THE MARTABE Au-Ag HIGH-SULFIDATION EPITHERMAL DEPOSITS, SUMATRA, INDONESIA: IMPLICATIONS FOR ORE GENESIS AND EXPLORATION

by

BRONTO SUTOPO

Submitted in fulfilment of the requirements
for the degree of Doctor of Philosophy

University of Tasmania
Australia
March 2013

STATEMENT AND AUTHORITY OF ACCESS

This thesis contains no material which has been accepted for a degree or diploma by the University or any other institution and, to the best of my knowledge and belief, no material previously published or written by another person except where due acknowledgement is made in the text of this thesis.

Authority of access:

This thesis is not to be made available for loan or copying for two years following the date of submission for examination (January 15, 2011). Following that time the thesis may be made available for loan and limited copying in accordance with the Copyright Act 1968.

Date:

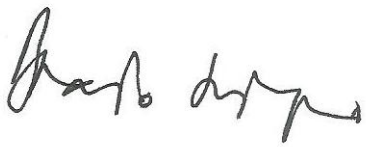

Bronto Sutopo

ABSTRACT

The Martabe gold district, situated on the north-west coast of Sumatra, Indonesia, consists of four high-sulfidation epithermal gold-silver deposits over an 8 km strike length: Purnama, Baskara, Kejora and Gerhana and one low-sulfidation epithermal gold-silver deposit, Pelangi. Resources have been estimated for the three principal known deposits, Purnama, Baskara and Pelangi. Resources (inferred, indicated and measured) are 91.2 Mt @ 1.5 ppm Au and 19 ppm Ag for Purnama, 36.6 Mt @ 1.0 ppm Au and 4 ppm Ag for Baskara, and 10.4 Mt @ 1.1 ppm Au for Pelangi. Reserves (proved and probable) are based on an optimized open-pit mine design which extends approximately 900 m north-south along strike; total Purnama reserves are identifying 35.7 Mt @ 1.9 ppm gold and 26 ppm Ag.

Martabe is located in the western Sunda Banda magmatic arc within and adjacent to a Late Tertiary porphyritic dacite and andesite dome and diatreme complex that was emplaced into a volcano-sedimentary sequence comprising interlayered sandstone, siltstone, carbonaceous mudstone and andesite lava flows. Martabe is located near a series of fault splays of the Sumatra Fault System and this structural framework has played an important role in the formation of the deposits.

At Martabe there are a wide variety of distinctive breccias within the dome and diatreme complex. The origins and processes of these breccias are varied and include phreatomagmatic, phreatic, tectonic and hydraulic brecciation. Recognition of stratified and unstratified breccias, base surge deposits and overlying airfall tuffs indicate that the initial setting was a maar volcanic field, containing multiple diatreme vents.

Intrusion of felsic magma into a fault-bounded block of brecciated carbonaceous mudstone (part of Sumatran Fault System) within an active hydrothermal system resulted in phreatomagmatic brecciation at Martabe. The presence of juvenile magmatic clasts with delicate wispy texture and cuspate margins, in situ rhyolite clasts associated with dacitic-andesitic dykes and base surge (stratified breccia) deposits are the key pieces of evidence for a phreatomagmatic origin.

The flow dome complex formed at ca. 3.8± 0.5 Ma (quartz-phyric dacite, U-Pb method) and 3.1±0.4 to 2.8± 0.3 Ma (hornblende-phyric andesite, U-Pb method), and extensive alteration closely followed emplacement of the domes at 3.30± 0.11 to 2.14± 0.10 Ma (alunite, K-Ar method). These periods of hydrothermal activity indicate the magmatic/hydrothermal system was active from 3.8 to 2.1 Ma and the main-stage alteration occurred within 0.5–0.8 Ma of dome emplacement.

All identified economic and sub-economic gold-silver mineralization of the district displays a zonal pattern of alteration typical of high-sulfidation epithermal systems, with the presence a low-sulfidation epithermal system at the periphery (i.e., Pelangi). In general, the alteration at Martabe consists of siliceous (quartz dominant), advanced argillic (alunitic and kaolinitic), argillic and propylitic alteration. The 'alunitic' alteration assemblage consists of quartz+alunite±dickite/kaolinite±pyrite; the 'kaolinitic' assemblage refers to quartz+kaolinite/dickite±alunite±pyrite; the argillic assemblage contains illite-smectite-pyrite±quartz; and the propylitic assemblage consists of chlorite+epidote+calcite ±illite/sericite±pyrite±quartz. Alteration is typically zoned from a core of brecciated, massive and vuggy quartz (siliceous alteration) that grades outwards through advanced argillic alteration (alunitic and kaolinitic) to argillic alteration that is surrounded by a peripheral zone of pervasive propylitic alteration. Economic mineralization is hosted within the siliceous and advanced argillic alteration zones. The alteration zones most likely occurred as multiple stages and formed contemporaneously with the Martabe dome magmatism.

The majority of epithermal Au-Ag mineralization in the district is characterized as high-sulfidation, based on the sulfide and sulfosalt mineral assemblage and advanced argillic alteration. Ore mineralization consists of enargite-luzonite+tetrahedrite-tennantite-pyrite in veins, vugs and as breccia matrix. Jarosite, hematite and goethite are the most common products of oxidation. Gold is present as micron-sized native gold grains associated with quartz, Fe-oxides, enargite-luzonite, tetrahedrite-tennantite and covellite-digenite.

Purnama consists of disseminated Au-Ag mineralization distributed sub-horizontally within and adjacent to the western perimeter of the diatreme with both strong lithological and structural control. A quartz matrix-supported breccia contains the majority of high-grade ore, although lower grade mineralized zones occur within pervasive advanced argillic-alunitic altered breccias and advanced argillic-kaolinitic altered andesite. At Baskara and Kejora, mineralization is sub-vertical and spatially associated with phreatic and phreatomagmatic breccia bodies emplaced along NE-striking faults. The best gold mineralization occurs at the contact between breccia bodies and the dacite-andesite dome. At Pelangi, gold- and silver-bearing, low-sulfidation, quartz veins and stockworks cross-cut the advanced argillic alteration. At Gerhana, the mineralization are with both lithology and structural controls and are likely similar to Purnama.

Results of a LA-ICP-MS study of trace-element mineral chemistry in pyrite and enargite indicate significant variability in trace-element compositions, particularly in Fe, Te, Bi, Sn, Se, Au, Pb, Mo, W and Ba. Three generations of pyrite are recognized. An early

stage of well-crystallized pyrite (stage-1) is enclosed by fine (submicron) overgrowths of second stage of poorly crystalline pyrite (stage-2). The stage-1 cores have relatively low trace element concentrations. Conversely, the stage-2 pyrites contain an abundant variety of trace elements with high concentrations. Stage-3 pyrite occurs as filling vugs or fractures and encompasses stage-1 and stage-2 pyrite. Stage-3 pyrite has a similar range of trace elements as stage 2 but at lower concentrations. In general, the most abundant trace elements in enargite are those that also form discrete sulfosalt, selenide and telluride accessory phases. Enargite in the Purnama and Gerhana deposits is enriched in Au, Se and Te.

The sequence of events that formed the Martabe diatreme/dome complex and associated alteration and mineralisation is interpreted to be:

(i) Down faulting of pre-Miocene sedimentary units.

(ii) Intrusion of felsic magma along existing structures. Interaction of meteoric water with magma initiated early hydrothermal convection (low-sulfidation fluid). Formation of argillic and propylitic alteration.

(iii) Felsic intrusions continued to move up along the existing faults and triggered phreatomagmatic and phreatic eruptions (diatreme formation).

(iv) Phreatomagmatic eruptions continued to excavate the conduit and widen the diatreme producing multiple crosscutting breccias.

(v) High temperature, extremely acid (high-sulfidation) fluids from condensation of magmatic volatiles caused advanced argillic alteration. No precious-metal mineralization accompanied this alteration.

(vi) The hydrothermal system returned to convection of meteoric water (low-sulfidation fluid). Formation of Au-Ag-bearing, quartz-chalcedony veins.

(vii) Intrusion of dacite and hornblende andesite into the diatreme creating the dome complex. Triggering of phreatomagmatic and phreatic eruptions.

(viii) Domes interacted with meteoric water causing hydrothermal convection of a low-sulfidation fluid with overpressure leading to hydrothermal brecciation.

(ix) Introduction of magmatic, metal-rich, high-sulfidation fluid depositing Cu-Au mineralization (disseminated and fracture-controlled pyrite-enargite-luzonite-tennantite-tetrahedrite).

(x) Late-stage phreatic brecciation.

(xi) Oxidation, erosion and weathering.

The Martabe Au-Ag deposits show a complex interplay of intrusive events, phreatomagmatic, phreatic, and hydrothermal brecciation and differing stages of hydrothermal (low- and high-sulfidation) fluid introduction. The superposition of both high- and low-sulfidation mineralizing events increases the precious metal content of the mineralization, and adds to the overall exploration potential of the district.

ACKNOWLEDMENTS

This thesis would not have been possible without the support, aid and guidance, and fruitful collaboration with, numerous people. I take this is opportunity to express my gratitude towards them.

I sincerely thank the management of Newmont Mining Corporation for providing financial support. In particular I would like to thank Brian Levet for encouraging me to undertake a PhD, prompting and releasing me from responsibilities in Indonesia. Brian, you have been far more than a supervisor, you are great friend and mentor. My ex-supervisor Martin Jones, thanks for your friendship during our time in Martabe. Stephens Enders and Jeff Huspeni I thank you for your support.

My deepest appreciation goes to my supervisors, Prof. J. Bruce Gemmell and Prof. David R. Cooke for their endless support, guidance, patience, teaching, hard work and enthusiasm throughout this project. Without them this thesis would not exist.
Bruce, thanks for your involvement in my research. I have been lucky to work with you. You were always available for me to discuss many things, no matter what the subject. I have learned a lot from you. Next, Dave, your guidance was essential to the clarity of this thesis. They have supported me while I was writing, across many islands and their efforts are greatly appreciated. Bruce and Dave, you are great supervisors.

I would like to thank all people at CODES for their generous contribution to my research. Professionally and personally, I would like to thank you for providing an incredible working atmosphere during my stay. Thanks for being great and friendly colleagues! Special thanks go to Masoe and Taka for discussing the study. CODES has been a fantastic place to work and study, and many people have provided tremendous support throughout my time here. Many thanks are due to June Pongratz, Di Steffens, Christine Higgins, Nilar Hlaing, Simon Stevens and Peter Cornish. Special thanks go to June Pongratz who assisted with the final production of my thesis.

Many thanks to all the personnel at the Martabe site who always welcomed me, worked with me for years, assisted in my mapping, logging and providing a warm friendship. To all of you at the Martabe project, thanks for the friendship and teamwork.

Particular thanks go to the many people from Newmont-Jakarta office, in particular mbak Tuti and mbak Virna; and Newmont-Perth office staffs, especially Sandra Brown and Jossiane who always made sure my family and I were fine in Hobart.

Thanks to my friends back in MGEI (Masyarakat Geologi Ekonomi Indonesia) for all their encouragement over the years. It was a challenging time to run and arrange many geological events in Indonesia, including seminars and workshops, while I was in Hobart. Thanks MGEIers, you make me proud of you.

I am also deeply indebted to my parents, who have always supported and encouraged me to pursue higher education. You are indeed my true teachers. To my late dad, this thesis I dedicate to you. To my parent in law, my brothers, sisters, cousins, thanks for your prayers.

Finally, a very special appreciation is due to my wife, Dewi Nursanti, not only for your constant encouragement and unreserved support in every circumstance but also for your love and sacrifice, without which completion of this thesis would not have been possible. Your patience and understanding has helped me tremendously throughout the many long years of our marriage. May God bless you in all your endeavours. I am also greatly indebted to my dear kids, the B-R-O (Balqis, Rahil and Omar) for always giving me their love. Sometimes when I accompany you to the school, I see your faces spurring me to spending more time with you. Dewi and BRO, many times we have had the wonderful experience to truly feel as a family. That means so very much to me. Thanks to all of you.

Hobart, 15 January 2011

TABLE OF CONTENTS

CHAPTER 5 : WHOLE-ROCK GEOCHEMISTRY

CHAPTER 6 : ALTERATION CHARACTERISTICS AND ZONATION

CHAPTER 7 : MINERALIZATION: GEOCHEMICAL SIGNATURE, ORE MINERALOGY AND METAL ZONATION

CHAPTER 8 : THE TRACE-ELEMENT COMPOSITION OF PYRITE AND ENARGITE

CHAPTER 9 : STABLE ISOTOPES GEOCHEMISTRY

CHAPTER 10 : EVOLUTION OF THE MARTABE VOLCANIC AND DOME COMPLEX AND MINERALISING HYDROTHERMAL SYSTEM

LIST OF FIGURES

CHAPTER 1: INTRODUCTION

CHAPTER 2: REGIONAL GEOLOGY AND SYNOPSIS REVIEW OF METALLOGENY OF SUMATRA

.

CHAPTER 3: DISTRICT GEOLOGY

CHAPTER 4 : GEOCHRONOLOGY

CHAPTER 5 : WHOLE-ROCK GEOCHEMISTRY

CHAPTER 6 : ALTERATION CHARACTERISTICS AND ZONATION

CHAPTER 7 : MINERALIZATION: GEOCHEMICAL SIGNATURE, ORE MINERALOGY AND METAL ZONATION

CHAPTER 8 : THE TRACE ELEMENT COMPOSITION OF PYRITE AND ENARGITE

CHAPTER 9 : STABLE ISOTOPES GEOCHEMISTRY

CHAPTER 10 : EVOLUTION OF THE MARTABE VOLCANIC AND DOME COMPLEX AND MINERALISING HYDROTHERMAL SYSTEM

LIST OF TABLES

CHAPTER 1: INTRODUCTION

CHAPTER 2: REGIONAL GEOLOGY AND SYNOPSIS REVIEW OF THE METALLOGENY OF SUMATRA

CHAPTER 3 : DISTRICT GEOLOGY

CHAPTER 4 : GEOCHRONOLOGY

CHAPTER 6 : ALTERATION CHARACTERISTICS AND ZONATION

CHAPTER 7 : MINERALIZATION: GEOCHEMICAL SIGNATURE, ORE MINERALOGY AND METAL ZONATION

CHAPTER 8 : THE TRACE-ELEMENT COMPOSITION OF PYRITE AND ENARGITE

CHAPTER 10 : EVOLUTION OF THE MARTABE VOLCANIC AND DOME COMPLEX AND MINERALISING HYDROTHERMAL SYSTEM

CHAPTER 1

INTRODUCTION

1.1 Preamble

Epithermal ore deposits form at shallow depth; this conclusion was initially based on geologic constructions, ore mineralogy and related textures (Lindgren, 1922; 1933). It has subsequently been refined with fluid inclusion data to indicate that epithermal ores form over the temperature range of <150°C to ~300°C, from the surface to as deep as 1 to 2 km (Berger and Eimon, 1983; White and Hedenquist, 1995; Cooke and Simmons, 2000). Such hydrothermal systems commonly develop in association with calc-alkaline to alkaline magmatism, in volcanic arcs at convergent plate margins, as well as in intra-arc, back-arc, and post-collisional rift settings (Buchanan, 1981; Heald et al., 1987; Sillitoe, 1993; White et al., 1995; White and Hedenquist, 1995; Hedenquist et al., 2000; Cooke and Simmons, 2000; Simmons et al., 2005). Precious metal Au-Ag mineralization develops in zones of high paleo-permeability, hosted within sequences of coeval volcanic and underlying basement rocks. Veins with steep dips are common and these tend to host highest grade ores. Precious metal mineralization also occurs in breccias, coarse clastic rocks, and intensely leached rocks; such disseminated ore is much lower in grade, but greater in total tonnage and may be amenable to bulk mining methods. Deposits and projects, comprising one or more orebodies, cover areas from <10 to ~200 km^2 (Simmons et al., 2005).

Epithermal deposits have been classified on the basis of alteration and gangue mineral assemblages, metal content, sulfide content and sulfide mineral assemblages, and each classification scheme has its merits (Hayba et al., 1985; Heald et al., 1987; White and Hedenquist, 1990, 1995; Hedenquist et al., 2000; Cooke and Simmons, 2000; Simmons et al., 2005). Initially two principal types of epithermal mineral in which gold is the dominant economic metal: low-sulfidation and high-sulfidation are recognized. The two deposit styles are formed from fluids of contrasting chemistry (White and Hedenquist, 1995). More recently, Sillitoe and Hedenquist (2003) and Hedenquist and Eunnadi (2005) argued that epithermal Au and Ag deposits of both vein and bulk-tonnage styles may be broadly grouped into high-sulfidation, intermediate-sulfidation and low-sulfidation types based on the sulfidation states of their hypogene sulfide assemblages.

In the low-sulfidation environment (White and Hedenquist, 1990), the mineralizing fluids are similar to those typically tapped by drilling into active geothermal systems

(Henley and Ellis, 1983). Low-sulfidation state sulfide minerals precipitate from reduced, near-neutral pH fluid (Barton and Skinner, 1979). The gold mineralisation related to near-neutral pH and relatively reduced fluids is associated with low-sulfidation-state minerals such as pyrite and pyrrhotite. This type of epithermal mineralization is called "low-sulfidation" (Hedenquist, 1987) or "adularia-sericite" (Heald et al., 1987). Epithermal deposits associated with quartz±calcite±adularia±illite (low-sulfidation) contain Au-Ag, Ag-Au, or Ag-Pb-Zn ores (Hedenquist et al., 2000; Cooke and Simmons, 2000; Simmons et al., 2005). Electrum, acanthite, Ag sulfosalts, Ag selenides, and Au-Ag tellurides are the main Au- and Ag-bearing minerals, with generally minor sphalerite, galena, and chalcopyrite; in some deposits base metals dominate the metal assemblage. Quartz is the principal gangue mineral accompanied by variable amounts of chalcedony, adularia, illite, pyrite, calcite, and/or rhodochrosite. Rhodochrocite is in more Ag- and base metal-rich deposits. Distinctively banded crustiform-colloform-cockade textures, and lattice textures comprising aggregates of platy calcite and their quartz pseudomorphs, are common. Hydrothermal alteration is zoned and comprises deep regional propylitic alteration, which gives way upward to increasing amounts of clay, carbonate, and zeolite minerals; whereas quartz, adularia, illite, and pyrite form proximal alteration zones enveloping orebodies. Ore-grade mineralization commonly terminates upward, and where there has been minimal erosion, it can be concealed beneath regionally extensive blankets of clay-carbonate-pyrite or kaolinite-alunite-opal ± pyrite alteration. Fluid inclusion data indicate salinities are commonly <5 wt. % NaCl equiv for Au-Ag deposits and <10 to >20 wt. % NaCl equiv for Ag-Pb-Zn deposits. Stable isotope data indicate that hydrothermal solutions were composed mostly of deeply circulated meteoric water, with a nil to small and variable component of magmatic water (Hedenquist et al., 2000; Cooke and Simmons, 2000; Simmons et al., 2005). Minor veins of this type of mineralization also occur in the Martabe project.

In contrast, the high-sulfidation-state minerals (Barton and Skinner, 1979) associated with mineralization include enargite, tennantite-tetrahedrite, and covellite, hence the term "high-sulfidation" (Hedenquist, 1987) for this type of deposit, also called the "acid-sulfate" type (Heald et al., 1987). The acid fluids responsible for leaching (Bethke, 1984) here and where are relatively oxidized. The style of alteration is advanced argillic, though the residual silica quartz is not included in this terminology (Meyer and Hemley, 1967). Epithermal deposits associated with quartz+alunite±pyrophyllite±dickite±kaolinite assemblages contain Au ± Ag ± Cu ores. Native gold and electrum are the main ore-bearing minerals, with variable amounts of pyrite, Cu-bearing sulfides and sulfosalts such as

enargite, luzonite, covellite, tetrahedrite, and tennantite, plus sphalerite and telluride minerals; enargite dominates the Cu sulfides and indicates a high-sulfidation state. Quartz (both massive and vuggy) and alunite are the main gangue minerals with kandite mineral group (dickite and/or kaolinite) and/or pyrophyllite. Concentric patterns of hydrothermal alteration envelop the zone of vuggy and massive quartz alteration, which hosts ore. Outward, these comprise zones of quartz and alunite, dickite, kaolinite or pyrophyllite, and illite or smectite alteration, surrounded by regional propylitic alteration. Zones of illite or pyrophyllite alteration occur in the roots beneath some deposits. Fluid inclusion data indicate that salinities are typically <5 to 10 wt. % NaCl equiv, but may be as high as >30 wt. % NaCl equiv. Stable isotope data indicate that the altering fluids are composed mostly of magmatic fluids with a minor to moderate component of meteoric water (Hedenquist et al., 2000; Cooke and Simmons, 2000; Simmons et al., 2005).

Critical genetic factors include: (1) at several-kilometer depth, the development of oxidized and acidic versus reduced and near-neutral pH fluids, controlled by the proportions of magmatic and meteoric components in solution, and the amount of subsequent water-rock interaction during ascent to the epithermal environment; (2) at epithermal depths, the development of boiling and/or mixing conditions which create sharp physical and chemical gradients conducive to precious and base metal precipitation; and (3) at shallow level, the position of the water table, which controls the hydrostatic pressure-temperature gradients at depth where epithermal mineralization forms. Epithermal mineralization can occur in large areas, with orebodies that range in shape, size, and grade and lie easily concealed beneath blankets of clay alteration or unaltered volcanic deposits. Efficient exploration requires integration of all geological, geochemical, and geophysical data, from regional to deposit scale. Vein mineralogy and texture, patterns of hydrothermal alteration, patterns of geochemical dispersion, and three-dimensional interpretation of related geophysical signatures are important guides (Buchanan, 1981; Heald et al., 1987; Sillitoe, 1993; White et al., 1995; White and Hedenquist, 1990, 1995; Hedenquist et al., 2000; Cooke and Simmons, 2000; Simmons et al., 2005).

High-sulfidation mineralization is increasingly being recognized throughout the world (Sillitoe, 1989; White and Hedenquist, 1990, 1995), with some deposits containing in excess of 100 tons of Au associated with Cu sulfosalts and sulfides (e.g., Goldfield, Nevada; Lepanto, Phillipines; Chinkuashih, Taiwan; El Indio; Chile; Pueblo Viejo; Dominican Republic; Yanacocha, Peru; Pierina, Peru and Alto Chicama, Peru). Ransome (1907) first proposed a deep hypogene origin for the acid fluids responsible for alteration at Goldfield. Steven and Ratte (1960) conducted detailed studies on similar alteration related

to the Summitville Au deposit in San Juan Mountains, Colorado, and recognizing the pattern of alteration characteristic of this style of mineralisation. Recent studies have focused on mineralogic and stable isotopic studies in an attempt to clarify the environment and evolution of the hydrothermal system in high-sulfidation environment (Stoffregen, 1987; Hedenquist et al., 1988; Rye et al.,1982; Arribas, 1995).

The high-sulfidation style of mineralization is typically hosted by calc-alkaline volcanic rocks (and associated sediments) which are strongly leached, typically leaving a vuggy silica residue, subsequently recrystallised to quartz. The vuggy quartz body has an abrupt contact outward with a zone of advanced argillic minerals assemblages (typically 1-10 m wide, though it can be in excess of 100 m in some deposits). This zone can include alunite, kaolinite and/or dickite, pyrophyllite and/or diaspore+zunyite, pyrite, barite; progressing outward through illite or smectite to extensive propylitic alteration and eventually fresh rock (Steven and Ratte, 1960). Sulfide and sulfosalt mineralization generally includes enargite/luzonite), pyrite, tetrahedrite, and/or tennantite, covellite with Au commonly closely intergrowth with or included in the sulfides and sulfosalts, or sometimes in crosscutting veinlets. Quartz which fills open space, although common, is mostly late stage (in contrast to the residual silica of leached host rock, which subsequently recrystalizes to fine-grained quartz). The late quartz deposition results in portions of deposit appearing massive. The sulfides and sulfosalt of the central zone are commonly oxidized to a variable extent as the result of late circulation of the surface water through the highly fractured orebody, causing some Au to be remobilized locally and concentrated with goethite (Urashima et al., 1981; Stoffregen, 1987; Sillitoe et al., 1990).

The form of the high-sulfidation deposits is variable, from strong fracture control resulting in dominant veins or lodes (e.g., Lepanto, Phillipines; El Indio, Chile) to lithologic control resulting in the typical mushroom shape of the Nansatsu deposits. Intermediate situations also occur, with permeability in some case enhanced by vertical zone of hydraulic fracturing, such as at Summitville, Lepanto, Nalesbotan and Nansatsu deposits. This style of alteration and mineralisation is most commonly preserved in Tertiary rocks, though it is recognized to have formed as far back as the Early Proterozoic in central Sweden (Enasen). The old examples are commonly highly metamorphosed and may be strongly sheared, resulting in a stratiform appearance. Some deposits have similar alteration but are distinct in having an Ag-Pb metal association.

So far, Martabe is the largest, high-sulfidation epithermal, gold-silver deposit located in the Sunda metallogeny belt, one of the favorable belts for mineral exploration in

Indonesia. Thus, this study was initiated to provide geologic information on the deposit and exploration criteria on the epithermal gold-silver deposits of the Martabe district.

1.2 Objectives of this study

The main aims and objectives of this PhD project are to examine the surface geology, drill core and existing information of the Martabe district in order to:

1. Characterise the geologic setting of the high-sulfidation mineralisation (Purnama, Baskara, Kejora and Gerhana deposits)
2. Describe the ore and gangue mineralogy and metal zonation
3. Document the alteration mineralogy, assemblages, paragenesis and geochemistry
4. Determine the characteristics of the mineralising fluids using stable isotopes.
5. Develop a genetic model for the mineralisation and useful criteria for exploration in the Martabe district.

1.3 Methodology

To accomplish these aims the following investigations were undertaken at Martabe:

A. Geology

1. Characterise the overall geologic setting (lithology, structure) for the district
2. Determine the breccia facies (structural, volcanic, phreatic, phreatomagmatic)
3. Date various igneous units using U-Pb ICP-MS on zircons.

B. Mineralogy and metal zonation

1. Identify ore and gangue mineralogy using hand sample identification, transmitted and reflected light microscopy, and SWIR data
2. Investigate ore and gangue mineralogical and textural zonation
3. Characterise the major and trace element geochemical signature and zonation of the mineralisation using Martabe assay and geochemical data, supplemented by electron microprobe and LA-ICPMS data.

C. Alteration mineralogy and geochemistry

1. Detailed identification of alteration mineralogy and assemblages using hand sample identification, transmitted light microscopy and SWIR data
2. Characterise the major and trace element whole-rock geochemical signature of the alteration using XRF and ICPMS data
3. Date alteration minerals (alunite) using Ar/Ar or K/Ar methods.

D. Implication for ore genesis and exploration

1. Develop a geologic and genetic model for mineralisation in the Martabe district
2. Propose exploration vectors, based on the geological, mineralogical and geochemical features, for use in the Martabe district.

1.4 Organization of the thesis

The thesis is organized into a total of 11 chapters. Chapter 1 outlines the study background, location of the study area and major objectives of the research project. Chapter 2 provides a background to the geology and magmatism of Sumatra, in particularly Sumatra metallogeny. The regional setting of host rocks of the Martabe is also given. The geological setting includes volcanic facies, and facies architecture is documented in Chapter 3. This chapter also describes the breccia system at Martabe. A geochronology study is given in Chapter 4. Chapter 5 addresses the whole rock geochemistry, which provides an insight into magmatic characteristic of Martabe district. Alteration characteristics at Martabe, including hydrothermal breccia stages, geochemistry of altered rocks and mass transfer are discussed in Chapter 6. Ore mineralogy, its geochemistry and metal zonation are presented in Chapter 7. Chapter 8 outlines the trace element geochemistry of pyrite and enargite. Chapter 9 documents stable isotope geochemistry. Chapter 10 addresses evolution of the Martabe volcanic dome/diatreme complex and the mineralizing hydrothermal system, including implications for exploration. Chapter 11 contains the conclusions and recommendations.

1.5 Previous studies at Martabe

Prior to this study, very little comprehensive research had been completed on the Martabe deposits. Only several papers had been published on the region (Levet et al., 2003; Sutopo et al., 2003; Harlan et al., 2005; Hertrijana et al., 2005; Sutopo et al., 2006); other studies were confidential internal company reports. None of the previous work contained any significant information on the regional geology. Details of the volcanological setting and igneous chemistry of the project were largely un-documented. The structural framework of the project had previously been described by Davies (2003).

1.6 Location, access and physiography

The Martabe gold-silver project is located in the province of North Sumatra, northwestern side of the island of Sumatra, approximately 3 km north of the village of Batangtoru and 40 km south of the port of Sibolga. The project lies about 200 km south of the provincial capital of Medan; regular daily flights link Medan from/to Jakarta and Singapore (Figure 1.1). Local commercial air services are available between Medan to Lumban Tobing airport in Sibolga or to Aek Godang airport in Padangsidempuan; and then followed by one or two hours by graded, locally rugged road to the Martabe camp.

The Martabe project has a wet, tropical environment that is rich in terrestrial and aquatic biodiversity. The area has tropical climate with temperatures consistent throughout the year at around 20-32°C with an average annual rainfall of between 4 to 5 m. The topography of the Martabe project is steep and extremely rough, with elevations of between 200-850 m above sea level. The Martabe project area is drained by the Aek Pahu Tombak and Aek Pahu Hutamosu sub-watersheds, which eventually flow into the Aek Garoga before discharging into the Indian Ocean.

The largest river in the vicinity of the project is the Batang Toru River, which originates close to Lake Toba and flows just south and east of the project. In Martabe, surface water quality is generally good in upper stream reaches, with near-neutral to slightly acidic pH (lowest pH levels observed in mineralised zones), low concentrations of trace metals, and variable levels of suspended solids depending on flow conditions. Bacteria levels are typically high in the lower reaches of the watershed due to widespread anthropogenic impacts. Vegetation consists of primary tropical rainforest, some of which has been planted and logged on a selective basis. Logging and cultivation have degraded zoned lowland tropical rainforest that existed over the area (Levet et al., 2003; Sutopo et al., 2003).

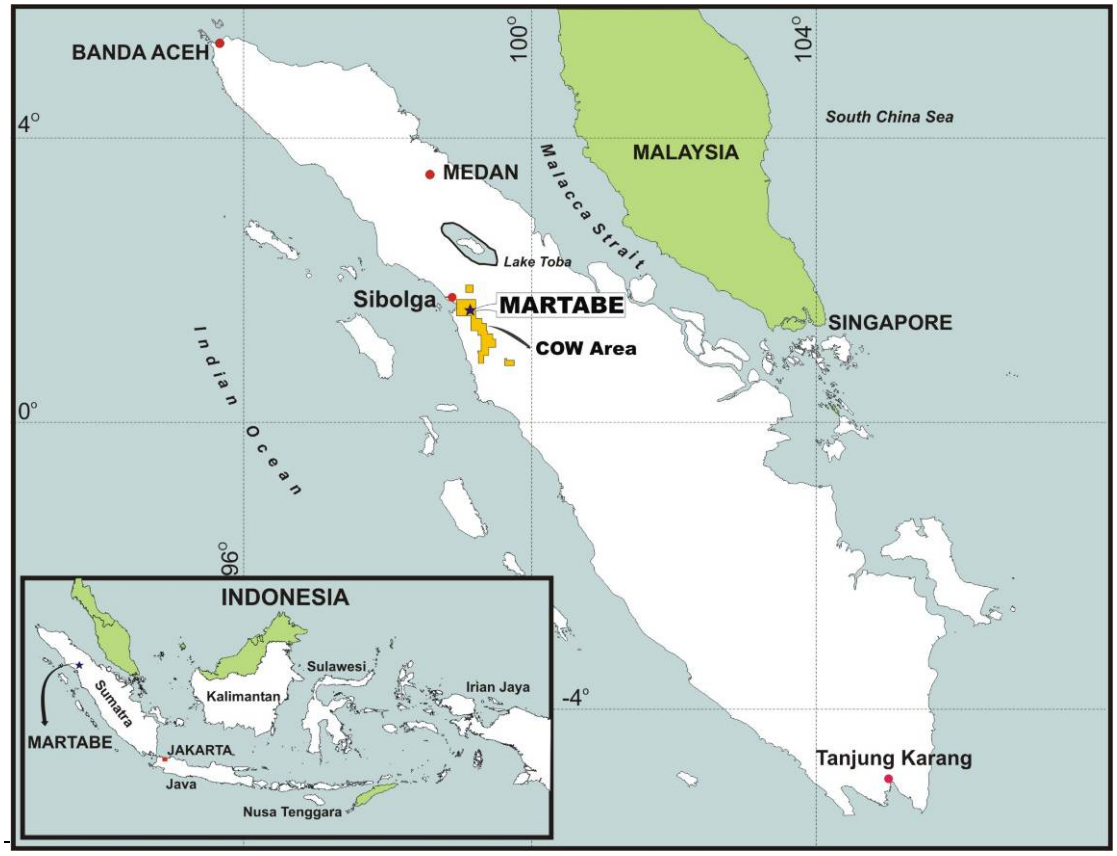

Figure 1.1. Location of the Martabe project, North Sumatra province, Indonesia.

The Martabe project area is a seismically active region which has experienced very large earthquakes in historical times including a magnitude 8.75 Richter Scale in 1833; and the December 2004 magnitude 9.3 Richter Scale that occurred in Aceh that resulted in a catastrophic tsunami.

Local inhabitants of the Batangtoru town area are predominantly Bataknese and Javanese immigrants. The population of Batang Toru has increased by almost 13,000 people over the past 22 years, from approximately 33,700 residents in 1980 to 45,000 today. It is estimated that 9,000 to 12,000 people live in villages situated in the immediate or surrounding areas of the Martabe project (Figure 1.2). Socially, the Batang Toru area is a complex community comprised of differing ethnic identities, claims to authority, power and natural resources, and livelihoods. Like much of Sumatra, the Batang Toru area is comprised in part by substantial plantations of rubber (Figure 1.3) and oil palm owned by the government, private businesses, and individuals.

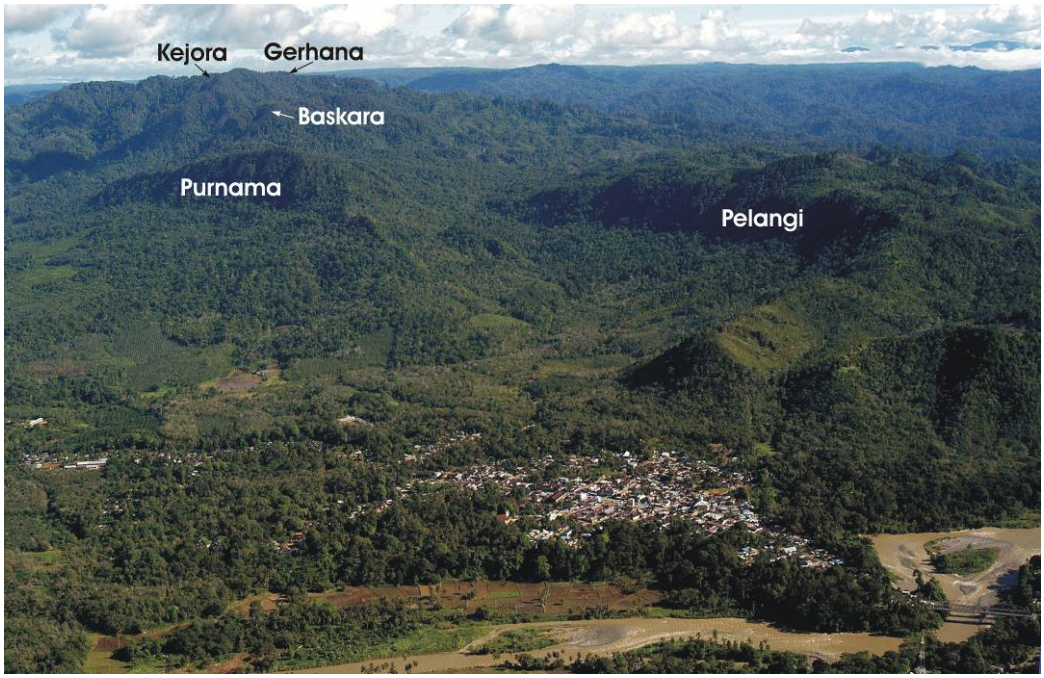

Figure 1.2. Batangtoru village in the foreground and Martabe district deposits in the background.

Figure 1.3. Martabe Camp with rubber trees. Photo taken in 2005.

1.7 Ownership

In October 1993, PT Danau Toba Mining (Normandy Anglo Asian Ltd, a joint venture between Normandy Mining, Anglo American and Austindo Nusantara Jaya) made an application for a 6th generation Contract of Work (CoW) in the Sibolga Project of North

Sumatra. The project was eventually granted by the Indonesian Government in April 1997. In July 2001, Anglo American sold their interest in the joint venture to Normandy. Following the merger between Newmont Mining Corporation and Normandy Mining Corporation, Newmont then acquired the project in 2002 and the operating entity is known as "PT Newmont Horas Nauli". At that time, Newmont held 95 percent interest and Austindo the remaining 5 percent. In September 2006, Agincourt Resources Limited (ARL) purchased the Martabe project from Newmont and then "PT Agincourt Resources" become the operator of the project. In April 2007, through a corporate takeover, Oxiana Limited acquired ARL and the Martabe project. The ownership and operating rights to Martabe were then held 95 percent by Oxiana and 5 percent by the Indonesian company, PT Artha Nugraha Agung. Following the merger between Oxiana and Zinifex, PT Agincourt Resources was owned by a new company, OZ Minerals. On April 2009, China Sci-Tech Holdings Limited, through its arm G-Resources, acquired the project from OZ Minerals. In 2011, the project was still operated under the entity "PT Agincourt Resources".

In April 1997 the CoW originally covered an area of 659,600 ha. The CoW was formed to explore for porphyry Cu-Au and epithermal gold mineralization. Progressive relinquishments which are required by the regulation mandate and continuous exploration have reduced the CoW area to 1639 km^2 or 25 percent of the original area. The Martabe project area itself occupies approximately 29 km^2.

1.8 Exploration history

Sumatra has long been known as a source of gold, the name of the island being derived from the Sanskrit word "Svarnadvipa" meaning 'Golden Island', dating from the importance of gold deposits to the rulers of the Hindu kingdoms that flourished in Sumatra from the 7^{th} until the 11^{th} century. The estimated total production of precious metals from Sumatra to 1994 was 91 tonnes of Au and 937 tonnes of Ag (van Leeuwen, 1994). The North Sumatra province is distinguished by the small size and relatively small number of known gold occurrences, except for the West Sumatra provinces. This situation combined with relatively presence of the young Toba Tuff (74,000 years ago), which covers most of northern Sumatra, has resulted in the discovery of few gold occurrences. Martabe was discovered by regional exploration in an area not known for high-sulfidation systems and when the copper gold exploration efforts in Indonesia decreased. It is remarkable that the Martabe project was only discovered in early 1997, just 2 km from the Trans Sumatra

Highway near the town of Batangtoru. The name Martabe is a Batak acronym from the saying "**Mar**sipature Hu**ta**na **Be"** meaning, "to develop our region by our people". The acronym was introduced by late North Sumatra Governor Radja Inal Siregar in 1989 to invite the successful Bataknese to develop and build their region.

In the early 1980s, the British Geological Survey (BGS) completed a stream sediment survey over a large portion of Sumatra including the Sibolga CoW and the Martabe area, but did not assay for gold. Regional geochemical drainage sampling was carried out intermittently by PT Danau Toba Mining within the CoW between 1994 and 1996. Gold mineralisation was discovered in 1997 using the company's in-house BLEG stream sediment sampling techniques. A 14 ppb Au BLEG anomaly was generated in the lower Aek Pahu drainage at Martabe (Figure 1.4). This BLEG anomaly was thought to be sourced from shearing and chalcedony veining in volcanic rocks. Subsequent BLEG assay samples of 157 ppb Au and 1,206 ppb Ag supported the early sampling and follow-up float samples assayed up to 20.3 ppm Au and 76 ppm Ag. Subsequent tape and compass geological mapping, ridge-spur soil and rock sampling as well as ground and airborne geophysical methods identified numerous prospects (Levet et al., 2003; Sutopo et al., 2003).

From 1998 to present, extensive exploration and definition drilling programs have been conducted on the project and confirmed the presence of gold, silver and copper hydrothermal mineralisation, within a sequence of lavas and volcanic and hydrothermal breccias. Five mineralized deposits, Purnama, Baskara, Pelangi, Kejora, and Gerhana, have been identified in north-trending corridors of about 7 km x 3 km. In recent reports the names of these deposits have been changed in accordance with the current owner (PT AR) or local usage to Pit 1, Ramba Joring, Barani, Tor Uluala and Uluala Hulu, respectively. In this thesis, the old names are used for consistency of when the data was collected.

The Martabe deposits are associated with silicified ridges or hills, covered in fairly dense vegetation. Some of the hills are extremely steep, and access is difficult. Drilling was carried out by drill rigs lowered into position by helicopter, or by man-portable rigs. The bulk of the work undertaken to date has focused on the Purnama deposit, with 257 diamond drill holes completed on approximately a 50 m spaced grid, with some infill drilling at a 25 m x 25 m spacing. Resources have been defined at Purnama, Baskara and Pelangi (Table 1.1) and open pit reserves have been defined at Purnama (Table 1.2).

A definitive feasibility study ("DFS") was completed in November 2007 based on open pit mining and carbon in leach ("CIL") processing of the Purnama ore. The DFS is based on mining and processing approximately 4.5 Mtpa of ore at an average grade of 1.9 ppm Au, producing approximately 200,000 oz of Au per annum together with 2 Moz of

Ag. The stripping ratio is low averaging 0.66:1. Metallurgical testing has indicated recoveries of 70–80% for gold and 60–80% for silver. The current mine plan has a life of nine years, however, there are good prospects for further extension from both the Purnama deposit at depth and the adjacent Baskara and Pelangi deposits and other prospects in the area (Behre Dolbear Australia, 2009).

Figure 1.4. The meandering Batangtoru River cutting across flat Quaternary alluvium. Photo is taken from the top of Purnama.

1.9 Resources/Reserves

The Martabe resource estimate, as of June 2008, is shown in Table 1.1. Resources have been estimated for the three principal known deposits namely, Purnama, Baskara and Pelangi, by independent specialist RSG Global Limited ("RSG Global"), now part of Coffey Mining fly Limited ("Coffey Mining"). No formal resource estimate of the other known prospects has been carried out to date. To date, reserves have been estimated only for Purnama (Figure 1.5), based on an optimised open-pit mine design which extends approximately 900 m north-south along strike; the Purnama reserves are shown in Table 1.2.

Table 1.1. Summary of Martabe resources per June 2008 (www.g-resources.com).

Deposit	Category	Tonnage (M Tonnes)	Gold Grade (ppm)	Silver Grade (ppm)	Contained Gold (M Ozs)	Contained Silver (M Ozs)
Purnama (Pit 1)	Measured	3.8	2.9	46	0.354	5.568
	Indicated	47.7	1.7	22	2.604	33.513
	Inferred	39.7	1.1	13	1.388	17.201
	Subtotal	91.2	1.5	19	4.345	56.282
Baskara (Ramba Joring)	Inferred	36.6	1.0	4	1.191	5.207
	Subtotal	36.6	1.0	4	1.191	5.207
Pelangi (Barani)	Inferred	10.4	1.1	-	0.368	-
	Subtotal	10.4	1.1	-	0.368	-
Total	Measured	3.8	2.9	46	0.354	5.568
	Indicated	47.7	1.7	22	2.604	33.513
	Inferred	86.6	1.1	8	2.947	22.408
	Subtotal	138.1	1.3	14	5.905	61.489

Note: cut off 0.5 ppm Au; Ag grade not determined for Pelangi and therefore omitted from totals; Pelangi Ag grade estimated at 1-3 ppm Ag but silver totals and grade calculated assuming no contribution from Pelangi.

Table 1.2. Summary of Martabe open pit reserves per June 2008 (www.g-resources.com).

Deposit	Category	Tonnage (M Tonnes)	Gold Grade (ppm)	Silver Grade (ppm)	Contained Gold (M Ozs)	Contained Silver (M Ozs)
Purnama (Pit 1)	Proved	3.9	2.7	42	0.336	5.288
	Probable	31.8	1.8	24	1.883	24.419
	Total	35.7	1.9	26	2.219	29.707

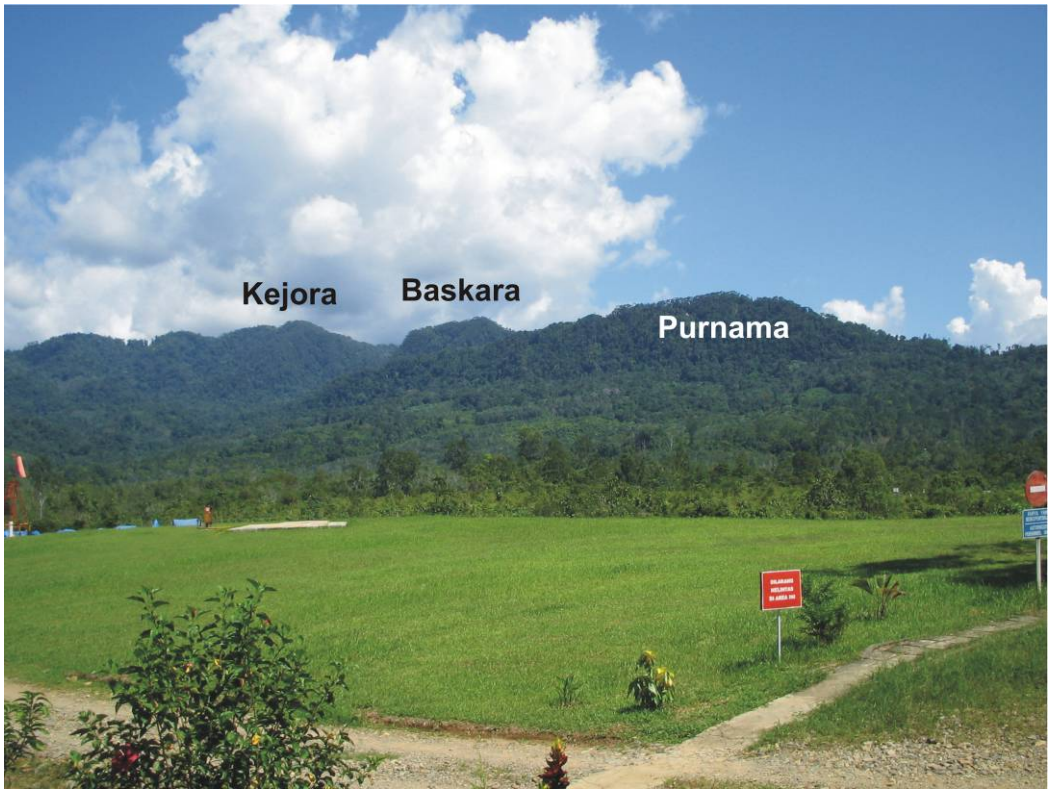

Figure 1.5. Purnama in the foreground and Baskara and Kejora deposits in the background.

CHAPTER 2

REGIONAL GEOLOGY AND SYNOPSIS REVIEW OF THE METALLOGENY OF SUMATRA

2.1 Introduction

Sumatra was explored by geologists working for mining and petroleum companies before World War II, but for commercial reasons most of the reports remained confidential and unpublished. However, some of the results were then made available to van Bemmelen (1949, 1970) during the preparation of his great synthesis of 'The Geology of Indonesia'. In 1970-80's, British Geological Survey (BGS) in collaboration with the Geological Survey of Indonesia (GSI) commenced mapping and reconnaissance geochemical surveys of northern Sumatra (Northern Sumatra Project, NSP). The structural, stratigraphy, geochemical and tectonic results of the of NSP have been presented in a series of papers (Page et al., 1978, 1979; Cameron et al., 1980; Rock et al., 1982; Aldiss and Ghazali, 1984; Aspden et al., 1982) and unpublished reports. Warren Hamilton prepared a series of maps and a memoir reviewing the geology of the Indonesia region in plate-tectonic terms (Hamilton, 1977, 1979). Recently, the tectonic setting of the South East Asia covered Sumatra Island has been presented by Metcalfe (1996, 2000, 2006) and Hall (1998, 2002). Their tectonic maps show present views of the tectonic setting of Sumatra. The geology of Sumatra has been also extensively reviewed by Barber et al. (2005). The Indonesian Petroleum Association (IPA) and the Indonesian Association of Geologist (IAGI) through their proceedings, provide an additional invaluable source of information on the geology of Indonesia, including Sumatra and north Sumatra in particular. The following discussion is based largely on these workers.

A general review of regional geology of Sumatra and the synoptically review of the Sumatera metallogeny is described here. This chapter will then detail the tectonics setting and magmatic activity of Sumatra in relation to the formation of Martabe epithermal deposits.

2.2 Physiography of Sumatra

Sumatra has an area of about 473,606 km^2, stretching across the equator for 1,760 km length from Banda Aceh in the north to Tanjungkarang in the south. Its width is about

100-200 km in the northern part and is up to 400 km in the southern part (Figure 2.1). The island's backbone is formed by the Barisan Mountains/Range which extends the whole length of the island; and divides the island into the west and the east coast. The Barisan Mountains is mainly a narrow belt, parallel to and generally only a few tens of kilometers from the west coast (Pulunggono, 2000). The main peaks, which are mainly Quaternary volcanoes, commonly rise about 2,000 m above sea level, culminating in Mt. Kerinci 3,805 m in the central Sumatra. Towards the Indian Ocean the west slope is generally short, and has rivers that drain towards the west-southwest and is mountainous. The eastern slope is broad, hilly tracts and flat areas of Tertiary formations and alluvium. The rivers in the east follow long meandering patterns across broad coastal plains and swamps to the Malacca Straits and continue to the southeast across the narrow Sunda Strait and the Java Sea.

2.3 Tectonic evolution of Sumatra

Sumatra is located on the southwestern edge of the Sundaland plate northeast of the Sunda Trench (Figures 2.1 and 2.2). The island has a classic tectonic setting of a subduction arc including trench, accretionary prism, outer-arc ridge, fore arc and volcanic chain with active andesitic volcanism (Karig et al., 1979). Sumatra has a very long tectonic history which extends back to at least 250 Ma (Katili, 1973; Hamilton, 1979; McCourt et al., 1996, Barber et al., 2005; Metcalfe, 2006). Sumatra is underlain by the Paleozoic continental crust of Gondwanaland origin that drifted away from the Australian continent, which were accreted to a number of plate fragments in several stages during the Mesozoic (Barber et al., 2005; Metcalfe, 1996, 2006). These plate fragments were then combined throughout a series of subduction-arc magmatism, collision and accretion events.

During the Devonian, southwestern Sumatra and the Tin Island were part of West Sumatra Block and East Malaya Block which rifted from Gondwanaland. In the Early Permian, the East Sumatra Block forms part of Sibumasu (**Si**am, **Bu**rma, **Ma**laya, **Su**matra), a continental fragment which detached from Gondwanaland and collided with Indochina Block later in the Permian or in the Early Triassic (Metcalfe, 2000) (Figure 2.3a).

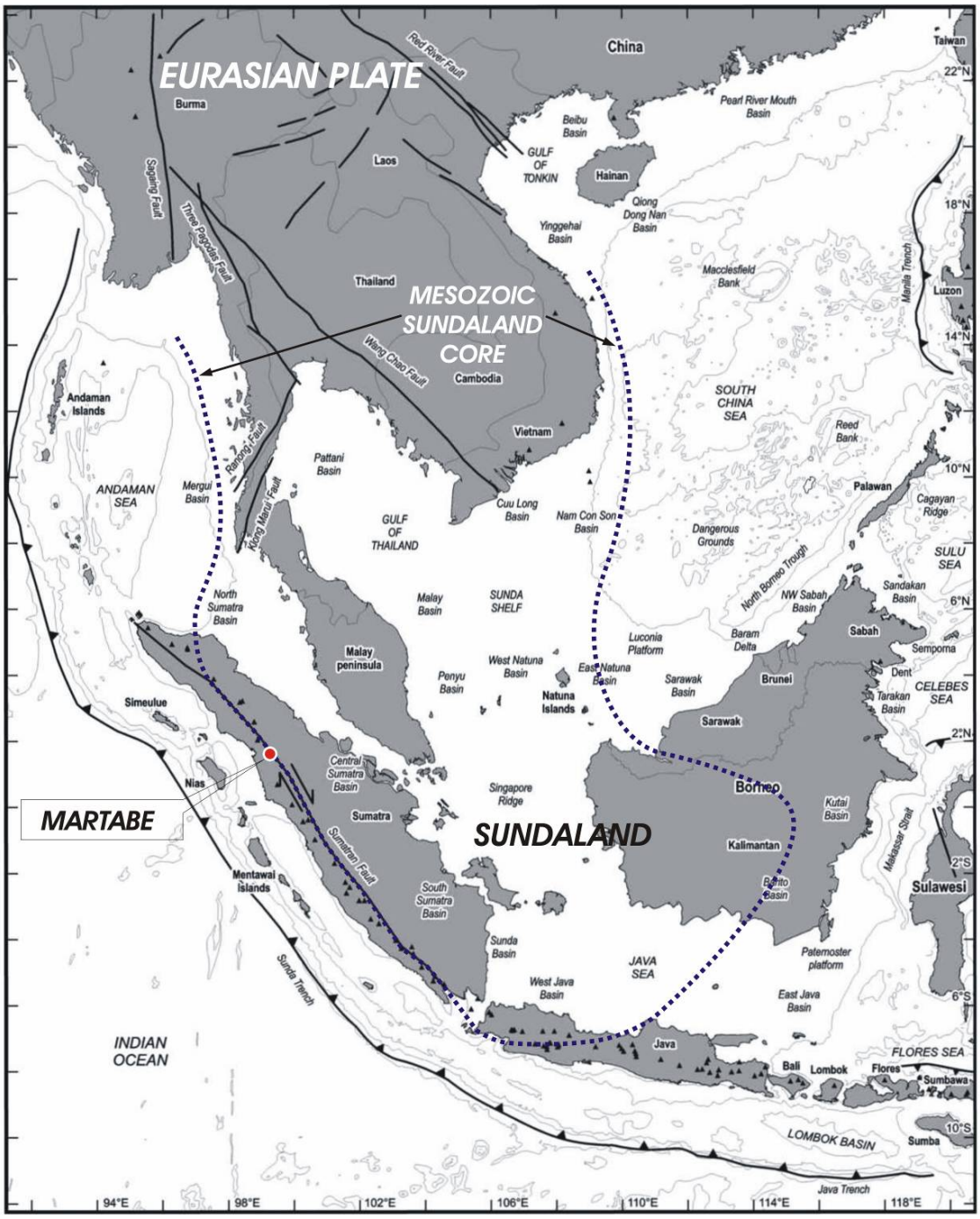

Figure 2.1. Present day Sumatra within the Indochina and Sundaland geographical setting. Red filled circle is the Martabe gold deposit. Small black filled triangles are volcanoes from the Smithsoman database. Gray shaded lines are bathymetric contours (modified from Hall, 2002).

During this event, the Paleo-Tethys was subducted beneath the East Malaya Block. The deformed remains of this accretionary complex form the Bentong-Raub Suture Zone (Metcalfe, 2006) extending from the Malay Peninsula into the Tin islands (Figure 2.2). Following the collision of the Sibumasu Block with the East Malaya Block, the West Sumatra Block became detached in the Triassic and was marked by transcurrent faulting or a strike-slip faulting along the Medial Sumatra Tectonic Zone and was accreted along the

outer margin of Sibumasu (contact between West and East Sumatra Block) (Figures 2.2 and Figure 2.3b).

During the Late Triassic-Early Jurassic subduction of the Meso-Tethys commenced along the margin of the combined West Sumatra Bock and Sibumasu continent (Barber et al. (2005); Metcalfe, 1996) (Figures 2.3b and 2.3.c). Following the subduction of the Meso-Tethys, accretion during Mid Jurassic-Early Cretaceous is recorded in the Oceanic Assemblage of the Woyla Group, comprising oceanic volcanics, sediments and oceanic crust fragments that accumulated in the Woyla accretionary complex (Barber, 2000; Barber and Crow, 2005; Crow, 2005) (Figure 2.3c). This phase of subduction/accretion was brought to a close by docking of a string of oceanic island arcs which had originated within the Meso-Tethys Ocean (Figure 2.3c).

The arrival of the Bentaro-Saling oceanic island arc terminated the subduction, and the Woyla Oceanic Assemblage and Volcanic Arc were thrusted over the margin of the West Sumatra Block as the Woyla Nappe. Subduction of the Meso-Tethys resumed late in the Cretaceous and the oceanward side of the Bentaro-Saling Volcanic Arcs (Crow, 2005) (Figure 2.3d).

A collision between Sumatra-West Java and the narrow Woyla Terrane terminated Mesozoic magmatic arc activity and Cenozoic rocks unconformably overlie Mesozoic rocks (Barber, 2000). The subduction direction changed from oblique to almost orthogonal between Sumatra and Java; and India plate-Sundaland plate motion is subdivided into trench-normal subduction and dextral slip on the Sumatran Fault System and related strands (Fitch, 1972) (Figure 2.1 and 2.2).

Since the Late Cretaceous, the paleogeographic setting of Sumatra is similar to what we see today (Hall, 1996, 2002; Metcalfe, 1996, 2006). At present, Sumatra forms the active southwestern margin of the Sundaland which is the southeastern of Eurasian Plate (Figure 2.1). The thickness of crust underneath Sumatra is approximately 30 km (Ben-Avraham and Emery, 1973; Hamilton, 1979). The north-northeast-directed motion of Indian Ocean results in oblique subduction and a northwestward movement of a sliver plate. There is a well-defined Wadati-Benioff seismic zone 200 km deep beneath Sumatra, which is much shallower than 600 km deep in Java to the south (Hamilton, 1979). However, recent tomography studies on the seismic velocity structure beneath Sunda Arc suggest that the lithospheric slab in both Sumatra and Java penetrates into the depth of more than 660 km or to the lower mantle (Widiyantoro and Van der Hilst, 1996; Hafkenscheid et al., 2001).

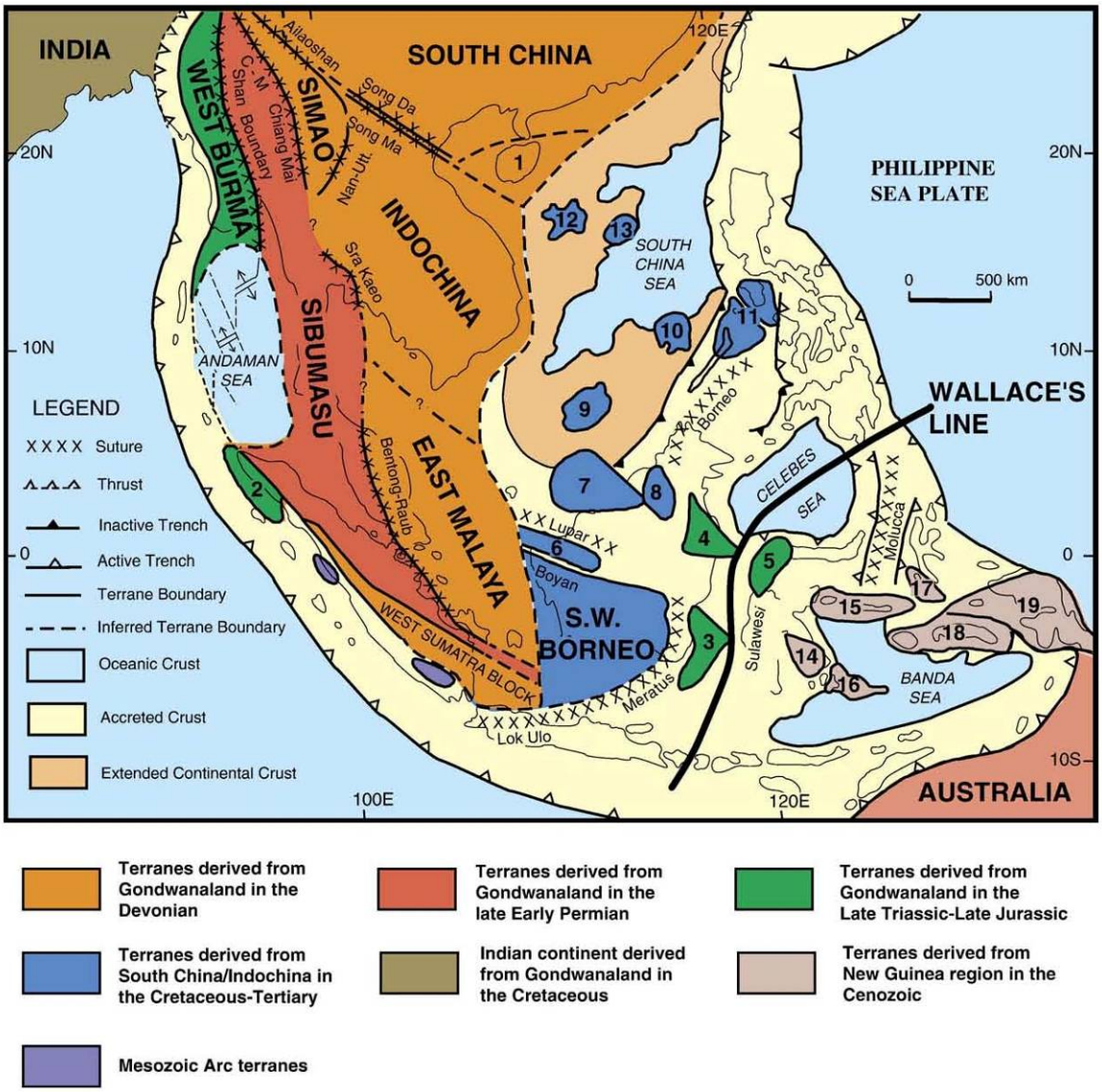

Figure 2.2. Distribution of principal blocks and sutures of Southeast Asia, including Sumatra (from Metcalfe, 2006).

In the early Cenozoic, regional uplift occurred and was followed by extension and subsidence although this is not well dated; the oldest parts of the sequence include volcanic rocks and sedimentary rocks devoid of fossils. The origin of the Sumatra Basins in the east is uncertain, partly because of the uncertainty in their age. There was short-lived plutonism in the Early Eocene (60-50 Ma), but most Cenozoic activity dates from the early Miocene (20-5 Ma) when the present fore arc - arc-back arc became established (McCourt et al., 1996). The most distinctive structural feature on land is the Sumatran Fault System (SFS), a major mid-Tertiary dextral strike-slip fault zone accompanied by a row of Quaternary volcanoes (Figure 2.1). Both strike-slip and extensional controls have been proposed (Williams and Eubank, 1995; McCarthy and Elders, 1997). The Sumatran fore-arc also dates from the early Miocene (Samuel and Harbury, 1996). Subsequent tectonism and uplift

in the Miocene and Plio-Pleistocene caused inversion of the Cenozoic basins, folding and fault reactivation. In summary, since the late Paleozoic, Sumatra is interpreted to be constructed through a series of collision, subduction-arc magmatism, accretion events, the creation of volcanic arcs, formation of compression, oblique slip structures and suturing of discrete microcontinents (Karig et al., 1979; Hamilton, 1979; Pulunggono and Cameron 1984; Barber, 1985; Metcalfe, 1996, 2006; Hall, 2002; Barber et al., 2005).

2.4 Stratigraphy of Sumatra

It is recognized that Pre-Tertiary basement outcrops widely in the Barisan Mountains in the western part of Sumatra and in the Tin islands (i.e., Bangka, Singkep, Bintan and Belitung) in the eastern part of Sumatra. These Pre-Tertiary rocks are variably metamorphosed and were termed as the "Barisan-Schiefer" and the "Old-Slates Formation" in Central Sumatra, and the "Crystalline Schists" in the Lampung area at the southern Sumatra.

Occurrences of granites in the eastern part of Sumatra and the Tin islands suggest that a large part of Sumatra is underlain by a highly differentiated Pre-Carboniferous crystalline continental crust, the age of which extends back into the Precambrian (Barber and Crow, 2005). However, Eubank and Makki (1981) obtained Rb-Sr ages of 426$\pm$41.5 Ma (Silurian) and 335$\pm$43 ma (Early Carboniferous) from granites in the basement beneath the Central Sumatra Basin. These granites suggest that an older basement underlies eastern Sumatra, although the Proterozoic and Lower Paleozoic rocks occur in the Malaysian Langkawi Islands only some 30 km to the NE of Sumatra (Barber and Crow, 2005). Oil wells drilled in eastern Sumatra intersected sedimentary rocks containing palynomorphs from near the Devonian-Carboniferous boundary (Eubank and Makki, 1981).

A stratigraphic scheme which divided the Pre-Tertiary rocks into: the Carboniferous-Permian Tapanuli Group, the Permo-Triassic Peusangan Group and the Jurassic-Cretaceous Woyla Group was proposed by Cameron et al.(1980) and Pulunggono and Cameron (1984). However, this stratigraphic terminology should be applied only to northern Sumatra where the units were first defined (Barber and Crow, 2005).

The oldest sedimentary rocks that have been reliably dated are Carboniferous-Permian, although Devonian rocks have been reported from a borehole in the Malacca Strait, and undated gneissic rocks in the Barisan Mountains may represent a Pre-Carboniferous continental basement. All the older rocks, which lie mainly to the northeast of the Sumatran Fault System (SFS), show some degree of metamorphism, mainly to low-

grade slates and phyllites, but younger Permo-Triassic sedimentary and volcanic rocks are less metamorphosed (Barber et al., 2005). The area to the southwest of the Sumatran Fault System (SFS) is composed largely of variably metamorphosed Jurassic-Cretaceous rocks. The Permo-Triassic is further divided by Barber and Crow (2005) into two units, Mid-Late Permian and Mid-Late Triassic. The Pre-Tertiary basement is cut by granite plutons that range in age from Permian to Late Cretaceous.

Locally within the Barisan Mountains the basement is intruded by Tertiary igneous rocks and is overlain to the east and west by volcaniclastic and siliciclastic sedimentary rocks in hydrocarbon-(oil and gas) and coal-bearing Tertiary sedimentary basins. These basins have back-arc, fore-arc and inter-arc relationships to the Quaternary to Recent volcanic arc. Lavas and tuffs from these young volcanoes overlie the older rocks throughout the Barisan Mountains and, in particular cover an extensive area in North Sumatra around Lake Toba. Recent alluvial sediments occupy small grabens within the Barisan Mountains, developed along the line of Sumatra fault and cover lower ground throughout Sumatra (Barber et al., 2005).

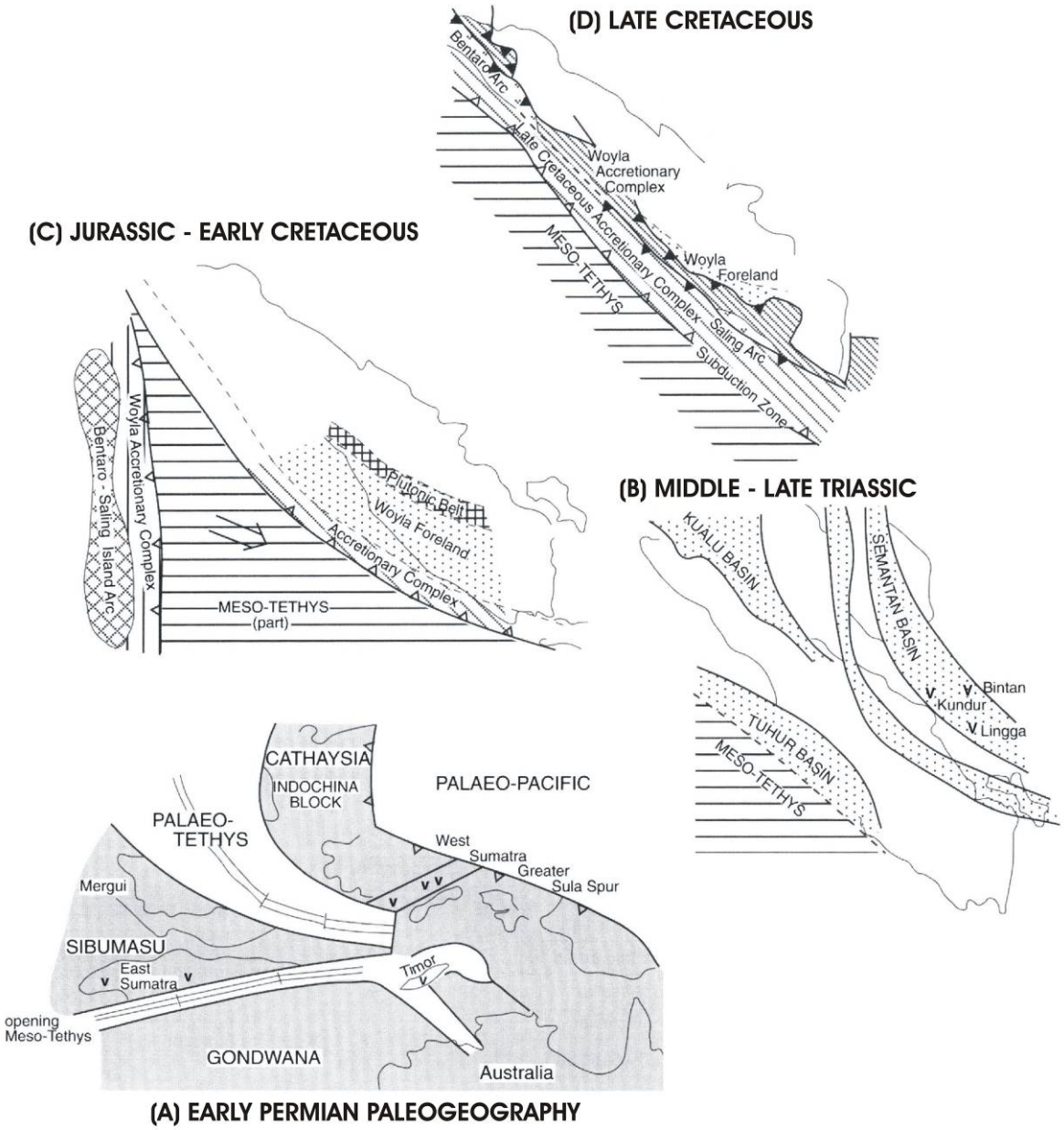

Figure 2.3. The main geological evolution of Sumatra and magmatism events from its dispersal from Gondwana to the collision of the Bentaro-Saling Oceanic Volcanic Arcs during Paleozoic to Mesozoic period (modified from Crow, 2005).

(a) The opening of Meso-Tethys in the Early Permian. In this period the West Sumatra Block is still in position between Cathaysia and the Greater Sula Spur, while East Sumatra is in the Sibumasu block.
(b) Sumatra and the Malay Peninsula in the Mid-Late Triassic showing the Pahang Volcanic Belt (V, volcanic localities) in the Semantan Basin.
(c) Subduction of the Meso-Tethys in the Jurassic-Early Cretaceous showing the Plutonic Arc-Woyla Foreland Assemblage in the east and Bentaro-Saling Arc with the Woyla Accretionary Complex in the west.
(d) Arrival in the Late Cretaceous of the Bentaro-Saling Oceanic Arc that has collided with and has been overthrust onto, Sumatra as the Woyla Nappe. This collision event terminated subduction in the Late Cretaceous.

2.5 Magmatism of Sumatra

2.5.1 Pre Tertiary magmatism

Magmatism in Sumatra occurred during several periods. The oldest magmatism is represented by a Silurian granite (426 ± 41.5 Ma), found in a borehole in the basement beneath the Central Sumatra Basin (Eubank and Makki, 1981). However, the Sibolga granite (264±6 Ma) and Ombilin granite (256±6 Ma), which are exposed along northwestern Sumatra, suggest Permian magmatism (McCourt et al., 1996).

Mesozoic and Cenozoic magmatism can be divided into several major events; Triassic-Early Jurassic (247-180 Ma), Middle Jurassic-Early Cretaceous (169-129 Ma), Mid-Late Cretaceous (120-75 Ma) and Cenozoic (65-0). They represent long-lived magma generation throughout the last 200 Ma (McCourt et al., 1996; Crow, 2005). Following the collision between the Sibumasu and East Malaya blocks during the Triassic, horst and graben structures were formed parallel to the orogen axis where the granites of the Main Range and Eastern Province of the SE Asia granite belts were subsequently emplaced (Crow, 2005).

Within the Malaysia peninsular, the Triassic-Early Jurassic magmatism is identified as I-type for the Eastern Province and S-type for the Central Range Province granitoids (Cobbing et al., 1992; Gasparon and Varne, 1995; Cobbing, 2005). The Pahang volcanics in east Malaya represent the volcanic carapaces of Eastern Province granites emplaced within the Semantan Basin (Crow, 2005) (Figure 2.3.b). In Sumatra, the Middle Triassic-Early Jurassic granites (250-143 Ma) are scattered along and east of Barisan Mountains and within the Tin Islands. These granites were mainly emplaced at 220 Ma, suggesting that most of the plutonism was post-orogenic and occurred at the southern-end extension of the SE Asia granites belt (Cobbing et al., 1992; Gasparon and Varne, 1995; McCourt et al., 1996; Cobbing, 2005). On mainland Sumatra, the Middle Triassic-Early Jurassic granites are identified as I-type, while in Tin Islands these granites are both I- and S-types. The occurrence of Meso-Tethys subduction along the margin of the West Sumatra Block is believed to contribute to the presence of I-type granites in Sumatra during this period (Figure 2.3b).

The Middle Jurassic-Early Cretaceous (169-129 Ma) magmatism formed an extensive I-type plutonic arc that can be correlated with the Western Province of SE Asia granites (McCourt et al., 1996). These granites are associated with subduction of Meso-Tethys to the northeast and the accretion documented within the Woyla accretionary

complex (Figure 2.3c). According to Crow (2005) another arc known as the Bentaro-Saling oceanic island arc was also formed along the western margin of the Meso-Tethys. In the latest Early Cretaceous both arcs were accreted towards the Sundaland (Figure 2.3c).

Resuming of Meso-Tethys subduction in the Mid-Late Cretaceous (Figure 2.3d) formed the Cretaceous and Cenozoic Sumatra arcs, including a new plutonic arc formed on the Woyla Nappe and the margin of the West Sumatra Block (Crow, 2005). The Mid-Late Cretaceous (120-75 Ma) was characterized by I-type granitoid magmas (McCourt et al., 1996) that were likely the continuation of the western Burma Arc or the Central Valley Province of SE Asia granites (McCourt et al., 1996; Cobbing, 2005). This magmatic belt continues to the Meratus Complex in South East Kalimantan, forming the Middle-Late Cretaceous Sumatra-Meratus Arc (Carlile and Mitchell, 1994).

2.5.2 Tertiary magmatism

Bellon et al. (2004) suggested that the continuation of Cenozoic magmatism in Sumatra began at 65 Ma after a general absence of magmatism during 75-65 Ma. Cenozoic volcanism occurs along the Barisan Mountains and the western coast of Sumatra (Figure 2.1 and 2.4). Main volcanic episodes recognized in Tertiary Sumatra are during the Paleocene (65-c.50 Ma; Bellon et al., 2004; Crow, 2005), Late Middle Eocene (c.46-40 Ma), Late Eocene-Late Oligocene (c.38-24 Ma), Late Early Miocene-Middle Miocene (c.22-14 Ma), Late Miocene-Pliocene (6-1.8 Ma) and Quaternary (1.8-0 Ma) (Crow, 2005). However, the youngest plutonic rock is 5±0.2 Ma (McCourt et al., 1996). Geochemical signatures of arc magmas suggest that they are of I-type continental margin type rather than the island arc type of Java (Whitford, 1975; McCourt et al., 1996; Crow, 2005). Therefore, this arc magma provided an abundance of young silicic volcanic rocks associated with caldera-forming events involving the melting of upper crustal material (Whitford, 1975; Hamilton, 1979; Gasparon and Varne, 1995; Gasparon, 2005).

2.5.3 Quaternary volcanism

The morphology and type of Quaternary volcanic activity was compiled by Neumann van Padang (1951) and Kusumadinata (1979). The Quaternary volcanoes along the Sunda-Banda arcs of Sumatra are a well-known example of subduction-related volcanism (Figure 2.1 and 2.2). Volcanic rocks associated with the active volcanic arc in Sumatra range in composition from calc-alkaline basalts to andesites and dacites, typical of

a volcanic arc built on continental crust (Gasparon, 2005). Gasparon (2005) identifies four major Pliocene to Quaternary pyroclastic deposits in Sumatra, namely the Lampung and Ranau tuffs in south Sumatra, the Padang tuffs in central Sumatra, and the Toba tuffs in north Sumatra. The Toba tuffs are associated with a very large eruption that formed the caldera now occupied by Lake Toba. Toba caldera is the earth's largest Quaternary caldera some 35 km x 100 km in dimension, formed during four major Pleistocene eruptions that produced over 25,000 km^3 of ejecta (Kusumadinata, 1979).

2.6 Regional metallogeny of Sumatra

The history and complexity of geological activity in Sumatra from the Paleozoic (detachment of Gondwanaland fragments) through the Triassic-Early Jurassic (collision-related magmatism) and post Early Jurassic-recent (subduction-related magmatism) have contributed different styles of mineralization (Figure 2.4). This review concentrates on the metallic minerals deposits and occurrences. Interpretation of mineralization events are mostly based on the radiometric ages of the host rocks and magmatism and/or tectonic events taken from various regional geological studies (Bemmelen, 1949; Leeuwen, 1994; Carlile and Mitchell, 1994; Hall, 2002; Barber, 2005 et al.; Crow and Leeuwen, 2005; Metcalfe, 2006).

2.6.1 Paleozoic sedimentary units

Lead-Zn mineralization occurs in the metasedimentary and metavolcanic rocks in the Nam Salu open pit at Billiton in the Tin Islands (van Leeuwen, 1994; Schwartz and Surjono, 1990), in the meta-argillites, subordinate meta-psammites and marbles at the Beukah area in South Aceh (Dalimunthe et al., 1996) and in the carbonaceous shales-dolosiltstones of the Dairi prospects, northwest of Lake Toba, North Sumatra (Middleton, 2003) (Figure 2.5).

The Pb-Zn mineralization is mainly associated with interbedded, iron-rich, chemical sedimentary rocks and basaltic tuffs, altered by metasomatic processes (Schwartz and Surjono, 1990) in the Bentong-Billiton Accretion Complex of the east Sumatra Block (Barber and Crow, 2003) and the Kluet Formation, a member of the Carboniferous-Permian Tapanuli Group on the west side of Sumatra. The origin is interpreted to be either: (i) sediment-hosted exhalative (Dairi deposit, Middleton, 2003); (ii) syngenetic/diagenetic related to volcanic exhalations and granite intrusions (van Leeuwen

and Poole, 1978); (iii) syntectonic formed from hydrothermal solutions derived from tectonically induced dewatering of the host sediments, with mineral deposition taking place in structurally dilated zones (Large, 1991); and (iv) vein-type related to hydrothermal fluids (Schwartz and Surjono, 1990). The Pb-Zn mineralization occurs as: (i) fine grained laminated massive sulfides of sphalerite, galena and pyrite, in places commonly containing fragments of quartz and mudstone; (ii) brecciated quartz veins and mudstones with selvages of Pb-Zn; (iii) disseminated sphalerite and galena in sandstone (Large, 1991).

Silver-Cu-(Pb-Zn) skarn mineralization was identified in the Sarkea area (Hendrawan et al., 2001) related to the intrusion of Sibolga complex granite into (calcareous?) beds of the Kluet Formation. Ores comprise of magnetite and pyrrhotite with minor sphalerite-molybdenite in a magnetite-quartz-chlorite-garnet±actinolite-epidote alteration. Late quartz veins with significant amounts of Ag-Cu and minor of Pb-Zn mineralization locally cut the skarn (Hendrawan et al., 2001).

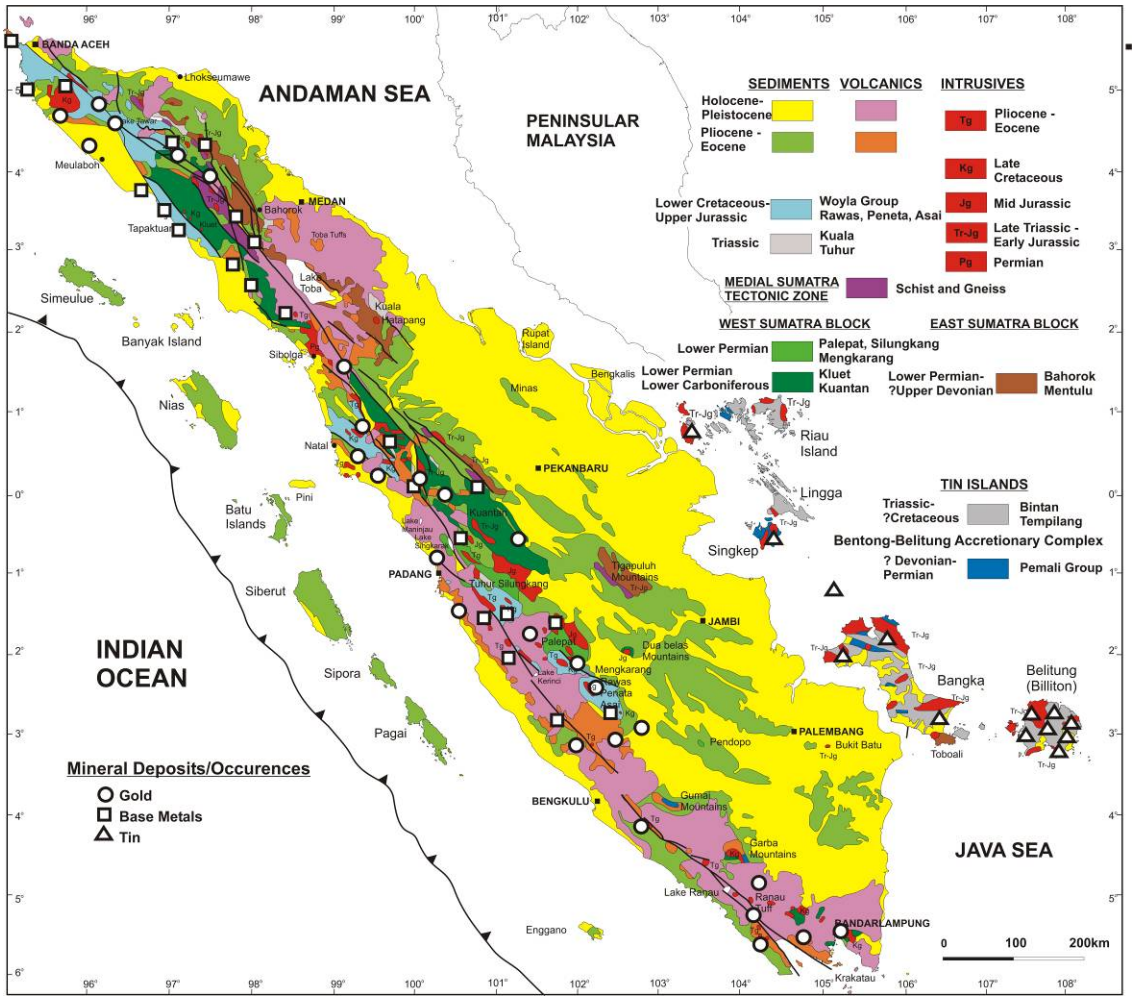

Figure 2.4. Simplified geological map of Sumatra and the Tin Islands, including mineral occurrences (modified from Crow and Barber, 2005).

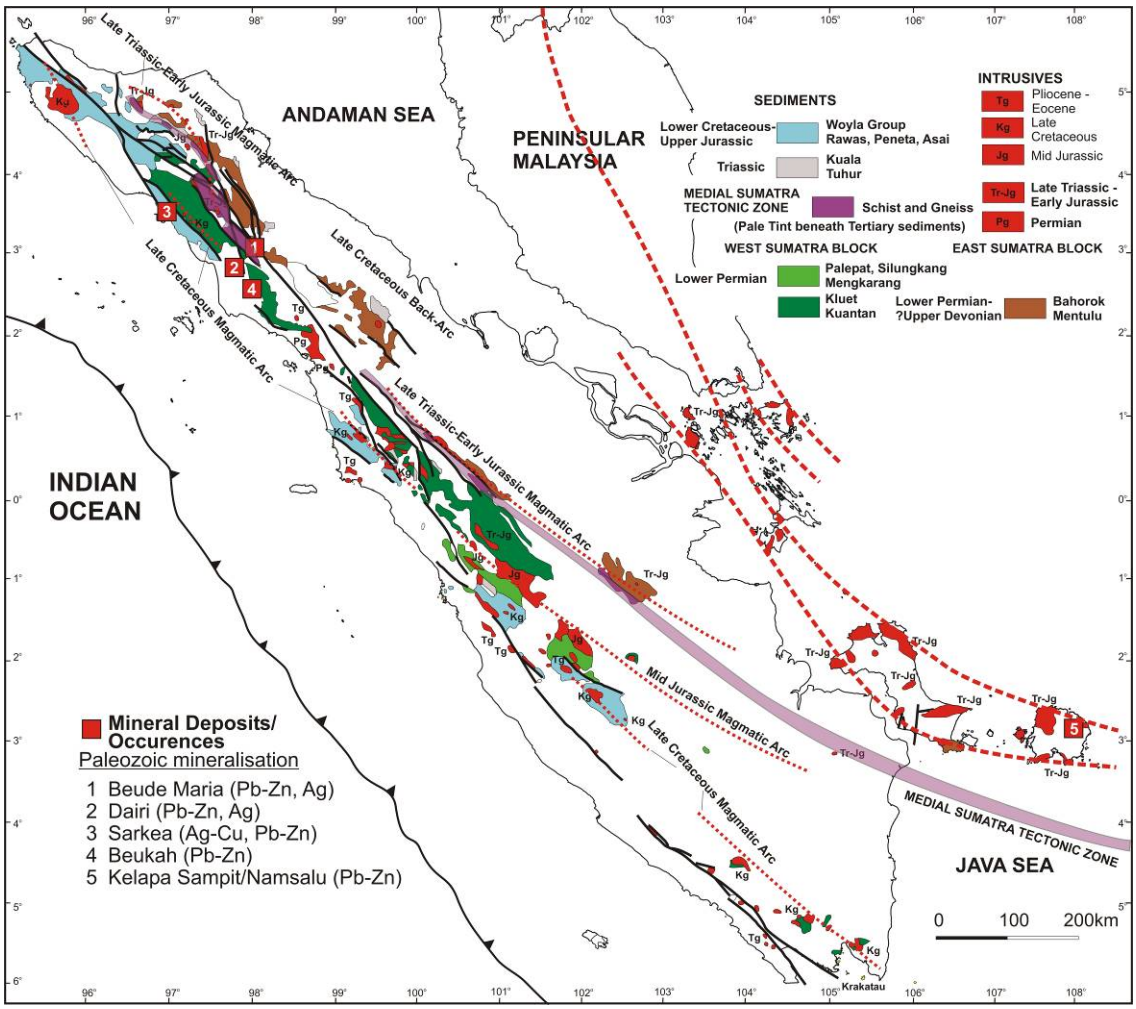

Figure 2.5. Mineral occurrences associated with the Paleozoic sedimentary basins. Data from Crow and Leeuwen (2005).

2.6.2 Mesozoic magmatic arc-related mineralization

In the Mesozoic, mineralization in Sumatra occurred in association with both magmatic arc and collision-related granites. Ishihara (1981) interpreted the granites in eastern Asia as older granites which are dominated by ilmenite-series (or S-type) and younger granites that are mainly composed of the magnetite-series (or I-type).

2.6.2.1 Late Triassic-Early Jurassic magmatic arc-related Sn-W-Fe mineralization

The older granite group in Sumatra is mostly Triassic-Jurassic (250-143 Ma) and is distributed as isolated plutons east of the Barisan Mountains Range and in the Tin Islands (Cobbing et al., 1992; Gasparon and Varne, 1995; Cobbing, 2005). Radiometric data suggest that tin-bearing granites of the Tin Islands are mostly Triassic and older than Early Jurassic (>180 Ma). Many of these granites are S- type (ilmenite-series) and peraluminous,

and have a narrow compositional range of generally >70% SiO_2. This granite group produced abundant Sn-(W)-Fe mineralization and can be correlated with the Central (Main Range) Province of the SE Asia granite belt in Thailand and Malaysian Peninsula (Hutchison, 1983; Cobbing et al., 1992). The major, primary Sn-(W) deposits are Pemali (Bangka Island) and Tikus (Belitung). Geochemical characteristics of the host granite suite suggest a collision to within plate setting (Cobbing et al., 1992; Cobbing, 2005). At both Bangka and Belitung, some I-type granitoids are also present. Although these rocks show a lack of tin mineralization, skarn-like iron ore occurs at Batubesi (Manggar district, eastern Belitung) near the I-type Gunung Mang Batholith. The Batubesi deposit (Figure 2.6), currently being mined for its iron ore, is a vein-shape body several kilometers long and several meters thick hosted by metasedimentaary rocks. Moreover, the nearest exposed granitoid rocks surrounding the Kelapa Kampit Sn-Fe-base metals mineralization are also of I-type. In mainland Sumatra, several S-type granites of similar age occur, such as a suite of tin-bearing granites in northern Sumatra (e.g. Sibolga) and within the Medial Sumatra Tectonic Zone (Tigapuluh Mountain and near Palembang).

2.6.2.2 Mid Jurassic-Early Cretaceous magmatic arc-related Cu-Au mineralization

The younger granitoid group (mainly Cretaceous, but also Jurassic) forms separated plutons and batholiths along the Barisan Mountains Range. Compositions range from gabbro to monzogranite of magnetite- or I-type granitoid. Cretaceous arc magmatism produced dominantly sulfide mineralization and rare tin mineralization.

The Mid-Jurassic-Early Cretaceous magmatic arcs have been largely eroded and are now exposed as batholiths and plutons. These intrusions are responsible for Cu-(Mo, Au) mineralization in Central Sumatra. Examples of intrusion-centered skarn and disseminated mineralization are Muarasipongi and Danau Ranau Kelayang in central Sumatra (Crow and Van Leeuwen, 2005), skarn mineralization related to emplacement of a batholith (158 ± 23) Ma at Muara Sipongi in North Sumatra (Beddoe-Stephens et al., 1987), porphyry-type mineralization related to the Sulit Air suite of plutons (192 ± 0.4 and 193 ± 4 Ma) in the Singkarak cluster, West Sumatra (Imtihanah, 2000; Crow and Leeuwen, 2005) and the low-grade Cu-Mo mineralization related to the Bungo batholith (169 and 129 Ma) at Danau Ranau Kelayang in the north Bangko cluster, Central Sumatra (McCourt et al., 1996) (Figure 2.7).

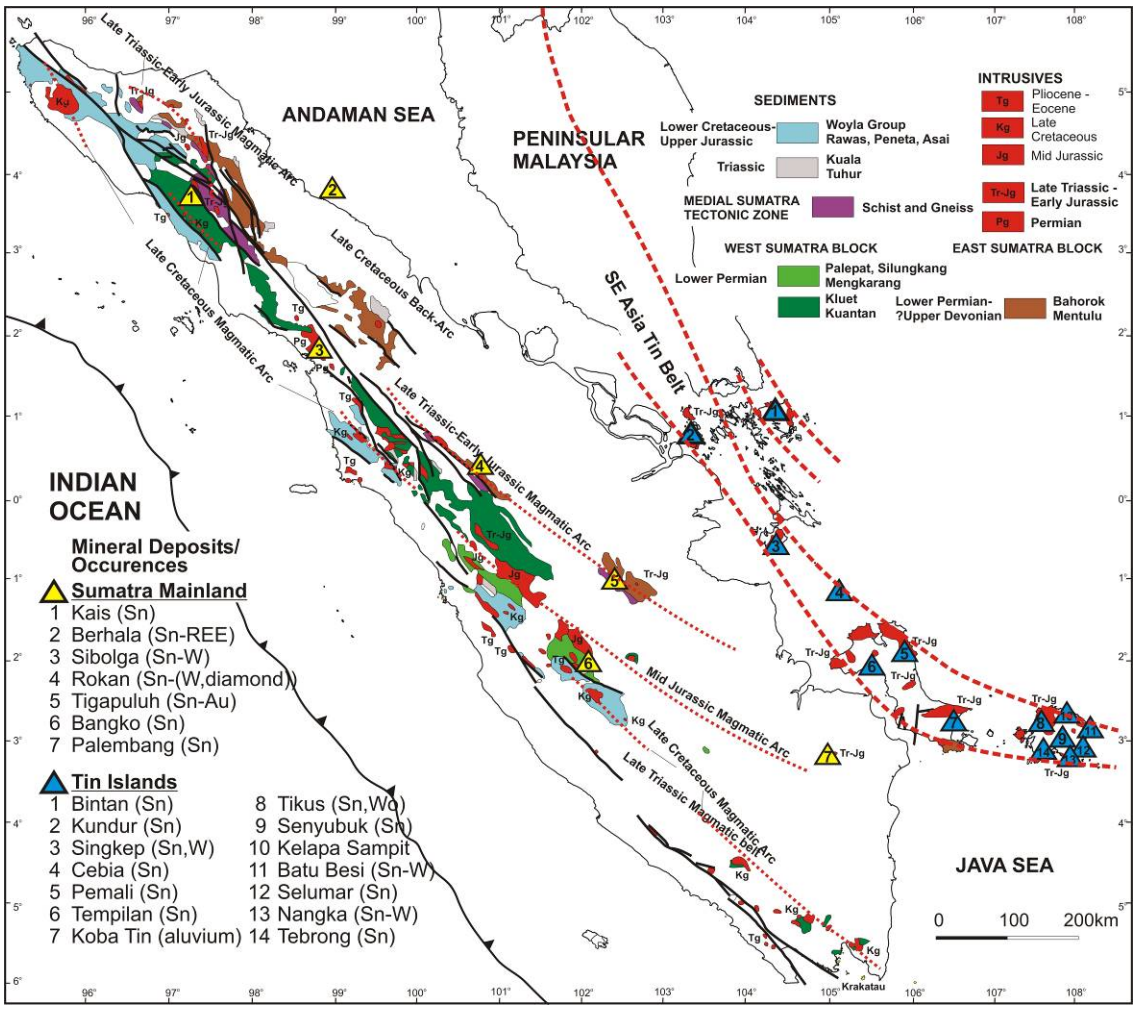

Figure 2.6. Mineral occurrences associated with the Early Mesozoic and granitoids in the Tin Island. Data from Crow and Leeuwen (2005).

2.6.2.3 Late Cretaceous magmatic arc (and Woyla Accretion Complex)-related Au-Ag, Pb-Zn, Sn mineralization

The collision of the Bentaro-Saling oceanic volcanic arcs with Sundaland in the Mid Cretaceous resulted in the reversal of subduction (Barber, 2000) and was recognized as important for mineralization by Carlile and Mitchell (1994) (Figure 2.7). The Cretaceous arc magmatism produced dominant sulfide mineralization and rare tin mineralization (Figure 2.7). This mineralization formed when the Cretaceous batholiths (i.e, Sikuleh, Garba, Hatapang and Manunggal) were emplaced. Precious metal and sulfide mineralization associated with magnetite bodies formed at the contact of the Manunggal Batholith (87 Ma, Rock et al., 1983) with the Woyla Group in the Natal district of central Sumatra. This skarn mineralization is the source of alluvial gold along the Natal River. Small amounts of gold in the Sikuleh area are hosted in skarns in reef limestones associated with emplacement of Sikuleh Batholith at c. 98 Ma (Crow and Leeuwen, 2005). For example, Late Cretaceous

magmas formed precious metal and sulfide mineralization associated with magnetite bodies in Natal, west Sumatra, at the contact of the Manunggal Batholith and the Woyla Group. Cretaceous (?) granite can also be related with Fe-Mn skarn mineralization occurrences such as observed at the Pringsewu area in Lampung. Only two tin mineralization zones formed in Late Cretaceous granitoids, i.e. Garba Batholith in southern Sumatra and the Hatapang Batholith in northeastern Sumatra (Crow and Van Leeuwen, 2005). However, an alluvial tin deposit in the Seputi is thought to be related with granite of Padean pluton (Crow and Leeuwen, 2005) (Figure 2.7).

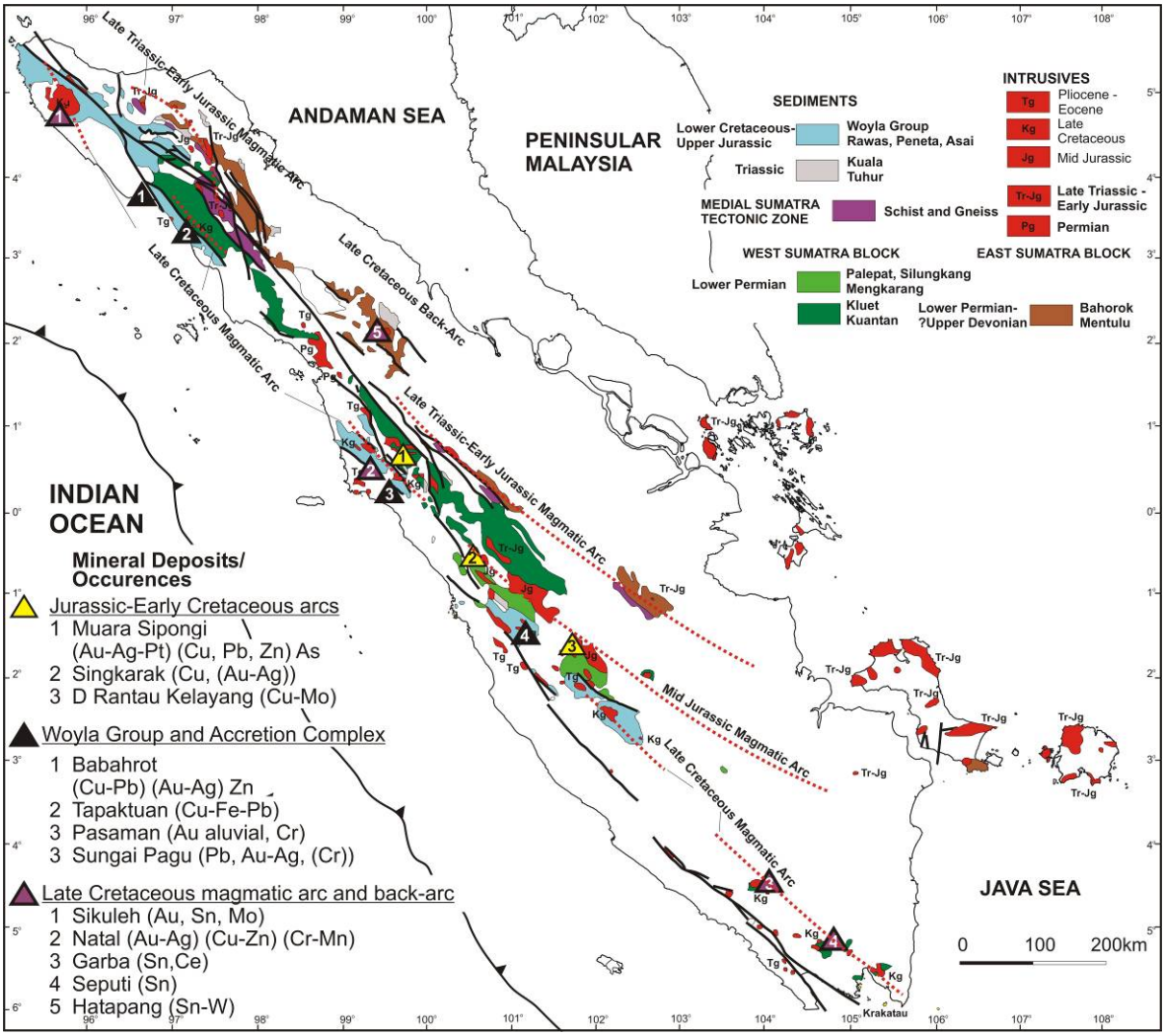

Figure 2.7. Mineral occurrences associated with the Mid-Mesozoic (Mid-Jurassic—Early Cretaceous and Late Cretaceous) magmatic arcs and Woyla Group Accretionary complex. Data from Crow and Leeuwen (2005).

Rare-earth mineralization also forms as a result of the fractionation of these granitoids (i.e., Garba). Several areas of auriferous magnetite and sulfides mineralization within the Woyla Group succession and Late Cretaceous intrusions occur along the western side of Sumatra (massive sulfides at Tapaktuan and Babahrot, northern Sumatra,

Cameron et al., 1982), alluvial gold derived from skarn-type deposits in Natal, alluvial Cr-Au related ophiolite body at Pasaman in west Sumatra (Crow and Leeuween, 2005), and the Pb-Zn mineralization at Sungei Pagu near Lubukgadang, central Sumatra (Hariwidjaja and Suharsono, 1990; Figure 2.7).

2.6.3 Tertiary-Quaternary mineralization

Tertiary magmatism and volcanism produced many arc-related porphyry and epithermal deposits along the Barisan Mountains range. Carlile and Mitchell (1994) suggested that in the northern part of Sumatra another Neogene magmatic arc is present running in an east-west direction (Aceh Arc). The Aceh Arc appears to be different from the adjacent Sunda Arc, as it is characterized by porphyry copper-molybdenum and high-sulfidation rather than low-sulfidation epithermal deposits.

2.6.3.1 Paleocene magmatic arc-related Cu-(Au-Ag) mineralization

Paleocene iron-rich skarns deposits occur at Rawas and Sungai Tuboh (Figure 2.8). At Rawas, the sulfide mineralization occurs at the contact with the Woyla Group and the Bukit Rajah Granite (54 $\pm$ 2 Ma). However, the Sungai Tuboh copper and precious metal skarn mineralization formed at the contact of a 40 $\pm$ 2 Ma quartz monzonite (Crow and Leeuwen, 2005).

2.6.3.2 Late Eocene-Early Miocene magmatic arc-related Cu-Au, Fe mineralization

Mineralisation associated with late Eocene-Early Miocene magmatic arc occurs in the Breueh cluster northwest of Banda Aceh where disseminated sulfides and quartz veins are related to a 19 $\pm$ 1 Ma diorite intrusion (Bennett et al., 1981) (Figure 2.8).

2.6.3.3 Miocene-Pliocene magmatic arc-related porphyry Cu-Mo mineralization

Miocene felsic intrusions are located in the Barisan Mountains of western Sumatra, but so far only very low grade porphyry- Cu-Mo mineralization associated with porphyritic diorite and granite has been discovered. This mineralization is associated with arc-parallel faults of the Sumatran Fault System (SFS), with plutons emplaced within segments and jogs of the main fault zone, or in fault splays (Figure 2.9).

Extensive exploration programs during 1970s located several Cu-Mo porphyries and associated skam prospects, but at the time of the exploration none of these prospects were considered economic; these prospects are Tangse, northern Sumatra (Young and Johari, 1978; Van Leeuwen et al., 1987), Danau Diatas, Siuluk Deras and Danau Dipatiampat in central western of Sumatra (Van Leeuwen et al., 1987). The only porphyry copper prospects associated with Miocene-Pliocene diorite-tonalite porphyry stocks that have been drill tested are the Upper and Lower Tengkereng and Upper Ise-Ise prospects in the Dusun cluster, northern Sumatra (Dalimunthe et al., 1997) (Figure 2.9).

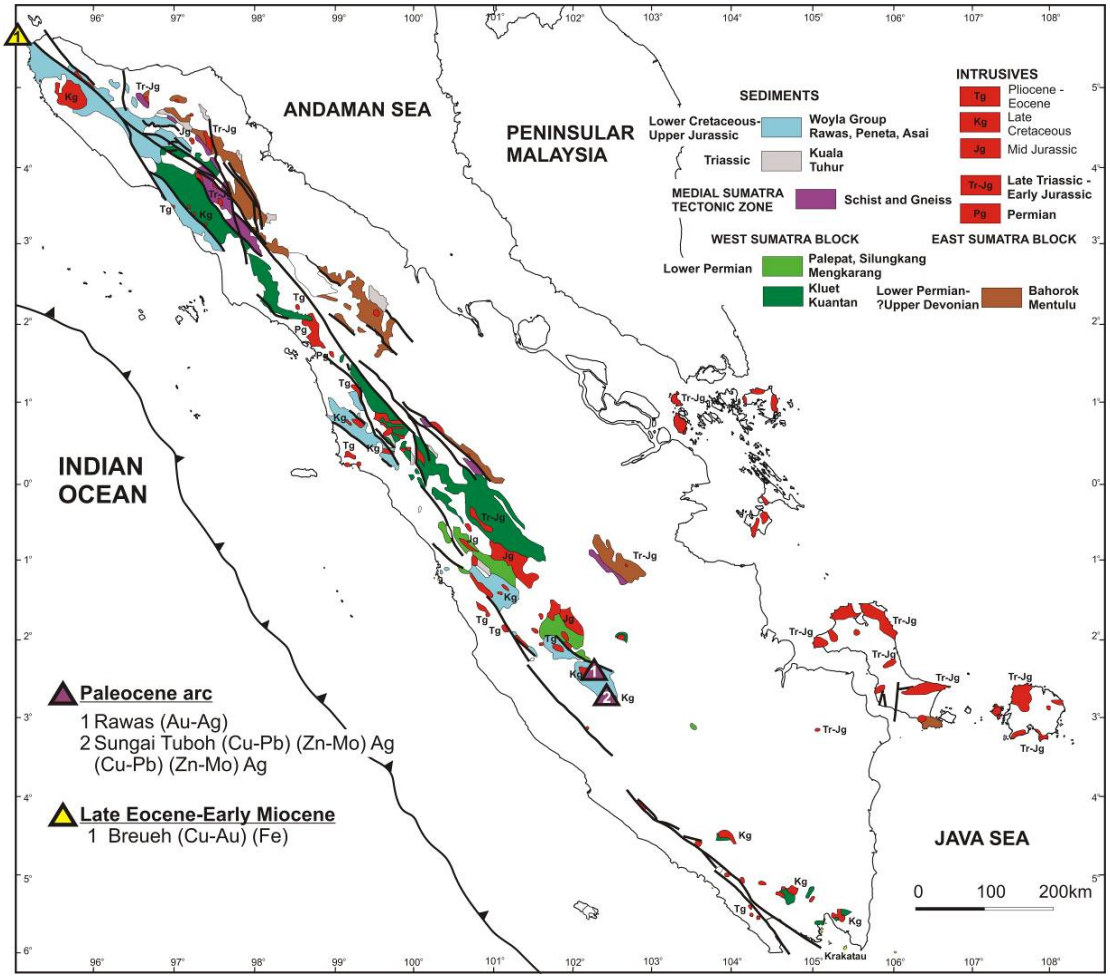

Figure 2.8. Mineral occurrences associated with the Paleocene and Late Eocene-Early Miocene magmatic arcs. Data from Crow and Leeuwen (2005).

2.6.3.4 Neogene magmatic arc-related Au-Ag mineralization

Epithermal mineralization in the Neogene magmatic arc is better documented, but the details of the gold mineralization remains poorly understood because of their perceived low economic potential (Figure 2.10). Only a few of the epithermal deposits have been dated, such as Lebong Donok at 1.2 Ma-1.3 Ma (Henley and Etheridge, 1995) and Martabe at 2.1-3.3 Ma (this thesis). The available data suggests that Neogene gold mineralization in Sumatra, at least in part, occurs in the period after 3.5 Ma, in an interval of tectonic reorganization following the collision of the Philippine Arc and the Eurasian Plate (Barley et al., 2002).

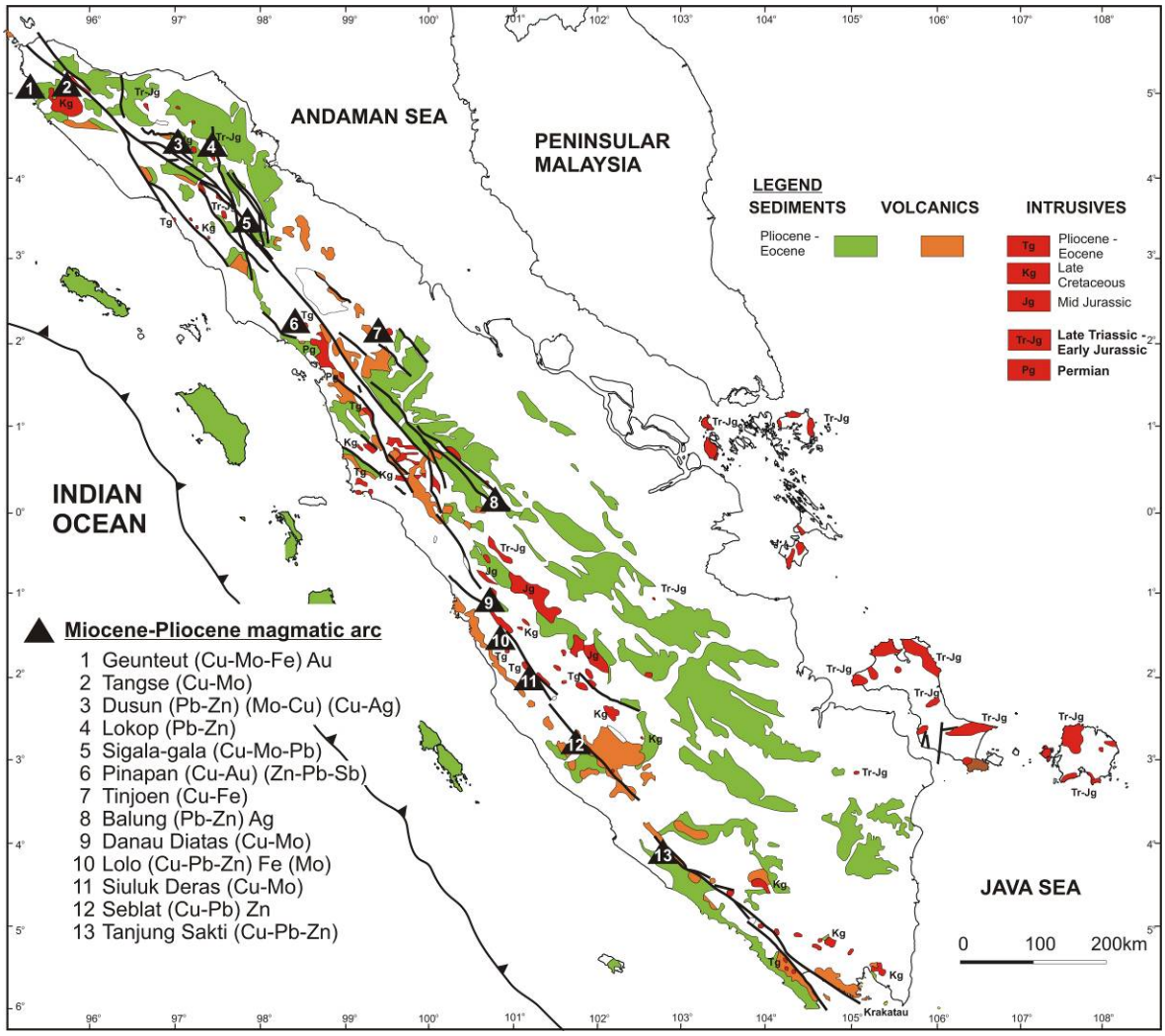

Figure 2.9. Mineral occurrences associated with the Miocene-Pliocene magmatic arcs. Data from Crow and Leeuwen (2005).

The epithermal deposits within Neogene magmatic arc in Sumatra are identified as (i) low-sulfidation, (ii) high-sulfidation and (iii) sediment-hosted mineralization systems.

These deposits occur in an Outer Neogene Gold Axis and an Inner Neogene Gold Axis (Figure 2.10) (Crow and Leeuwen, 2005). The classic quartz-vein, low-sulfidation epithermal deposits are commonly found in the southern half of the island, Mangani district, central Sumatra (van Bemmelen, 1949; Kavaleries, 1988), Lebong districts, western Sumatra (van Leeuwen, 1994; Henley and Etheridge, 1995; van Bemmelen, 1949) and the Lampung district, southern Sumatra (Andrews et al., 1991; Crow, 1995; Andrews, 1996). However, high-sulfidation epithermal deposits are located in northern Sumatra, at Martabe (Levet et al., 2003; Sutopo et al., 2003), Miwah (Williamson and Fleming, 1995) and Meluak (www.corona.com.au). Only one prospect has been discovered in southern Sumatra (Bengkulu). The third type of deposit consists of sediment-hosted mineralization that occurs in the northern Sumatra at Abong (Hendrawan et al., 1996) and Sihayo (www.oropa.com.au).

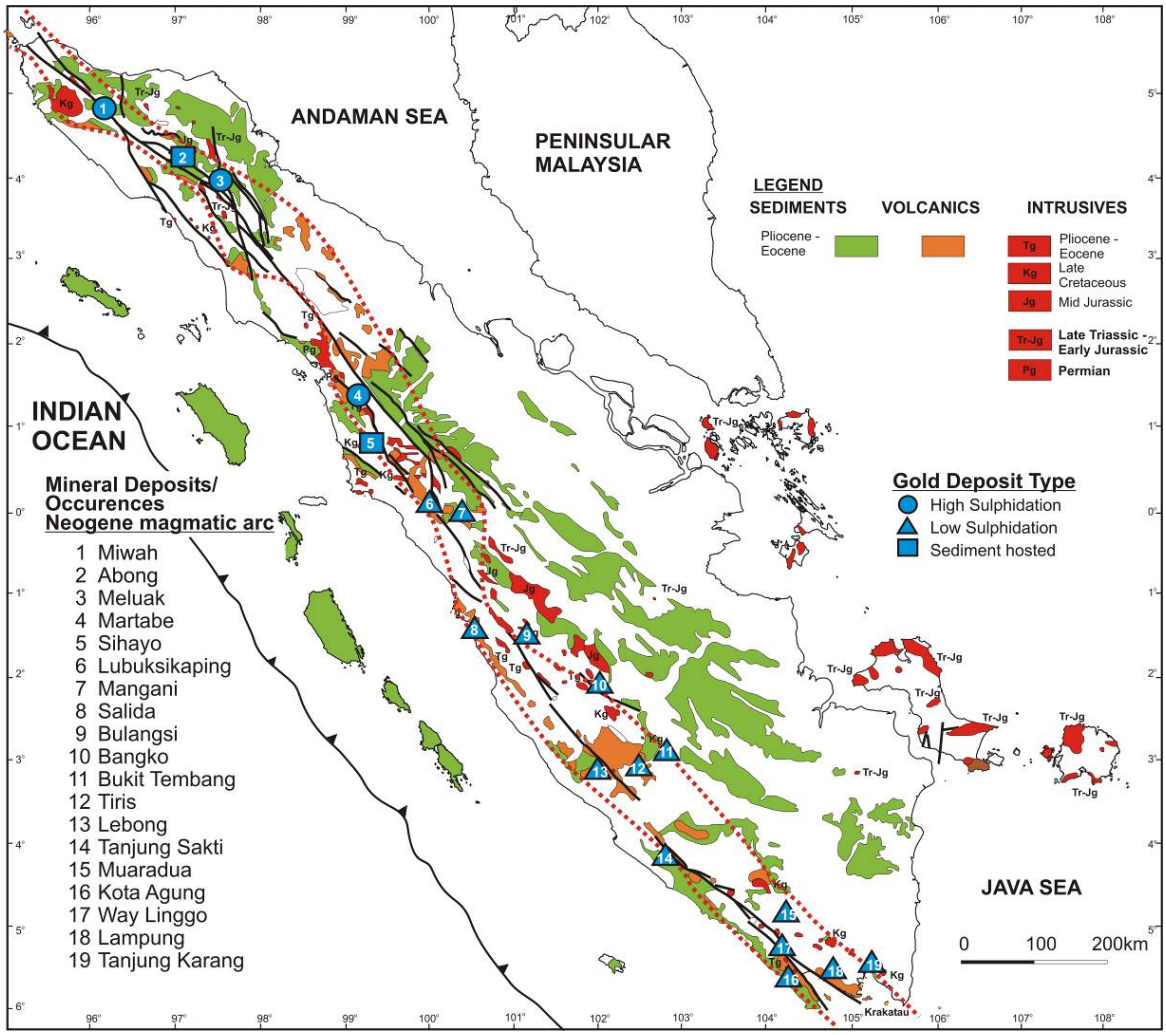

Figure 2.10. Mineral occurrences associated with the Pliocene-Pleistocene magmatic arcs. Data from Crow and Leeuwen (2005).

The majority of Neogene epithermal gold occurrences in Sumatra are hosted in Tertiary volcanics and sedimentary rocks which overlie the Woyla Group. Carlile and Mitchell (1994) suggest that this relationship may be related indirectly to the arc reversal and emplacement of the oceanic volcanic arcs onto the Sundaland margin in the Cretaceous (Crow and Leeuwen, 2005). The Sumatran Fault System (SFS), which controls the emplacement of intrusions, helps to explain the concentration of epithermal occurrences in the Neogene Gold Belt. In southern Sumatra, several precious metal prospects are associated with arc-parallel fault segments of the Sumatran Fault System (e.g., Tanjungsakti, Way Linggo and Martabe) or proximal to fault splays.

Three known high-sulfidation deposits (Martabe, Meluak and Miwah) were discovered in the mid 1990s in areas of good access that had no previously recorded gold occurrences. The Martabe gold deposit is currently the largest known gold deposit in Sumatra (Levet et al., 2003), with a resource of 5.9 Moz of Au and 61.5 Moz of Ag. It is associated with an intrusive dacitic dome and diatreme complex, proximal to a fault splay of the Sumatran Fault System (this thesis). The Meluak area of north Sumatra is located in a rift formed by the sub parallel Blangkejeren-Toru and Kla-Alas faults that form part of the Sumatran Fault Zone. Mineralization is associated with hydrothermal breccias, massive and vuggy quartz and clay-pyrite alteration within the Quaternary Kembar volcano (www.coronagold.com.au). The Miwah prospect in Aceh is hosted within interbedded Pliocene sedimentary and andesitic volcanic rocks associated with normal faulting. This prospect is likely related to a buried intrusion (Williamson and Fleming, 1995).

The Abong and Sihayo sediment-hosted gold deposits are both located in northern Sumatra. The Abong prospect is hosted in mudstone/black shale underlain by limestone of the Upper Oligocene to Middle Miocene Bampo Formation. Andesitic volcanic rocks are interbedded with this unit. The northwest-trending mineralization is associated with an irregular zone of gold-bearing, stratiform, jasperoid and silicified shale/siltstone which is present at, or close to, the hanging wall of the limestone (Hendrawan et al., 1996).

The Sihayo gold prospect in northern Sumatera has a strike length of 1 km and is up to 450 m wide, containing an inferred gold resource of about 600,000 ounces of Au (www.oropa.com.au). The zone is inferred to extend discontinuously for more than 4-km of strike length to adjacent prospects. Gold mineralization is hosted by regolith and silicified breccias related to a sequence of Permian limestones, and in tuffaceous siltstone intercalations within the limestones. The breccias were interpreted to form by karst dissolution and subsequent collapse. Pyrite is the dominant sulfide phase and is accompanied by arsenopyrite and stibnite.

The two major structures/alignments are recognized to be responsible for Neogene gold mineralization in Sumatra (Posavec et al., 1983). The northwest-southeast "Neogene Gold Axes" are volcanic-tectonic alignments which represent the migration of older Quaternary to Recent volcanic centres in response to progressive displacement along the Sumatran Fault System. Whilst less common east-west alignments of active Quaternary volcanic centres thought to be related to large buried dioritic intrusions based on aeromagnetic signatures (Posavec et al., 1983).

2.7 Discussion

Sumatra has been influenced by multiple tectonic, magmatic and metallogenic processes which are responsible for formation of the diverse styles of precious and base metals deposits. Many different deposits types and mineralization styles appear to occur in clusters and belts. At least five different mineralization belts/events have been recognized such as: (i) base metal mineralization related to Paleozoic sedimentary basins, (ii) tin mineralization related to Early-Mesozoic magmatism, (iii) base metal mineralization related to Mid-Late Mesozoic magmatism (iv) base-precious metal mineralization related to Early Tertiary and Miocene-Pliocene magmatism and (v) precious metal mineralization related to Neogene magmatism (Table 2.1, Figure 2.11).

At least three different styles of lead-zinc-(silver) mineralization occur in Sumatra, such as SEDEX (Dairi, Beukah), MVT (Dairi), skarn and porphyry related skarn and veins (Sarkea). All Paleozoic base metal related-mineralisation is situated along the western part of Barisan Range or Sumatran Fault System, except for the Nam Salu mineralization at the Kelapa Kampit mine in the Tin islands. In general, SEDEX type deposits are the most important style for lead-zinc mineralization in Sumatra, followed by MVT and skarn deposits.

The Sumatra region has many clusters of porphyry Cu-Mo-(Au) mineralization (Tangse in Aceh and Ise-ise, in North Sumatra). Katili (1974) argued that the general low tenor of the porphyry copper occurrences found in Sumatra may be due to the poor copper content of the crust that was subducted beneath the island during the Neogene, whilst Hutchison and Taylor (1978) suggested that the process of subduction was too young to have generated suitable melts. Sillitoe (1997) suggested another possible explanation that the Neogene subduction occurred (most of the time) at an even velocity, a condition which is not conducive to the generation of large and high grade deposits.

The primary precious metal (gold-silver) deposits occur as (i) low-sulfidation epithermal deposits (ii) high-sulfidation epithermal deposits, and (iii) sediment-hosted deposits (jasperoid and/or karst dissolution). The quartz-vein, low-sulfidation epithermal deposits are common in the middle to southern part of the island (Mangani district and Lebong) and the high-sulfidation epithermal deposits are found in the northern part of Sumatra (Martabe, Meluak and Miwah). These low- and high-sulfidation deposits are hosted in Miocene-Pliocene volcanic-sedimentary units. Neogene sediment-hosted gold mineralization occurs on Sumatra — the Abong and Sihayo deposits which are both located in northern Sumatra.

Table 2.1. Metallogenic characteristics of Sumatra. See text for references.

Time of mineralization	Main lithological Setting	Main associated pluton	Main orebody form	Main alteration and mineralization	Main ore elements
PALEOZOIC					
Paleozoic Permian?	Metasedimentary rocks, meta-argillites Kluet Formation carbonaceous shales, dolosiltones, calcareous siltstone	Sibolga granite complex in northern Sumatra (264 Ma)	Massive and vein sulfides hosted in carbonaceous shales with shear zones parallel to banding Banded and laminated sulfides Bedding plane in lenses Brecciated quartz vein SEDEX and Mississippi Valley Type (MVT) Skarn aureole	Fine-grained, disseminated sphalerite-galena-pyrite Banded, layered of pyrite-pyrrhotite-sphalerite-galena Skarn: magnetite-pyrrhotite-sphalerite-molybdenite in magnetite-quartz-chlorite-garnet±actinolite-epidote	Pb-Zn-(Ag) Ag-Cu-(Pb-Zn)
MESOZOIC					
Early Mesozoic (mainland Sumatra)	Calcareous sinter (travertine?) Metasedimentary rocks-metavolcanics Tapanuli Group (metasedimentary rocks)	Kais Complex (granite-diorite), Berhala granite, Sibolga granite complex, Rokan granodiorite, Tantan granite, Tigapuluh granite pluton, Palembang syenite (264±6 Ma to 160-150 Ma)	Alluvium, placers, beach sand, disseminated sulfides, greisen, pegmatite, quartz-cassiterite veins, granite roofs	Locally prophylitized, chloritized and silicified granite, veined granite, diorite altered, greisen	Sn-(W-REE) Minor Au from pegmatite, Trace diamond probably from weathered Tapanuli group
Early Mesozoic (Tin island)	Granitoids and metasediments, metavolcanics Tuff and iron formation	Lagoi Granite, Karimun Granite, Kundur Granite, Danai Granite, Dabo Granite, Tujuh Granite, Permali Granite, Menumbig Granite, Tempilan Granite, Mangkol, Tanjungpandang Granite, Nangka Granitoid (from selected age dating: 211±3 Ma to 193±12 Ma) Rare dacite porphyry dykes	Greisen, fissure/veins-stockworks, sheeted veins, cross cutting and bedding plane, replacement Vertical veins, tabular ore to a lenticular body Bedding plane lode	Albitization, kaolinization, hydrothermal alteration Rare metasomatism to stilpnomaline-biotite-chlorite-phyllite Cassiterite±tourmaline-wolframite, molybdenite-pyrite-arsenopyrite, pyrrhotite, marcasite, sphalerite, galena, tennantite, chalcopyrite, magnetite, fluorite, rutile, apatite, siderite, garnet, amphibole, topaz, titanite Ilmenite+magnetite Banded magnetite+iron sulfides-quartz	Sn-(W-Fe)
Jurassic and Early Cretaceous arcs	Permian metasediments-metavolcanics, volcanics	Muarasipongi batholith, quartz diorite, Bungo batholith granodiorite (200-129 Ma)	Skarns, hydrothermal veins, gossans, disseminated vent/joints Intrusion centred mineralization	Chlorite-calcite alteration of skarns Quartz-feldspar-epidote magnetite skarn Silicification, pyritization, propylitisation	Au-Ag-(Pt-As) Cu-(Mo-Pb-Zn)
Woyla Group and Accretion Complex	Tapaktuan Volcanics Formation-andesites, basalts Woyla Group-metasediments	Samadua Granite (51±1 Ma), Pasaman ultramafic, diorite, dacite, diatreme	Stockwork, disseminated sulfides, sulfides in quartz stringers, carbonates, oxidized-vein Massive volcanic exhalative Au magnetite and sulfides	Pyritic, hydrothermal alteration, silicified, argillized, oxidation	Cu-Pb-(Zn-Fe) Au-Ag-(Mn-Cr)

Table 2.1. Metallogenic characteristics of Sumatra (continued). See text for references.

Time of mineralization	Main lithological Setting	Main associated pluton	Main orebody form	Main alteration and mineralization	Main ore elements
Late Cretaceous magmatic arc and back arc	Woyla Group metasedimentary rocks, metavolcanic rocks Tapanuli group metasedimentary rocks	Older Sikuleh (diorite, gabbro) and younger Complex (granodiorite 98+1 Ma), Manunggal Batholith *c.* 87 Ma, Garba Batholith (86-82 Ma), Way Pubean granite *c.* 85 Ma , Hatapang granite (80±1 Ma)	Alluvial Au from skarn, greissen and pegmatite in cupola intrusive origin), dyke (?), silicification, ore in magnetite at batholith contact, minor disseminated in serpentinites	Silicification, magnetite, skarn Alteration in pluton and country rocks Disseminated magnetite body at contact of batholith, cassiterite	Au-Ag, Cu-Zn, Cr-Mn, Sn-(W-Ce) Skarn : Au Dykes : Sn and Mo
CENOZOIC					
Paleocene	Woyla Group metasedimentary rocks, metavolcanic rocks	Bukit Raja granite (54±2Ma, Sungai Tuboh quartz monzonite. Post intrusion hydrothermal activity *c.* 40±2 Ma)	Quartz veins, skarns, alluvium	Chlorite, sericite and silica	Au-Ag Cu-Pb Zn-Mo
Late Eocene-Early Miocene	Basalts, pyroclastic rocks, dykes	Diorite (19±1 Ma)	Quartz vein, disseminated	Epidote	Cu-Fe Au
Miocene-Pliocene	Miocene-pliocene volcanics, limestone-mudstone Tapanuli groups-metasedimentary rocks Intrusion-related mineralization Bampo Formation, pyritic mudstone	Mainly diorite stocks and intrusive swith minor dacite, tonalite and less granodiorite (range from 14 to 9 Ma)	Disseminated and veins, gossan boxwork, disseminated, skarn	Argillic, kaolinization, propylitized, epidote-chlorite-(barite), quartz-sericite, clinopyroxene-biotite	Cu-Mo-Fe Pb-Zn-(Sb-Ag) Cu-Au (trace Au in supergene) Fe in gossan/boxwork
Pliocene-Pleistocene	Miocene volcanic rocks, Oligocene-Pliocene sedimentary rocks Pliocene-Pleistocene age mineralization	Dacite, porphyritic andesite, Miocene volcanics, diatreme breccia	Dome-related, brecciated quartz bodies, quartz vein and stockworks, sulfides vein and disseminate	Dome-related, high-sulfidation (silicification-advanced argillic), enargite-luzonite, tennantite, low-sulfidation (adularia, prophylitic, argillic), sulfides, jasperoid	Au-Ag with traces Pb-Zn

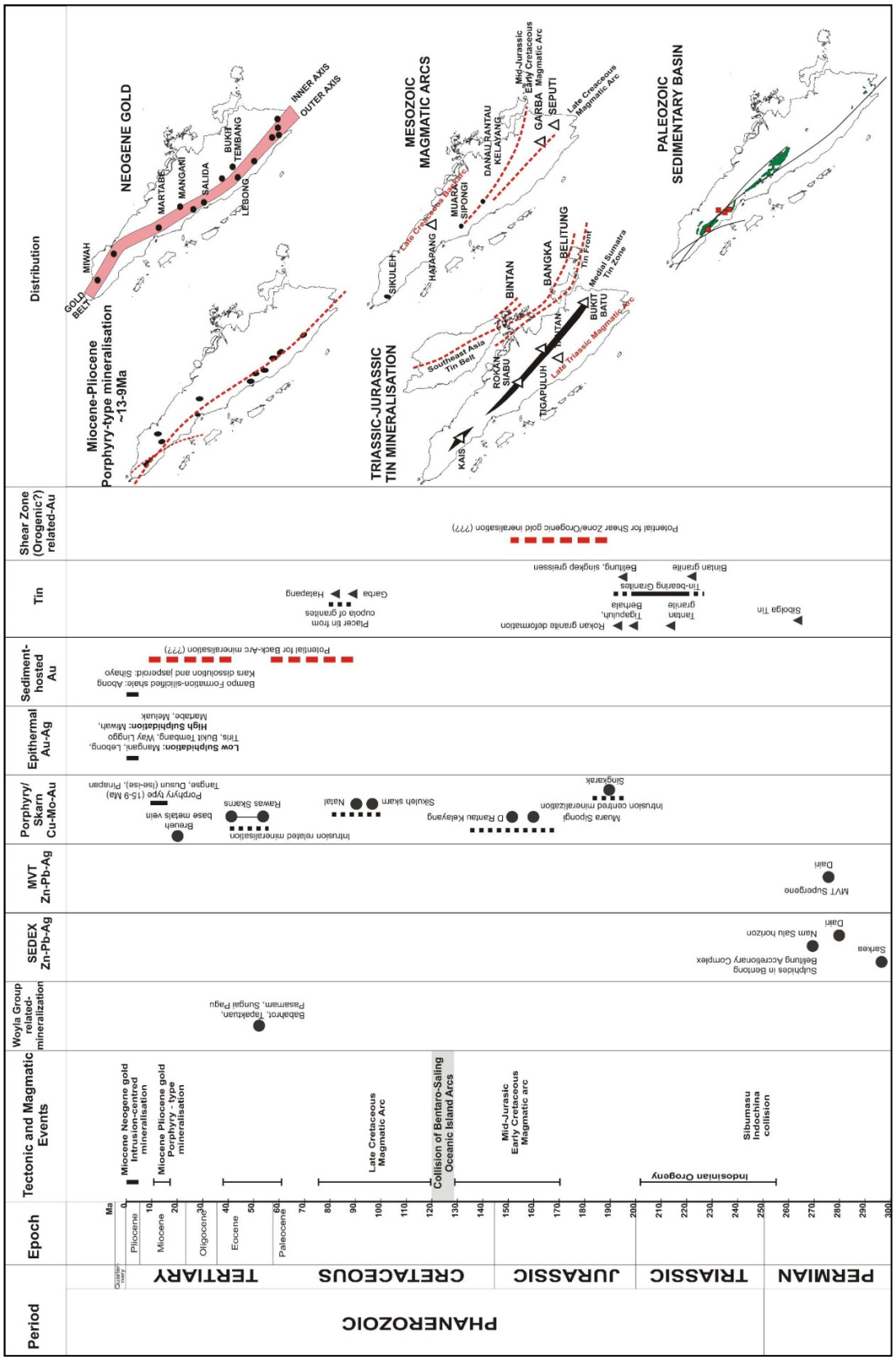

Figure 2.11. Timing of the main mineralisation events and their distribution in Sumatra and the Tin islands. Black and dashed lines are the known ages of mineralization. Red dashed line is the speculative age of the mineralization. Dots and triangles are the known deposits (modified from Crow and Leeuwen, 2005)

CHAPTER 3

DISTRICT GEOLOGY

3.1 Introduction

This chapter describes the lithologies and their environments of deposition in the Martabe district. The lithology descriptions are based on author and company geological mapping, detailed drill core logging and observation of hand specimens and thin sections.

Volcanic and breccia facies and their environment of formation were also studied, although most volcanic and breccias facies have showed varying degrees of alteration. However their primary textures were often still preserved, therefore allowing interpretation of their fragmentation and depositional characteristics.

The older rocks, such as granitic batholith and Tapanuli metasedimentary unit of the western of north Sumatra are well documented (e.g., Aspden et al, 1982; Barber, 2005). However, as these units do not host gold mineralization in the Martabe district, they will be only briefly described in this study. In contrast, the age and origin of the Tertiary sedimentary, volcaniclastic, volcanic and intrusive rocks exposed at Martabe have previously been poorly described and detailed documentation of these rocks are given in this chapter.

3.2 Geologic setting

The Martabe district is located in fore arc region within the Western Barisan physiographic region, which includes a subduction zone to the west and active volcanism to the east (Barisan Mountains) of the northern Sumatra (Figure 3.1). The district lies within the Sumatra Faults System (SFS), which is locally known as Sibolga Fault and Angkola-Gadis Fault, and a structurally uplift zone of metasedimentary, sedimentary, volcaniclastic and volcanic rocks (Figure 3.2).

The district is composed of Tertiary volcano-sedimentary units floored by and in structural contact with Pre-Tertiary basement. Dioritic to granitic intrusions were emplaced during the Permian-Triassic, Eocene, Miocene and Pliocene (Aspend et.al., 1982). Within the uplifted zone, numerous faults have disrupted bedding orientations and complicated the distribution of sedimentary units. Intermediate (andesitic and dacitic) intrusions have intruded sedimentary and volcaniclastic rocks within and to the west of the structural linier.

Plio-Pleistocene mafic lava flows and volcaniclastic units are widespread, particularly to the east and northeast of the Martabe district. These mafic units uncomformably underlie the intrusive rocks. Multiple phases of magmatism and sedimentation have been recognized in Martabe district, are provisionally divided into six major units:

(1) Palaeozoic carbonaceous metasedimentary rocks of the Tapanuli group (Put),

(2) Palaeozoic Uluhalanagodang granite, coralated to the Sibolga granite complex (Mpi),

(3) Tertiary Sibarus formation mainly composed of siltstone, sandstone and conglomerate (Tms),

(4) Tertiary Angkola volcanics of basalt-trachyte-andesite composition (Tmav),

(5) Tertiary Toru volcanics of porphyritic andesite (Tmtv),

(6) Late-Tertiary dacitic-andesitic Martabe dome/intrusion (Tpid and Tpia) and diatreme.

The Martabe gold district is hosted in a sequence of Tertiary volcanics/instrusions and sedimentary rocks with the principal host rocks being a series of multiphase phreatic and phreatomagmatic breccia units that show temporal and spatial variability in texture and composition. The Martabe district geology is presented in Figure 3.3 and the stratigraphy is illustrated schematically in Figure 3.4. Detailed geological cross-sections for the Purnama (Figure 3.5) and Baskara (Figure 3.6) and Gerhana (Figure 3.7) depositss show the spatial relationships between the major lithologies.

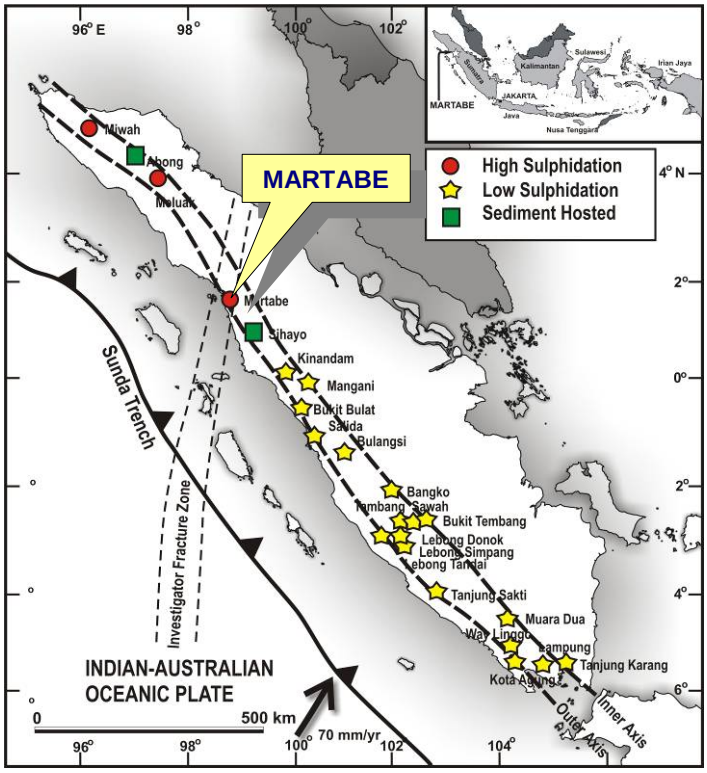

Figure 3.1. Regional location map showing the Martabe epithermal high-sulfidation gold deposits and Neogene gold depositsin Sumatra (modified from Crow and van Leuween, 2005).

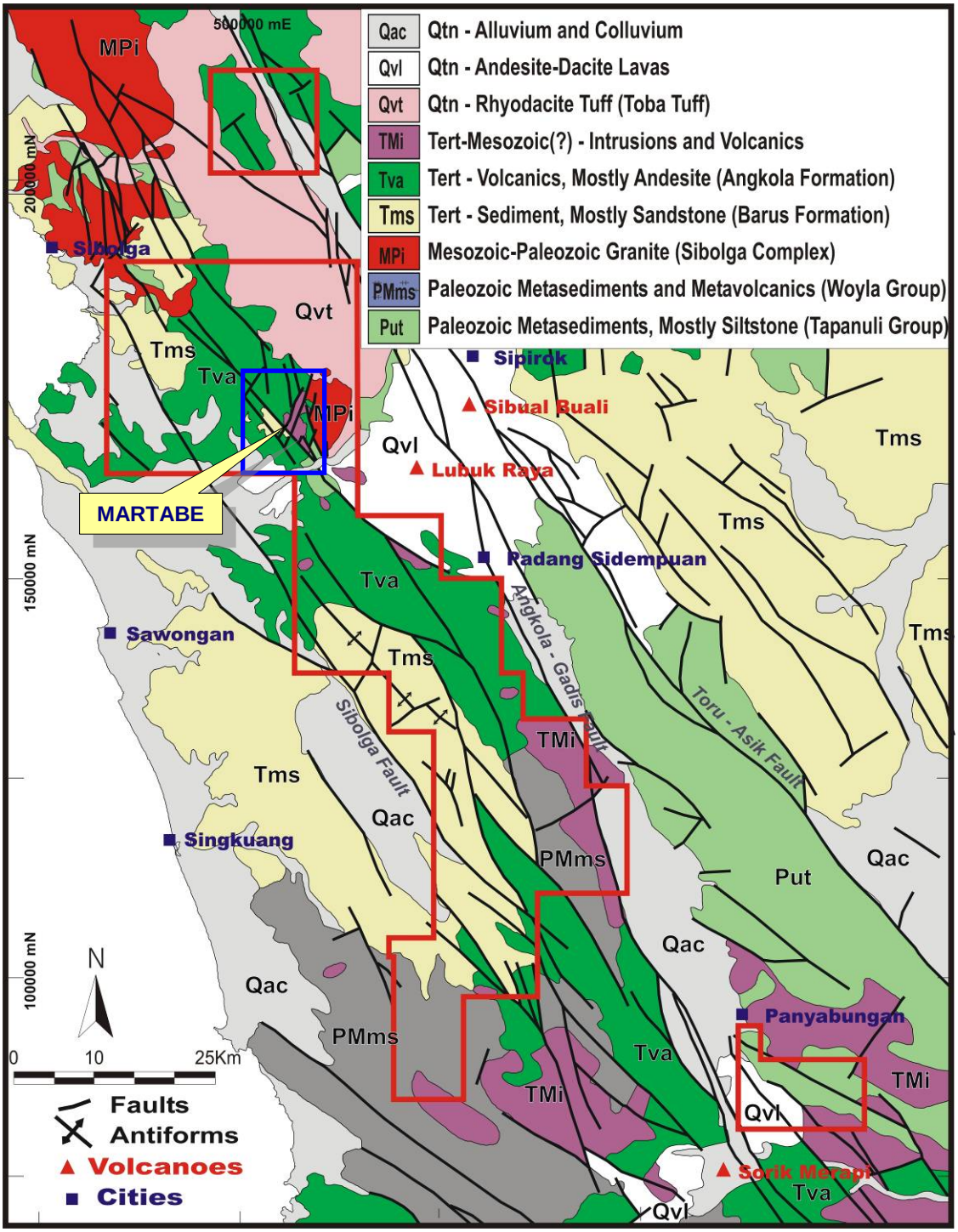

Figure 3.2. A simplified geological regional map of the northwestern Sumatra, Indonesia. Martabe district is shown in blue box within the Sibolga Contract of Work (CoW) tenement that isoutlined in red (courtesy G-resources).

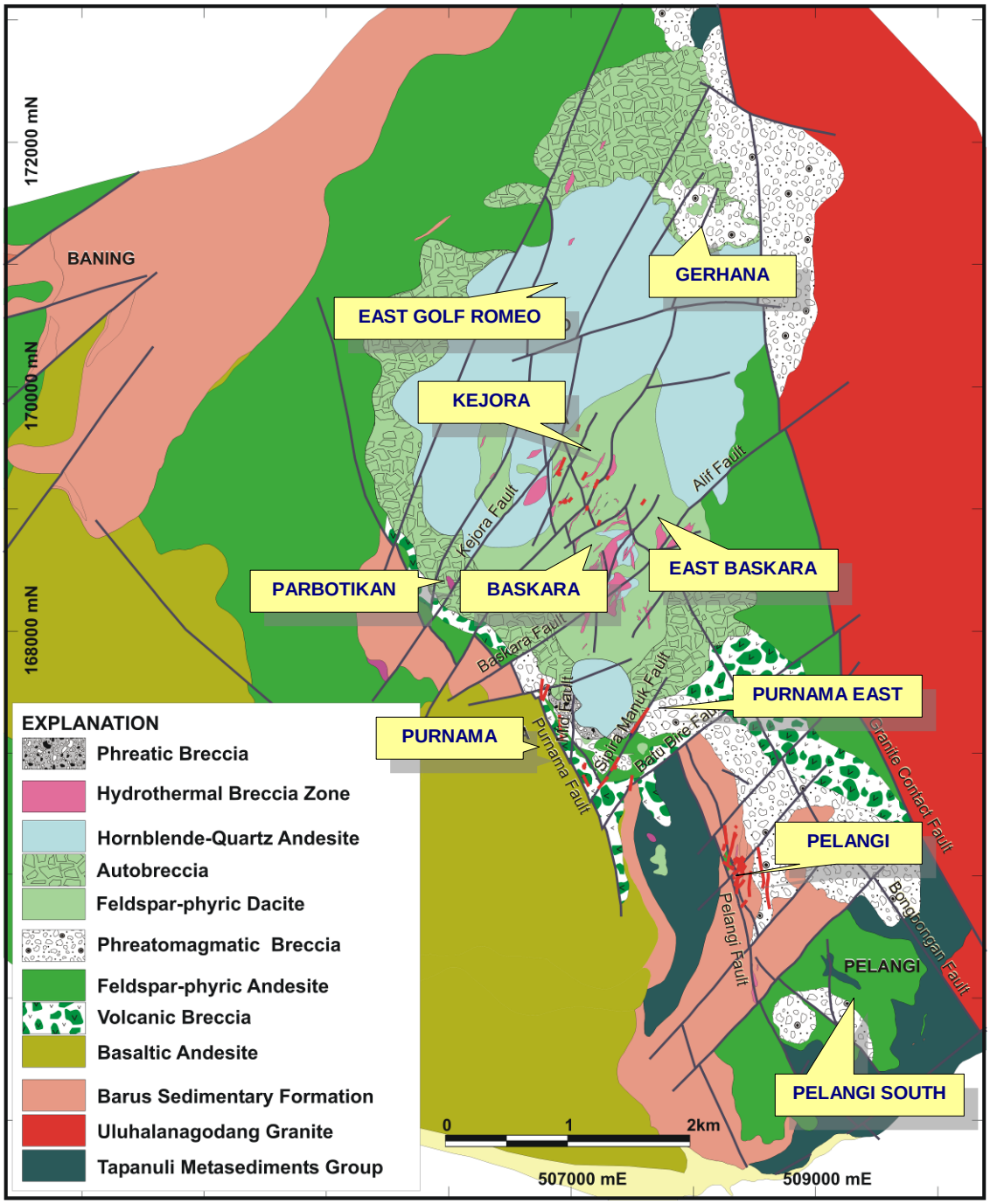

Figure 3.3. Geology of the Martabe district showing the location of epithermal deposits (courtesy G-resources).

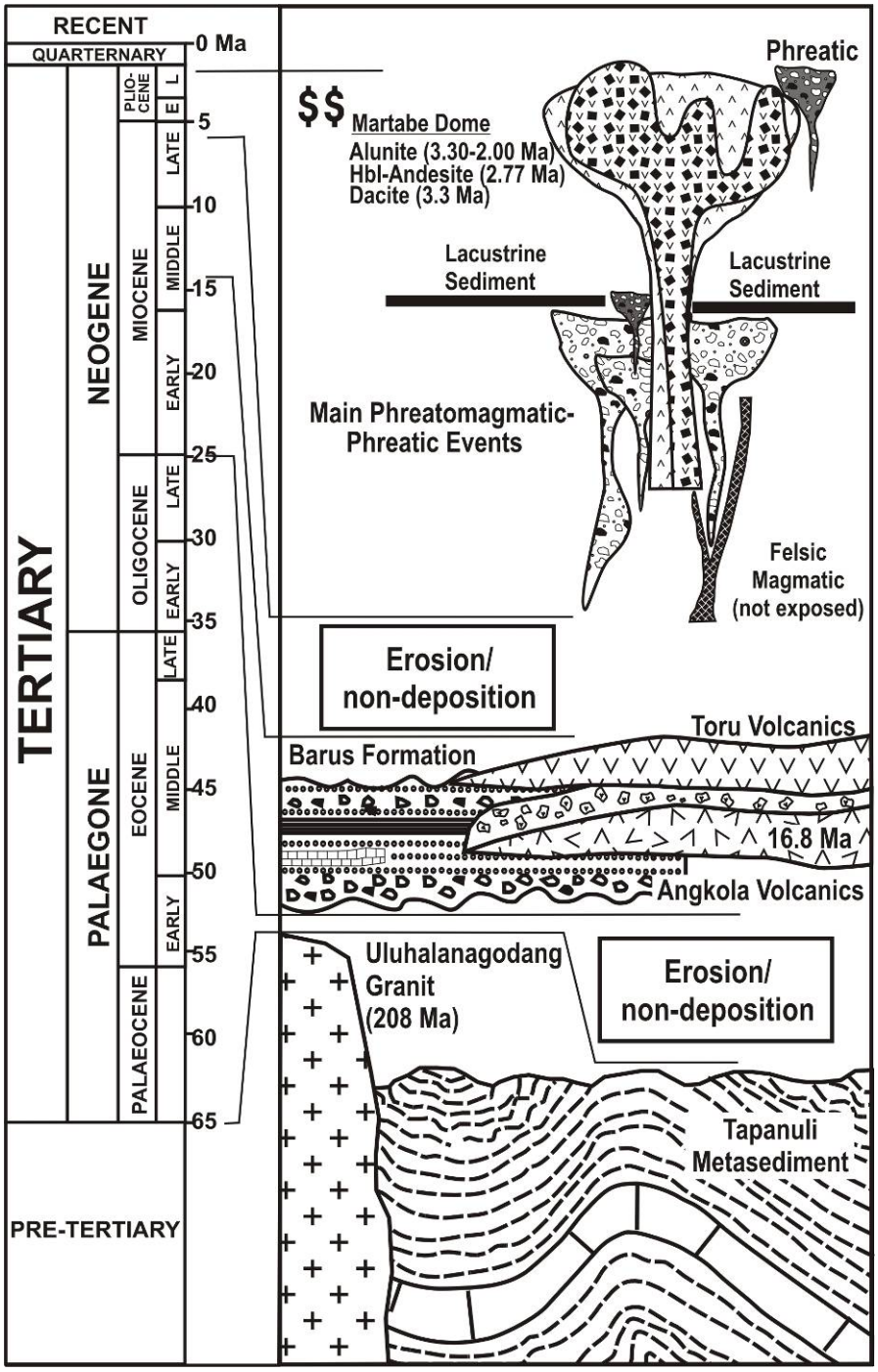

Figure 3.4. A simplified geological event diagram for the Martabe district. Stratigraphy modified from Crow (2005), Hickman et al. (2004) and De Smet and Barber (2005).

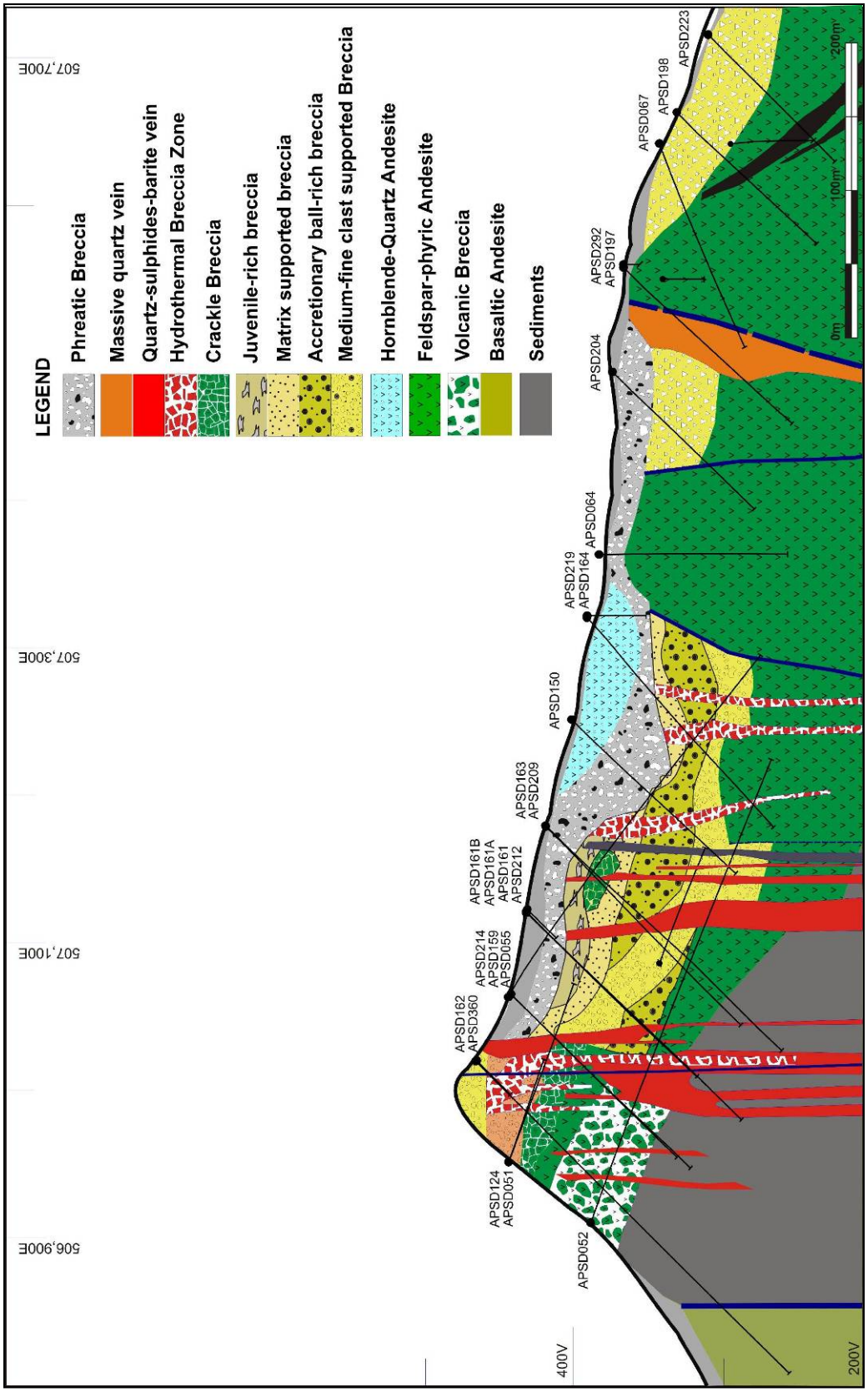

Figure 3.5. An interpreted east-west geological cross section (section 167200 mN) at Purnama.

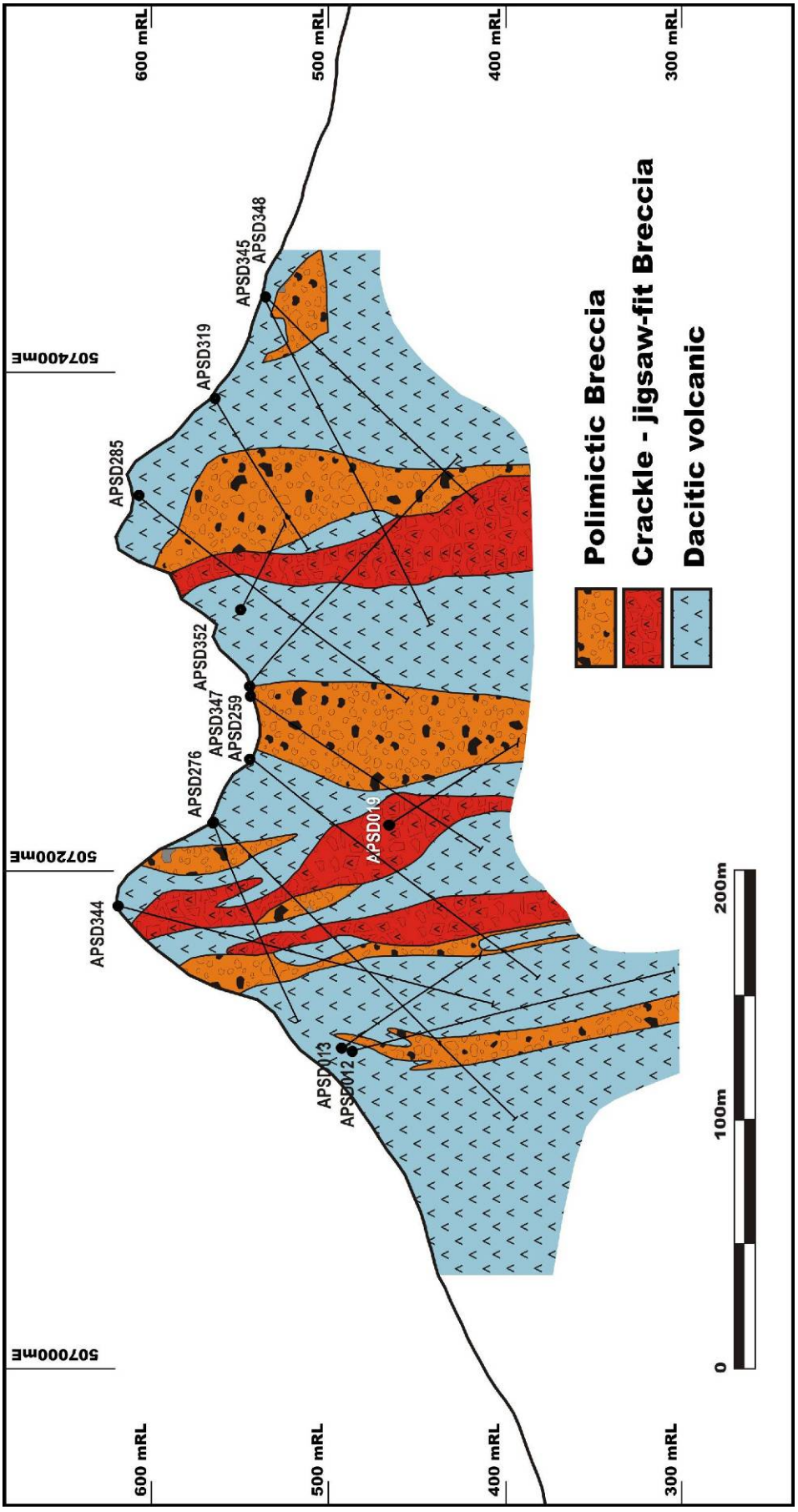

Figure 3.6. An interpreted northwest-southeast geological cross section (section OB-96) at Baskara.

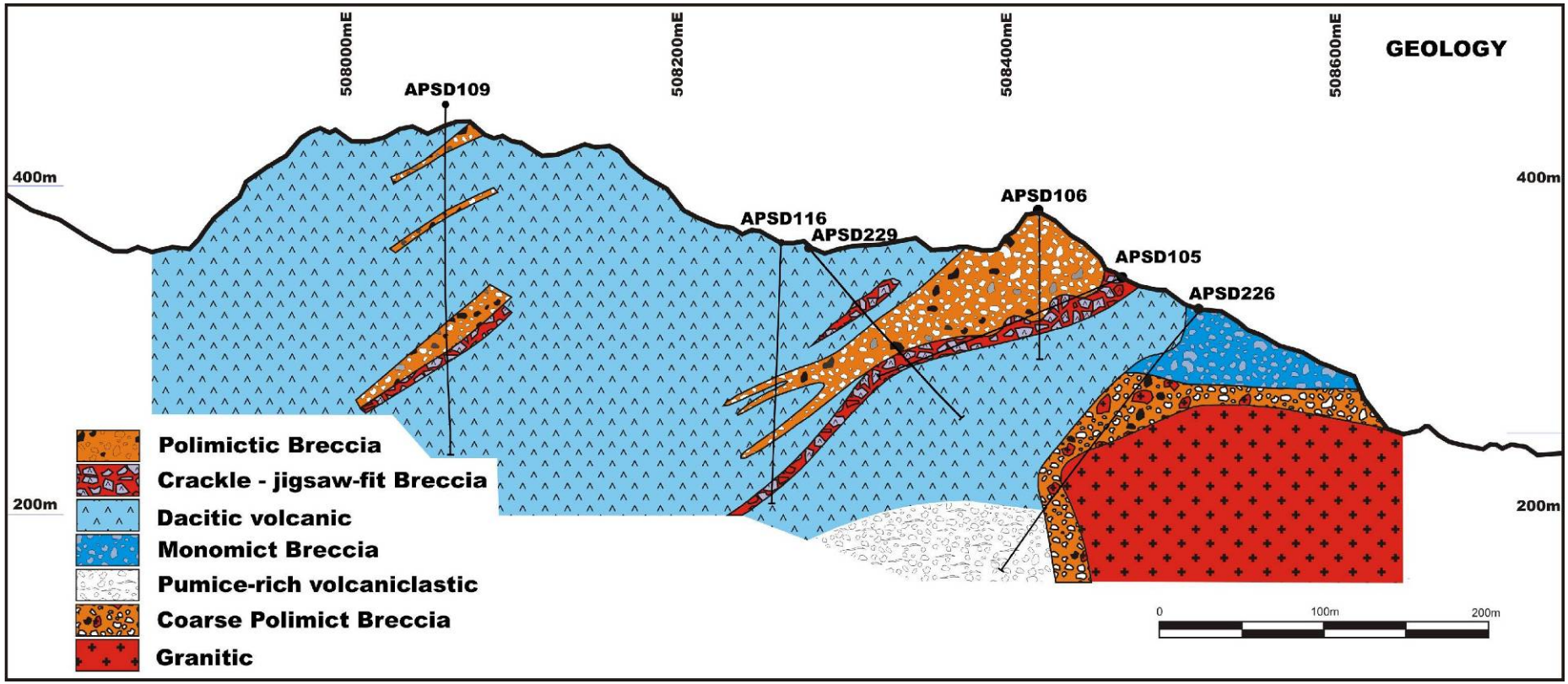

Figure 3.7. An interpreted east-west geological cross section (section 172000 mN) at Gerhana.

3.3. Pre Tertiary Lithologies

3.3.1 Late Palaeozoic-Tapanuli Metamorphic Group (Put)

Throughout the Sibolga Contract of Work (CoW) tenement (Figure 3.2) and the Martabe district (Figure 3.3), the oldest recognised rocks have been assigned to the Permian-age Tapanuli Group (Put). This group is interpreted as metasedimentary and carbonate rocks that form the basement to the area. The lithologies consist primaly of flysch-type sedimentary rocks; comprising gray to black meta-greywacke, carbonaceous mudstone-siltstone, shale-slate, fine-grained sandstone and minor conglomerate; with minor volcanic and epiclastic rocks. The major lithology is massive, oftenly unbedded, wackes (pebbly mudstones) which have clasts of schist, quartzite, vein quartz, granite and limestone. Locally occurring sedimentary textures include local graded bedding and small-scale ripple laminations. Metamorphic effects are generally weak. The structure, thickness and facies distributions remain unclear at this stage, although they are clearly associated with a west-northwest – east-south east trending zone of exposed basement rocks throughout the CoW, particularly in the northern of the CoW.

3.3.1.1 Tapanuli Group - origin and regional correlation

In the Martabe district, these rocks are exposed within the Batangtoru River to the east, where they are locally contact metamorphosed by the Uluhalanagodang Granite (Figures 3.8 and 3.9). The Tapanuli Group was intensely deformed during late Early to Middle Permian times. This major orogenic event was also accompanied by regional (greenschist facies) metamorphism, and at this time the major phase of the Sibolga granite (and Uluhalanagodang granite) was emplaced (Cameron et al. 1980). The Tapanuli Group is interpreted as being a submarine turbidite deposit that has been subjected to low-grade metamorphism (Aspden et al., 1982).

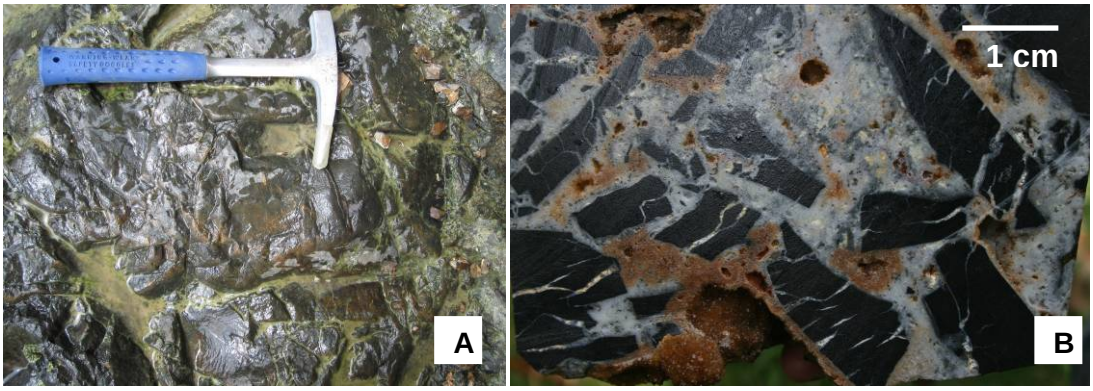

Figure 3.8. (A) A gray to black, intensively fractured, unbedded, meta-greywacke to siltstone, exposed in the Batangtoru river. (B). A monomict breccia consisting of Tapanuli metasedimentary clasts, cemented by quartz.

Figure 3.9. Tapanuli metasedimentary rocks on the banks of the Batangtoru river, locally contact metamorphosed by the Uluhalanagodang granite.

3.3.2 Permo-Triassic - Uluhalanagodang granite intrusive (Mpi)

The Uluhalanagodang granite is a large composite batholith of granite to diorite composition, which outcrops extensively at the eastern part of the Martabe district (Figures 3.2 and 3.3). The granite forms both intrusive and fault contacts with the metasedimentary Tapanuli Group. The granitic complex is tectonised in part, with areas of mild sericite-chlorite-pyrite alteration adjacent to regional structures.

Aspend et al. (1982) proposed that the Uluhalanagodang granite is Miocene, in age that was obtained from the Timbahan granite complex to the west of the Panyabungan graben (Figure 3.2). The age of the Uluhalanagodang granite remained poorly constrained until 2004. However, based on two ^{40}K-^{40}Ar ages, the granite is between 208.59 $\pm$ 0.07 Ma and 209.26 $\pm$ 0.19 Ma (Turner, 2004), or approximately the same age as the Sibolga granite

complex (212±3 Ma, McCourt, 2005) that forms a batholithic size intrusion complex 20 to 40 kilometres northwest of Martabe (Figure 3.2).

Two samples of granite were collected for age dating (Figure 3.10). Both samples are a coarse-grained quartz-phyric, biotite-hornblende granite. The samples were collected at about 2 km east of the Gerhana deposit, on the western side of Uluhalanagodang granite.

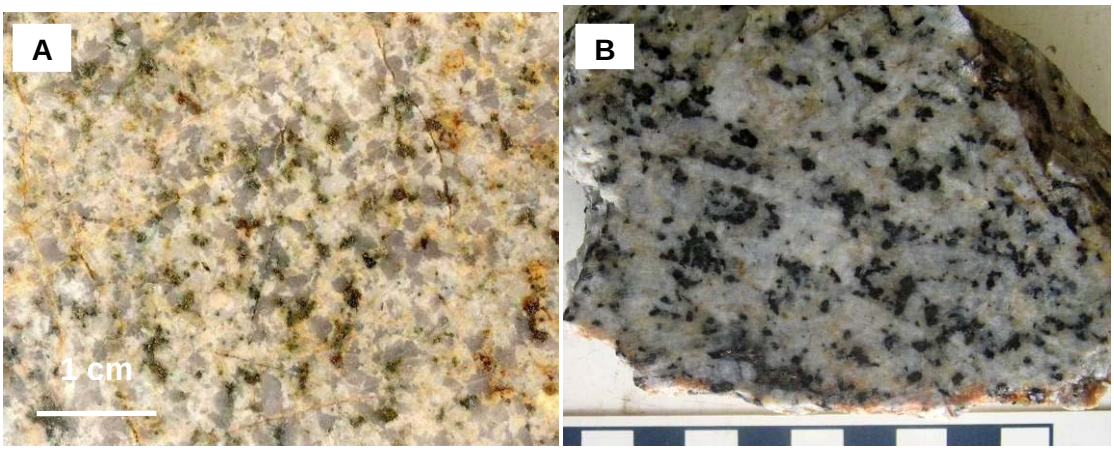

Figure 3.10. Uluhalanagodang granite (A) pinkish-white-greenish coarse-grained variety and (B) white-dark medium-grained granite (Sample No: Ulu-Granite_01 and Ulu-Granite_2).

3.3.2.1 Uluhalanagodang granite - origin and regional correlation

The main phase of Sibolga granite complex is Permo-Triassic, but younger centres are known to exist (e.g. in the Aek Haporas near the Sibolga town) (Aspden et al., 1982). This partially unroofed Sibolga Granite Complex is the oldest dated intrusion of the CoW. The Uluhalanagodang granite is probably separated from the main mass of the batholith (the Sibolga Granite Complex) by over 20 km of right-lateral, strike-slip offset related to the Sumatra Fault System (Figure 3.2). It is likely that the granite formed as a young intrusive satellite of Sibolga Granite. The granite's geochronology is discussed in a Chapter Four.

3.4 Tertiary lithologies

The Tertiary lithologies in the Martabe district are composed of a late Oligocene to middle-Miocene age of Sibarus sedimentary formation (Tms – 'Tertiary Miocene Sibarus'), the Miocene-Pliocene of series the Angkola mafic lava flows (Tmav – 'Tertiary Miocene Angkola volcanic'), volcaniclastic sequences (Tmab – 'Tertiary Miocene Angkola volcanic

breccia'), and the Toru porphyritic andesite intrusive (Tmtv – 'Tertiary Miocene Toru volcanic').

3.4.1 Tertiary sedimentary rocks of Sibarus Formation (Tms)

The late Oligocene to middle Miocene Sibarus sedimentary formation consists of conglomerate, sandstone (sometimes micaceous) and siltstone with minor sandy limestone and carbonaceous shale that is exposed in the central and southeastern parts of the Martabe district (Figure 3.3) and at numerous locations within the CoW (Figure 3.2). Cross-bedded and massive units are most common but fine laminated units are also present. Purnama and Pelangi drill data and regional mapping suggest that the Sibarus sedimentary rocks underlie most of the Martabe district. A fossil, globacirena from sandy limestone collected below the Angkola volcanics (Tmav), is interpreted to be 12-25 Ma, early to mid-Miocene (Lunt, pers. com., 2001). Thick layered, gently- to moderately dipping, medium- to coarse-grained sandstone and conglomerate are exposed at the Pelangi deposit, forming prominent cliffs (Figure 3.11). These rocks are strongly silicified and therefore resistant, whereas the Sibarus formation elsewhere in the district tends to be friable and weakly indurated. Well-bedded to massive carbonaceous siltstone and sandstone crops out below andesitic volcanic breccias in the southern part of Purnama.

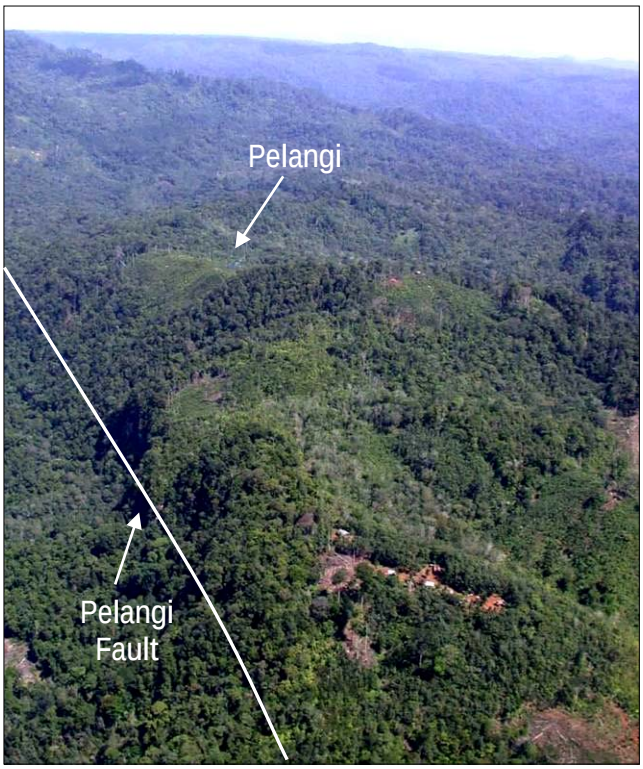

Figure 3.11. Thick layered gently- to moderately east dipping sandstone and conglomerate of Sibarus Formation at the Pelangi prospect. View toward north.

3.4.1.1 Facies Tms 1 – Laminated carbonaceous mudstone

This facies consists of dark grey to black, finely laminated (1-3 mm) carbonaceous mudstone (Figure 3.12). Laminations are generally planar, but are locally wavy planar. Light to medium grey laminae consist of fine sand- to silt-sized quartz grains. Dark grey laminae consist of clay- to silt-sized grains and are rich in organic material. This unit is locally bioturbated, especially where fine sand to silt component increases. Rich fossil beds from 1-2 cm occur locally in very fine-grained, clay-rich, black carbonaceous mudstone beds. This facies crops out at the Baning prospect, 3 km to the west form Baskara deposit.

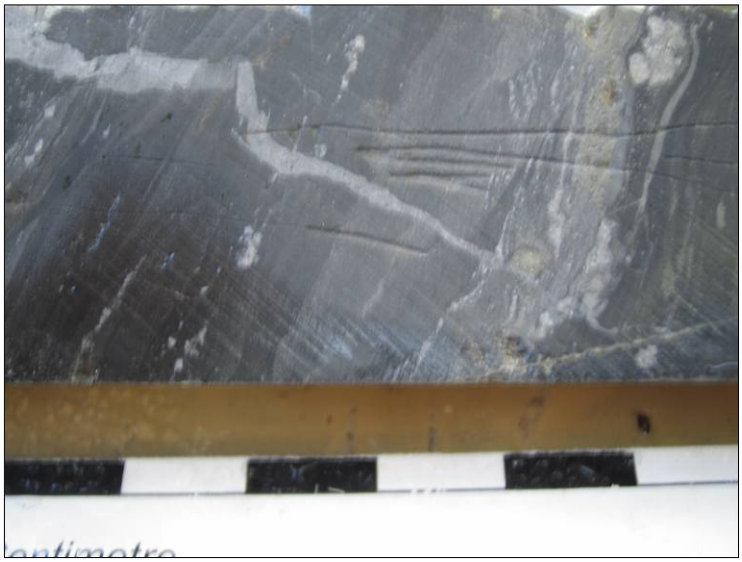

Figure 3.12. Dark grey, finely laminated carbonaceous mudstone that is rich in organic material (Tms1). Sample APSD441 depth 113m.

3.4.1.2 Facies Tms 2 – Thinly-interbedded carbonaceous mudstone and fine sandstone

This facies consist of interbedded carbonaceous mudstone and fine-grained quartz sandstone (Figure 3.13). In drillcore, it varies from light to dark grey in color depending on the abundance of carbonaceous mudstone. The sandstone component is well-sorted and consists of rounded to sub-rounded, quartz-dominated and fine-sand sized grains (<1mm), whereas mudstone layers contain abundant carbonaceous organic material. Mudstone/siltstone beds are typically 0.5 to 10 cm thick, however, sandstone beds can be as thick as 1.5 m, particular at higher stratigraphic levels. Thinly-bedded intervals are typically characterized by lenticular bedding and less commonly wavy planar bedding. Medium to thick quartz-sandstone (>0.10 m to 1.5 m) beds are light grey and locally

trough cross-bedded. Abundant, discontinuous wisps of black organic material are present throughout the sandstone beds.

Figure 3.13. Light to gray laminae consists of interbedded fine sand and carbonaceous siltstone (Tms2). Sample APSD442, depth 105 m.

3.4.1.3 Facies Tms 3 – Thinly to thickly bedded quartz sandstone with thin carbonaceous mudstone interbeds

This facies varies from thinly- to thickly bedded sandstone, with subordinate interbedded thinly- to very thinly- bedded carbonaceous mudstone (Figure 3.14 and 15). The sandstone is light grey, well sorted, and consists of sub-rounded to rounded quartz grains. Thin beds are planar wavy planar and laminated. Medium to thickly-bedded (2 to 30 cm) quartz arenite beds rarely show cross-bedding. Thick quartz sandstone beds (> 5 m) are locally present. Fine carbonaceous wisps commonly define laminations or ripple troughs in the sandstone units. These quartz-sandstone beds are interbedded with 1 to 2 cm lenticular carbonaceous siltstone and fine sandstone beds. Cross bedding is not consistently oriented. In general, bed thickness of both quartz sandstone and carbonaceous siltstone beds increases up section.

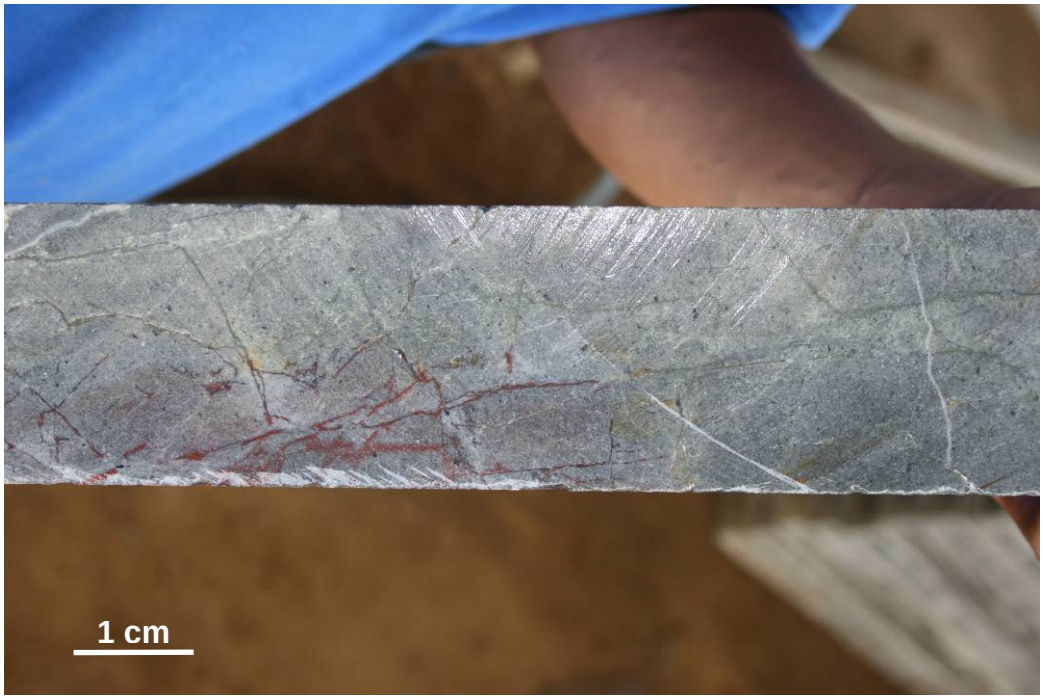

Figure 3.14. Light grey sandstone that is well-sorted and consists of rounded to sub-rounded, quartz grains (Tms3). Sample APSD442, depth 70 m.

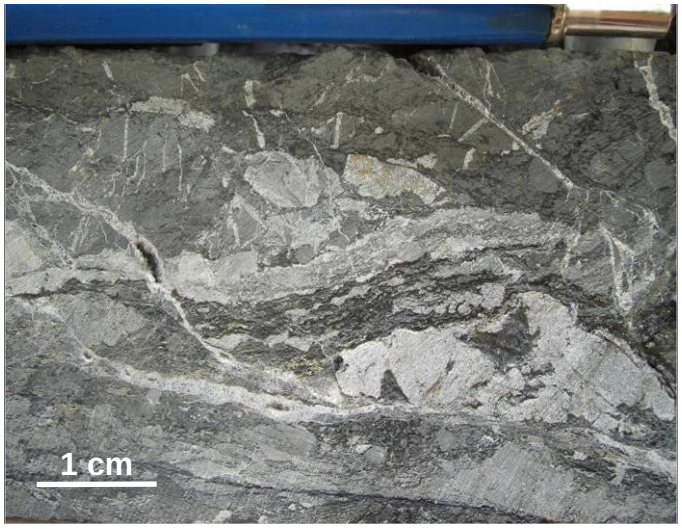

Figure 3.15. Thinly to thickly bedded quartz sandstone with thin carbonaceous mudstone interbeds (Tms3). Sample APSD412, depth 50 m.

3.4.1.4 Facies Tms 4 – Quartz sandstone and lithic conglomerate

Well-sorted, quartz and lithic-rich sandstone and conglomerate (Figure 3.16) is exposed at the southern end of the Martabe district, in particular forming cliffs at the Pelangi deposit (Figure 3.11). Thick to very thick (up to 5 m) planar quartz sandstone-conglomeratic sandstone beds are massive to weakly trough cross-bedded. Medium wavy beds show low angle cross stratification and broad channels are locally visible. In contrast

to other Sibarus facies, this unit lacks an abundant carbonaceous organic component and the sandstone is buff to light orange.

Figure 3.16. Conglomerate consisting of well-sorted, sub-round to round coarse-grained quartz and lithic fragments in sandy matrix (Tms4). Sample APSD410, depth 12.8 m.

3.4.1.5 Sibarus formation- origin and regional correlation

Based on regional correlations, these sedimentary rocks belong to the late Oligocene to middle Miocene Sibarus sedimentary formation (Aspden, 1982). However within the Martabe district, the oldest facies of the Sibarus sedimentary rock is the Tms1 carbonaceous mudstone unit, as seen in Pelangi drillcore and sections. Overall, there is a progressive change up-section from carbonaceous mudstone to siltstone and then sandstone through facies Tms2, Tms3 and Tms4. A general change to the tractional bedfroms and bioturbation in facies Tms2, and the presence of coal beds in facies Tms3, indicates a change from deep to shallow water sedimentation and a shift to more terrestrial depositional environments up-section. Tms4 is tentatively placed stratigraphically above Tms1 and to Tms3, but structural complexities have prevented observation of key contact relationships.

3.5 Tertiary volcanic lithologies

In Sumatra, the late Early to Mid Miocene-volcanic episode consists of two phases. A volcanic arc was formed parallel to the west coast and high-K and shosonitic magmatism

occurred in the Central Sumatra Back arc Basin. Similar igneous activity occurred in the South Sumatra Basin between 17 and 12 Ma (Crow, 2005).

Although volcanic clasts are present in the conglomeratic sandstone of the Sibarus sedimentary formation at Sibolga town, the oldest volcanic rock outcrops recognized at Martabe are Miocene volcanic rocks of basaltic and andesitic composition. The volcanics lie above, or are sometimes interbedded (?), with the Sibarus formations (Figure 3.3).

At Martabe overlying the Sibarus sediments are coherent mafic volcanic flow and volcaniclastic rocks. This volcanic sequence is of unknown thickness, and consists of near flat lying basaltic, trachytic and andesitic lava flows and volcanic breccias facies.

3.5.1 Miocene Angkola Volcanic Formation (Tmav)

The Angkola Volcanic Formation (Tmav) is widespread and divided into four facies (Figure 3.3).

3.5.1.1 Facies Tmav 1 – Coherent basalt

The coherent basaltic facies is observed in the Aek Pahu river, at the Pelangi deposit to the southeast and at the Parbotikan prospect to the west. Generally these units could be mapped along the strike for tens of meters but their overall extent was difficult to determine due to vegetation and erosion. Several flows were mapped within the volcanic breccia (Tmab) sequence at Parbotikan. Exposures at the Parbotikan prospect and in the Aek Pahu river show that flow thickness can be as great as 5–10 m. The coherent basaltic lava facies is aphanitic, black to dark greenish, unaltered to weakly altered with a weak magnetic response (Figure 3.17 and 3.18). It consists of fine laths of plagioclase with lesser amount of olivine, pyroxene and relict magnetite (?) set in a glass groundmass (Figure 3.18). Phenocryst abundances range from 2 to 5%. Sub- to euhedral tabular plagioclase exhibits multiple twinning and oscillatory zoning that ranges from 1 to 3 mm. The fine grained groundmass consists of mafic minerals and feldspar. Weak fracture-controlled alteration consisting of chlorite, clays and calcite is observed.

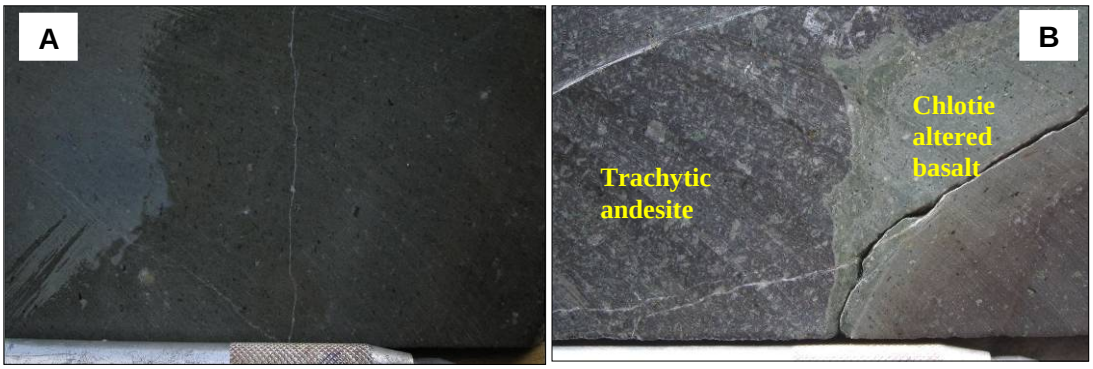

Figure 3.17. (A) Aphanitic, black unaltered basaltic lava (APSD001_55.2). (B). Contact between coherent porphyritic trachytic-andesite and chloritic-altered basaltic andesite (APSD001_35.3).

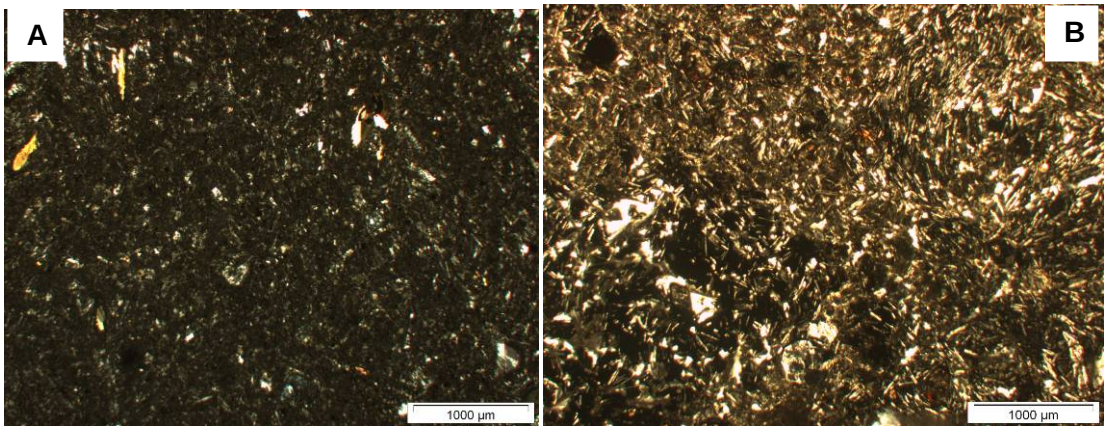

Figure 3.18. (A) Aphanitic, fine grained plagioclase laths and olivine in glass groundmass (APSD001_55.2). (B) Fine laths of plagioclase showing flow texture in basaltic lava. (APSD001_55.2).

Numerous basaltic dykes and minor sills occur in the basaltic lavas at Purnama. They are grey to dark green, massive and typically aphyric. Locally, fine pyroxene and/or olivine phenocrysts are visible. Wall rock contacts are either sharp or irregular and marked by zones of basalt-cemented, wall-rock-clast breccia as seen at Pelangi. Dykes range in thickness from 10 cm to 5 m, but are generally 1 to 3 m thick, and they are predominantly hosted by basaltic flow facies. The flows range from 3 to more than 40 m in thickness. At Purnama, dykes occur in drill cores APSD001, APSD003 and APSD005. A few dykes have also intruded the Sibarus formation at Pelangi. Due to the limited amount of drill core, the dykes can not be correlated.

The coherent basalt facies is commonly associated with coherent basaltic andesite, coherent andesite, volcaniclastic and/or volcanic breccia facies. Textures associations indicate that the coherent basalt facies represents the coherent parts of basalt dikes and flows. The majority of this facies is extrusive flows.

3.5.1.2 Facies Tmav2 - Coherent trachytic-basalt

This facies is part of the mafic rocks with trachytic texture. This facies consists of mainly augite, labradorite- bytownite and titanomagnetite±ilmenite. A subparallel arrangement of microcrystalline lath-shaped feldspars in the groundmass of the holocrystaline or hypocrystalline rock is common (Figure 3.19).

The coherent trachytic-basalt facies is commonly associated with the coherent basaltic facies. It has been identified only in drillcores APSD001, APSD003 and APSD005.

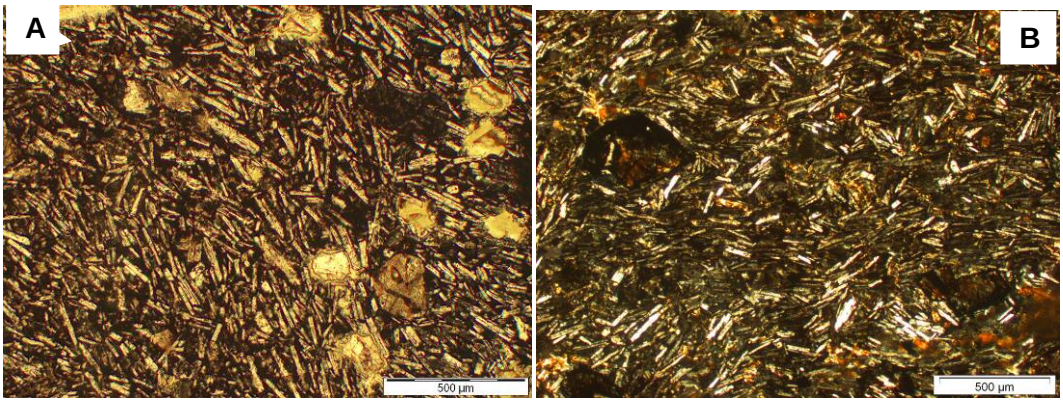

Figure 3.19. (A) Fine laths of aligned plagioclase showing flow texture in trachytic basaltic (APSD003-86.9). (B) Fine- to medium olivine phenocrysts in groundmass (APSD089_9).

3.5.1.3 Facies Tmav3 - Coherent andesitic basalt

The coherent andesitic basaltic facies contains fine grained phenocrysts of dull white feldspar in a dark brown to grey, bleached, weakly to moderately altered, aphanitic matrix (Figure 3.20). Phenocryst abundances range from, 2 to 15% (average of 5%) and are predominantly plagioclase with smaller amount of pyroxene, amphibole and magnetite (Figure 3.21). Sub- to euhedral tabular plagioclase phenocrysts, that can exhibit flow alignment, range in size from 1 to 5 mm. The fine-grained groundmass consists of micro-granular feldspar and glass. This facies is variably altered to chlorite, calcite and illite.

This facies is commonly associated with other coherent basalt, tuff, non-stratified monomict andesite breccia facies and non-stratified sediment matrix andesite monomict breccia facies. Textures and facies association indicate that the coherent andesitic basalt facies represents extrusive lava flows.

The coherent andesitic basalt facies is observed throughout the Purnama and Pelangi deposits. It is dominant facies in the Purnama footwall, but is rare in the Baskara. Lithologic contacts between coherent flows are not always clearly defined. Single units range in thickness from 50 cm in Purnama to 20 m at Pelangi footwall. Varying degrees of

alteration along contacts and variations in phenocryst size between layers are the discriminator of unit boundaries.

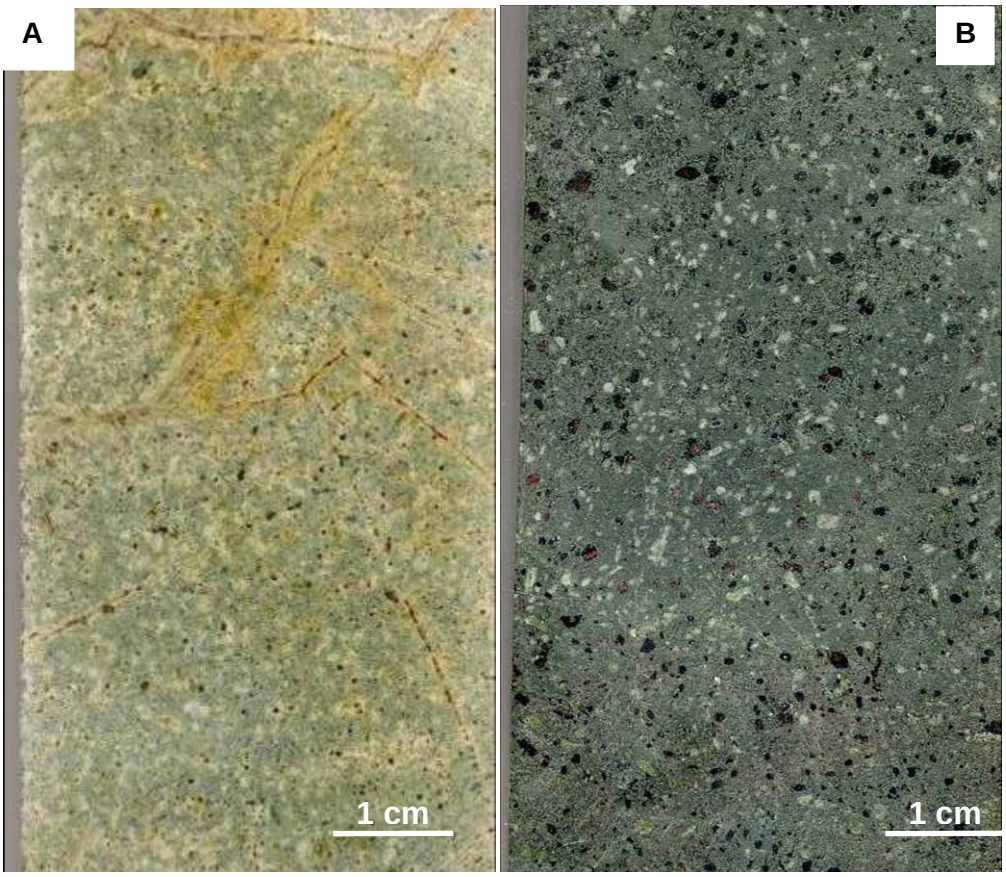

Figure 3.20. (A) Coherent andesitic basalt altered to chlorite (APSD003_15). (B) Weakly to unaltered coherent andesitic basalt with abundant hornblende and plagioclase phenocrysts (APSD005_24).

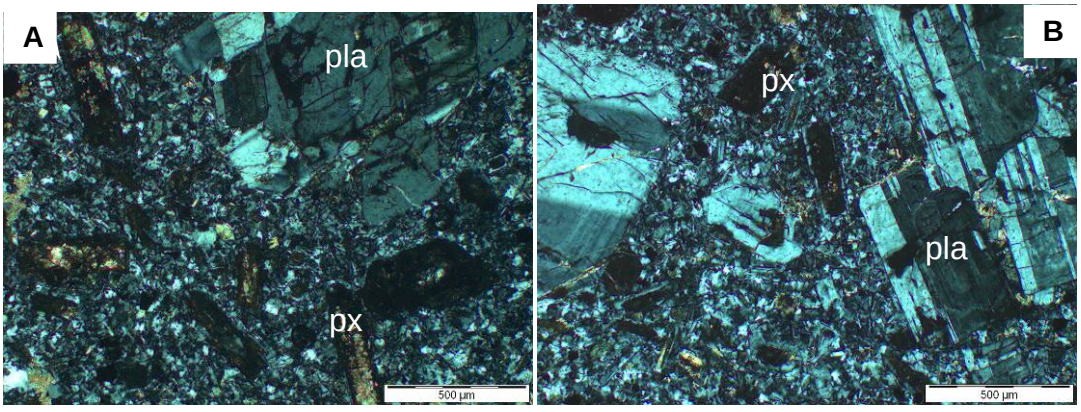

Figure 3.21. (A) Coherent andesitic basalt with pyroxene and plagioclase phenocrysts set in a fine grained groundmass. The rocks are weakly altered to chlorite and calcite (APSD090_98-2). (B). Euhedral plagioclase and pyroxene in a fine grained groundmass. Plagioclase, pla and pyroxene, px (APSD090_98-2).

3.5.1.4 Facies Tmab – Basaltic-andesite volcanic breccia

This volcanic breccia is a coarse, heterolithic, fragmental rock composed primarily of sub-rounded, volcanic clasts but locally contains sandstone and siltstone clasts. It is unstratified, greenish to reddish to grey, often bleached, clast- to matrix-supported and poorly sorted.

The clasts consist of coherent porphyritic, coherent andesite facies (Tmav 3) and trachytic basaltic facies (Tmav2) as polyhedral blocks, ranging in size from 1 to 10 cm, with curvi-planar and angular surface set in fine-grained matrix (Figure 3.22). The primary minerals of the fresh volcanic rock are quartz, andesine, hornblende, pyroxene, biotite, titanomagnetite and magnetite. Basaltic (Tmav2) clasts, consisting of plagioclase, augite and a small proportion of magnetite, show a range in sizes of plagioclase and augite crystals (<0.01-0.5 mm). Phenocryst abundances range from 2 to 10% and are predominantly remnants of plagioclase with lesser amounts of pyroxene and amphibole. Phenocrysts range from 1 to 3 mm in size. The fine grained groundmass consists of micro-granular feldspar (Figure 3.23). The matrix is fine grained, hematitic mudstone that is composed of micro-granular feldspar.

An intense quartz alunite alteration commonly occurrs at the contact between the Tmab and the porphyritic andesite (Tmtv) or diatreme breccias. Some basaltic andesite clast are strongly bleached, oxidized and have illite-altered rims (Figure 3.22). Alteration intensity may vary between clast and matrix. These are generally weakly- to strongly-altered to dickite and kaolinite at Purnama, while clasts in this breccia west of the Purnama fault are generally unaltered to weakly altered. This volcanic breccia is an upper part of the sequence of the Angkola volcanic unit.

This monomict andesite breccia facies occurs above the coherent andesite (Tmav 3) flows at the Purnama, but rarely at Pelangi. Individual beds range from 1 to 5 m in thickness. This facies is gradational into the coherent basaltic andesite (Tmav 1) facies and is commonly associated with other flow, coherent porphyritic andesites (Tmtv), coherent trachytic basalt andesite (Tmav 2) and coherent basalt (Tmav 1).

The clast shapes, monomict composition and association with coherent andesite facies of the same composition suggest that the monomict breccia facies represents the clastic portion of andesite lavas. These clasts likely formed from brittle fragmentation (autobrecciation; Pichles, 1965) of solidified magma, due to tensile stresses exerted by adjacent or underlying ductile flowing magma.

The Tmab volcanic breccias were mapped at southeastern of Pelangi close to other breccias body (Pelangi breccias. The volcaniclastic (Tmab – 'Tertiary Miocene Angkola breccia') is observed on the Purnama cliff and at northern part of Pelangi. These coherent volcanic are generally unaltered to weakly altered and massive unit. On the contrary, the volcanic breccia is mostly altered to chlorite, kaolinite and dickite, in particular along the contact with upper unit.

In some intervals in the Purnama drill core, this volcanic breccia shows vuggy and massive quartz alteration. The coherent basaltic lava is likely the lower most facies of the Tmav with grading into trachytic-textured volcanic and andesitic lava composition. A volcanic breccia appears to be an upper part of the sequence. The volcanic breccia is mostly overlain by the andesite Toru volcanic unit (Tmtv). However, little is known about exploration potential of this facies to the west of Purnama Fault due to the lack of significant alteration and also because of the mostly gentle relief and infrequent exposure.

Figure 3.22. Comparison between weakly altered (bottom) and oxidized-kaolinite altered volcaniclastic (top). The volcanic breccias are coarse, heterolithic fragmental rocks composed primarily of sub-round volcanic clasts, but locally contains sandstone and siltstone fragments. The clasts commonly show hyaloclastic texture.

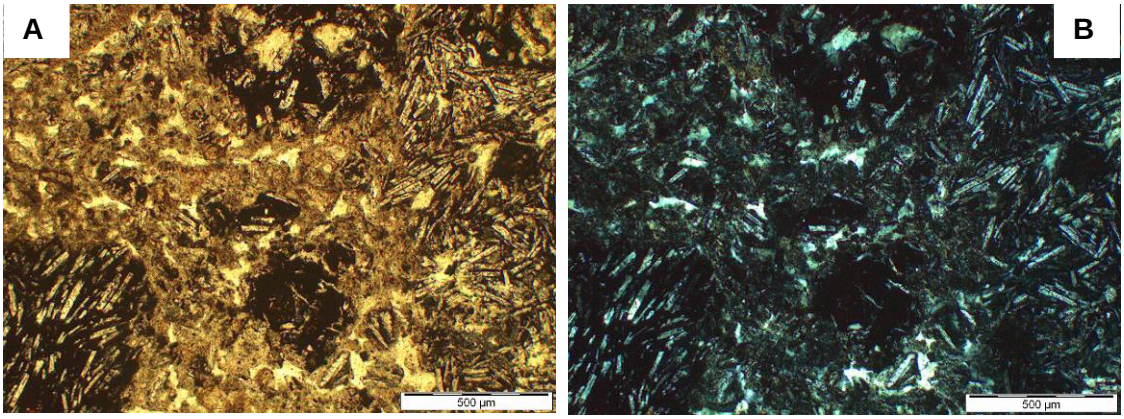

Figure 3.23. Clasts of trachytic basaltic set in fine grained plagioclase groundmass (A) in plain light. (B) in cross-nichols (APSD003_86.9).

3.5.1.5 Miocene Angkola Volcanic - origin and depositional environment

A K/Ar age of 18.91 ± 0.07 Ma (Turner, 2004) was obtained from basaltic andesite samples in drill hole APSD001_23. Other radiometric ages for the Angkola Volcanic unit are as young as 17 Ma (Barber, 2005). In the Martabe district, basalt lavas overlie the Sibarus formation units, therefore the extrusive basaltic units in the Martabe district are interpreted to have been deposited in a proximal volcanic setting during the early Miocene. Basalt dykes are inferred to be the sub-volcanic feeders to the extrusive units.

3.5.2 Miocene Toru coherent andesite (Tmtv)

This volcanic facies consists of plagioclase-phyric porphyry andesite. The andesite contains about 10–20% by volume of 1–3 mm of plagioclase phenocrysts and it is porphyritic. Primary mineralogy principally consists of plagioclase, hornblende, minor quartz, apatite and feldspar set in a fine-grained, interlocking groundmass (Figures 3.24 and 25). Trace pyroxene was observed locally and relict, primary magnetite crystals were also observed in some thin sections.

This facies is referred to as the Toru volcanic units (Tmtv). It is interpreted as lava flows because they have overlying contacts with coherent volcanic and volcanic breccia facies of the Angkola volcanic unit (Tmav) and/or non-volcanic sedimentary units. Several smaller andesite intrusions occur as dykes and plugs, such as at Pelangi and may be similar in age.

The Tmtv is an important host rock at Purnama, particularly where it is fractured and brecciated adjacent to the diatreme breccia. The margins of Tmtv are bounded by

northwest-trending fault in the west at Purnama and north-trending fault orientation in the eastern part (Figure 3.3).

Tmtv is typically moderate to strongly chlorite altered in the Martabe district, and it is difficult to find samples with well-preserved primary mineralogy.

It is unclear whether the andesite is single lava flow or consisting of texturally and compositionally multiple flows.

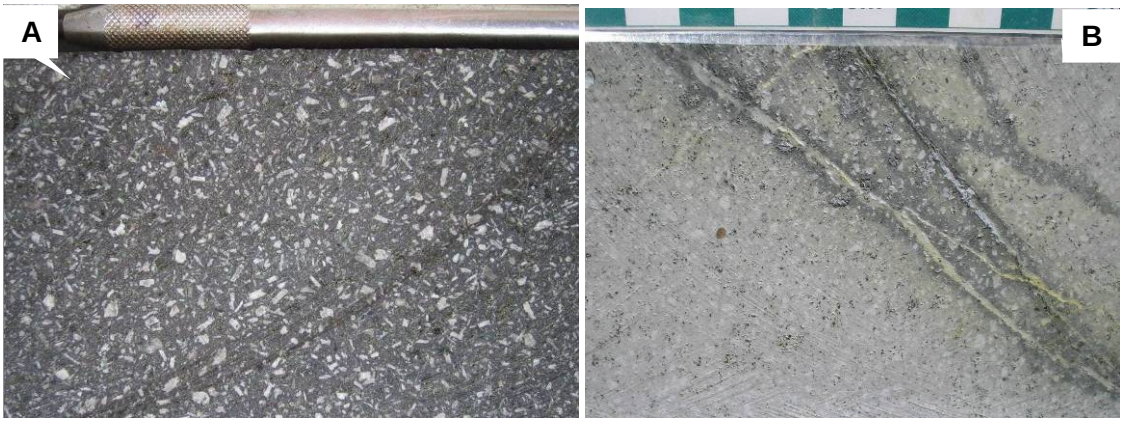

Figure 3.24. (A) Coherent andesite with hornblende and plagioclase phenocrysts. Sample from drillhole APSDD005. (B) Sample is altered to quartz- kaolinite with late pyrite-dickite veinlets. Sample from drillhole APSD067.

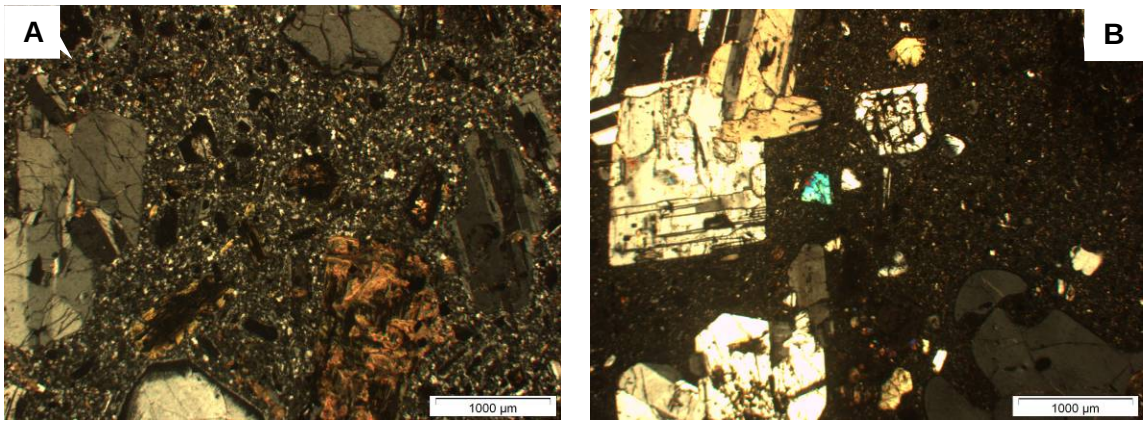

Figure 3.25. (A) Coherent andesitic basalt showing hornblende and plagioclase phenocryst set in fine plagioclase, pyroxene and hornblende groundmass with varying degrees of chlorite and carbonate prophylitic alteration (APSD090_98.5). (B) Euhedral plagioclase set in fine groundmass. Quartz with embayment texture at right bottom. In Tmtv, quartz is rarely present.

3.5.3 Pliocene Martabe dome complex (Tpi)

Multiple intrusions were emplaced along the north-trending fault on the western margin of the Uluhalanagodang granite complex (Figure 3.3). Emplacement of relatively coarse-grained porphyritic intrusions occurred late with regards to phreatomagmatic-phreatic brecciation. The intrusions are separated into two types; quartz-phyric dacite porphyry (Tpid) and hornblende-phyric andesite (Tpi). Overall, the intrusions and the phreatomagmatic-phreatic breccias are referred to as the Martabe dome complex.

3.5.3.1 Facies Tpid - quartz-phyric dacite

The dacite intrusion (Tpid) is porphyritic with plagioclase and quartz phenocrysts. The quartz-phyric dacite crops out north of Purnama and more extensively at Baskara and Kejora (Figure 3.3). The dacite contains phenocrysts of plagioclase (20-30%), biotite and hornblende (5-10%) and quartz (3-7%) (Figure 3.26). Textures include flow banding and autobreccia. Locally there are fine- to coarse grained pyroclastic rocks having the same composition. Flow banding is locally present near the margin of the intrusive bodies. The dacite is an important host for mineralization at the Baskara, Kejora and Gerhana deposits, but not at Purnama deposit.

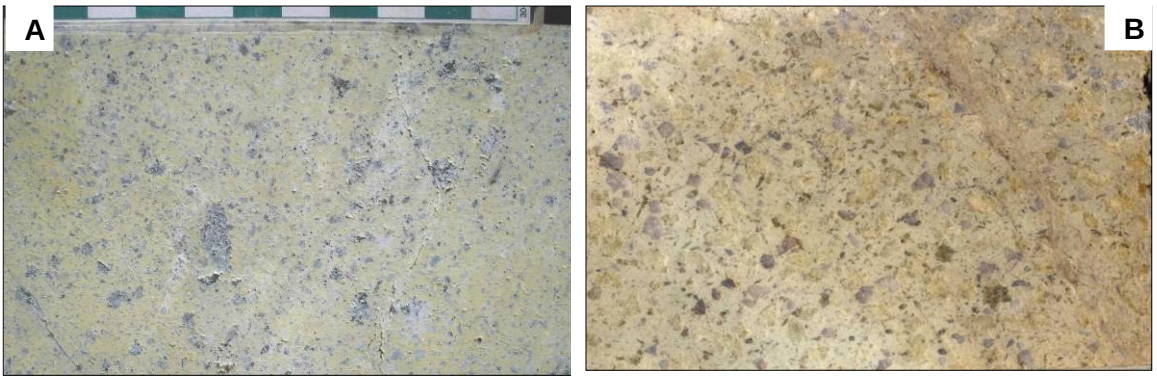

Figure 3.26. (A) Intense quartz-kaolinite altered-dacite with distinct quartz phenocryst (grey). (B). Quartz-alunite altered dacite, same scale as A. Sample from APSD125 at Purnama East.

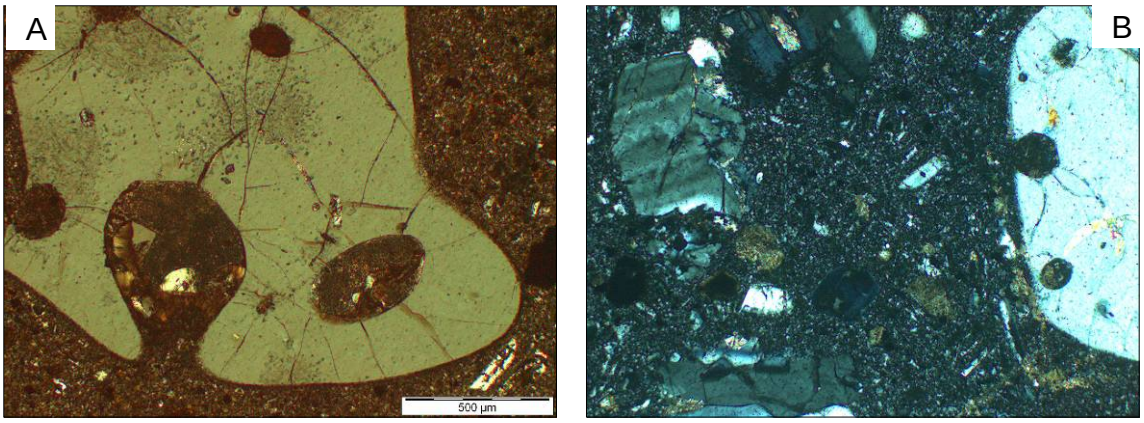

Figure 3.27. (A) Coarse (>3mm) embayed quartz set in fine groundmass of quartz-phyric dacite (APSD350_39-1). (B) Plagioclase and rounded quartz in groundmass. Hornblende altered to calcite (APSD350_39-1).

3.5.3.2 Facies Tpia – hornblende-phyric andesite

The hornblende andesite (Tpia) is a porphyritic rock with 10–15 % hornblende phenocrysts, commonly up to 10 mm in length, 15–25 % plagioclase feldspar grains and rare quartz (<2%) phenocrysts. The feldspar phenocrysts may be complexly zoned and embayed. The phenocrysts are in andesine, hornblende ± biotite and pyroxene(s) groundmass.

Mapping and drilling indicates that the Tpia occurs as a near-circular intrusion at Purnama (Figure 3.28). However, it occurs as irregular, mostly north trending dikes and small stocks at Baskara and Kejora. The rock is typically weakly propylitic altered at Purnama and is considered to be a late-stage intrusion, although vuggy-quartz alteration is present in it at Baskara. It is unclear whether the Tpia is a single intrusion, or consists of multiple, texturally and compositionally similar intrusions.

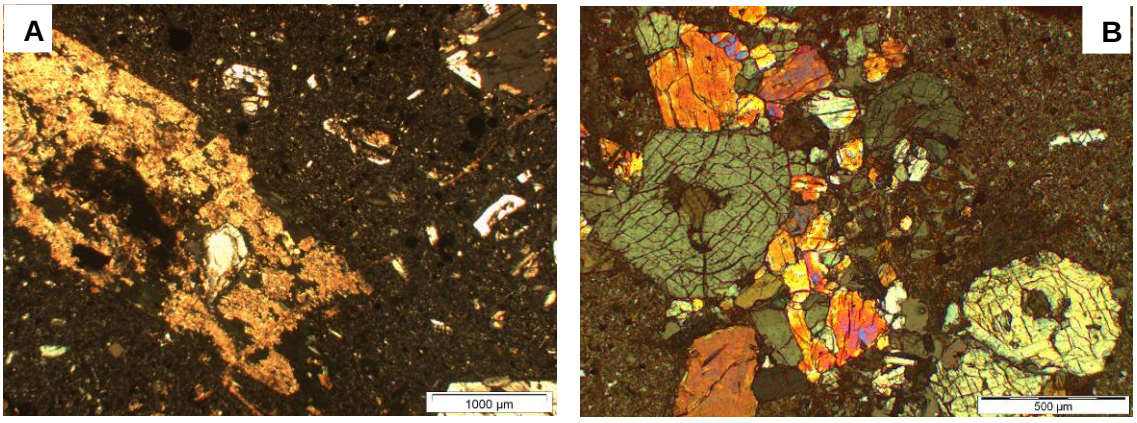

Figure 3.28. (A) Calcite replacing hornblende (APSD350_39-1). (B) Cluster of hornblende crystals (APSD350_39-1).

3.5.4 Late Tertiary phreatic and phreatomagmatic breccias

The Martabe deposit is hosted in the sequences of Tertiary carbonaceous mudstone and sandstone sedimentary rocks, volcanics and breccias. There are distinctive groups of hypogene breccias at Martabe that are mainly distinguished by the abundance of clasts and/or matrix of carbonaceous sedimentary lithologies and by alteration type, in particular from clay and quartz content in the cement and/or matrix (Levet, 2003). Collectively these hypogene breccias were described as diatreme breccias which have temporal and spatial variability in texture and composition.

During the Martabe exploration stage (1999-2005) these breccias were described using a combination of descriptive and genetic terminology and were classified into two groups 'sBPM' and 'cBPM'. The first breccia group is intensively silicified and was classified as 'quartz-altered phreatomagmatic breccia' or 'sBPM'. This breccia is a light to dark gray, 'muddy matrix breccia' that contains abundant finely comminuted carbonaceous mudstone wall rock and is completely or partially silicified with fine-grained disseminated pyrite (Turner, 2002; Levet, 2003).

The second breccia group is poorly lithified, dark gray and strongly clay altered with fragments of monomict to polymict clasts and was classified as 'clay-altered phreatomagmatic breccia' or 'cBPM'. At Purnama, cBPM occupies the near vertical to sub-horizontal zone between the 'quartz-altered phreatomagmatic breccia' or 'sBPM' and the weakly altered intrusive rocks. The 'clay-altered phreatomagmatic breccia' or 'cBPM' commonly contains abundant shear laminations and slickensides suggesting displacement between the silicified breccia and intrusive rocks is concentrated along this contact. In similar breccia occurrences at Kelian, these breccias have been described as 'muddy breccias' by previous workers (Lawless, 1988; van Leeuwen et al., 1990; Corbett and Leach, 1998).

In this study, hypogene breccias are associated with the Martabe dome complex and are described and re-interpreted using the breccia description and classification scheme presented by Davies (2004) in his Kelian study. The breccias have been classified into two facies groups: unstratified (A facies) and stratified (B facies), where each group can consist of several facies and sub-facies. The breccias are referred to as 'carbonaceous matrix-supported breccias' to emphasize the common, characteristic component, a carbonaceous mudstone matrix which was originally interpreted to be from the Tapanuli group and/or Sibarus sedimentary rocks.

The A facies breccias consist of monomict carbonaceous sediment breccias, polymict sediment-bearing breccias, and monomict-polymict volcanic breccias with carbonaceous matrix. Facies A vary in breccia composition (monomict versus polymict) and diagnostic clast types. Sub-facies are characterized by subtle variations in the dominant clast-lithology (i.e. sediment, andesite, volcaniclastic, dacite) other than carbonaceous mudstone matrix, or modal mineralogy of the clasts (i.e., feldspar versus quartz). Collectively, these breccias vary in appearance due to clast abundance, size, lithology and degree of clast rounding, but where intensely clay-altered, the breccia is generally black or dark grey or, whereas it is intensely quartz±alunite±dickite±kaolin-altered, light grey.

The majority of these breccias are matrix-supported, although there are clast-supported breccias within this group. All polymict facies have similar matrix components (sand-sizes fragments of quartz, polymict lithic clasts, volcanic clasts and abundant milled carbonaceous mudstone and sandstone) but variable in clast population. Clast populations vary from one facies to another, and consist of various combinations of andesite, dacite, volcaniclastic rocks, earlier-formed breccias (all breccia groups), accretionary lapilli, charcoal and rare vein fragments. Eight facies have been defined for the A facies breccias.

The B facies have similar clast and matrix components to the A facies breccias but differ in that they are stratified. Facies B breccias have been defined by variation in stratification and the principal clasts components (dacite dominated versus wall rock dominated). Sub-facies of the B facies breccias are distinguished by variations in grain size (sandstone to breccia).

3.5.4.1 Facies A – Unstratified breccia facies

3.5.4.1.1 Facies A1 - Unstratified monomict sediment clast, carbonaceous matrix-supported breccia

Facies A1 breccia is unstratified, dark grey to black, clast- to matrix-supported, unsorted-poorly monomict carbonaceous sedimentary clasts in the carbonaceous-matrix (Figure 3.29, Table 3.1). Clasts are angular to sub-rounded, that generally range from 0.5 to 5cm but be up to 50 cm. Clast compositions mainly vary from mudstone, siltstone to sandstone with very a few others from rock units. Matrix comprises up to 50% of the rock and is composed of mud- to silt-sized fragments of carbonaceous sedimentary rocks.

This facies typically occurs within narrow irregular zones as stringers or dykes, in gently to moderately dipping tabular bodies, that crosscut volcanic breccia (Tmab), quartz-

phyric dacite (Tpid) and hornblende-phyric andesite (Tpia). This breccia facies occurs mainly within carbonaceous sedimentary rocks or in between carbonaceous sedimentary rocks and volcaniclastic rocks. It also occurs within laminated to thinly-bedded carbonaceous mudstone and sandstone. In these settings, there is a strong spatial association between the breccias and either faults or faults projections.

Sharp or gradational wall rock contacts are typical. Where graded, there is typically a transition from monomict moderate-/fine-sized clasts, carbonaceous matrix-supported breccia into jigsaw-fit breccia and then into unbrecciated sedimentary wall rocks.

In some locations, the facies A1 breccias contain abundant clay gouge and occupy moderately to steeply inclined tabular zones. These zones have sub-parallel planar to sub-planar contacts with carbonaceous mudstone/sandstone wall rocks. Internal banding, defined by aligned clasts, gouge and/or foliation, is common. It is also common on the surface at Purnama and Pelangi to find lacustrine sedimentary rocks.

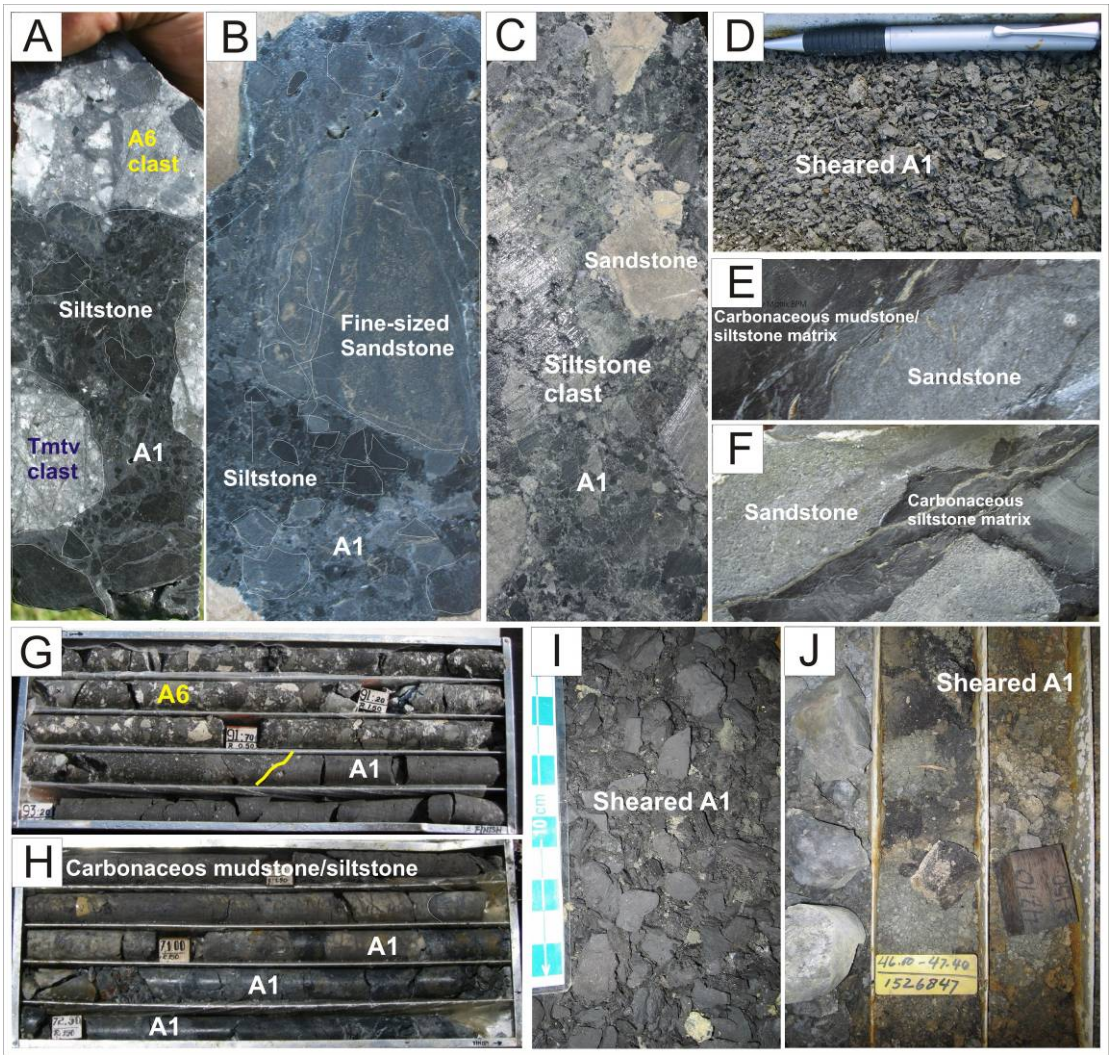

Figure 3.29. Facies A1 - Unstratified monomict sediment clast, carbonaceous matrix-supported breccia.

(A).Clast- to matrix-supported A1 breccia with clasts of kaolinite-altered porphyritic andesite (Tmtv) and A6 facies breccia (APSD420_12). (B). Jigsaw-fit to moderate clast-rotated A1 breccias. Several of larger sandstone clasts have some internal fractures. Between the black siltstone, there is a zone of matrix- to clast-supported A1 breccia with aligned clast which is interpreted to be a fault zone (APSD423-20).
(C). Clast-supported A1 with sandstone-siltstone clast (APSD420_25).
(D, I and J). Sheared of carbonaceous silt one-mudstone matrix supported. Sample from APSD055 at Purnama.
(G and H). Matrix-supported A1 breccia with clasts and A6 facies breccia contact with A7 facies. It is also showing gradation from mudstone to monomict A1 facies breccia.

Table 3.1. Summary description of facies A1 – Unstratified monomict sediment clast to matrix supported- breccia.

Faces	**A1–Unstratified monomict sedimentary clast, with carbonaceous matrix-supported breccias**
Sub Facies	None
Internal Organization	Unstratified, unsorted-poorly sorted, monomict, clast- to matrix-supported. Gradational from in-situ to jigsaw-fit and/or clast-rotated texture. Sheared is commonly observed in many places.
Components:	
Clasts :	Dark grey to black, angular to sub-rounded, thin-layered carbonaceous sedimentary rocks Clast sized decreases outwards from sedimentary wall-rock contacts.
Matrix :	Silt- to sand-sized of carbonaceous sedimentary matrix; locally carbonaceous clay gouge due to shearing.
Cement :	None
Open Space :	None
Grain Size:	Generally medium- to coarse-grained clast, 0.5 cm to 5 cm. Large sedimentary block/clast is commonly present within breccia.
Geometry:	
Morphology :	Irregular to tabular-shaped inclined to sub-vertical zones m's to tens m's across. As sub-horizontal zones on nearly surface. It mainly occurs at contacts between carbonaceous sediment and volcaniclastic rocks and within carbonaceous sedimentary rock.
Contacts :	Structurally controlled, sharp or gradational from jigsaw-fit into un-brecciated carbonaceous sedimentary rock.
Distribution :	Common on near surface in Purnama and Pelangi, it might be a lacustrine phase. Also as result north-northwest structurally controlled near contact hornblende-bearing andesite (Tpia) and quartz-dacite (Tpid) at northeastern part of Gerhana. Irregular dykes of A1 breccia cut many others polymict breccia facies. Present in spatial association with north-northeast and/or north-northwest fault-striking at Pelangi.
Alteration and Mineralization:	Intensively illite±smectite-pyrite alteration, with local gouge development. No mineralization.
Interpretation	Tectonic (fault), phreatic and possibly hydraulic breccia.

3.5.4.1.2 Facies A2 – Unstratified monomict volcanics [andesite porphyritic (Tmtv) and/or volcanic breccia (Tmab)] clast, carbonaceous matrix-supported breccia

The A2 facies is typically monomict, jigsaw-fit texture, clast- to matrix-supported breccia (Figures 3.30 and 3.31; Table 3.2). This facies is commonly observed to have gradational contacts with the coherent porphyritic andesite (Tmtv) or volcanic breccia (Tmab) to facies A4, A5 and A6. The matrix (5 to 20%) consists of one or more of fine-grained polymict carbonaceous breccia (A5 facies), sand-to mud sized polymict lithic fragments dominated by carbonaceous sedimentary rocks (A5 and A6 facies); and/or clay gouge and rhyolitic fragments.

Two sub-facies are distinguished by the presence dominant volcanic clasts: sub-facies A2_1 is a volcanic breccia with curviplanar margin-textured clasts (Tmab) and sub-facies A2_2 has angular and blocky porphyritic andesite of Toru volcanic (Tmtv) as the dominant clast type. Clasts of both sub-facies range from 0.2 to 20 cm. A2 facies breccias have been observed at Purnama, mainly at the contact between coherent porphyritic andesite (Tmtv) or volcanic breccia (Tmab) and other polymict facies breccias. Generally A2 breccias occur in irregular fingers or dykes (10 cm to 20m wide). In several locations, a complete gradation from coherent porphyritic andesite (Tmtv) into A2 facies to polymict carbonaceous matrix-supported breccia occurs over strike lengths of several meters.

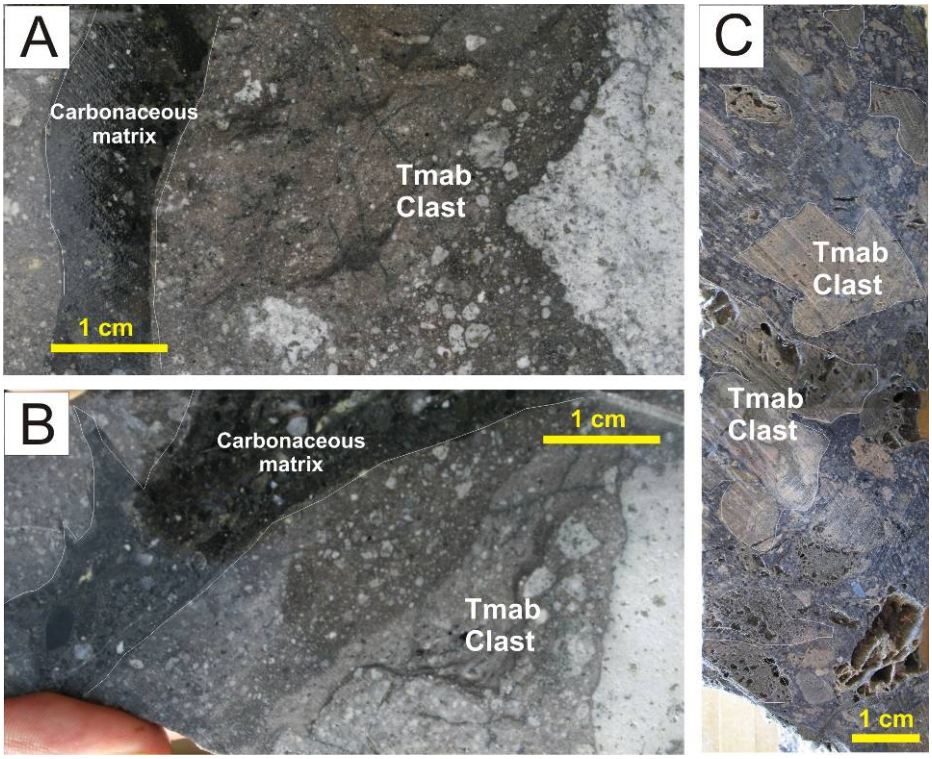

Figure 3.30. Facies A2 – Unstratified monomict volcanic [andesite porphyritic (Tmtv) and/or volcanic breccia (Tmab)] clast, carbonaceous matrix-supported breccia, subfacies A2_1. A and B shown how the original volcaniclastic (Tmab) is intruded by carbonaceous matrix-supported breccia (APSD029). C. Tmab clast set in carbonaceous matrix, with pervasively siliceous alteration of both clasts and matrix (APSD052_41)

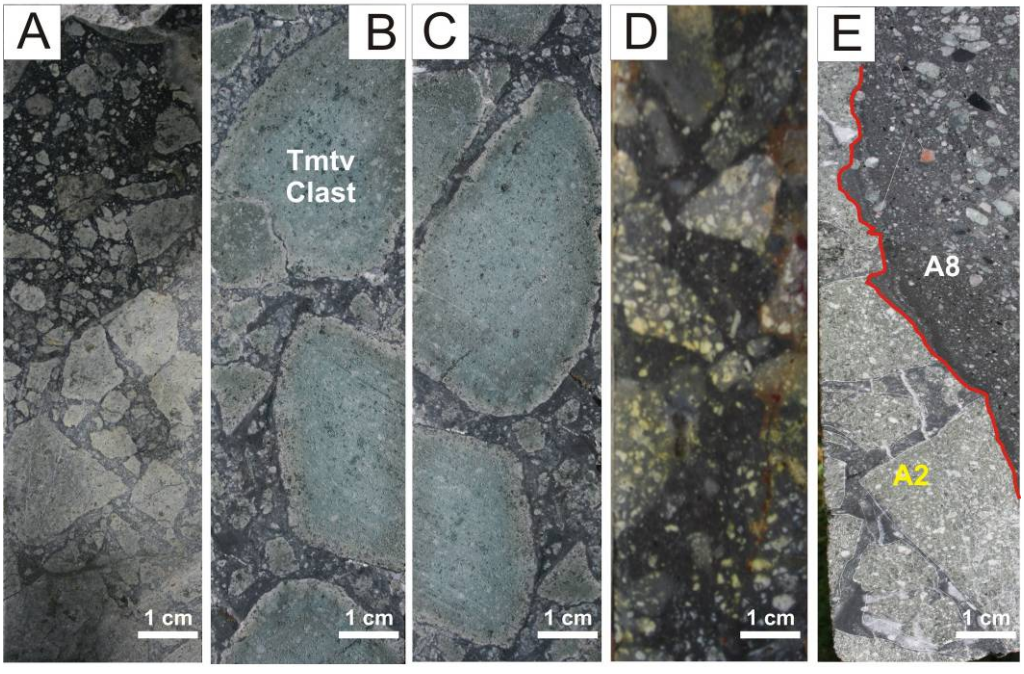

Figure 3.31. Facies A2 – Unstratified monomict volcanics [andesite porphyritic (Tmtv) and/or volcanic breccia (Tmab)] clast, carbonaceous matrix-supported breccia, subfacies A2_2. (A) Gradational from coarse- to medium-grain clast size (APSD030). B and C. Jigsaw-fit breccias with chloritic clasts rimmed by kaolinite (APSD067). D. Clast- to matrix-supported breccia with clasts of kaolinite-altered porphyritic andesite (Tmtv) with siliceous overprint (APSD055_230). E. A2 facies breccia cut by A8 facies breccia (APSD055_135).

Table 3.2 Summary description of facies A2 – Unstratified, monomict volcanics clast, with carbonaceous sedimentary matrix-supported breccia.

Facies	**A2 – Unstratified, monomict volcanics clast, with carbonaceous sedimentary matrix- supported breccia**
Sub Facies	A2_1 Volcanic breccia (Tmab) clast-bearing A2_2 Andesite porphyritic (Tmtv) clast-bearing
Internal Organization	Unstratified, monomict, poorly- to moderately-sorted, clast- to matrix-supported. Variation in clast proportions of Tmtv and Tmab, and abundancy of clast to matrix. Sharp to gradational from in-situ, jigsaw-fit and/or clast-rotated textures from Tmtv and Tmab wall rocks into facies A2 breccia. Local gradation from facies A2 breccia into polymict breccia (facies A4, A5 and A6).
Components:	
Clasts :	Angular to sub-angular of fine-medium feldspar-rich andesite porphyry (Tmtv). Andesite porphyry clasts comprise up to 60% of the A2 breccias. Most andesite porphyry clasts are leached and silicified. Sub-angular to sub-round of Tmab clast at the contact between carbonaceous sediment and volcaniclastic rocks. Volcanic breccia clast is characterised by curviplanar shape showing its original clast texture of volcanic breccia (Tmab). Clast angularity increases inwards to andesite porphyritic (Tmtv)/volcanic breccia (Tmab) wall-rock contacts.
Matrix :	Silt- to sand-sized carbonaceous mudstone/siltstone/sandstone.
Cement :	quartz±alunite overprint
Open Space :	None
Grain Size	: Commonly 0.2 cm to 20 cm generally less than 10 cm.
Geometry:	
Morphology :	Irregular inclined to sub-horizontal zones m to tens m across.
Contacts :	Sharp of gradational into massive andesite porphyritic (Tmtv).
Distribution :	Mainly occurs in western part of the main Purnama but also common of Purnama East. Minor occurrences in the Baskara, Kejora and Gerhana. Occurs also at contacts between carbonaceous and volcaniclastic rocks.
Alteration and Mineralization:	Advanced argillic-kaolinitic and prophylitic alteration. Weak-moderate kaolinitic alteration of clasts and argillic alteration of matrix.
Interpretation	Hydraulic breccia and possibly phreatic breccia.

3.5.4.1.3 Facies A3 – Unstratified, monomict intrusion clast, with carbonaceous sediment matrix-supported breccia

The A3 facies is also identified by monomict, jigsaw-fit texture, clast- to matrix-supported breccia which is commonly observed in gradational contact with the intrusions of coherent hornblende-physic andesite (Tpia) or quartz-phyric dacite (Tpid) (Figures 3.32; Table 3.3). The matrix is up to 30%, consisting of fine-grained polymict carbonaceous breccia (A4, A5or A6 facies); and/or clay gouge and rhyolitic fragments. Clasts range from 0.2 to 20 cm. Two sub-facies are indicated by the presence dominant bimodal mineral or rock composition of clasts: sub-facies A3_1 has quartz-phyric dacite (Tpid) clasts and sub-facies A3_2 has hornblende-phyric andesite (Tpia) clasts.

Facies A3 breccias are mainly at the contact between coherent porphyritic andesite (Tmtv) and quartz-hornblende phyric andesite (Tpia) or quartz-phyric dacite (Tpid) at Baskara, Kejora, Purnama and East Purnama. There is sharp to gradational transition from in-situ, jigsaw-fit and/or clast-rotated textures from Tmtv and Tmab wall rocks into facies A2 breccia.

Figure 3.32. Facies A3, subfacies A2_1. A, B and C. Strong quartz-kaolinite altered A3 facies. The clasts were originally quartz-phyric dacite (Tpid).

Table 3.3 Summary of facies A3 – Unstratified, monomict intrusion clast, with carbonaceous sediment matrix-supported breccia.

Facies	**A3 – Unstratified, monomict intrusion clast, with carbonaceous sedimentary matrix-supported breccia**
Sub Facies	Hornblende-phyric andesite (Tpia) Quartz-phyric dacite (Tpid)
Internal Organization	Unstratified, monomict (with minor polymict), poorly- to moderately-sorted, clast- to matrix-supported. Variation in clast proportions and clast to matrix. Sharp to gradational from in-situ, jigsaw-fit and/or clast-rotated textures from Tpia and Tpid wall rocks into A3 breccias.
Components	
Clasts :	Clast shapes are variable but generally sub-angular. Angular to sub-round of Tpia and Tpid clasts are the most dominant, up to 60%. Minor sub-angular to sub-rounded carbonaceous mudstone/sandstone clasts are present. Accretionary lapilli are observed but rare. Clast size increases inwards to the centre to Tpia and Tpid wall-rock contacts.
Matrix :	Dominant of silt- to sand-sized fragment of carbonaceous sediments, minor polymict lithic fragments and broken quartz crystals. Up to 70% matrix, typically 20 to 50%.
Cement :	quartz±alunite
Open Space :	None
Grain Size	Commonly fine- to coarse-grained clasts range 0.2 cm to 20 cm, generally less than 10 cm. Locally blocks up to 20 cm occur within medium- to coarse-grained breccia.
Geometry	
Morphology :	At Baskara and Gerhana, these breccias occur as sub-vertical, irregularly-shaped, vary from 1 m to >20 m wide and are vertically continuous over 10's to hundreds of meters.
Contacts :	Wall-rock contacts with Tpia and Tpid can have a zone of coarse breccia, up to 20 m wide. Thin fingers and dykes of A3 breccia locally extend into the wall rocks for 10's m. Sharp to gradational into Tpia and Tpid. Breccias have locally followed pre-existing fault zones, and are also crosscut by later movement on the same faults. In Purnama, these breccias facies observed at margins or contact between feldspar-phyric andesite of Toru volcanic (Tmtv) and hornblende-phyric andesite (Tpia) quartz-phyric volcanic dacite (Tpid).
Distribution :	Common occurs along the north-northeast and northeast trending faults at Baskara, Kejora and Gerhana. Minor occurrences in the in Purnama at southern margin of Tpia and Tpid.
Alteration and Mineralization	Moderately to strong quartz± alunite and/or quartz±kaoline alteration in Baskara, Kejora and Gerhana. Weak to strong prophylitic of the clast and argillic alteration of matrix in Purnama zones. Dominant pyrite and enargite mineralization in Baskara. None to weak pyrite mineralization in Purnama
Interpretation	Hydraulic breccia and possibly phreatic breccia.

3.5.4.1.4 Facies A4 – Unstratified, monomict wispy-texture clasts, with carbonaceous matrix breccia

The A4 facies is a monomict, wispy-textured rhyolitic to dacitic, clast- to matrix-supported breccia. (Figure 3.33. Table 3.4). This breccia is moderately- to poorly-sorted with a carbonaceous matrix. The A4 breccia is distinguished from other breccias by the clast components. A4 facies is characterized by a distinctive wispy texture of rhyolite or dacitic clasts. The texturally distinctive rhyolite or dacite clasts range from 0.2 to 7 cm and generally comprise 5 to 25 % (locally up to 40%) of the A4 breccia. Minor to rare sub-angular to sub-rounded rounded quartz grain, siltstone, basalt, andesite and/or volcaniclastic clasts are also typically present. The breccia matrix (up to 60%) consists of silt- to sand- sized grains of all host-rocks and fine (<2 mm) wispy and angular grains of rhyolite and dacite. In some instances it also consists of one or more of fine-grained polymict carbonaceous breccia; sand- to mud-sized polymict lithic fragments dominated by carbonaceous sedimentary rocks and volcanics fragments and/or clay gouge.

Clasts are irregular in shape with curviplanar margins or swirly texture and can be ragged, whereas others are blocky with curviplanar margins or have partial wispy and partial blocky, curviplanar margins. Minor amounts of accretionary lapilli are locally present. Accretionary lapilli (2-8 mm diameter) comprise up to 3 % of some A4 breccias. The wispy-texture rhyolitic or dacitic clasts have commonly been subject to texturally destructive moderately to intense kaolinite$\pm$illite alteration. All other clast types identified in the A4 facies are consistently more rounded than swirly-wispy rhyolitic clasts.

This breccia facies has been observed in transitional contact with the fine grained facies polymict carbonaceous breccias (A5 and A6 facies). Although, the clasts are entirely composed of coherent rhyolitic or dacitic, this facies is not observed in gradational contact with these intrusions.

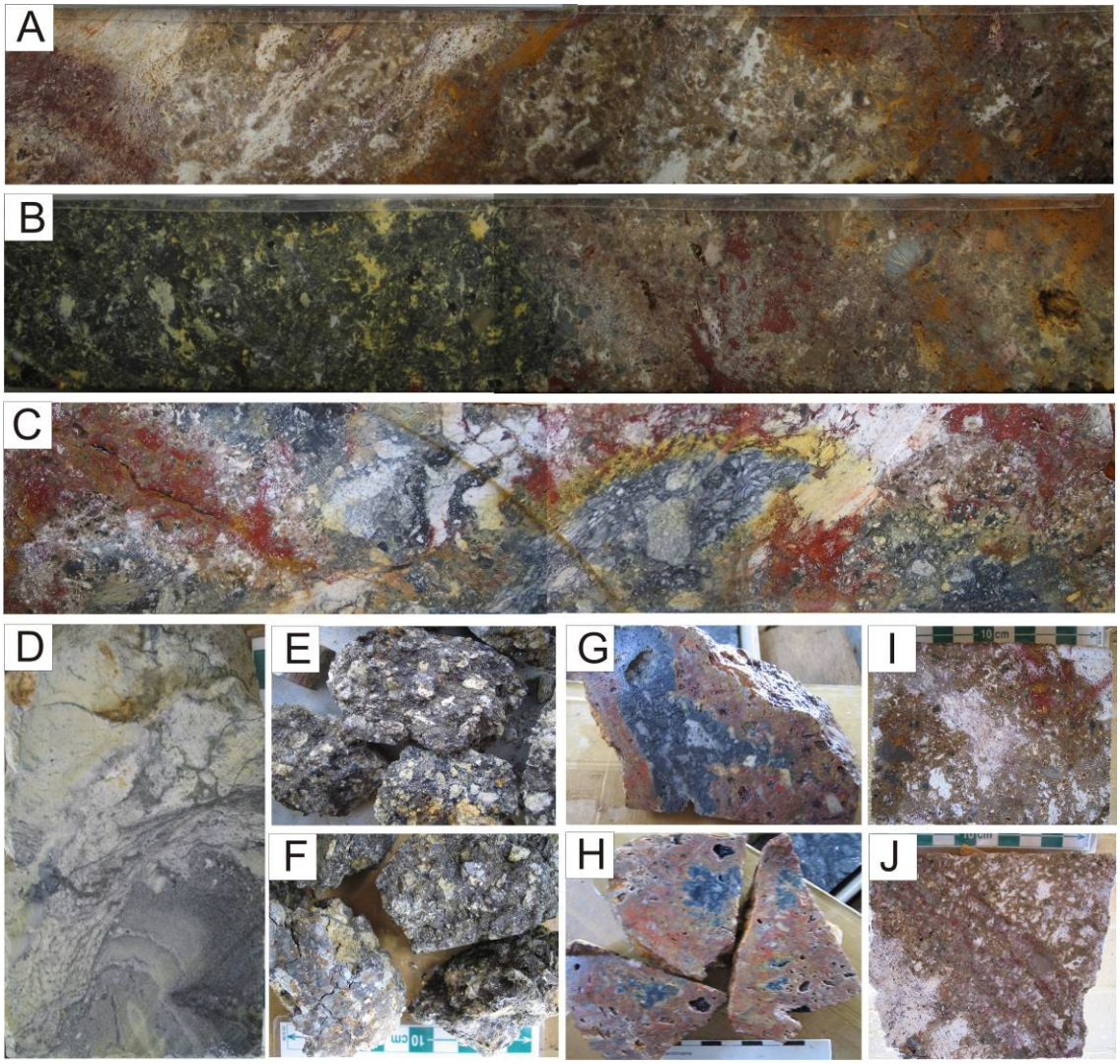

Figure 3.33. Facies A4 Unstratified, monomict wispy-texture clasts, with carbonaceous matrix breccia.

A. B and C. Examples of wispy-texture (white color) with ragged margins in fine- to medium grained A4 breccia. Some clasts display small scale jigsaw-fit texture. Other clasts in these breccias are carbonaceous sediment and volcaniclastic rocks.
D. Jigsaw-fit A3 breccia with rhyolitic clasts separated by a matrix of carbonaceous sediment.
E and F. Wispy texture clast of rhyolite in an illite altered carbonaceous matrix.
G. H. I and J. Examples of oxidized A4 breccia withcharacteristic textures still visible.

Table 3.4. Summary of facies A4 – Unstratified, monomict wispy clasts, with carbonaceous matrix-supported breccia.

Facies	**A4 – Unstratified, monomict wispy clasts, with carbonaceous matrix-supported breccia**
Sub Facies	**None**
Internal Organization	Unstratified, unsorted, monomict (with minor polymict), clast- to matrix-supported Clast-rotated, no jigsaw-fit texture.
Components	
Clasts :	Wispy-texture of rhyolitic and dacitic clasts comprise up to 40% of the A4 breccias. Clasts range from finely (<2 mm) to coarsely (>5 cm) grained. The clasts have wispy, delicate margin and some showed blocky with the curviplanar margins.
Matrix :	Comprises up to 60% of black to dark grey sand- to mud-sized fragments of carbonaceous sandstone and mudstone, with minor volcaniclastic rocks. Fine-grained wispy rhyolite fragments (<2 mm) up to 10%, and locally angular to sub-round lithic clasts.
Cement :	None
Open Space :	None
Grain Size	Rhyolite clasts vary from 2 mm to 10 cm and are generally less than 5 cm.
Geometry	
Morphology :	Irregular to shell-shaped sheet, common found on or near surface. Locally gradational into A5 and A6 breccias.
Contacts :	Irregular at mm- to cm-scale, with transition from other carbonaceous matrix-supported breccias. Direct contact with rhyolite intrusive never found.
Distribution :	Common at Purnama with irregular distribution. Rare at in Baskara, Kejora and Gerhana.
Alteration and Mineralization	Moderate-strong kaolinite alteration of rhyolite clast and quartz-illite-pyrite alteration of matrix.
Interpretation	Phreatomagmatic breccia with juvenile rhyolitic clasts.

3.5.4.1.5 Facies A5 – Unstratified polymict, medium clast, with carbonaceous matrix-supported supported breccia

A5 breccia is unstratified, well to poorly sorted, with polymict clasts set in a carbonaceous matrix (Figures 3.34 and 3.35; Table 3.5). All A6 breccias contain carbonaceous sedimentary rock clasts and typically also contain clasts of rhyolite, andesite and/or volcaniclastic rocks. Clasts are dominantly sub-rounded to sub angular with variable proportion of carbonaceous mudstone/siltstone, sandstone, volcaniclastic (Tmab) and andesite (Tmtv) clasts. Clasts range from 2 mm to 10 mm and comprise 10 to 80% of the breccias. The largest blocks are in excess of 15 cm in diameter, although most of the A5 breccias are fine to medium-grained.

Andesite and volcaniclastic rock clasts are commonly altered to quartz-dickite/kaolinite-pyrite. The A5 breccias are distinguished from other breccias by their components (clast-sized) and internal organizations (polymict vs. monomict). A5 facies is characterized by various clasts that are fine- to medium-grained, sub-angular to sub-rounded to rounded quartz grains and siltstone, basalt, andesite and/or volcaniclastic clasts. Rare rhyolite clasts ranging from 1 to 3 mm are present. They can have wispy fine margins or have partial wispy and partial blocky, curviplanar margins. The wispy rhyolitic clasts have texturally destructive moderately to intense kaolinite$\pm$illite alteration. Minor clasts of quartz veins and accretionary lapilli are present locally. Accretionary lapilli (2-5 mm diameter) can comprise up to <1 % in some A5 breccias.

The breccia matrix (up to 60%) consists of sub-angular to sub-round lithic of sediments rock (carbonaceous mudstone/sandstone), andesite, volcaniclastic rocks, crystal (quartz, feldspar) fragments, fine (<2 mm) wispy and angular grains of rhyolite and dacite clasts. The matrix is typically sand to fine-sand size but the grain size decreases to silt-size where carbonaceous mudstone is the abundant clasts and/or wall rock.

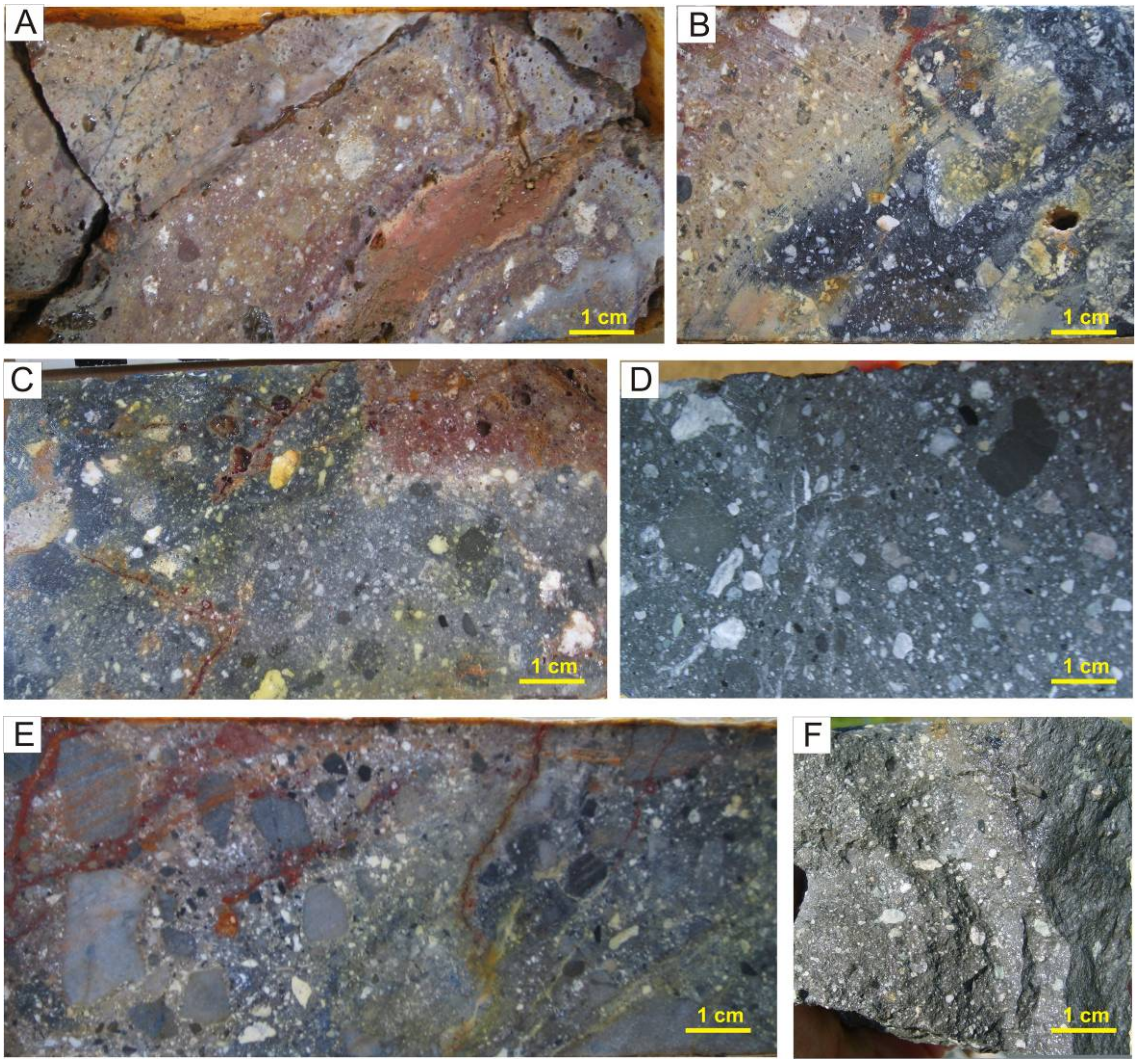

Figure 3.34. Facies A5-Unstratified polymict, medium clast, with carbonaceous matrix-supported supported breccia.

Six examples of fine-grained A5 breccias with 5–10% wispy texture. Clast consist of polymict fine-medium-grained variable proportion of carbonaceous mudstone/siltstone, sandstone, volcaniclastic (Tmab) and andesite (Tmtv) clasts.

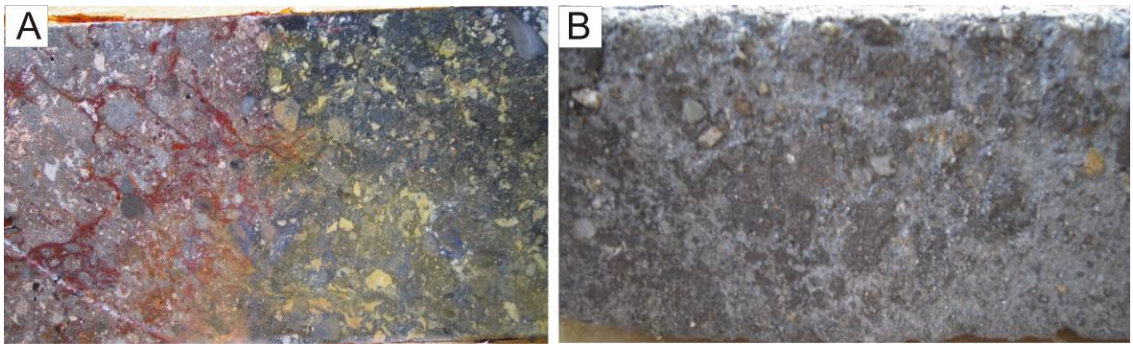

Figure 3.35. Facies A5 Facies A5-Unstratified polymict, medium clast, with carbonaceous matrix-supported supported breccia.
A. Fine- to moderate breccias with 2–5% of wispy texture.
B. Illite altered A5 facies matrix.

Table 3.5. Summary of facies A6 - Unstratified, polymict, medium clast, with carbonaceous matrix-supported breccia.

Facies	**A5 – Unstratified, polymict, medium clast, with carbonaceous matrix-supported breccia**
Sub Facies	Sub-equal, sedimentary rocks, volcaniclastic (Tmab) and andesite (Tmtv) clasts dominated
Internal Organization	Polymict, massive and moderately sorted. Dominantly matrix-supported but locally clast-supported. Local lateral and vertical gradations into A4 or A6 fine breccias.
Components:	
Clasts :	Typically sub-rounded to sub-angular clasts with variable proportions of carbonaceous mudstone/siltstone, sandstone, volcaniclastic (Tmab) and andesite (Tmtv) clasts. There are no hornblende-phyric andesite (Tpia) and quartz-pyric dacite (Tpid) clasts. Minor juvenile wispy texture clasts. Clast type is strongly controlled by local wall-rock lithology. Carbonaceous mudstone/sandstones are the most abundant clast lithology.
Matrix :	Up to 60% matrix, dominated by sand-sized fragments of carbonaceous sandstone and siltstone, also lithic fragments and broken quartz crystals.
Cement :	None
Open Space :	None
Grain Size:	Dominant fine-grained breccia with locally medium-grained breccia.
Geometry:	
Morphology :	Irregular along sheets with 1 to 50 m across and extending up to several hundred meters strike.
Contacts :	Typically gradational into polymict carbonaceous breccias with rhyolite clasts (A4 or A6 facies), locally sharp shapes, polymict hydrothermally cemented breccias, unbrecciated Tmtv, unbrecciated carbonaceous sedimentary rocks or unbrecciated Tmab rocks.
Distribution :	A6 breccia occurs at the margins of the Purnama Breccia, in particular at its western end; at Baskara near it margins, and in northwest-trending zones in the west wall of the northern Gerhana area. In Gerhana, the A5 breccias are spatially associated with northwest trending faults, although the breccias are both cut but and crosscut fault zones.
Alteration and Mineralization	Moderate to intense quartz±dickite-kaolinite-pyrite altered matrix and clasts. Tmtv and Tmab clasts are moderately to intensively quartz-dickite-kaolinite-pyrite altered and contain stage LS veins. Alteration and veining pre-dates brecciation. Rare clasts are also cut by pre-breccia quartz-illite-pyrite vein.
Interpretation	Phreatomagmatic breccia, tectonic, gravitational collapse

3.5.4.1.6 Facies A6- Unstratified, polymict coarse clast carbonaceous sediment matrix-supported breccia with wispy texture

Facies A6 consists of polymict, clast-supported to locally matrix-supported, poorly- to moderately sorted breccia (Figure 3.36; Table 3.6). A6 breccias are distinguished from A5 breccias by the abundance of sub-angular to rounded clasts and their coarse size. This facies has similar composition and appearance to the facies A5 and shares similar matrix and textural characteristics with other polymict facies breccias. In some places the A6 breccia facies gradually changes into A5 breccis.

In general, the A6 breccias consist of clasts that are more angular and, on average, larger than those observed in the A5 breccias. The A6 breccias also typically have less matrix (generally <50%) than the A5 breccias. A6 facies generally contain clasts of porphyritic andesite (Tmtv) and volcaniclastic (Tmab) (rare basaltic andesite) up to (30-60%), carbonaceous mudstones/siltones and sandstone and swirly-wispy textured rhyolitic clast. Porphyritic andesite (Tmtv) clasts in A6 breccia are rare at Baskara and Kejora. Clast component locally includes minor accretionary lapilli, sandstone and finely laminated stratified carbonaceous sandstone breccia. White, sub-angular to sub-rounded, distinctive wispy and blocky (with curviplanar margins) clast shapes are a common component (up to 10%).

Matrix is dominated by carbonaceous mudstone, lithic clasts, fine wispy rhyolite clasts and broken quartz crystals. The A6 facies is common breccia at Purnama, typically occuring within the A4 or A5 breccia body. It also occurs on the peripheral areas of the hornblende-phyric andesite (Tpad) and quartz-phyric dacite (Tpid) intrusions.

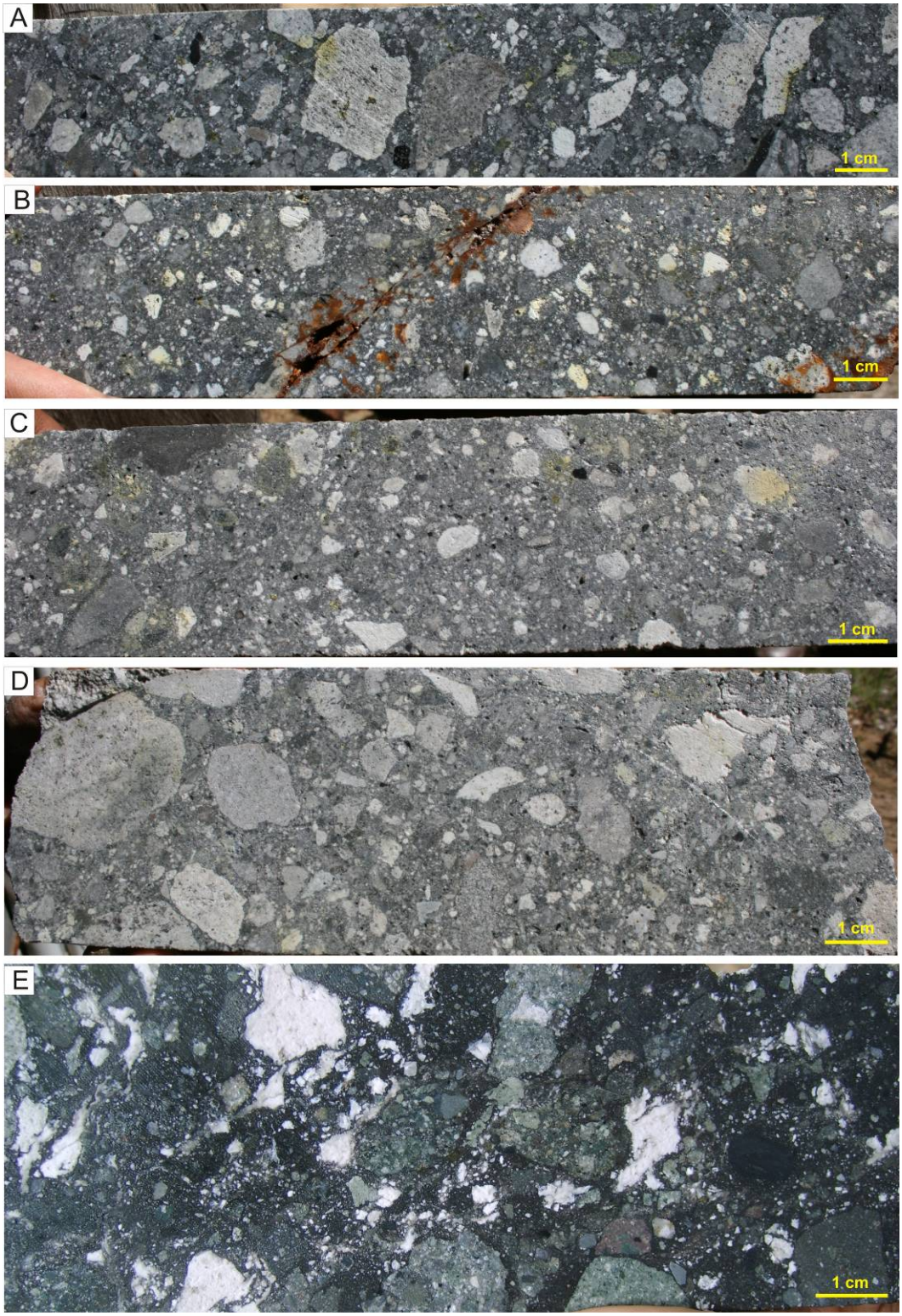

Figure 3.36. Facies A6 – Unstratified, polymict coarse clast, carbonaceous matrix-supported breccia with presence of wispy clasts.
A. Medium- to coarse-grained with sub-angular to angular polymict clasts. Blocky rhyolitic or dacitic clasts set in carbonaseous sandy matrix. Clasts altered to quartz-kaolinite.
B and C. Fine- to medium-grained A6 breccia with subround to subangular clasts. Clasts mainly altered to quartz+kaolinite, whereas the matrix has undergone quartz-illite±kaolinite alteration.
D. As A, but the matrix has more advanced argillic-kaolinitic alteration.
E. Fine- to coarse-grained polymict clasts with carbonaceous matrix. Volcanic clasts have been has altered to chlorite, whereas white-colored clasts (blocky and wispy-textured rhyolite have kaolinite altered.

Table 3.6. Summary of facies A6 - Polymict coarse clast, with carbonaceous matrix-supported breccia with presence of wispy clasts.

Facies	**Facies A6 – Unstratified, polymict coarse clast, carbonaceous matrix-supported breccia with presence of wispy clasts**
Sub Facies	None
Internal Organization	Unstratified, unsorted, polymict, clast- to matrix-supported Gradational variations in clast proportions and clast to matrix ratio Local gradations from A4 and A5 into A6 breccia.
Components	
Clasts :	Clasts of porphyritic andesite (Tmtv) and volcaniclastic (Tmab) (rare basaltic andesite) up to (30-60%), carbonaceous mudstones/siltones and sandstone and swirly-wispy textured rhyolitic clast. Porphyritic andesite (Tmtv) clasts in A7 breccia are rare at the Baskara and Kejora. Sub-angular to sub-rounded clast. Minor clast component locally include: fine-grained A5, accretionary lapilli and sandstone and finely laminated stratified carbonaceous sandstone breccia. White sub angular to sub rounded with the distinctive wispy and blocky (with curviplanar margins) clast shapes are a common component (up to 10%). All clasts other than the wispy and blocky rhyolite clasts are typically sub-angular to sub-rounded.
Matrix :	Up to 60% silt- to sand sized fragments dominated by carbonaceous mudstone, lithic clast, fine wispy rhyolite clasts and broken quartz crystals.
Cement :	Quartz-dickite-kaolinite
Open Space :	None
Grain Size	Varies from moderate-grained breccia to very coarse-grained breccia with average clast size range 0.2 to 150 cm, average 1-3 cm in diameter. Wispy rhyolite clasts range from 1 cm to 3 cm; and are generally less than 3cm. Locally blocks up to 5 m. Sand-sized compositional similar to as A5 facies.
Geometry	
Morphology :	Irregular sub-vertical to sub-horizontal tabular. Multiple generations of brecciation are indicated by crosscutting breccia body, clasts of early breccias in later breccias and disaggregation of early breccias at contacts with later breccias.
Contacts :	Sharp to irregular, erosional and penetrating contacts with earlier breccia phases.
Distribution :	Common facies breccias at Purnama. Typically occurs internal to the A4 or A5 breccia body. Minor occurrences peripheral to Baskara hornblende-phyric andesite (Tpad) and quartz-phyric dacite (Tpid) intrusion.
Alteration and Mineralization	Moderate to intense quartz-dickite-kaolinite-pyrite-alteration of matrix and clasts. Tmtv and Tmab clasts are moderately to intensively quartz-dickite-kaolinite-pyrite altered and contain stage LS veins. Alteration and veining pre-dates brecciation. Clast alteration: Tmtv and rare Tmab are typically moderately to strongly quartz+dickite altered where the matrix is quartz+dickite-kaolinite.
Interpretation	Phreatic and Phreatomagmatic breccia with juvenile rhyolite clasts.

3.5.4.1.5 Facies A7 – Unstratified monomict, fine lithic-accretionary balls clast carbonaceous matrix-supported breccia

Facies A7 are well sorted, monomict, matrix-supported breccias with a carbonaceous matrix. (Figures 3.37–3.39; Table 3.7). Clasts are dominantly sub-rounded to rounded, range from 2 mm to 10 mm and comprise 10 to 60% of the breccias. The most common clast types are accretionary lapilli and fine carbonaceous mudstone/sandstone. The A7 breccias are distinguished from other facies by their clast components, which are characterized by presence of texturally distinctive of accretionary lapilli and rock-flour matrix breccia.

Two sub-facies are observed by the presence dominant clasts or matrix: sub-facies A7_1 is accretionary lapilli-rich with rimmed-ball texture at the margins, and subfacies A7_2 that has a dominant, very fine grained, rock-flour matrix. Both sub-facies have very few other clast types. Accretionary lapilli (2–10 mm in diameter) comprises up to 60 % of some A7 breccias. In rock flour breccias sub facies, the matrix (up to 90%) consist of fine (<0.5 mm) mud- to silt-sized grains.

Accretionary lapilli commonly occurs in the centre of pipes; and also can be part of pyroclastic base surges. Facies A7 breccias are common in Purnama and also as isolated layers in Purnama East and northern Pelangi (along the Aek Pahu creek). Individual A7 breccia bodies vary from thin layer of 5 cm to 15 m to irregular, commonly downward tapering zones 10–20 m wide. Multiple phases of brecciation and subsidence in the diatreme pipe make correlation of individual accretionary layers difficult. In outcrop (i.e., Purnama and Aek Pahu creek, northern Pelangi) it is also difficult to discriminate individual zones of A7 breccia due to complex overprinting facies relationships.

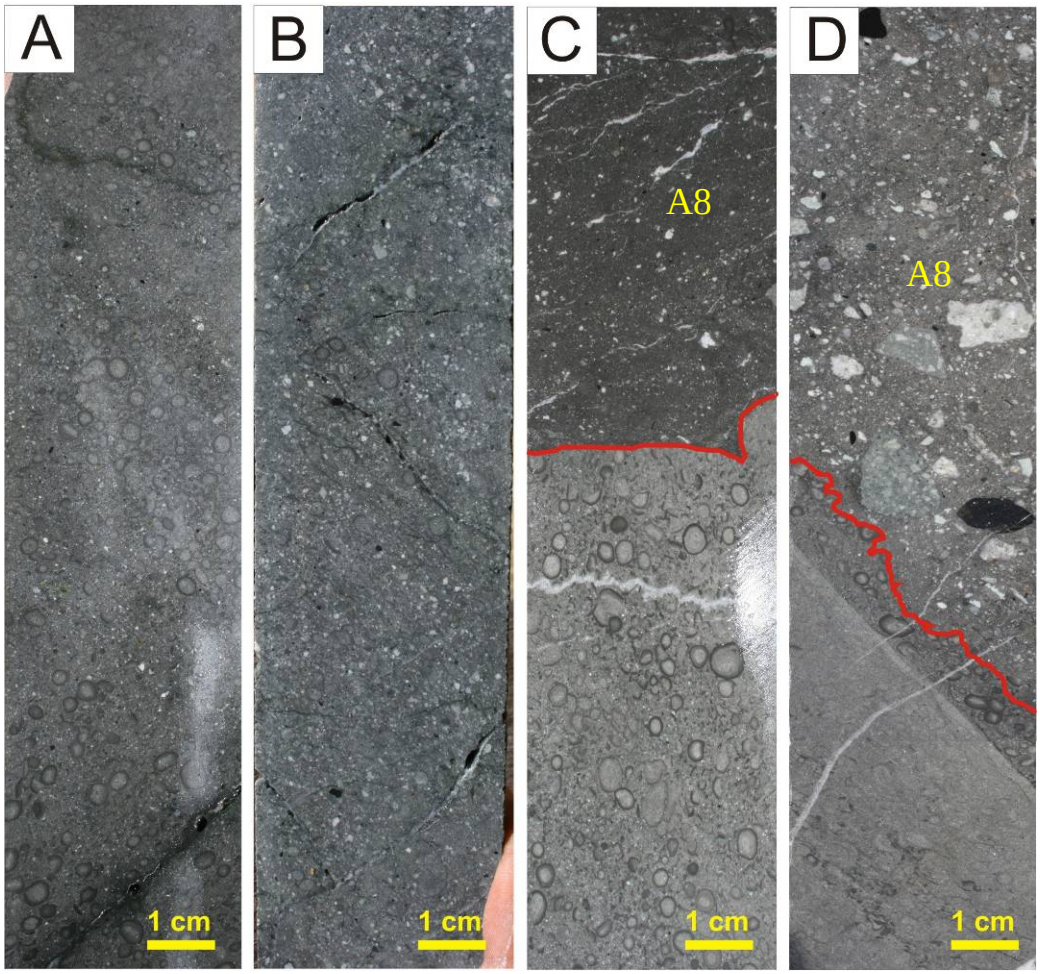

Figure 3.37. Facies A7 – Unstratified monomict, fine lithic-accretionary balls clast carbonaceous matrix-supported breccia. Sub facies A7_1.
A and B. Accretionary lapilli-rich facies.
C and D. Accretionary lapilli-rich facies cut by A8 facies breccia.

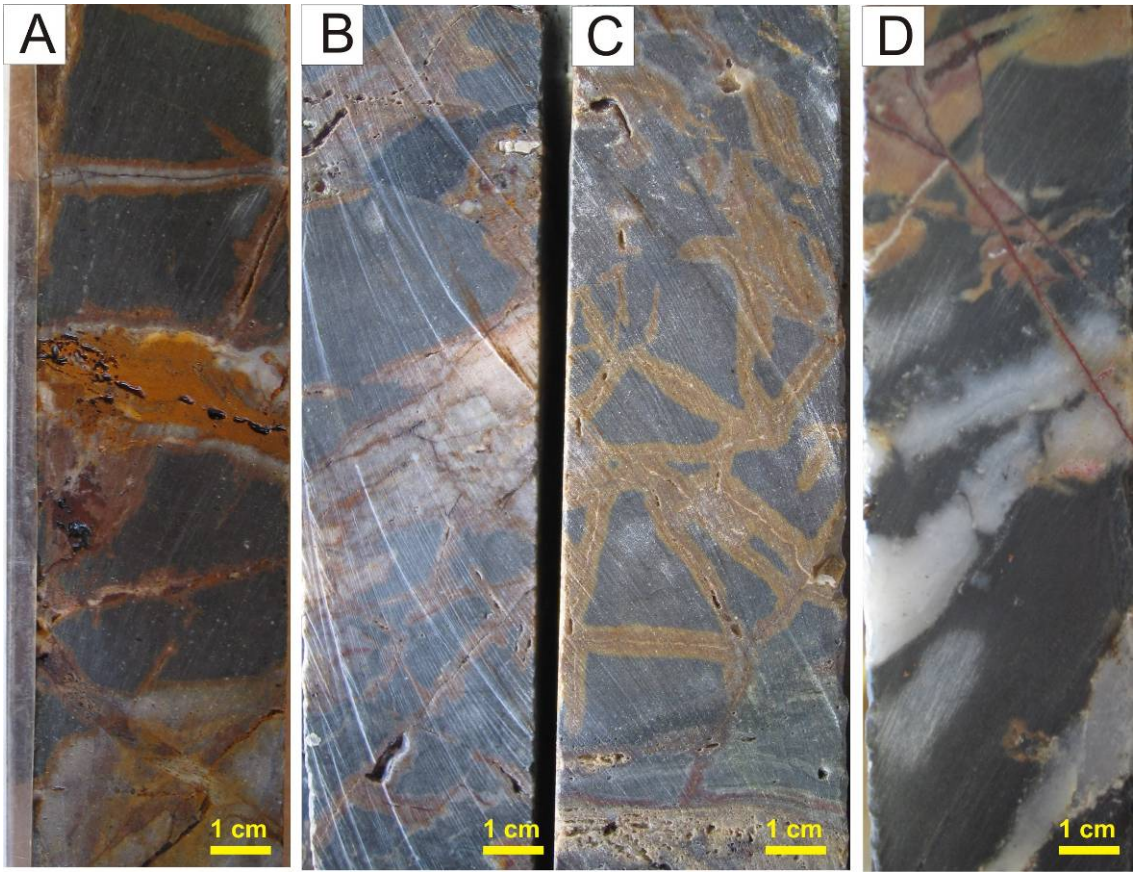

Figure 3.38. Facies A7 – Unstratified monomict, fine lithic-accretionary ball clast, carbonaceous matrix-supported breccia. Sub-facies A7_2.
A, B and C shows typical fine grained rock flour of A7 matrix.
D. Rock flour cut by quartz veining.

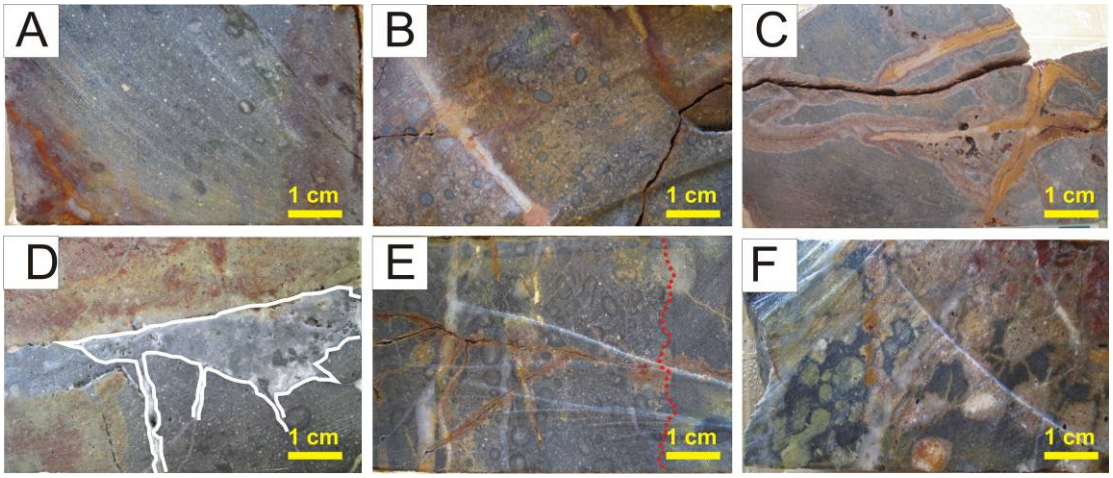

Figure 3.39. Facies– Unstratified monomict, fine lithic-accretionary balls clast carbonaceous matrix-supported breccia. Sub-facies A7_2.
A, B, C, D, E and F are examples of typical fine grained rock flour.

Table 3.7. Summary of facies A7 – Unstratified monomict, fine lithic-accretionary balls clast in carbonaceous matrix-supported breccia.

Facies	**A7 – Unstratified, monomict, fine lithic-accretionary balls clast, with carbonaceous matrix-supported breccia**
Sub Facies	Accretionary lapilli dominated (AL) Rock flour, fine-grained, crystal-rich dominated (RF)
Internal Organization	Monomict, massive, well-sorted. Dominant matrix supported with accretionary lapilli. Local lateral and vertical gradations into fine crystal-rich breccias.
Components	
Clasts :	Typical sub-rounded to rounded of accretionary lapilli. The balls range 2 to 10 mm is present up to 60%. Broken crystals are common. Abundant fine-grained lithic clast.
Matrix :	Up to 90% matrix, dominated by silt- to sand-sized fragments of carbonaceous sediment, also lithic fragments and broken quartz crystals.
Cement :	None
Open Space :	None
Grain Size	Dominantly fine-grained breccia, very few locally medium-grained breccias.
Geometry	
Morphology :	Irregular sheets with 1 to 50 m across and extending laterally possibly up to several hundred metres.
Contacts :	Typically gradational into other polymict carbonaceous breccias with rhyolite clasts (A5 and A6 facies). Locally sharp shapes with other breccias, polymict hydrothermally cemented breccias, unbrecciated carbonaceous sedimentary rocks or unbrecciated of Tmab rocks.
Distribution :	A7 breccia occurs in widespread in Purnama, in particular at its western end and in Aek Pahu creek at the northern Pelangi. A7 is difficult to find at the Baskara and Kejora.
Alteration and Mineralization	Moderate to intense quartz-dickite-kaolinite-pyrite-alteration of matrix and clasts.
Interpretation	Phreatomagmatic breccia, gravitational collapse, as interlayered unit in base surge.

3.5.4.1.8 Facies A8 – Unstratified, polymict, fine-coarse grain clast carbonaceous sediment matrix-supported, with oxidized breccia clast

Facies A8 is a polymict, moderately-sorted, carbonaceous sediment matrix-supported breccia. It consists of sand- to mud-sized grains of all host rocks, broken quartz, quartz veins and feldspar crystals (Fig 3.40; Table 3.8). The predominant components are fragments of volcanics, carbonaceous mudstone and sandstone. Fine fragments of porphyry andesite (Tmtv) and volcanic breccia (Tmab) are ubiquitous. A8 facies has also similar composition and appearance with facies A6 with more clay and sandy matrix. It shares similar matrix and textural characteristic as the other polymict A facies breccias, but with no distinctive wispy and blocky (with curviplanar margins) clast shapes as clasts. Overall, A8 facies is defined by the presence of distinctive fine to moderate sized, oxidized clasts (2–8 mm) and cross cuts all earlier breccias.

Accretionary lapilli are also present. A8 facies occurs either as the only facies in a breccia pipe, or as a fine-grained facies that grades into A5, A6 or A7 facies within a breccia body. The facies has sharp contact to A2, A3 and A4 facies. A8 facies typically occurs as a late facies in all Martabe diatreme.

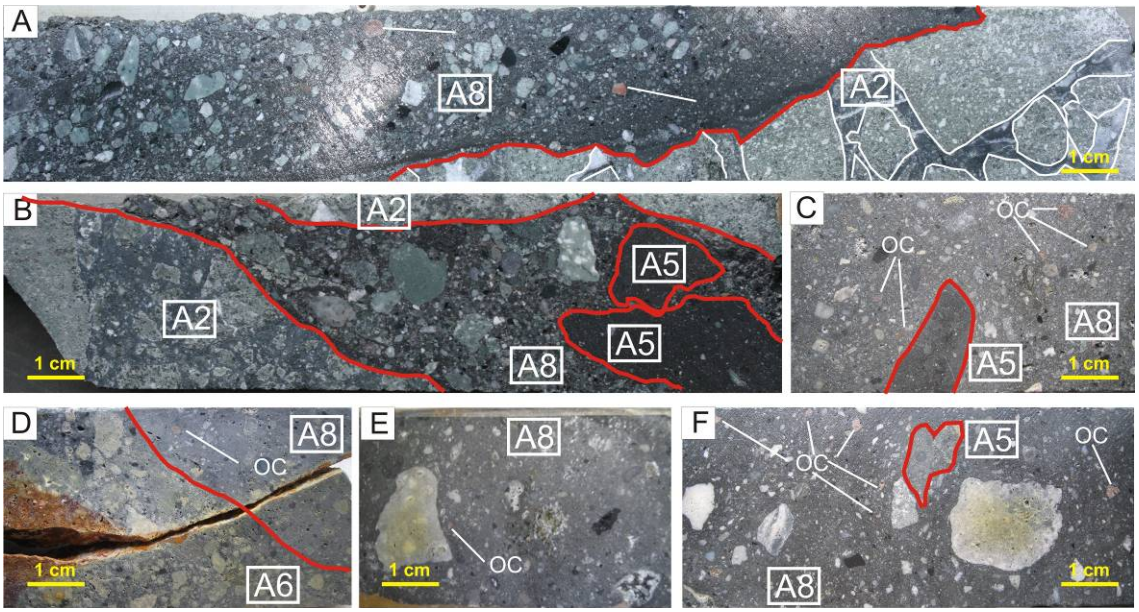

Figure 3.40. Facies A8 – Unstratified, polymict, fine-coarse grain clast carbonaceous sediment matrix-supported, with oxidized breccia clast.
A., B, C, D, E and F illustrate how A8 facies crosscuts almost all other facies breccias. A8 facies is defined by the presence of distinctive fine to moderate oxidized clasts.

Table 3.8. Summary of facies A8 - Polymict discordant, fine-coarse grain clast carbonaceous sediment matrix supported, with oxidized breccia clasts.

Facies	**A8-Unstratified, polymict, fine-coarse grain clast carbonaceous sediment matrix supported, with oxidized breccia clast**
Sub Facies	None
Internal Organization	Unstratified, polymict, moderately to finely-sorted sandstone clast
Components	
Clasts :	Compositionally equivalent to A5, A6 and A7 breccias, but with average grain size <2 mm. Clasts include Tmtv, carbonaceous mudstone and fine sandstone, andesite, volcaniclastic rocks and abundant broken quartz crystals. Accretionary lapilli minor present with range 1 to 5 mm is present. Clasts are sub angular to sub-rounded. Subrounded-subangular oxidized clast is most distinguished Oxidized clast is a distinctive clast type. Contains other earlier breccias as clasts
Matrix :	Mud-sized lithic fragments
Cement :	None
Open Space :	None
Grain Size	Fine-grained to medium-grain breccia
Geometry	
Morphology :	A8 facies occurs in small to medium irregular sub-vertical dikes up to 15-20 meters wide, locally in narrow zones cut all breccias.
Contacts :	Typically sharp and less commonly gradational.
Distribution :	A minor, but widespread facies at the Purnama, where the A8 facies is generally a late phase, although clasts are similar to the other breccias.
Alteration and Mineralization	Matrix is weak illite – pyrite alteration Clasts have undergone intense chloritic, quartz, quartz-dickite-alunite kaolinite
Interpretation	Phreatic breccia

3.5.4.2 Facies B - Stratified breccia facies

3.5.4.2.1 Facies B1 - Well-stratified, polymict, volcanicclast and sediment clasts dominant, carbonaceous matrix-supported breccia

B1 facies breccias are moderately sorted, light medium to grey-greenish, polymict and matrix to locally clast-supported (Figure. 3.41; Table 3.9). This facies consists of angular to sub angular clasts of white, fine-medium quartz-phyric dacite, volcaniclastic rocks, carbonaceous sediment and minor accretionary lapilli.

The B1 breccias are dominated by dacitic, volcaniclastic clasts and sediment clasts. Matrix consists of sand-sized dacitic, lithic grains and quartz-crystal fragments. B1 breccias form beds with planar or wavy-planar at cm- to m-scale. Some beds are normally graded, while others have well-sorted coarser fragments in a single bed. But most of the individual beds grade upward from medium to fine-grained breccia and some have volcanic sandstone tops. Many of the beds are moderately to wellsorted, in contrast to the B2 facies that are poorly- to moderately-sorted. One to 8 mm accretionary lapilli are abundant in the B1 breccias and in some cases occur in thin (1–5 cm) beds consisting of closely packed accretionary lapilli.

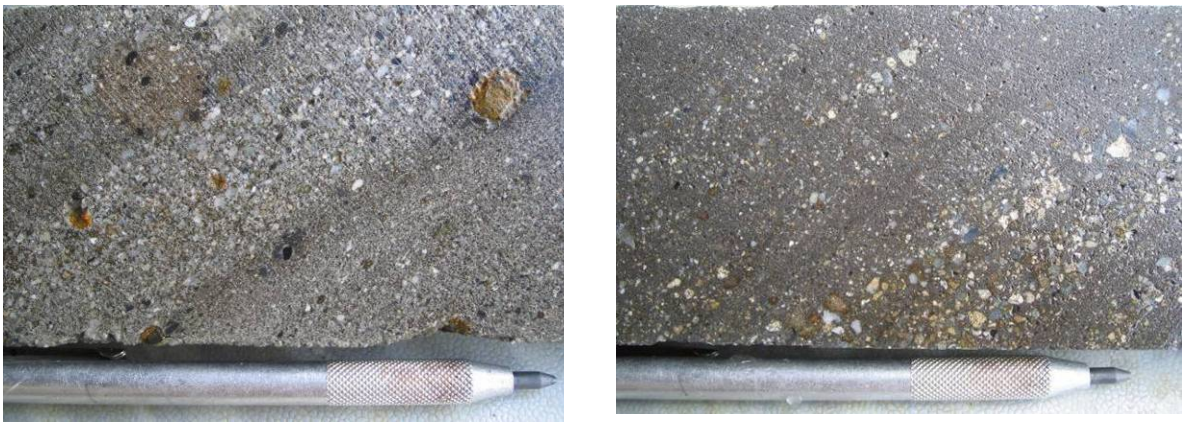

Figure 3.41. Facies B1 - Well-stratified, polymict, volcaniclastic and sediment clast, carbonaceous matrix-supported breccias. A and B. B1 breccias form beds with planar or wavy-planar in cm- to m-scale. Some beds are normally graded.

Table 3.9. Summary of facies B1 - Well-stratified, polymict, volcanic-clast and sediment dominant, carbonaceous-matrix supported breccia.

Facies	**Facies B1 - Well-stratified, polymict, volcanic-clast and sediment dominant, carbonaceous-matrix supported breccia**
Sub Facies	A) Medium-grained breccia B) Fine-grained breccia
Internal Organization	Light to medium grey and green. Polymict fine to medium-sorted, clast- to matrix- supported, and moderately to well-graded. Tabular and layered beds.
Components	
	Clasts : Sub-angular to sub-rounded fragments of carbonaceous sediments, volcanics, rare coal fragments, broken lithic and accretionary lapilli. Matrix : Matrix of sand-sized polymict lithic fragments and broken crystals. Cement : None Open Space : None
Grain Size	0.2 to 10 cm
Geometry	
	Morphology : Observed in wide distribution in the eastern past of Purnama, as indicated in APSD125 and ASPD123. It has also observed in outcrop at Gerhana. Well-developed beds (1 cm to 10 cm) with normal grading within fine grained clasts; and moderate sorting (10 to 20 cm beds) Diffuse normal and reverse grading; syn-deposited faults, flame and slumps structures. Interbedded medium-grained and fine-grained breccia. Contacts: Diffuse and erosional. Distribution: Purnama East and Gerhana.
Alteration and Mineralization:	Weak smectite, illite-kaolinite and trace disseminated pyrite.
Interpretation	Slumping, gravitational collapse and reworking in other breccias, or deposition from turbulent flow in A4, A5, A6 and A7 breccia pipe during phreatomagmatic explosions. Phreatomagmatic base-surge deposits.

3.5.4.2.2 Facies B2 - Weakly-Stratified, polymict, clast-rich, volcanic-clast and sediment dominant, carbonaceous-matrix supported breccia

The B2 breccias are weakly stratified, polymict, light to dark grey, unsorted- to moderately sorted and matrix-supported. The facies consist of angular to sub-angular clasts, clasts of volcaniclastic sandstone and siltstone, carbonaceous mudstone and sandstone, dacite. The B3 facies in the Purnama also contain andesite clasts. Accretionary lapilli are locally present and range from 1 to 8 mm. They have cores of fine-sand to mud-sized polymict grains surrounded by dark grey rims of mud-sized grains (Figure. 3.42; Table 3.10.

Matrix consists of sand to mud-size, lithic and crystal fragments, equivalent in composition and proportions to the lithic clasts. B2 breccias have the same range of bed forms as the B1 facies. However, B2 facies are predominantly weakly stratified and planar-bedded.

The B2 facies occur in medium to thick beds with diffuse to sharp, planar or channel bed forms. At East Purnama, a diffuse to sharp, undulose, erosional contact have separated the underlying well-bedded B1 facies from overlying weakly stratified B2 breccia. The average grain size of the B2 facies is coarser than the B1 facies. Normal grading is common, although individual beds have been observed with both normal and reverse grading around a core of clast-supported B1 facies breccia. B1 and B2 facies can be interbedded occur in alternating bed sets each consisting of multiple beds, or grade from B1 to B2 facies or vice versa in a single bed.

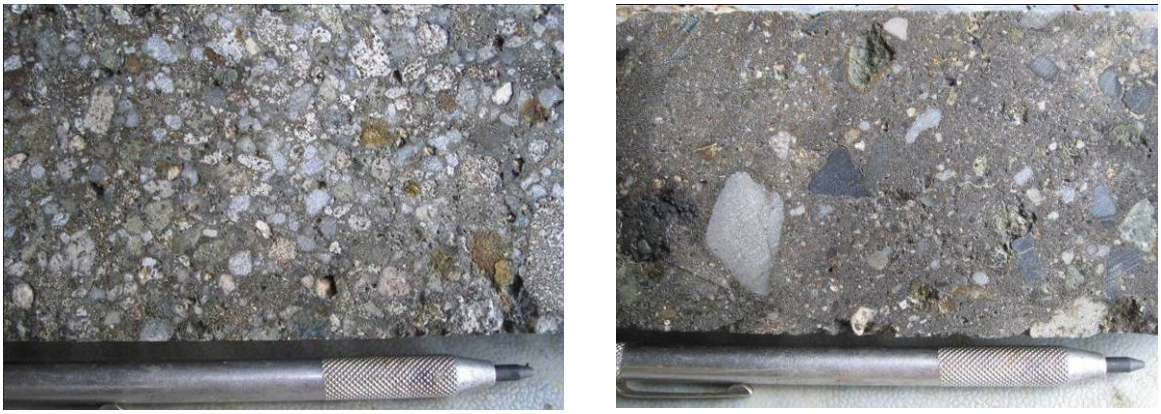

Figure 3.42. Facies B2 -Weakly-Stratified, polymict, volcanic-clast clast-rich and sediment dominant, carbonaceous-matrix supported breccia.
A. Weakly stratified B2 facies with polymict clasts.
B. Poorly sorted with coarse angular sediment clasts set in light grey carbonaceous matrix.

Table 3.10. Summary of facies B2 -Weakly-Stratified, polymict, volcanic-clast clast-rich and sediment dominant, carbonaceous-matrix supported breccias.

Facies	**Facies B2 -Weakly-Stratified, polymict, volcanic-clast clast-rich and sediment dominant, carbonaceous-matrix supported breccia**
Sub Facies	Medium-grained breccia Fine-grained (2-4mm) breccia
Internal Organization	Dark to medium grey and green Polymict, poorly- to good- sorted, matrix-to clast- supported Planar, diffuse normal, reserve and some beds normally graded
Components	
Clasts :	Dominated by sub-angular to sub-rounded white, green and grey of andesite and white dacite clasts with broken wispy margins. Sub-angular to sub-rounded carbonaceous mudstone/sandstone clasts are common, but generally finer-grained than other clast types. Rare angular to sub-angular broken quartz veining and vitreous coal fragments are present. 2-8 cm accretionary lapilli observe, especially in fine-breccia to medium-breccia. It has rims of fine sand- to silt-sized crystal and lithic fragments.
Matrix :	Fine- to sand- grained carbonaceous mudstone/sandstone sand-sized lithic fragments and broken quartz crystals.
Cement :	None
Open Space :	None
Grain Size	Predominantly medium-grained breccia with rare clasts up to 15 cm with interlayered with fine-grained breccia and volcanic lithic; minor-coarse breccia
Geometry	
Morphology :	Tabular with erosional contact. It is observed overlying porphyritic andesite at Purnama East. Poorly-developed beds with normally graded medium to coarse clasts. Poorly interbedded medium-grained and fine-grained breccia.
Contacts :	Contacts at boundaries are either sharp or gradational between facies and also sub-facies within individual beds are also gradational.
Distribution :	Purnama East and Gerhana North East
Alteration and Mineralization	Weak smectite, illite-kaolinite alteration Weak mineralization of trace disseminated pyrite
Interpretation	Phreatomagmatic base-surge deposits

3.5.4.3 Facies distribution and interpretation

The Martabe breccias formed by multiple brecciation episodes, thus it displays complex contact relationships, including multiple individual pipes and dykes, each of which consist of one or more A and B facies. Both internal and country rock contacts are typically gradational over meters to tens of meters, especially where earlier breccias are crosscut or removed by emplacement of later breccias. Breccias facies can be distinguished by variation in the clast to matrix proportions, degree of milling and clast type and morphology,

The Martabe breccias share many similarities with breccias that have been interpreted as diatremes (e.g., Yanacocha, Kelian, Montana Tunnels, Cripple Creek, Wau, and Baguio). The breccias have commonly large, extents, taper downwards, contain

abundant rock flour matrix, wall rock clasts and distinctive magmatic clast component that is more abundant than expected based on wall rock lithologies.

Phreatomagmatic brecciation is the product of direct magma-water interaction and by definition must incorporate juvenile magmatic material into the resulting deposits (Sheridan and Wohletz, 1981). A combination of phreatomagmatic and phreatic brecciation processes are inferred to form the diatremes (Lorenz, 1973; Lorenz, 1986), and identification of juvenile magmatic component in the former is the key to making a diatreme interpretation. Wall rock and pre-brecciation lithology played a key role in the location, geometry and clast types of all breccia bodies at Martabe. The combination with facies distribution, facies associations, breccia body geometry and wall rock relationships, enables the origins of the group A and B breccias to be determined.

A1 breccia: facies associations and interpretation

Carbonaceous sedimentary rock (siltstone and sandstone) clasts in the A and B facies breccias are from the carbonaceous sedimentary units, Sibarus formation (Tms) or Tapanuli group (Put). The clasts have similar compositions to these rocks and the clast gradations are from in-situ sedimentary units into monomict and then polymict A facies breccias. Presence of clay gouge, sheared and clast orientation suggest that some A1 breccias were tectonic in origin. In drillcore, A1 breccia tends to develop in spatial association with faults or projected faults. Some A1 breccias are sheared, following the intrusion margin (hornblende-phyric andesite (Tpia)) such as at Purnama. It is interpreted that the carbonaceous sedimentary rocks surrounding the intrusions were disrupted during emplacement of the intrusions and may have been phreatically brecciated due to boiling of ground water. As dykes, A1 breccia crosscut the polymict breccia A facies and stratified B facies. It is interpreted that the active structures that caused tectonic/fault breccia (A1 facies) continued after the main phreatomagmatic eruptions ceased.

A2 and A3 breccias: facies association and interpretations

The monomict, jigsaw-fit texture of A2 and A3 breccias occur as marginal phases to polymict A5 and A6 breccias. They are interpreted to have formed during the phreatomagmatic explosion that generated the A4, A5 and A6 breccias by fragmentation of wall rocks by mechanical abrasion; and/or hydraulic fracturing or phreatic brecciation in response to pressure gradients between the wall rocks and evacuated conduits. At Purnama, the A2 breccias occur at the Tmtv, Tmab, and Tpia intrusions margins. They also have no direct evidence for phreatomagmatic fragmentation (i.e. juvenile rhyolite

clasts). The jigsaw-fit texture and less clast-rotated texture of A2 and A3 breccias are interpreted to have formed by explosive phreatic fragmentation and tectonic fragmentation related to late-stage normal faults.

A4, A5 and A6 breccias: facies association and interpretations

Wispy and blocky felsic intrusion clasts found in the carbonaceous sandy- or matrix-supported breccias in facies A4, A5 and A6 are interpreted to be the juvenile magmatic component clasts, as seen at Kelian (Davies, 2002) and many similar geologic settings (i.e., Yanacocha, Turner, 1997; Wau, Sillitoe et al., 1984). These breccias are matrix-supported and lack the jigsaw-fit textures of the A2 and 3 breccias, indicating that disaggregation of the rhyolite magma was more advanced in the A4, A5 and A6 breccias.

Polymict, fine- to coarse-grained clast, silty-sandy matrix-supported with presence of wispy textures of the A5 and A6 breccias have similar internal organization to the *dispersed peperite* of Hanson and Wilson (1993), that are produced by intrusion of rhyolite magma into wet, unconsolidated fault breccia and gouge, wet A1 facies breccia or wet carbonaceous mudstone.

A4 breccias containing blocky rhyolite clasts with curviplanar margins are texturally similar to *blocky peperite* and A4 breccias containing wispy rhyolite clasts are a variety of *fluidal peperite* (cf. Busby-Spera and White, 1987; Hanson and Hargrave, 1999).
The A4 breccia with wispy and blocky rhyolite clasts are also interpreted to be a variety of intrusive peperite produced by mingling of rhyolite magma with unconsolidated, wet, clastic material including one or more of carbonaceous mudstone and sandstone; fault gouge; A1 breccia; and/or A5 and A6 breccia. Roache et al. (2000) described similar wispy and blocky rhyolite clasts set in a matrix of polymict breccia and inferred that wispy clast morphology was produced via squashing of plastic rhyolite clasts by the relatively coarse clasts of the host breccia.

Interaction between the intruding rhyolite and the wet unconsolidated sediment could have resulted in purely explosive phreatomagmatic fragmentation, non-explosive quench fragmentation, or a combination of both explosive and non-explosive fragmentation. Although gradations between wispy rhyolite-rich A4 breccia to jigsaw-fit A2 breccia, A3 breccia and coherent rhyolite have been observed locally, typically the A4 breccias have no identifiable magmatic 'roots'.

It is interpreted that rhyolite dissagregation into wispy and blocky clasts generally resulted in complete fragmentation of the intruding magma batch within the unconsolidated sediment. The magma – wet sediment interaction was sufficiently energetic

to disperse the clasts away form the coherent rhyolite feeder. Clast transport is interpreted to have been explosive and driven by phreatomagmatic explosions. The A4 breccias contain wispy-rich textured (with less jigsaw-fit) rhyolite clasts, that might be interpreted to be the preserved roots of the A5 and A6 breccias, and their rare occurrence is most likely related to destruction of the magmatic root zone by explosive fragmentation.

The predominance of sub-rounded, lithic fragments in the A5 and A6 breccias suggests that development of these clasts resulted from greater clast transport and abrasion than the juvenile rhyolite clasts (cf. Roache et al., 2000), perhaps due to recycling during multiple brecciation events (e.g., Houghton and Smith, 1993).

Preservation of the wispy- and blocky-shaped juvenile magmatic clasts in A4 breccias is interpreted to indicate only minor clasts transport. In the A5 and A6 breccias, equivalent juvenile magmatic components occur, however they lack the wispy or cuspate morphology of those in the A4 facies. A5/A6 breccias are interpreted to be the product of progressive transport and abrasion of A4 breccia components, either in single brecciation events or during repeated brecciation cycles (either phreatic or phreatomagmatic; Houghton and Smith, 1993). The observations made during this study support this interpretation.

A4 facies contain mostly juvenile clasts that are interpreted to have a phreatomagmatic origin. There is a gradational transition from A4 facies (monomict wispy-texture) to A5 and A6 (polymict, vary in clast size and angularity and wispy-texture content) indicating that there is a direct link between magma intrusion and generation wispy-texture rhyolite clast brecciation. More commonly, an igneous-clast phase is inferred to represent the juvenile component (e.g., dacite porphyry clast at Wau, Sillitoe et al., 1984).

This A4 facies breccia has been observed in transition with the fine grained facies polymict carbonaceous breccia (A5 and A6 facies). Although, the clasts are entirely composed of coherent rhyolitic or dacitic, the facies has not been observed in gradational contact with these intrusions.

A7 breccias: facies association and interpretation

The occurrence of abundant accretionary lapilli is consistent with deposition from wet, gas-rich particle systems (Walker, 1984). Accretionary lapilli are sometimes used to indicate formation the in sub-aerial environment; however, they have been identified in both subvolcanic breccias at Mt Leyshon (Wormald, 1991), in gas segregation pipes in the

Oruanui Ignimbrite in New Zealand (Self, 1983), in dykes cutting breccias at the Rain mine (Williams et al., 2000) and at Lihir (Carman, 1994).

At Martabe, water supply and magma-sediment mixing may have become greater later in the evolution of the diatreme complex due to the increased abundance of sand- to silt-sized 'sediment" in the pipes after successive explosions events. Very fine-grained matrix or rock flour is inferred to have formed during high-water-magma ratio explosions and/or as a result of highly efficient fuel-coolant mixing.

A8 breaccias: facies association and interpretation

Based on their contact relationships, the A8 facies and accretionary lapilli-bearing sandstone formed in the subsurface. Since the components and textures of the A8 facies are identical to those of the polymict A5 and A6 breccias, their origin is inferred to be equivalent. In particular, the presence of <2 mm cuspate and wispy juvenile rhyolite clasts indicates that some A8 sandstones formed as the result of discrete phreatomagmatic explosions rather than progressive grain size reduction during multiple brecciation events.

The occurrence of clast of hydrothermal breccias cemented breccias in the A8 breccias, and vice versa indicates that formation of some A8 breccias occurred during the post-phreatomagmatic phase of breccia development.

B breccias: facies interpretation

B1 facies shares similar matrix and textural characteristics as the other polymict breccias, such as A5 and A6 facies breccias. But they contain less distinctive wispy and blocky (with curviplanar margins) rhyolite clast shapes. This may be because the wispy and blocky shapes were eroded or reworked. Overall, B facies breccia is defined by the presence of stratification, such as in planar, dune bed and minor low angle cross beds, which are consistent with deposition from turbulent, gas-rich flows at the transition from low to high-flow regimes (Walker, 1984; Valentine and Fisher, 2000).

Accretionary lapilli are also present together with soft sediment or plastic deformation structures. The B1 facies are interpreted to have been deposited by a combination of wet, pyroclastic base surge, fall out and co-surge fallout (Fisher and Waters, 1970; Walter, 1984).

Presence of interbedded facies B1, with uniformly thick beds of accretionary lapilli and sand to silt sized grains, suggests that this facies formed as a combination of surge fallout of fine ash after passage of the turbulent 'wet' surge (Walter, 1984). This type of deposition is inferred to have occurred at the surface from cohesive, wet, cold (<100°C,

Valentine and Fisher, 2000) base surge generating phreatomagmatic-eruptions. At Martabe, deposition is inferred to have occurred in a wet, terrestrial environment, based on the presence of interbedded carbonaceous mudstone (containing wood fragments) within the B facies sandstone and breccias.

The B2 breccia is interpreted as re-working of B1 facies breccia. It may also occur within the breccia pipe and likely formed from turbulent flow during brecciation events, or slumping of material back down the evacuated conduit or by gravitational collapse into polymict A facies breccia during phreatomagmatic explosions. The B2 breccias may also have formed by syn-eruptive resedimentation of the B1 breccia and sandstone either due to rainfall, eruption of water from the volcano (Walker, 1984), or collapse of the inferred maar deposits into the maar crater.

3.5.5 Discussion

At Martabe there are a wide variety of distinctive breccias within the dome and diatreme complex. The origins and processes of these breccias are varied and include phreatomagmatic, phreatic, tectonic and hydraulic brecciation. There are complex overlaps in these processes and it is likely the breccias preserved today are the product of hybrid brecciation processes.

Intrusion of rhyolitic magma into a fault-bounded block of brecciated carbonaceous mudstone (part of Sumatran Fault System) within an active hydrothermal system resulted in phreatomagmatic brecciation at Martabe. The presence of juvenile magmatic clasts with delicate wispy texture and cuspate margins, in situ rhyolite clasts associated with dacitic-andesitic dykes and base surge (stratified breccia) deposits are the key pieces of evidence for a phreatomagmatic origin.

The A2 and A3 breccias and rhyolite dykes are interpreted to be the root zones to the phreatomagmatic breccias and are 'frozen' examples of the magma-sediment mixing event. The transition from in-situ rhyolite dykes through A2 breccias and into the juvenile clast bearing A3 breccias has not been documented previously in a subsurface breccia complex, likely perhaps due to the poor preservation potential of these facies.

Stratified breccia is found in some locations at depth. It is interpreted as a result of collapse and down-dropped blocks into the eruption pipes of phreatomagmatic base-surge deposits from the near surface maar environment. Structure played a key role in the localization of the diatreme breccias. The pre-cursor sedimentary rocks were brecciated

tectonically during faulting. At Martabe, pre-existing faults and structural weakness controlled felsic magmas emplacement along northeast- and northwest-striking fault.

3.6. Conclusion

At Martabe, detailed drill core logging and mapping has led to a better understanding of the diatreme breccias and associated intrusions, which are closely associated with the Purnama, Baskara, Kejora, Pelangi and Gerhana epithermal deposits. There are a wide variety of distinctive breccias within the dome and diatreme complex. The origins and processes of these breccias are varied and include phreatomagmatic, phreatic, tectonic and hydraulic brecciation.

CHAPTER 4

GEOCHRONOLOGY

4.1 Introduction

The first geochronological investigation in North Sumatra were performed in the 1970's when the region was mapped by the Indonesian Directorate of Mineral Resource (DMR) and the British Geological Survey (BGS) with the aim of identifying mineral resources and providing a geological database of Sumatra (Hehuwat, 1976; Cameron et al., 1980; Aspend et al., 1982; Rock et al., 1982). More recently, ^{40}K-^{40}Ar age dating was undertaken to determine the age of rocks dating back as far as 65 Ma (Bellon et al., 2004).

This chapter integrates the results derived from several separate stages of geochronology in the North Sumatra region, and in particular the Martabe district. In an effort to improve the accuracy ofthe age dating, ^{40}Ar/^{39}Ar and U-Pb ICPMS dating was conducted in the Martabe district. The U-Pb ICPMS dating method was undertaken on the Martabe flow dome complex. The^{40}Ar/^{39}Ar method was previously used in the district on intrusive granite, volcanics and alunite (Turner, 2002). Therefore, new ^{40}Ar/^{39}Ar and U-Pb ICPMS data are integrated with existing published K/Ar and Rb/Sr data from the region. Locations of the samples used to dating are shown in Figure 4.1. Taken together, and integrated with field relationships from regional and detailed mapping, these data constrain the age of the epithermal systems and identify the existence of different volcanic and intrusive rock successions within the Martabe district. These data allow the establishment of temporal relationships between igneous intrusions and the associated hydrothermal system in the Martabe district.

4.2 Review of previous data

Prior to this study, several geochronological studies were conducted in Northern Sumatra, including in the Sibolga and South Tapanuli regions where the Martabe district is located (Table 4.1 and Table 4.2). The age dating methods include K-Ar and Rb-S on biotite, hornblende or whole rock samples from granite and volcanic rocks (Hehuwat, 1976; Aspend et. al., 1982; Fontaine and Gafoer, 1989; Clarke, 1990; Kallagher, 1990; McCourt, 1996; Bellon et. al., 2004).

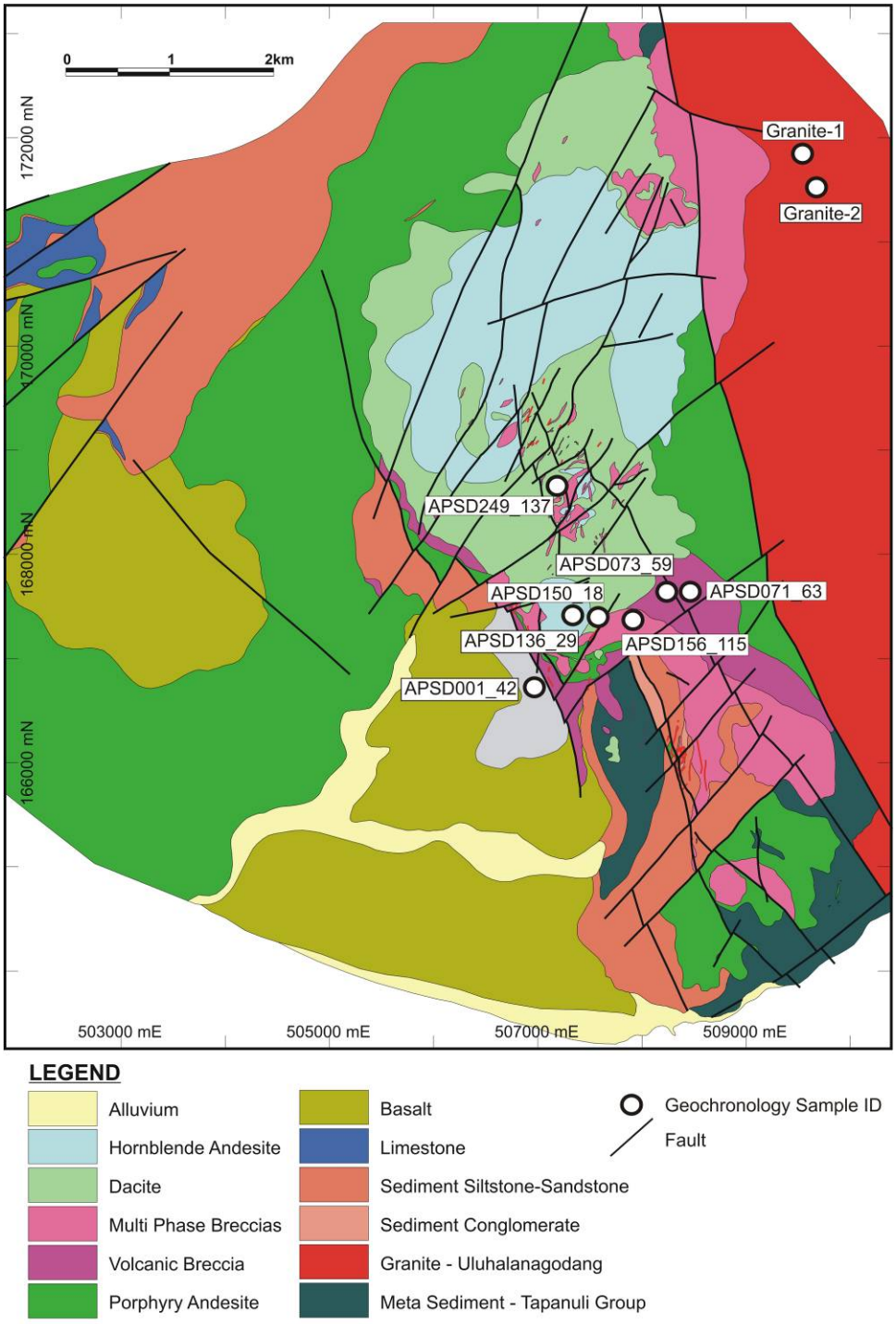

Figure 4.1. Geological map of the Martabe district showing the location of samples used to the geochronological investigation.

4.2.1 Early Jurassic Plutonic episode in Sumatra – Triassic Sibolga Granite

The granites of Sumatra form two distinct groups. The older group is widely distributed as isolated plutons and batholiths over the entire island, but mainly in the area to the east of the Barisan Range. Some of these granites have associated tin-mineralisation and have a narrow compositional range of SiO_2 values, generally above 70 wt. %. These

older granites are correlated with granites of the Central (Main Range) province of the Southeast Asian Tin Belt of Malaysia and Thailand. A younger group of granites and other intrusion rocks form the plutonic component of a volcanic arc suite. They are confined to the Barisan Range and form small batholiths and separated plutons with compositions ranging from gabbro to monzogranite (Cobbing, 2005).

Many of the published isotopic ages of granites from Sumatra are not accompanied by petrographic descriptions or whole-rock geochemical analyses. Moreover, in some cases isotopic ages determined for particular plutons have large error bars and, therefore, do not constrain the exact age of emplacement. In other cases, the available geochemistry is sufficiently anomalous to cast doubt on the well reliability of the reported isotopic age. The Sibolga Batholith in the northwest Sumatra is an example of difficulties in interpreting the isotopic age of granites of Sumatra (Cobbing, 2005). This pluton has yielded a wide range of isotopic ages from 264-75Ma (Bellon et al., 2004; Table 4.1). It is a very large body, and may well be composite, comprising several distinct units of different ages. In the hinterland of Sibolga, these granites consist of biotite-hornblende granite and granodiorite with pink alkali-feldspar megacrysts, mafic enclaves and mafic dykes. These characteristics are typical of the Eastern Province Granite of the Peninsular Malaysia and the Tin Islands, and distinguish these rocks from the tin-mineralized granites in the same areas (Cobbing et al., 1986, 1982). The location of the Sibolga granite is anomalous, as it crops out on the far west coast of Sumatra, 300 km way from the Eastern Province Granites of Peninsular Malaysia. An age of 264 Ma (Aspden et al., 1982) may represent the age of the emplacement of the Sibolga granite, but the 13 other ages recorded from this body that range from 75 to 264 Ma may have been obtained from satellite plutons in the Sibolga region (Cobbing, 2005). In the northwest, the partially unroofed Sibolga granite, which is of batholitic proportion, is the oldest dated intrusion. The main phase is Permo-Triassic but younger centres are known to exist (Aspden et al., 1982).

The Uluhalanagodang granite is well exposed at the eastern part of the Martabe district. It forms both intrusive and fault contacts with the Tapanuli Group. This granite remained undated until 2002, however Aspend et al. (1982) assumed a Miocene age.

Table 4.1. Radiometric age dates for the Triassic - Early Jurassic intrusions and plutons in the Sibolga region, north Sumatra (Bellon et al., 2004).

Lithology	Dating Method	Age (Ma)	Reference
Sibolga Granites	Rb-Sr, isochron	264 ± 6	Aspden et al. (1982)
Sibolga Granites	Rb-Sr, ? whole rock	257 ±24	Fontaine & Gafoer (1989)
Sibolga Granites	K-Ar, biotite	211 ±5	Aspden et al. (1982)
Sibolga Granites	K-Ar, biotite	211 ±3	Hehuwat (1976)
Sibolga Granites	K-Ar, biotite	206 ±3	Fontaine and Gafoer (1989)
Sibolga Granites	K-Ar, biotite	206 ±2	Fontaine and Gafoer (1989)
Sibolga Satellite Granites	K-Ar, biotite	217 ±4	Fontaine and Gafoer (1989)
Sibolga Satellite Granites	K-Ar, biotite	212 ±3	Fontaine and Gafoer (1989)
Sibolga Satellite Granites	K-Ar, biotite	147 ±2	Aspden et al. (1982)
Sibolga Satellite Granites	K-Ar, hornblende	144 ±2	Aspden et al. (1982)
Sibolga Satellite Granites	K-Ar, biotite	75 ±1	Hehuwat (1976)

4.2.2. Late Early Miocene - Mid Miocene Angkola Volcanic Formation

In northern Sumatra, numerous late Early Miocene - Mid-Miocene volcanic formations have been mapped. Several plutons were emplaced into the volcanic arc. ^{40}Ar-^{39}Ar ages obtained by Imtihanah (2000) from the Lolo Batholith show that the Sumatra Fault Zone was active during the latter part of the Late Early - Mid-Eocene volcanic phase. Sub-volcanic and other intrusions are observed to be associated with several of the Mid Miocene volcanic formations and have been dated by Bellon et al. (2004) and Aspden et al. (1982). South of Lake Toba, volcanic rocks become more extensive, with lavas and volcaniclastic rocks forming a discntinuous linear zone (Crow, 2005). Dykes and flows in the Sibolga area have been dated between 17 and 20 Ma (Bellon et al., 2004). The andesites within a ^{40}K-^{40}Ar age range of 17 Ma to 19 Ma occurs within the Angkola Volcanic Formation (Table 4.2).

Table 4.2. Radiometric age dates for the Angkola Volcanic Formation of the Late Early Miocene-Mid Miocene volcanic episode in the Sibolga region, North Sumatra (Bellon et al., 2004).

Lithology	Dating Method	Age (Ma)	Reference
Andesite dyke in Barus Formation	^{40}K-^{40}Ar	19.6 ± 0.58	Bellon et al. (2004)
Andesite flow in Angkola Volcanic	^{40}K-^{40}Ar	18.2 ± 0.45	Bellon et al. (2004)
Andesite dyke in Angkola Volcanic	^{40}K-^{40}Ar	16.8 ± 0.47	Bellon et al. (2004)
Andesite dyke in Angkola Volcanic	^{40}K-^{40}Ar	16.8 ± 0.39	Bellon et al. (2004)
Andesite, Musala island	^{40}K-^{40}Ar, whole rock	17.2 ± 5	Aspden et al. (1982)

4.3 Geochronology of the Martabe district

4.3.1 Analytical methods

The U-Pb dating was determined by LA-ICPMS at CODES, University Tasmania. The U-P zircon age dating used an HP4500 quadrupole ICP-MS with a 213nm New Wave Laser. Zircons were extracted from crushed fresh rock samples of about 1-2 kg to <400 micron using heavy liquid separation techniques. Individual crystals were hand-picked and mounted on double-sided adhesive tape and enclosed in epoxy resin discs. The discs were polished and then cleaned. The samples were then washed in distilled water in an ultrasonic bath. Scanning electronic microscopy (SEM) and/or cathodoluminescence (CL) imaging were deformed on the zircon grains prior to U-Pb analyses to reveal textures and to guide the ICPMS analyses (Figure 4.2). Zircons were ablated in He atmosphere in a custom-made chamber with the laser pulsing at 5 Hz and a 30 micron meters diameter beam delivering ~12 J/cm^2 and drilling at approximately 1 micron meter/sec. A total of 11 masses were measured (^{96}Zr, ^{146}Nd, ^{178}Hf, ^{202}Hg,^{204}Pb, ^{206}Pb, ^{207}Pb, ^{208}P, ^{232}Th, and ^{238}U), with longer counting times on Pb isotopes giving a total quadrupole cycling rate of 0.2 sec.

Each analysis began with 30 seconds of background gas followed by 30 seconds with the laser switched on. Four primary (Temora zircons of Black et al., 2004) and two secondary (91500 of Wiedenbeck et al., 1995) standards were analyzed both before and after every 12 zircon analyses to correct for instrumental drift. Repeated monitoring of U/Pb mass fractionation during drilling showed an average fractionation of U/Pb varying from 0.050 at the start of a 30 sec analysis to 0.053 at the deepest level of laser ablation. More detailed analytical procedures are described by Compston et al. (1984, 1992) and Williams (1998). Decay constants used are those recommended by Steiger and Jager (1977), and common Pb correction used the ^{204}Pb methods of Compston et al. (1984). The U-Pb LA-ICPMS analytical data in Tabel 4.4 are the mean values of twelve consecutive scans for each zircon spot.

Some Ar-Ar dating has been performed by Turner (2004). Biotite, alkali-feldspar, alunite and hornblende were extracted from crushed rock samples using a floatation method, and was then handpicked to a purity of >99%. Apparent ages were calculated using decay constants recommended by Steiger and Jager (1977). Argon data were evaluated using age spectra, apparent ^{39}Ar/^{37}Ar ratios (for whole rock and hornblende samples), and ^{39}Ar/^{40}Ar versus ^{36}Ar/^{40}Ar isochron diagrams. The determination of whether the individual apparent ages in an age spectrum yielded a "plateau" was made using the criteria of Fleek et al. (1977). Following these criteria, a plateau is defined as comprising

two or more contiguous gas fractions, which yield apparent ages that are statistically indistinguishable at the 95% confidence level. Plateau ages were calculated using a weighted mean based on the proportion of $^{39}Ar_K$ released during incremental heating experiment. Plateau ages are given at ± 1σ and include the analytical uncertainty in the determination of the fluency parameter.

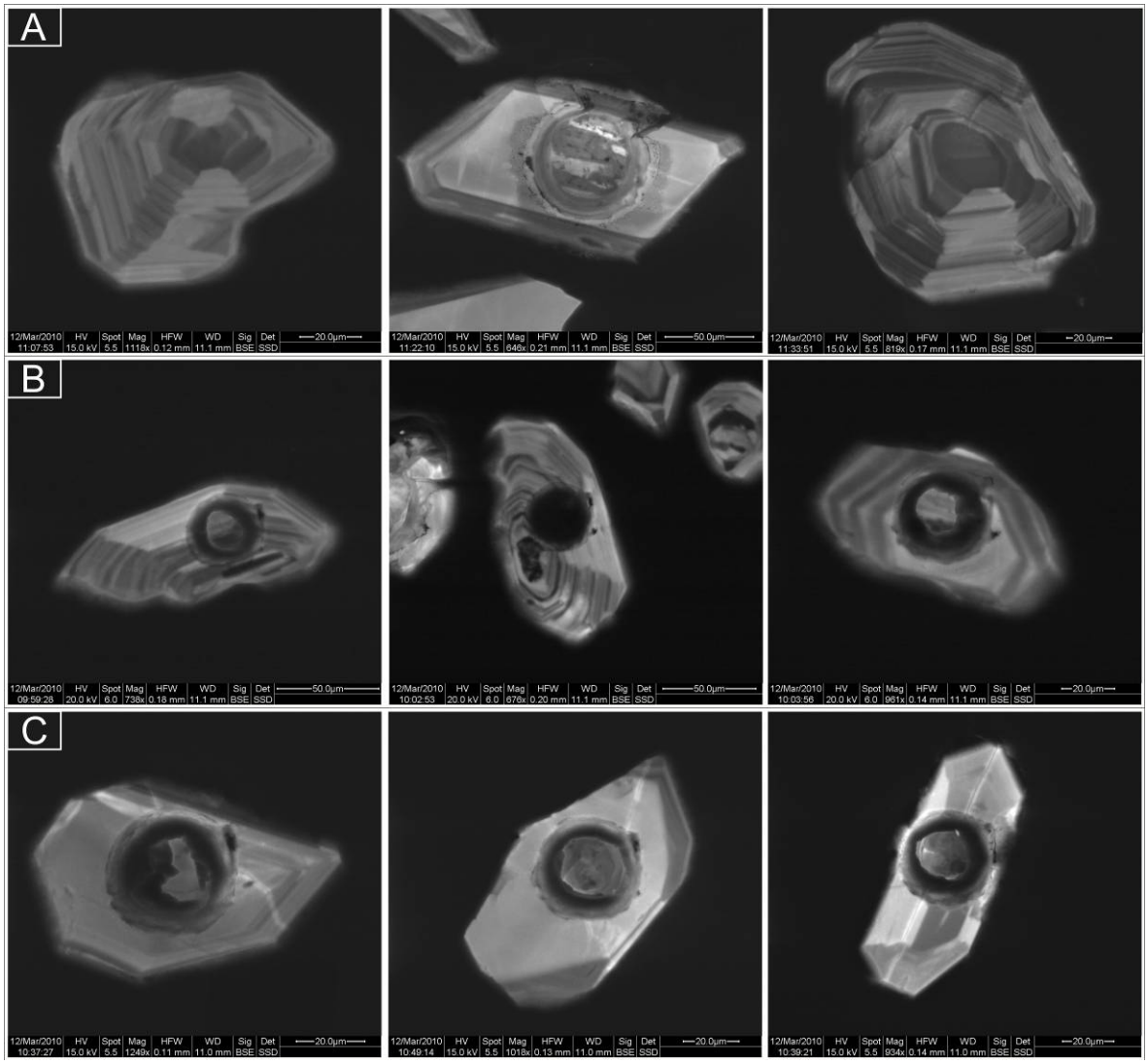

Figure 4.2. Representatitive cathodoluminescence images showing the morphology and internal textures of zircon grains from the Martabe district. Photos (A) and (B) are images of zircons from hornblende-quartz andesite (APSD150_18 and APSD249_137). Photos (C) are images of zircons from a dacite (APSD071_63) at the Purnama deposit. The distinct oscillatory zonation of these zircon grains indicates they are of magmatic origin. The circles represent positions of LA-ICP-MS analytical spots.

4.3.2 Samples

Nine samples were selected for geochronological study: (a) three for zircon U-Pb LA-ICPMS dating and (b) six for Ar-Ar dating. The six Ar-Ar dating samples were collected by the author and performed by Turner (2004). Samples include primary biotite, hornblende and alkalic-feldspar from the relatively fresh Uluhalanagodang granite, hornblende from a hornblende-pyric andesite of the Martabe volcanic dome, groundmass from basaltic andesite of Angkola volcanic formation and two samples of alunite from the advanced-argillic alteration zone. These samples were analyzed by the Ar–Ar stepped heating technique. Ar–Ar ages were determined from age spectrum diagrams and all data are reported at the 2σ level of uncertainty.

A summary of the results of the U-Pb ICPMS and $^{40}Ar/^{39}Ar$ incremental heating experiments are listed in the Table 4.3 and are discussed following a description of each sample. Individual spectra are shown in Figures 4.3 through 4.8. The detail Ar-Ar and zircon U-Pb LA-ICPMS analytical data are listed in Tables 4.4 and 4.5.

Table 4.3. A summary of new $^{40}Ar/^{39}Ar$ and U-Pb age data from the Martabe district.

Sample No	Description	Mineral	Preferred age (Ma)		Methods
			Apparent	±Error	
Granite-1	Granite	Biotite	208.6	0.07	Ar-Ar Total Fusion
Granite-1	Granite	K-feldspar	-	-	Failed
Granite-2	Granite	Biotite	209.3	0.19	Ar-Ar Total Fusion
Granite-2	Granite	K-feldspar	-	-	Failed
APSD001_42.3	Basaltic Andesite	Matrix	18.9	0.07	Ar-Ar Whole rock matrix
APSD071_63	Dacite	Zircon	3.8	0.5	U-Pb Zircon
APSD150_18	Hornblende Andesite	Zircon	3.1	0.4	U-Pb Zircon
APSD249_137	Hornblende Andesite	Zircon	2.8	0.3	U-Pb Zircon
APSD136_29.6	Hornblende Andesite	Hornblende	2.8	0.12	Ar-Ar Isochron
APSD156_115.3	Alunite#1	Alunite	3.3	0.02	Ar-Ar Total Fusion
APSD156_115.3	Alunite#1	Alunite	3.3	0.11	Ar-Ar Isochron
APSD073_59.75	Alunite#2	Alunite	2.1	0.04	Ar-Ar Total Fusion
APSD073_59.75	Alunite#2	Alunite	2.0	0.02	Ar-Ar Step-heated
APSD073_59.75	Alunite#2	Alunite	2.1	0.10	Ar-Ar Isochron

4.3.2.1 Uluhalanagodang granite sample

The eastern part of the study area is occupied by the unaltered to extensively deformed Uluhalanagodang granite suite. This granite intrudes the Tapanuli Group; its contact with the dacitic dome complex is either a fault or an inferred intrusive contact.

Sibolga plutonic rocks of similar texture and compositional range occur 20 km north of the Martabe district, where they might be separated by the fault.

The Uluhalanagodang granite is characterized by coarse porphyritic quartz-feldspar, with a distinctive pink, white and green coloration due to weak to pervasively chlorite-sericite-epidote alteration. In many places it is affected by brecciation. The sample selected for dating was a coarse-grained quartz-phyric, biotite-hornblende granite; collected about 2-km east of Gerhana deposit, on the western side of the Uluhalanagodang granite. Biotite separates from the Uluhalanagodang granite-1 and granite-2 samples have near identical Ar-Ar ages of 208.5± 0.07 Ma and 209.2± 0.19 Ma, respectively (Figure 4.3). No plateau was defined for the alkalic-feldspar from the two granite samples.

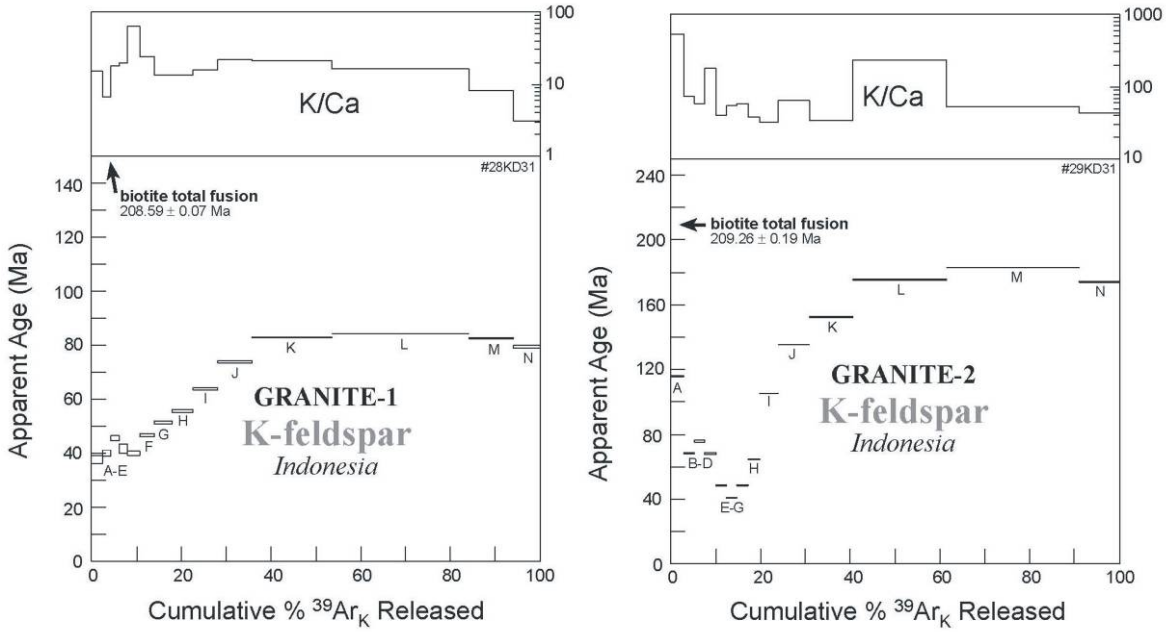

Figure 4.3. $^{40}Ar/^{39}Ar$ spectra from Uluhalanagodang granite-1(A) and granite-2 (B) samples.

4.3.2.2 Angkola Volcanic Formation sample

The Angkola Volcanic Formation (Tmd) occurs in the western part of the district (Figure 4.1). This formation is characterized by aphyric and porphyritic andesite flows, lithic-rich volcanic breccias, and less extensive ash-flow tuffs. One sample of matrix from a basaltic andesite in Angkola Formation Volcanic was dated. Sample (APSD001_42.3), which was collected from a drilhole on the southern side of the Purnama fault, returned an Ar-Ar age of 18.9± 0.7 Ma (Figure 4.4).

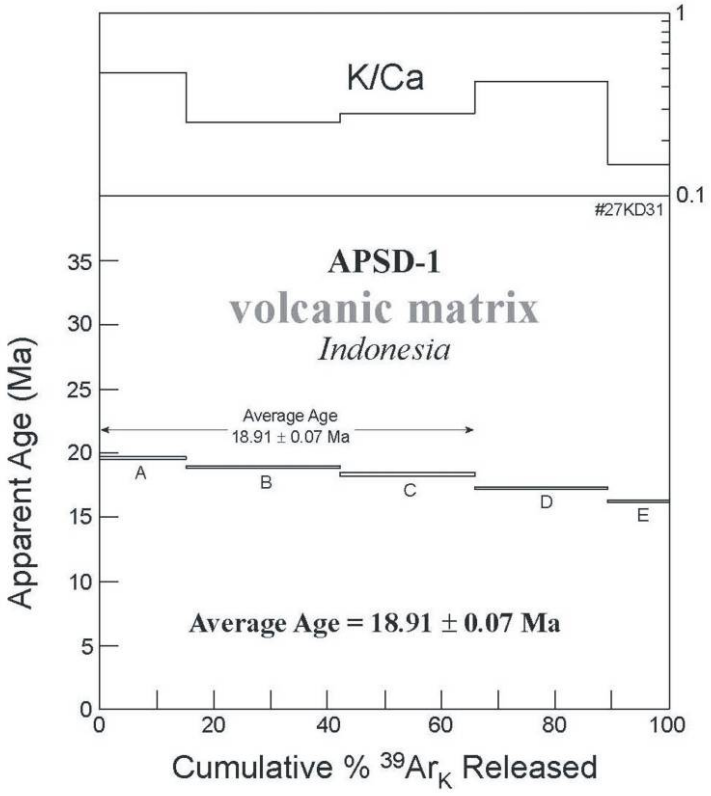

Figure 4.4. ^{40}Ar-^{39}Ar spectra of whole rock from volcanic matrix of APSD001_42.3.

4.3.2.3 Martabe flows dome samples

Four samples from the Martabe flows dome complex were selected; three for zircon U-Pb LA-ICPMS dating and one for $^{40}Ar/^{39}Ar$ dating. The samples were representative of least altered hornblende-quartz andesite (APSD136_29.6, APSD150_18 and APSD249_137) and dacite (APSD71_63). Based on mapping, these volcanics units are the youngest known in the district and host the high-sulfidation systems.

One andesite sample (APSD136_29.6) from the Purnama deposit had a spectra with increasing radiogenic yield over the initial heating steps that are correlated with decreasing apparent ages. Analysis of this sample had nine stepwise-heating stages as listed in Table 4.4. The fourth and fifth stages yielded a plateau. The remaining seven stages formed a range of apparent ages. Plotting the$^{39}Ar/^{40}Ar$ vs.$^{36}Ar/^{40}Ar$ data gives an isochron age of 2.8± 0.12 Ma (Figure 4.5), with an MWSD of 3.4.

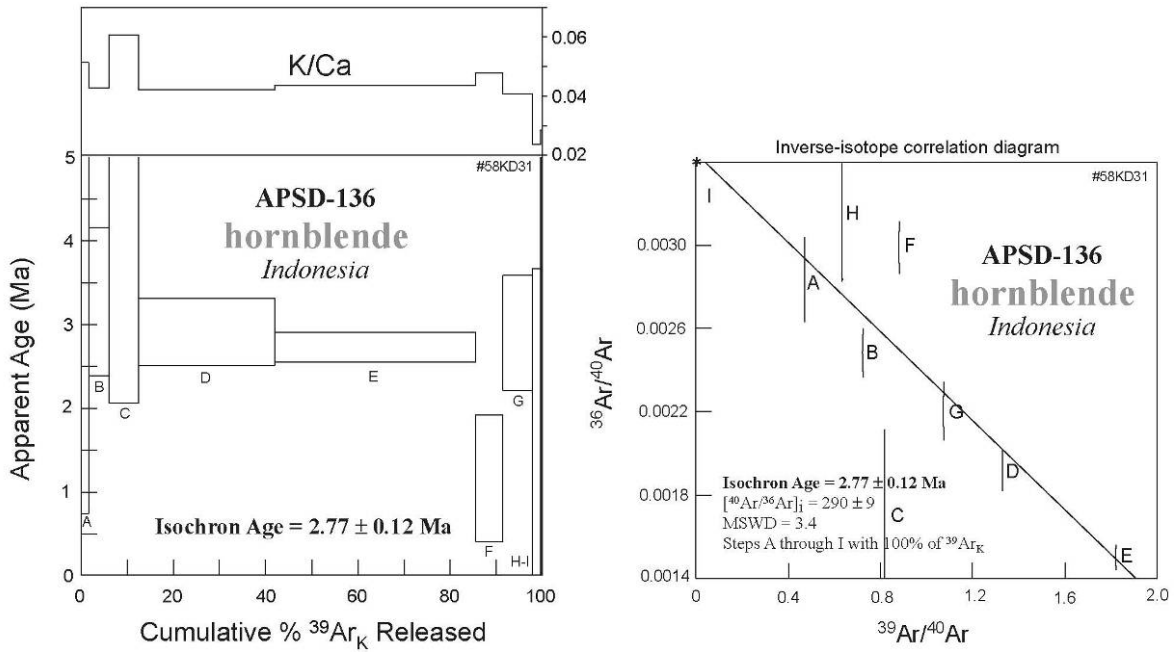

Figure 4.5. ^{40}Ar-^{39}Ar spectra of hornblende from fresh hornblende-phyric andesite show an isochron age of 2.8±0.12 Ma.

Zircon grains were obtained from three samples at two different locations in the Martabe flow domes. These samples were intended to evaluate the apparent close similarity between the ages of hornblende-quartz phyric andesite and dacite flow domes at Martabe. As noted above, a hornblende-phyric andesite sample that was previously dated in 2002 using Ar-Ar isotope analysis came from APSD 136_29.6 (Purnama). In this study, zircon grains were analyzed from APSD249_137 (Baskara) and APSD150_18 (Purnama), which are similar to the hornblende-pyric andesite. The third sample is a dacite that form the upper part of the dome (APSD071_63). The U-Pb data for the three samples (Table 4.5) were plotted on a concordia diagram (Figures 4.6–4.8) to test for multiple age populations.

APSD249_137

Sample APSD249_137 was collected from a hornblende-quartz andesite of Baskara (Figure 4.6). This andesite has a porphyritic texture of plagioclase (50 to 65 vol. %) and hornblende (up to 35 vol. %), with minor quartz (<5 vol. %) and accessory magnetite, sphene, zircon and apatite. The hornblende has been weakly altered by chlorite and carbonate. The plagioclase has generally been replaced by clays and carbonate. Zircons from this sample are mostly stubby or rounded grains, with length/width ratios ~2:1. Cathodoluminescence (CL) imaging indicates that all zircon grains have similar internal structures; a large core with an oscillatory rim and a very thin overgrowth (Figure 4.2a), suggesting a magmatic origin for the zircons with a late thermal event. Twelve analyses on the zircon grains from APSD249_137 (each grain with 12 analyses) yielded ages from 2.3±

0.6 Ma to 3.6± 0.7 Ma (Table 4.5, Figure 4.6). All the data form a coherent group which give a weighted mean $^{206}Pb/^{238}U$ age of 2.8± 0.3 Ma with mean squared weighted deviation (MSWD) of 0.39. The 2.8± 0.3 Ma age is interpreted as the youngest age of intrusion of the hornblende-quartz andesite.

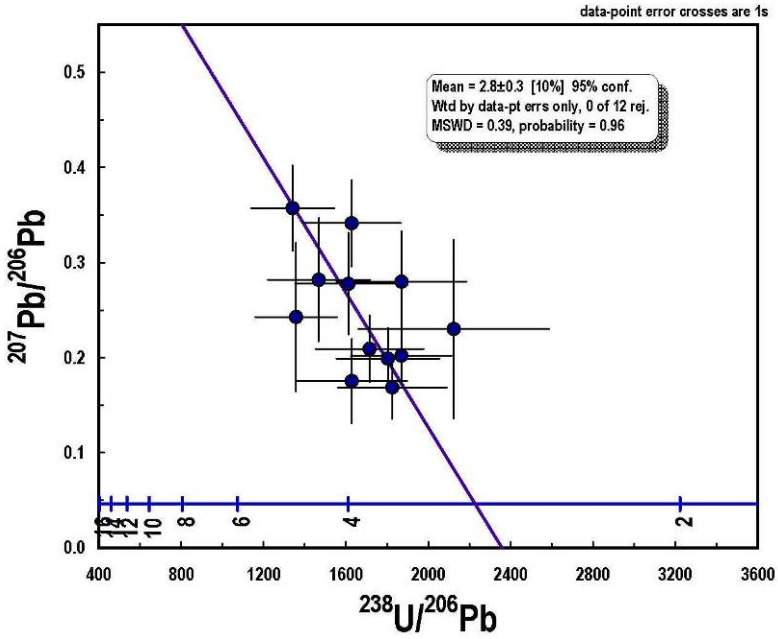

Figure 4.6. Reverse concordia plot of U-Pb LA-ICPMS on zircon from hornblende phyric-andesite of APSD249_137. The best fit regression and ^{207}Pb corrected age calculated using the Isoplot 30 software assuming common Pb composition based on the two stage model of Stacey and Kramer (1975).

APSD150_18

Sample APSD150_18 was taken from a near surface ourcrop exposure of hornblende-quartz andesite at the Purnama deposit (Figure 4.7). This andesite is similar to sample 249_137 and is composed of hornblende, plagioclase and quartz with accessory magnetite, apatite, zircon and sphene. Microscopic observations suggest that this andesite has been altered, with the hornblende partially replaced by chlorite and plagioclase by sericite. No obvious cleavage observed within the sample, except for quartz locally exhibiting some undulatory extinction. Zircon grains from this sample show similar features and are elongate prisms, mostly 50–150 μm by 20–70 μm in size. A total of 12 zircons from this sample were analyzed. All the data form a coherent group which give a weighted means $^{206}Pb/^{238}U$ age of 3.1± 0.4 Ma with points (MSWD)=0.39. This age is interpreted as the oldest age of intrusion of the hornblende-quartz andesite.

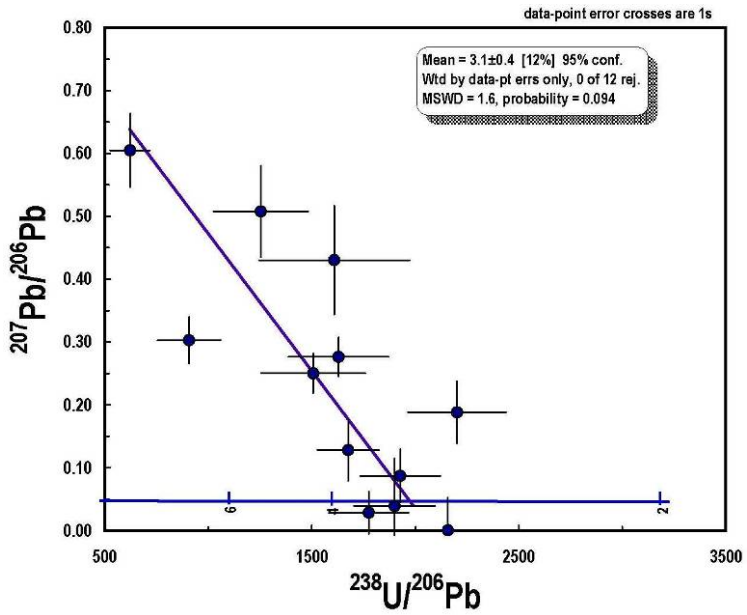

Figure 4.7. Reverse concordia plot of U-Pb LA-ICPMS analyses on zircon grain from hornblende-phyric andesite ASPD150_18. Best fit regression and ^{207}Pb corrected age calculated using the Isoplot 30 software assuming common Pb composition based on the two stage model of Stacey and Kramer (1975).

APSD71_63

Sample APSD71_63 is a quartz-bearing dacite taken from the eastern part of the Purnama deposit. The sample is white and displays a porphyritic texture. Phenocrysts are mainly feldspar (~20 vol. %) and quartz (~10 vol. %) and the groundmass includes feldspar (~50 vol. %), quartz (up to 10 vol. %), biotite (~5 vol. %) and hornblende (2–3 vol. %), with accessory magnetite, apatite and zircon. At the Baskara deposit, this lithology occurs in the same area as the main gold mineralisation. Twelve analyses made on 12 zircons from this sample gave $^{206}Pb/^{238}U$ ages between 2.6± 1.2 Ma and 6.0± 1.1 Ma. The data points from a coherent group which gives a weighted means $^{206}Pb/^{238}U$ age of 3.8± 0.5 Ma with a MSWD value of 1.3. The 3.8± 0.5 Ma age is interpreted as the time of intrusion of the dacite (Figure 4.8).

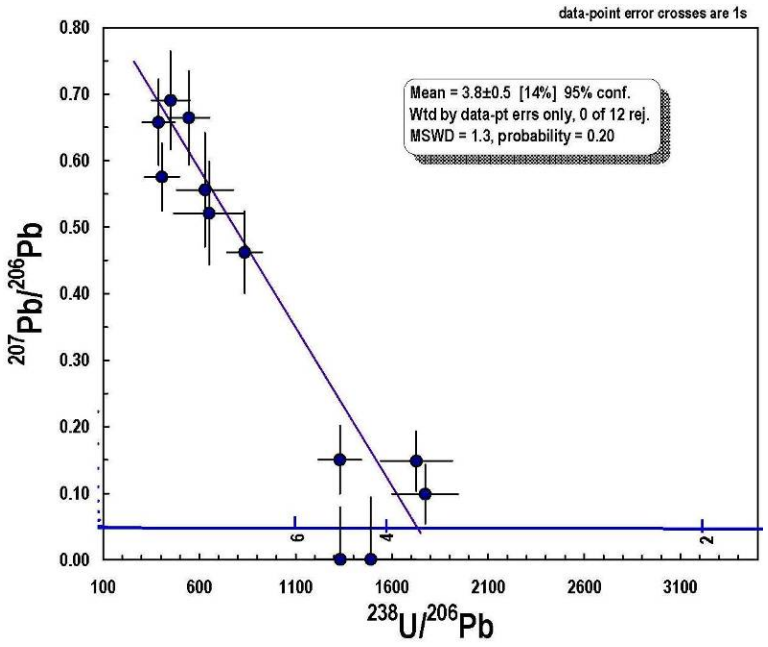

Figure 4.8. Reverse concordia plot of U-Pb Pb LA-ICPMS analyses on zircon grain from dacite APSD71_63. The best fit regression and ^{207}Pb corrected age calculated using the Isoplot 30 software assuming common Pb composition based on the two stage model of Stacey and Kramer (1975).

4.3.2.4 Alunite samples

Two samples of alunite were collected from drill core at Purnama and chosen for Ar-Ar dating. One sample is from an alunite vein (APSD156_115.3) and the other is alunite replacing feldspar (APSD73A_59.75m) within the advanced argillic alteration zone.

APSD156_115.3

The alunite vein (APSD156_115.3) shows two distinctly different apparent ages (Table 4.4.) The fourth or last stage yielded a relatively young apparent age of 1.37±0.13 Ma. The remaining three stages formed a well-defined plateau, with an average age of 3.30±0.02 Ma (Table 4.4). These three data points define a well-correlated isochron on an ^{39}Ar/^{40}Ar vs. ^{36}Ar/^{40}Ar diagram which gives an isochron age of 3.30±0.11 Ma (Figure 4.9b), with an MWSD of 0.044 and an initial ^{40}Ar/^{36}Ar of 294.48±37.24 Ma. The isochron and plateau ages, high percentage (100%) of the ^{39}Ar released during three stages, and approximation of the initial ^{40}Ar/^{36}Ar to that of the atmosphere suggest that the age is reliable. Therefore, the age of 3.30±0.11 Ma is interpreted to be the time of formation of this alunite (alunite-1).

APSD73A_59.75

The analytical results for the replacement alunite (APSD73A_59.75) are listed in Table 4.4. All four stages formed a well-defined plateau, with an average age of 2.00±0.02

Ma (Table 4.4). These four data points define a well-correlated isochron on an $^{39}Ar/^{40}Ar$ vs. $^{36}Ar/^{40}Ar$ diagram which gives an isochron age of 2.14±0.10 Ma (Figure 4.9), with an initial $^{40}Ar/^{36}Ar$ of 285±6.43 and an MWSD of 0.211. The isochron and plateau ages, high percentage (94.6%) of the ^{39}Ar released during four stages, and approximation of the initial $^{40}Ar/^{36}Ar$ to that of the atmosphere suggest that the age is reliable. Therefore, the age of 2.14±0.10 Ma is interpreted to be the time of formation of the second phase of alunite.

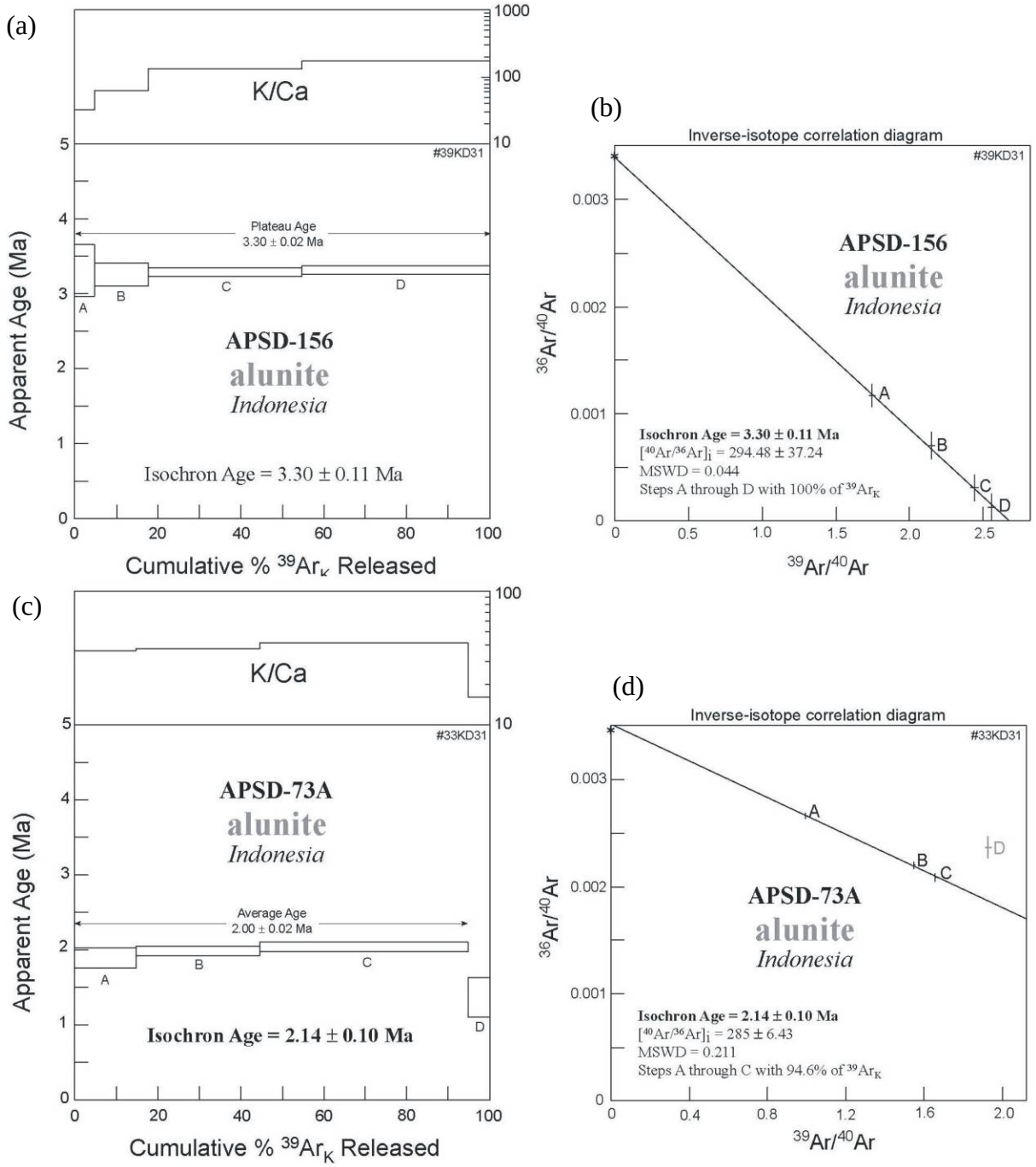

Figure 4.9. ^{40}Ar-^{39}Ar spectra step-heating and isochron age diagrams of alunite from samples APSD156_115.3m and ASPD73A_59.75m. (a) and (b) The older age (3.30±0.11 Ma) is interpreted as the age of early stage of advanced-argillic alteration. (c) and (d) the younger age (2.14+0.20 Ma) is interpreted as second phase of alunite. All error boxes are shown at the 2σ level of uncertainty.

4.4. Discussion and conclusion

4.4.1 Discussion

Figure 4.10 summarizes the new and existing geochronolgical data for the Martabe district. Emplacement of the granite in the Sibolga began at 264 Ma and intrusive activity continued until about 75 Ma (Aspden et al., 1982; Bellon et al., 2004; Crow, 2005). However, ages ranging from 75 to 264 Ma may have been obtained from the many satellite plutons in the Sibolga region (Cobbing, 2005). ^{40}Ar /^{39}Ar dating from the Martabe revealed that the Uluhalanagodang granite is 208.6± 0.07 Ma and 209.3± 0.19 Ma, suggesting that it might be co-eval with the Sibolga pluton or its satellite plutons.

An $^{40}Ar/^{39}Ar$ plateau age on the groundmass from a basaltic andesite (APSD001_42.3) gives an age of 18.9± 0.07 Ma. This age is similar to the numerous volcanic rocks belonging to the late Early Miocene-Mid Miocene Volcanic episode in northern Sumatra (Bellon et al., 2004). These volcanics outcrop more extensively as lavas and volcanoclastics to the south of Lake Toba forming a discontinuous linear belt. The late Early to Mid Miocene volcanics episode is composed of two phases. First, a volcanic arc was formed parallel to the west coast (at western part and eastern of Sumatran Fault System (SFS), and secondly, the magmatism in the Central Sumatra Back Arc Basin, which is similar igneous activity that occurred in the South Sumatra Back Arc Basin, formed between 17 and 12 Ma (Crow, 2005). Sample (APSD001_42.3) is interpreted to belong to the Angkola Volcanic Formation. U-Pb age dating on the other volcanics series (i.e., Toru volcanic unit) at Martabe was also conducted, however the lack of zircons in basaltic andesite, volcanic breccia and porphyritic andesite prevented age determinations. Thus, the Mid-Miocene age for the Toru volcanic unit is estimated from its relative position to Angkola Volcanic Formation.

The U-Pb zircon age of 3.8± 0.5 Ma (APSD71_63) for the dacite is considered the minimum age for this unit. Zircon U-Pb dating gives two ages of 2.8± 0.3 Ma (APSD249_137) and 3.1± 0.4 Ma (APSD150_18) for the hornblende-phyric andesite intrusive. The age difference can be interpreted in two ways. First, magma was emplaced at two times during the history of the instrusive or that the intrusive is 3.1 Ma or older. However from a similar rock, the $^{40}Ar/^{39}Ar$ plateau age on hornblende provides an age of 2.8± 0.12 Ma (APSD136_29.6). These ages suggest multiple periods of emplacement occurred in a short time for hornblende phyric-andesite flow dome. Crosscutting relationships between the dacite, hornblende phyric-andesite and breccias; or dacite and the sulfide veins indicates that the dacite formed earlier than, or at least coeval with, the

gold mineralisation.

The two alunite $^{40}Ar/^{39}Ar$ plateau ages (3.30± 0.11 Ma and 2.14± 0.10 Ma) suggest two different genetic types of alunite or at least two periods of advanced argillic alteration. The older age from a vein alunite is interpreted to be hypogene in origin. The younger alunite likely formed from steam-heating in the vadose zone as supergene alunite.

If two periods of hydrothermal activity did occur, this would indicate that the magmatic hydrothermal system was active from ≥3.8 to ≤2.1 Ma. This age range is also consistent with the general interpretation that several periods of magmatic activity with resultant heat and fluid flow occurred in the Late Miocene through Pliocene in Sumatra, in particularly in southern Sumatra (Crow, 2005).

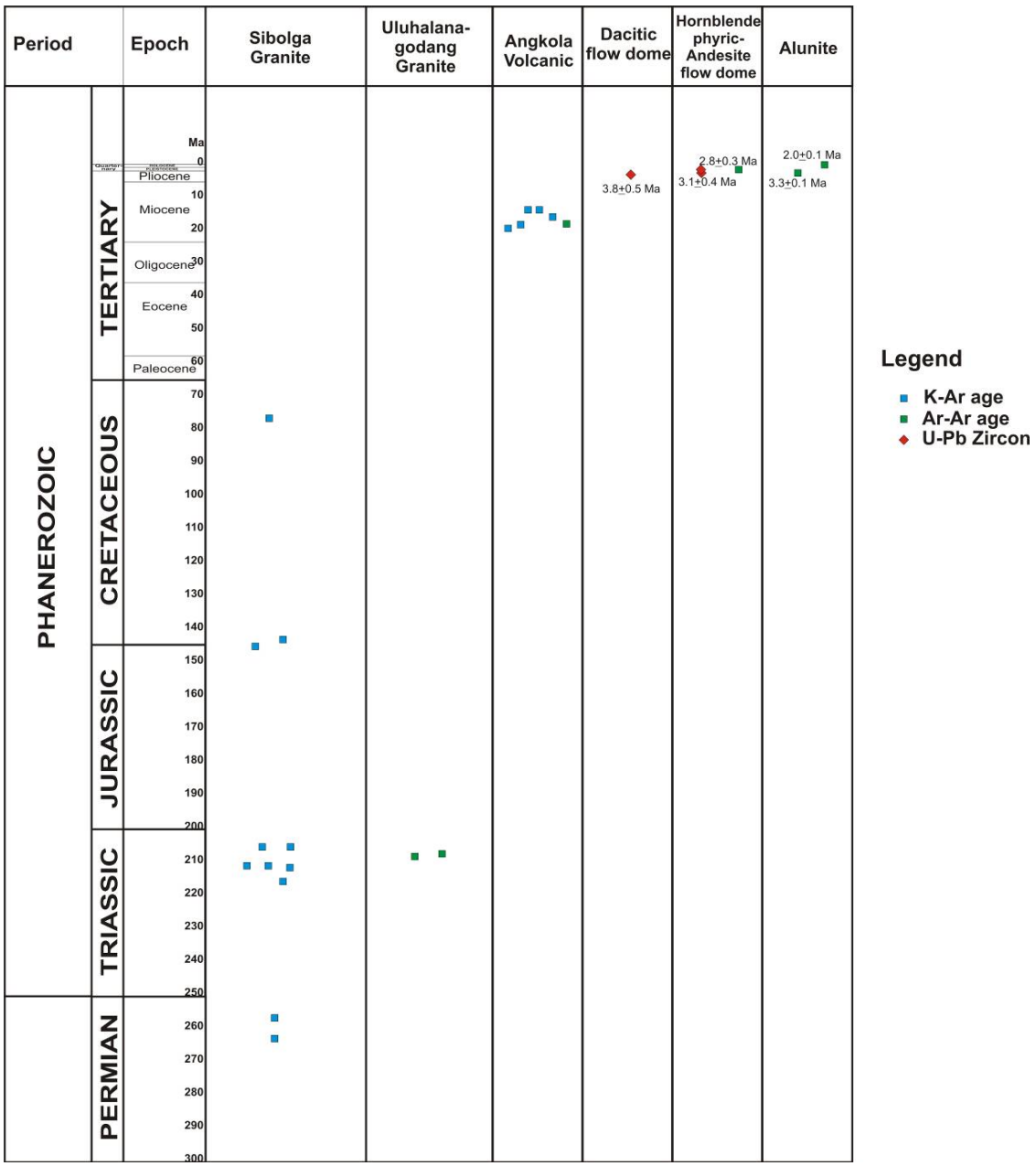

Figure 4.10. Summary of geochronological data for the Martabe district, including the Sibolga area. Data from Turner (2002), Bellon et al. (2004) and this study.

4.4.2 Conclusions

Five fundamental conclusions can be derived from the geochronology study at Martabe (Figure 4.10):

(i) Major magmatism, recorded by the widespread granitic plutons of Sibolga, occurred between 264 and 75 Ma.

(ii) The flow dome complex, host to the high-sulfidation mineralisation and alteration, formed by the emplacement of magmas by 3.8 Ma (or ~4Ma).

(iii) The high-sulfidation system was formed at approximately 3.3 Ma, with formation of multiple stages of advanced argillic alteration up to $\leq$0.5 Ma after the dacitic dome emplacement.

(iv) The andesitic dome formed between 3.1 and 2.8 Ma.

(v) A second phase of hydrothermal advanced argillic alteration occurred at 2.1 Ma.

Table 4.4. ^{40}Ar /^{39}Ar step-heating data of the Martabe district samples.

Step	Temp. °C	%^{39}Ar of total	Radiogenic Yield (%)	$^{39}Ar_k$ (Moles x 10^{-12})	$^{40}Ar^*$ / $^{39}Ar_k$	Apparent K/Ca	Apparent K/Cl	Apparent Age (Ma)	Error (Ma)
APSD-1	*Indonesia*	***volcanic matrix***	*J = 0.004827 ± 0.25%*	*wt = 247.4 mg*	*#27KD31*				
A	850	15.1	75.7	0.21346	2.268	0.47	3367	19.64	± 0.07
B	950	27.2	76.8	0.38542	2.181	0.25	3677	18.89	± 0.04
C	1050	23.5	94.4	0.33302	2.118	0.28	1838	18.35	± 0.06
D	1150	23.3	90.2	0.32991	1.992	0.42	542	17.26	± 0.04
E	1250	10.8	84.9	0.15289	1.869	0.15	252	16.20	± 0.05
Total Gas		100.0	84.8	1.41470	2.101	0.32	2096	18.21	
65.9% of gas on plateau-like in 850 through 1050 steps							**Average Age =**	**18.91**	**± 0.07**
APSD-73A	*Indonesia*	***alunite***	*J = 0.004887 ± 0.25%*	*wt = 30.7 mg*	*#33KD31*				
A	650	14.6	21.3	0.18402	0.215	36	2732	1.89	± 0.07
B	675	29.8	35.0	0.37457	0.226	37	8121	1.99	± 0.03
C	700	50.2	38.4	0.63058	0.231	41	8950	2.04	± 0.03
D	725	5.4	30.1	0.06733	0.156	16	4994	1.37	± 0.13
Total Gas		100	34.4	1.25650	0.223	38	7580	1.97	
94.6% of gas on plateau-like in 650 through 700 steps							**Average Age =**	**2.00**	**± 0.02**
APSD-73A	*Indonesia*	***alunite TF***	*J = 0.004858 ± 0.25%*	*wt = 12.1 mg*	*#34KD31*				
A	1000	100	25.8	0.51441	0.242	41	2931	2.12	± 0.04
Total Gas									
APSD-73	*Indonesia*	***alunite TF***	*J = 0.004888 ± 0.25%*	*wt = 5.7 mg*	*#41KD31*				
A	1000	100	27.9	0.15191	0.237	16	1478	2.09	± 0.07
Total Gas									
APSD-156	*Indonesia*	***alunite***	*J = 0.004901 ± 0.25%*	*wt = 32.1 mg*	*#39KD31*				
A	600	4.8	65.4	0.05976	0.375	32	1495	3.31	± 0.17
B	625	12.9	79.2	0.16008	0.369	62	2091	3.26	± 0.08
C	650	37.0	90.9	0.45690	0.372	136	30831	3.29	± 0.03
D	675	45.3	96.2	0.55943	0.376	172	57027	3.32	± 0.03
Total Gas		100.0	90.6	1.23617	0.374	138	37546	3.30	
100% of gas on plateau in 600 through 675 steps							**Plateau Age =**	**3.30**	**± 0.02**
APSD-156	*Indonesia*	***alunite TF***	*J = 0.004901 ± 0.25%*	*wt = 17.3 mg*	*#40KD31*				
A	1000	100	76.9	0.923831	0.377	262	4553	3.33	± 0.01
Total Gas									

Table 4.4. ^{40}Ar /^{39}Ar step-heating data of the Martabe district samples (*continued*).

Step	Temp. °C	%^{39}Ar of total	Radiogenic Yield (%)	$^{39}Ar_k$ (Moles x 10^{-12})	$^{40}Ar^*$ / $^{39}Ar_k$	Apparent K/Ca	Apparent K/Cl	Apparent Age (Ma)	Error (Ma)
Granite-1	*Indonesia*		***biotite TF***	*J = 0.004851 ± 0.25%*		*wt = 4.5 mg*	*#35KD31*		
A	1450	100	99.4	0.23478	25.268	101	22	208.59	± 0.07
Total Gas									
Granite-1	*Indonesia*		***K-feldspar***	*J = 0.004845 ± 0.25%*		*wt = 25.2 mg*	*#28KD31*		
A	800	2.5	95.7	0.01636	4.367	15	842	37.78	± 0.82
B	850	1.8	95.3	0.01142	4.650	7	817	40.19	± 0.57
C	900	1.7	96.4	0.01115	5.309	18	768	45.82	± 0.48
D	950	2.0	98.5	0.01313	4.845	20	1138	41.86	± 0.88
E	1000	2.6	97.3	0.01668	4.643	64	2502	40.13	± 0.35
F	1050	3.4	99.5	0.02209	5.426	25	2518	46.81	± 0.30
G	1100	3.9	99.2	0.02535	5.957	13	834	51.33	± 0.29
H	1150	4.5	98.3	0.02906	6.467	13	456	55.66	± 0.23
I	1200	5.7	96.8	0.03670	7.454	16	536	64.00	± 0.16
J	1250	7.5	97.0	0.04860	8.647	22	372	74.04	± 0.16
K	1300	17.8	98.1	0.11451	9.713	21	443	82.96	± 0.07
L	1350	30.5	98.6	0.19705	9.885	16	560	84.40	± 0.07
M	1400	10.1	98.4	0.06515	9.694	8	631	82.80	± 0.10
N	1650	5.9	95.7	0.03779	9.316	3	530	79.64	± 0.32
Total Gas		100.0	97.9	0.64504	8.559	17	679	73.30	
No Plateau									
Granite-2	*Indonesia*		***biotite TF***	*J = 0.004892 ± 0.25%*		*wt = 4.6 mg*	*#37KD31*		
A	1450	100	99.4	0.24071	25.142	116	18	209.26	± 0.19
Total Gas									
Granite-2	*Indonesia*		***K-feldspar***	*J = 0.004920 ± 0.25%*		*wt = 26.9 mg*	*#29KD31*		
A	750	2.9	98.2	0.05064	13.512	537	425	116.11	± 0.14
B	800	2.3	98.6	0.04107	7.850	75	1131	68.36	± 0.19
C	850	2.4	98.5	0.04172	8.715	58	1194	75.74	± 0.25
D	900	2.4	99.1	0.04228	7.835	180	1431	68.23	± 0.25
E	950	2.4	98.9	0.04136	5.537	40	2786	48.49	± 0.16
F	1000	2.3	98.2	0.04094	4.677	55	4440	41.04	± 0.16
G	1050	2.5	99.6	0.04398	5.543	59	4022	48.54	± 0.18
H	1100	2.7	99.2	0.04754	7.395	38	1950	64.47	± 0.20
I	1150	4.0	98.8	0.07083	12.223	32	771	105.35	± 0.13
J	1200	7.0	99.0	0.12290	15.857	65	514	135.52	± 0.09
K	1250	9.7	99.2	0.17012	17.925	35	494	152.47	± 0.07
L	1300	20.8	99.5	0.36528	20.796	234	511	175.73	± 0.15
M	1350	29.5	99.5	0.51833	21.687	53	606	182.90	± 0.09
N	1400	9.1	99.6	0.15921	20.628	44	954	174.38	± 0.17
Total Gas		100.0	99.3	1.75621	17.483	105	911	148.86	
No Plateau									

Table 4.4. ^{40}Ar /^{39}Ar step-heating data of the Martabe district samples (*continued*).

Step	Temp. °C	%^{39}Ar of total	Radiogenic Yield (%)	$^{39}Ar_k$ (Moles x 10^{-12})	$^{40}Ar^*$ / $^{39}Ar_k$	Apparent K/Ca	Apparent K/Cl	Apparent Age (Ma)	Error (Ma)
APSD-136	*Indonesia*		***hornblende***	*J = 0.004934 ± 0.25%*		*wt = 20.1 mg*	*#58KD31*		
A	1150	1.7	16.1	0.00251	0.341	0.05	3.5	3.04	± 1.16
B	1175	4.4	26.5	0.00419	0.366	0.04	3.5	3.26	± 0.44
C	1200	6.5	55.2	0.00542	0.674	0.06	3.4	6.00	± 1.97
D	1225	29.4	43.3	0.01523	0.326	0.04	3.6	2.90	± 0.20
E	1250	43.7	55.6	0.01657	0.305	0.04	3.4	2.72	± 0.09
F	1275	5.8	11.5	0.00453	0.130	0.05	3.1	1.16	± 0.38
G	1300	6.4	34.8	0.00412	0.324	0.04	2.9	2.89	± 0.35
H	1350	1.8	7.4	0.00190	0.118	0.02	0.7	1.05	± 1.30
I	1450	0.3	4.2	0.00277	0.611	0.03	0.7	5.45	± 8.27
Total Gas		100.0		0.05723				2.92	

Ages calculated assuming an initial $^{40}Ar/^{36}Ar = 295.5 \pm 0$.
All precision estimates are at the one sigma level of precision.
Ages of individual steps do not include error in the irradiation parameter J.
No error is calculated for the total gas age.

	206Pb/238U age (Ma)	+/-1s	Th	U	Th/U	207Pb/ 206Pb	+/-1s	206Pb/ 238U	+/-1s	238U/ 206Pb	+/-1s	207Pb 235U	%rse	208Pb/ 232Th	%rse	207Pb/ 206Pb	%rse
Sample APSD249_137 Hornblende-phyric Andesite																	
APSD249-137	2.3	0.6	81	159	0.51	0.230	0.094	0.000	0.000	2124.29	461.69	0.011	26.3%	0.0005	14.3%	0.230	40.9%
APSD249-137	2.4	0.5	147	240	0.61	0.280	0.053	0.001	0.000	1870.49	315.40	0.016	17.1%	0.0004	13.4%	0.280	18.9%
APSD249-137	2.5	0.4	247	319	0.77	0.341	0.046	0.001	0.000	1627.90	239.95	0.019	11.4%	0.0004	8.2%	0.341	13.3%
APSD249-137	2.8	0.4	248	368	0.67	0.202	0.029	0.001	0.000	1869.96	245.14	0.012	14.9%	0.0004	6.9%	0.202	14.5%
APSD249-137	2.8	0.5	104	175	0.59	0.278	0.054	0.001	0.000	1612.88	259.22	0.021	16.7%	0.0006	11.7%	0.278	19.3%
APSD249-137	2.9	0.4	314	420	0.75	0.199	0.032	0.001	0.000	1803.97	250.71	0.010	16.4%	0.0003	8.5%	0.199	16.1%
APSD249-137	2.9	0.5	156	283	0.55	0.357	0.045	0.001	0.000	1341.42	202.25	0.027	11.6%	0.0009	7.3%	0.357	12.6%
APSD249-137	3.0	0.5	192	340	0.56	0.209	0.035	0.001	0.000	1715.56	261.97	0.014	14.7%	0.0006	12.2%	0.209	16.8%
APSD249-137	3.0	0.5	235	383	0.61	0.169	0.033	0.001	0.000	1825.66	264.64	0.010	15.9%	0.0005	13.5%	0.169	19.7%
APSD249-137	3.1	0.6	215	318	0.68	0.282	0.065	0.001	0.000	1469.08	248.74	0.017	19.9%	0.0006	9.9%	0.282	23.0%
APSD249-137	3.3	0.6	122	228	0.53	0.175	0.044	0.001	0.000	1628.57	268.21	0.014	20.4%	0.0006	14.1%	0.175	25.3%
APSD249-137	3.6	0.7	77	158	0.49	0.243	0.078	0.001	0.000	1358.17	197.60	0.030	13.3%	0.0011	8.6%	0.243	32.3%
Sample APSD150_18 Hornblende-pyric Andesite																	
APSD150-18	2.1	0.6	139	232	0.60	0.430	0.086	0.001	0.000	1608.09	363.99	0.033	14.5%	0.0010	9.2%	0.430	20.0%
APSD150-18	2.1	0.6	192	247	0.78	0.508	0.073	0.001	0.000	1253.00	228.06	0.038	12.5%	0.0010	6.6%	0.508	14.3%
APSD150-18	2.4	0.3	232	346	0.67	0.188	0.050	0.000	0.000	2201.56	237.11	0.012	34.7%	0.0001	40.1%	0.188	26.4%
APSD150-18	2.8	0.4	283	412	0.69	0.277	0.031	0.001	0.000	1629.21	242.38	0.018	10.8%	0.0004	7.8%	0.277	11.2%
APSD150-18	3.0	0.9	64	128	0.50	0.605	0.058	0.002	0.000	621.90	95.33	0.108	10.0%	0.0043	7.8%	0.605	9.7%
APSD150-18	3.2	0.4	128	261	0.49	0.087	0.042	0.001	0.000	1927.36	193.61	0.004	85.8%	0.0000	-514.9%	0.087	48.5%
APSD150-18	3.2	0.6	258	374	0.69	0.250	0.031	0.001	0.000	1506.86	251.58	0.021	16.5%	0.0005	11.2%	0.250	12.5%
APSD150-18	3.3	0.4	181	286	0.63	0.001	0.052	0.000	0.000	2157.20	244.32	0.005	73.2%	0.0002	23.1%	-0.026	-200.4%
APSD150-18	3.4	0.5	145	269	0.54	0.039	0.075	0.001	0.000	1899.45	196.03	0.014	28.6%	0.0002	35.6%	0.039	191.6%
APSD150-18	3.4	0.4	173	291	0.60	0.128	0.049	0.001	0.000	1675.51	148.63	0.007	61.6%	0.0003	21.2%	0.128	37.8%
APSD150-18	3.7	0.4	116	238	0.49	0.029	0.034	0.001	0.000	1774.66	192.82	-0.001	-456.6%	0.0001	156.1%	0.029	116.5%
APSD150-18	4.8	0.9	462	454	1.02	0.303	0.037	0.001	0.000	906.43	151.76	0.037	13.4%	0.0007	8.4%	0.303	12.3%
Sample APSD71_63 Dacite																	
APSD71-63	2.6	1.2	82	172	0.48	0.664	0.071	0.002	0.000	545.15	107.06	0.151	8.0%	0.0052	6.9%	0.664	10.7%
APSD71-63	2.6	1.5	171	239	0.71	0.691	0.074	0.002	0.000	450.72	99.31	0.181	8.8%	0.0036	7.2%	0.691	10.7%
APSD71-63	3.2	0.4	87	193	0.45	0.148	0.045	0.001	0.000	1727.12	185.60	0.005	90.3%	0.0003	45.2%	0.148	30.4%
APSD71-63	3.4	0.4	233	324	0.72	0.099	0.044	0.001	0.000	1773.20	170.77	0.005	86.2%	0.0003	20.6%	0.099	44.9%
APSD71-63	3.6	1.4	133	227	0.59	0.556	0.086	0.002	0.000	629.52	148.10	0.091	12.4%	0.0029	10.2%	0.556	15.4%
APSD71-63	3.7	0.7	54	113	0.47	0.462	0.062	0.001	0.000	834.80	91.95	0.063	20.6%	0.0026	14.9%	0.462	13.3%
APSD71-63	3.7	1.6	117	189	0.62	0.658	0.065	0.003	0.001	387.58	84.27	0.214	11.6%	0.0061	5.4%	0.658	9.8%
APSD71-63	3.9	1.5	168	276	0.61	0.521	0.077	0.002	0.000	650.65	183.82	0.104	14.0%	0.0032	9.3%	0.521	14.9%
APSD71-63	4.2	0.5	103	234	0.44	0.151	0.051	0.001	0.000	1330.15	111.10	-0.007	-62.4%	0.0002	54.8%	0.151	34.1%
APSD71-63	5.2	1.6	168	365	0.46	0.576	0.051	0.002	0.001	405.54	89.68	0.164	10.6%	0.0061	10.2%	0.576	8.8%
APSD71-63	5.3	0.7	81	172	0.47	0.001	0.078	0.001	0.000	1331.72	138.41	0.032	21.9%	0.0014	12.3%	-0.026	-295.6%
APSD71-63	6.0	1.1	70	116	0.60	0.001	0.093	0.001	0.000	1490.93	234.55	0.037	25.2%	0.0005	30.8%	-0.264	-35.4%

Table 4.5. Zircon LA-ICPMS U-Pb analysis of the Martabe district samples.

CHAPTER 5

WHOLE-ROCK GEOCHEMISTRY

5.1 Introduction

This chapter describes the geochemistry of the coherent volcanic facies hosting the Martabe deposits, including the major-, trace- and immobile-element chemistry, to provide constraints on the source of the magmas and their evolution. Prior to this study, limited geochemical investigations had been conducted on the Tertiary volcanic rocks of the Martabe district (Aspden et al., 1982; Bellon et al., 2004) and very little was known on the geochemistry of volcanic and intrusive rocks in the district. Geochemical data from selected volcanic occurrences in northern Sumatra are reported in Aspden et al. (1982), Rock et al. (1982), Wajzer (1986), Kallagher (1989), Gasparon and Varne (1995), Bellon et al. (2004) and Crow (2005). The majority of analyses include major elements only and these have been discussed by Rock et al. (1982), Bellon et al. (2004), and Crow (2005). However, there are more chemical analyses available for the Neogene than for the Paleogene volcanic rocks.

The aim of this study was to (1) characterize the geochemical signature of the least-altered host rocks, (2) determine the magmatic affinity, (3) define trends of magma composition through time, and (4) provide a baseline of geochemical data with which to compare altered rocks at Martabe. In this chapter, most of the newly analyzed samples are accompanied by petrographic descriptions.

5.2 Sampling and analytical methods

A total of 28 samples of least-altered, coherent volcanic facies were analyzed for major and trace element compositions. These samples were selected from drill holes at the Purnama, Baskara and Gerhana deposits, except for one sample (RO5000468PUR) which was taken from the outcrop of an intrusive unit at the Pelangi deposit (Appendix 1).

Samples are grouped based on their stratigraphic position, namely; (i) Angkola Volcanic Formation (Tmav), (ii) Toru Volcanic Formation (Tmtv), and (iii) Martabe flow domes complex (Tpid and Tpia). Rocks were grouped based on the rock texture and description rather than the sample locations or deposits. The lithological formation names of the Early to Mid-Miocene of Angkola Volcanic Formation (Tmav) and Toru Volcanic Formation (Tmtv) are taken from Aspden et al. (1982), Bellon et al. (2004) and Crow (2005) (Chapter Three); while the Martabe flow domes complex is the local terminology for Pliocene age intermediate-felsic intrusions (Tpid-'Tertiary Pliocene intrusion Dacite' and Tpia-'Tertiary Pliocene intrusion andesite') which occur in the Martabe or Batangtoru districts.

It was hard to find fresh or unaltered rock because sampling was mostly restricted to drill holes that were associated with mineralization and alteration. Least-altered samples were selected based on hand specimen and thin section observations. The geochemistry of altered samples (i.e., those with high LOI value, or a high Alteration Index of Ishikawa et al., 1979) is not included in this sample set, but discussed in following chapter.

All whole-rock samples were analyzed for major and trace elements using the X-ray fluorescence (XRF) facility at CODES, University of Tasmania. All sample preparation was carried out at the facilities. Samples were initially crushed using a steel jaw crusher to produce fragments of about 0.5 cm^3 or less. Samples were then ground in a tungsten carbide ring mill for approximately 3 minutes to produce a rock powder of less than 200 μm. The mill was cleaned with 1 to 2 passes of high purity quartz and between each sample run. Approximately 1 gram of each samples was ignited, initially at 500ºC for 4 hours and then at 1000ºC overnight. Loss on ignition (LOI) was determined by weighing the samples before and after ignition. Major elements where determined as oxides: SiO_2, TiO_2, Al_2O_3, Fe_2O_3, MnO, MgO, CaO, Na_2O_3, K_2O, P_2O_5, BaO and S using fused disk. Trace elements Nb, Zr, Sr, Cr, Ba, V, La, Y, Rb, U, Th, Pb, As, Bi, Zn, Cu, Ag, Ni and Se were determined using pressed powder pellets. Both major and trace elements were analyzed using a Philips 1480 automated XRF with ScMo and Au tubes using standard procedures outlined by Norrish and Chappel (1977) and Robinson et al. (2003). Sample standards were run every 6-10 samples to ensure analytical precision. Certain trace elements (Sc, Y, Nb, Ag, Cd, Sn, Sb, Te, Bi, Th, and U) were also analyzed by ICP-MS using an Agilent HP4500 ICP-MS. No rare earth elements (REE) were analyzed during this study.

All whole rock geochemistry data generated in this study are listed in Appendix 1. Representative data from earlier studies and comparisons to other Tertiary volcanic rocks

from Northern Sumatra as reported in Bellon et al. (2004) and Crow (2005) are given in Appendix 1.

5.3 Major element geochemistry

The discrimination of coherent volcanic host rocks in the Martabe district is based on classification of total alkalies versus silica (TAS) (Le Maitre et al., 1989) and K_2O-SiO_2 (Pecherillo and Taylor, 1976) diagrams (Figure 5.1). On Figure 5.1a, volcanic rocks may be subdivided into members of two major magma series, alkalic and sub-alkalic, as defined by Miyashiro (1978). The TAS diagram shows that the volcanic rocks at Martabe mostly plot within basalt, basaltic andesite, basaltic-trachyandesite, andesite and dacite fields of sub-alkalic affinity. This diagram illustrates that the Angkola volcanic samples plot in the basalt to basaltic-andesite fields, with one sample being of basalt-trachyandesite composition. Toru volcanic samples fall in the andesite to dacite fields. Martabe flow dome samples plot in the andesite to dacite fields. All rocks plot in the subalkaline to tholeiithic fields.

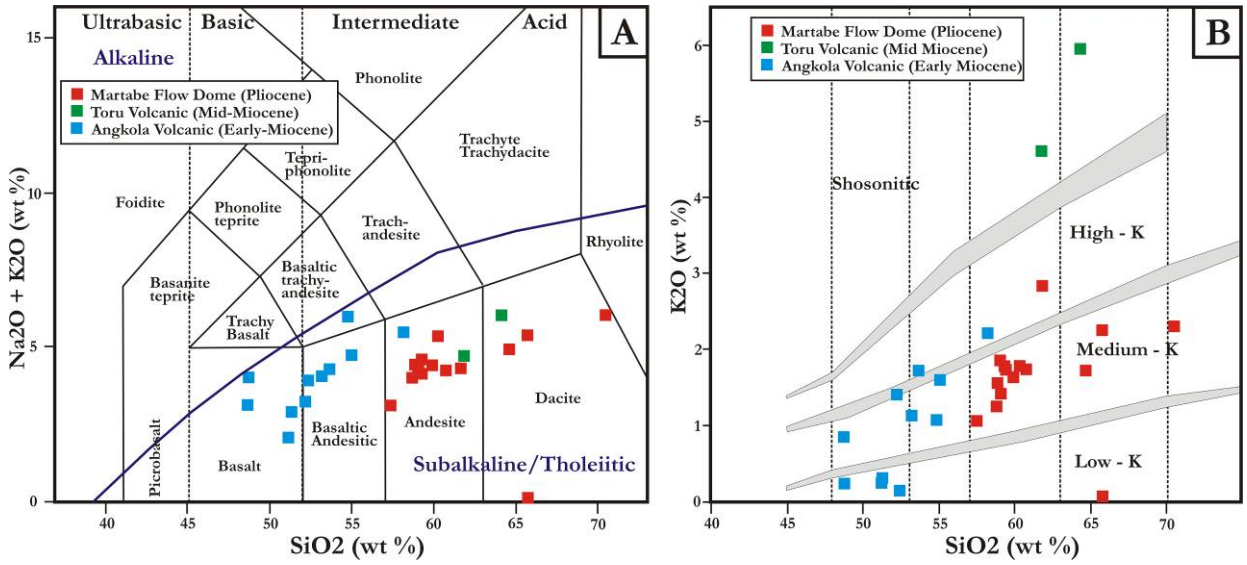

Figure 5.1. (A) SiO_2 vs K_2O+Na_2O (TAS) diagram field from Le Maitre et al. (1989). The dividing line between alkalic and subalkalic magma series is from Misyashiro (1978). (B) SiO_2 vs. K_2O diagram fields from Pecherillo and Taylor (1976).

In general, the rocks range in composition from 48 to 58 wt.% of SiO_2 for Early-Miocene of Angkola Volcanic Formation which range from basaltic to andesite; 61 to 64 wt.% of SiO_2 for Mid-Miocene of Toru Volcanic Formation which extent from andesite to dacite; 57 to 70 wt.% of SiO_2 for Pliocene of Martabe flow dome complex which arrange from andesite

to dacite in composition (Figure 5.1a). The Toru volcanic samples have a slightly high SiO_2 content (61 to 64 wt. % of SiO_2) and plot marginally within the dacite field despite the more mafic to intermediate mineralogy. The Toru volcanic samples have a slightly higher SiO_2 content which is probably caused by minor siliceous alteration. Data from this study agrees with Bellon et al. (2004) and Crow (2005), in that the Tertiary volcanic rocks in Sumatra are mostly basaltic-andesitic composition; with dacite compositions for Pliocene volcanic rocks.

A diagram of wt. % K_2O-SiO_2 may also be used to differentiate basaltic members of the subalkalic series (Middlemost, 1975). On the SiO_2-K_2O diagram (Figure 5.2b) of Peccerillo and Taylor (1976), most Martabe volcanic rocks have a low- to medium-K composition, with exception of Toru volcanic andesite rocks which have a shoshonitic composition. These diagrams show that the early Miocene Angkola volcanic formation has a wide range of low- to medium-K of basaltic andesite to andesite composition, while most of the Martabe flow dome complex rocks plot within the medium-K alkaline andesite to dacite fields. However, the lavas or shallow intrusive sills of the Toru Volcanic Formation are high-K to shoshonitic andesite. These data agree with Aldiss et al. (1983) who reported that the Toru volcanic andesite had a shoshonitic affinity.

The sub-alkalic magma series can be subdivided into a high alumina or calc-alkaline series and a low-K tholeiitic series. The two series can be differentiated in terms of their trends on the AFM ($A=Na_2O+K_2O$, $F=FeO+Fe_2O_3$, $M=MgO$) diagram (Figure 5.2), in which tholeiitic suites commonly show a strong trend of iron enrichment in the early stages of differentiation, whereas calc-alkaline suites trend directly across the diagram, due to the suppression of iron enrichment by the early crystallization of Fe-Ti oxides.

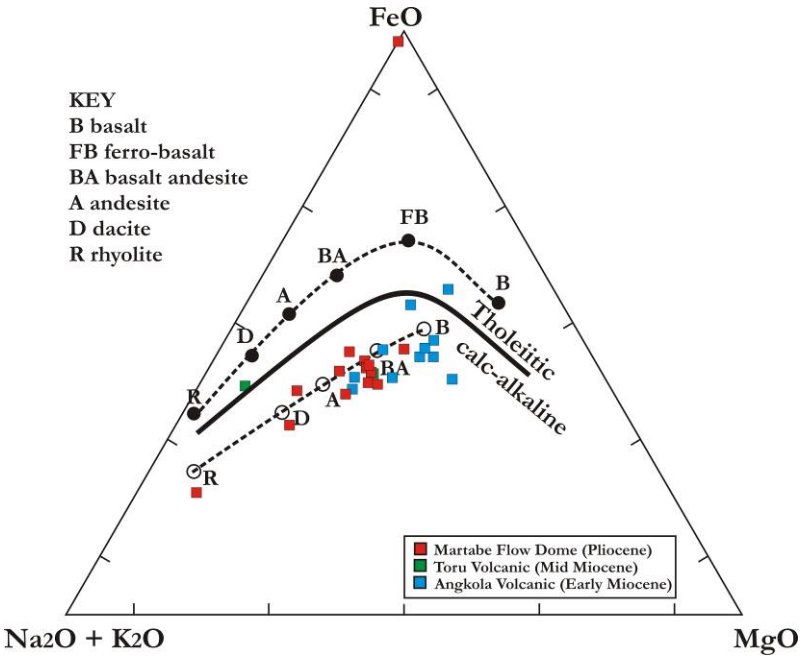

Figure 5.2 AFM diagram illustrating the calc-alkaline trend of the Martabe volcanic rocks with the field boundaries after Kuno (1969) and Irvine and Barager (1971).

The AFM diagram illustrates that volcanic rocks at Martabe mostly plot in the calc-alkali field of sub-alkali magma series. The FeO and MgO concentrations decrease with fractionation and alkali enrichment, which points to the importance of ferromagnesian minerals, such as olivine and pyroxene in the evolution of both types of magma. However, few volcanic rocks at Martabe have higher FeO/MgO ratios and plot in the tholeiitic field. The AFM diagram (Figure 5.2) shows a clear calc-alkaline trend with FeO and MgO depletion and alkali enrichment. FeO and MgO depletion and alkali enrichment correlate with decreasing amounts of ferromagnesian minerals from basalt of Angkola volcanic to felsic in Martabe flow dome. Such magma compositions are typical of subduction-related tectonic settings, but in detail there are differences from typical or average magma compositions (Ewart, 1982; Thorpe et al., 1982).

However, the products of volcanism in island arcs vary with the stage of evolution of the arc, with vertical distance above the Benioff zone and, in some cases laterally along the arc (Wilson, 1989).

Harker variation diagrams for major elements vs. SiO_2 are presented in Figure 5.3. The SiO_2 content increases with decreasing TiO_2, Al_2O_3, Fe_2O_3, MgO, CaO and MnO contents, whereas K_2O and Na_2O contents, show a poor correlation but generally increase with

increasing SiO_2. On the SiO_2-Na_2O diagram, samples with higher SiO_2 define a separate, but similar trend to more mafic samples, even for the three samples (B14, B15 and B28, see Appendix 1) that have very low Na_2O contents (LOI up to 10.89%). According to Wilson (1989) a marked linear correlation of major elements on the variation diagrams is evidence for the formation of felsic magmas by fractional crystallization from the parent magma.

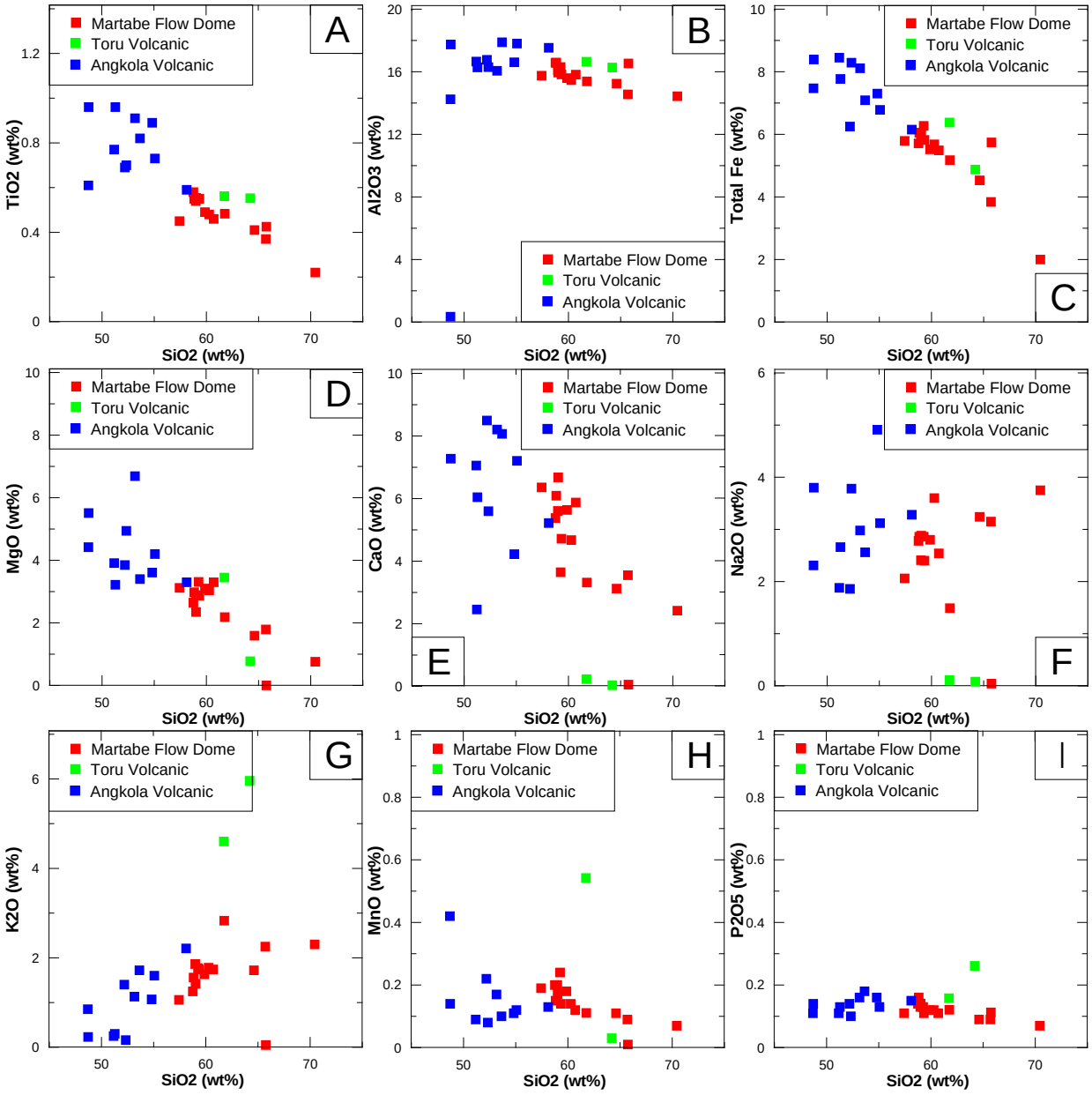

Figure 5.3. Harker variation diagrams for major elements as a function of SiO_2 for coherent volcanic rock in the Martabe district.

Decreasing trends in TiO_2 and Fe_2O_3 likely reflect the removal and crystallization of magnetite, titanomagnetite and sphene from the magma (i.e., basaltic to dacitic rocks). A decrease in Al_2O_3 and CaO contents but increase in Na_2O with increasing SiO_2 reflects the crystallization

of clinopyroxene and plagioclase. However, these changes may be also attributed to the effects of hydrothermal alteration. Na_2O generally shows a poor correlation with SiO_2, while K_2O increases with increasing SiO_2. In the Martabe flow dome samples, there is a slightly decrease in Al_2O_3 and in MgO contents, reflecting little, if any, removal of plagioclase during fractionation. For MgO <2%, there is a decrease in Al_2O_3 contents for the Martabe flow dome complex, possibly reflecting significant plagioclase extraction. Felsic intrusions of the Martabe flow dome have moderate P_2O_5 contents, which then slightly decreases with fractionation or with increasing SiO_2. This most likely indicates apatite-saturation at the andesitic to dacitic stage of magmatic evolution. By comparison with the Angkola volcanic samples, which have more constant P_2O_5 contents, samples from the Toru volcanic unit at 61-64 wt% SiO_2, have notably relatively high P_2O_5 contents. These volcanic rock analyses show MgO, TiO_2, Fe_2O_3 and CaO depletions with fractionation that typifies sub-alkaline suites, which also confirm similar results from the total alkalies versus silica diagram.

Fractional crystallization of ferromagnesian phases such as olivine and clinopyroxene leads to systematic depletion in FeO and MgO and enrichment in elements such as SiO_2, Na_2O and K_2O. When plagioclase appears on the liquidus, the remaining liquid becomes depleted in CaO and Al_2O_3. The overall result is that mafic liquids evolve towards more intermediate and felsic compositions. Basalts in subduction zone environments are characterized by high Al_2O_3 (17.0-21.0 wt. %) and low MgO (< 6 wt. %), compared with basalts in other tectonic settings, and are known as high-alumina basalts. However, basalts from Angkola have a relatively high Al_2O_3 content of 14-15 wt. % (Appendix 1). Although their origin is unclear, their low MgO content suggests that they are fractionated (by removal of olivine and clinopyroxene). The high Al_2O_3 implies that plagioclase was not a liquidus phase.

5.4 Trace element geochemistry

Harker-type variation diagrams plotted using trace elements as well as major elements oxides and may be interpreted in a similar way. The trace element geochemistry as function of SiO_2 abundance is illustrated in Figure 5.4. Highly incompatible trace elements such as Zr may be useful as an index of differentiation if SiO_2 or MgO are inappropriate. Those elements which are incompatible with respect to normal mantle minerals (olivine, pyroxene, spinel and garnet) are termed lithophile or large-ion lithophile (LIL), e.g. K, Rb, Sr, Ba, Zr, Th and light

REE. Concentrations of large lithophile elements such as Sr, Sc and Ba show a high degree of scatter, reflecting their tendency to be mobilized during hydrothermal alteration. Zr and La show gently increases with increasing SiO_2 up to 55 wt. %, but decrease or disperse at >55 wt.% SiO_2. This may reflect removal of high field strength elements (HFSE) such as Ti, V, Zr, Nb, Hf and Ta in the andesites, compared with basalts, basaltic andesites, or could reflect the removal of HFSE phases through the crystallization of sphene and zircon. Hutton (1950) showed that sphene could contain Nb, La and Y in significant amounts. Zircon was observed in coherent hornblende-pyric andesite and dacite from Martabe flow dome but it was not identified in Toru volcanic andesite.

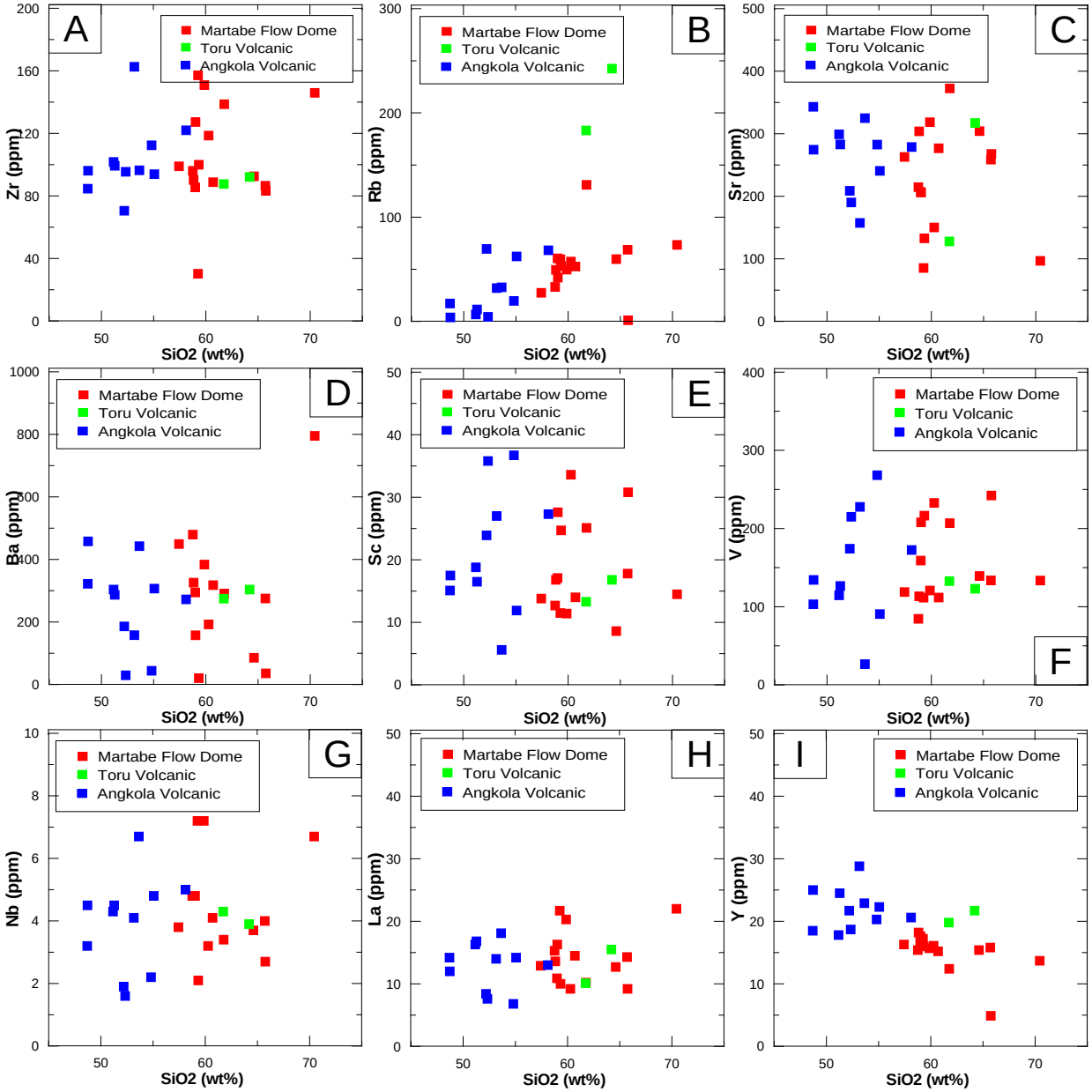

Figure 5.4. Harker variation diagrams for trace elements as a function of SiO_2 for coherent volcanic rock in the Martabe district.

5.5 Immobile element geochemistry

Several immobile elements were used to examine the geochemistry of the Martabe host rocks and their genetic origins. Elements that remain relatively immobile under hydrothermal alteration are Ti, Zr, Y, Nb, Ga, P, REE, V, Cr, Sc, Hf, T and Th (Winchester and Floyd, 1977).

Linear correlation of high field strength elements (HFSE) reflects primary elemental ratios, due to their assumed immobility (MacLean and Barret, 1993). At Martabe Nb, Zr and Y are relatively immobile as demonstrated by constant Nb/Zr and Nb/Y ratios that are projected through the axis origin (Figure 5.5). Figure 5.5 illustrates differences between Martabe and other Tertiary volcanic rocks in Sumatra that were analyzed by various workers (Appendix 1). There is a high degree of variability in the existing geochemistry data for other Sumatra volcanic rocks (Figure 5.5)

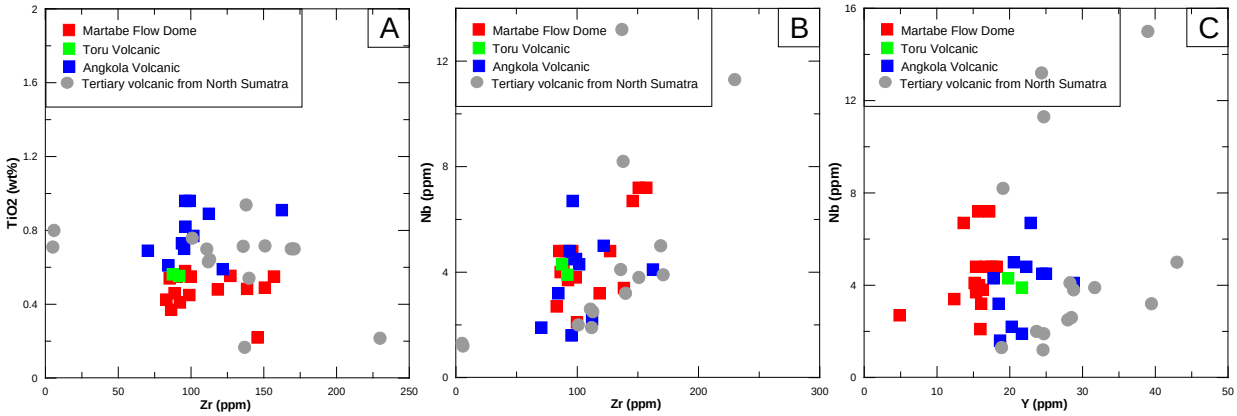

Figure 5.5. TiO_2-Zr, Nb-Zr and Nb-Y discrimination bivariate diagrams for Martabe volcanics and other tertiary volcanics in Sumatra.

A. TiO_2-Zr diagram showing Martabe volcanic rocks and the fields for andesite to basalt (based on the data of Bellon (2004) for 19 unaltered Tertiary volcanic rocks from north Sumatra). Fields were defined by comparing Ti/Zr ratio against SiO_2 content of known unaltered volcanics Empirical Ti/Zr ratios were defined for andesite with 58 to 63wt% SiO_2, basaltic andesites with 52 to 58 wt% SiO_2 and basalts with less than 52wt.% SiO_2. The Martabe volcanic rocks plot in the fields of basalt, andesites and dacite.

B. Nb-Zr diagram showing constant Nb/Zr ratio for the Martabe samples that projects through the axis origin. This trend suggests relative immobility of Nb and Zr.

C. Nb-Y diagram showing poor correlation of Nb and Y, suggesting possible element mobilization during hydrothermal alteration.

5.6. Discussion

5.6.1 Rock types discrimination based on immobility elements

The ratio of Zr/TiO_2 and Nb/Y are indices of alkalinity and differentiation, respectively (Winchester and Floyd, 1977). Therefore these ratios can be used to discriminate between different magma series and rock types (Figures 5.6 and 5.7). Samples plot mostly within the field of andesite to basalt compositions (Figure 5.7), which is consistent with hand specimen and petrographic studies, as well as whole rock geochemistry discussed in section 5.3. Some samples plot within the dacite field, which is also supported by the petrographic observations. Andesites of the Toru Volcanic Formation and the hornblende-phyric andesites to dacites of the Martabe flow dome complex have intermediate Zr/TiO_2 and low Nb/Y ratios. The basalts show slightly lower Zr/TiO_2 and Nb/Y ratios (Figure 5.5 and 5.6). Low Nb/Y ratios suggest a subduction-related magma source rather than an intraplate source of magmatism for Martabe (Winchester and Floyd, 1977).

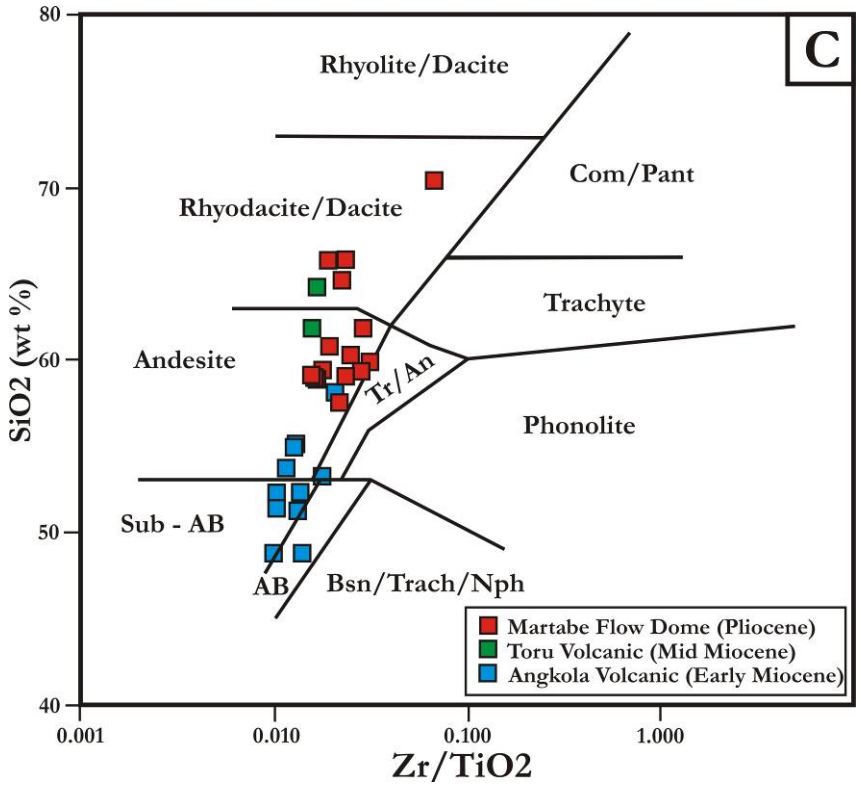

Figure 5.6. Zr/TiO_2 vs. SiO_2 diagram field. These diagrams show the Angkola volcanic formation plot in the basalt to basaltic andesite fields with one sample having basalt-trachyandesite composition. Toru Volcanic Formation samples plot in the andesite to dacitic fields. Martabe flow dome samples plot in the andesite to dacite fields.

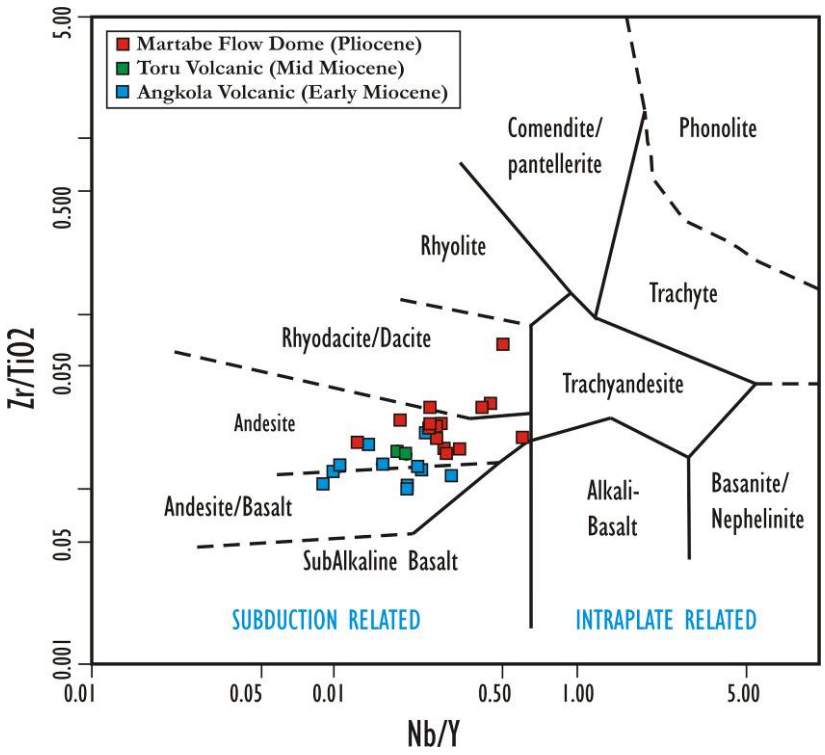

Figure 5.7. Nb/Y and Zr/TiO_2 discrimination diagram for coherent volcanic facies at Martabe. The diagram showing distribution of coherent volcanics for different rocks types and fields for subduction and intraplate related magmatism (diagram from Winchester and Floyd, 1977).

5.6.2 Magma type discrimination

The Ti-Zr-Y diagram (Figure 5.8) is used to discriminate between different types of within-plate basalts (i.e. OIB (Ocean Island Basalts) and continental flood basalts and other basalt types) (Rollinson, 1993). The coherent volcanics facies at Martabe plot largely within the sub-alkaline field, as in Figure 5.1, with basalts and basaltic andesites plotting toward the MORB (Mid Ocean Ridge Basalts), island-arc thoelitic and calc alkali basalt fields (Figure 5.8A). Samples were also plotted on a Ti-Zr diagram to better discriminate the samples in the MORB, island-arc thoelitic and calc alkaline basalt fields (Pearce and Cann, 1973). All Martabe coherent facies plot within the calc-alkaline basalt field (Figure 5.8B). This diagram also shows that the basalt and basaltic andesite of the Angkola Volcanic Formation generally have higher Ti values than the andesitic Toru volcanic formation and andesitic-dacitic Martabe flow dome complex, while the dacite of the Martabe flow dome has higher Zr values. The discriminatory field used in this plot compares well with the empirically derived field in Figure 5.8A.

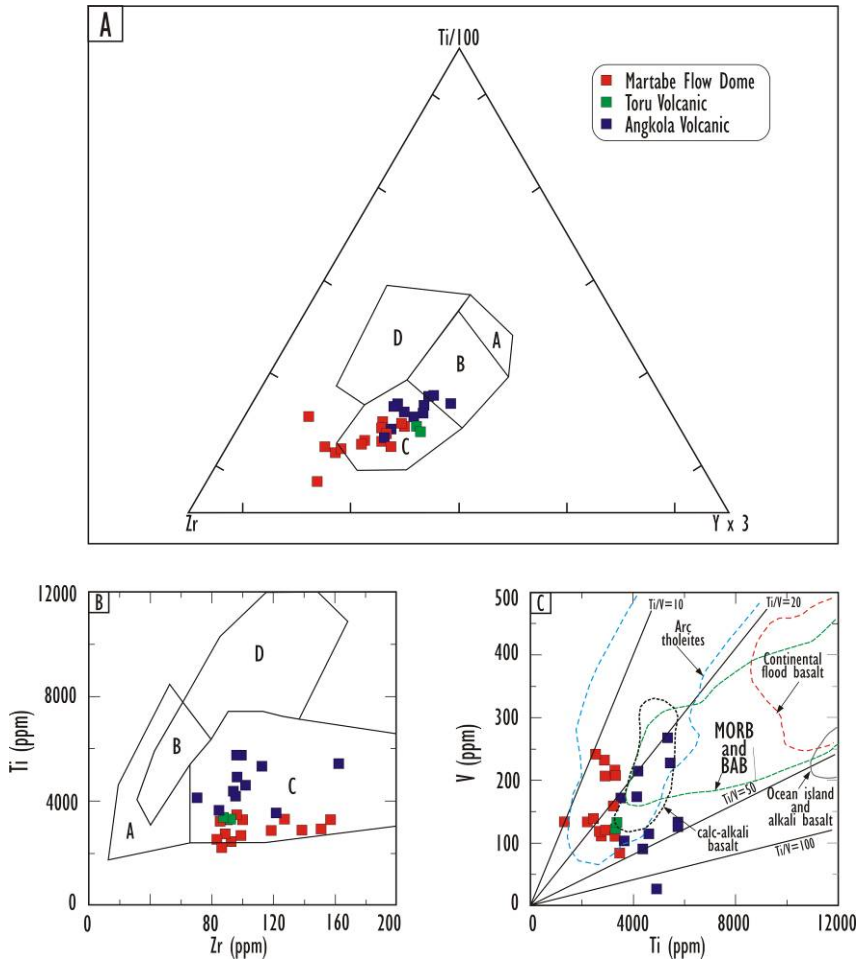

Figure 5.8. Ti-Zr-Y, Ti-Zr and Ti-V discrimination diagrams for coherent volcanic facies at Martabe district.

A. Ti-Zr-Y discriminant diagram for basalts (after Pearce and Cann, 1979; Rollinson, 1993). The fields correspond to: (A) island-arc tholeites; (B) MORB, island-arc tholeites, and calc alkaline basalts; (C) calc-alkaline basalts; and (D) within plate basalts. Rocks plotting in field B can be further separated on a Ti-Zr diagram (Figure 5.9B).
B. Ti-Zr discriminant diagram for basalts (after Pearce and Cann, 1973; Rollinson, 1993). The fields correspond to: (A) island-arc tholeites; (B) MORB, island-arc tholeites; and calc alkaline basalts; (C) calc alkaline basalts; and (D) MORB.
C. Ti-V discriminant diagram for basalts (after Shervais, 1982; Rollinson, 1993). Fields of arc tholeites (blue line), MORB and back-arc basin (BAB) (green line), continental flood basalts (red lines) and ocean island and alkali basalt (grey lines) can also be recognized by their Ti/V ratio. Calc alkaline basalts (black lines) show varying Ti/V ratios and low Ti concentrations.

The Ti-V diagram of Shervais (1982) uses the different behavior of Ti and V to distinguish between volcanic arc tholeites, MORB and alkali basalt (Figure 5.8C). Variations of Ti and V can be related to the oxygen activity of magma and the crystallization processes that have taken place (a detailed explanation is given in Shervais, 1982 and Rollinson, 1993). These variations can also be related to the environment of eruption. Titanium and V are assumed to

be immobile under hydrothermal alteration and high grades of metamorphism, and therefore are useful in discriminating volcanic groups (Rollinson, 1993). The basaltic andesites and basalts at Martabe generally plot with higher Ti and V values, whereas the andesites have comparatively lower values (Figure 5.8C). Most basalts from the Angkola volcanic formation are characterized by Ti/V ratios greater than 20 and less than 50, consistent with back-arc basin basalts (BAB) and plot within the empirically determined field (from Shervais, 1982) of calc-alkaline basalts. All the Martabe flow dome complex samples plot within the arc tholeite field (Figure 5.8C).

5.6.3 Tectonic setting discrimination

Pearce and Norry (1979) used the Zr/Y-Zr diagram (Figure 5.9A) to subdivide basalts formed at active continental margins and arcs from those of the oceanic crust. Values for coherent basaltic rocks at Martabe suggest that they formed in a continental arc setting (Figure5.9A). Basalt and basaltic-andesite samples have comparatively lower Zr/Y and Zr values than the andesite and dacite samples, reflecting their more mafic character.

The Ti/Y-Nb/Y diagram (Figure 5.9B) is used by Pearce and Gae (1977) to discriminate between within-plate basalts and other basalts (collectively termed plate-margin basalts; Rollinson, 1993). Values for coherent basalt rocks at Martabe suggest a within-plate margin affinity (Figure 5.9B) with some sample in the intra-plate field. The basalt and basaltic andesite plot with comparatively lower Zr/Y than the andesite and dacite, reflecting their more mafic character, while Ti/Y remains constant. The Pliocene Martabe flow dome complex rocks are compositionally similar to the dominantly andesitic-dacitic hosting the Pinapan porphyry copper deposit, 30 km to the northwest of Martabe district (Appendix 1). The Pinapan volcanic rocks exhibit a wider range of composition, from basalts through dacite with >50 wt% SiO_2 (Rock et al., 1982).

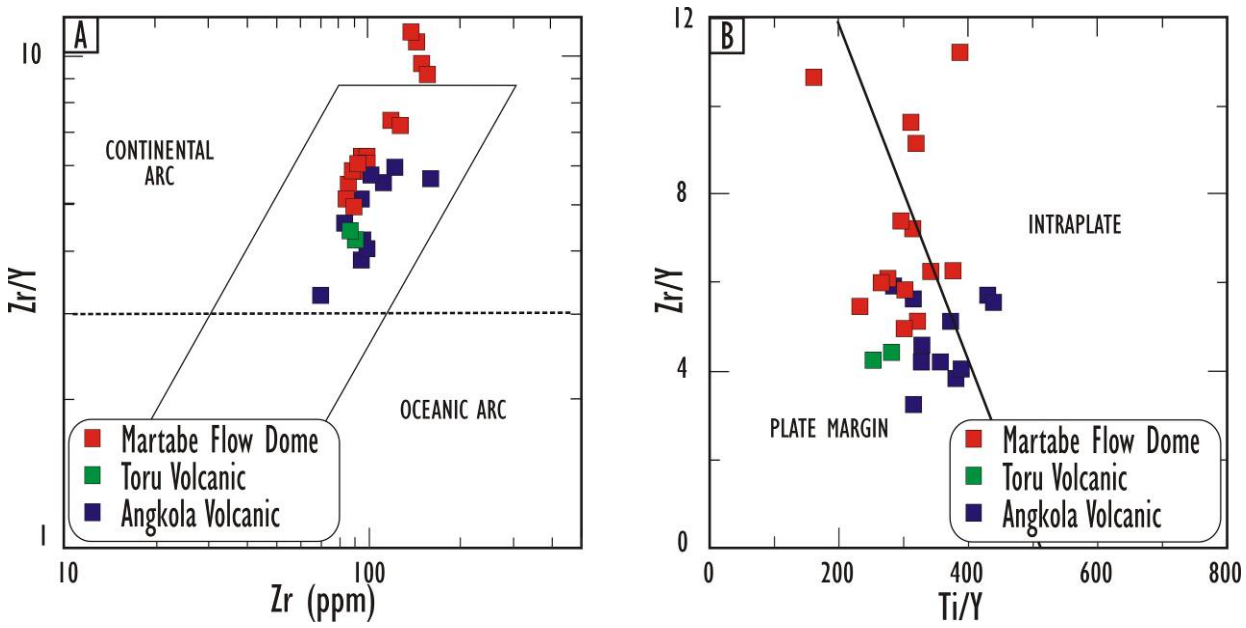

Figure 5.9. Zr/Y-Zr and Zr/Y-Ti/Y discrimination diagrams for coherent volcanic facies at Martabe
A. Zr/Y-Zr diagram showing fields of oceanic arc basalts and continental arc basalts
B. Zr/Y-Ti/Y diagram showing division of plate margin basalt and within-plate basalt

5.7 Conclusions

Geochemical data for coherent volcanic rocks at Martabe can be divided into four characteristically different volcanic suites; a basalt suite, a basaltic-andesite suite, an andesite suite and a dacite suite. These may correlate with the Late Early Miocene-Mid Miocene of Angkola volcanic and Toru volcanics formations, respectively. These results are consistent with a back-arc environment. The Martabe coherent volcanic rocks have geochemical similarities and appear to be genetically related. Generally, these have similar immobile elements characteristics that are indicative of andesitic to basaltic volcanism, generated at a plate margin in a back arc setting.

Data from this study agree with the data of Bellon et al. (2004) and Crow (2005), in that the Tertiary volcanic rocks in Sumatra are mostly of basaltic-andesitic composition; with dacite compositions for Pliocene volcanic rocks. The volcanic rocks at Martabe mostly plot within basalt, basaltic-andesite, basaltic trachyandesite, andesite and dacite fields of sub-alkalic magmas, with most samples having a low- to normal-K composition, with exception of Toru volcanic andesite rocks which have a shoshonitic composition. These diagrams show that the early Miocene Angkola Volcanic Formation has a wide range of low- to normal- K of basaltic andesite to andesite composition, while most of the Martabe flow dome complex rocks are

classified as medium-K alkaline andesite to dacite. However, the lavas or shallow intrusive sills of the Toru volcanic are high-K to shoshonitic andesite.

The AFM diagram illustrates that the volcanic rocks at Martabe plot in the calc-alkaline field of the sub-alkali magma series. The FeO and MgO decreases with fractionation and alkali enrichment, which suggests the importance of ferromagnesian minerals, such as olivine and pyroxene in the evolution of both types of magma. However, few volcanic rocks at Martabe have higher FeO/MgO ratios and plot in the tholeiitic field. The AFM diagram (Figure 5.2) shows a clear calc-alkaline trend with FeO and MgO depletion and alkali enrichment. FeO and MgO depletion and alkali enrichment correlate with decreasing of ferromagnesian minerals from basalt of Angkola Volcanic Formation to rhyolite in Martabe flow dome. Such magma compositions are typical of subduction-related tectonic settings, but in detail there are differences from typical or average magma compositions (Ewart, 1982; Thorpe et al., 1982).

CHAPTER 6

ALTERATION CHARACTERISTICS AND ZONATION

6.1 Introduction

The Martabe district is located within the Sumatran Fault System (SFS) zone, which locally formed the northwest-trending Purnama fault-related mineralization. The mineralization extends along strike for 8 km (Figure 6.1). It is enveloped by a wide alteration system with a footprint of over 45 km^2. Both lithological and structural features have influenced the alteration characteristics and zonation (Figures 6.1 and 6.2).

To date several deposits have been recognized in Martabe district, namely Purnama, Baskara, Kejora, Pelangi and Gerhana. All identified economic and sub-economic gold-silver mineralization and the alteration of the district displays a zonal pattern of alteration typical of high-sulfidation epithermal system (Figure 6.3), with the presence a low-sulfidation epithermal system at the peripheral (i.e., Pelangi prospect). In this study alteration minerals were identified by hand specimen observation, petrography, K-feldspar staining, XRD and SWIR analysis.

In general, the alteration at Martabe is classified as siliceous, advanced argillic (alunite- and kaolinite-rich zone), argillic and propylitic following the terminology defined by Lowell and Guilbert (1970), Meyer and Hemley (1976), Rose & Burt (1979) and Sillitoe (1989) (Table 6.1). The core of the Martabe system, which has a cm- to m- scale size of structural (i.e., Baskara, Kejora and Gerhana) and sub-horizontal/stratigraphical (i.e., Purnama) control, is typically zoned from brecciated, massive quartz and vuggy quartz, outwards to an advanced argillic altered zone of the alunitic and kaolinitic sub-types. The advanced argillic alteration passes outwards to an argillic altered zones of illite that is surrounded by a peripheral zone of pervasive propylitic alteration, consisting of epidote, chlorite and calcite. The alteration zones most likely occurred as multiple stages within combining centers and formed approximately contemporaneously with the Martabe flow dome magmatism.

The spatial distribution of mineral assemblages for each deposit within the Martabe district is slightly different from each other. In general, alteration occurs in the flow dome, breccias and andesitic volcanic units whilst the unaltered rocks are mainly the basaltic volcanic units at the periphery (i.e., southern part of Purnama and Pelangi, and Baskara East). The quartz matrix-supported breccias contain the majority of high-grade Au, whereas lower-grade mineralized zones mainly occur within the pervasive alunitic altered

breccias. In addition, kaolinitic altered rock units contain some lower-grade mineralization. A late-stage advanced argillic alteration overprint is due to acidic supergene oxidation. The contacts are typically gradational between the argillic and advanced argillic alteration zones, whereas contact zones are sharp where identified between the siliceous and advanced argillic and/or argillic alteration zones. At Martabe, the alteration zones are based on the presence and abundance of alteration minerals and textural characteristics (Tables 6.1 to 6.4). The '*alunitic*' alteration assemblage mainly consists of quartz+alunite± dickite/kaolinite±pyrite; the '*kaolinitic*' assemblage refers to quartz+kaolinite/dickite± alunite±pyrite; the '*illitic*' assemblage is used for illite-smectite-pyrite±quartz; and the '*propylitic*' assemblage consists of chlorite+epidote+calcite ±illite/sericite±pyrite±quartz (Table 6.1).

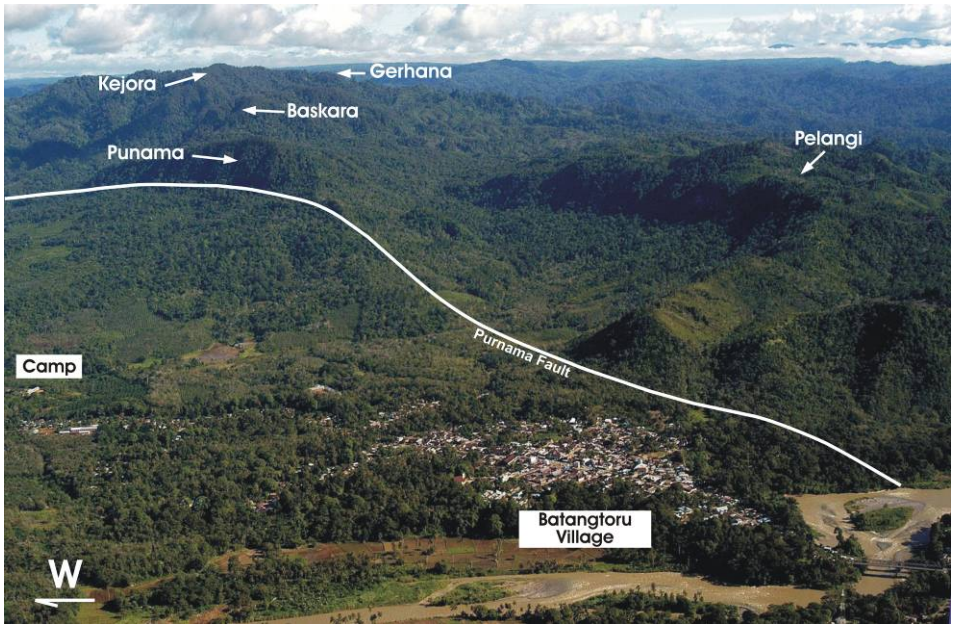

Figure 6.1. Martabe district viewed from south east showing quartz altered ledges. These ridges are mostly made up of massive-vuggy quartz and advanced argillic alteration surrounded by argillic alteration at lower elevations. The Batangtoru village is as in the foreground (bottom left).

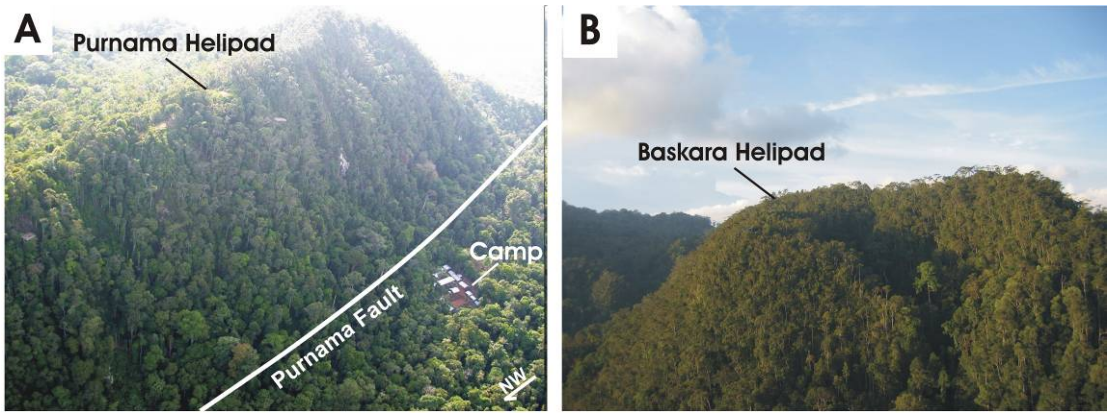

Figure 6.2. (A) Purnama ridge and Purnama fault scrap. View is toward southeast. (B) Baskara ridge as viewed from the south. The middle of the Baskara ridge is occupied by intense argillic alteration.

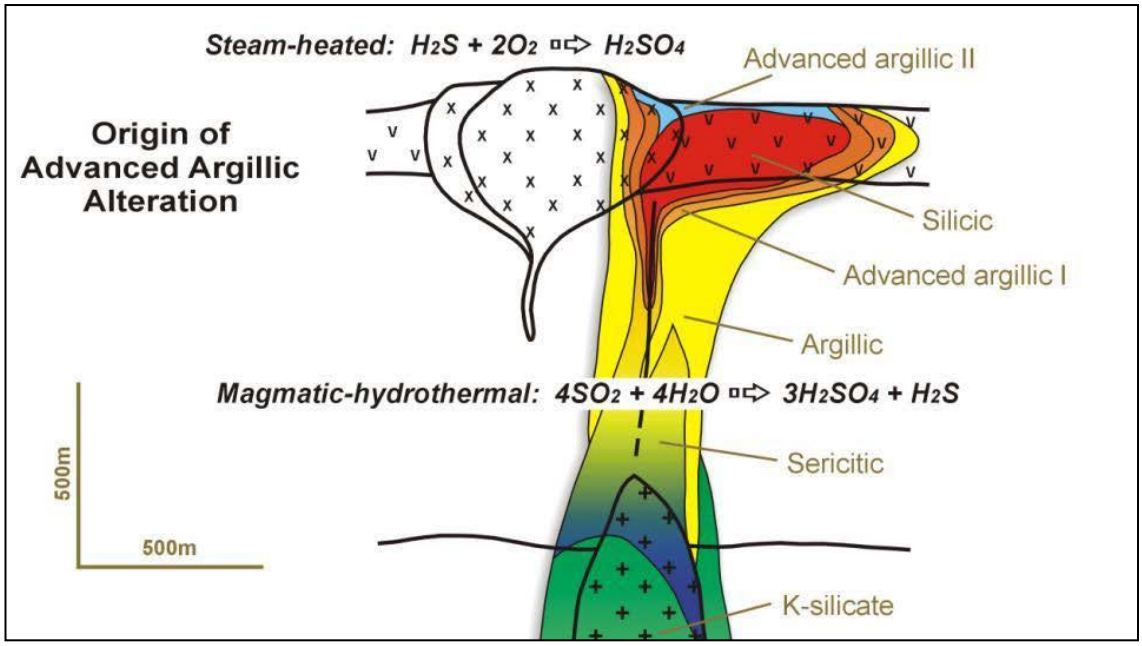

Figure 6.3. Schematic section illustrating the alteration relationship of the high-sulfidation epithermal system in a flow dome setting (Arribas et al., 2000 modified from Sillitoe, 1999).

Table 6.1. Summary of alteration types and mineral assemblages in the Martabe district.

Alteration type	Mineral assemblage	Minerals with diagnostic spectral features (PIMA infrared analyses result)	Petrographic dominant features	Hand specimen description
Siliceous				
Massive quartz and vuggy quartz	quartz	not applicable	~>85-95% quartz	very hard, massive, distinctive voids texture in vuggy quartz, trace of alunite-kaolinite
Opal/chalcedony	opal/chalcedony, cristobalite	not applicable	amorphous silica	cryptocrystalline to amorphous silica, powdery to sandy
Quartz veining	opal/chalcedony	not applicable	amorphous silica to fine grained quartz	opal/chalcedony to crystalline quartz
Advanced Argillic				
Alunitic	quartz, alunite ±kaolinite/dickite ±pyrite	alunite	quartz, alunite	dominant alunite+kaolinite /dickite, jarosite
Kaolinitic	quartz, kaolinite/ dickite±alunite ±pyrite	kaolinite/dickite	kaolinite/dickite quartz	dominant kaolinite/dickite pyrite, jarosite ±alunite
Argillic				
Illitic	illite, smectite, pyrite, quartz, smectite	illite smectite	illite smectite ±pyrite	grayish clay to more kaolinite in weathered zone, swelling clay
Propylitic				
Chlorite, epidote and calcite	chlorite, epidote calcite±pyrite illite or sericite quartz	chlorite, epidote calcite, illite or sericite	chlorite, epidote calcite, illite orsericite	greenish rock with distinctive of chlorite, calcite, epidote

6.2 Alteration facies

A variety of methods, including field mapping, drill-hole logging, hand specimen description, K-feldspar staining, transmitted and reflected light optical microscopy, XRF analysis (Appendix 2), X-Ray Diffraction analysis (Appendix 3), Electron Microprobe analysis (Appendix 4) and PIMA analysis (Appendix 6) were used to identify the alteration facies in this study. XRD and PIMA were used to determine clay minerals (i.e., kaolinite/dickite, halloysite and illite-smectite clays).

6.2.1 Siliceous alteration

Siliceous alteration forms the core of the hydrothermal alteration system and results in prominent ridges, which are distinctive features in the Martabe district. The siliceous alteration is classified separately from the advanced argillic zone; and is interpreted to have about >~80-95 vol. % of quartz. The alteration zone varies from massive quartz, vuggy quartz (with or without sulfide and Fe-oxide) to chalcedony/opal (Table 6.2). In addition, quartz veining is also included as siliceous alteration. The silicification is pervasive, varying both in grain size and the degree of vugginess. Overprinting textural relationships indicate at least two main stages of silicification, an early vuggy quartz development and 'multiple' later silicification events.

Massive silicification is widespread in all deposits of the Martabe district, particularly at Purnama, Baskara and Gerhana, while fractured and brecciated massive quartz is the main ore host in Purnama. In hand specimen, massive quartz is typically hard, dense and obliterates original textures. In thin section, the silicification commonly has a domainal texture with variations in crystallinity that shows that it was not a single-stage process, initiating from very fine and cherty to later coarser crystalline quartz. Blurred, dull, textureless, pale white to brown, fine-grained quartz and locally weak colloform and fibrous textures, are probably derived from the recrystallisaton of chalcedony or opal. Original textures are mainly destroyed, but locally there are taint remains of original phenocryst or fragmental texture. The field-based description of 'silica flooding' or 'quartz flooding' was used to describe the chalcedony and/or quartz that partially or completely filled the vugs, fractures and obliterated the textures. Fine-grained quartz may replace both phenocrysts and groundmass.

Alteration Type	**SILICEOUS**						
Alteration assemblage/ Sub-type	Vuggy quartz	Massive quartz	Chalcedonic/ opal	Quartz sulfide	Quartz – Fe-oxide	Residual silica	Quartz veining
Mineral assemblage (dominant)	qtz+alu-(kao/di) py-(en/luz)	qtz	qtz	qtz-py-(en/luz)	qtz-goe-hm-(jar)	qtz+kao/di-alu	qtz+(kao/di)
Location, extent and Temporal relation to ore	Core Syn-mineralization, centimeters to 10's meters, cryptocrystalline quartz with void > 5% voids	Core to proximal Syn-mineralization, centimeters to 10's meters, massive-compact quartz <5% voids	Distal to medial Pre-mineralization Cryptocrystalline to amorphous silica, due to acid fluid at water table and often at peripheral	Core to proximal Syn-mineralization centimeters to 10's meters, compact to vuggy quartz with disseminated, veined and matrix sulfide in breccias	Proximal to core Post-mineralization Upper part, related to fault/structures and contact units, pervasive matrix and selective veins, centimeters to 10's meters	Distal, upper part Pre-mineralization Acid leaching Upper part and peripheral to volcanic contacts, patchy in andesite porphyritic. Abundant in flows dome	Distal to medial Pre-post mineralization Centimeters to meters, crystalline quartz, kaolinite/dickite associated with veins are common
Alteration style[1]	P, V, F	P	P	SP, V	SP, V	SP	V
Relevance to mineralization	Mod- to high-grade	Low to mod-grade	Barren to trace	Mod- to high-grade	Mod- to high-grade	Barren to trace	Barren to mod-grade
HOST ROCK							
Sediments	Not applicable	Not applicable	Minor	Minor	Trace	Not applicable	Common
Angkola Volcanic							
Basaltic Andesite	-	-	-	-	-	-	-
Volcaniclastic rocks	Minor	Minor	Rare	Minor to common	Minor to common	Rare	Minor to common
Lithic fragments	qtz-*(alu-kao)*	qtz	qtz	qtz-py	qtz-*(goe)*	qtz	qtz+(kao/di)
Crystals	qtz-*(alu-kao)*	qtz	qtz	qtz	qtz	qtz	qtz+(kao/di)
Matrix	qtz-*(kao)*	qtz	qtz	qtz-py	qtz-*(goe)*	qtz	qtz+(kao/di)
Toru Volcanic							
Porphyritic andesite	Common to major	Common to major	Common	Common to major	Common	Rare to minor	Common to major
Feldspar	qtz-*(kao)*	qtz	qtz	qtz	qtz	qtz	qtz
Mafic	qtz	qtz	qtz	qtz-*(py-en)*	qtz-*(goe-hm-jar)*	qtz	qtz
Groundmass	qtz-*(kao)*	qtz	qtz	qtz-*(py-en)*	qtz-*(goe-hm)*	qtz	qtz
Martabe Flow Dome							
Hornblende andesite	Minor to major	Minor to major	Rare	Common-Major	Minor to common	Common	Trace
Feldpsar	qtz-*(alu-kao)*	qtz	qtz	qtz	qtz	qtz	qtz
Mafic	qtz	qtz	qtz	qtz-*(py-en)*	qtz-*(goe-hm-jar)*	qtz	qtz
Groundmass	qtz-*(alu-kao)*	qtz	qtz	qtz-*(py-en)*	qtz-*(goe-hm)*	qtz	qtz
Dacite	Common to major	Common to major	Rare	Common to major	Minor to common	Common	Trace
Feldpsar	qtz-*(alu-kao)*	qtz	qtz	qtz	qtz	qtz	qtz
Mafic	qtz	qtz	qtz	qtz-*(py-en)*	qtz-*(goe-hm-jar)*	qtz	qtz
Groundmass	qtz-*(alu-kao)*	qtz	qtz	qtz-*(py-en)*	qtz	qtz	qtz
Phreatomagmatic breccia[2]	Common to major	Common to major	Common to major	Common to major	Common to major	Common to major	Common to major
Clast and matrix	qtz-*(alu-kao)*	qtz	qtz	qtz-*(py-en)*	qtz-*(goe-hm-jar)*	qtz-kao-*alu*	qtz-kao/di
Phreatic breccia[3]	Trace	Trace	Trace	Trace	Trace	Minor	Trace
Matrix and clast	*qtz-(alu-kao)*	-	*qtz*	*qtz*	qtz	qtz-kao	-

Table 6.2. Summary of siliceous alteration characteristics at Martabe.

Abbreviation: qtz = quartz, alu=alunite, kao=kaolinite, di=dickite, sul=sulfide, py=pyrite, en=enargite, lim=limonite, jar=jarosite, goe=goethite, hm=hematite, nat-s=native sulfur.

Underline = principal alteration mineral and/or complete replacement; italics = partial replacement; parentheses = minor occurrence

[1]SP = selective pervasive alteration, P=pervasive alteration, V = vein- and/or vug related; F=fault related,

[2]Clast alteration may pre- and/or postdate brecciation

[3]Qtz-alu-kao clast alteration typically predates brecciation; all other alteration styles typically postdate brecciation.

Vuggy quartz altered rock appears in hand specimen to be nearly pure quartz, but upon microscopic observation, significant amounts (5-10 vol.%) of sulfates (e.g., barite and jarosite), goethite and hematite are identified. The vugs vary from mm to cm scale and are white to grayish. The vugs may be lined with fine or drusy quartz crystals, and/or hematite and limonite (mainly goethite).

In thin section, the vuggy quartz forms a dense mosaic texture and exhibits similar variations in crystallinity as massive quartz. A progression is observed from vuggy quartz with open voids to massive quartz in which later, coarser quartz has totally infilled the void space. Coarser crystals occur in vugs and fractures can be up to 1 mm in size. The vuggy quartz is therefore early, and was converted to a compact from by later deposition of quartz. Both vuggy and massive quartz alteration have been overprinted by brecciation and fracturing with variable amounts jarosite, hematite, goethite and barite. The protholith rocks that have been altered to vuggy quartz can be distinguished miscroscopically. The volcanic rocks commonly show angular to sub-angular and more uniform vugs. Whereas the volcaniclastic rocks and breccias consist mostly of multi-shaped vugs and very fine vugs. Andesites are dominated by a matrix of fine-grained quartz, probably representing original volcanic glass (Figures 6.4 to 6.6).

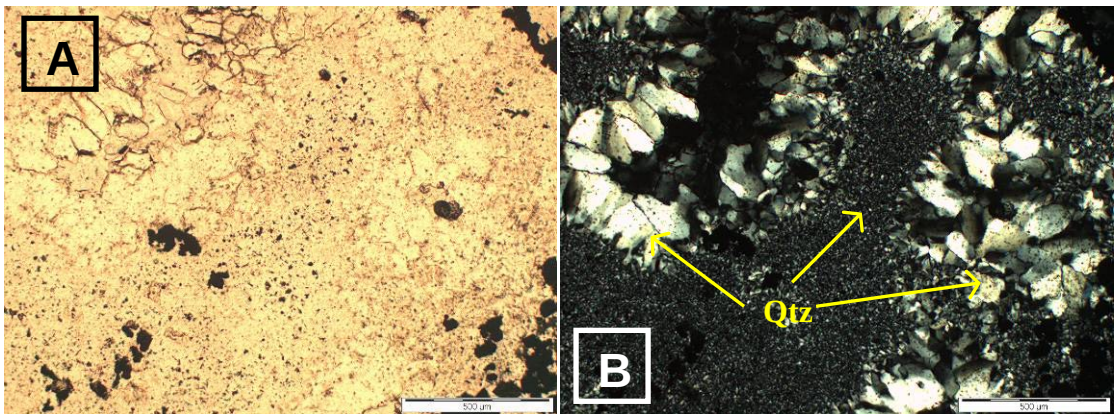

Figure 6.4. Vuggy quartz forms a dense mosaic texture; and coarser quartz has totally infilled the void space (B-right centre) and partially outlined vug (B-top left). (A). Transmitted light (B) Transmitted light/cross polar. Sample APSD198_66.5 taken from Purnama.

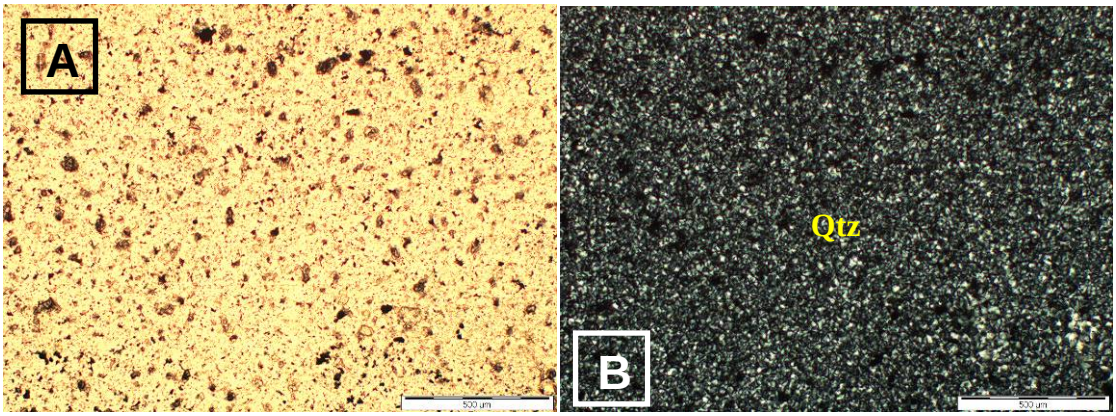

Figure 6.5. Fine-grained interlocking quartz dominated matrix of fine-grained quartz. Sample probably representing original volcanic glass. (A) Transmitted light. (B) Transmitted light/cross polar. Sample APSD 198_66.5 taken from Purnama.

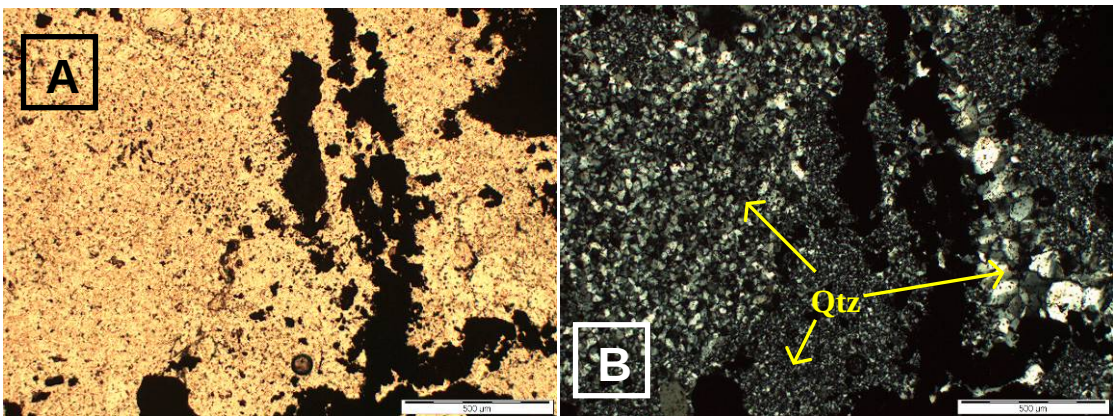

Figure 6.6. Vuggy quartz exhibits variations in crystal size of quartz with coarse grained Fe oxides. (A) Transmitted light. (B) Transmitted light/cross polar. Sample APSD198_66.5 taken from Purnama.

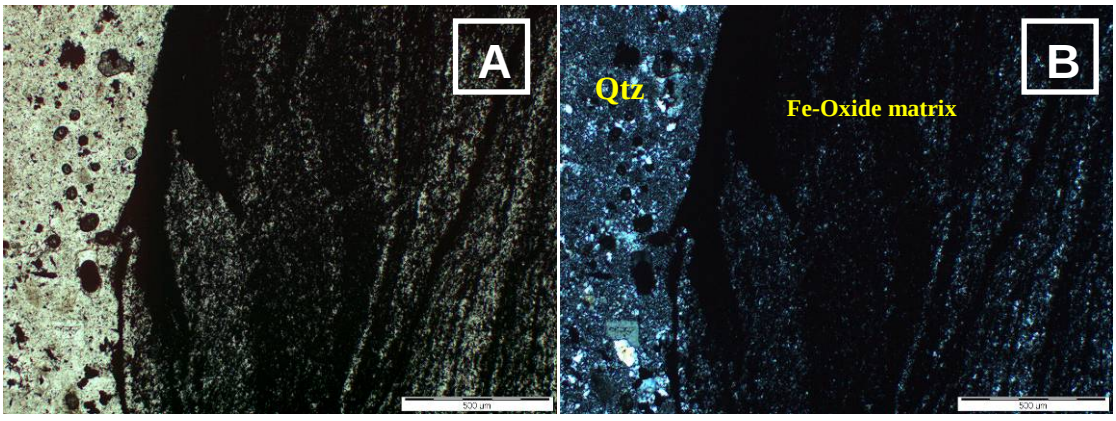

Figure 6.7. Fine-to medium-grained subangular quartz clast with Fe-oxide and quartz matrix breccia. (A) Transmitted light. (B) Transmitted light/cross polar. Sample APSD156_122.5 taken from Purnama.

In contrast, quartz in the altered dacite is generally coarser-grained, with some finer-grained domains. Large zircon crystals are present in the most intensely altered rock. Residual iron oxides are also very common in the altered andesite and dacite, but do not

define relict mineral grains, they may reflect preexisting mafic minerals. Limonite and jarosite fills small vugs and coats larger vugs in the breccia. Euhedral barite is commonly found in vuggy quartz zones in vugs or on fractures (Figure 6.8 and 6.9).

Chalcedony and opal are observed as white to gray, blue-grey to dark-grey with a waxy luster or porcellaneous appearance. Chalcedony and opal are mainly found at the periphery of the main alteration centers (i.e. Parbotikan, Purnama East and peripheral to the Baskara deposit), but are rarely present at Kejora and Gerhana. In thin section, chalcedony appears as very fine-grained, porcellaneous and amorphous to cryptocrystalline in texture.

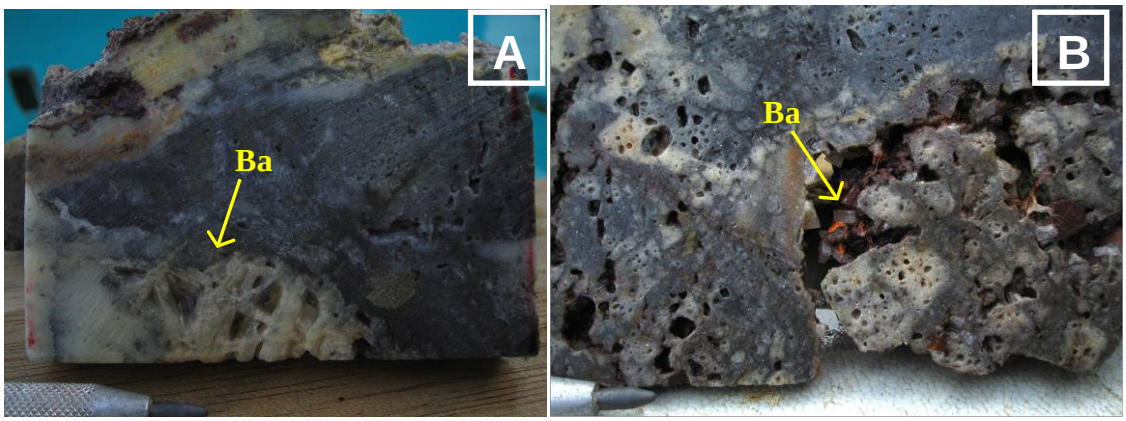

Figure 6.8 (A) Bladed barite texture and quartz cut massive quartz. (B) Barite, as prisms fills void in vuggy quartz and encrust by hematite-goethite. Sample APSD159_122.5 taken from Purnama.

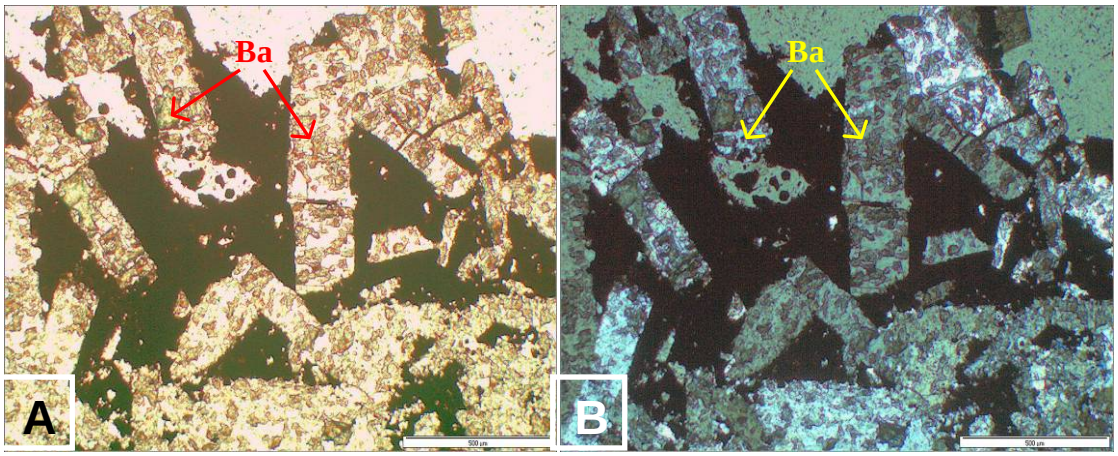

Figure 6.9. (A) Coarse-grained tabular barite is encrusted by goethite (A) Transmitted light parallel polar. (B) Transmitted light/crossed polars. Sample APSD159_122.5 taken from Purnama.

At Martabe, geophysics has been successful in locating and defining the siliceous alteration through Induced Polarization (IP) pole-dipole and airborne HoisTEM resistivity methods (Fig 6.10 and 6.11). These data have sufficient resolution to accurately target the siliceous alteration beneath soil, such as at East Baskara. The siliceous alteration has a resistivity in the order of thousands of ohm-meters compared with the resistivity of tens of ohm-meters

from marginal argillic alteration and propylitic alteration. This contrast has clearly shown the shape of the siliceous zones beneath argillic alteration or soil. At Baskara East and Purnama, the siliceous alteration can be detected 20-100 m below surface. At Purnama and Gerhana, the siliceous alteration mainly forms subhorizontal bodies, whereas in Baskara, the siliceous alteration generally forms vertical tabular bodies thinner with depth. Alteration in high-sulfidation epithermal deposits commonly has a large area of magnetite destruction, although it does not appear to have a large vertical extent depending on the underlying lithologies (Hoschke, 2007).

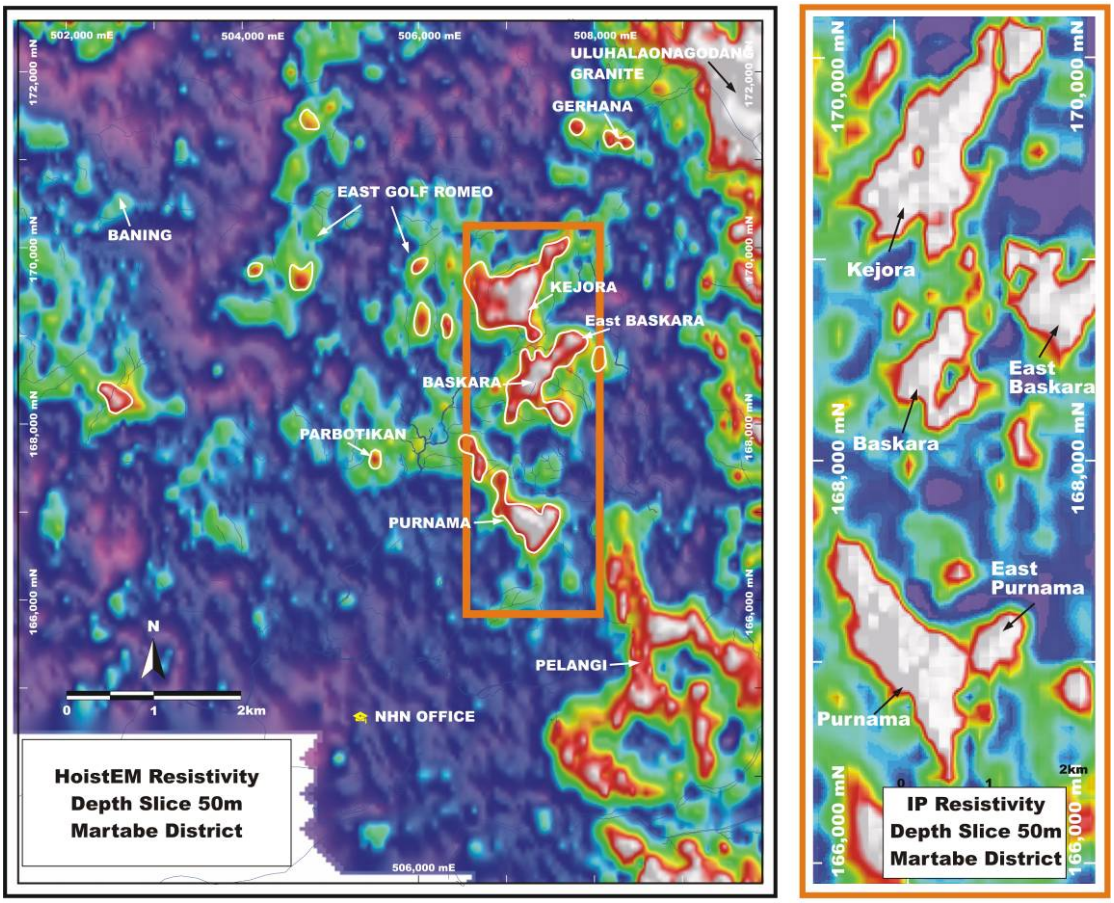

Figure 6.10. (a) Airborne TEM resistivity map of the Martabe district (b) Pole-dipole resistivity map of the Purnama deposit (modified from Hoschke, 2007).

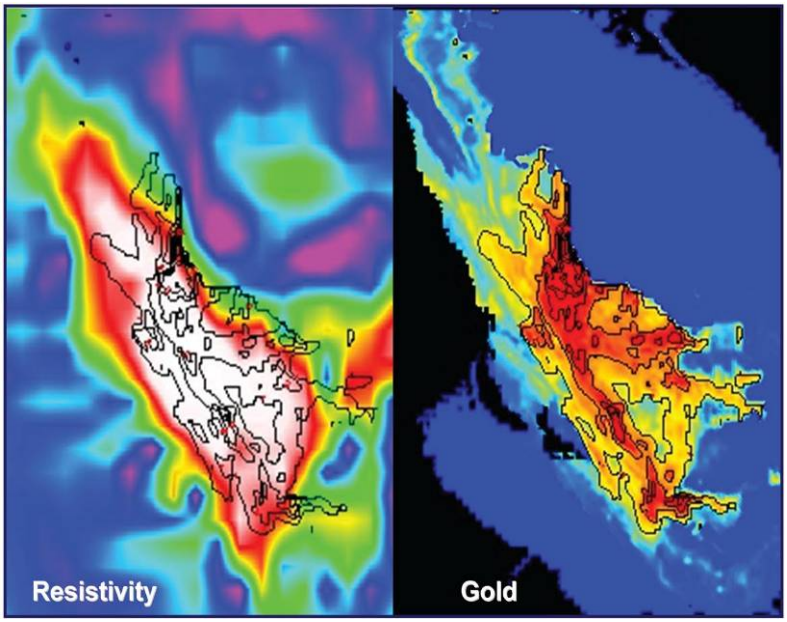

Figure 6.11. Depth slice of (a) resistivity at 50 meters depth and (b) gold at 50 m depth below topography through the Purnama (contours represent gold distributions at above intervals of 1 g/t) (modified from Hoschke, 2007).

6.2.2 Advanced argillic alteration

The terminology 'advanced argillic' is commonly used to defined an alteration zone in which alunite, quartz, kaolinite and dickite (a high temperature polytype of kaolinite) form an assemblage. An 'ideal' advanced argillic mineral alteration assemblage should included quartz, alunite, kaolinite/dickite, pyrophyllite, diaspore, barite and jarosite (Hedenquist, 1994). At Martabe, hydrothermal breccias and siliceous alteration are common features present in the rocks or adjacent to the advanced argillic alteration zones. The advanced argillic alteration surrounds and partly overlaps the core zone of siliceous alteration laterally and at depth, and its distribution varies widely. However, clay content increases toward the outer margin. Therefore, there are locally subdivisions in the advanced argillic alteration zone at Martabe district (Table 6.3). Alunite-dominated alteration envelops the siliceous zones and these facies together comprise the highest grade zones of the deposit. Alunite is easily identified in Baskara, Kejora and Gerhana in hand specimen. At Purnama, advanced argillic alteration consists of quartz and dickite±kaolinite with rare alunite. Alunite may constitute up to 30 vol. % of the altered rock as determined by petrographic observation and semi-quantitative XRD analysis

Table 6.3. Summary of advanced argillic alteration characteristics at Martabe.

Alteration Type	**ADVANCED ARGILLIC**				
Sub-type	**Alunitic**			**Kaolinitic**	
Alteration assemblage	Quartz-alunite replacement	Quartz-alunite hydrothermal	Quartz Dickite/kaolinite ±(alunite)	Quartz kaolinite Alunite Supergene	Quartz kaolinite
Mineral assemblage (dominant)	qtz-alu	qtz-alu	qtz-di/kao+(*alu*)	qtz-kao+ (alu)	qtz-kao+ mixed-layer clays-(alu)
Location and extent	Proximal-medial	Proximal-medial	Medial to distal	Distal	Distal
Temporal relation to Ore	Syn-mineralization centimeters to 10's meters, acid leaching,	Syn-mineralization 10's to 100's meters, acid leaching,	Pre-Syn-mineralization, acid leaching, patchy flows dome in, abundant in andesite porphyritic	Pre-mineralization Acid leaching water table centimeters to 10's meter	Syn-mineralization, centimeters to 10's meter
Alteration style[1]	P, SP	SP	SP, P	SP, P	SP, P
Relevance to mineralization	Low- grade	Low grade	Low grade to barren	Barren to low grade	Barren to low grade
HOST ROCK					
Sediments	Rare to minor	common	common	Minor	Minor
Angkola Volcanic	Minor	Minor	Minor	Minor	Minor
Basaltic Andesite	Trace	Trace	Trace	Trace	Trace
Volcaniclastics rocks	Common	Common	Major	Minor	Common-Major
Lithic fragments	qtz-di+*(alu)*	qtz-di+*kao-py)*	qtz-di-*(kao-py)*	qtz-di+*(kao-py)*	qtz-di+*(kao-py)*
Crystals	qtz-di+*(kao-py)*	qtz-di+*(kao-py)* qtz-di+*(kao-py)*	qtz-di+*(kao-py)*	qtz-di+*(kao-py)*	qtz-di+*(kao-py)*
Matrix	qtz-di+*(alu)*		qtz-di+*(kao-py)*	qtz-di+*(kao-py)*	qtz-di+*(kao-py)*
Toru Volcanic					
Porphyritic andesite	Common to minor	Minor	Common to major	Common to major	Common to major
Feldpsar	qtz-alu-di-*(py)*	qtz-alu-*(py)*	qtz-kao-*(alu)*	qtz-kao-*(alu)*	qtz-kao-*(alu)*
Mafic	qtz-*(kao-py)*	qtz-*(kao-py)*	qtz-*(kao-py)*	qtz-*(kao-py)*	qtz-*(kao-py)*
Groundmass	qtz-alu-di-*(py)*	qtz-kao-*(alu-py)*	qtz-kao-*(py)*	qtz-kao-*(py)*	qtz-kao-*(py))*
Martabe Flow Dome					
Hornblende andesiteFeldpsar	Minor to common	Common to major	Common to major	Common to major	Common to major
Mafic	qtz-alu-*(kao-qtz)*	qtz-alu-*(qtz)*	qtz-kao-*(alu)*	qtz-kao-*(alu)*	qtz-kao-*(alu)*
Groundmass	qtz-*(kao-py)* qtz-*(alu-kao-py)*	qtz-*(kao-py)* qtz-kao-*(alu-py)*	qtz-*(kao-py)* qtz-kao-*(py)*	qtz-*(kao-py)* qtz-kao-*(py)*	qtz-*(kao-py)* qtz-kao-*(py)*
Dacite	Common to major	Common to major	Common to major	Common to major	Common to major
Feldpsar					
Mafic	qtz-alu-*(kao-qtz)*	qtz-alu-*(qtz)*	qtz-kao-*(alu)*	qtz-kao-*(alu)*	qtz-kao-*(alu)*
Groundmass	qtz-*(kao-py)* qtz-*(alu-kao-py)*	qtz-*(kao-py)* qtz-kao-*(alu-py)*	qtz-*(kao-py)* qtz-kao-*(py)*	qtz-*(kao-py)* qtz-kao-*(py)*	qtz-*(kao-py)* qtz-kao-*(py)*
Phreatomagmatic breccia[2]	Common	Common	Common to major	Minor	
Clast and matrix	qtz- di-alu-*(py)*	qtz- di-alu-*(py)*	qtz- di-alu-*(py)*		
Phreatic breccias[3]	Rare to minor	Rare to minor	Rare to minor		
Matrix and clast	Qtz-*(kao-py)*	qtz- di-alu-*(py)*	qtz- di-alu-*(py)*		

Abbreviation: qtz=quartz, alu=alunite, kao=kaolinite, di=dickite, sul=sulfide, sm=smectite, py=pyrite, lim=limonite, jar=jarosite, goe=goethite, hm=hematite

Underline = principal alteration mineral and/or complete replacement; italics = partial replacement; parentheses = minor occurrence

[1]SP = selective pervasive alteration, P=pervasive alteration, V = vein- and/or vug related; F=fault related,

[2]Clast alteration may pre- and/or postdate brecciation

[3]Qtz-alu-kao clast alteration typically predates brecciation; all other alteration styles typically postdate brecciation.

Chemically, the alunite varies from K-rich to natroalunite ($NaKAl_3(SO_4)_2(OH)_6$) with increasing substitution of Na. This variation can be recognized from XRD, PIMA and EMP. To confirm this variation, several grains were analyzed by EMP (Table 6.4). EMP indicates most samples are K-rich alunite with varying amounts of Na.

Table 6.4. List of alunite EMP composition from Purnama (all values in wt.%). Negative values indicate below detection.

Sample_Ref	Al	K	Na	Ca	S	P	Pb	Fe	Ba	Sr	O	Total
164_156.8-1	19.33	9.19	0.04	0.00	15.21	0.06	-0.03	0.01	0.14	0.04	41.95	85.97
164_156.8-2	18.88	8.16	0.04	0.21	13.79	0.79	-0.01	0.00	1.37	0.31	40.45	84.02
164_156.8-3	19.30	9.24	0.04	0.00	14.96	0.03	-0.07	0.01	0.07	0.06	41.54	85.26
164_156.8-4	18.90	9.35	0.06	-0.01	14.96	0.05	-0.03	0.02	0.12	0.04	41.24	84.74
164_156.8-5	18.88	9.11	0.02	-0.01	15.17	0.00	-0.07	0.05	-0.01	-0.02	41.38	84.62
164_156.8-6	19.15	9.03	0.05	0.01	14.93	0.11	0.00	0.06	0.29	0.06	41.45	85.14
164_156.8-7	19.23	8.74	0.02	0.01	15.07	-0.01	-0.04	0.01	0.05	0.00	41.46	84.59
164_156.8-8	19.06	9.03	0.03	0.02	15.22	0.00	-0.01	-0.02	0.09	-0.06	41.60	85.05
164_156.8-9	19.07	9.05	0.07	0.06	15.21	0.24	-0.01	0.04	0.46	0.02	42.02	86.26
164_156.8-10	18.78	9.12	-0.01	-0.01	15.25	0.00	-0.07	0.03	0.14	0.04	41.43	84.80
164_156.8-11	18.74	9.07	0.10	0.01	15.01	0.03	-0.15	0.01	0.01	0.07	41.07	84.12
164_156.8-12	18.79	9.14	0.07	-0.01	14.92	0.01	-0.12	0.03	0.12	0.00	40.98	84.06
164_156.8-13	19.15	8.22	0.04	0.13	14.25	0.49	-0.02	0.03	0.89	0.19	40.89	84.28
164_156.8-14	19.24	8.97	0.03	0.01	14.70	0.05	-0.11	0.04	0.14	0.06	41.06	84.30
164_156.8-15	18.45	8.54	0.06	0.16	14.18	0.86	-0.09	0.05	1.20	0.36	40.80	84.65
164_156.8-16	19.06	8.90	0.04	0.09	14.81	0.32	-0.02	0.04	0.56	0.27	41.54	85.64
164_156.8-17	18.97	9.37	0.09	0.00	15.02	0.06	-0.10	0.04	0.07	0.07	41.42	85.12
164_156.8-18	18.85	9.16	0.06	0.01	14.98	0.06	-0.08	0.04	0.05	-0.29	41.13	84.33
164_156.8-19	19.07	9.17	0.06	0.01	15.29	0.01	-0.02	0.15	0.00	0.12	41.82	85.69
135_47.3_1	15.73	5.23	0.70	0.17	11.82	0.38	0.39	0.09	0.85	0.52	33.82	69.72

In the Martabe district, alunite occurs in veins, filing vugs or voids and as replacement masses in andesite, dacite, hornblende-pyric andesite and breccias. Three types of alunite are recognized:

(i) Euhedral (acicular) alunite is a characteristic of hypogene acid-sulfate alteration related to magmatic-hydrothermal environments (Rye et al., 1992; Deyell et al., 2005). It is generally tabular, ranging in length from 10 μm to 200 μm and may be zoned. The tabular alunite infills vugs and finer-grained crystals with quartz in the groundmass and is partially replaced (rimmed) by supergene jarosite. Alunite is pervasive and replaces feldspars. Disseminated, coarse-grained alunite gives a sparkly appearance to the rock. Alunite in the matrix of the hydrothermal breccias is relatively fine to medium grained bladed and yellow to brownish.

(ii) Alunite in veinlets or veins. In hand specimen, this alunite may be white, pink or tan; dominated by fine to medium coarse-grained crystals. In thin section, this alunite is up to 0.5 mm, often zoned and crystals may form seams or frostwork-like agglomerates in vugs.

(iii) Very fine-grained alunite intermixed with kaolinite. In hand specimen, it is commonly white to tan, and may be massive porcellanous texture to extremely porous texture and replace plagioclase. It is typical of a near-surface steam-heated environment in the vadose zone and is interpreted to be supergene.

Alunite-rich alteration envelopes the siliceous zones, occupies a broadly vertical zone in the central part of the Purnama deposit, and is also concentrated along faults. Alunite extends down to the inferred hypogene feeder system below 425 masl at Baskara. Locally in the oxidized zone, alunite is found throughout the rock in patches. In much of the oxidized zone, jarosite partially or completely replaces alunite. Alunite crystals are observed replacing fine-grained kaolinite crystals.

Kaolinite is a clay mineral with the chemical composition $Al_2Si_2O_5(OH)_4$. It is a soft, whitish to creamy, earthy material, produced by the alteration or chemical weathering of aluminosilicate minerals like feldspar. In hand specimen, kaolinite also selectively replaces feldspar phenocrysts and occurs as pervasive alteration in the groundmass. In thin section, kaolinite occurs in replacement masses and as void infill. It is typically fine-grained (<0.05 mm), occurs as anhedral crystals, platy flakes, and crystals with hexagonal, square and triangular outlines. Dickite is a high temperature polytype of the kaoline group. In hand specimen, dickite is typically greenish color, and typically occurs as a pervasive replacement, as selective alteration of feldspar phenocrysts, or as infill in veins and cavities (Figures 6.12 to 6.18).

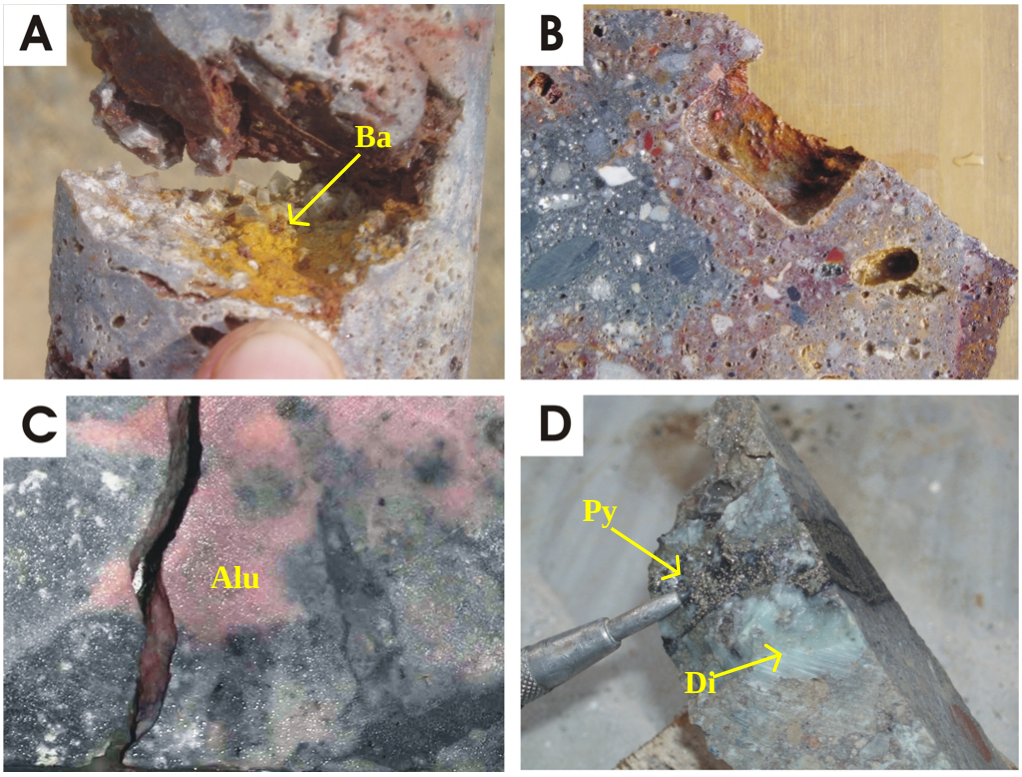

Figure 6.12. (a) Large tabular crystals of barite (Ba) occur as vug infill in silicified polimictic breccia, (b) Vuggy texture up to 3 cm in diameter which is due to dissolved clast in very intense silicified polymict breccias, (c) Medium to fine-grained, pinkish alunite (Alu) in veins, this type is characteristic for hypogene acid-sulfate alteration, (d) Very fine-grained dickite (Di) and pyrite (Py) in a vein.

Varying proportions of kaolinite/dickite are typically present with the quartz and alunite dominated alteration zones. Dickite distribution is restricted to the 'high temperature' environment of this epithermal system, within quartz-alunite and/or close to siliceous alteration, whereas kaolinite is more widely dispersed. Quartz-kaolinite±(smectite) mineral assemblages in altered rocks at Martabe are typically very fine-grained, white or tan to pink-orange-red and may have a brown oxidized surface due to weathering of pyrite.

In many cases, the advanced argillic zone contains more clay than alunite, however quartz is still very abundant, exceeding 50 vol.% in places. On the surface, siliceous ridges may grade down into clay alteration within a few meters. This may be due to remnant, thin quartz-rich caps from early alteration, or a supergene effect of groundwater movement and deposition of silica. Both processes are probable and have preserved some clay alteration zones from erosion. Pyrophyllite was identified in few samples by SWIR. It occurs in the siliceous and quartz-alunite zones. SWIR analysis also identified some diaspore associated with the pyrophyllite. In thin section diaspore occurs as distinct, pale green to yellow pleochroic, prismatic crystals in veinlets.

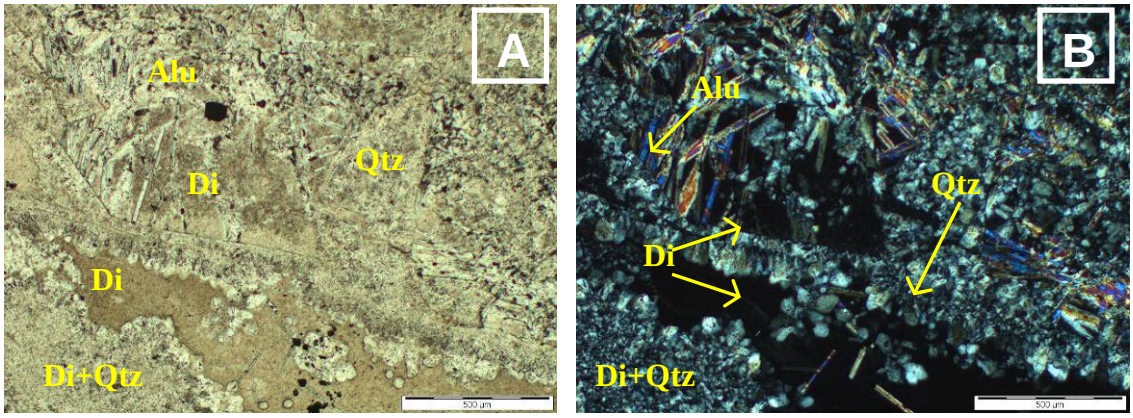

Figure 6.13. Tabular alunite between medium-grained silieous altered rock. Quartz and dickite fills vug or vein. (A) Transmitted light. (B) Transmitted light/cross polar. Sample APSD198_66.5 taken from Purnama.

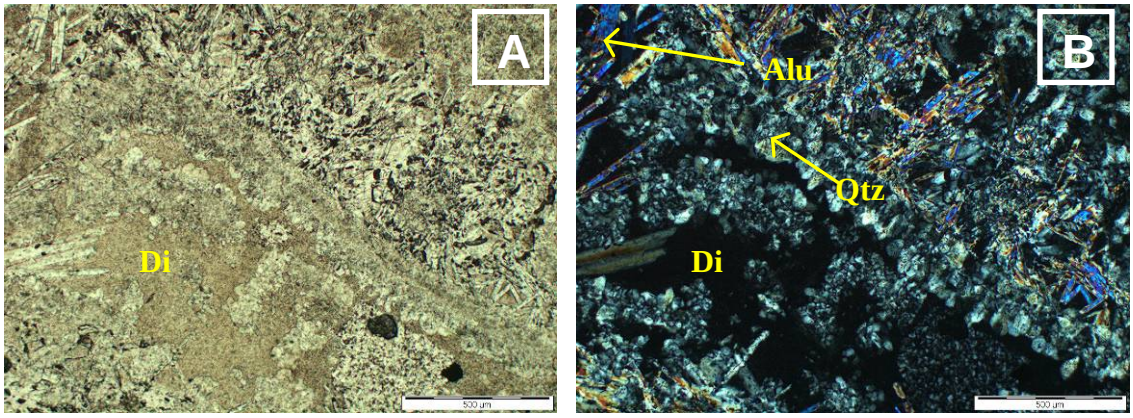

Figure 6.14. Tabular alunite between medium-grained quartz altered rock. Quartz and dickite fills vug or vein. (A) Transmitted light. (B) Transmitted light/cross polar. Sample APSD198_66.5 taken from Purnama.

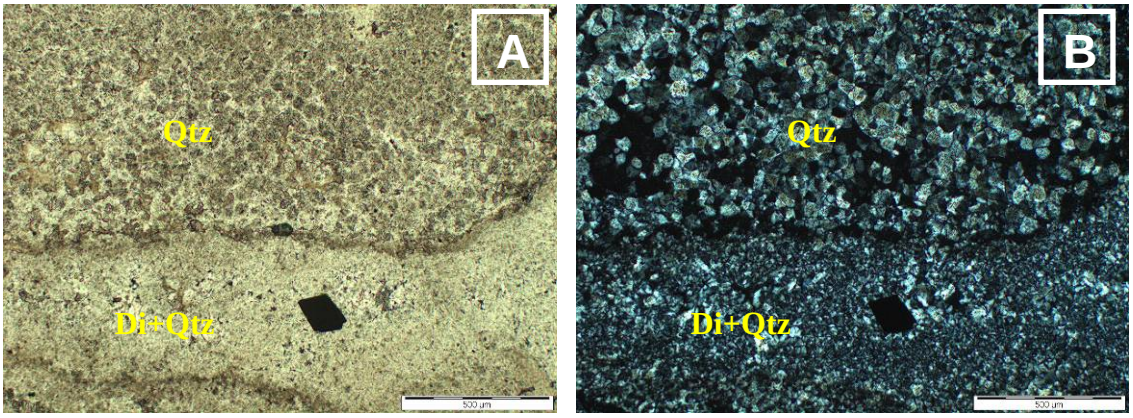

Figure 6.15. Variations in crystal size of quartz in vuggy quartz alteration with coarse-grained Fe-oxides. (A).Transmitted light. (B) Transmitted light/cross polar. Sample no APSD198_66.5 taken from Purnama.

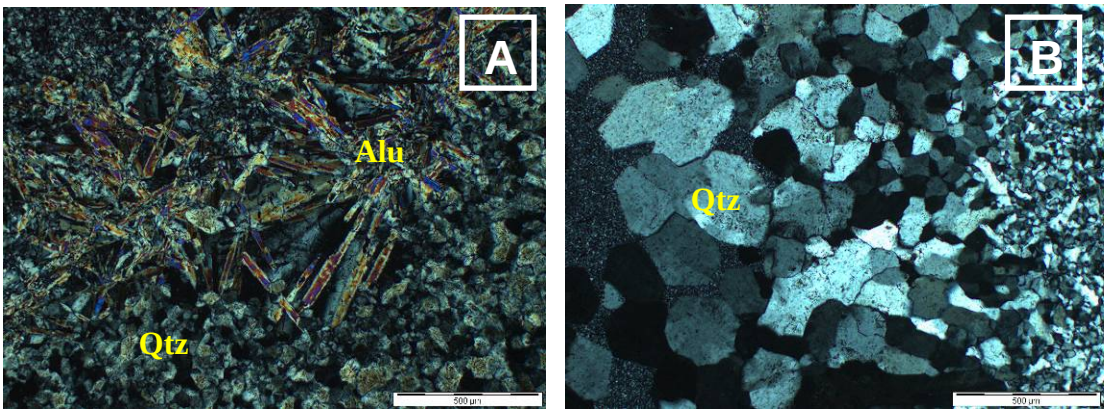

Figure 6.16. (A) Coarse crystalline alunite (alu) occupying former site of feldspar phenocryst in a groundmass altered to quartz. (A)Transmitted light.
(B) Variation of grain size of quartz showing a progression from vuggy quartz with open voids to become massive quartz in which later. Coarser quartz has totally infilled the void space. Coarser crystals occur in vugs and fractures and can be up to 1 mm in size. The vuggy quartz is therefore early, and was converted to a compact form by later deposition of quartz. Transmitted light/cross polar. Sample APSD198_66.5 taken from Purnama.

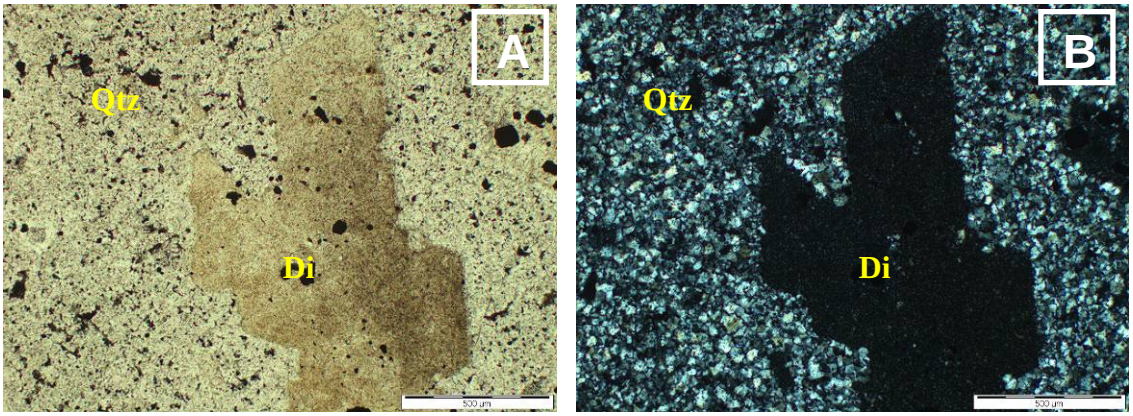

Figure 6.17. Very fine-grained dickite altering a phenocryst within fine-grained interlocking quartz. (A).Transmitted light. (B) Transmitted light/cross polar. Sample APSD198_66.5 taken from Purnama.

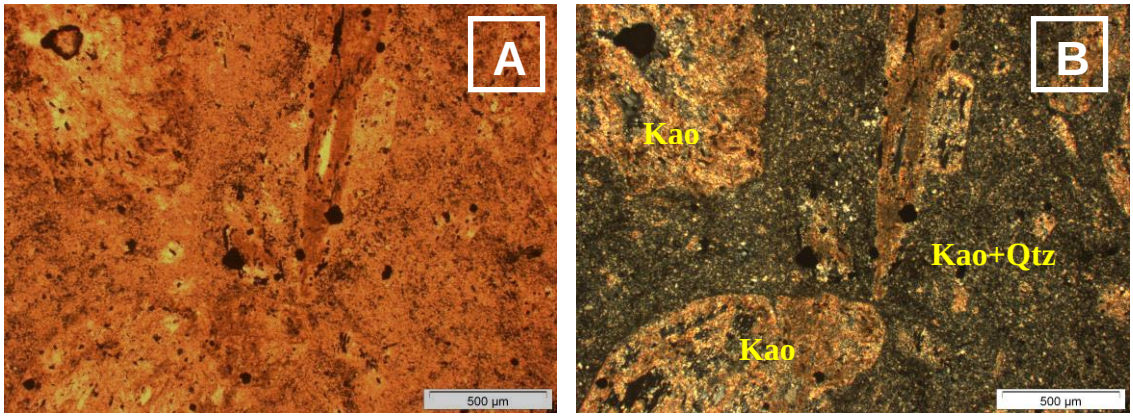

Figure 6.18. Pervasively kaolinitic (kaolinite-quartz) altered porphyritic andesite. (A) Transmitted light. (B) Transmitted light/cross polar. Sample APSD198_66.5 taken from Purnama.

6.2.3 Argillic alteration

The argillic alteration zone defines the periphery of the hydrothermal alteration halo and ore-grade mineralization. It occurs in later structural zones (i.e., Baskara) or in phreatic breccias (i.e., Purnama and Baskara). This alteration envelopes the advanced argillic and siliceous alteration zones. Illite is the dominant mineral recognizable at hand-specimen scale, but PIMA analysis identifies smectite and halloysite (?). The argillic altered rocks are characteristically soft, incompetent, pyrite-rich and easily swell on exposure to air and water. The presence of smectite induces swelling, in contrast to the kaolinite/dickite clay dominant assemblages in the advantage argillic zone (Table 6.5). In hand specimen, the argillic alteration varies from pale gray, pale green to pale white. Very fine-grained smectite replaces primary minerals and volcanic glass. Interlayered illite/smectite with minor kaolinite-quartz, altered rocks are very fine-grained and white or tan. The pyrite content is variable, ranging from <1 to about 10 vol.%. The highest pyrite contents can be found near the contact with the advanced argillic alteration.

6.2.4 Propylitic alteration

A broad zone of 'greenish' alteration is the most distal manifestation of hydrothermal alteration. Propylitic alteration is characterized by the presence of epidote, chlorite, calcite and minor quartz-illite (Table 6.5). Original rocks textures are commonly been preserved or enhanced.

Table 6.5. Summary of argillic and propylitic alteration zones at Martabe.

Alteration Type	ARGILLIC	PROPYLITIC	
Alteration assemblage	Clay-Pyrite-Quartz	Chloritic dominant	Chlorite-Calcite-Epidote
Mineral assemblage	Ill-(ser), sm, mixed layer ill-sm-py	Chl-ill-carb	chl-cal-ep
Location and extent	Distal to medial	Distal to peripheral	Distal to peripheral
Temporal relation to Ore	Pre to Syn mineralization	Pre to Syn mineralization	Pre to Syn mineralization
	Proximal to quartz-alunite-kaolinite/dickite and siliceous alteration, intensive in phreatic and phreatomagmatic breccias , 10's to 100's metres	Centimeters to 10's meters, peripheral to kaolinite zone	Proximal to core of volcanics/flow s dome and volcaniclastic, 10's to 100's meters
Alteration style[1]	P	SP, P	SP, P
Relevance to mineralization	Barren	Barren	Barren
HOST ROCK			
Sediments[2]	Common	Minor	Minor
Angkola Volcanic[2]	Common	Common	Common
Basaltic Andesite	ill-py	chl-*(ill)*-carb	chl-cal-*(ill)*
Volcaniclastic rocks	ill-sm-*(py-kao)*	chl-*(ill)*-carb	chl-cal-*(ill)*
Lithic fragments	ill-sm-*(py-kao)*		
Crystals	ill-sm-*(py-kao)*		
Matrix	ill		
Toru Volcanic			
porphyritic Andesite	Common to major	Common to major	Common to major
Feldpsar	ill-sm-*(qtz)*	ill-*carb*	cal-*(ill)*
Mafic	ill-sm-*(py-kao)*	ill-chl-*carb*	chl-epi-*cal-(ill)*
Groundmass	ill-sm-*(py-kao)*	chl-ill-*carb*	chl-*cal-epi-(ill)*
Martabe Flow Dome			
Hornblende andesite	Minor to common	Common to major	Common to major
Feldpsar	ill-sm-*(qtz)*	ill--*carb*	cal-*(ill)*
Mafic	ill-sm-*(py-kao)*	ill-chl-*carb*	chl-epi-*cal-(ill)*
Groundmass		chl-ill-*carb*	chl-*cal-epi-(ill)*
Dacite[2]	Common to major	Common to major	Common to major
Feldpsar	ill-sm-*(qtz)*	ill--*carb*	cal-*(ill)*
Mafic	ill-sm-*(py-kao)*	ill-chl-*carb*	chl-epi-*cal-(ill)*
Groundmass	ill-sm-*(py-kao)*	chl-ill-*carb*	chl-*cal-epi-(ill)*
Phreatomagmatic breccia[2]	Common	Minor	
Clast and matrix	ill-sm-*py-(qtz)*		
Phreatic breccias[3]	Major	Trace	
Matrix and clast	ill-sm-*py-(qtz)*		

Abbreviation: qtz=quartz, kao=kaolinite, ill=illite, sm=smectite, py=pyrite, carb=carbonate, epi=epidote, chl=chlorite, lim=limonite, jar=jarosite, goe=goethite, cal=calcite hm=hematite

Underline = principal alteration mineral and/or complete replacement; italics = partial replacement; parentheses = minor occurrence

[1]SP = selective pervasive alteration, P=pervasive alteration, V = vein- and/or vug related; F=fault related,

[2]Clast alteration may pre- and/or postdate brecciation

[3]Qtz-alu-kao clast alteration typically predates brecciation; all other alteration styles typically postdate brecciation

In thin section, feldspar crystals are replaced by aggregates of illite or sericite, chlorite, epidote and calcite. Epidote replaces plagioclase and hornblende. Chlorite, calcite and trace illite partially to completely replace amphibole. Calcite also occurs in veinlets. Chlorite-rich alteration mainly occurs in andesitic flows and flow domes. Typically plagioclase is altered to chlorite; carbonate and illite after chlorite. Chlorite, illite, quartz and minor carbonate completely replace the groundmass (Figures 6.19 to 6.22). Trace clay (kaolinite) replacement of plagioclase and wall-rock xenoliths has occurred locally. Chlorite-rich alteration is less well developed in the Purnama, it is observed locally where argillic alteration grades into fresh rock. However, chlorite-rich alteration is found beneath the mineralization zone and zone of advanced argillic alteration at Baskara. This implies that a feeder zone, which should have higher temperature alteration assemblages, may not have developed below this deposit.

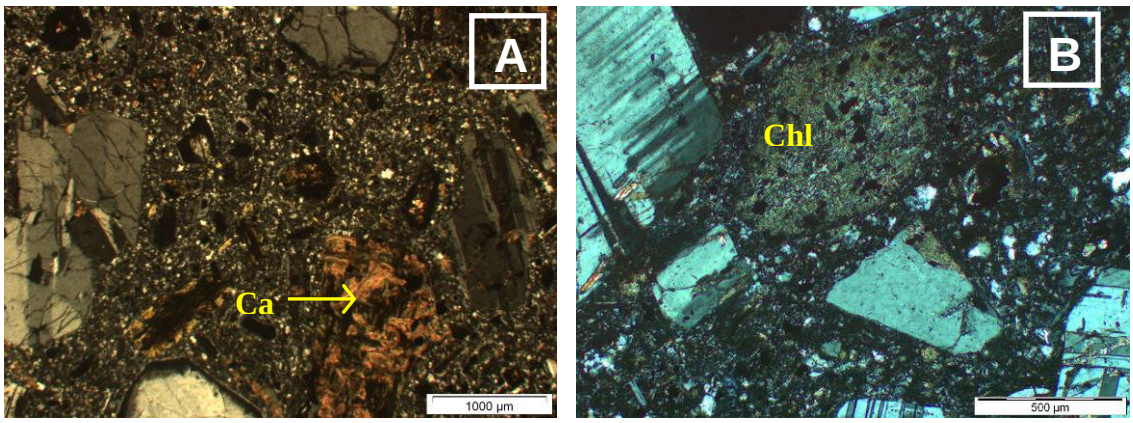

Figure 6.19. (A) Calcite replacing a mafic mineral. (B) Chlorite and opaque mineral replacing hornblende. (A) Transmitted light. (B) Transmitted light/cross polar. Sample APSD198_66.5.

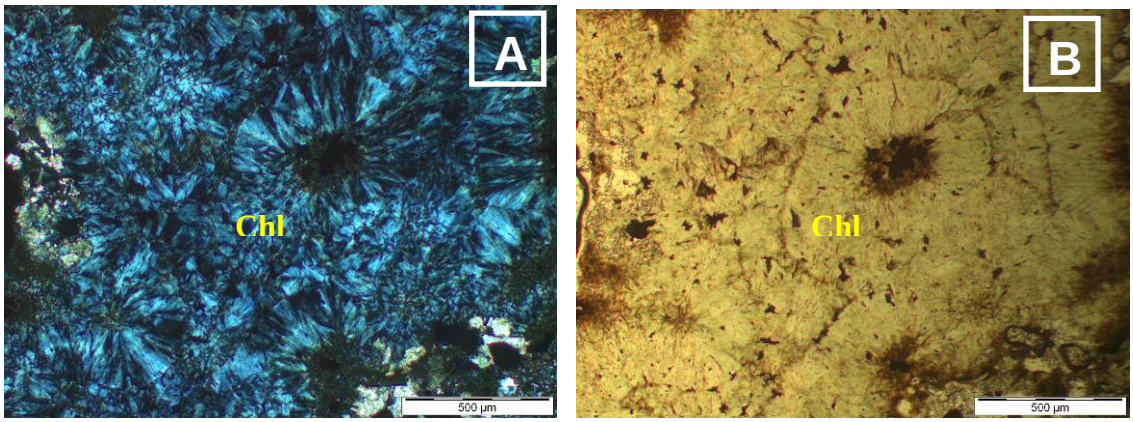

Figure 6.20. Pervasive chlorite in the matrix. (A) Transmitted light. (B) Transmitted light/crossed polars. Sample APSD198_66.5.

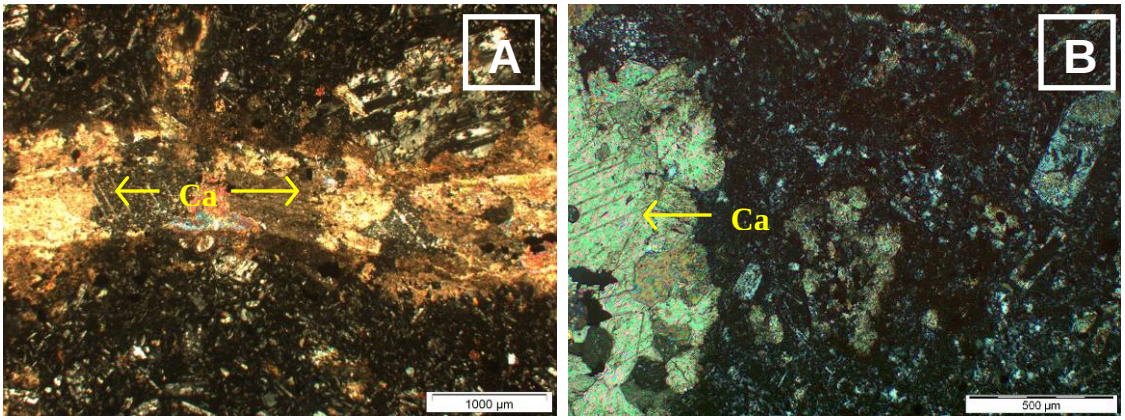

Figure 6.21. (A) Calcite vein cutting a propylitic altered volcanic rock. (B) Coarse calcite fills vug in propylitic altered volcanic rock. Sample APSD198_66.5.

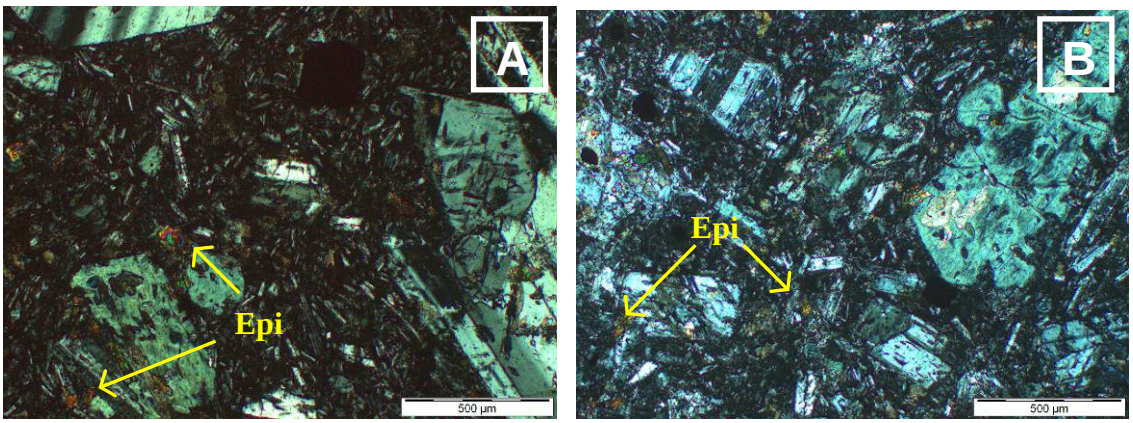

Figure 6.22. Fine grained epidote in andesitic basalt. (A) Transmitted light. (B) Transmitted light/crossed polars. Sample APSD198_66.5.

6.3 Residual quartz alteration

In the some acid sulfate deposits, zones of barren granular quartz have been recorded (i.e., Yanacocha; Turner et al., 1999). This alteration is attributed to the alteration of the steam-heated zone above the paleo-water table. At Purnama, granular or possibly remnant residual quartz form some outcrops. In some location, porous quartz is completely disaggregated to a fine silt to clay sized, powdery quartz. The leached zones are characterized by an absence of Au, and lack most other metals apart from Hg. They are small zones of whitish, grayish, incompetent and friable quartz. Residual quartz is found predominantly above 350 masl. The distribution of residual quartz appears to have a blanket like morphology and overlie the ridges. This morphology suggests that the residual quartz zones are the eroded remnants of an originally extensive sheet, which is best preserved on high elevations of the district. Outcrops are only a few meters thick and grade down to very hard, massive porcellanous quartz. Residual quartz is also found on top of Baskara and Kejora occurs in many places. It is also probably a thin extensive zone of

continuous microcrystalline silica which is thought to represent the groundwater surface at the time steam heated alteration.

6.4. Supergene oxidation and weathering

Supergene oxidation affects the surface outcrops. It has an irregular base and may extend down fractures/faults to unknown depth. In the oxide zone, most of the primary sulfides have been destroyed. Hematite, goethite, kaolinite, scorodite, jarosite and supergene alunite after sulfides and sulfosalts are the most common products of oxidation. The oxidation is variable throughout the district, ranging from down to 100 m in Purnama and less than 100 m in Baskara. In Gerhana, the depth of oxidation is thin approximately ~15 m depth in the eastern part but extends down to 50 m in the west. Oxidation of sulfides consists of Fe-oxides and sulfates in siliceous rocks and kaolinite and Fe-oxides in argillized rocks. The original sulfide content has probably significantly affected the intensity of the supergene alteration processes (Bladh, 1992).

Scorodite, from the oxidation of arsenic-rich sulfosalts, is also present. Barite commonly occurs in these late-stage iron oxide fractures and vugs filled up to 2 cm wide. Kaolinite is present as an alteration formed through reaction in acidic meteoric water or plagioclase phenocrysts in the breccia fragments, andesite and dacite volcanic rocks. It is difficult to distinguish from hypogene kaolinite in the argillic alteration zones. Jarosite is an iron analogue of alunite in which Fe^{3+} replaces the aluminium.

Oxidation and transitional mineralization grade down into the primary sulfide mineralization. The transitional zone is characterized by partial oxidation above the sulfide zone, in which cores of the sulfide are still preserved in strongly silicified rock. The pyrite content may locally range from several volume percent to over 20 vol. %, forming patches of semi-massive pyrite. In the intense supergene oxidation near-surface, pyrite is not preserved. Late-stage gold mineralization is temporally distinct from the earlier quartz–pyrite alteration. As it is predominantly fracture and breccia controlled, this style of mineralization is more susceptible to oxidation than the earlier quartz pyrite mineralization.

Although some remobilization of gold can be expected in the oxidized zone, the lack of coarse-sized free gold and the presence of high silver values, indicates that there has not been significant supergene upgrading of the gold values. The percentage of late stage iron oxide in fractures and crackle breccias rather than the proportion of sulfide in the rock is likely to be the best indicator of the gold leachability of the rock (Levet et al., 2003; Sutopo et al., 2003). The presence of luzonite/enargite–covellite± pyrite/marcasite in fractures represents the unoxidized equivalent of the late-stage mineralization, which is

likely to be refractory. At Martabe, sulfide sulfur assays were used to define oxide, transitional and sulfide interfaces.

6.5 District-scale alteration

The distribution of alteration mineral zones in part of the Martabe district is shown in Figures 6.23 and 6.24. Some of the alunite-rich zones follow northwest-southeast structures. Siliceous alteration passes outwards into advanced argillic alteration which passes outwards to argillic and propylitic alteration. At Martabe, hydrothermal alteration, especially advanced argillic and siliceous alteration, is generally located in areas recognized as steep and/or distinctive topographic highs. The zones are mostly situated in hilly terrain at the east side of the Purnama fault. Whereas the moderate to flat areas are dominated by widespread propylitic and argillic zones, as notably the abrupt low elevation on the west side (foot wall) of the Purnama Fault (Figures 6.2 and 6.3). The Purnama deposit is associated with the NW trend of the Purnama fault which controls weathering-resistant silicified ridge of the hypogene breccias and porphyritic andesite of Toru Volcanic Formation. As the Baskara and Kejora deposits are situated within the centre of a dome, their topographic high is mainly controlled by siliceous alteration. Minor intense kaolinite alteration and quartz veining zones are recognized at the small ridge in the Parbotikan area associated with a NW trending fault at the west (Figure. 6.23). To the southeast, subsequent faulting and ore mineralization associated with quartz veins along these structures occurred during a possible younger, low-sulfidation hydrothermal episode in Pelangi. Vuggy quartz is best developed at Baskara and Gerhana. At Purnama, siliceous alteration forms extensive sub-horizontally zones of massive microcrystalline quartz with minor vuggy quartz texture, associated with dickite, pyrite, enargite/luzonite and minor tennantite-tetrahedrite. The contact between advanced-argillic and argillic/propylitic altered rocks on the west-slope at Purnama follows the structure and lithological sharp contact between breccias and lavas of the Toru Volcanic Formation. Figure 6.24 shows the distribution of hydrothermal alteration zone in the Martabe district.

There are some zones of kaolinite$\pm$alunite that occur in weakly altered Angkola Volcanic andesites down a ridge to the west at Parbotikan, indicating that the alteration probably extended down this ridge. Compared to the Purnama area, alteration at Baskara is more alunite-rich, with very little dickite. A propylitic-altered intrusion (hornblende-bearing andesite) was mapped at Purnama, but at Baskara and Kejora this intrusion is partly altered to siliceous and advanced argillic alteration. Overall, in the Martabe district propylitic alteration is widespread, and also adjacent to structures along which mineralized high-

sulfidation veins occur. Several small 'alunitic' and 'kaolinitic' zones are also mapped in the Golf Mike area, approximately 4 km south of the Martabe district (Figures 6.23 and 6.24). Breccia-hosted siliceous and advanced argillic outcops were also observed at about 800 meters to the south-southeast of Pelangi. This area is also adjacent to the north-northwest structure which controlled the formation of the Pelangi deposit.

At Purnama, the vuggy quartz zone has mainly developed from polymict-monomict breccia and porphyritic andesite of the Toru Volcanic Formation; while at Baskara and Kejora, the vuggy altered zone is predominantly hosted in a hornblende-phyric andesite to dacite dome. At Baskara and Kejora, the vuggy quartz zone occurs persistently at the elevations of 425 m and 575 m above sea level. Large vuggy textures are found in Pelangi and Gerhana, showing vugs up to 30 cm in diameter which is due to solution of large breccia clasts. The existence of a vertical feeder, probably associated with a remnant fault, is indicated by Induced Polarization/resistivity anomaly. This distribution suggests that hydrothermal fluid flow was channeled preferentially along faults and lithological contacts (Figure 6.24). Chalcedony veins are ubiquitous at Purnama. In contrast, quartz veins of low-sulfidation epithermal character are also clearly exposed on the ridges at Pelangi deposit 2 km to SE of Purnama. At Purnama, the advanced argillic alteration is identified by quartz+dickite± kaolinite±alunite which are mostly hosted in breccias and andesite volcanic rocks. At Baskara, Kejora and Gerhana, quartz+alunite is the characteristic of the advanced argillic alteration which occurs in the dacitic-andesitic dome and breccias. Kaolinite is observed to replace feldspar in both volcanic and volcaniclastics rocks as well as in breccias fragments. In sedimentary rocks, kaolinite and dickite infill cavities and fractures and coexists with quartz veinlets. At Baskara the advanced argillic alteration is restricted to a narrow, <20 m wide zone on the margin of the ore deposit. The argillic mineral assemblage passes outward into the propylitic altered rocks at Baskara and Kejora, which are mainly hosted by dacitic-andesitic intrusions. The western limit of mineralization at Purnama is controlled by structure with patchy to intensive argillic alteration (Figure 6.24).

The three cross sections (Figures 6.25 to 6.27) demonstrate the spatial relationship of the alteration zones in Purnama, Baskara and Gerhana, respectively. Figure 6.25 is the east-west Purnama cross-section compiled using all available drill hole data within 25 m of the line of intersection. This cross-section illustrates the dominant sub-horizontal and minor sub-vertical nature of the hypogene alteration and the spatial relationships of the propylitic alteration in the western part of the Purnama deposits. Figure 6.26 is the east-west cross-section of the Gerhana deposit. Figure 6.27 is the oblique northwest-southeast cross-section of Baskara. These cross-sections illustrate the dominant vertical nature of the

hypogene alteration which is structurally controlled. Figure 6.28 is a conceptual long section showing district wide alteration.

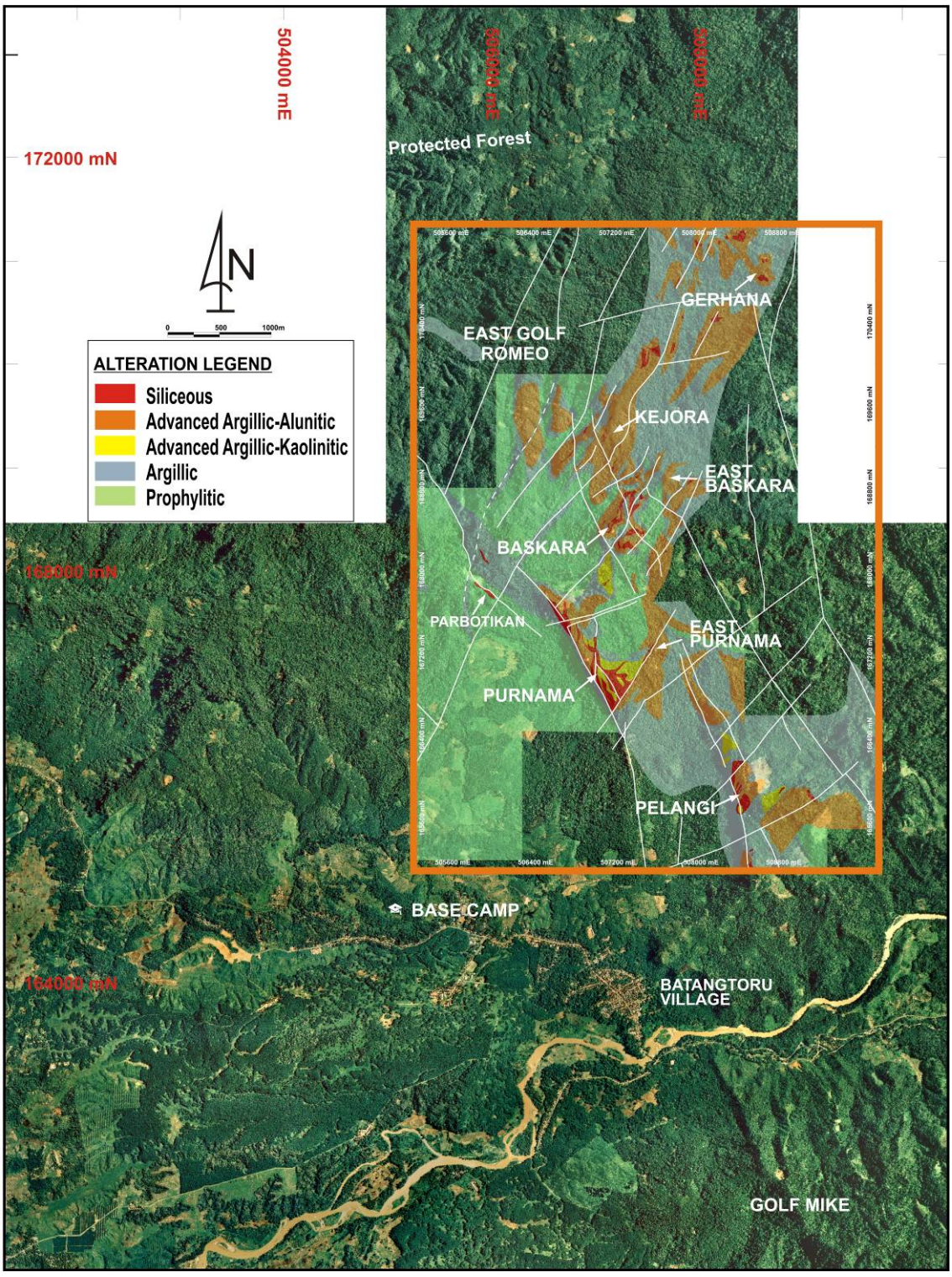

Figure 6.23. District alteration map showing the location of the deposits overlain on the digital orthophoto image of the Martabe district. The lines and transparent polygons are the structure (white lines) and alteration zones, respectively. Siliceous zones are shown in red, alunitic zones in orange, kaolinitic zones in yellow, argillic zones in light blue and propylitic zones in green.

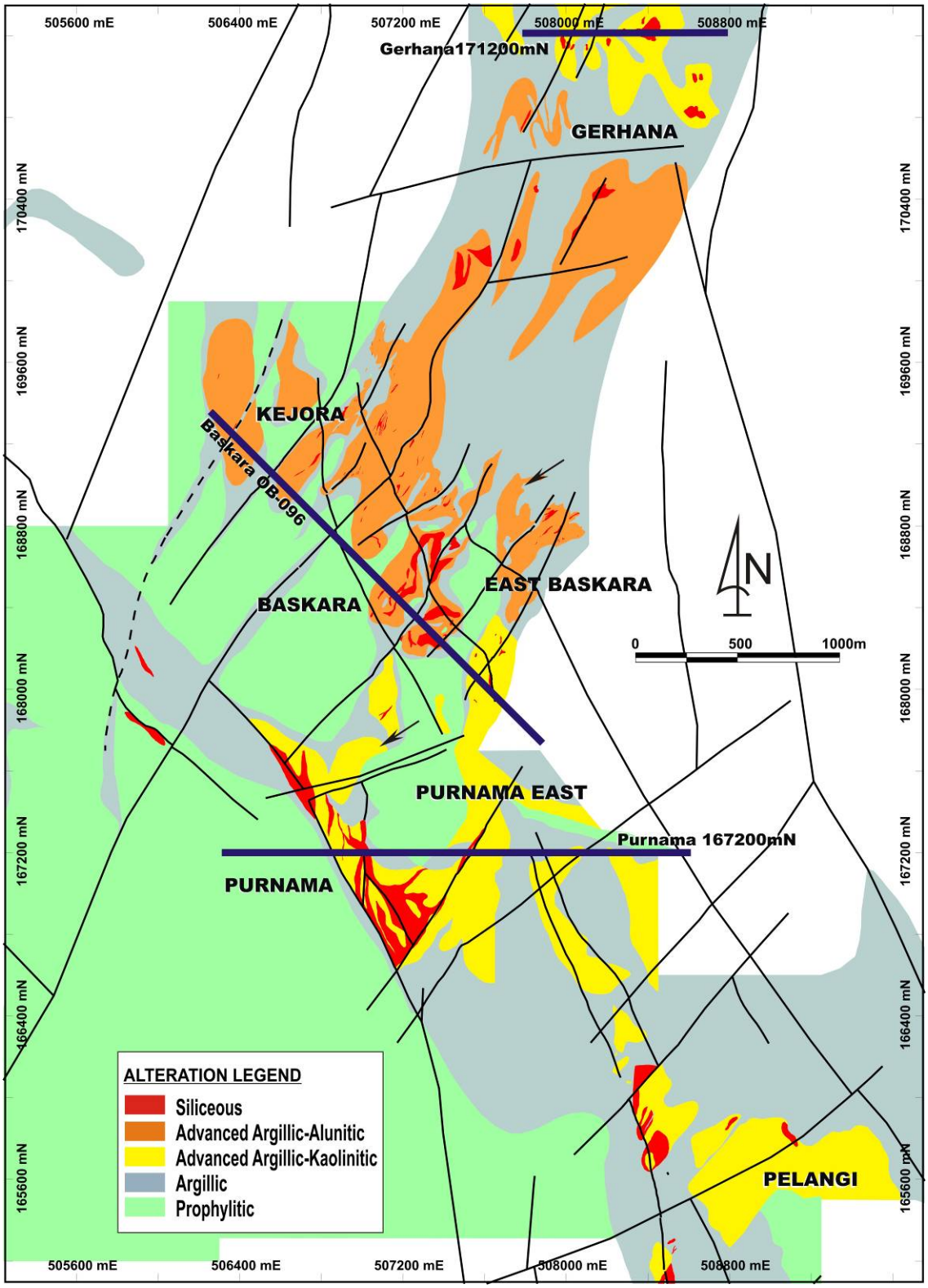

Figure 6.24. Alteration zones and main structures of the Martabe district. Structural control on the distribution of the 'alunitic' and siliceous alteration zone is illustrated.

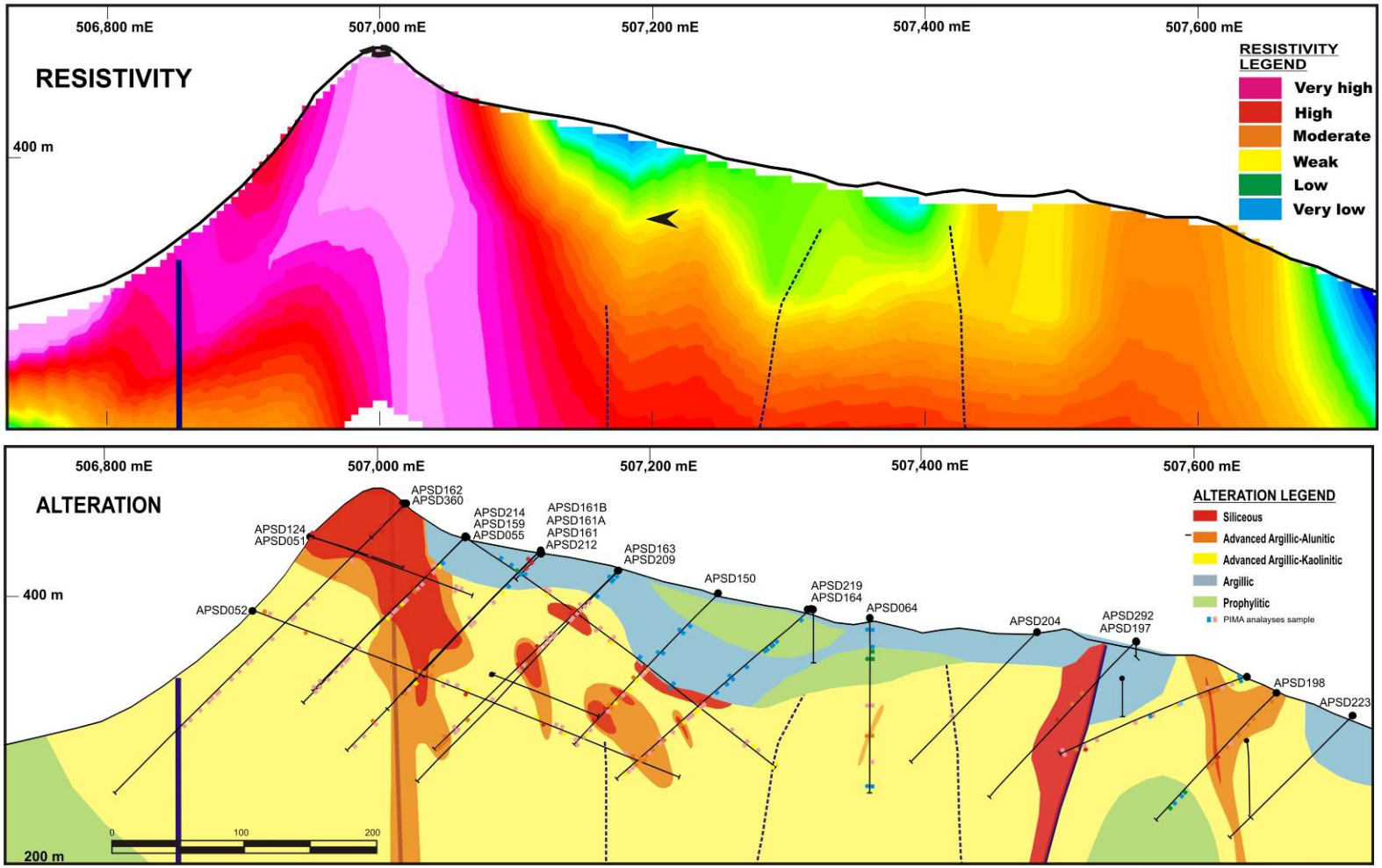

Fig. 6.25.East-west cross-section of the Purnama deposit (Section 167200 mN) showing (a) resistivity and (b) the distribution of alteration zones. Sections were prepared from logging of diamond drill-core holes, petrographic investigation, PIMA and XRD data.

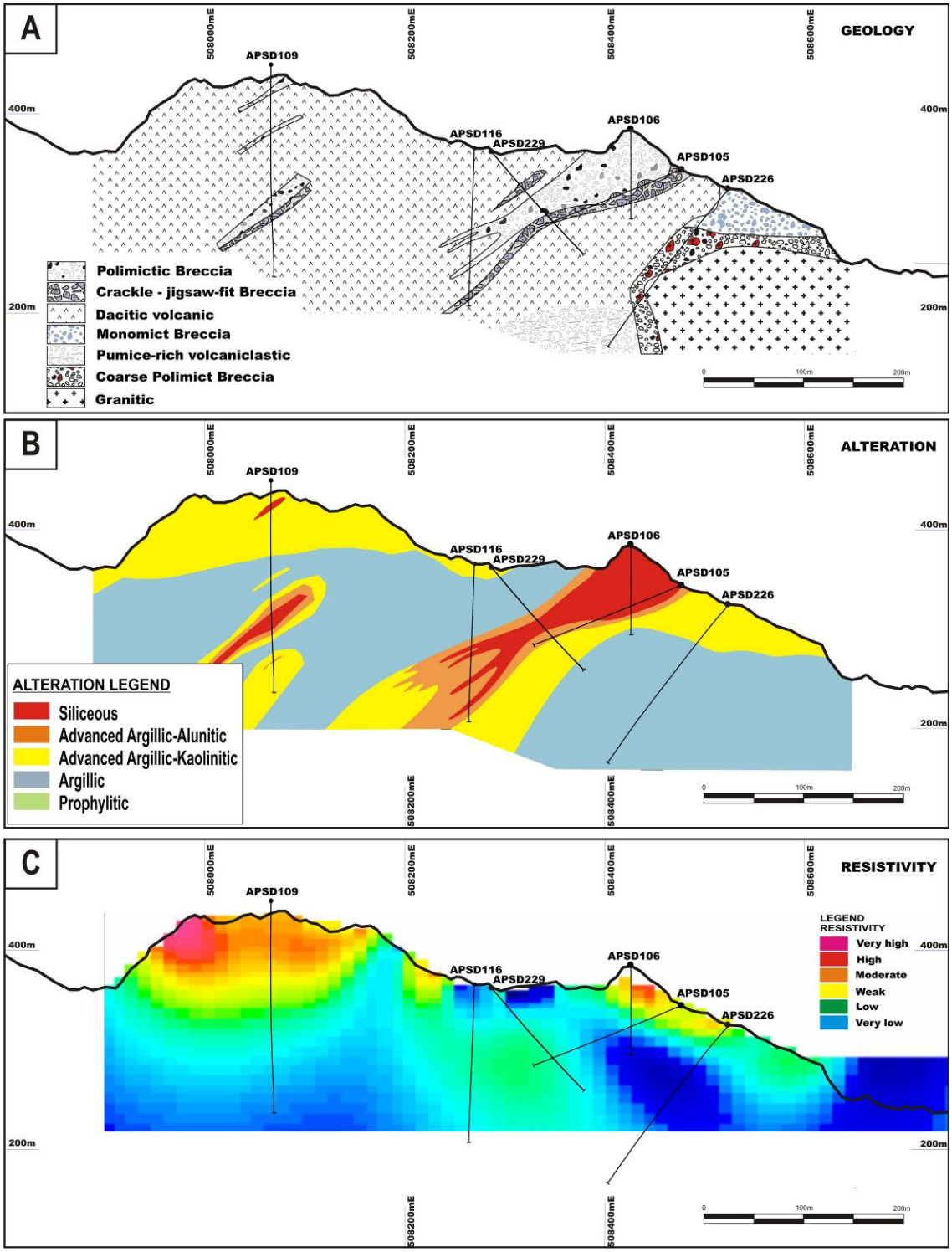

Figure 6.26. East-west cross-section of the Gerhana deposit (Section 171200 mN) showing comparison between (a) geology, (b) distribution of alteration zones and (c) resistivity data. Sections were prepared from logging of diamond drill-core holes, petrographic investigations, PIMA and XRD data. Induced polarization geo-modeled section illustrates the thickness of the siliceous alteration and small root zones.

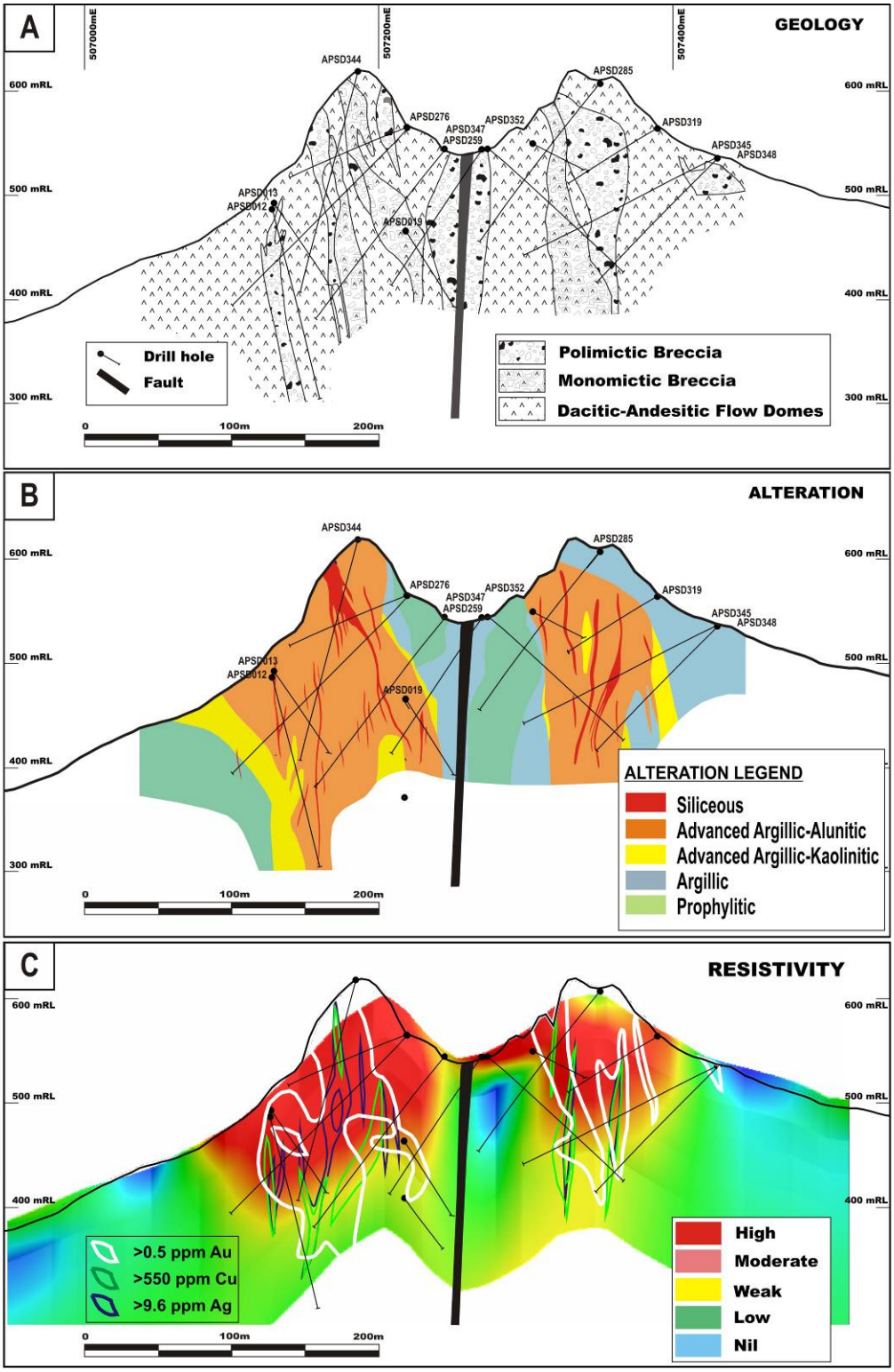

Figure 6.27. Northwest-southeast cross-section of the Baskara deposit (section OB-096) showing comparison between (A) geology, (B) distribution of alteration zones and (C) gold, Cu and Ag grades and resistivity data. Induced polarization geo-modelled section illustrates the thickness of the siliceous alteration and small root zones. Sections were prepared from logging of diamond drill-core holes, petrographic onvestigation, PIMA and XRD data.

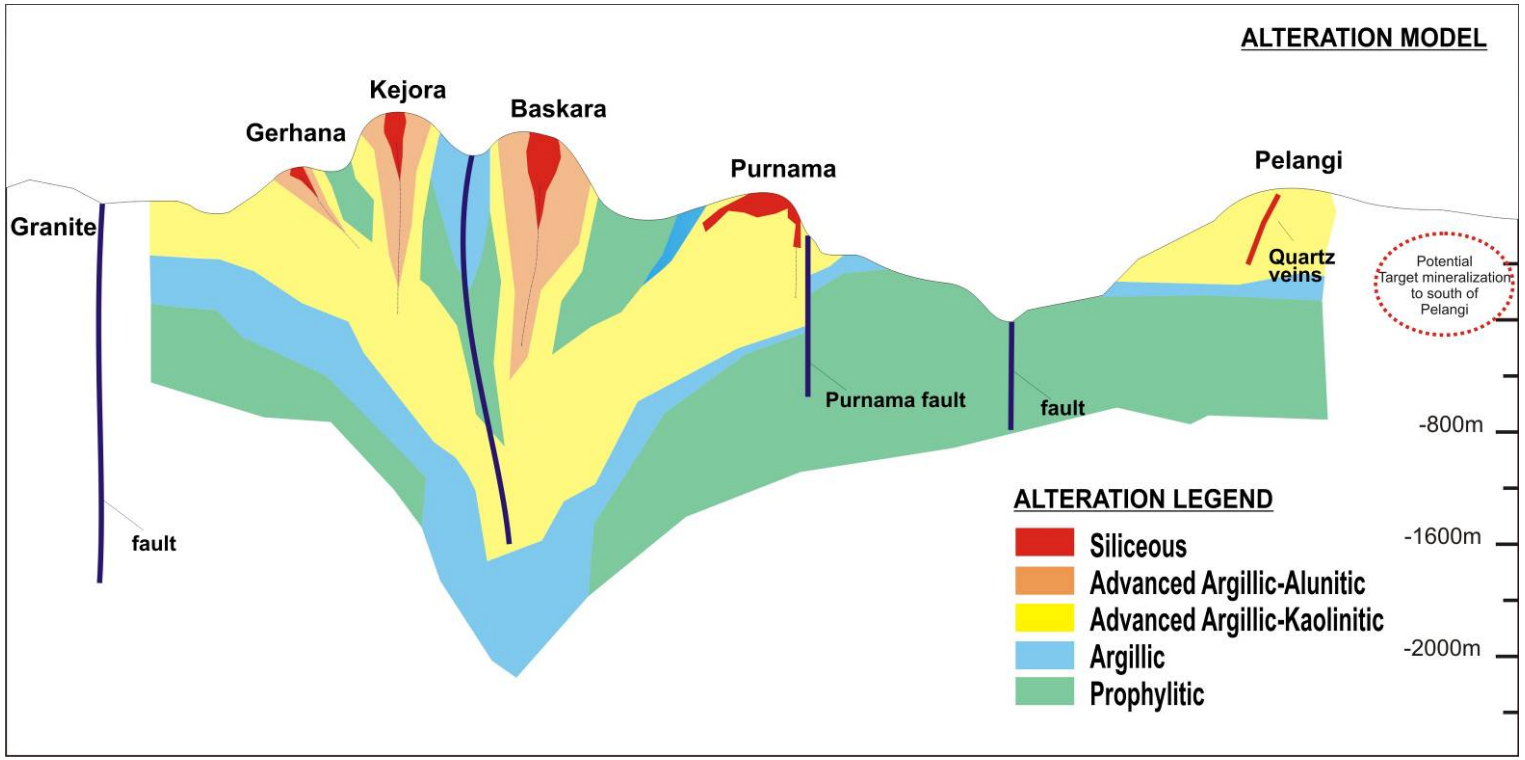

Figure 6.28. Schematic north-south (or longitudinal) section through the central part of the Martabe district showing spatial distribution of the alteration zones interpreted from diamond drillcore, petrographic investigation, PIMA and XRD data.

6.6 Mass transfer

Mass transfer techniques aim at quantifying the amounts of individual elements added and subtracted from the rock during alteration. There are several approaches to estimating mass transfers, including the method of Gresens (1967), subsequently modified by Grant (1986) and Huston (1993) to produce the isocon method, the Pearce element ratio analysis of Stanley and Madeisky (1996), and the immobile element techniques of MacLean and Barrett (1993). These techniques all depend on recognition of immobile elements. They also, with the exception of the Pearce element ratio analysis, depend on the identification of precursor-rock compositions (Gifkins, 2005).

The method of Gresens (1967), as modified by Grant (1986), was employed to calculate the mass balances using the isocon diagram which is constructed using a double-logarithmic plot following the suggestions of Baumgartner and Olsen (1985). The identified immobile elements were used to graphically define an isocon line, using standard deviations of the immobile element analyses. The gradient of the isocons were defined by mass of the original samples against the mass of the altered samples (M^o/M^a). Once this reference frame of immobile elements has been established, geochemical variations can be discussed in terms of element mobility (i.e., gains or loss of elements). Elements that plot above the reference isocon were enriched during the alteration, whereas elements that plot below were depleted (Grant, 1986).

In an intense leaching process, such as in the acid alteration of Martabe district as demonstrated by differences in bulk rock densities between rocks (Table 1), there is a progressive loss of rock mass and/or volume that accompanies the sequence from least altered, through altered to leached rocks. It is very difficult to accurately measure the bulk density of residual quartz or leached quartz rocks, but measurement obtained are extraordinary low, and significantly affect tonnage estimates. Traditional mass balance calculations (Gresens, 1967; Grant, 1986) may not be valid for rocks in which leaching indicates extremely acidic conditions, because assumptions of element immobility are invalid. Aluminium has been totally removed from many leached rocks and trails of TiO_2 mineral group (i.e., rutile and anatase) in silicified rocks demonstrate that Ti is also mobile. Other normally immobile elements may also have been mobile under these conditions.

Table 6.6. Bulk density data for alteration types at the Purnama, deposit,. A 'typical' unaltered andesitic rock should have a density of ~2.4 to 2.8 (Birch et al., 1942).
[1] Determined by routine density measurements at Martabe.

Alteration Type	Bulk Density[1] (gm/cc^3)	N (total sample)
Siliceous Alteration		
- Massive quartz	2.50	358
- Vuggy quartz	2.36	50
- Leached quartz	1.85	23
Advanced argillic		
-Quartz-alunite (Baskara)	2.25	1557
-Quartz-dickite/kaolinite (Purnama)	2.42	2034
Argillic	2.25	2059
Propylitic	2.42	1082

The safest approach in this study is to consider the geological context, established from field relationships and rock textures observations, in combination with various immobile element tests (e.g. MacLean and Barrett, 1993; Stanley and Madeisky, 1996). This ensures that precursors are appropriately matched to the altered rocks under investigation. The isocon method does not include a procedure for selecting precursors and it commonly produces erroneous results because incorrect geological assumptions are made. The Pearce element ratio analysis method (Stanley and Madeisky, 1996) and the multiple-precursor variant of the MacLean and Barret (1993) method attempt to overcome the limitations of primary variability. For these reasons, as suggested in Gifkins et al. (2005), the more rigorous MacLean and Barrett (1993) method, which is also simplest to calculate is used.

6.6.1 Analytical methods

Petrographic analyses were undertaken on thin and polished sections using transmitted and reflected light. A total of 138 thin and polished sections from drill holes were analyzed in detail**.** This analysis is necessary to identify least-altered rocks and hydrothermal minerals, typical of the different alteration zones and their textural relationships. It also allows the recognition of diagnostic hydrothermal minerals typical of each alteration zone. More than 100 fresh/least-altered and altered samples were analyzed

using XRF for major oxides at the University of Tasmania. In addition a total of 77 samples were analyzed by XRF atNewmont Mining Services, Colorado.

6.6.2 Alteration geochemistry and elemental mass balance

The average geochemical compositions of the least-altered rocks and various alteration zones associated with the basaltic-andesite, basaltic volcaniclastic, porphyry andesite, hornblende-phyric andesite, quartz-phyric dacite and breccias are given in Appendix 1.

For the mass balance calculations only two major alteration zones: the advanced argillic zone, which may be subdivided into (i) kaolinitic and (ii) alunitic; and the siliceous alteration zone are considered. Mass balance calculations for the siliceous zone were mainly based on samples from polymic-monomict breccia and porphyritic andesite, whereas samples of the basaltic andesite, basaltic volcaniclastic and porphyritic andesite rocks were used for the advanced argillic zones. These alteration zones were chosen because they also represented the main ore host rocks. The other reason is, it was almost impossible to find 'least altered' example of polymict-monomict breccia because the clast and/or matrix were altered to clay and siliceous alteration. Thus, it was decided to use advanced argillic altered breccia as 'the least-altered' rocks to calculate a relative mass balance of siliceous altered breccia relative to advanced argillic.

The method of MacLean and Barrett (1993) was employed to calculate the mass balances. The selection of immobile elements is the most important aspect of the mass balance analysis. The potentially immobile elements (i.e. Al, Ti, Nb, Y and Zr) from variably altered and unaltered samples are calculated, whereas the gains and losses of major element concentration are illustrated graphically (Figures 6.29, 6.30 and 6.31). The correlation coefficient, r, provides an estimate of the relative immobility of one element with respect to another element with relation to any change in mass or volume in a sample suite (MacLean and Kranidiotis, 1987). The existence of highly correlated (i.e., $r > 0.85$) trends that pass through the origin enables selection of the optimal element to be used as the immobile monitor in the mass change calculations. The graphical process also highlights any samples from different precursors, which should be eliminated or treated separately. Nb and Zr have been shown to the relatively immobile during hydrothermal alteration although the 'r' was not highly correlated.

The single-precursor mass transfer method proceeds by calculating the ratios of the proportions of an immobile element in the altered and unaltered samples. Each of the mobile element proportions is then multiplied by that ratio to obtain a reconstructed composition (Figures 6.29, 6.30 and 6.31). The mass change of each element is found by subtracting its percent proportion in the precursor from that in the reconstructed composition. The steps and the flow chart outlining the procedure for estimating mass changes in single-precursor system are described in Gifkins et al. (2005).

The absolute mass composition change (Δ^a) is defined as the concentration change of each oxide/element referenced to its original concentration, and can be visualized in the graph, calculated using the following equation:

$$\Delta^a = [Z^o/Z^a * C^a] - C^o$$

Where Δ^a is absolute mass exchange expressed in g/100 g

C^a= wt% proportion of component in altered rock

C^o= wt% proportion of component in precursor

Z^a= proportion of immobile element in altered rock

Z^o= proportion of immobile element in precursor.

The mass changes may be calculated from compositions of individual altered samples or from average compositions of sample groups representing certain mineral assemblages or alteration zones (Gifkins et al., 2005).

6.6.2.1 Basaltic volcaniclastic rocks

For the volcaniclastic rocks, the mass change of the major elements is calculated from the weakly altered kaolinitic altered zone to the strongly siliceous zone. The result can be obtained by reading the plotted histogram bar (Figure 6.29). From the weakly altered to the strongly altered zone, SiO_2 and S were gained, whereas Al_2O_3, Fe_2O_3, MgO, CaO, and Na_2O were lost. Moreover, the trend of mass transfer for several component induced by the progressive alteration can also be readily interpreted. With an increase in the alteration intensity, Al_2O_3 shows a progressive loss. After having been gained from 'weak altered quartz-dickite zone', SiO_2 was progressively lost towards the vuggy quartz zone. Fe_2O_3 underwent loss in the weakly altered quartz-dickite zone, but then was progressively gained toward to more intense of strongly altered advanced argillic and/or siliceous zones.

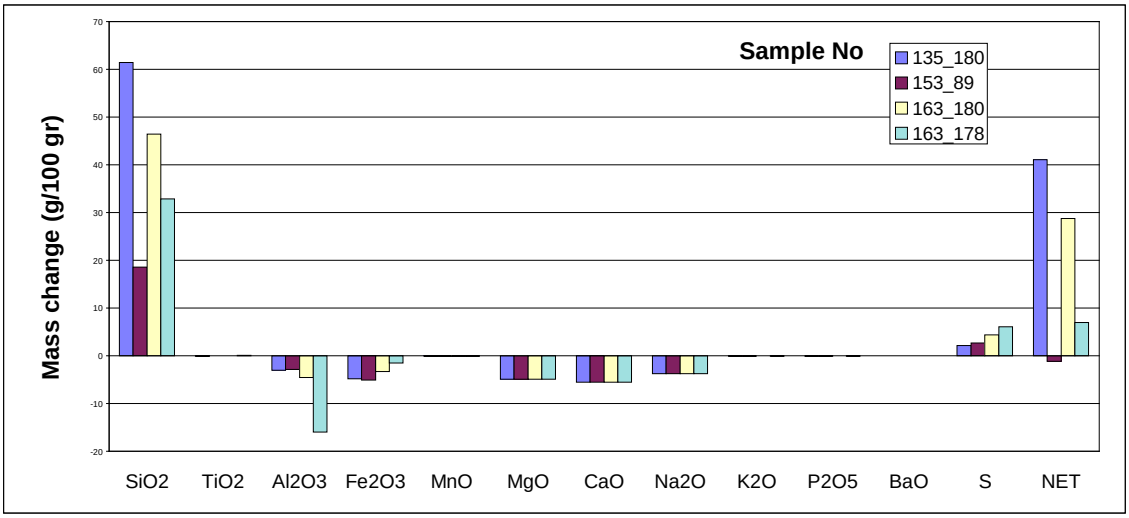

Figure 6.29. Bar graph showing estimated absolute mass changes of major elements in four samples of advanced argillic alteration from weakly altered quartz-dickite rocks to strongly/partly siliceous altered rocks in volcaniclastic. Sample numbers in legend box.

Large positive and negative net mass changes are mainly due to SiO_2 and S gains, or loss of Al_2O_3 in the samples (Figure 6.29). However, Al_2O_3 are lower in concentration in siliceous altered rocks when compared to quartz-dickite altered rocks. Increasing S and decreasing Fe_2O_3 indicate a trend towards increasing concentration of a sulphide mineral. The plagioclase breakdown may lead to the depletion of Al and K. These are consistent with the observed destruction of plagioclase in intensely siliceous altered rocks.

6.6.2.2 Basaltic- andesite and porphyritic andesite

Similar to absolute mass changes in the volcaniclastic breccia (Figure 6.30), net mass changes of basaltic- to porphyritic andesite involve SiO_2 and S gains and a loss of Al_2O_3. SiO_2 underwent an initial loss in weakly kaolin altered zone, but then was progressively gained toward massive quartz. Sulfur was also gained in similar order with S gained in volcanic breccia. Al_2O_3 initially underwent little loss in the weakly altered zone, but then was progressively decreased towards siliceous rocks through advanced argillic zone. CaO_2 exhibits the strongest depletion among the alkalis. This may reflect the destruction of Ca-rich plagioclase at a rate greater than the depletion of K_2O and Na_2O, which are incorporated into alunite and natroalunite, respectively. From the weakly altered zone to the siliceous alteration, Fe_2O_3, MgO and K_2O were consistently and almost constantly lost.

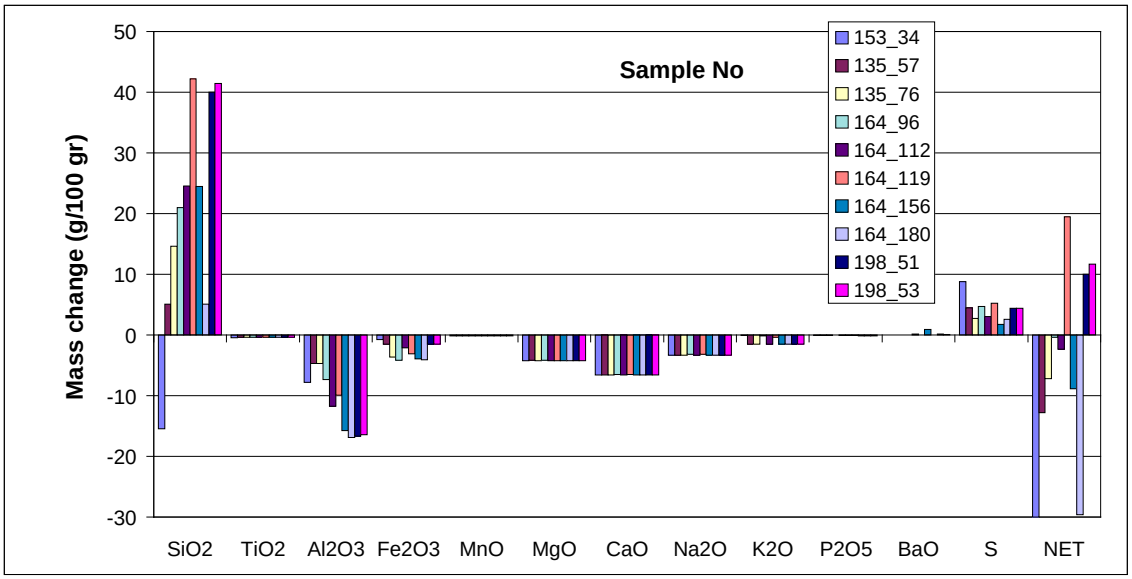

Figure 6.30. Bar graphs showing estimated absolute mass changes of major elements in ten samples of advanced argillic alteration from weakly kaolinitic altered to strongly/partly siliceous altered andesite. Sample numbers in legend box.

6.6.2.3 Polymict-monomict breccia

In comparison to the alteration related to basaltic volcaniclastic and basaltic-andesite and porphyritic andesite, alteration of the polymict-monomictic breccia displays more significant increases in mass. The mass increase would be even greater in siliceous-altered breccia, if it is normalized to "the least-altered" rocks due to the complete destruction of primary mafic minerals and plagioclase. The altered rocks have an increase in all major oxides, with an exception of Al_2O_3 and K_2O which decrease (Figure 6.31). The addition of Fe_3O_2 may correspond to the high abundance of hematite (after pyrite). Sulfur in the rocks shows a high enrichment compare to the advanced argillic altered samples. This is consistent with the high abundance of pyrite and other sulfides. The changes in concentrations of the trace elements involve a moderate enrichment of Ba, which may be in barite that occurs as vug fill in siliceous rocks, and a slight increase in P_2O_5, possibly reflecting the presence of phosphate minerals. The S decrease in weakly altered samples and is strongest in massive quartz corresponding to the presence changes from oxidation zone to more sulfidic alteration.

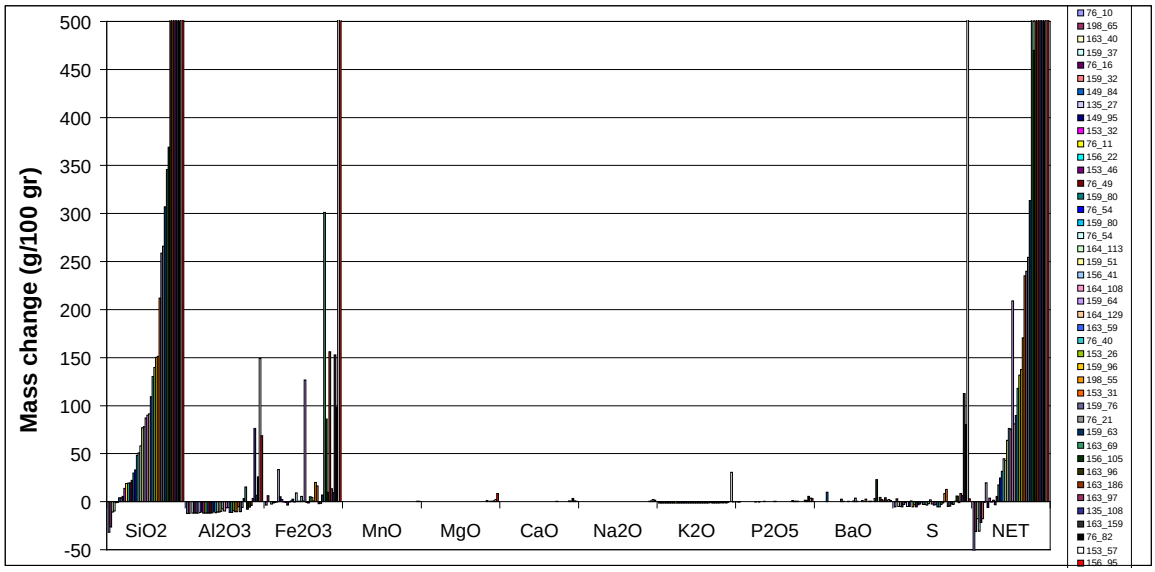

Figure 6.31. Bar graphs showing estimated absolute mass changes of major elements of breccia from least-altered to strongly/partly siliceous alteration. Sample numbers in legend box.

6.7 Discussion

6.7.1 Chemical discriminations between hydrothermal alteration zones

The chemical discrimination between the hydrothermal alteration zones enable a comprehensive understanding of the processes and fluids involved, which may also be applied to potential exploration targets. There are two possible methods to chemically distinguish between the alteration zones: (i) variation in the bulk rock chemistry, which is illustrated using e.g. millicationic R_1-R_2 diagram (De La Roche et al., 1980), and (ii) chemical compositional variations of diagnostic hydrothermal minerals. This section focuses on the first method.

6.7.1.1. Major element geochemical discrimination

In this section, the chemical discriminations are only emphasized on the bulk rock chemistry of the advanced argillic (kaolinitic and alunitic) and siliceous-altered rocks. The rock types are selected due to their presence in all hydrothermal alteration zones within Purnama deposit. For comparative purposes, the geochemical data of both least-altered basaltic volcaniclastic and porphyritic andesite are also incorporated (Figure 6.32).

The R_1-R_2 diagrams take into consideration all the major cations, the degree of silica saturation and the combined change in Fe/(Fe +Mg) and (Ab +Or)/An, in the formulas:

$R_1 = 4Si - 11(Na + K) - 2(Fe + Ti)$ and $R_2 = 6Ca + 2Mg + Al$ (plotted along the *x* and *y* axis, respectively, Figure 6.32; De La Roche et al., 1980). The R_1-R_2 diagram appears to be more suitable in evaluating the dispersion of the hydrothermal mineral assemblages.

The trend of hydrothermal alteration signature, as represented by the arrows in Figure 6.32, reflect an increase in the alteration intensity, from the least-altered rock, through advanced argillic (kaolinitic and alunitic) to siliceous alteration zones. The replacement of primary mafic minerals by pyrite then hematite, depicts a trend from the least altered rock, through advanced argillic to siliceous alteration zones, respectively. The destruction and/or replacement of the plagioclase by kaolinite and alunite portray a trend in advanced argillic alteration zones.

Chemically, the alteration trend may be attributed to the general decrease in Ca, Mg, Na and K, as a consequence of the destruction and/or replacement of the mafic minerals and plagioclase. The chemical discrimination also indicates that R_1 increases and R_2 decreases with increasing alteration intensity, from the least-altered (shaded area; Figure 6.32), through advanced argillic (kaolinitic and alunitic) and siliceous alteration zones. The increase of R_1 and the decrease of R_2 correspond to the general increase of mass of the altered rocks associated with the subsequent alteration zones.

6.7.1.2 Origin of hydrothermal alteration zones

The siliceous and advanced argillic-alunitic alteration are mainly associated with the highest gold and silver grades. These alteration zones predominantly formed from magmatic hydrothermal fluids. In Purnama, the lack of alunite in the advanced argillic alteration zone may, in part reflect a low primary K-feldspar content of the original wallrock (basaltic andesite and porphyritic andesite). Whereas alunite is mainly observed the quartz-phyric dacite and hornblende-phyric andesite rocks, as well as in structures or conduits that fed the hydrothermal system (i.e., Baskara, Kejora and Gerhana).

Mass balance calculations indicate that the advanced argillic (kaolinite and alunitic) altered rocks are generally enriched in S and Si, but generally depleted in Al and K. During the consumption of primary mafic minerals (pyroxene and hornblende) and Ca-rich plagioclase, Ca and probably Mg and Ba are removed. In solution, the aqueous sulfur species may be represented by sulfuric acid (H_2SO_4) and hydrogen sulfide (H_2S).

Weakly altered rocks and propylitic (chlorite-epidote) alteration is typically characterized by a high CaO content. The relatively high CaO is clearly influenced by the presence of the secondary Ca-rich minerals, i.e. epidote and calcite. The epidote replacing plagioclase is represented by the following chemical reactions (cf. Meyer and Hemley, 1967; Bowman et al. 1987):

$2NaCaAl_3Si_5O_{16} + SiO_2 + Na^+ + H_2O = Ca_2Al_3Si_3O_{12}(OH) + NaAlSi_3O_8 + H^+$

The chloritization in the propylitic alteration and the breakdown of plagioclase are expressed by a general depletion of ferromagnesian oxides and alkalis. Some K_2O liberated through chloritization may, in part, be fixed into illite. The illite-dominated alteration (argillic) alteration zone is typified by variably low contents of Fe and Mg oxides. The low concentration of these elements is consistent with the complete destruction and replacement of preexisting hornblende pyroxene and plagioclase by fine to medium grained clay (illite). The complete destruction of the preexisting minerals is consistent with the overall decrease of mass of the advanced argillic rocks with respect to their precursors.

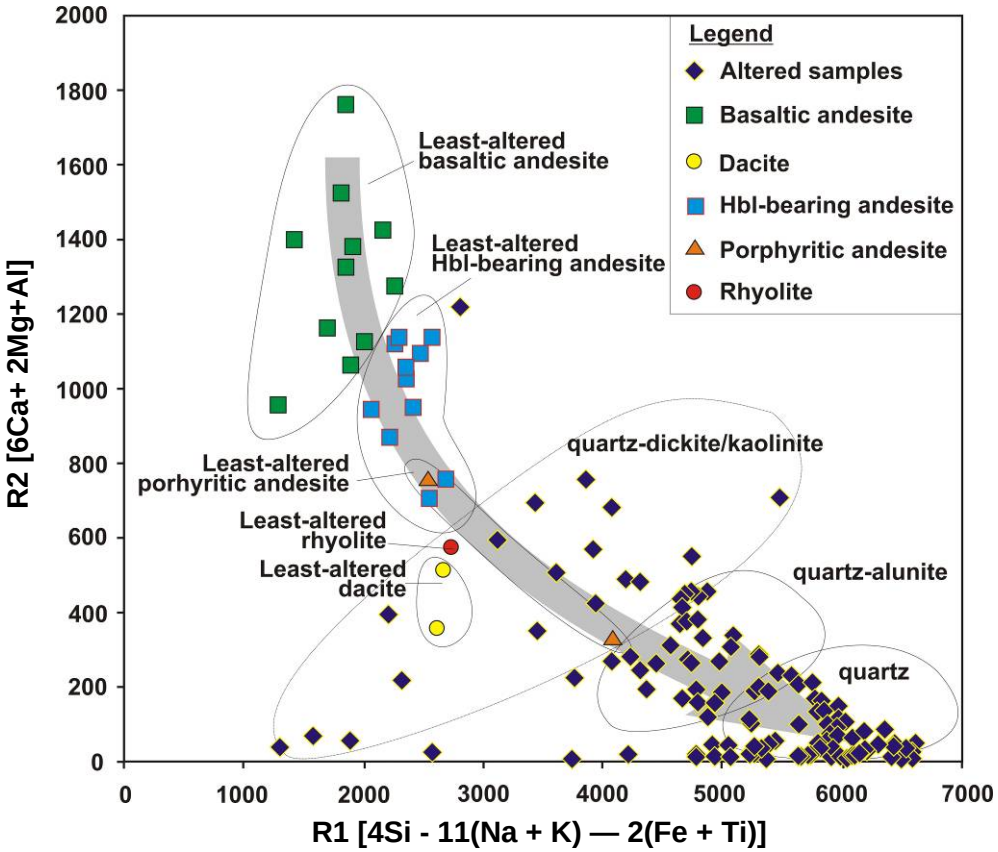

Fig.6.32. R_1-R_2 diagrams (after De La Roche et al., 1980) discriminating various alteration zones advanced argillic (kaolinitic and alunitic) and siliceous rocks within the Purnama deposit with respect to the host rock: volcaniclastic rocks, basaltic-andesite, porphyritic andesite, hornblende-phyric andesite, quartz-phyric dacite (and rhyolite). The chemical discrimination indicates that R_1 increases and R_2 decreases with increasing alteration intensity, from the least-altered (shaded area), through advanced argillic (quartz-kaolinite/dickite and quartz-alunite) and siliceous alteration zones.

6.8 Airborne radiometric data

Airborne radiometric data are often combined with satellite imagery to provide a composite tool for alteration and mineralization interpretation and mapping. The distribution of radiometric isotopes of the elements potassium (K), uranium (U) and thorium (Th) within the project area gives an indication of the degree of weathering and alteration, and also the type of source rocks from which the altered or weathered material is derived. The weathered bedrock has generally reduced levels of K concentration due to chemical breakdown of mica and feldspar minerals. In addition, weathered felsic rocks usually show reduced U and Th, whereas weathered mafic rocks exhibit elevated concentrations of U and Th. Laterites and residual soil horizons generally exhibit elevated U and Th concentrations. Alluvial and colluvium regolith units usually show a variable radiometric signature, depending on the source rocks from which these depositional units were derived.

Figures 6.33 and 6.34 show the airborne radiometric maps, including potassium and K/Th ratio images of the Martabe district. In the potassium and K/Th ratio map, the white to red (K/Th) region along the east of the image typically represents the outcropping of the Uluhalanagodang granite. The high K/Th ratio value is controlled by the higher K concentrations of least-altered felsic volcanic rocks (Figure. 6.33b). Slightly lower K/Th ratios are associated with the weathered/altered bedrock indicating a decrease in K and an increase in Th concentration due to the weathering/alteration process. The northwest trending low tone color (blue color in Fig 6.33b) in the central portion of the image likely represents weathered bedrock (saprolite) and scree.

The potassium data delineate a circular region of high values (approximately 3 x 3 km diameter) centered on the Martabe district (Figure. 6.33a). This survey also shows a zone of high total K/Th/U values in a similar location (Figure. 6.33b). Combining these two maps/images suggest the location of flow domes with weak to moderate anomalies. The areas of moderate to low total radiometric value are controlled by a northwest-southeast and north-south trending lineament. Empirically, the Purnama, Baskara and Gerhana deposits are situated within low total K/Th anomalies, while Kejora is located within moderate total K/Th anomaly (Fig 6.34) Colluvium at south of Martabe shows high K/Th isotope concentrations (K and Th) (Figures 6.34). As the composition of the colluvium material reflect that of the source rocks, initial mapping recognized soil in this area contains abundant coarse quartz grains and gravels which originated from the Uhulanagodang granite.

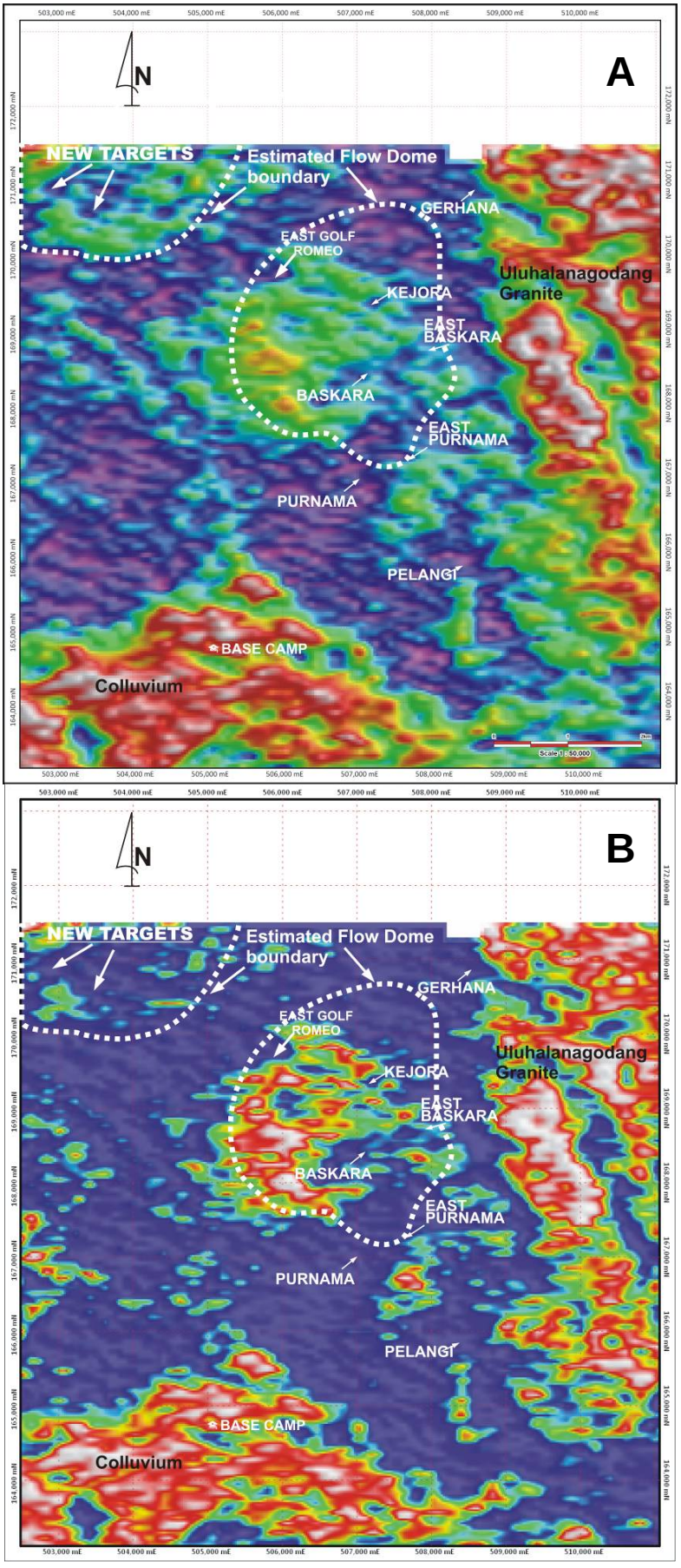

Figure 6.33. (A) Potassium and (B) K/Th map showing location of epithermal deposits within the Martabe district. The arrows in the upper left corner the map indicate future exploration targets.

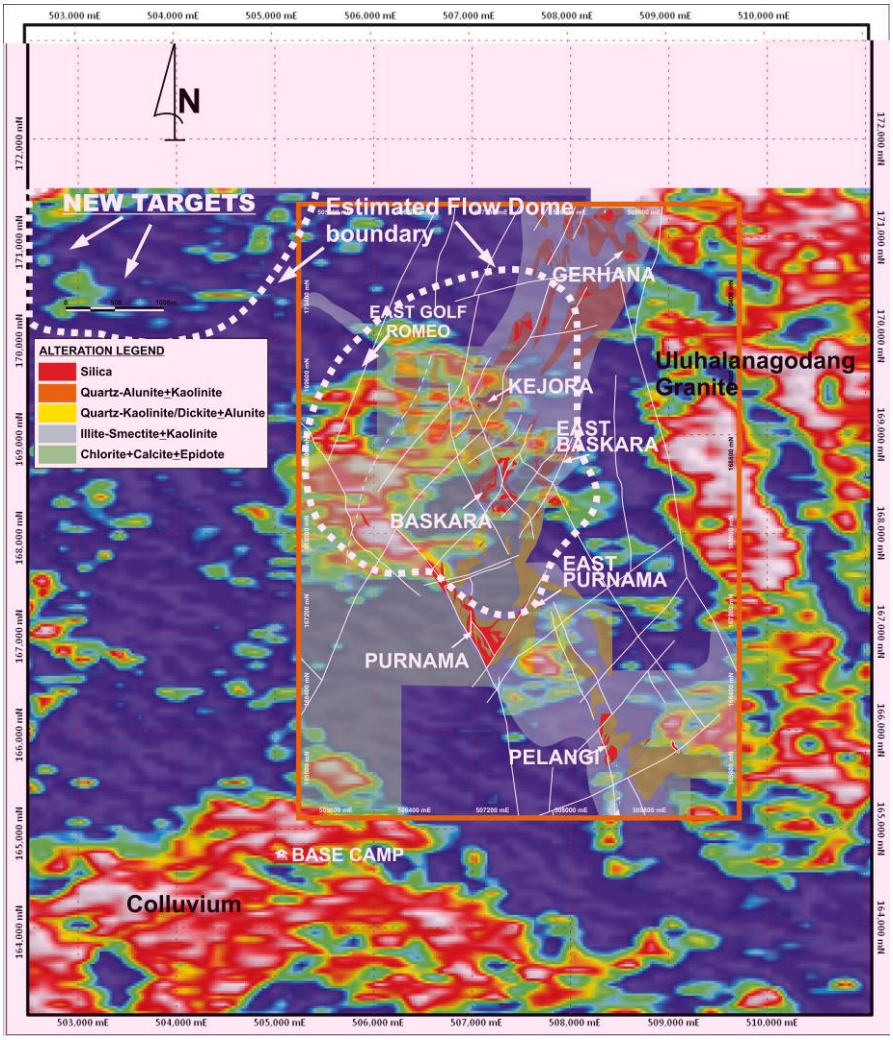

Figure 6.34. Alteration map overlain on K/Th ratio map of the Martabe district.

Another circular feature is identified at the northwestern part of the radiometric map. This area shows a depletion of K/Th which has a similar appearance to the Martabe district with a depletion of the radiometric ratio at the centre. This area is probably a good target for further exploration in the Martabe district.

6.9 Conclusions

Compared to other known world class of similar deposits (i.e., Yanacocha and Pierina), Martabe has a medium-sized (5-10 Moz Au) of magmatic hydrothermal, high-sulfidation type alteration zone. The hydrothermal alteration is divided into four facies: propylitic, argillic, advanced argillic (kaolinitic and alunitic) and siliceous alteration. Advanced argillic (quartz-dickite/kaolinite, quartz-alunite) and siliceous alteration zones are the primary ore-related hydrothermal alteration in the Martabe district. The kaolinitic zone

is predominantly enriched in Si and S with an increase of net mass. The alunitic zone shows a general enrichment of Si and is characterized by a destruction of pre-existing mafic minerals and plagioclase. Gold and silver enrichments are more significant in the alunitic alteration zone compare to the kaolinitic alteration. Siliceous alternation shows significant increases of Si, S and other oxides and mass balance.

In general, major elements (Al, Fe, Ca, Mg, Na and K) and some minor elements elements decrease from least altered rocks towards the siliceous alteration zones as a consequence of breakdown of pyroxene, hornblende, biotite and plagioclase. Si and S increase as a consequence of hydrothermal fluids. The chemical discrimination also indicates that R1 [4Si - 11(Na + K) – 2(Fe + Ti)] increases and R2 [6Ca+ 2Mg+Al] decrease with increasing alteration intensity, from least-altered, through kaolinitic, alunitic to siliceous alteration zones. Degree of mass gain increases during the alteration stages. A decrease of the elements from weak alteration, argillic, advanced argillic to siliceous alteration zones implies a general decrease of the element activities in hydrothermal fluids during the formation of the alteration zones.

CHAPTER 7

MINERALIZATION: GEOCHEMICAL SIGNATURE, ORE MINERALOGYAND METAL ZONATION

7.1 Introduction

In high-sulfidation epithermal deposits, gangue and ore mineralization varies laterally and vertically in response to variations in temperature, pressure, fluid composition and wall rock interaction (Lindgren, 1922; Sillitoe, 1977; Buchanan, 1981; Berger and Henley, 1989; White and Hedenquist, 1995; Cooke and Simmons, 2000; Hedenquist et al., 2000; Sillitoe and Hedenquist, 2003; Einaudi et al., 2003).

Prior to this study, documentation of mineralization at the Martabe district was limited to internal company memos and consultants reports, based mainly on selected rock chip and early drill core samples. All of the geochemical data were collected during drilling exploration when the quality control was not rigorous. Because of these limitations, the data are treated with only basic statistics, and used to define general patterns of elemental distributions. No mining had begun when this study was completed.

This chapter documents the geochemical signatures of mineralization, ore mineralogy and metal distribution at the various deposits and prospects; and their effectiveness in delineating Au mineralization.

7.2 Geochemical signatures

In the early 1980s the British Geological Survey (BGS) conducted a stream sediment survey covering most parts of Sumatra including the Martabe area, but did not assay for gold. The survey identified several base metal anomalies; elevated arsenic was also detected in the vicinity of Martabe.

Normandy Anglo Asian Limited ("NAAL") believed that North Sumatra had potential for epithermal Au-Ag deposits, as well as porphyry Cu-Au deposits and skarn-related mineralization. Normandy commenced a regional geochemical drainage sampling, including BLEG (Bulk Leach Extractible Gold) under a "SIPP" (Preliminary Exploration Permit) agreement in August 1994. The regional geochemical drainage sampling was carried out intermittently within the area between 1994 and 1996 with vehicle and helicopter support.

7.2.1 Stream-sediment signature

Martabe was discovered in 1997 by follow-up of a 14 ppb Au BLEG anomaly collected from the Aek Pahu River (Figures 7.1 and 7.2). Subsequent BLEG assay samples up to 157 ppb Au and 1206 ppb Ag (Figure 7.1) supported the early sampling; follow-up float samples assayed up to 20.3 ppm Au and 76 ppm Ag. The BLEG anomaly was thought to be related to a series of prominent north-trending silica ledges and sourced from sheared chalcedony veins up to 5–10 m wide that were mapped in volcanic rocks in the upper tributaries. Subsequent 1:5000 mapping, rock chip sampling, "ridge and spur" soil sampling and 650-line-km of combined aeromagnetic/radiometric surveying was completed over the central part of the CoW in early 1998. These surveys identified numerous deposits, including Purnama, Baskara, Pelangi, Kejora, and Gerhana, which occurred along a north-south trending corridor, approximately 7 km x 3 km in size (Levet et al., 2003; Sutopo et al., 2003).

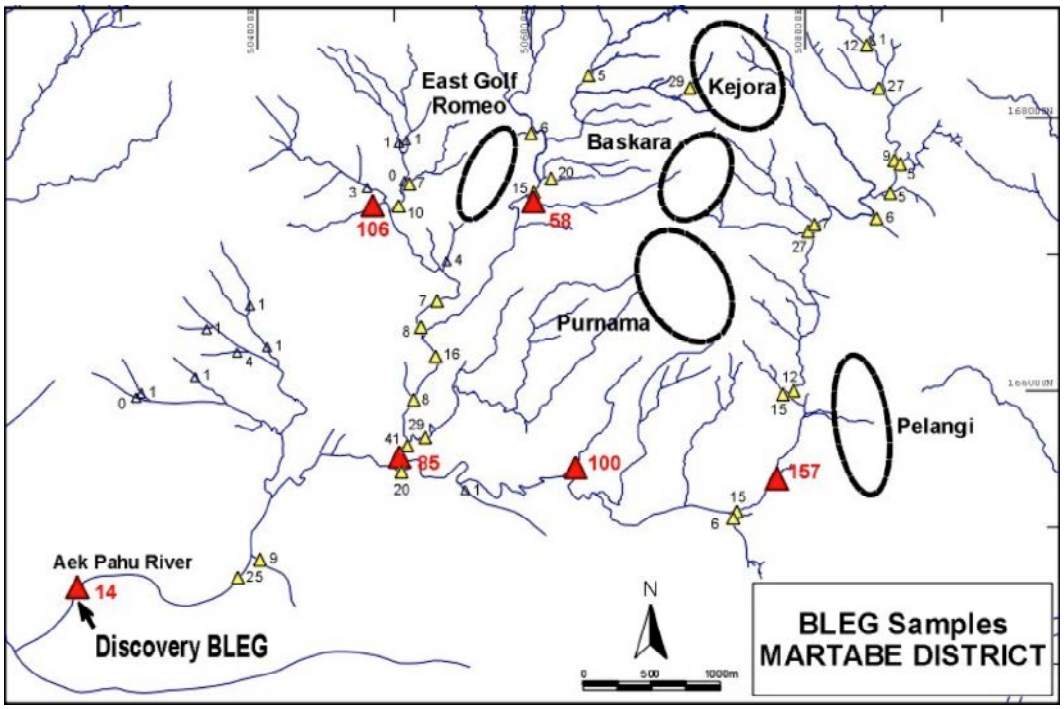

Figure 7.1. BLEG sample results for Au (in ppb) in the Martabe drainage district (Sutopo et al., 2003).

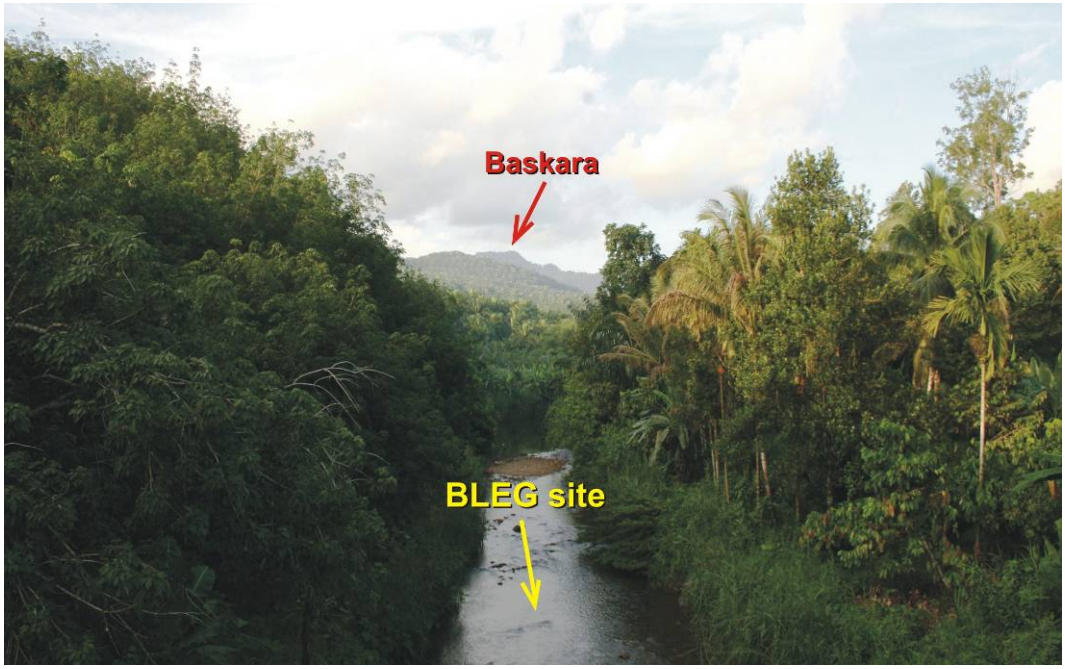

Figure 7.2. The 'discovery' BLEG location of 14 ppb Au in Aek Pahu River. Baskara hill is about 6 km northeast of the BLEG site.

7.2.2 Soil geochemistry signature

Soil sampling was initially completed on ridges and spurs at 50 m spacing followed later by soil sampling on a 100 m by 50 m grid over the main deposits. Soil sampling programs were conducted by hand augering to 1.5 m. When possible, samples where taken from the C-horizon. Samples were routinely assayed for Au, Ag, As, Cu, Sb, Pb and Zn.

The most significant gold soil geochemical anomaly (>1 ppm Au) was identified in talus, near the base of the cliffs southwest of Purnama, below Purnama hill on the western margins of the Purnama fault (Figure 7.3A). The first three holes drilled at Purnama in October 1998 were designed to test the strong western gold-in-soil anomaly some 160 m west from the base of the hill. Drilling intercepted up to 12 m from surface of high-grade mineralized scree (5– 25 ppm Au) overlying unaltered basaltic andesite, suggesting that the gold in soil anomaly was the result of mechanical transport. It was later interpreted that the soil anomaly resulted from transported scree and slope wash material. Similarly, at Baskara the gold in soil anomaly occurs west of the deposit at the base of a steep slope (Figure 7.3A).

However, the gentle slopes on the east side of Purnama are characterized by weakly anomalous or barren gold in soil even though latter drilling confirmed much of this area overlies significant widths of high-grade (5–25 ppm Au) mineralization at depth. Low gold soil geochemistry on the east side of Purnama is explained by masking due to un-

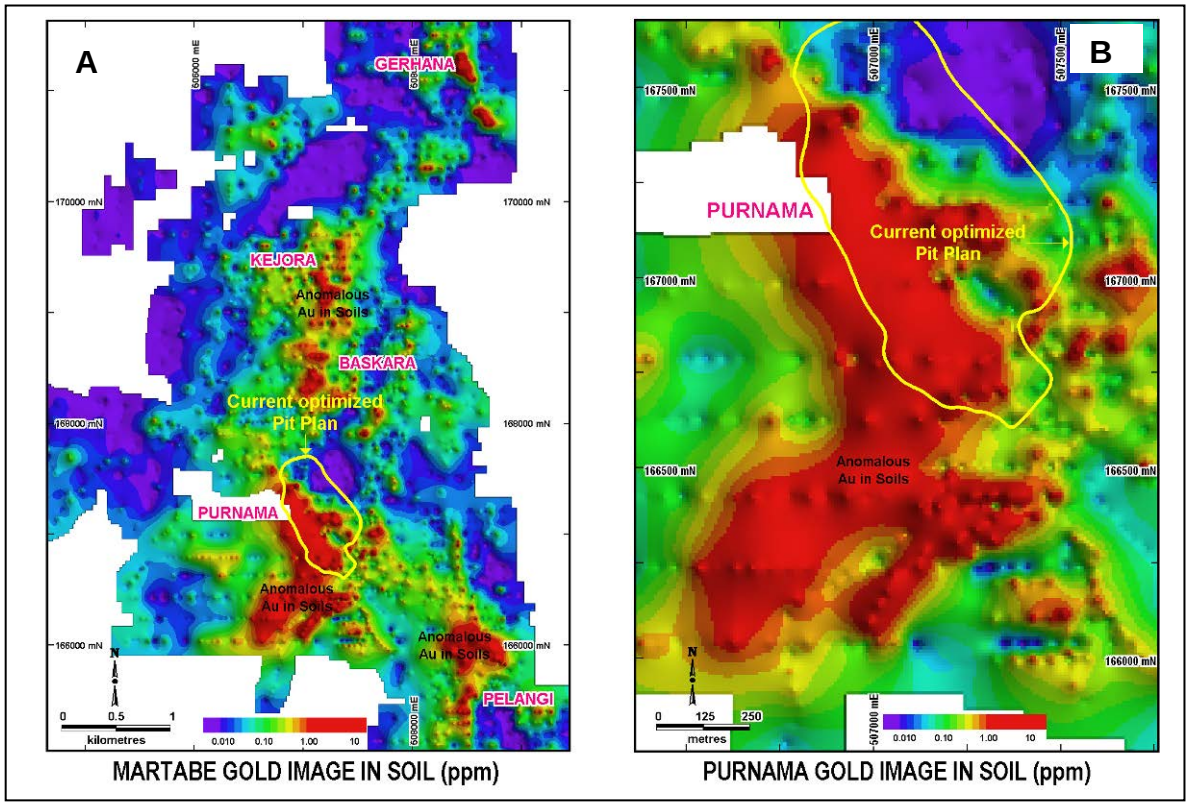

Figure 7.3. Soil geochemistry distribution of gold in (A) Martabe district and (B) Purnama deposit (Sutopo et al., 2003).

mineralized clay altered breccia and unaltered hornblende andesite overlying the siliceous altered breccia and associated high-grade Au zone.

The distribution pattern of gold in soil shows to varying directions, mostly following the structures or lineament (i.e., the NE soil anomaly trending at Baskara-Kejora and NW soil anomaly trending at Purnama, Figure 7.3). However, in detail these anomaly patterns are interpreted to be complex as a result of both mechanical and chemical transport. Locally widespread and strong copper-in-soil (>100 ppm Cu) anomalies occur in two locations in the Martabe district (Figure 7.4).

One location is west of the northwest striking Purnama fault in an area where most other ore-forming elements are at background levels (Figure 7.3A). The other location is in a structurally complex zone of low topography southeast of the Purnama deposit, where As, Sb and Au are also anomalous. The northwest Cu anomaly remains unexplained, while the southeast Cu anomaly is believed to result from both physical transport of Au-bearing material and chemical transport of more mobile Cu, As and Sb from Purnama. High-grade gold mineralization at Purnama is related to pyrite, enargite and luzonite fracture-filling. This element dispersion suggests that Cu and As are highly mobile in this environment. The fact that moderate Cu and As levels are observed over Baskara and Kejora is explained

by enargite-luzonite occurring as void-filling in strongly silicified rock rather than the much more common fracture-controlled mineralization, which is typical for Purnama (Figures 7.4 and 7.5). The other possibility is that Baskara and Kejora are less oxidised than Purnama.

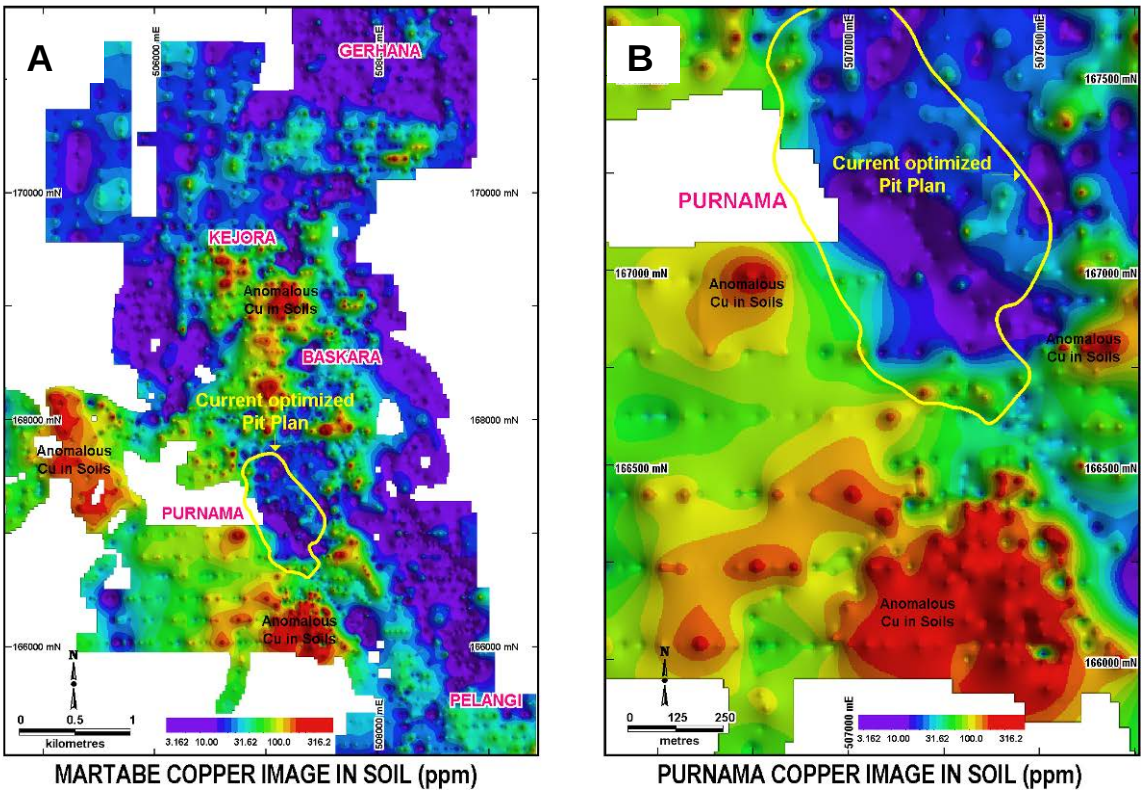

Figure 7.4. Distribution of soil geochemistry for copper in (A) Martabe district and (B) Purnama deposit. (Sutopo et al., 2003).

At both Baskara and Purnama, soils are anomalous in Ag (Figure 7.6) and Sb. These elements show similar patterns to Au suggesting they are less mobile than Cu and As. The soil geochemistry over Purnama is very low in Pb and Zn, but Pb is moderately anomalous at Baskara. Pelangi has strong north-south trending Au, Sb and As soil anomalies reflecting the low-sulfidation vein system. Mercury in soil is also moderately anomalous.

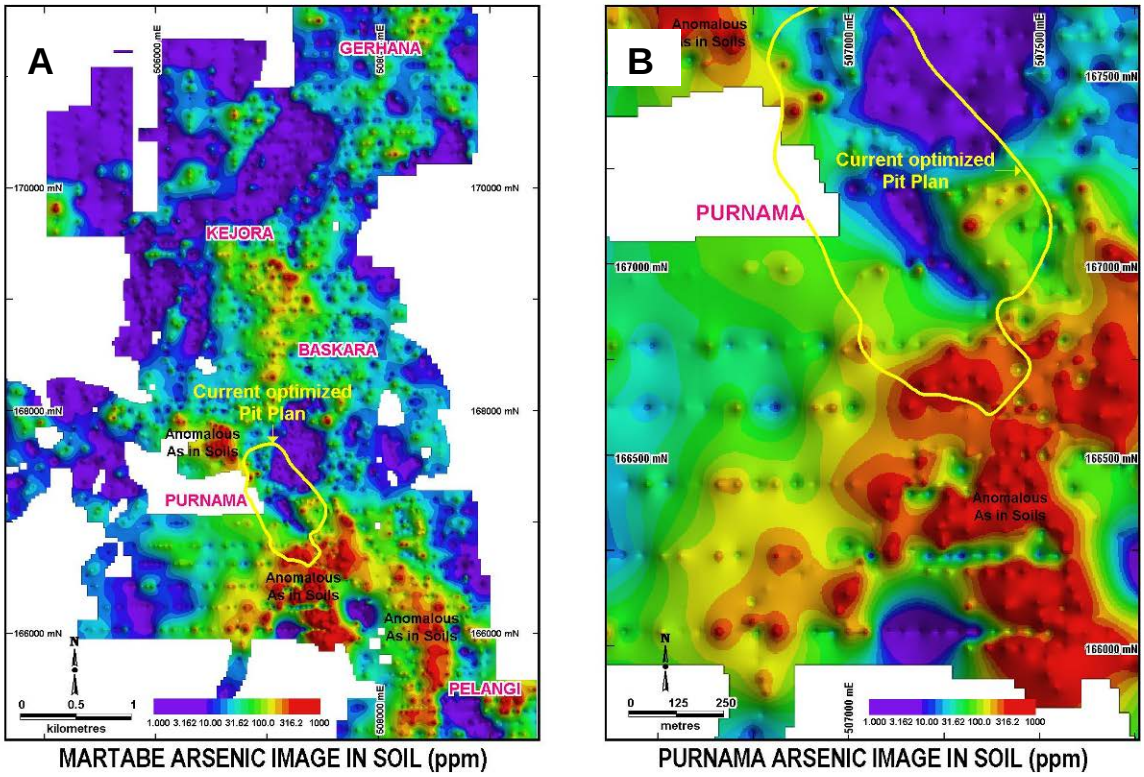

Figure 7.5. Distribution of soil geochemistry for arsenic in (A) The Martabe district and (B) The Purnama deposit. (Sutopo et al., 2003).

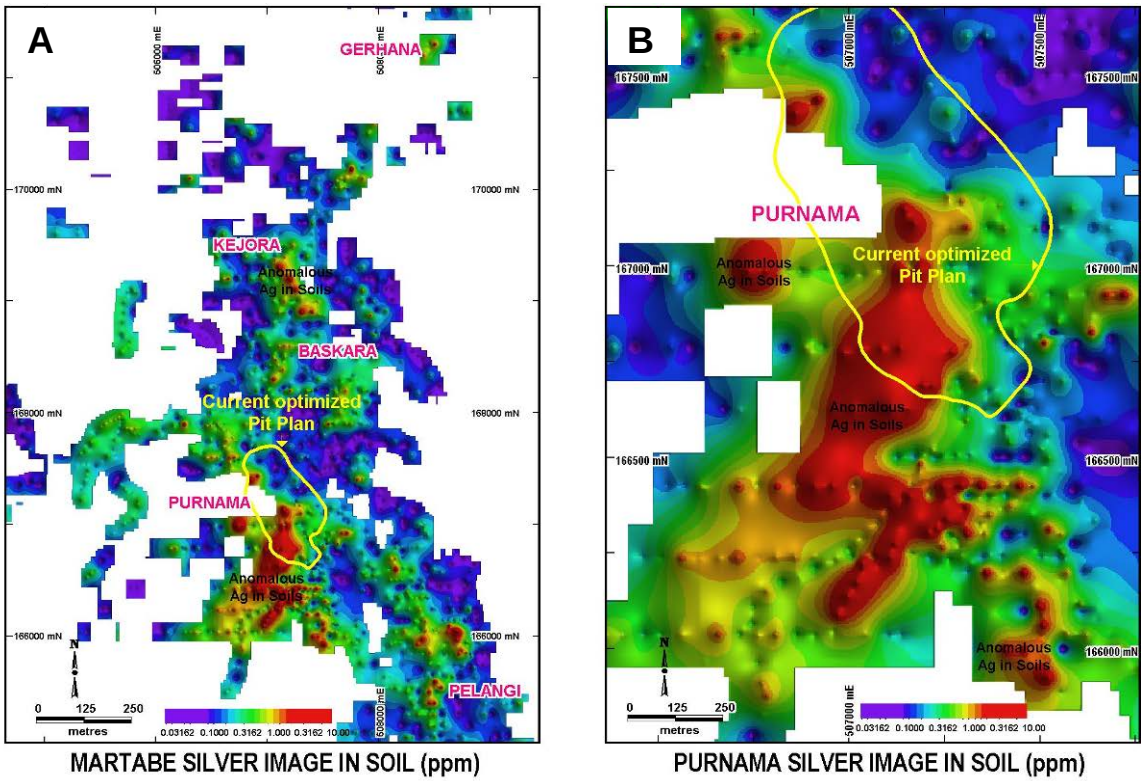

Figure 7.6. Distribution of soil geochemistry for silver in (A) The Martabe district and (B) The Purnama deposit (Sutopo et al., 2003).

7.2.3. Rock chip geochemical signature

During early exploration, selective rock chip samples were taken from mineralized outcrops, float of silicified and advanced argillic altered rocks. Float samples were collected near the in-situ outcrops or subcrops. Gridded rock chip sampling was not considered because of insufficient outcrops and the deposits are mostly covered by thick soil. Most rock chip samples were assayed for Au, Ag, Cu, As, Sb, Hg, Pb and Zn. These data have been combined with drillhole samples to characterize the geochemical response for all the known deposits and prospects.

Rock chips from a silicified outcrop on the western escarpment at Purnama produced gold results up to 14.3 ppm Au, however the majority of rock samples from the east side contain less than 500 ppb Au, even though drilling indicates an ore zone crops out nearby (Figure 7.7). As mentioned above, the majority of Au at Purnama is associated with main stage pyrite-enargite-luzonite fracture fill. This material is readily oxidized, which causes it to become weak and friable and easily washed away during the torrential rains (four to six meters of rain per year). The results of Au and Ag analyses of rock chips are shown in Figure 7.7. Gold and Ag from the rock chip samples are patchy in their correlation. In Purnama, moderate gold grades are associated with high grades of Ag; but high Au grades are correlated with low silver at Baskara. At Golf Romeo (top left) and Gerhana, gold and silver correlate strongly.

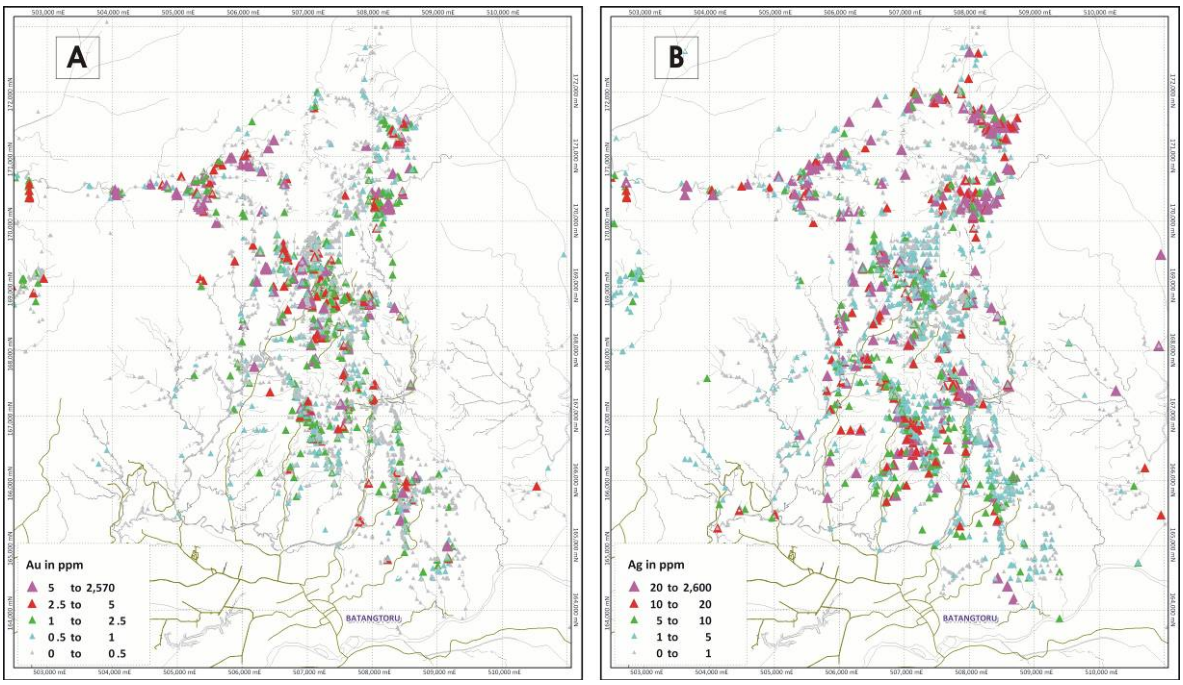

Figure 7.7. Rock chip geochemistry distribution for (A) gold and (B) silver in the Martabe district.

Copper and Sb enrichment in rock chips were mostly recorded for the northern part of Martabe (East Golf Romeo and Gerhana south) (Figure 7.8). The samples from Golf Romeo are almost entirely from float, likely derived from the Gerhana deposit to the east. In south Gerhana, moderate to high grade rock chips were taken from a structurally controlled north-south trend of silicified rocks, about 2 m x 25 m in dimension. However, sampling in a zone of reddish hematite altered breccia returned up to ~2,500 ppm Au in Gerhana. At the other deposits, the Cu and As contents are low. At Martabe, rock chip analyses define distinct surface Au anomalies, with no consistent trend, but in general these anomalies fall within the ENE-trending corridor that hosts the Martabe flows dome. High grades of gold in the rock chips which are from the northwestern part of Figure 7.7 (in the Garoga prospect) are probably the result of transported scree and slope wash material from western Kejora.

The rock chip samples define discrete surface metal anomalies, especially Au anomalies, but with no consistent trend. Rock chip analytical data are of limited statistical validity in most areas due to selective and oxidized samples. However, drilling confirms that mostly the in-situ rock chips are consistent with drill core sample grade at depth, with little upgrading or leaching. These generally fall within the north-south or north-north east trending corridor that hosts the Martabe mineralization.

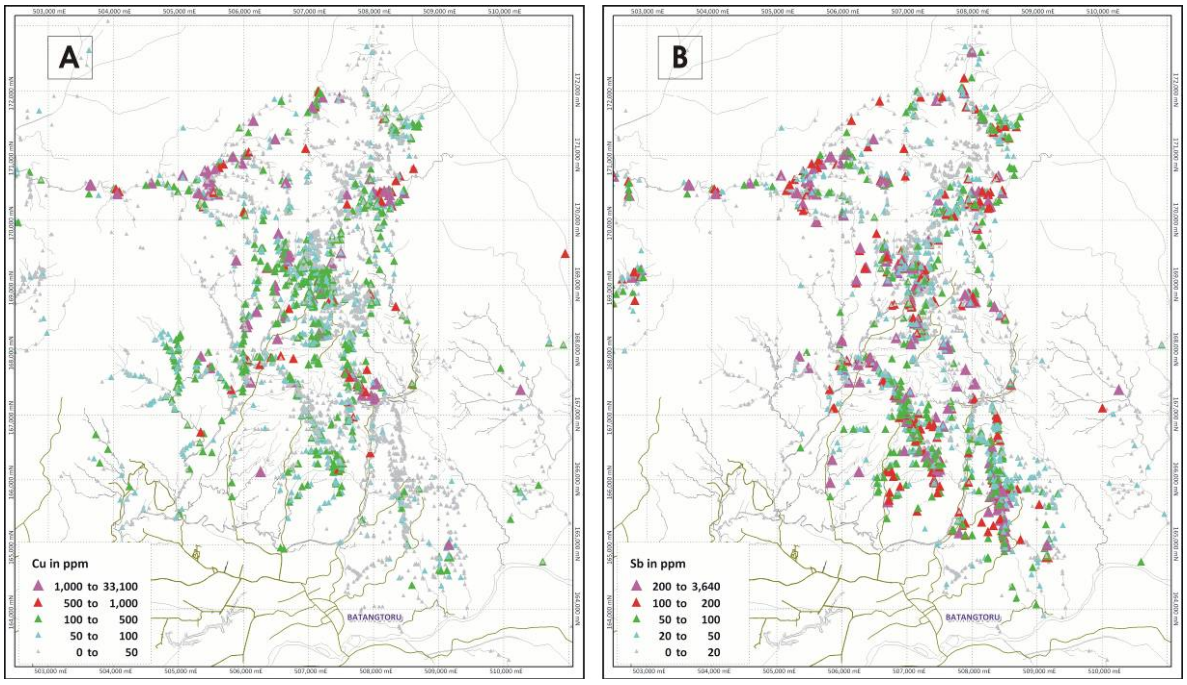

Figure 7.8. Rock chip geochemistry distribution for (A) copper and (B) antimony in the Martabe district.

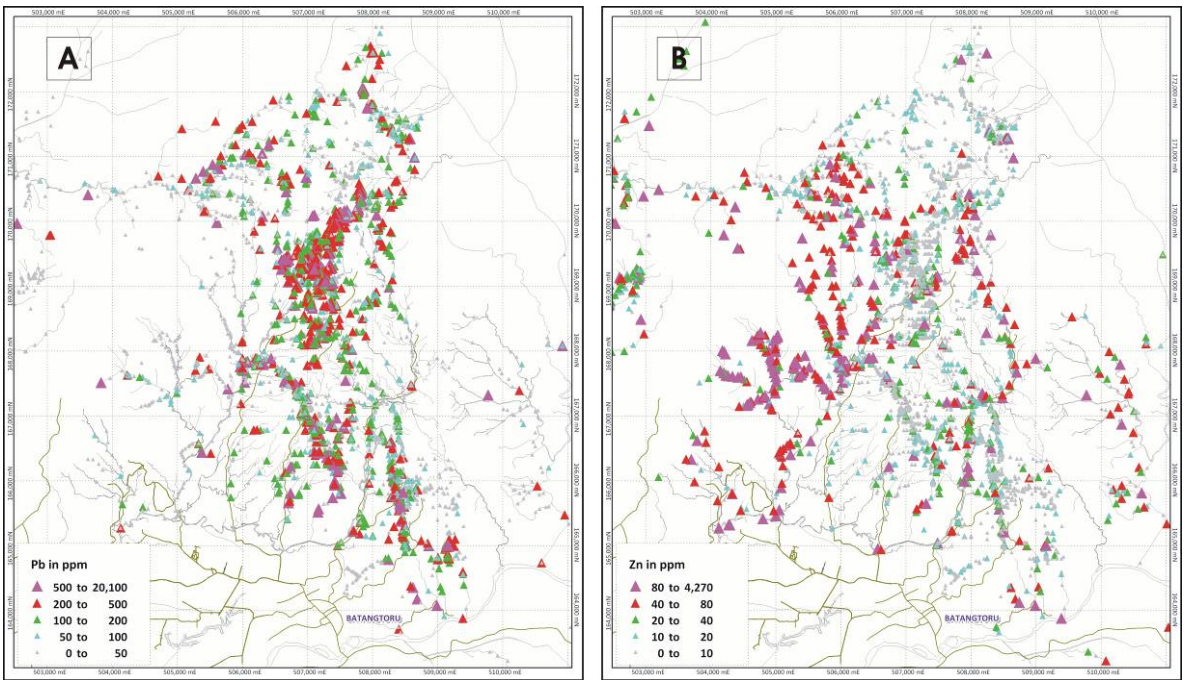

Figure 7.9. Rock chip geochemistry distribution of (A) lead and (B) zinc in the Martabe district

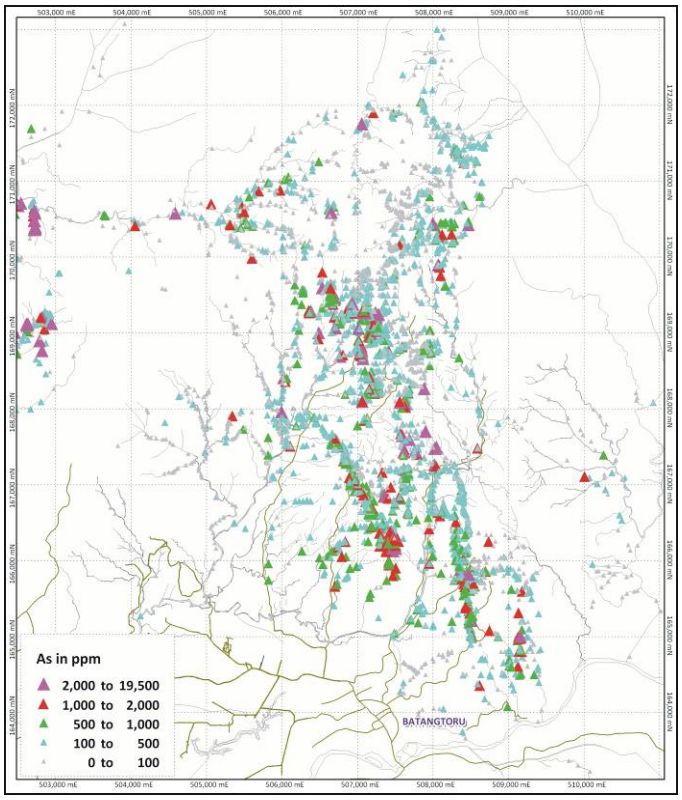

Figure 7.10. Rock chip geochemistry distribution of arsenic in the Martabe district.

7.3 Ore mineralogy

The mineralogy of the ores, including sulfides, sulfosalts and oxides, was determined from field and logging observations and optical microscopy on polished and thin sections (118 samples). In addition, XRF (140 samples), XRD (41 samples) and EMP

(56 spots) analyses were carried out. Most samples were taken from Purnama and Baskara, with a few samples collected from Gerhana. EMP analyses were conducted to identify fine-grained and unknown minerals, using the laboratory at the University of Tasmania. A complete listing of samples and results are included in Appendices 2–6.

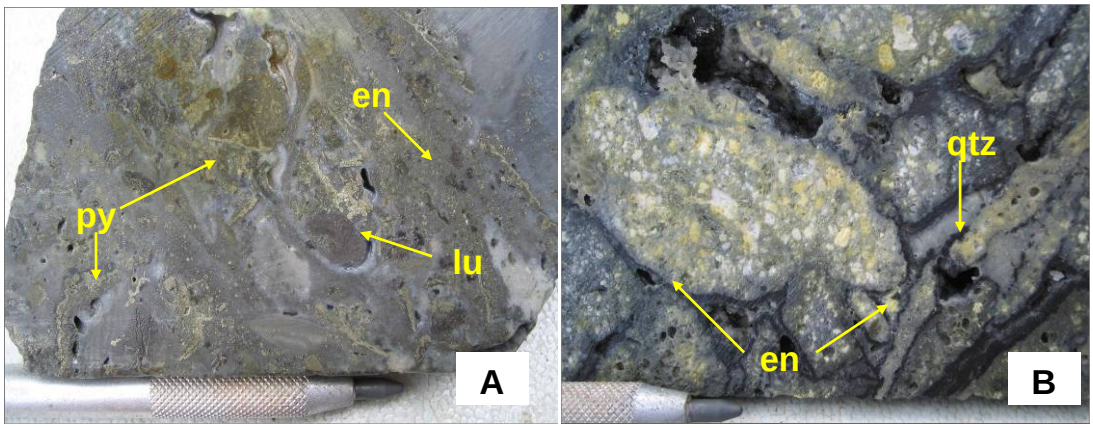

Figure 7.11. (A) Massive sulfide with siliceous alteration. Sulfides consist of luzonite (lu), enargite (en) and pyrite (py). (B) A jigsaw-fit breccia with porphyritic andesite clasts. Enargite (en) forms a cement and also encrusts the andesite. Vugs are filled by quartz (qtz). Samples taken from Baskara.

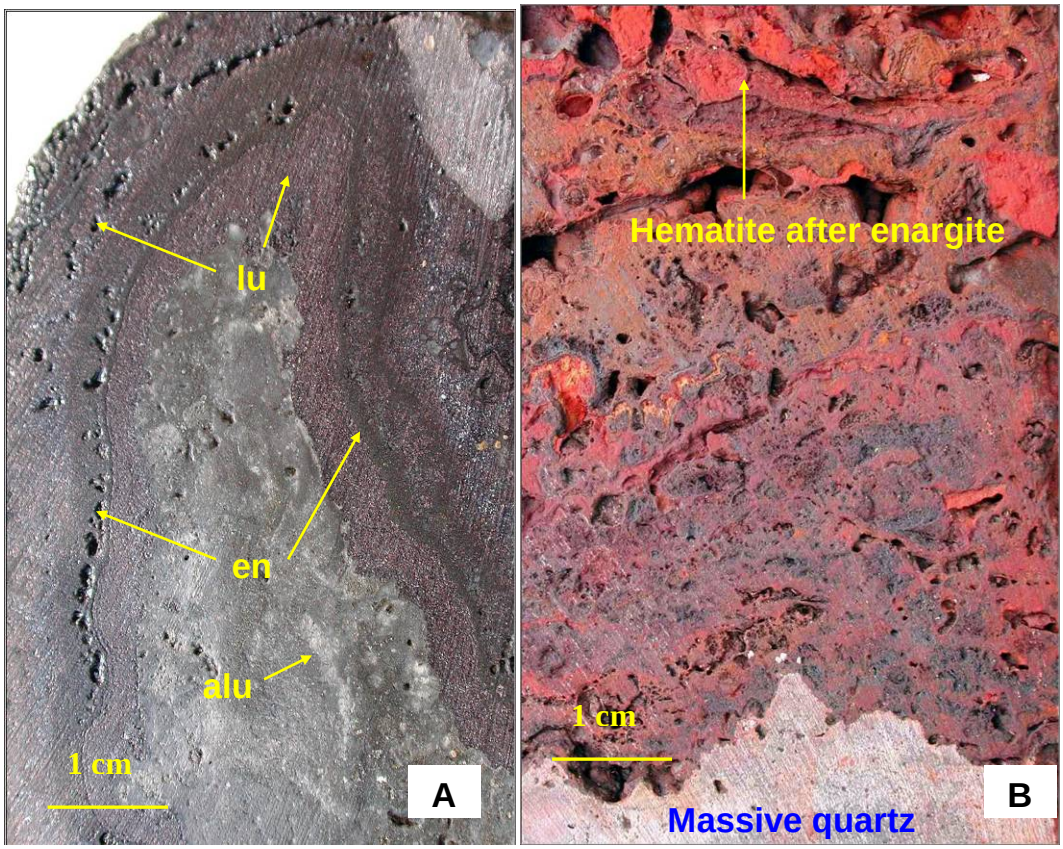

Figure 7.12. (A) Luzonite (lu, pinkish) and enargite (en, dark gray) are present as cement in a hydrothermal breccia. Minor white pinkish alunite (alu) within massive quartz clast. (B) Hematite after enargite encrusts a massive quartz clast. Samples taken from Gerhana.

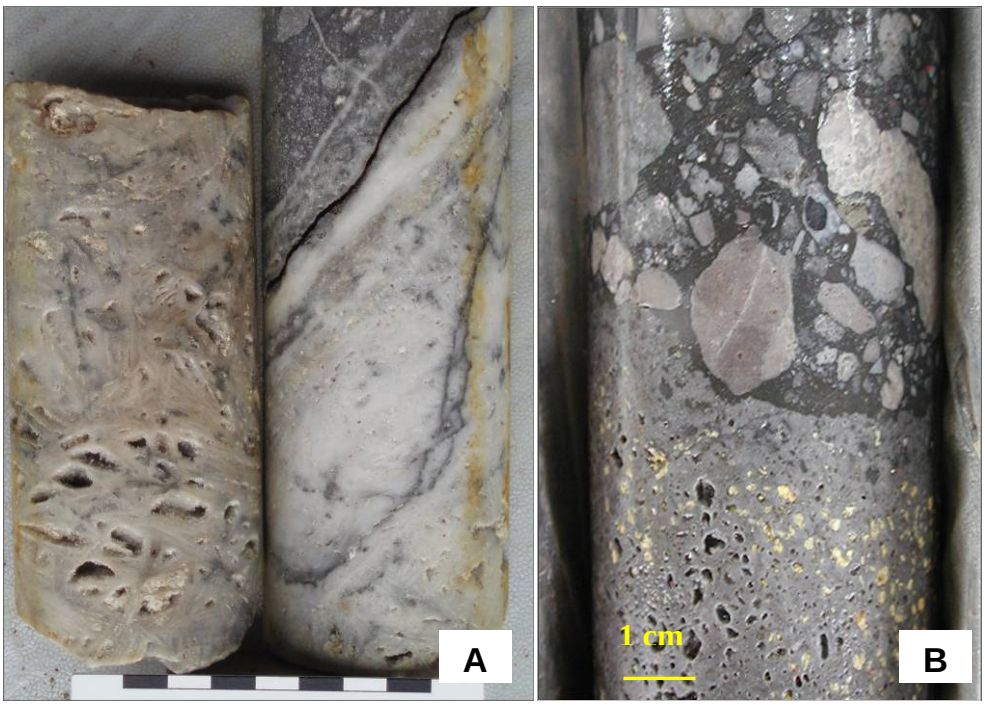

Figure 7.13. (A). Massive bladed texture after coarse barite (left) with chalcedony vein (center) cut polymict breccia. (B). Polymict clast, hydrothermal breccia cemented by fine pyrite cut vuggy quartz alteration. Native sulfur fills vugs in vuggy quartz. Samples taken from Purnama.

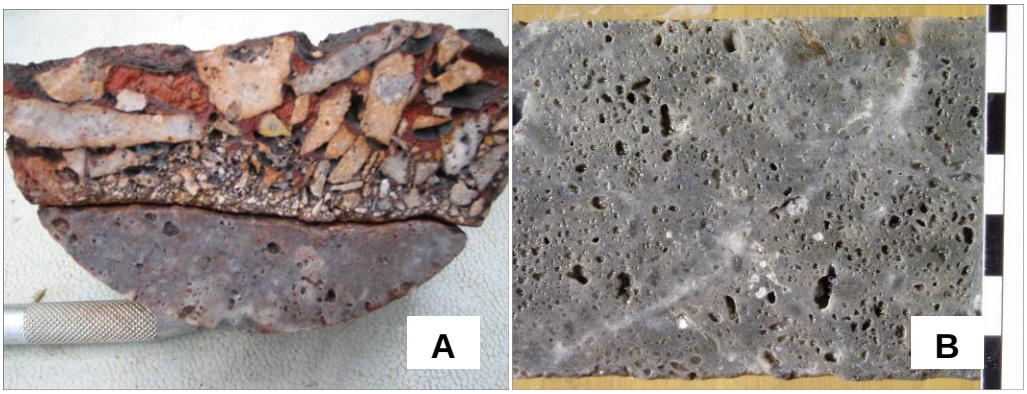

Figure 7.14. (A). Clast supported hydrothermal breccia cut by massive quartz. Breccia cement which was enargite is altered to hematite. (B) Vuggy quartz partially infilled by latest stage quartz. Samples taken from Purnama.

7.3.1 Sulfide and sulfosalt zone

Pyrite (FeS_2) is the most abundant sulfide and has a complex paragenetic at Martabe. Pyrite forms in three distinct generations. Detailed geochemistry of these pyrites is described in Chapter Nine. Pyrite occur as disseminations, veinlets, in breccia matrix and as semi-massive sulfide. Some pyrites show episodic growth.

Early (stage-1) pyrite is fine to coarse grained with a common subhedral shape. This pyrite occurs in breccia matrix and as clusters after replacement of mafic minerals with zone overgrowths. It rarely contains magnetite or anatase inclusions and/or is

inclusion free (Figure 7.15). This pyrite is present in all mineralized and altered zones. Late (stage-2) pyrite mostly forms as porous-textured rims of stage-1 pyrite, is dark yellow and anhedral and often formed contemporaneously with coarse anatase. Stage-2 pyrite has a poor polish and abundance of pits. Stage-2 pyrite is also associated with brecciation and/or leaching of stage-1 pyrite. Late (stage-3) pyrite is commonly euhedral, coarse grained, and has a clean surface (Figure 7.16). This pyrite is more common in veins and breccia matrix. Some framboidal pyrite is recognized primarily in sedimentary host units (Figure 7.17b). In this study, no analysis for framboidal pyrite was undertaken.

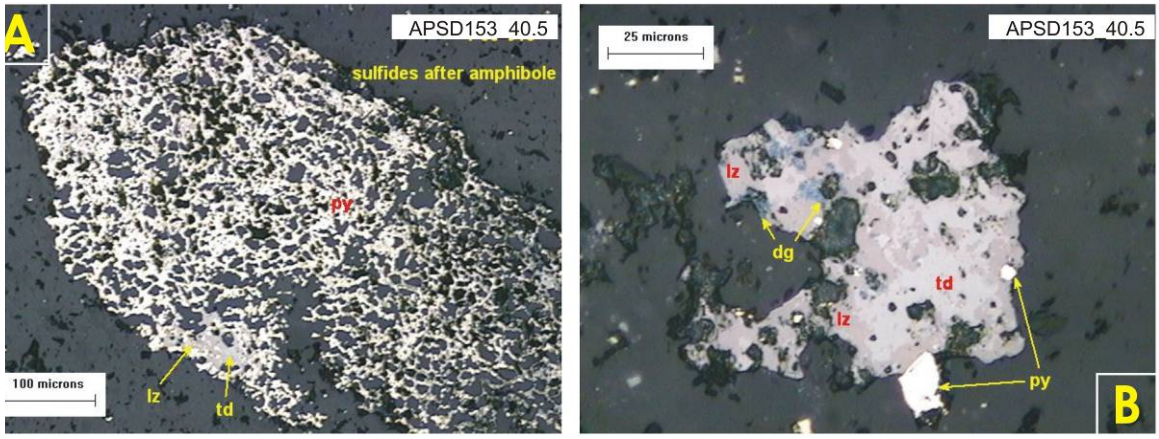

Figure 7.15. (A) Amphibole phenocrysts replaced by stage-1 pyrite (py), tetrahedrite (td), luzonite (lz), and quartz (gray areas). (B) Subhedral pyrite (py) before tetrahedrite (td), before luzonite (lz), before digenite (dg). Sample APSD153_40.5 taken from Purnama.

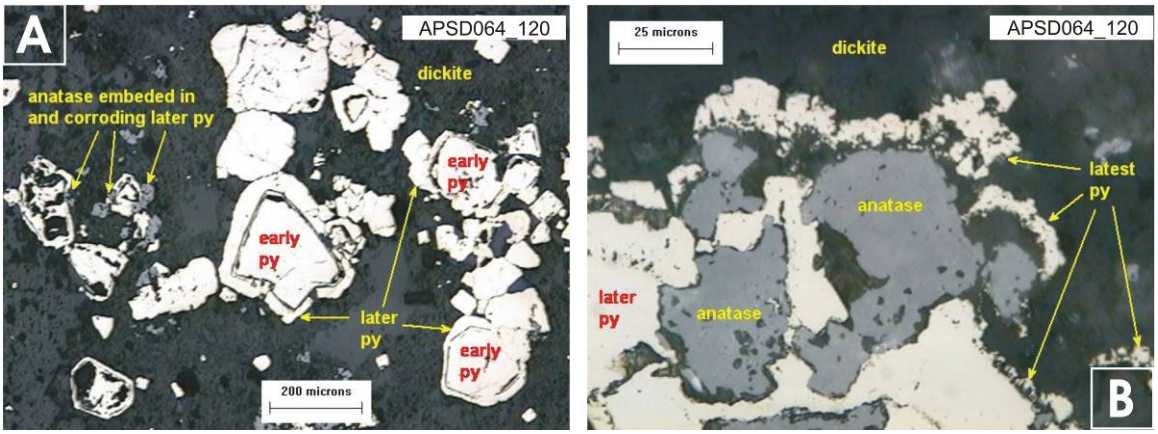

Figure 7.16. (A) Early (stage-1) pyrite (py) coated by later (stage-2) pyrite. Anatase has grown contemporaneously with or after later (stage-2) pyrite. (B) Anatase corroded by and coating later (stage-2) pyrite. Latest (stage-3) pyrite crust coats anatase and later (stage-2) pyrite. Dickite (tansparant blue gray) coats pyrite and anatase. Sample APSD064_120 taken from Purnama.

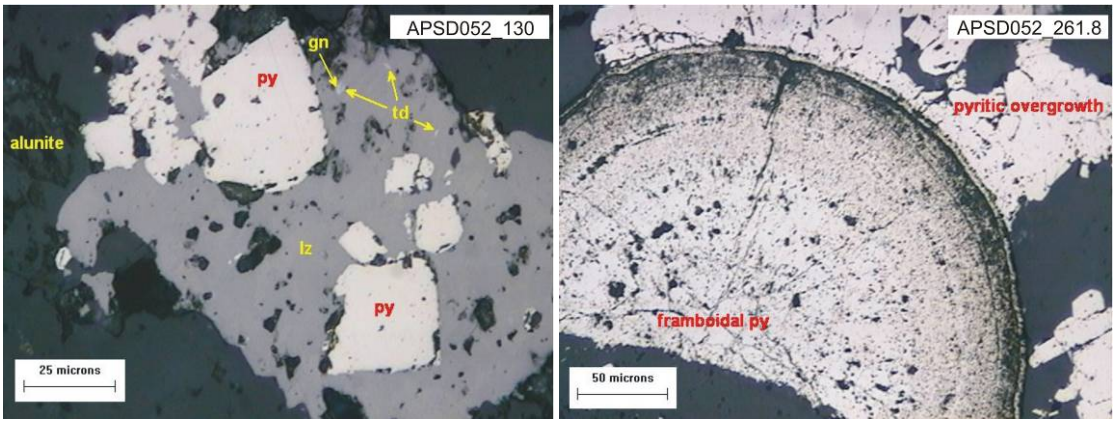

Figure 7.17. (A) Subhedral pyrite (py), fine grained tetrahedrite (td), and galena (gn) inclusions in luzonite. (B) Framboidal pyrite (py) coated by later (stage-2) pyrite overgrowth. Sample APSD052_130 taken from Purnama. Sample APSD052_130 and APSD052_261.8 taken from Purnama.

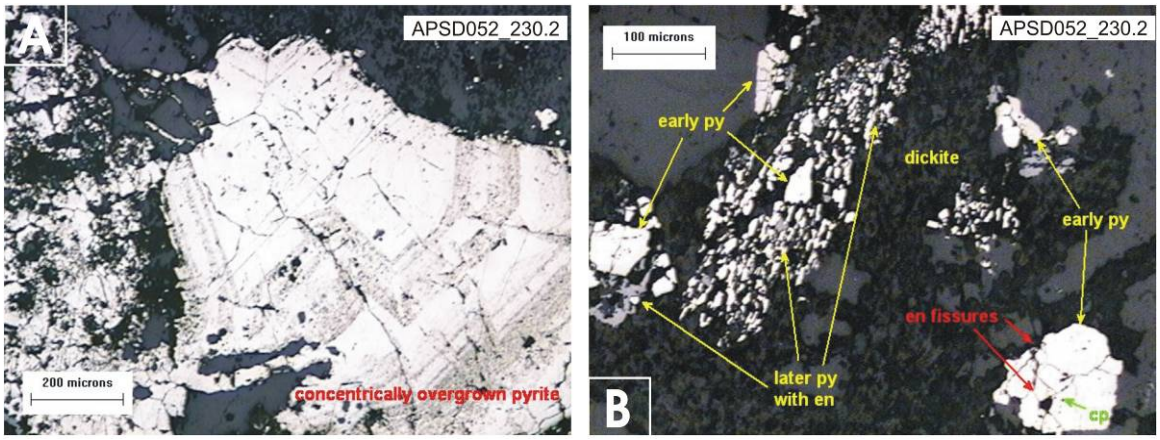

Figure 7.18. (A) Pyrite with concentric overgrowths. Pyrite also cuts quartz (gray) in upper left of view. (B) Early (stage-1) pyrite (py) coated by blades of later (stage-2) pyrite. Stage-2 pyrite with enargite (en) grains. Dickite appears as the darkest aggregates in the vug. Enargite has cut early (stage-2) pyrite that contains a chalcopyrite inclusion (cp) in the lower right of view. Sample APSD052_230.2 taken from Purnama.

Enargite (Cu_3AsS_4) and luzonite (Cu_3SbS_4) are the most common copper sulfosalt minerals at Martabe. In hand specimen, enargite is dark grey, commonly fine grained and with vertical striations on the crystal faces of larger grains. These occur filling leached voids and fractures which cut earlier (stage-1) pyrite and/or together with late (stage-2) pyrite (Figure 7.18B). In polished sections, enargite is typically grey, whereas luzonite, which is a dimorph of enargite is more pinkish but does not show the strong anisotropy or lamellar twinning. Enargite and luzonite also rim early (stage-1) pyrite and may be intergrown with Bi-bearing minerals, tennantite-tetrahedrite and trace galena ±sphalerite. In some cases enargite is altered to covellite and digenite (Figures 7.19A and 7.20A). Enargite and luzonite appears to be the earliest Cu mineral in the quartz-sulfide zone. Tennantite ($Cu_{12}As_4S_{13}$)-tetrahedrite ($Cu_{12}Sb_4S_{13}$) forms in small blebs and also surrounds enargite. It is very fine grained and irregular in shape (Figures 7.19–7.21).

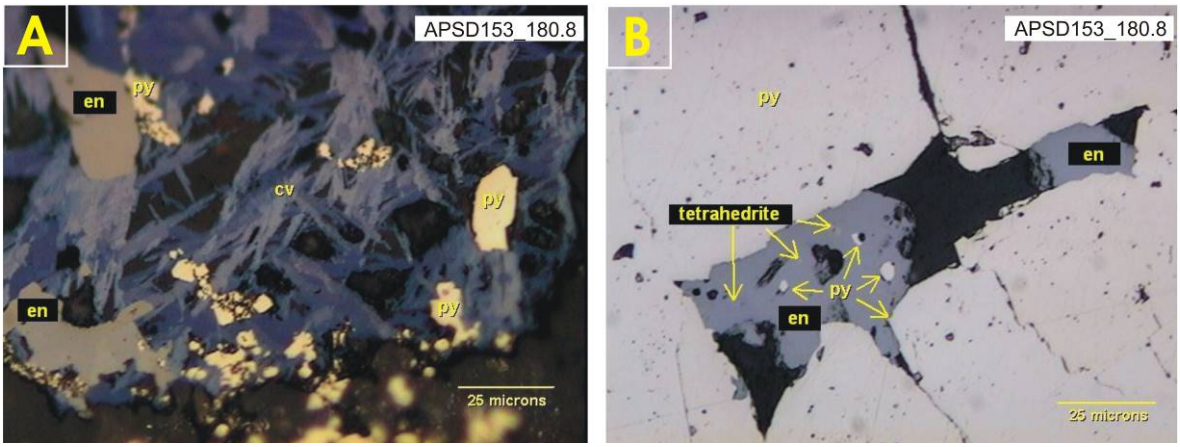

Figure 7.19. (A) Pyrite (py) and enargite (en) coated by covellite (cv) blades. (B) Gap between coarse pyrite (py) blades partially filled with enargite (en). The enargite also contains small inclusions of tetrahedrite that are hard to see in this photomicrograph, as well as some pyrite inclusions. Sample APSD153_180.8 taken from Purnama.

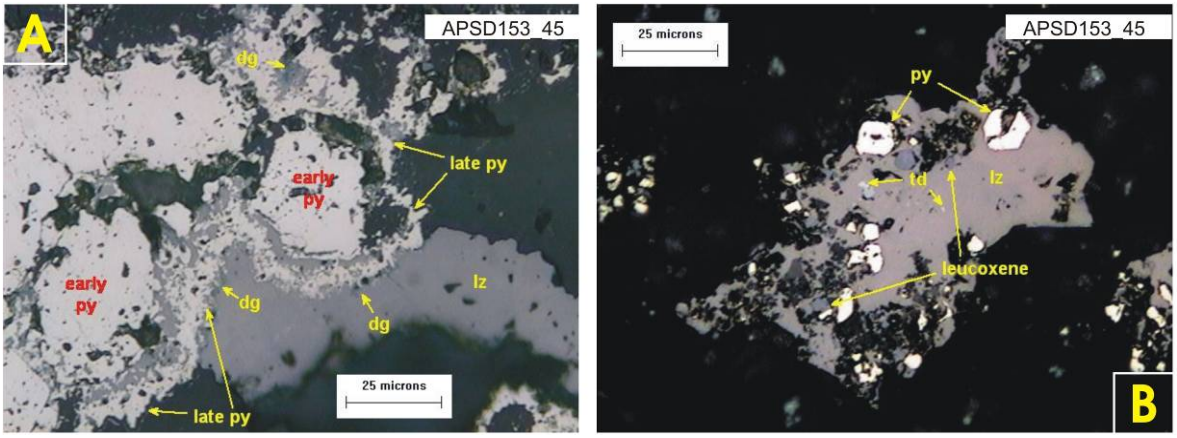

Figure 7.20. (A) Early (stage-1) pyrite coated by late pyrite, which have been infilled by luzonite. Note local alteration of luzonite to digenite (dg), particularly near late pyrite contacts.
(B) Early (stage-1) pyrite (py) cut and replaced by luzonite (lz). Leucoxene and tetrahedrite (td) inclusions in luzonite. Sample APSD153_45 taken from Purnama.

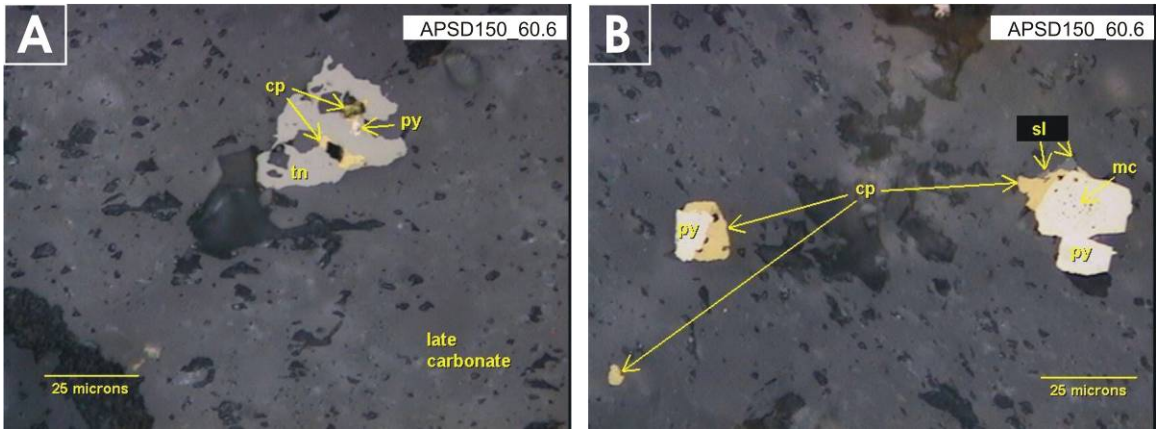

Figure 7.21. (A) Tennantite (tn) grain with pyrite (py) and chalcopyrite (cp) inclusions, within rhodochrosite? (late carbonate) vug.
(B) Possible marcasite (mc) inclusion within pyrite grain, coated by chalcopyrite and sphalerite (sl). This is the same rhodochrosite vug as photographed in Figure 8.17A. Sample APSD150_60.6 taken from Purnama.

Covellite (CuS) and/or digenite (Cu_9S_5) are easily recognized in both hand specimen and polished thin section as dark blue, and they are the most common Cu sulfides. Covellite and/or digenite occur as fracture fill and in leached voids. They may form as early more crystalline intergrowths with enargite and as later rims around enargite. These latter covelite and/or digenite encrust remant enargite. Supergene covellite is an alteration product of sulfosalts such as enargite/luzonite and tennantite-tetrahedrite (Figures 7.19A and 7.20A).

Chalcopyrite is rarely observed. It is commonly present in early pyrite with galena, sphalerite and kaolinite/dickite. It occurs mainly in veinlets. Chalcopyrite may also occur within hematite.

Sphalerite (ZnS) and galena (PbS) are rare elsewhere in the district, consistent with the low geochemical levels of Zn and Pb. In polished thin section, sphalerite and galena are mostly very fine grained and intergrown with enargite; and occur in voids around early (stage-1) pyrite. Some galena and sphalerite are also recognized together in kaolinite/dickite veinlets that cut across the quartz-sulfide zone and extend into zones of advanced argillic and argillic alteration. The sphalerite encloses smaller grains of euhedral pyrite.

Pyrrhotite ($Fe_{1-x}S$) is rare, also and occurs as small inclusion in early pyrite (stage-1) grains (Figure 7.23). Trace magnetite is identified as inclusion in early (stage-1) pyrite.

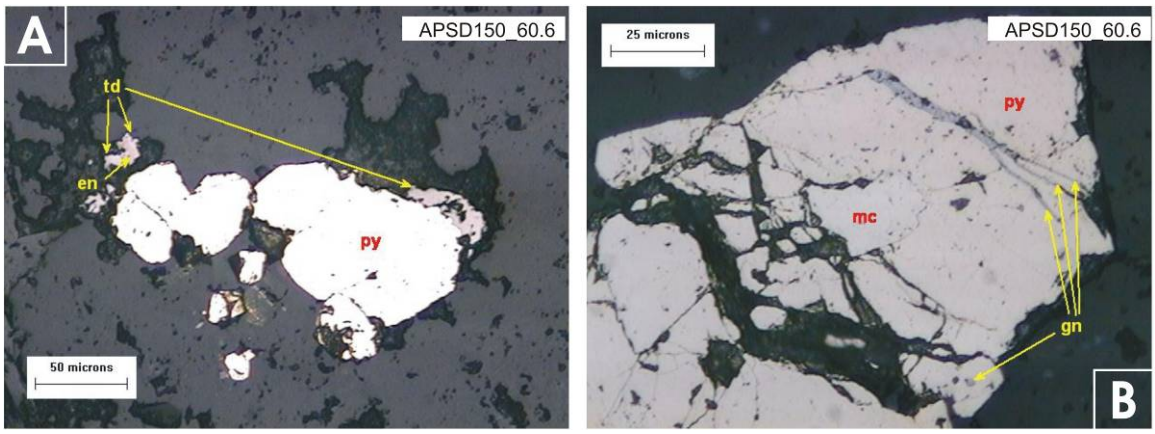

Figure 7.22. (A) Pyrite (py) coated by tetrahedrite (td) and enargite (en). (B) Marcasite (mc) grain coated by pyrite that is cut by a galena veinlet (gn). Sample APSD150_60.6 taken from Purnama.

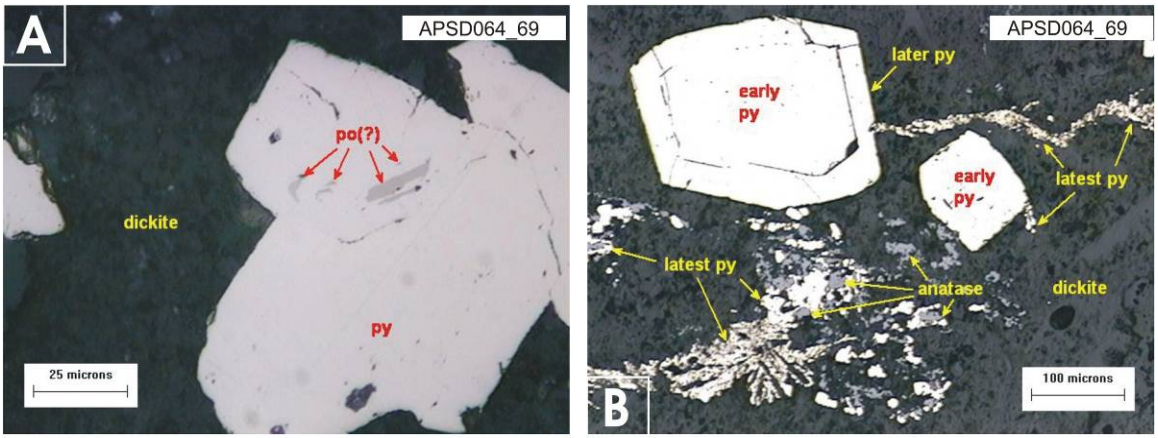

Figure 7.23. (A) Subhedral pyrite (py) with pyrrhotite (po?) inclusions in a dickite-altered phenocryst. (B) Early (stage-1) pyrite coated by later pyrite and dickite. Late (stage-2) pyrite cuts dickite and infiltrates anatase. Sample APSD064_69 taken from Purnama.

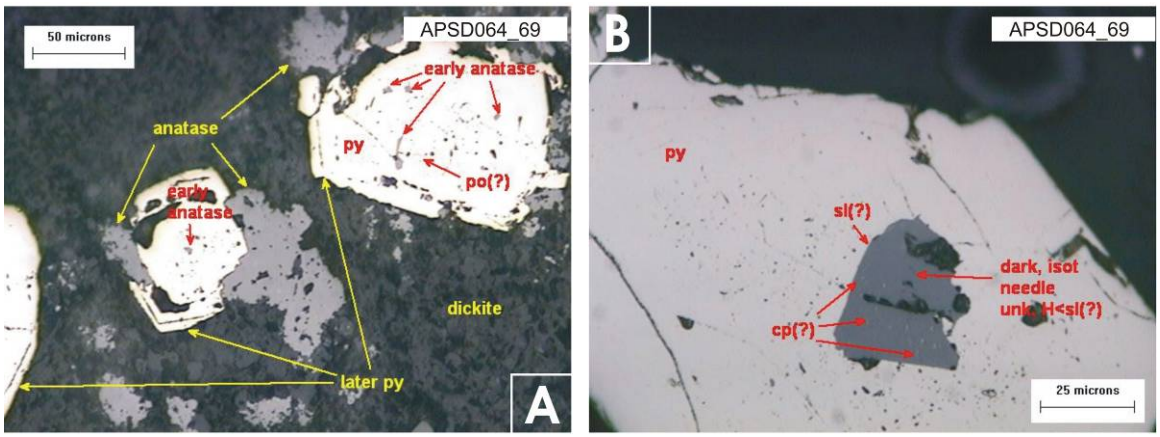

Figure 7.24. (A) Early (stage-1) pyrite (py) with pyrrhotite (po?) and early anatase inclusions. Later pyrite rims early pyrite, but is cut by late anatase. Dickite filled phenocryst after late anatase.
(B) Pyrite with inclusion of sphalerite (sl?) with chalcopyrite (cp?). Sample APSD064_69 taken from Purnama.

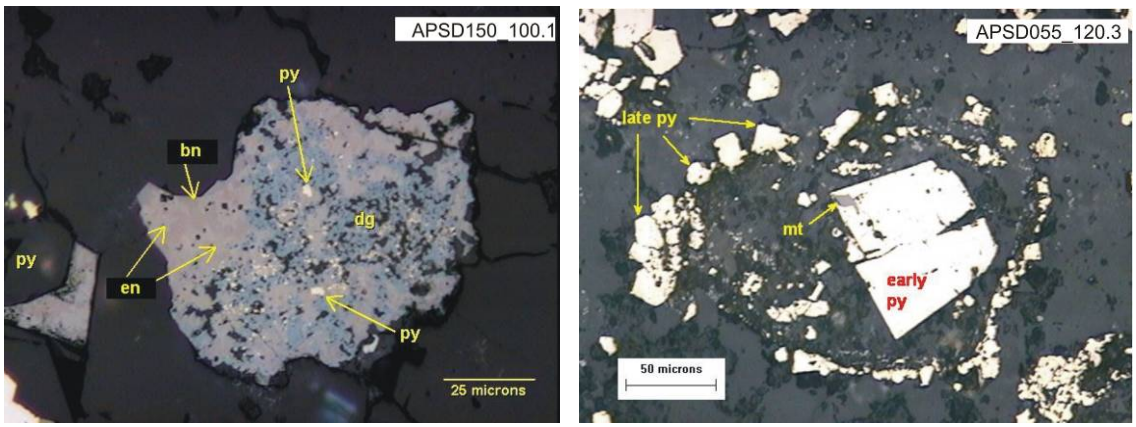

Figure 7.25. (A) Copper sulfide aggregate containing bornite (bn), enargite (en), pyrite stage-2, and digenite (dg). Note the similarity between bornite and enargite, but the former is faintly darker.
(B) Magnetite (mt ?) inclusion in early stage-1pyrite(py) rimmed by late stage-2 pyrite. Sample (a) APSD150_100.1 and sample APSD055_120.3 taken from Purnama.

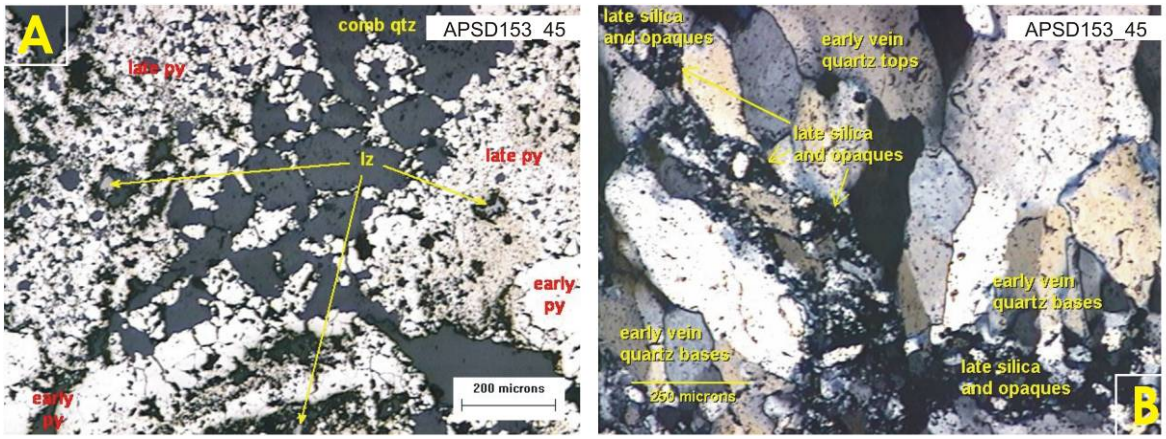

Figure 7.26. (A) Comb quartz infilled by early (stage-1) and late (stage-2) pyrite (py). Luzonite (lz) fills voids in late (stage-2) pyrite and locally replaces it. (B) Comb quartz cut and infilled by fine-grained quartz and opaque phases. Sample APSD153_45 taken from Purnama.

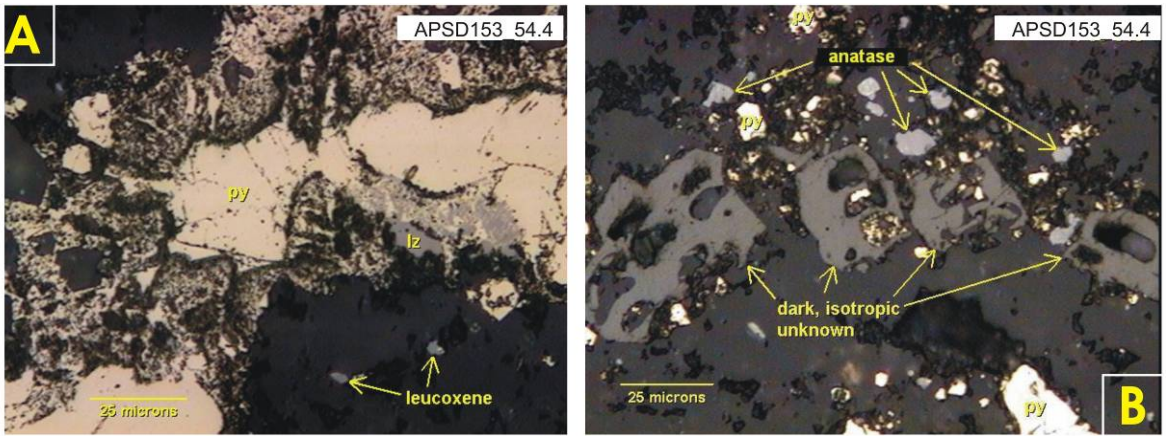

Figure 7.27. (A). Coarse early (stage-1)pyrite(py) coated by late (stage-2) pyrite, corroded by luzonite (lz) in breccia matrix. (B) Dark isotropic unknown mineral with anatase and pyrite stage-1. The dark unknown is likely organic matter (?) and was corroded by quartz. Sample APSD153_54.4 taken from Purnama.

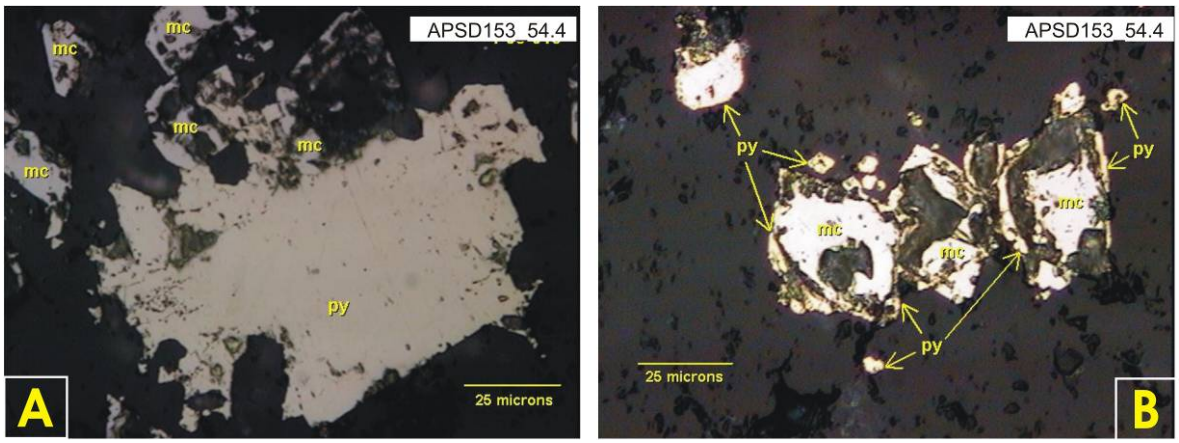

Figure 7.28.(A) Subhedral pyrite stage-1 (py) rimmed by marcasite (mc) in breccia matrix. (B) Marcasite (mc) rimmed by pyrite stage-2 (py) in breccia matrix. Sample APSD153.54.4 taken from Purnama.

7.3.2 Transitional and oxide zone

The transitional and oxidation zones have an irregular shape. Detailed logging indicates that oxidation mostly occurs near the surface and along lithological contacts. However, the oxidation extends to deeper levels along fracture and fault zones. Silver and Au grades do not vary markedly through this zone, but Cu grades are probably enhanced

Goethite and hematite are the main Fe oxides; and their abundance is probably related to the early sulfide distribution and content. Colloform goethite commonly fills voids and fractures as late-stage oxidation. They are most abundant in the oxide siliceous zone, but decrease in the advanced argillic zone. Reddish or purple, finely dispersed hematite is more common in the outer part of the advanced argillic zone.

Titaniferous minerals mainly occur as anatase; and mostly in the sulfide zone. A titaniferous phase in the vuggy quartz is formed because of progressive removal of Fe from titanomagnetite during progressive alteration leaves a skeletal intergrowth which consists of rutile or anatase (Figure 7.30). These minerals are characterized by distinctive white internal reflections. Anatase is also formed as inclusion in pyrite. Late anatase occupies phenocryst with dickite and pyrite, but occurs before dickite and probably after stage-2 pyrite.

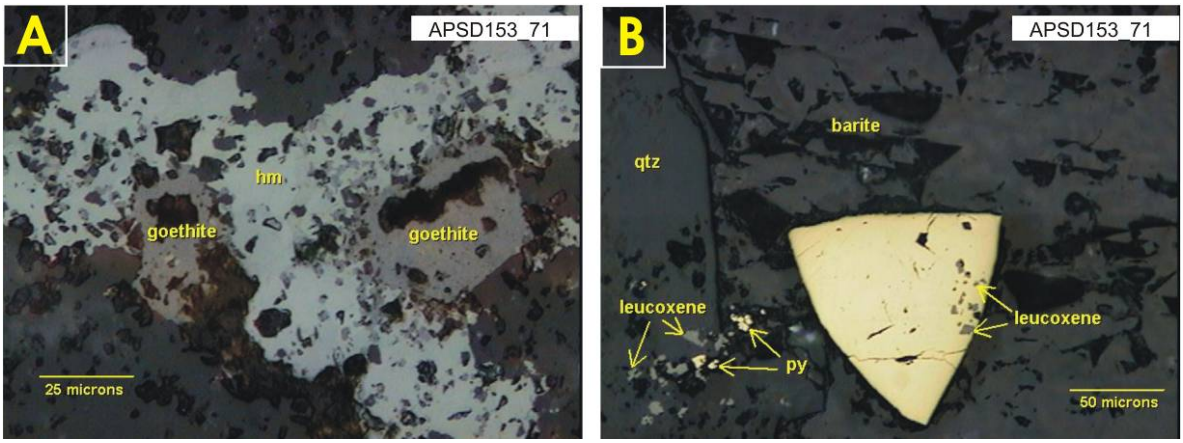

Figure 7.29.(A) Hematite (hm) replacing goethite. (B) Pyrite stage-1 (py) and leucoxene or anatase in quartz (qtz) vug wall, and as inclusions in barite. Sample APSD153_71 taken from Purnama.

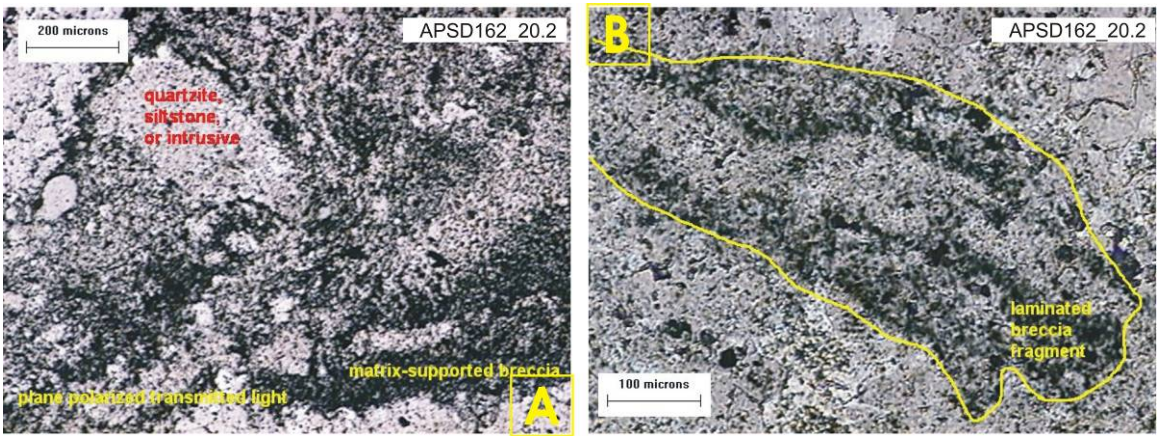

Figure 7.30. (A) Equigranular fragment in upper left corner and breccia contrast created by anatase (dark grains) (plane polarized transmitted light). (B) Dark bands from pyrite stage-1 and anatase distribution in the laminated breccia fragment (plane polarized transmitted light). Sample APSD162_20.2 taken from Purnama.

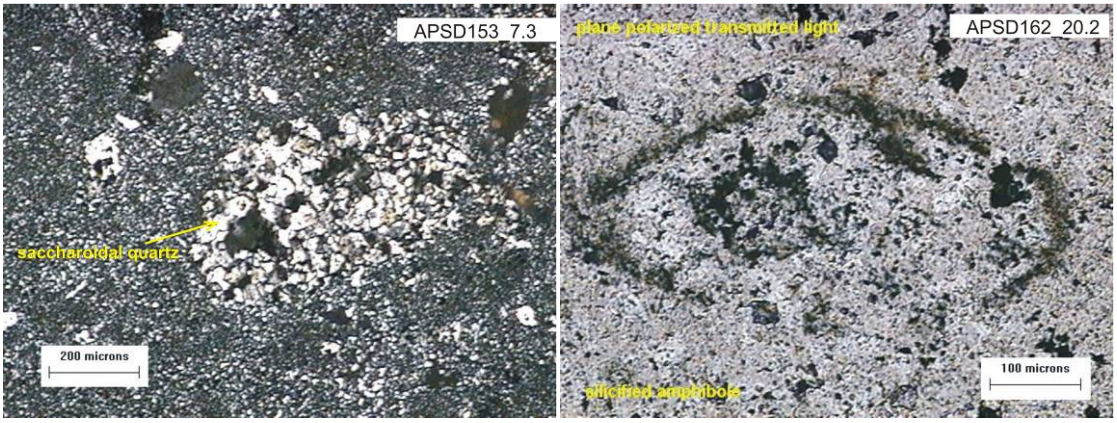

Figure 7.31(A) Silicified amphibole phenocryst outlined primarily by anatase. Plane polarized transmitted light. (B) Saccaroidal quartz (once sandstone?) texture of breccia fragment in microcrystalline quartz (devitrified glass and ash debris) seen in cross-polarized transmitted light. Sample APSD153_7.3 and APSD162_20.2 taken from Purnama.

Jarosite and barite are typical sulfates in Martabe. Jarosite is common in the oxidized zone, however, barite can be present in both the oxidized and sulfide zones. In hand specimen, jarosite is identified as earthy yellow encrustations and staining. Barite is common in late-stage fractures and vugs, mostly at Purnama and Gerhana. It forms tabular to more complex prismatic crystals (Figure 7.32).

Figure 7.32. Barite crystals, filling a vug and encrusting jarosite (yellow). Goethite (dark brown) coating fractures after pyrite. Sample taken from Purnama.

Native sulfur is common, mainly occuring as vug fill in the oxide zone, but is also present to depth in the vuggy quartz or sulfide zones. It forms bright yellow crystals up to 1 cm in size. Locally sulfur occurs also in fractures in the advanced argillic alteration halo.

7.4 Metal zonation signatures

This study was undertaken to define district patterns scale distribution of minor and trace elements in deposits and prospects throughout the Martabe district. The distribution of elements is grouped as the data is based on oxide, transition and sulfide zones for each deposit/prospect.

7.4.1 Methods of analysis

A total of 34 chemical elements (Ag, Al, As, Ba, Bi, Ca, Cd, Co, Cr, Cu, Fe, Ga, K, La, Li, Mg, Mn, Mo, Na, Nb, Ni, Pb, Sb, Sc, Sn, Sr, Ta, Te, Ti, V, W, Y, Zn and Zr) were measured using the ICP at the Intertek Laboratory in Jakarta, Indonesia on 9043 core samples from 79 drill holes (Figure 7.33). Details of the multi-element analyses, including data acquisition and, statistical analysis are summarized in Appendix 7. A correlation matrix for all elements was also calculated. Based on observations from petrography, 15 elements (Ag, Cu, Pb, Zn, Mo, Bi, As, Sb, Hg, Te, Ba, Ni, Cr and Mg) were selected to determine their relation to the gold deposition in the Martabe district.

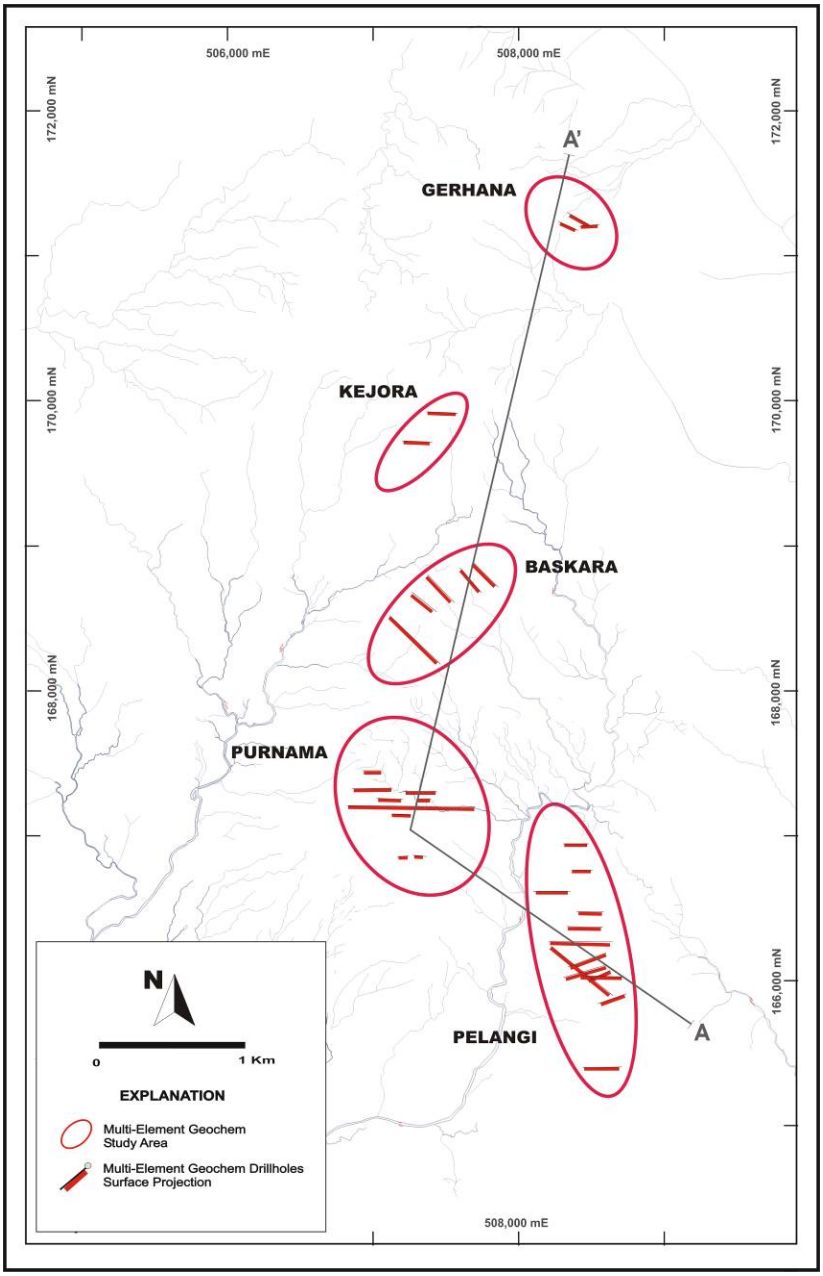

Figure 7.33. Location of the multiple element samples used in this study. Red lines are multi element geochemical surface projection from drillholes at Pelangi, Purnama, Baskara, Kejora and Gerhana.

Table 7.1. Summary of selected element data obtained drill core for the Martabe district. Data are also given for the Purnama and Baskara deposits. Note: AuFA= Fire assay analytical method for gold; AuCN, an analytical method for gold cyanide using the hydrogen cyanide.

	MARTABE (n=9043) DISTRICT					PURNAMA (n=2956)					BASKARA (n=2189)				
Elements	**Mean**	**Median**	**StdDev**	**Min**	**Max**	**Mean**	**Median**	**StdDev**	**Min**	**Max**	**Mean**	**Median**	**StdDev**	**Min**	**Max**
	(ppm)	**(ppm)**	**(ppm)**	**(ppm)**	**(ppm)**	**(ppm)**	**(ppm)**	**(ppm)**	**(ppm)**	**(ppm)**	**(ppm)**	**(ppm)**	**(ppm)**	**(ppm)**	**(ppm)**
AuFA	0.9	0.3	2.3	0.001	94	1.2	0.5	2.6	0.0	51	1.0	0.3	1.9	0.001	25
AuCN	0.6	0.1	1.9	0.1	90	0.9	0.3	1.8	0.1	24	0.8	0.2	1.7	0.1	23
Ag	7	1	23	0	569	14	4	35	0	569	3	1	6	0	70
Cu	137	32	534	1	12800	162	58	539	1	10000	226	60	714	1	12800
Pb	84	36	231	1	8210	136	54	354	1	8210	70	49	104	1	2300
Zn	57	10	354	1	18500	102	9	589	1	18500	30	10	78	1	2030
Mo	2.6	1.0	8.1	0.5	651	3.3	2.0	4.0	0.5	65	1.9	1.0	2.3	0.5	43
Bi	10.4	2.5	68.2	2.5	3820	14.2	2.5	108.5	2.5	3820	11.6	5.0	36.4	2.5	986
As	243	156	350	3	8940	327	255	356	3	7860	147	79	289	3	4580
Sb	26	6	98	3	4600	47	16	154	3	4600	8	3	21	3	446
Hg	0.2	0.1	0.6	0.0	36	0.2	0.1	0.8	0.0	36	0.1	0.1	0.2	0.0	3
Te	10.5	5.0	34.1	5.0	2000	16.6	5.0	57.0	5.0	2000	7.3	5.0	9.7	5.0	380
Ba	53.0	21.0	127.3	0.5	1720	113.6	42.0	204.0	1.0	1720	14.3	8.0	18.7	0.5	288
Ni	9.1	6.0	11.0	0.5	185	11.5	7.0	14.9	0.5	185	4.1	3.0	4.5	0.5	36
Cr	145.0	107.0	133.2	0.5	1550	130.9	87.0	130.4	0.5	1550	104.9	64.0	114.2	0.5	742
Ca	1852	50	7375	50	183000	2184	50	7591	50	141000	2042	50	6844	50	49700
Mg	1040	50	3345	50	49800	1242	50	4058	50	49800	1522	50	4000	50	34400
Ag/AuFA	7.8	4.2	9.8	100	6	12.1	8.1	13.9	100.0	11	3.2	3.7	3.1	20.0	3
Cu/AuFA	156.3	123.1	228.1	500	136	136.8	107.4	211.2	1000.0	196	233.1	200.0	377.8	200	512
AuCN/AuFA	0.7	0.4	0.8	50	1	0.7	0.6	0.7	50.0	0	0.8	0.7	0.9	10.0	1

Table 7.1 (*Continued).* Summary of selected element data obtained drill core for the Martabe district. Data are also given for the Kejora, Gerhana and Pelangi deposits. Note: AuFA= Fire assay analytical method for gold; AuCN, an analytical method for gold cyanide using the hydrogen cyanide.

Elements	KEJORA (n=289)					GERHANA (n=695)					PELANGI (n=2914)				
	Mean (ppm)	Median (ppm)	StdDev (ppm)	Min (ppm)	Max (ppm)	Mean (ppm)	Median (ppm)	Std Dev (ppm)	Min (ppm)	Max (ppm)	Mean (ppm)	Median (ppm)	StdDev (ppm)	Min (ppm)	Max (ppm)
AuFA	0.6	0.2	1.4	0.0	14.9	1.3	0.2	5.0	0.0	94	0.4	0.1	1.1	0.0	28
AuCN	0.5	0.1	1.2	0.1	12.7	0.7	0.1	4.0	0.1	90	0.3	0.1	1.0	0.1	27
Ag	2	1	5	0	51	12	1	29	0	256	1	1	5	0	207
Cu	98	33	399	1	5690	249	40	842	1	8240	21	14	49	1	2130
Pb	143	112	183	19	2300	47	29	53	1	489	44	19	147	1	3950
Zn	10	5	59	1	1010	53	4	224	1	2720	38	12	131	1	4060
Mo	1.7	1.0	1.6	0.5	14.0	6.4	3.0	25.6	0.5	651	1.7	1	4.7	0.5	150
Bi	25.0	5.0	86.8	2.5	1060	16.7	2.5	52.7	2.5	680	2.6	3	1.8	2.5	67
As	134	59	309	3	2860	209	86	583	3	8940	249	181	288	3	4400
Sb	20	6	52	3	546	23	3	66	3	776	19	8	60	3	1850
Hg	0.3	0.2	0.3	0.0	3.6	0.1	0.0	0.2	0.0	3	0.3	0	0.7	0.0	14
Te	12.5	5.0	15.3	5.0	120	15.4	10.0	22.6	5.0	260	5.2	5	3.3	5.0	130
Ba	12.3	7.0	26.0	1.0	304	40.1	24.0	56.1	1.0	578	27.5	19	35.8	0.5	774
Ni	3.3	2.0	2.9	0.5	17	7.3	6.0	5.6	0.5	65	11.4	9	9.7	0.5	179
Cr	187.8	178.0	79.1	29.0	516	115.4	74.0	110.0	0.5	473	192.2	159	143.1	1.0	874
Ca	60	50	136	50	2300	1272	50	4401	50	29400	1688	50	8369	50	183000
Mg	65	50	175	50	2800	287	50	776	50	5800	748	50	2311	50	19500
Ag/AuFA	3.3	4.0	3.5	20.0	3.4	8.9	4.3	5.7	20.0	3	3.2	4	4.3	20.0	7.4
Cu/AuFA	176.1	220.0	280.7	100.0	381.9	190.7	173.9	168.0	100.0	88	50.9	100	44.7	100.0	76.1
AuCN/AuFA	0.8	0.7	0.8	10.0	0.9	0.5	0.4	0.8	10.0	1	0.8	1	0.9	10.0	1.0

Table 7.2. Mean of values of selected elements and ratios in Martabe district as a whole and the Purnama and Baskara deposits . The distribution of multi elements is grouped as the data variation based on oxide, transition and sulfide zones.

Element	Martabe (n=9043)				Purnama (n=2956)				Baskara (n=2189)			
	All Samples (ppm)	Sulfide (ppm)	Transition (ppm)	Oxide (ppm)	All Samples (ppm)	Sulfide (ppm)	Transition (ppm)	Oxide (ppm)	All Samples (ppm)	Sulfide (ppm)	Transition (ppm)	Oxide (ppm)
AuFA	0.88	0.46	1.39	1.32	1.19	0.63	1.80	1.83	0.97	0.52	1.42	1.18
AuCN	0.63	0.23	0.81	1.14	0.87	0.33	1.08	1.71	0.79	0.25	1.05	1.06
Ag	6.93	5.15	13.82	7.72	14.37	9.46	23.32	18.83	3.14	2.49	5.65	3.23
Cu	142.5	186.5	174.4	76.4	162.4	215.2	158.12	84.86	226.4	409.6	424.76	103.48
Pb	83.9	59.0	104.7	111.8	136.1	106.5	175.46	167.67	70.0	45.7	66.96	83.88
Zn	57.4	99.8	19.9	9.5	101.6	177.5	28.30	11.70	30.4	70.3	18.00	9.48
Mo	2.6	2.5	2.9	2.7	3.3	2.7	3.65	3.98	1.9	1.8	2.07	1.93
Bi	10.4	7.8	13.0	13.3	14.2	11.0	17.03	18.02	11.6	7.6	16.67	13.29
As	243.2	224.4	303.2	253.6	327.2	281.7	362.53	384.06	146.7	146.1	227.41	138.48
Sb	25.7	16.5	38.7	34.9	47.0	27.8	64.77	69.96	7.9	7.4	12.19	7.66
Hg	0.2	0.14	0.22	0.32	0.24	0.17	0.26	0.34	0.12	0.07	0.14	0.15
Te	10.5	8.9	12.4	12.1	16.6	13.0	17.27	21.90	7.3	7.1	7.34	7.37
Ba	53.0	33.4	55.5	78.5	113.6	51.2	101.71	211.24	14.3	16.0	13.86	13.43
Ni	9.1	13.0	8.6	4.0	11.5	15.5	11.34	5.58	4.1	6.2	5.78	2.74
Cr	145.0	142.6	174.9	141.3	130.9	114.2	168.74	143.51	104.9	86.4	144.00	111.15
Ca	1851.7	3395.4	418.1	131.0	2183.6	3767.0	795.18	264.26	2042.0	5877.5	372.30	83.45
Mg	1039.6	1848.9	270.0	140.7	1242.1	2054.2	465.5	278.6	1521.8	4332.5	306.8	85.8
Ag/Au	7.91	11.29	9.93	5.87	12.11	15.12	12.93	10.29	3.23	4.82	3.97	2.75
Cu/Au	162.52	408.50	125.40	58.10	136.82	344.01	87.67	46.39	233.11	792.44	298.30	87.97
AuCN/AuFA	0.72	0.49	0.58	0.87	0.73	0.52	0.60	0.93	0.81	0.48	0.74	0.90

Table 7.2. (*Continued).* Mean of values of selected elements and ratios for the Kejora, Gerhana and Pelangi deposits showing the differing geochemical signatures, The distribution of multi elements is grouped as the data variation based on oxide, transition and sulfide zones.

Element	Gerhana (n=695)				Kejora (n=289)				Pelangi (n=2914)			
	All Samples (ppm)	Sulfide (ppm)	Transition (ppm)	Oxide (ppm)	All Samples (ppm)	Sulfide (ppm)	Transition (ppm)	Oxide (ppm)	All Samples (ppm)	Sulfide (ppm)	Transition (ppm)	Oxide (ppm)
AuFA	1.31	0.86	3.95	1.76	0.56	0.30	1.14	0.56	0.42	0.19	0.38	0.99
AuCN	0.66	0.27	1.77	1.43	0.47	0.20	0.70	0.49	0.35	0.14	0.29	0.87
Ag	11.71	9.41	37.01	10.11	1.82	4.91	10.46	1.01	1.34	1.14	1.68	1.72
Cu	249.5	279.4	398.4	111.2	98.0	354.7	402.8	51.8	21.3	23.8	15.6	16.9
Pb	47.2	41.7	95.2	47.5	143.1	87.3	113.5	151.3	44.3	28.6	38.2	83.6
Zn	53.5	74.3	3.3	8.0	9.6	11.1	88.3	5.2	38.4	54.5	10.7	8.0
Mo	6.4	7.0	8.4	4.1	1.7	1.2	1.8	1.8	1.7	1.5	1.4	2.3
Bi	16.7	17.2	30.6	10.7	25.0	12.9	16.7	26.9	2.6	2.7	2.5	2.6
As	209.5	226.2	247.2	147.0	133.8	133.0	272.2	126.7	249.5	208.2	280.4	339.6
Sb	22.6	23.1	47.7	13.0	19.7	8.3	24.3	20.8	19.0	9.0	18.9	43.2
Hg	0.10	0.09	0.16	0.12	0.30	0.19	0.30	0.32	0.30	0.16	0.24	0.68
Te	15.4	13.3	31.9	16.4	12.5	10.2	18.5	12.4	5.2	5.1	5.0	5.5
Ba	40.1	36.7	56.1	44.9	12.3	5.1	5.9	13.5	27.5	24.9	21.9	35.9
Ni	7.3	8.0	7.7	5.0	3.3	9.8	7.0	2.3	11.4	14.9	7.0	4.4
Cr	115.4	118.0	136.2	100.6	187.8	198.9	169.4	187.4	192.2	193.4	205.4	185.3
Ca	1271.6	1814.0	61.1	60.6	59.7	146.6	50.0	50.0	1688.1	2573.4	65.1	69.8
Mg	287.4	389.3	53.7	62.1	65.1	167.2	50.0	53.8	747.9	1109.5	64.0	89.7
Ag/Au	8.95	10.96	9.36	5.74	3.28	16.37	9.18	1.81	3.19	5.94	4.36	1.73
Cu/Au	190.7	325.4	100.8	63.1	176.09	1182.30	353.61	93.19	50.87	123.81	40.72	17.06
AuCN/AuFA	0.50	0.31	0.45	0.81	0.85	0.66	0.61	0.88	0.82	0.73	0.76	0.88

Table 7.3. Correlation coefficient of elements with gold for all deposits in Martabe district. Red text indicates a strong positive correlation with gold (coefficient >0.5).

Element	Martabe (n=9043)				Purnama (n=2956)				Baskara (n=2189)			
	All samples	Sulfide	Transition	Oxide	All samples	Sulfide	Transition	Oxide	All samples	Sulfide	Transition	Oxide
AuFA	1.00	1.00	1.00	1.00	1.00	1.00	1.00	1.00	1.00	1.00	1.00	1.00
AuCN	**0.87**	**0.78**	**0.90**	**0.95**	**0.88**	**0.79**	**0.93**	**0.96**	**0.91**	**0.83**	**0.96**	**0.96**
Ag	**0.70**	**0.81**	**0.72**	**0.59**	**0.75**	**0.82**	**0.71**	**0.65**	**0.66**	**0.85**	**0.68**	**0.53**
Cu	0.41	**0.56**	**0.50**	0.31	0.43	**0.59**	0.44	0.45	0.45	**0.80**	**0.51**	0.31
Pb	**0.56**	**0.60**	**0.65**	0.38	**0.60**	**0.60**	**0.72**	**0.52**	**0.50**	**0.71**	0.24	0.27
Zn	-0.38	-0.36	-0.09	-0.09	-0.43	-0.37	-0.05	-0.22	-0.47	-0.62	-0.40	-0.16
Mo	0.28	0.26	0.38	0.29	0.31	0.19	0.29	0.44	0.16	0.15	0.30	0.13
Bi	0.38	0.44	0.42	0.25	0.38	0.39	0.33	0.35	0.44	**0.56**	0.43	0.34
As	0.49	**0.57**	**0.53**	0.45	**0.58**	0.63	**0.68**	**0.57**	**0.50**	0.68	0.41	0.38
Sb	**0.62**	**0.64**	**0.61**	**0.55**	**0.74**	**0.72**	**0.68**	0.68	0.44	0.46	0.41	0.43
Hg	0.46	**0.52**	0.26	0.21	0.49	0.49	0.38	0.26	0.47	**0.74**	0.54	0.12
Te	0.47	0.47	**0.58**	0.41	**0.57**	0.49	**0.60**	**0.59**	0.37	0.45	0.35	0.33
Ba	0.13	-0.12	0.31	0.30	0.20	-0.06	0.20	0.14	-0.21	-0.63	0.00	0.13
Ni	-0.01	0.16	0.20	0.25	-0.08	0.11	0.06	0.09	0.23	0.51	0.41	0.35
Cr	0.17	0.17	0.12	0.18	0.31	0.29	0.26	0.28	0.18	0.15	0.20	0.14
Ca	-0.55	-0.64	-0.35	-0.19	-0.71	-0.76	-0.63	-0.42	-0.54	-0.72	-0.41	-0.17
Mg	-0.58	-0.67	-0.39	-0.26	-0.73	-0.76	-0.67	-0.60	-0.60	-0.82	-0.51	-0.22

Element	Gerhana (n=695)				Kejora (n=289)				Pelangi(n=2914)			
	All samples	Sulfide	Transition	Oxide	All samples	Sulfide	Transition	Oxide	All samples	Sulfide	Transition	Oxide
AuFA	1.00	1.00	1.00	1.00	1.00	1.00	1.00	1.00	1.00	1.00	1.00	1.00
AuCN	**0.74**	**0.72**	**0.52**	**0.86**	**0.94**	**0.82**	**0.95**	**0.95**	**0.87**	**0.77**	**0.91**	**0.99**
Ag	**0.77**	**0.85**	**0.83**	**0.59**	**0.41**	**0.75**	**0.87**	**0.40**	**0.59**	**0.72**	**0.46**	**0.14**
Cu	**0.61**	**0.73**	0.38	0.33	0.05	**0.51**	**0.58**	0.00	0.07	0.13	0.27	0.31
Pb	**0.57**	**0.56**	**0.60**	0.46	0.13	0.42	0.26	0.10	**0.58**	0.49	**0.65**	0.33
Zn	-0.42	-0.47	0.15	0.03	-0.19	0.04	-0.48	-0.21	-0.32	-0.21	0.11	0.08
Mo	0.39	0.37	0.55	0.41	0.08	0.10	0.32	0.05	0.21	0.22	0.02	0.60
Bi	**0.63**	**0.65**	**0.70**	**0.50**	0.27	0.40	**0.73**	0.25	0.10	0.15	0.11	0.11
As	0.32	0.34	0.30	0.22	0.11	0.59	**0.51**	0.05	**0.57**	0.58	**0.67**	0.29
Sb	0.71	**0.72**	**0.74**	**0.65**	0.47	0.45	**0.58**	0.46	**0.70**	0.61	**0.66**	**0.68**
Hg	0.45	0.57	-0.10	0.02	0.00	0.66	0.20	-0.10	**0.64**	0.56	0.44	0.32
Te	**0.68**	**0.67**	**0.91**	**0.56**	0.27	0.48	0.69	0.21	0.20	0.17	0.18	0.63
Ba	0.14	-0.01	0.27	0.50	0.21	-0.10	-0.15	0.26	0.07	-0.12	0.40	0.14
Ni	0.30	0.34	0.46	0.47	0.22	0.02	-0.01	0.33	-0.28	-0.03	0.12	-0.03
Cr	0.37	0.35	0.37	0.43	0.47	0.59	0.00	0.49	0.10	0.11	-0.02	0.07
Ca	-0.67	-0.75	-0.30	-0.25	-0.16	-0.50	-	0.00	-0.48	-0.52	-0.09	-0.05
Mg	-0.62	-0.72	0.26	0.08	-0.19	-0.50	-	-0.12	-0.54	-0.59	-0.17	-0.05

Table 7.4A. Pearson Product-Moment Correlation for all Martabe drillcore (n=9043). Red bold text in yellow box indicates strong positive correlation (>0.5). Bold, black italic text in green box indicates strong negative correlation (>-0.5).

	AuFA	AuCN	Ag	Cu	Pb	Zn	Mo	Bi	As	Sb	Hg	Te	Ba	Ni	Cr	Ca	Mg
AuFA	1.00																
AuCN	**0.87**	1.00															
Ag	**0.70**	**0.57**	1.00														
Cu	0.41	0.29	**0.58**	1.00													
Pb	**0.56**	0.50	**0.55**	0.41	1.00												
Zn	-0.38	-0.39	-0.19	0.05	-0.10	1.00											
Mo	0.28	0.23	0.32	0.28	0.23	-0.09	1.00										
Bi	0.38	0.37	0.39	0.44	0.38	-0.15	0.20	1.00									
As	0.49	0.32	0.48	0.40	0.46	0.02	0.16	0.21	1.00								
Sb	**0.62**	**0.55**	**0.63**	0.30	**0.55**	-0.15	0.28	0.32	**0.61**	1.00							
Hg	0.46	0.40	0.39	0.04	0.41	-0.31	0.11	0.09	0.35	0.49	1.00						
Te	0.47	0.48	0.49	0.42	0.42	-0.15	0.31	**0.56**	0.35	**0.55**	0.11	1.00					
Ba	0.13	0.20	0.21	0.00	0.18	0.06	0.20	-0.01	0.16	0.34	0.02	0.22	1.00				
Ni	-0.01	-0.18	0.19	0.14	-0.04	0.32	0.14	-0.08	0.17	0.12	-0.09	-0.04	0.05	1.00			
Cr	0.17	0.10	0.15	-0.08	0.11	-0.11	0.16	0.02	0.11	0.24	0.21	0.07	-0.02	0.40	1.00		
Ca	-0.55	-0.39	-0.40	-0.17	-0.34	**0.53**	-0.07	-0.19	-0.32	-0.31	***-0.50***	-0.17	0.20	0.13	-0.18	1.00	
Mg	-0.58	-0.42	-0.44	-0.16	-0.38	**0.55**	-0.09	-0.21	-0.34	-0.34	***-0.54***	-0.18	0.22	0.12	-0.20	**0.89**	1.00

Table 7.4B. Pearson Product-Moment Correlation for all Martabe drillcore sample (for gold >=0.2 ppm) (n=5023). Red text indicate strong positive correlation (>0.5).

	AuFA	AuCN	Ag	Cu	Pb	Zn	Mo	Bi	As	Sb	Hg	Te	Ba	Ni	Cr	Ca	Mg
AuFA	1.00																
AuCN	**0.85**	1.00															
Ag	0.45	0.26	1.00														
Cu	0.27	0.03	**0.53**	1.00													
Pb	0.32	0.26	0.40	0.29	1.00												
Zn	-0.10	-0.25	0.12	0.23	0.21	1.00											
Mo	0.25	0.15	0.28	0.22	0.12	-0.05	1.00										
Bi	0.39	0.27	0.32	0.42	0.27	-0.03	0.18	1.00									
As	0.19	0.08	0.33	0.35	0.41	0.28	0.06	0.16	1.00								
Sb	0.43	0.33	**0.50**	0.20	0.45	0.10	0.26	0.25	**0.61**	1.00							
Hg	0.08	0.18	0.13	-0.17	0.19	-0.01	0.03	-0.09	0.18	0.37	1.00						
Te	**0.55**	0.41	0.46	0.40	0.36	-0.05	0.32	**0.56**	0.34	**0.52**	-0.06	1.00					
Ba	0.21	0.25	0.34	-0.07	0.29	-0.10	0.24	0.02	0.23	0.44	0.20	0.26	1.00				
Ni	-0.02	-0.25	0.32	0.23	0.03	0.32	0.24	-0.01	0.13	0.15	-0.04	0.01	0.01	1.00			
Cr	0.09	0.05	0.09	-0.07	0.07	0.00	0.27	0.00	0.06	0.22	0.14	0.07	0.06	0.45	1.00		
Ca	-0.08	-0.14	-0.01	-0.02	-0.03	0.23	0.09	-0.06	0.07	0.01	-0.04	-0.01	0.09	0.17	0.01	1.00	
Mg	-0.08	-0.12	-0.05	-0.02	-0.04	0.21	0.09	-0.07	0.05	-0.01	-0.06	0.01	0.12	0.14	0.01	**0.67**	1.00

7.4.2 Results

The distribution of samples collected for multi-element geochemical analysis is generally too patchy to define district wide patterns and zonation. However, histograms and cumulative frequency diagrams of the main pathfinder elements define the types of mineral distribution. Patterns of element distribution are recognized by a determined background population and a log-normally distributed anomalous population (i.e., Figure. 7.34). Data in Tables 7.1 to 7.4 (and Appendix 7) characterize the known deposits, and show the differing geochemical signatures for each area. In the case of Au, the pattern generally reflects anomalous Au in the advanced argillic and siliceous zones, with no detectable Au in the argillic alteration zone. The lower threshold between local background and anomalous Au enrichment is important for exploration, whereas higher thresholds may reflect different conditions of Au concentration, such as fracture-controlled Au or remobilized Au in the oxide zone. In several deposits, such as Purnama, the Ag values are also log-normally distributed but several populations are present, with several different thresholds.

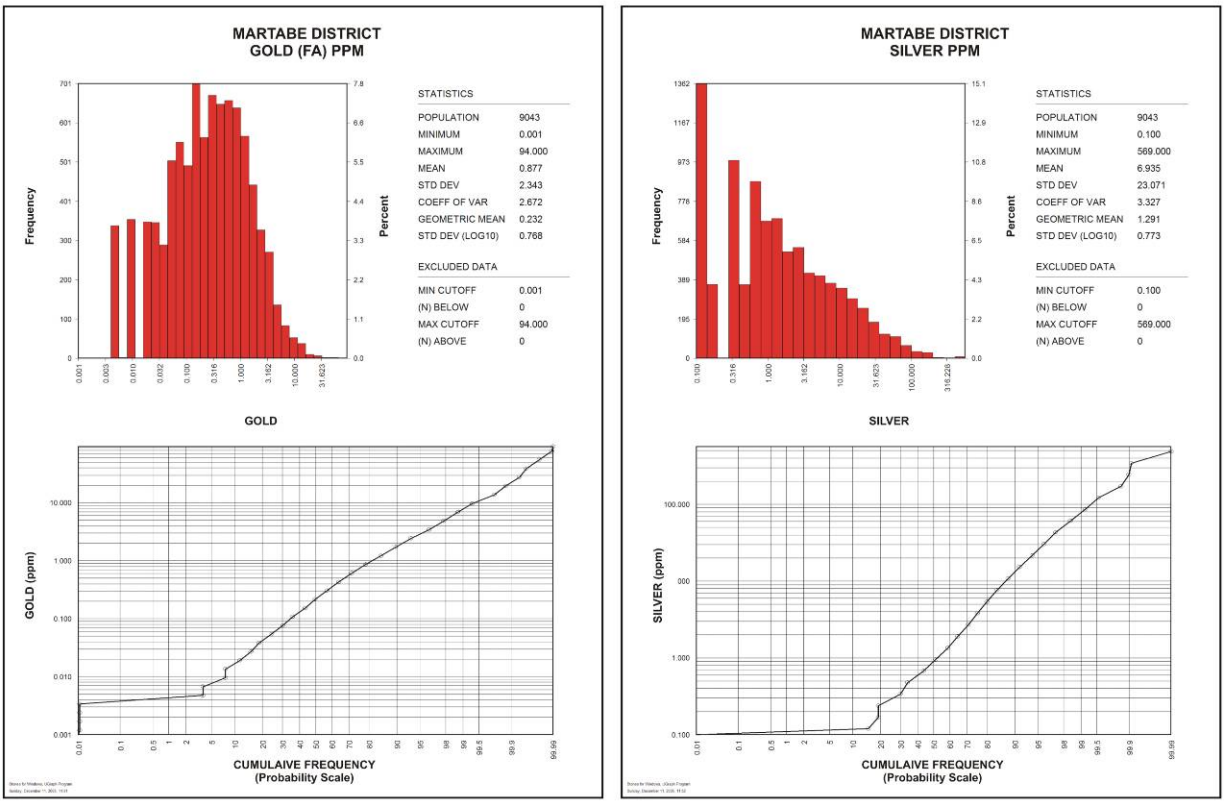

Figure 7.34. Cumulative frequency and log-scale histogram for (a) gold and (b) silver from Martabe drill core samples. These data comprise samples from the oxide, transition zone and sulfide zones.

7.4.2.1 Martabe district geochemical signatures

The following section discusses the spatial variation analysis and shows the differing geochemical signatures for the Martabe district in general and specifically for the Purnama and Baskara deposits.

Gold

In the Martabe district, gold shows a range in concentration from the detection level to a maximum of 94 ppm Au with a mean of 0.88 ppm (Table 7.1). Oxide ore grades are up to 94 ppm Au with a mean of 1.32 ppm Au and sulfide ore contain up to 19.4 ppm Au with an mean of 0.46 ppm Au. The highest mean value for gold occurs in the transition zone (1.39 ppm Au) with maximum values up to 70 ppm Au.

For all Martabe samples, the range in Au content of the sulfide zone is generally similar to that in the oxide zone, although some very high grades occur (Table 7.2). This is simply reflected by a smaller population of data of high grade interval. The mean and median values of the oxide and sulfide zones are different, suggesting that supergene upgrading of the Au content within the oxide zone is significant. The presence of upgrading indicates mobilization of Au in the oxide zone. The correlation coefficient of some elements (Cu, Pb, Bi, As, Sb and Hg) with gold is decreasing as observed from the sulfide to oxide zone, but Au grade increases form sulfide to oxide zone (Table 7.3).

In the Martabe districts gold has a strong correlation with Ag, Pb and Sb and a moderate correlation with As, Cu, Hg and Te (Table 7.4A). In the sulfide zone, Au has a strong correlation with Cu, Ag, Pb, As, Sb and Hg; whereas in the oxide zone, Au has a strong correlation with Ag and Sb only. In particular for Au >0.2 ppm, the Au correlation with all elements is mainly moderate to weak; however, a strong correlation Au-Te is indicated (Table 7.4B).

From logging and field observations, higher gold concentrations occur at the contact between the volcanic and dacitic flow dome within the breccias. Overall zone, Au mineralization in the Martabe district is strongly coincident with the siliceous alteration zone within envelopes of advanced argillic alteration. The high grade zone is mostly found in the lithology-controlled zones, averaging tens of grams of Au over several meters along the contact between clay-altered and siliceous-altered breccias or at the contact between the

volcanic and dacitic flow dome with the breccias. However, Au grades may be much higher, as in structurally-controlled zones in the Purnama orebody (Figure 7.35), but these comprise only a very small proportion of the total mineralization.

In addition to the alteration, the degree of brecciation and the iron content are also believed to influence the Au grade. But it is not a clear linear relationship between Au and degree of brecciation and iron content or rock type at Martabe. These characteristics were determined the Purnama, Baskara and Gerhana sections. At Baskara, from the drillcore observation suggests high grades of Au are found within breccias or at the contact between breccias and more competent rock. At Gerhana, high Au grades accompany Fe-oxides and the high degrees of brecciation. However, on a district scale, many areas with strong development of Fe oxides and hydrothermal brecciation lack Au mineralization.

Base Metals, Silver, Arsenic, Antimony, Mercury and Barium

Antimony values range up to 4600 ppm with a mean of 26 ppm (Table 7.1). Within the sulfide zone, the Sb-Au correlation is 0.64 (Table 7.3). This correlation may suggest an association of gold with luzonite. Antimony correlates well with Ag, Cu, and As.

In the sulfide zone, the As-Pb correlation is very weak, but Cu-Ag is anomalous. Mercury and Ba have no strong correlation with any element. Mercury has shown moderate correlation with Au and Ag (Table 7.4B). Te has a moderate correlation with Au, Ag and Cu and a strong correlation with Bi and Sb. With respect to gold, Pb, Sb and Ag consistently have strong positives correlation coefficients and have high concentrations in the sulfide, transition and oxide zone, whereas Cu and As are only anomalous in the sulfide zone (Table 7.4A). The As-Pb correlation is very weak in the sulfide zone, but Cu-Ag has a positive correlation.

Te has a moderate correlation with Au, Ag and Cu, but has a strong correlation with Bi and Sb. Arsenic is strongly correlated with Sb (coefficient value=0.61) and Pb, but weakly correlated with Bi, Zn and Mo. For all Martabe samples, arsenic is strongly correlated with Sb (coefficient value = 0.61) and Pb, and weakly correlated with Bi, Zn and Mo. These high correlation coefficients can be explained by the presence of Au in luzonite. Mercury and Ba have no strong correlation to any element. Mercury has shown moderate correlation with Au and Ag (Table 7.4B).

Silver concentrations range up to 569 ppm, with a mean value of 7 ppm (Table 7.1). Ag has a strong correlation coefficient of 0.81 with Au in the sulfide zone, but only a correlation of 0.59 in the oxide zone (Table 7.3). Silver is present in both the oxide and sulfide

zones at Baskara and Gerhana. Silver generally correlates well with Au, Cu, Pb and Sb; moderate correlated with As and Te; and weakly with Ba, Bi, Hg, Ni and Mo (Table7.4A).

Copper has low mean value (143 ppm) (Table 7.1) and moderate correlation with gold (coefficient value of 0.4) (Table 7.3). Copper is weakly anomalous in the oxide zone, but strongly anomalous in the sulfide zone, where it correlates with Ag, Pb and Bi. At higher grades, copper shows a tendency to occur at the base of oxidation or within the sulfide zone. Copper decrease significantly from the sulfide and transition zone to the oxide zone (Table 7.2). This indicates that Cu is elevated the sulfide zone.

Lead assays range up to 8210 ppm with a mean value of 84 ppm (Table 7.1). Lead has a strong correlation with gold (correlation coefficient of 0.71) (Table 7.3). Lead is concentrated within the oxide zone. Lead also correlates with Sb and As. Zinc is not anomalous in most places. In contrast to Au, base metals have elevated values in the peripheral argillic alteration, even though geochemical data are sparse. This relationship is confirmed by the presence of base metal sulfides in the argillic alteration zones. Zinc occurs widespread surrounding the gold mineralization zone, as well as below the zone of oxidation or within the sulfide zone. Zinc shows a reverse relationship with gold as shown by the low correlation coefficient within the sulfide zone (Table 7.3).

Other elements

Molybdenum has a low correlation coefficient with Au and does not show a coherent relationship in all zone. In a broad context, Mo values of >2 ppm seem to correlate well with the presence of the breccia body (i.e., Figure 7.36 and 7.37).

Bismuth concentrations fall into the range from the detection level of 2.5 ppm to a maximum of 3820 ppm, with a mean of 10.4 ppm (Table 7.1). Although Bi shows a moderate correlation with Au with coefficient value of 0.38 (Table 7.3), bismuth has the same special association as the gold distribution (i.e., Figure 7.36).

Nickel values are up to 185 ppm with mean value of 9 ppm (Table 7.1). Nickel shows a correlation coefficient to gold of 0.16 within the sulfide zone (Table 7.3). Nickel is concentrated at the base of the oxidation zone or within the sulfide zone. The correlation of Ni with Au is also reflected in their spatial distribution as higher grades of Ni seem to be in the sulfide zone, and developed at the base or margin in the oxide zone.

Barium has weak correlations with all elements, but is only moderate correlated with Sb. A strong negative correlation of Au is observed with Zn and Mg.

7.4.2.2 Purnama metal zonation and multi-element geochemical signatures

The Purnama deposit is elongated in a northwest direction and measures approximately 1200 m x 400 m in a zone between the southern margin of the diatreme-dome complex and the northwest-striking Purnama fault. As described previously, mineralization is mostly hosted in siliceous and advanced argillic altered rocks.

The data base used in this study comprised 2956 data records from 27 drillholes. Each correlation coefficient with any Au and >0.2 ppm of Au are tabulated in the Tables 7.5a and 7.5b. A cross section along line 167200mN was selected as a type section to examine the distribution and zoning of precious and base metals at Purnama. This section was also used in the detail examination of geology and alteration, and therefore has the most geological constraints as shown in Figure 7.36. Precious and base metals are confined to the main Purnama fault (main structure). Cu values are elevated across the whole structure, in particular the east Purnama structure. In general metal distribution on the 167200mN section is consistent with the pattern observed for the whole of Purnama deposit (Figures 7.35 and 7.36).

7.4.2.2.1 Purnama metal zonation

Gold occurs as a sub-horizontal northeast dipping zone that corresponds to the siliceous alteration zone and Te, Ba, Sb, Hg, Pb, and Bi, and is within the broader halo of Ag, As and Mo. Chromium has a distribution similar to that of Ag, but less broad. Gold distribution is also structurally controlled as seen at section 507000 mE. The metal zonation and siliceous alteration distribution highlights structures/faults as sites of hydrothermal fluid flow.

A strong Au-Te association throughout the deposit might be caused by Te replacing S in enargite-luzonite and the presence of other Au-Te association minerals (e.g., cavalerite). The Au-Te association is not present at depth, where Au might be occurring as electrum. Gold and Bi correlate well in places where Bi- bearing minerals (i.e., bismuthinite) occur.

The ratio AuCN (Au assay by Cyanide method) and AuFa (Au assay by Fire Assay method) correlates well with the visual oxidation zone. The ratio shows Au recovery is moderately high (>0.7) above 300 masl and indicates that it is possible to leach gold out of sulfide. In the oxidation zone, secondary Au is partitioned from the more mobile Cu, which was transported downwards and to a lesser extent, laterally. The distribution of Ag is similar to that of Cu but is boarder, both laterally and vertically.

The widespread Ag-Cu-As-Sb-Au association is related to the enargite-luzonite mineral assemblage. Copper and As correlate moderately well in most western part of the Purnama deposit. In the eastern part, Cu without As or Sb occurs where covellite is the dominant Cu-sulfide. Comparison of As to Sb shows the distribution and content of enargite to luzonite. Sb anomalies lie with and above the As, indicating the deposition of low temperature luzonite and/or stibioluzonite at shallower levels in the system than enargite.

Zinc and Mg display an inverse relationship with respect to the alteration and Au. In the illitic alteration zone, the Zn and Mg values are elevated, but in the siliceous and advanced argillic alteration zone, the Zn and Mg values progressively decrease inwards, possibly recording the intensity of leaching that may indicate conduit fault structures as seen at 507000 mE. It may also suggest low concentration or absence of Zn in the mineralizing fluids.

Nickel correlates well in weakly-unaltered basaltic volcanic (Tmav) in the west. Although it is not shown in Figure 7.35, the broad distribution of S relates to the overall distribution of sulfates, sulfides and native S. Sulfur is generally coincident with Cu and Au occurrences except in the oxidized portions of the deposit. Sulfur and Cu were leached and remobilized vertically and laterally.

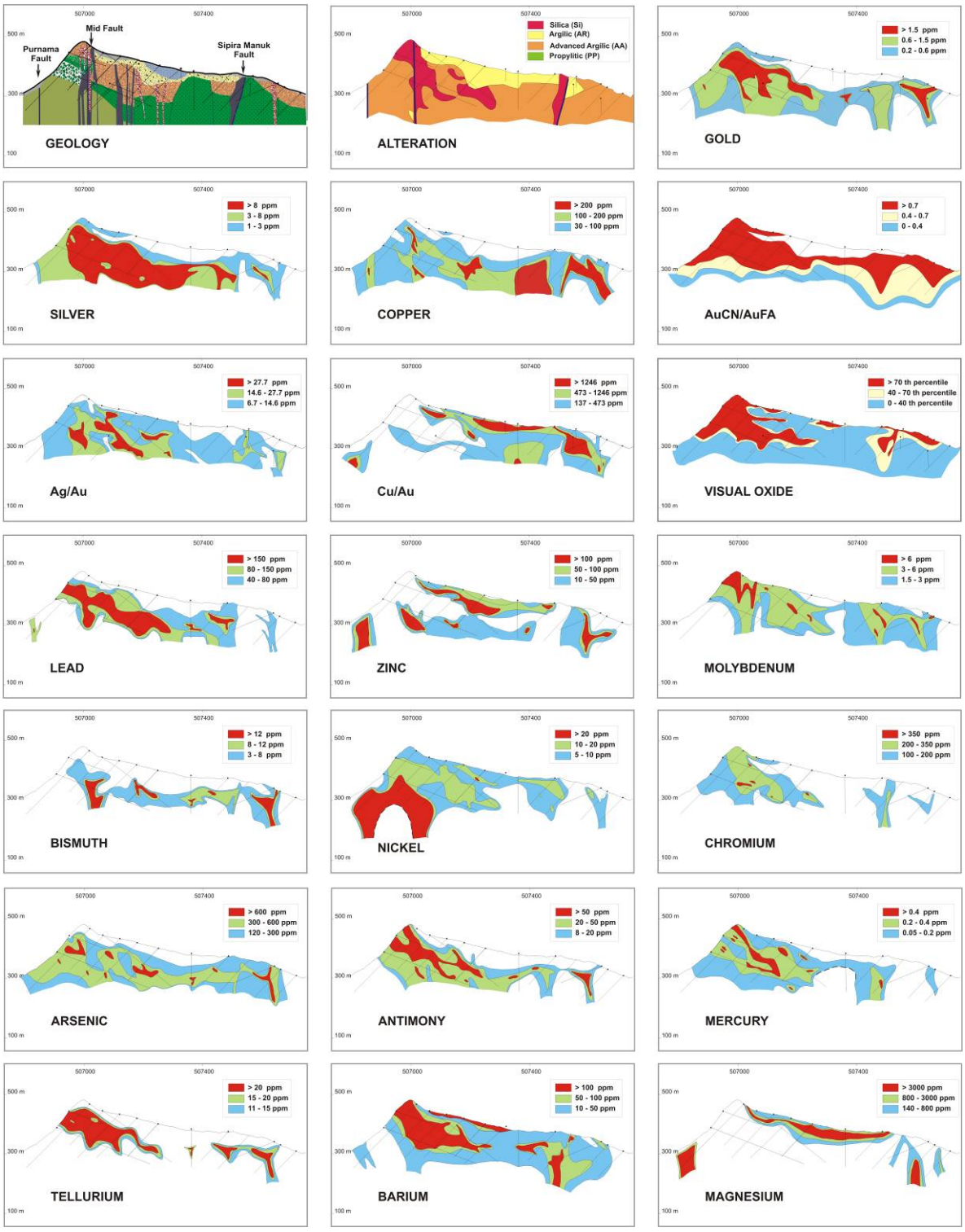

Figure 7.35. Metal zonation at Purnama (section 167200 mN).

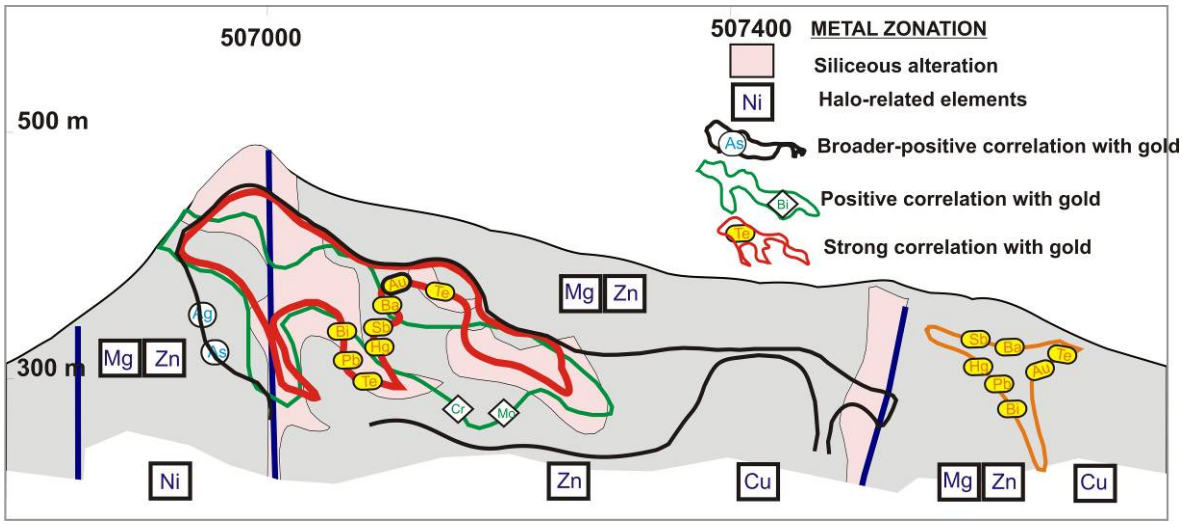

Figure 7.36. Schematic representation of metal zoning at Purnama. Siliceous alteration and Te, Ba, Sb, Hg, Pb, Bi and Au values correlate well. Silver, As, Mo and Cr are also correlated with Au but have a broader, more lateral dispersion. Zinc, magnesium and nickel form a halo to the gold mineralization.

7.4.2.2.2 Purnama multi-element geochemical signatures

Gold

For all the Purnama samples, gold has a general strong positive correlation with Ag, Pb, Sb, As and Te and a moderate correlation with Cu and Hg. In the sulfide zone, Au has a strong correlation with Ag, Cu, Pb, As and Sb; whereas in the oxide zone, Au has a good correlation with Ag, Sb, As and Te (Tables 7.5 and 7.6). For all the Purnama samples, gold shows up to a maximum of 51 ppm Au with a mean of 1.2 ppm (Table 7.5A). The higher mean Au value is found in the oxide zone (1.83 ppm Au) with maximum values up to 51 ppm Au. The transition zone returns a gold value range to a maximum of 47.8 ppm Au with a mean value of 1.8 ppm Au. Gold in the sulfide zone has values up to 19.4 ppm Au with low mean value (0.63 ppm Au). In particular for gold >2 ppm (Table 7.4B), the Au correlation with all elements is analysed is mainly moderate to weak; however, a strong correlation for Au-Te-Sb is indicated.

The correlation coefficients of all the elements analysed with Au generally decreases from the sulfide to oxide zone, except for Mo (Table 7.5). However, Au grade increases from the sulfide to the oxide zone (Table 7.5). Most high Au concentrations appear to occur along the contact between clay-altered and siliceous altered breccias. Overall, Au mineralization in the Martabe district is strongly coincided with the siliceous and advanced argillic alteration.

Nickel occurs at the base of the oxidation zone or within the sulfide zone. Similarly, higher Cu concentrations occur at the sulfide zone or at the margin with the oxidation zone. A strong negative correlation of Au is observed with Zn and Mg. Zinc occurs surrounding the Au mineralization zone, as well as below the zone of oxidation or within the sulfide zone. Magnesium correlates well with the clay-altered breccia and unaltered host rocks.

Table 7.5A Correlation coefficients for elements with gold in Purnama drillcore

	All Samples			Sulfide			Transition			Oxide		
Element	n	Corr	Mean	n	Corr	Mean	n	Corr	Mean	n	Corr	Mean
AuFA	2956	1.00	1.19	1568	1.00	0.63	342	1.00	1.80	1045	1.00	1.83
AuCN	2201	0.88	0.87	1230	0.79	0.33	240	0.93	1.08	730	0.96	1.71
Ag	2956	**0.75**	14.37	1568	**0.82**	9.46	342	**0.71**	23.32	1045	**0.65**	18.83
Cu	2956	0.43	162.4	1568	**0.59**	215.2	342	0.44	158.12	1045	0.45	84.86
Pb	2956	**0.60**	136.1	1568	**0.60**	106.5	342	**0.72**	175.46	1045	**0.52**	167.67
Zn	2956	-0.43	101.6	1568	-0.37	177.5	342	-0.05	28.30	1045	-0.22	11.70
Mo	2956	0.31	3.3	1568	0.19	2.7	342	0.29	3.65	1045	0.44	3.98
Bi	2956	0.38	14.2	1568	0.39	11.0	342	0.33	17.03	1045	0.35	18.02
As	2956	**0.58**	327.2	1568	**0.63**	281.7	342	**0.68**	362.53	1045	**0.57**	384.06
Sb	2956	**0.74**	47.0	1568	**0.72**	27.8	342	**0.68**	64.77	1045	**0.68**	69.96
Hg	2463	0.49	0.24	1284	0.49	0.17	284	0.38	0.26	894	0.26	0.34
Te	2956	**0.57**	16.6	1568	0.49	13.0	342	**0.60**	17.27	1045	**0.59**	21.90
Ba	2956	0.20	113.6	1568	-0.06	51.2	342	0.20	101.71	1045	0.14	211.24
Ni	2956	-0.08	11.5	1568	0.11	15.5	342	0.06	11.34	1045	0.09	5.58
Cr	2956	0.31	130.9	1568	0.29	114.2	342	0.26	168.74	1045	0.28	143.51
Ca	2956	-0.71	2183.6	1568	-0.76	3767.0	342	-0.63	795.18	1045	-0.42	264.26
Mg	2956	-0.73	1242.1	1568	-0.76	2054.2	342	-0.67	465.5	1045	-0.60	278.6
Ag/Au			12.11			15.12			12.93			10.29
Cu/Au			136.82			344.01			87.67			46.39
Cn/FA			0.73			0.52			0.60			0.93

Table 7.5B Correlation coefficients for elements with gold (>0.2 ppm) in Purnama drillcore.

Element	All Samples			Sulfide			Transition			Oxide		
	n	Corr	Mean	n	Corr	Mean	n	Corr	Mean	n	Corr	Mean
AuFA	2139	1.00	1.61	894	1.00	1.05	315	1.00	1.95	930	1.00	2.05
AuCN	1510	0.91	1.24	649	0.85	0.57	216	0.96	1.19	645	0.98	1.92
Ag	2139	0.48	19.40	894	0.53	15.78	315	0.53	24.94	930	0.51	20.99
Cu	2139	0.17	195.3	894	0.26	313.2	315	0.35	165.69	930	0.38	92.0
Pb	2139	0.38	175.9	894	0.31	161.7	315	0.58	187.86	930	0.39	185.5
Zn	2139	-0.09	98.1	894	-0.11	215.2	315	0.24	27.90	930	0.16	9.3
Mo	2139	0.31	3.8	894	0.22	3.2	315	0.17	3.85	930	0.39	4.3
Bi	2139	0.36	18.6	894	0.36	17.3	315	0.36	18.27	930	0.36	19.9
As	2139	0.26	395.8	894	0.21	380.8	315	0.41	381.56	930	0.28	415.0
Sb	2139	0.60	62.9	894	0.55	45.2	315	0.63	69.63	930	0.59	77.7
Hg	1797	0.05	0.30	745	0.12	0.24	260	-0.06	0.28	792	-0.15	0.36
Te	2139	0.65	20.8	894	0.60	18.5	315	0.69	18.25	930	0.66	23.9
Ba	2139	0.28	132.8	894	0.21	54.7	315	0.21	105.62	930	0.17	217.2
Ni	2139	-0.06	11.2	894	0.04	16.5	315	-0.03	11.77	930	0.14	5.8
Cr	2139	0.19	157.5	894	0.15	153.5	315	0.14	179.27	930	0.24	154.1
Ca	2139	-0.07	154.4	894	-0.12	264.4	315	-0.04	83.33	930	0.06	72.8
Mg	2139	-0.08	126.0	894	-0.10	201.1	315	-0.14	73.3	930	-0.04	71.6
Ag/Au			12.02			15.08			12.78			10.27
Cu/Au			121.0			299.3			84.9			45.0
Cn/FA			0.77			0.55			0.61			0.94

Table 7.6A. Pearson Product-Moment Correlation for all samples from Purnama drillcore.

	AuFA	AuCN	Ag	Cu	Pb	Zn	Mo	Bi	As	Sb	Hg	Te	Ba	Ni	Cr	Ca	Mg
AuFA	1.00																
AuCN	0.88	1.00															
Ag	0.75	0.64	1.00														
Cu	0.43	0.26	0.51	1.00													
Pb	0.60	0.51	0.64	0.42	1.00												
Zn	-0.43	-0.52	-0.21	-0.01	0.00	1.00											
Mo	0.31	0.33	0.27	0.13	0.23	-0.08	1.00										
Bi	0.38	0.39	0.31	0.37	0.35	-0.10	0.18	1.00									
As	0.58	0.39	0.53	0.53	0.65	-0.12	0.12	0.31	1.00								
Sb	0.74	0.72	0.75	0.46	0.68	-0.21	0.29	0.46	0.55	1.00							
Hg	0.49	0.46	0.51	0.09	0.42	-0.26	0.15	0.06	0.29	0.49	1.00						
Te	0.57	0.66	0.44	0.37	0.42	-0.20	0.28	0.59	0.39	0.63	0.09	1.00					
Ba	0.20	0.36	0.19	-0.12	0.24	-0.19	0.13	0.15	-0.04	0.20	0.13	0.22	1.00				
Ni	-0.08	-0.26	0.15	0.23	0.05	0.36	0.20	0.03	0.02	0.03	-0.09	-0.10	-0.27	1.00			
Cr	0.31	0.27	0.35	0.19	0.26	-0.07	0.37	0.19	0.15	0.33	0.19	0.18	0.04	0.50	1.00		
Ca	-0.71	-0.55	-0.58	-0.37	-0.39	0.50	-0.09	-0.19	-0.47	-0.50	-0.50	-0.25	-0.04	0.16	-0.18	1.00	
Mg	-0.73	-0.57	-0.63	-0.38	-0.46	0.51	-0.14	-0.20	-0.52	-0.55	-0.57	-0.26	-0.03	0.15	-0.18	0.91	1.00

Table 7.6B. Pearson Product-Moment Correlation for Purnama drillcore samples (gold >=0.2 ppm)

	AuFA	AuCN	Ag	Cu	Pb	Zn	Mo	Bi	As	Sb	Hg	Te	Ba	Ni	Cr	Ca	Mg
AuFA	1.00																
AuCN	0.91	1.00															
Ag	0.48	0.35	1.00														
Cu	0.17	-0.03	0.37	1.00													
Pb	0.38	0.28	0.47	0.30	1.00												
Zn	-0.09	-0.31	0.22	0.29	0.32	1.00											
Mo	0.31	0.31	0.18	0.07	0.08	-0.03	1.00										
Bi	0.36	0.29	0.22	0.35	0.29	0.02	0.15	1.00									
As	0.26	0.15	0.28	0.48	0.59	0.19	-0.07	0.30	1.00								
Sb	0.60	0.52	0.62	0.36	0.56	0.14	0.24	0.42	0.45	1.00							
Hg	0.05	0.20	0.25	-0.22	0.17	0.02	0.04	-0.08	-0.08	0.21	1.00						
Te	0.65	0.63	0.34	0.32	0.35	-0.06	0.26	0.56	0.38	0.60	-0.10	1.00					
Ba	0.28	0.41	0.23	-0.18	0.27	-0.20	0.14	0.12	-0.02	0.21	0.16	0.21	1.00				
Ni	-0.06	-0.30	0.28	0.29	0.07	0.35	0.23	0.05	0.01	0.07	-0.07	-0.09	-0.27	1.00			
Cr	0.19	0.13	0.25	0.10	0.16	0.07	0.40	0.14	0.05	0.24	0.06	0.12	0.01	0.57	1.00		
Ca	-0.07	-0.14	-0.11	-0.03	-0.02	0.18	0.09	-0.03	-0.02	-0.12	-0.08	-0.03	-0.05	0.12	-0.02	1.00	
Mg	-0.08	-0.11	-0.19	-0.07	-0.06	0.18	0.10	-0.05	-0.07	-0.16	-0.09	-0.04	-0.03	0.11	0.02	0.78	1.00

Silver, Copper, Lead, Arsenic and Antimony

Silver has values up to 569 ppm with a mean value of 14 ppm (Table 7.1). The Ag occurrence is similar to gold, as indicated by a strong correlation coefficient of 0.82 in the sulfide zone that gradually decreases to 0.65 in the oxide zone.

Copper has a low mean value (162 ppm), but has a moderate correlation with gold (coefficient value of 0.43). Copper has a higher tendency to occur at the base of the oxidation zone or within the sulfide zone (Figures 7.35 and 7.36). Copper significantly decreases in concentration from sulfide and transition zones to the oxide zone. This relationship suggests copper mineralization has a tendency to concentrate in the sulfide zone.

Lead has a maximum of 8210 ppm and mean value of 136 ppm. Lead has a strong correlation with Au (correlation coefficient of 0.60). Higher grades of Pb are recorded within the oxide zone.

Arsenic assays are up to 7860 ppm with a mean value of 327 ppm. It has a strong correlation with Au. Antimony results are up to 4,600 ppm with mean value of 47 ppm. Antimony also has a strong correlation with Au (0.74).

Zinc, Molybdenum, Bismuth and Nickel

Zinc shows a reverse relationship with Au as shown by the negative correlation coefficient within the sulfide zone (Table 7.6A). A higher concentration of anomalous zinc seems to correlate with the clay-altered phreatomagmatic breccia unit, and also forms a general broad halo (Figures 7.35 and 7.36).

Molybdenum has a low correlation coefficient with Au. Molybdenum values correlate well with the breccia body (Figures 7.35 and 7.36).

Bismuth is up to 3820 ppm, with a low correlation coefficient to Au. Bismuth values increase in the sulfide zone. Nickel has low correlation with Au and seems to be concentrated in the sulfide zone, with local concentrations at the base or margin in the oxide zone.

7.4.2.3 Baskara metal zonation and multi-element signature

Baskara is situated within the diatreme-dome complex, with a northeast trend of approximately 400 m x 200 m. The alteration is mainly siliceous and advanced argillic in the quartz-phyric dacite and hornblende andesite. The multi-element database at Baskara comprises 2189 data records from 23 drilholes. Each correlation coefficient with gold content and >0.2 ppm gold is tabulated in the Tables 7.6A and 7.6B. A cross section along line OB-96 (16 drillholes) was selected as a type section to examine the element distributions and metal zoning (Figure 7.37). Schematic representation of metal zoning at Baskara is shown in Figure 7.38.

7.4.2.3.1 Baskara metal zonation

At Baskara, gold correlates well with Ag, As, Sb, Pb and Bi. At Baskara, the Au distribution clearly shows a structural control, following the distribution of the breccias and siliceous alteration. Copper and Pb form a broader halo than Au. A strong correlation between As and Sb indicates that enargite and luzonite are present in almost equal proportions. Tellurium correlates with Au in the near surface only, close to the same area where As and Sb are well correlated.

The ratio AuCN (Au assay by Cyanide method) and AuFa (Au assay by Fire Assay method) correlates very well with the visual oxidation zone. The ratio shows Au recovery is moderately high (>0.7) above 400 masl and indicates that it can possibly be leached from sulfides. In the oxidation zone, Cu values decrease, indicating that Cu is a mobile element.

Arsenic, Cu and Sb correlates moderately well at depth. Barium, Cr and Mo show a weak correlation with Au. Zinc and Mg values correlate with argillic alteration and a fault zone. The Zn and Mg values are elevated, but in the siliceous and advanced argillic alteration zones, Zn and Mg values are progressively higher in fault clay alteration. Nickel shows a very weak presence in this deposit.

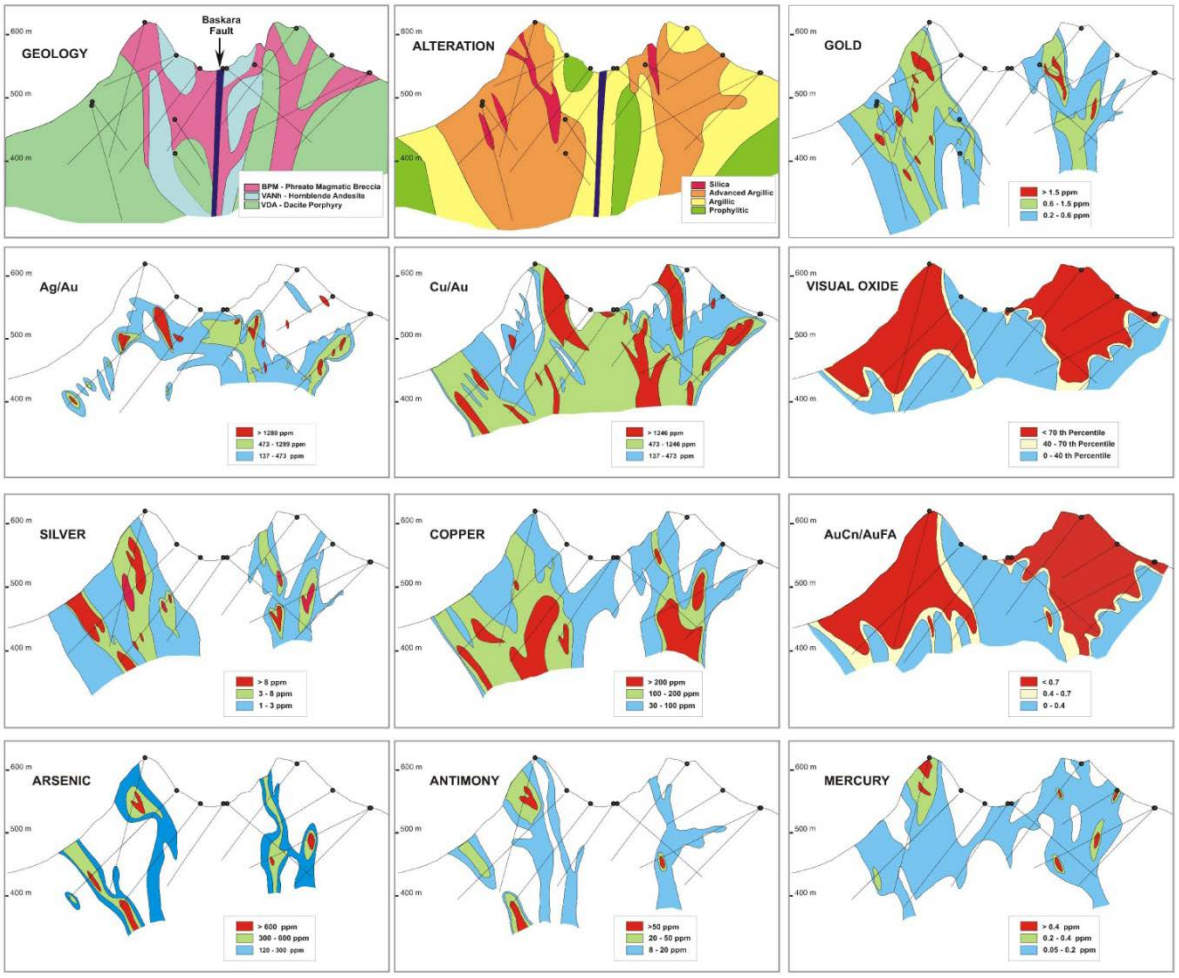

Figure 7.37. Metal zonation at Baskara (cross section OB-96).

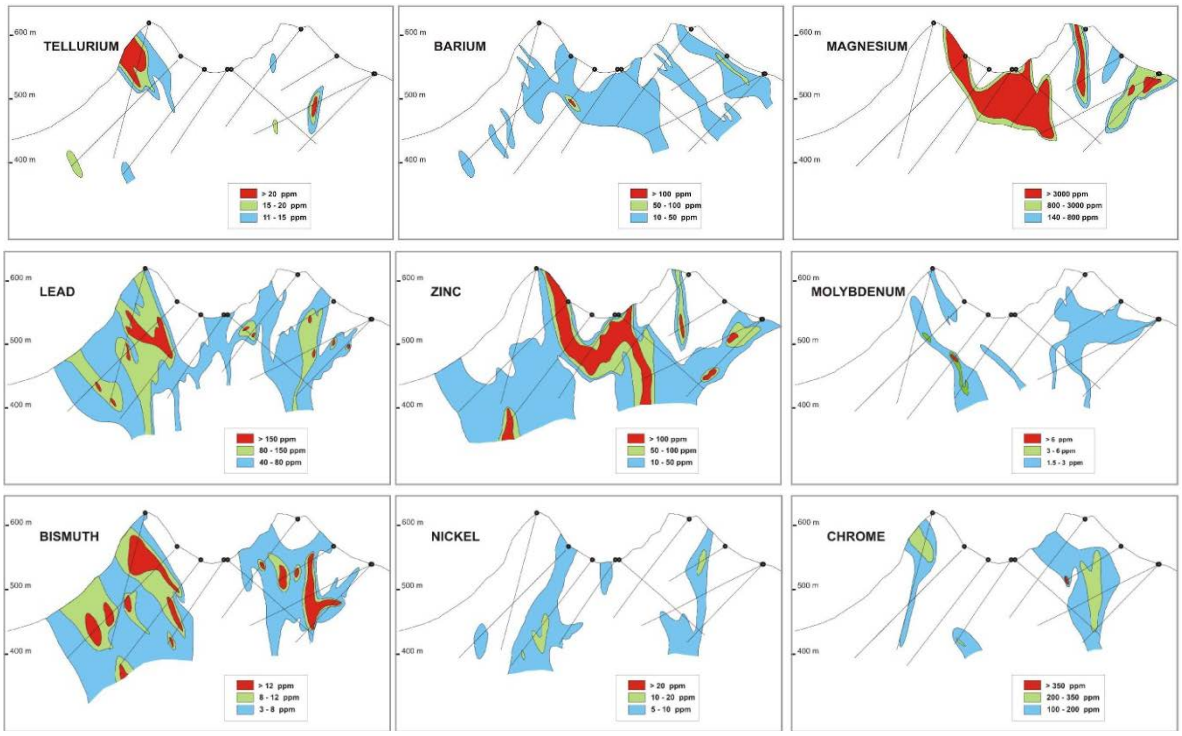

Figure 7.37. Metal Zonation at Baskara (cross section OB-96) (continued).

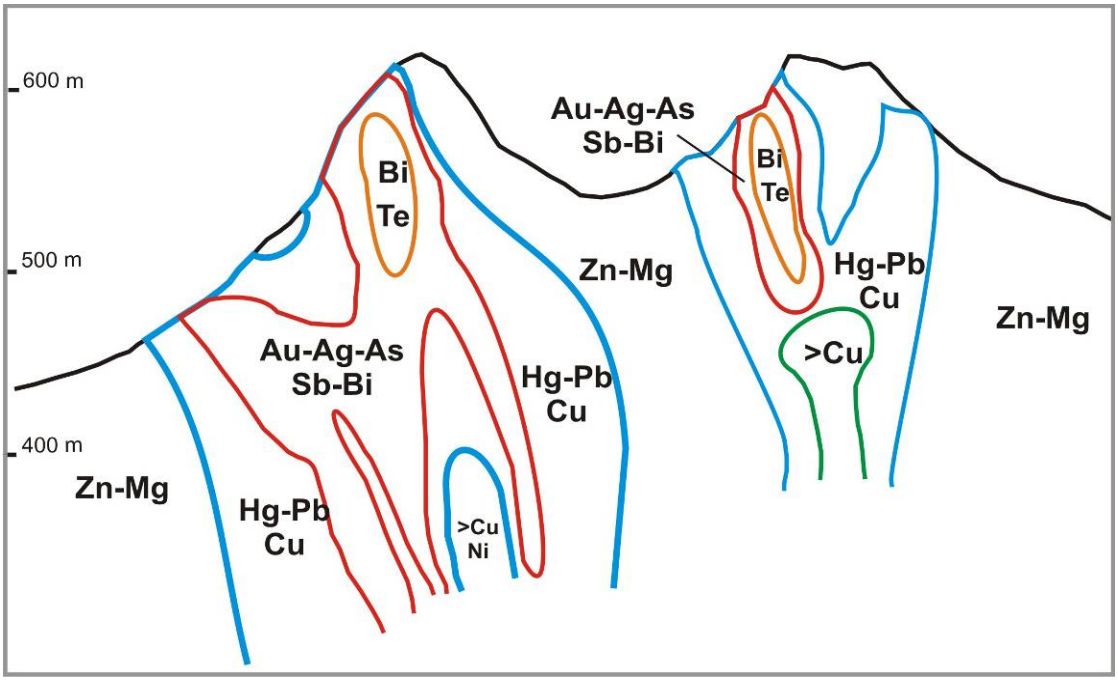

Figure 7.38. Schematic representation of metal zoning at Baskara. Gold correlates well with Ag, As, Sb, Pb and Bi. Copper, Hg and Pb form a broader halo than Au. Bismuth and Te correlate with Au in the near surface. The Cu and Ni concentration increase with depth.

7.4.2.3.2 Baskara multi-element signature

Gold

At Baskara gold has a general strong correlation (coefficient >0.5) with Ag, Pb and As (Table 7.7a). In the sulfide zone, Au has a strong correlation with Ag, Cu, Pb, Bi, As, Hg and Ni, whereas Au only has a strong correlation with Ag in oxide zone gold.

Gold has values up to 25 ppm, with mean of 0.96 ppm Au (Table 7.1). Higher gold values are found in the transition zone with a mean value of 1.42 ppm and maximum values of 12.4 ppm. The oxide zone returns Au values up to 25 ppm with a mean value of 1.18 ppm. Gold in the sulfide zone has a maximum of 8.32 ppm with a mean value of 0.52 ppm. At Baskara, higher Au concentrations occur in the contact zone between the dome and breccia body. This Au mineralization also coincides with the siliceous alteration within zones of broad advanced argillic alteration. For gold >2 ppm (Table 7.7b), the correlation of all elements with gold is generally moderate to weak; however a strong correlation is shown with Ag in sulfide zone. In general, the correlation coefficient for elements with Au decreases from the sulfide through to the oxide zone.

Silver, Copper, Lead, Arsenic and Antimony

Silver ranges from the detection level to a maximum of 69.5 ppm, with a mean of 3.14 ppm. The distribution of Ag is similar to that of gold (Figure 7.38). The mean value for Ag is highest in the transition zone (Table 7.3). The correlation coefficient of Ag within the sulfide zone (0.85) gradually decreases to 0.53 in the oxide zone (Table 7.3).

Copper is up to 1.28% with mean of 226 ppm, and has a moderate correlation with gold (0.45).The highest mean value for copper is found in the transition zone with a value of 425 ppm, while a mean value for copper at the sulfide zone of 410 ppm and 104 ppm in the oxide zone.

Lead has the maximum value of 2300 ppm and a mean value of 70 ppm. There is strong correlation of Pb with Au (0.50). Lead is concentrated in the oxide zone.
Arsenic ranges from 2.5 ppm to a maximum of 4580 ppm with a mean value of 147 ppm. Arsenic has a strong correlation with Au (0.68) in the sulfide zone. Antimony is up to 446 ppm with a mean of 7.66 ppm. Antimony has a moderate correlation with Au (0.44).

Table 7.7a Correlation coefficients for elements and ratios with Au for Baskara drillcore samples. Red letters indicate strong correlation with Au (coefficient >0.5).

	All Samples			Sulfide			Transition			Oxide		
Element	n	Corr	Mean	n	Corr	Mean	n	Corr	Mean	n	Corr	Mean
Au	2188	1	0.96	732	1	0.52	140	1	1.41	1316	1	1.16
Ag	2189	0.657	3.14	732	0.85	2.5	140	0.675	5.63	1317	0.53	3.2
As	2189	0.503	146.7	732	0.684	146.2	140	0.407	226.2	1317	0.379	138.5
Bi	2189	0.438	11.6	732	0.557	7.6	140	0.436	16.57	1317	0.336	13.29
Cu	2189	0.446	226.4	732	0.796	410.1	140	0.508	422.5	1317	0.311	103.5
Ni	2189	0.232	4.1	732	0.514	6.24	140	0.422	5.75	1317	0.352	2.7
Pb	2189	0.504	70.02	732	0.714	45.73	140	0.243	66.7	1317	0.278	83.9
Mg	2189	-0.6	1522	732	-0.82	4338	140	-0.51	306.1	1317	-0.22	85.76
Zn	2189	-0.47	30.38	732	-0.62	70.29	140	-0.41	18.26	1317	-0.17	9.5
Sb	2189	0.438	7.85	732	0.461	0.461	140	0.415	12.12	1317	0.125	1.93
Mo	2189	0.161	1.87	732	0.154	0.154	140	0.286	2.07	1317	0.428	7.66
Ag/Au	2188	-0.59	13.58	732	-0.61	13.94	140	-0.65	17.48	1316	-0.57	12.96
Cu/Au	2188	-0.7	1136	732	-0.55	1930	140	-0.7	1371	1316	-0.76	669.4
CN/FA	2194	0.043	63.87	733	0.061	5.75	140	-0.06	52.73	1321	-0.16	97.29

Table 7.7b.Correlation coefficients for elements and ratios with Au (>0.2 ppm) for Baskara drillcore samples. Red letters indicate strong correlation with Au (coefficient >0.5).

	All Samples			Sulfide			Transition			Oxide		
Element	n	Corr	Mean	n	Corr	Mean	n	Corr	Mean	n	Corr	Mean
Au	1222	1	1.68	306	1	1.19	94	1	2.1	822	1	1.81
Ag	1222	0.402	4.96	306	0.545	5.3	94	0.393	7.54	822	0.401	4.55
As	1222	0.26	208.8	306	0.316	276.8	94	0.129	297.9	822	0.28	173.3
Bi	1222	0.335	15.52	306	0.205	13.1	94	0.353	21.8	822	0.359	15.72
Cu	1222	0.132	359.2	306	0.258	900.4	94	0.08	575.9	822	0.206	132.9
Ni	1222	0.142	5.16	306	-0.05	9.44	94	0.253	6.98	822	0.276	3.36
Pb	1222	-0.02	89.56	306	0.048	77.2	94	-0.24	77.1	822	0.009	95.6
Mg	1222	-0.64	66.4	306	-0.12	113.4	94		50	822	0.034	50.8
Zn	1222	-0.13	10.92	306	-0.05	18.9	94	-0.15	10.37	822	-0.13	8.02
Sb	1222	0.404	11.62	306	0.372	13.87	94	0.272	15.84	823	0.436	10.3
Mo	1222	0.157	1.98	306	0.095	1.86	94	0.391	2.34	823	0.144	1.99
Ag/Au	1222	-0.28	4.52	306	-0.26	5.5	94	-0.51	6.64	822	-0.26	3.92
Cu/Au	1222	-0.44	350.1	306	-0.35	876.6	94	-0.57	509.7	822	-0.51	135.9
CN/FA	1222	0.021	71.2	306	0.095	8.54	94	-0.01	52.16	822	-0.21	96.73

Zinc, Molybdenum, Bismuth and Nickel

Zinc has a maximum of 2030 ppm with a mean value of 30 ppm (Table 7.1). Zinc has a inverse relationship with gold. Figure 8.34 illustrates how Zn forms a broad halo.

Molybdenum is up to 43 ppm, with a mean of 1.88ppm. A broad molybdenum (>2 ppm) zone correlates well with the phreatomagmatic breccia body.

Bismuth is up to 986 ppm with a mean of 11.6 ppm (Table 8.1). Bismuth shows a good correlation with Au, with coefficient value of 0.56. Bismuth has a similar distribution to Au.

Nickel ranges from a detection level of 1ppm to the maximum of 36 ppm, with a mean of 4.1 ppm. Nickel has a good correlation with Au (0.56) within the sulfide zone. But this relationship decreases at the oxide zone.

7.5. Discussion and Conclusion

Development of the main fault (i.e., Purnama and Pelangi faults) in Martabe was crucial for the emplacement of the intrusions and subsequent mineralization at Martabe. In addition, syn-mineral faulting, brecciation and fracturing provided numerous permeable zones within the altered rocks allowing enhanced movement of metal-bearing fluids and localization of Au. The Purnama deposit is a composite structurally-lithology controlled, while Baskara is more structurally controlled system.

In general multi-element data from Baskara and Purnama shows a strong correlation between Au and Ag. While As, Sb, Te and Pb have higher levels at Purnama and have a stronger correlation with Au than at Baskara, Baskara has higher Cu and Bi levels and greater positive correlation with Au suggesting it may be closer to the mineralising fluid source. Nickel is concentrated at the base of the oxidation zone or within the sulfide zone. Similarly, higher Cu concentrations occur in the sulfide zone or at the margin with the oxidation zone. A strong negative correlation of Au is observed with Zn and Mg.

Zinc and Mg occur surrounding the gold mineralization zone, as well as below the zone of oxidation or within the sulfide zone. The occurrence of these elements correlates well with the argillic altered rock and unaltered host rocks in both Purnama and Baskara deposits.

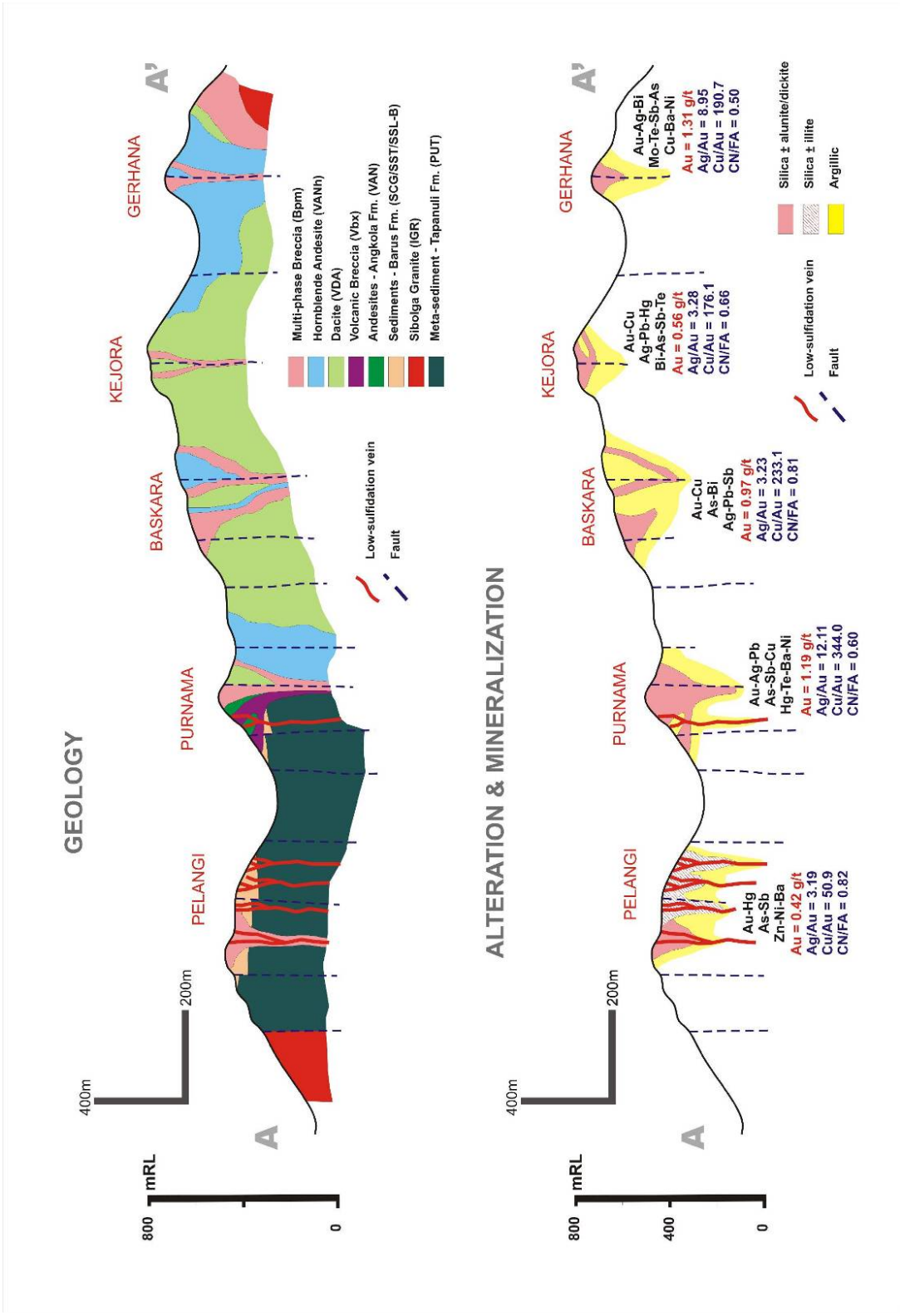

Figure 7.39. Schematic long section illustrating the geology, alteration and multi-element metal zoning for each deposit/prospects in the Martabe district. Correlation coefficients are calculated using Pearson product.

CHAPTER 8

THE TRACE ELEMENT COMPOSITION OF PYRITE AND ENARGITE

8.1 Introduction

At Martabe, gold is rarely observed in either hand samples or via optical microscopy, suggesting that the sulfide and sulfosalt minerals contain significant sub-microscopic gold. In general, in many similar high-sulfidation systems pyrite and enargite occur as the primary sulfide and sulfosalt phases, with lesser amounts of tetrahedrite-tennantite, galena and tellurides. Enargite is intimately involved with the Au-stage mineralization in many high-sulfidation systems (Hedenquist et al., 1998; Arribas et al., 1995; Claveria, 2001). In other studies, the distribution of Au is also recognized in the ore-stage pyrite of the high-sulfidation Au-Ag-(Cu) deposits (Chounirard et al., 2005; Rae and Davidson, 2006). However, pyrite has also occurred as a Au carrier in sediment-hosted deposits (Davidson, 2006; Large et al., 2009).

The development of laser ablation ICP-MS (LA-ICP-MS) offers an inexpensive and reliable method for in-situ microanalyses of a diverse suite of elements at low detection limits. Several studies have applied this technology to the examination of trace elements in sulfides, in particularly pyrite (Davidson, 2006; Large et al., 2009), while the trace element chemistry of enargite has been rarely investigated (Deyell et al., 2007). No detailed mineralogical geochemical trace element studies have been previously undertaken on samples from Martabe.

Martabe provides a good case study to investigate the trace element composition of pyrite and enargite using LA-ICP-MS and electron microprobe (EMP) techniques (Figure 8.1). In this chapter, LA-ICP-MS analyses of trace element concentrations in pyrite and enargite from the Au-stage of the paragenesis from the Martabe gold district are reported and discussed. Particular attention was placed on the presence of submicroscopic gold in pyrite and enargite.

8.2 Methods of analysis

The sample suite used in this study was collected from drill core samples from deposits throughout Martabe district, including the Purnama, Baskara and Gerhana depos-

its/prospects (Figure 8.1). The main criterion used for sample selection was to obtain samples from ore zones (Au-stage mineralization) associated with semi-massive sulfide, advanced argillic or siliceous alteration. Ore microscopy was undertaken mainly to ascertain the textures as well as the temporal relationships of pyrite and enargite to other sulfides minerals.

Prior to LA-ICP-MS analysis, a set of the pyrite (n=3) and enargite (n=8) samples were analyzed by electron microprobe (EPM) at the CSL, University of Tasmania to determine their major and selected trace element compositions. The sample suite of pyrites (n=19) and enargite (n=10) were analyzed by LA-ICPMS at CODES to determine their trace element compositions. 141 pyrite and 98 enargite grains were examined (Figure 8.1; Appendix 5). These samples were analyzed for 26 elements: Ti, Cr, Mn, Fe, Cu, Co, Ni, Zn, As, Se, Zr, Mo, Ag, Cd, Sn, Sb, Te, Ba, La, W, Au, Tl, Pb, Bi, Th and U. Beam size varied between 30 and 40 μm with mostly 40 μm, depending on pyrite and enargite grain size. Multiple grains were analyzed from each sample, and the number of analysis spots per grain was dependent on the crystal size. Data reduction and quantification used stoichiometric Fe for pyrite and Cu for enargite as the internal standard. Detection limits (averaged over all analyses) for the LA-ICP-MS data are also given in Appendix 8.1. Details of the LA-ICP-MS methodology, including descriptions of instrumentation, sample preparation, laser analysis, data reduction and interpretation are given by Danushevsky et al. (2006).

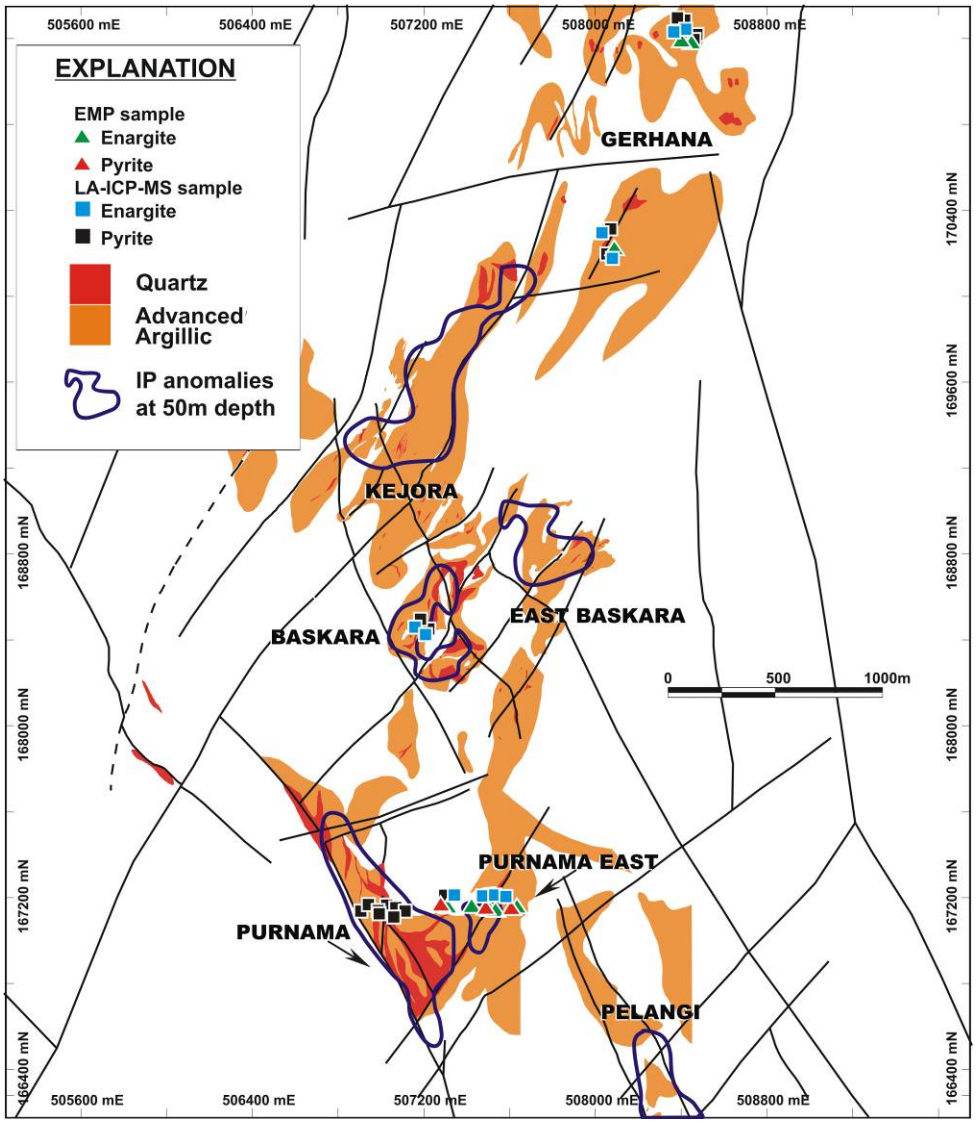

Figure 8.1. Map showing the location of all pyrite and enargite samples analyzed by EMP and LA-ICP-MS. Sample locations are superimposed on areas of siliceous and advanced argillic alteration and the resistivity anomalies.

8.3 Pyrite

8.3.1 Morphology and occurrence

A summary of the observations made from the ore microscopy study of pyrite is given. Pyrite is the most ubiquitous sulfide and most complex in term of its morphology. Observations show a range of textural features that seem to indicate several generations of pyrites. Pyrite occurs as disseminations, in veinlets and in breccia cements that commonly occur with siliceous and advanced argillic alteration, and in localized overgrowth zones that occur mainly in the semi-massive sulfide.

Three groups of pyrite are observed, based on different morphologies or textures:

1. An early stage (stage-1) pyrite that is typically subhedral to euhedral, disseminated, with inclusion or inclusion free, 10-300 μm, and forms as clusters around sites of former mafic phenocrysts in the host rock. This pyrite is present in all mineralized and altered zones, but is more abundant and coarser-grained in the silicified rocks, with zones of pyritohedral overgrowths (Figure8.2). The pyrite is mostly homogeneous and may be less pitted.
2. A second stage (stage-2) pyrite is commonly identified by a poor polish and abundance of pits (10–40 vol. %). This pyrite is usually dark yellow, poorly crystalline, anhedral and porous and commonly surrounds the earlier stage of pyrite (Figure 8.3). This second stage pyrite is also associated with brecciation and/or leaching of earlier stage pyrite and mainly occurs in the semi-massive sulfide.
3. The last generation (stage-3) pyrite is well crystallized, moderate to coarse grained and has a clean, polished surface. It forms cubes or is irregular in shapes. This pyrite mostly occurs in veins, fills vugs or fractures and surrounds the stage-1 and stage-2 pyrite (Figure 8.4).

8.3.2 EPM results

A summary of the EPM analysis data of pyrite is given in Table 8.1 and Appendix 5. Analyses indicate near-stoichiometric pyrite compositions for the majority of samples analyzed. The Cu contents are variable, with up to 3.2 wt % in one sample (sample EMP064-85.2 C4). In general, for most EPM analyses, concentrations of most minor elements (As, Au, Ag, Zn, Bi and Te) are below detection limits.

For the stage-1 pyrite, EMP analyses indicate no compositional variations and the growth discontinuity texture is sharp. The EMP results demonstrate that stage-1 subhedral-euhedral pyrite has no detectable Au, whereas the stage-2 pyrite has significant concentrations of Cu (up to 3.2 wt. %) and 0.04 wt.% of Sb. In other high-sulfidation systems, zoned pyrite has been also observed and results from early alteration (Turner, 1986; Chouinard et al., 2005).

Table 8.1. Summary of EMP data for individual grains of selected pyrite samples (in wt. %). Lines (-) indicates below detection limit.

Elements Sample_Id	Pyrite Stage	Fe (%)	As (%)	S (%)	Au (%)	Cu (%)	Zn (%)	Pb (%)	Bi (%)	Ag (%)	Sb (%)	Te (%)	Se (%)	Total
EMP198_194.8 C1a	1	45.36	-	53.31	-	0.08	-	-	-	-	-	-	-	98.75
EMP198_194.8 C1b	1	45.52	-	53.30	-	0.07	-	0.03	-	-	-	-	-	98.93
EMP198_194.8 C1c	1	45.32	-	53.45	-	0.09	-	-	-	-	-	-	-	98.86
EMP198_194.8 C3e	2	44.77	-	53.67	-	0.19	-	-	-	-	-	-	-	98.59
EMP198_51.8 C1a	2	43.62	-	53.13	-	1.91	-	-	-	-	-	-	-	98.62
EMP064_85.2 C3a	2	45.18	-	53.58	-	0.74	-	-	-	-	-	-	-	99.50
EMP064_85.2 C2b	2	44.41	-	54.22	-	0.48	-	-	-	-	-	-	-	99.07
EMP064_85.2 C2c	1	45.82	-	53.94	-	0.06	-	-	-	-	-	-	-	99.76
EMP064_85.2 C4	2	42.68	-	53.43	-	3.21	-	-	-	-	0.04	-	0.05	99.41
EMP064_85.2 C2	2	43.80	-	53.32	-	2.33	-	-	0.10	-	-	-	0.05	99.60

Two pyrite samples (64_68.5 and 198_51.8) are associated with enargite. In these pyrites, Cu content is variable with no significant As content. The Se is slightly elevated (~540 ppm) in some pyrite grains, but this is close to the detection limit of the electron microprobe for Se (400 ppm).

8.3.3 LA-ICP-MS results

LA-ICP-MS microanalyses from 19 samples produced 141 pyrite analyses. The average compositions from each sample are presented in Appendix 5. Direct comparison between the LA-ICP-MS and EPM analyses data cannot be made, because the sample size of the two techniques is significantly different. However, only Cu values are consistently high in both techniques. The LA-ICP-MS analyses provide a better estimate of the bulk composition of individual pyrite grains and can be used to analyse across small zones of compositional variability.

The compositional variability in individual pyrite grains can be recognized from the LA-ICP-MS data as a result from either inclusion and/or growth zones, although the samples can exhibit relatively simple LA-ICP-MS compositional patterns (Figures 8.5 and 8.6). Many elements are contained in small mineral inclusions (<5 μm) within the pyrite. Only a few elements are present as solid solution within the pyrite structure (Figure 8.5). The chalcophile elements (As, Cu, Pb, Sb, Bi, Sn, Sb and Te) are generally concentrated within mineral inclusions (Figure 8.6). The least mobile lithophile elements (Ti, Zr, Cr) tend to occur in various resistant phases (zircon, rutile) and were incorporated during the pyrite growth.

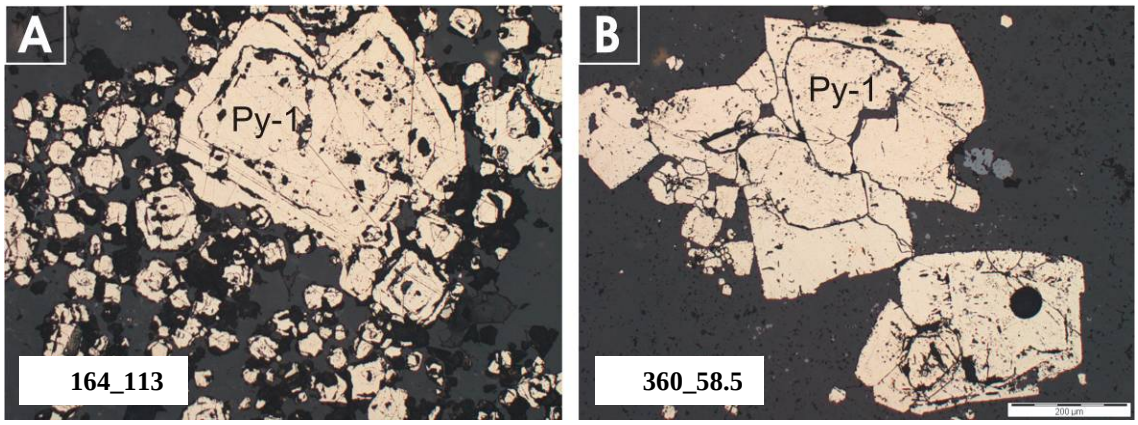

Figure 8.2. Two images showing zonation of stage-1 pyrite, pyritohedral overgrowths in siliceous alteration. Black spot in (B) is LA-ICP-MS analysis location. Sample 164_113 and 360_585 taken from Purnama

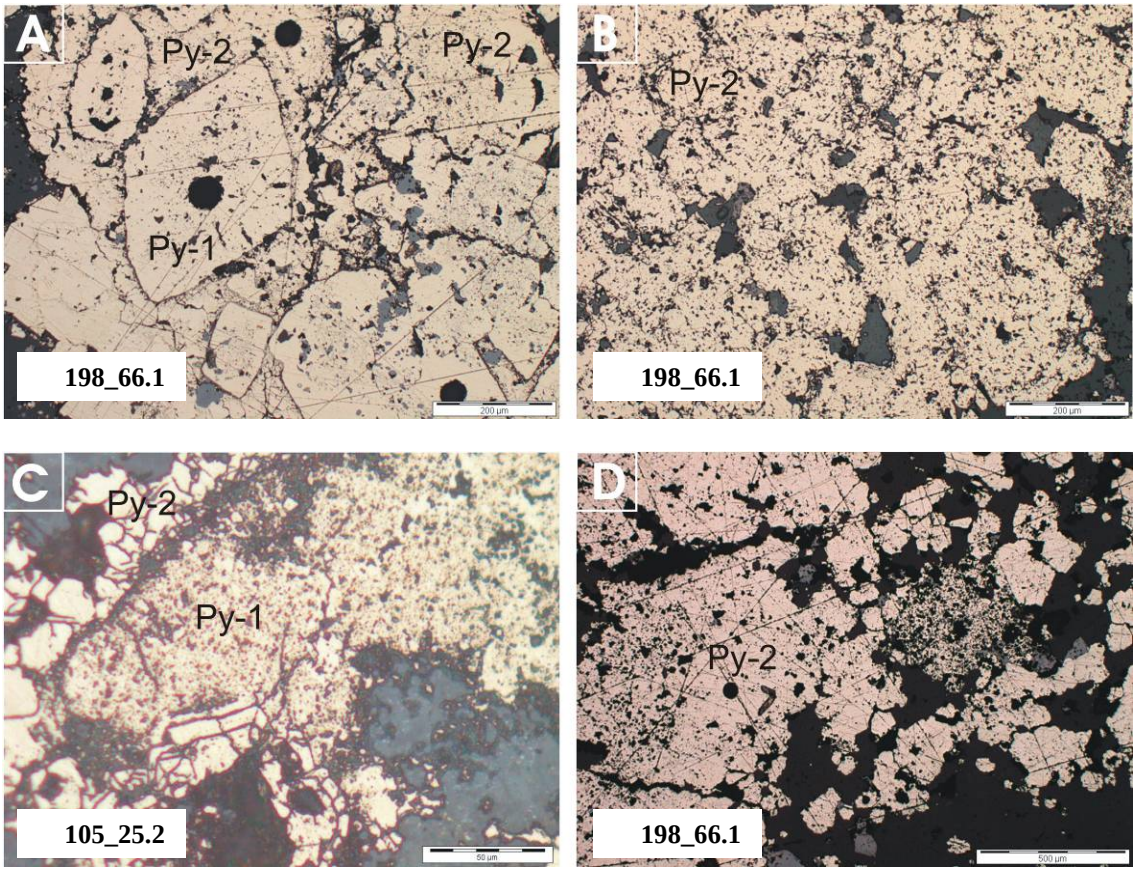

Figure 8.3. (A) Stage-1 of pyrite (Py-1) enclosed by fine overgrowths of an intensely pitted, poorly crystalline stage-2 pyrite (Py-2). (B) Stage-2 pyrite with a poorly crystalline, abundance of void space (10-40 vol.%) and spongeous-like texture. (C) Stage-2 pyrite surrounded by well crystalline stage-3 pyrite (Py-3). (D) Stage-2 pyrite with abundant void space or pits. Black spot in (B) is LA-ICP-MS analysis location. Sample 198_66.1 and 105_25.2 taken from Purnama.

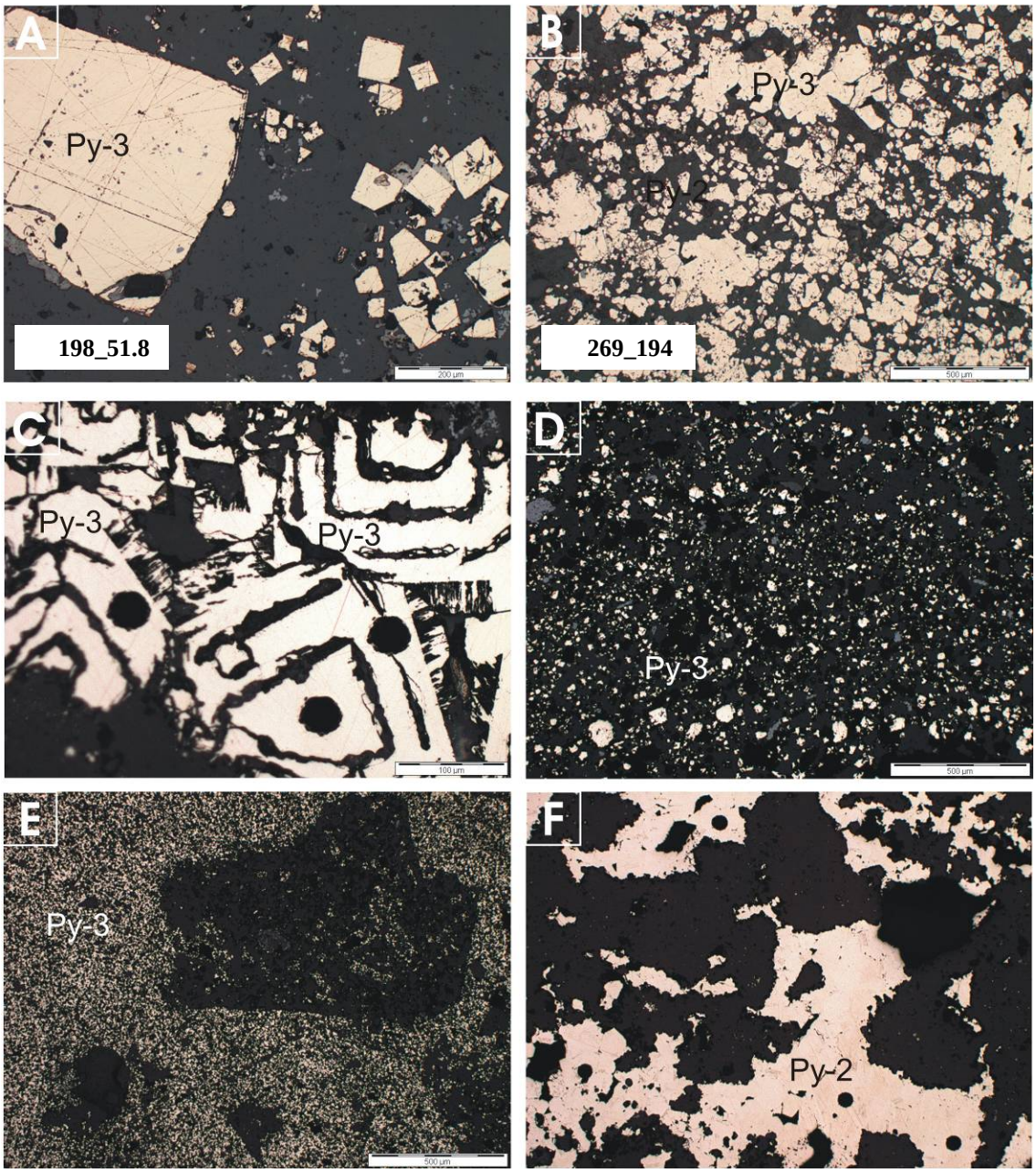

Figure 8.4. Stage-3 pyrite (py-3) is well crystallized, fine to coarse grained and has a clean polished surface. Textures include cubic (A and B), overgrowth zones (C) and breccia cement (D and E). Stage-2 (py-2) or Stage-3 (py-3) pyrite present as filled fractures and vugs (F). Black spot in (B) is LA-ICP-MS analysis location. Sample 164_113 and 360_585 taken from Purnama.

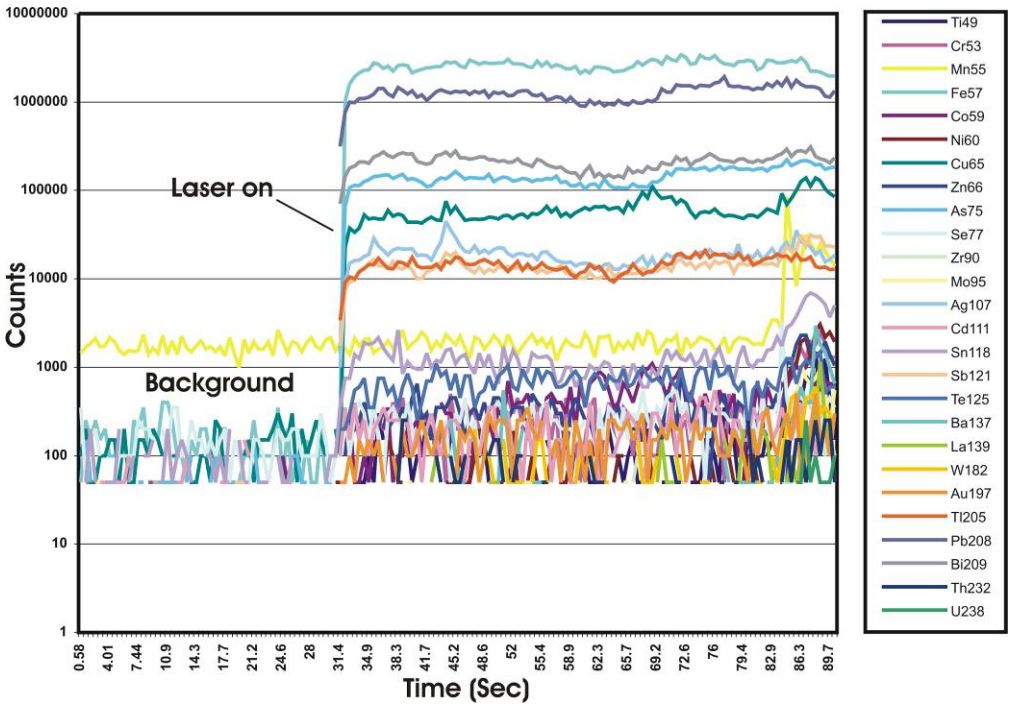

Figure 8.5. Laser ablation trace for selected trace elements in stage-3 pyrite from the Martabe district. Flat to smooth traces indicated elements within crystal lattice. This chart shows pyrite with elevated concentrations of Pb, Bi, As, Cu, Ag and Sb.

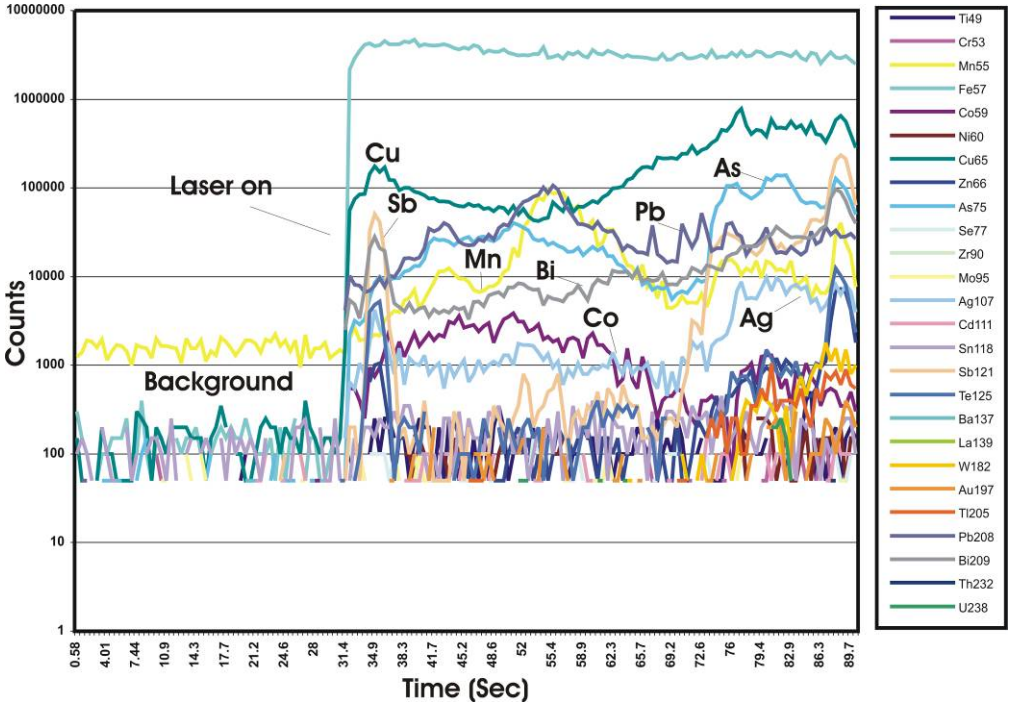

Figure 8.6. Laser ablation trace for selected trace elements in stage-2 pyrite from the Martabe district. This time chart shows pyrite with complex variations of Sb, Bi, Ag, As, Pb and Mn concentrations. Enargite inclusions (high Cu and As) are observed near the surface and within the pyrite.

8.3.4. Trace element variation in different textural types of pyrite

Pyrites from three prospects (Purnama, Baskara and Gerhana) in which representing Martabe deposit have been analyzed based on stages and textures. Each texture has a significant difference in trace element concentrations (Figures 8.5 and 8.6). Described below are the laser ablation results for the three stages or textures of pyrite.

Pyrites from all stages have highly variable compositions with ranges that span several orders of magnitude for most trace metals (Figure 8.7).

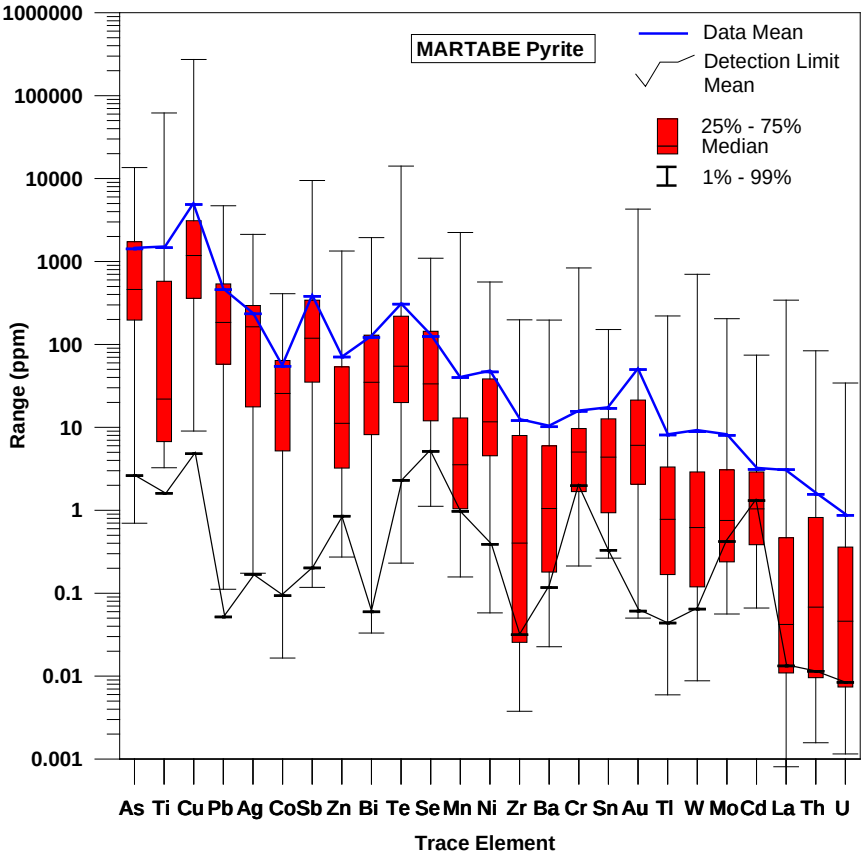

Figure 8.7. LA-ICPMS concentration range for all pyrite grains from three deposits (Purnama, Baskara and Gerhana) analyzed in this study. The mean of all analyses (blue line) and detection limits (black line) for each element are shown.

To simplify the comparison of the pyrite with different textures, the mean values of the measured elements in each texture were used. The results show distinct variations in the concentration of Au and associated elements in different growth zones or textures. Gold is highly concentrated in the heavy-pitted and spongy texture of stage-2 pyrite (Figure 8.3).

For all Martabe pyrite, stage-2 pyrites contain a greater variety of detectable elements and the highest concentrations of total trace elements (Figures 8.8b and 8.8d). In general, the stage-2 pyrite has the highest concentration of Cu, Sb, Au, Bi, Te, Se and Au

compared to stages-1 and stage-3 pyrite. There is a positive correlation between Cu, Ag, Sb, Te and Se with Au in stage-2 pyrite (Figure 8.8; Appendix 5). Comparison between stage-2 and stage-3 pyrite shows that these two stages have similar concentrations of their trace element contents, with the exception of Au which is less in stage-3 pyrite. Meanwhile, the stage-3 pyrite has similar Au contents to stage-1 pyrite, but stage-3 pyrite is enriched in the Cu, Sb, Bi, Te, Se, Mn, Sn and W compared to stage-1 pyrite.

Selected trace elements in pyrite are presented in scatter plots (Figures 8.9 and 8.10). The covariance relationships of Au to Cu-Ag-Se-Te-Sb and Sb to Ag-Te-Se-As have linear, positive trends. The relationships between other elements are not easily distinguished (Figures 8.10). This may be because, in rare cases the stage-1 and stage-3 pyrite plots overlap each other. However, the ratios or covariant plots involving Au and Sb with Ag-Te-Se in pyrite could be used for distinguishing between the various ore systems in the Martabe district.

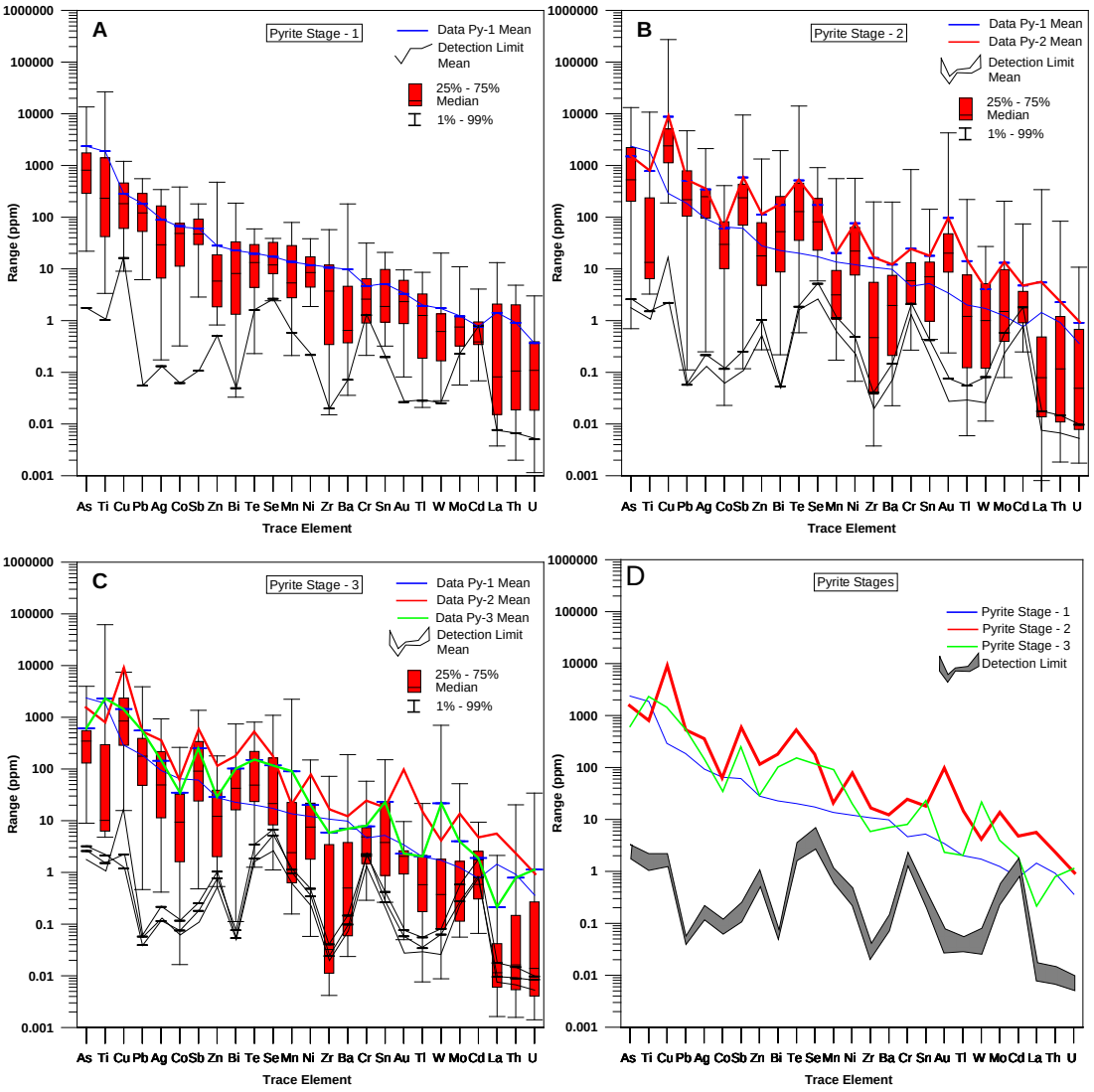

Figure 8.8. Range and mean of pyrite trace element contents of (A) stage-1 pyrite, (B) stage-2 pyrite and (C) stage-3 pyrite. (D) Comparison of the average of trace element LA-ICP-MS results from all stages of pyrite at Martabe.

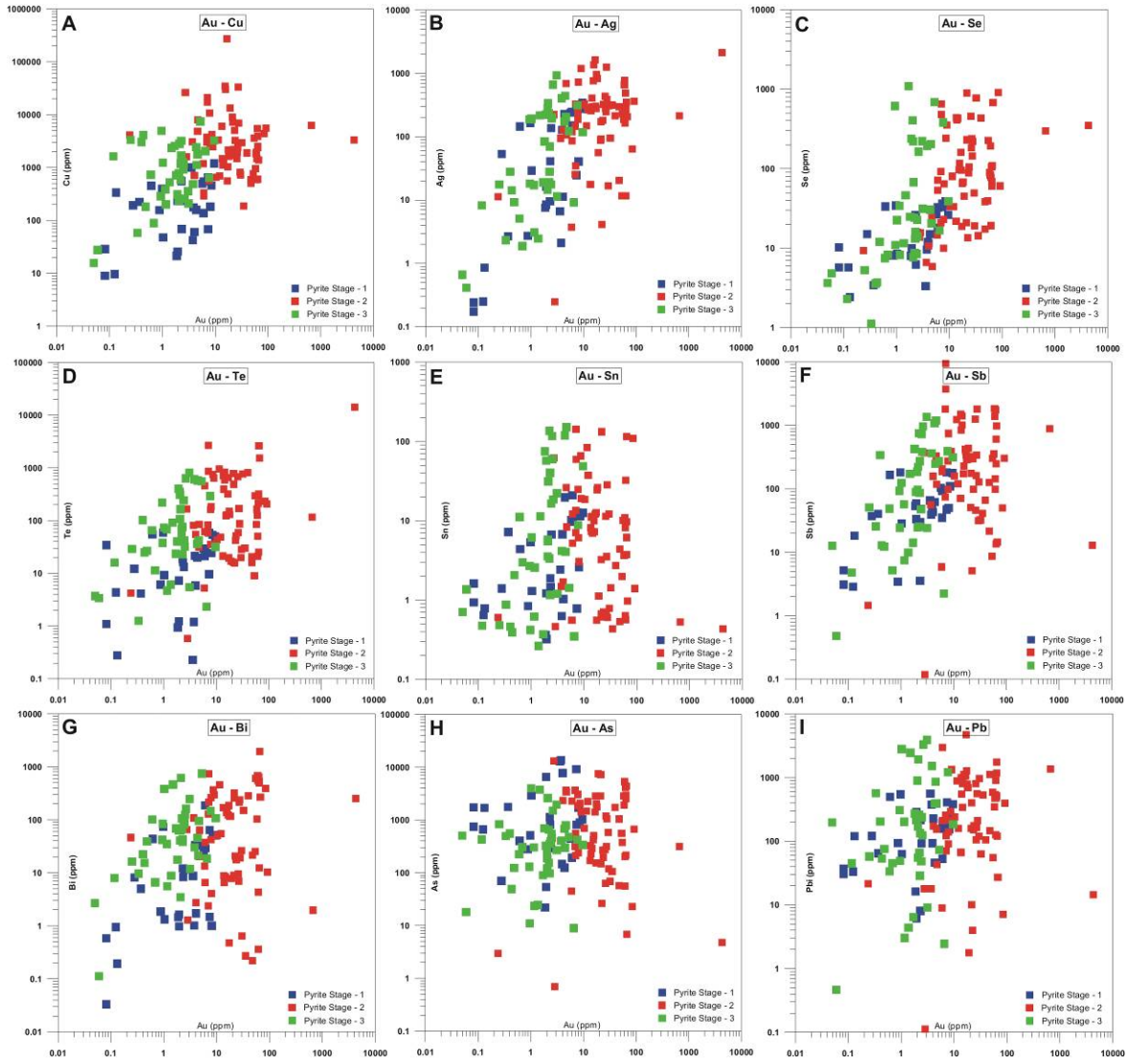

Figure 8.9. Covariations of: A) Au and Cu; B) Au and Ag; C) Au and Se; D) Au and Te; E) Au and Sn; F) Au and Sb; G) Au and Bi; H) Au and As; H) Au and Pb. Analyses have been categorized based on the pyrite stages.

8.3.5 Trace element variation in different deposits

Pyrite is considered to be useful for investigating the spatial variation of compositions of those hosted in advanced argillic and siliceous alteration or those occurring as overgrowths in the semi massive pyrite zones, as they have the greatest trace element concentrations and variability. The mineralization stage related-pyrite at Martabe has total trace element concentrations ranging from below the detection limit to more than 1%. There is significant variability in most elements analyzed (Figures 8.7 and 8.11; Appendix 5). Almost all elements are consistently above LA-ICP-MS detection limits, with the exception of Cd whose mean value (3.1 ppm) is close to its detection limit (1.3 ppm) (Figures 8.7 and 8.11; Appendix 5).

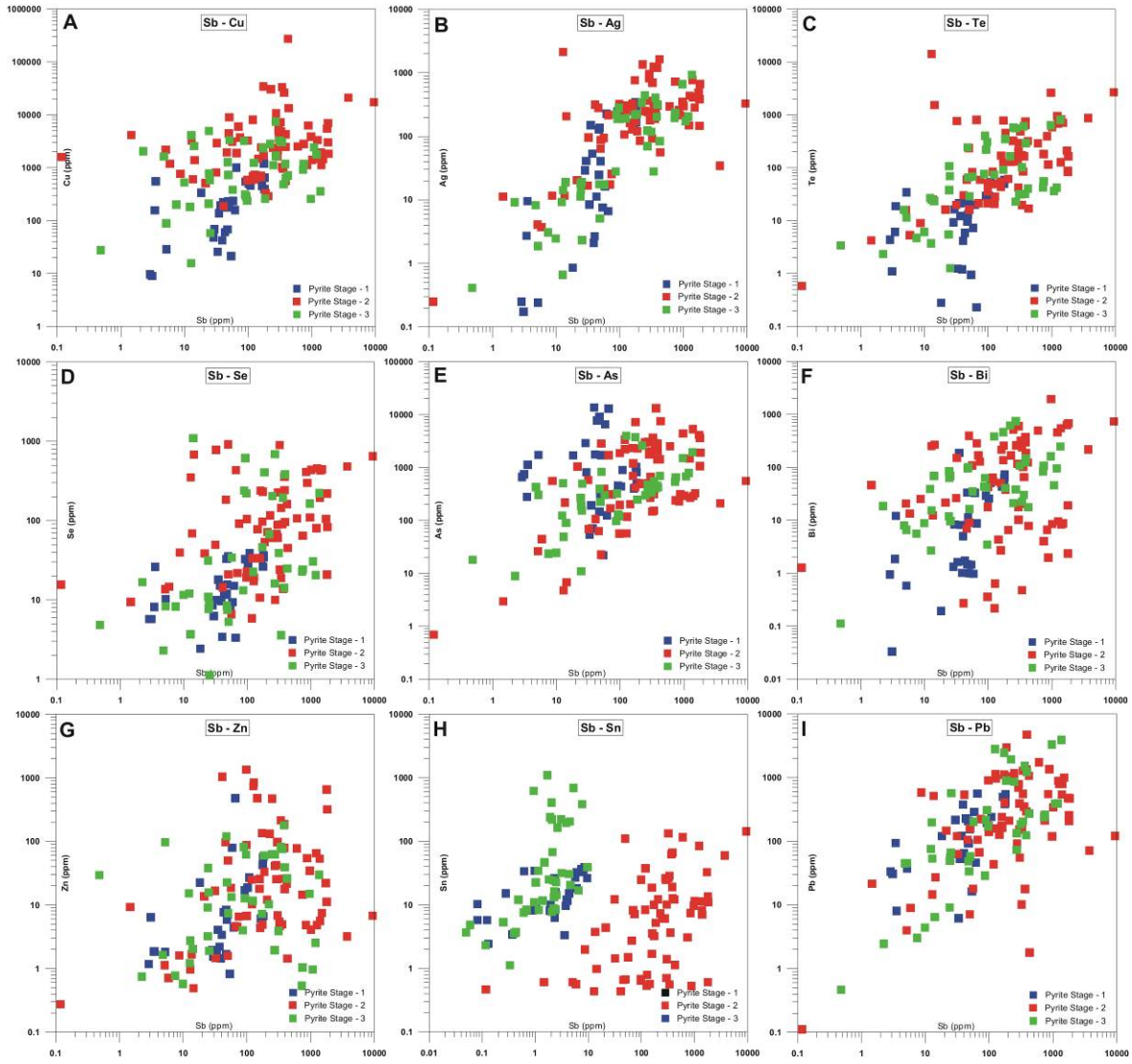

Figure 8.10. Covariations of trace elements in the 3 stages of pyrites from Martabe.

Purnama, Baskara and Gerhana pyrites have As, Ti and Cu in the highest concentrations (>1,000 ppm). In order of decreasing concentration, the following trace elements have mean concentrations >100 ppm: As, Cu, Ti, Pb, Sb, Ag, Te, Se and Bi (Figures 8.7 and 8.11; Appendix 5). The Purnama and Gerhana pyrites have higher values of trace elements than the Baskara pyrite. Pyrite from Purnama and Gerhana shows similar patterns of distribution in Cu, Pb, Ag, Co, Sb, Zn, Bi, Te and Se; while the Purnama and Baskara pyrite have similar patterns of Sn, Au and Tl (Figure 8.11).

Pyrites from the Purnama deposit are considerably richer in trace elements than the other deposits, especially in As, Pb, Ti, Sb, Ag, Tl, Bi, Te, Se, Au and Sn. However, pyrite from Purnama contains lower concentrations of Mn than Gerhana or Baskara pyrites (Figure 8.11D). Meanwhile pyrite from Gerhana has Cu and W in the highest concentrations. In general, Baskara pyrite has the lowest mean concentration of all trace elements among

the three deposits. There is also a general trend of decreasing concentration of most elements in pyrite from Purnama and Gerhana to Baskara.

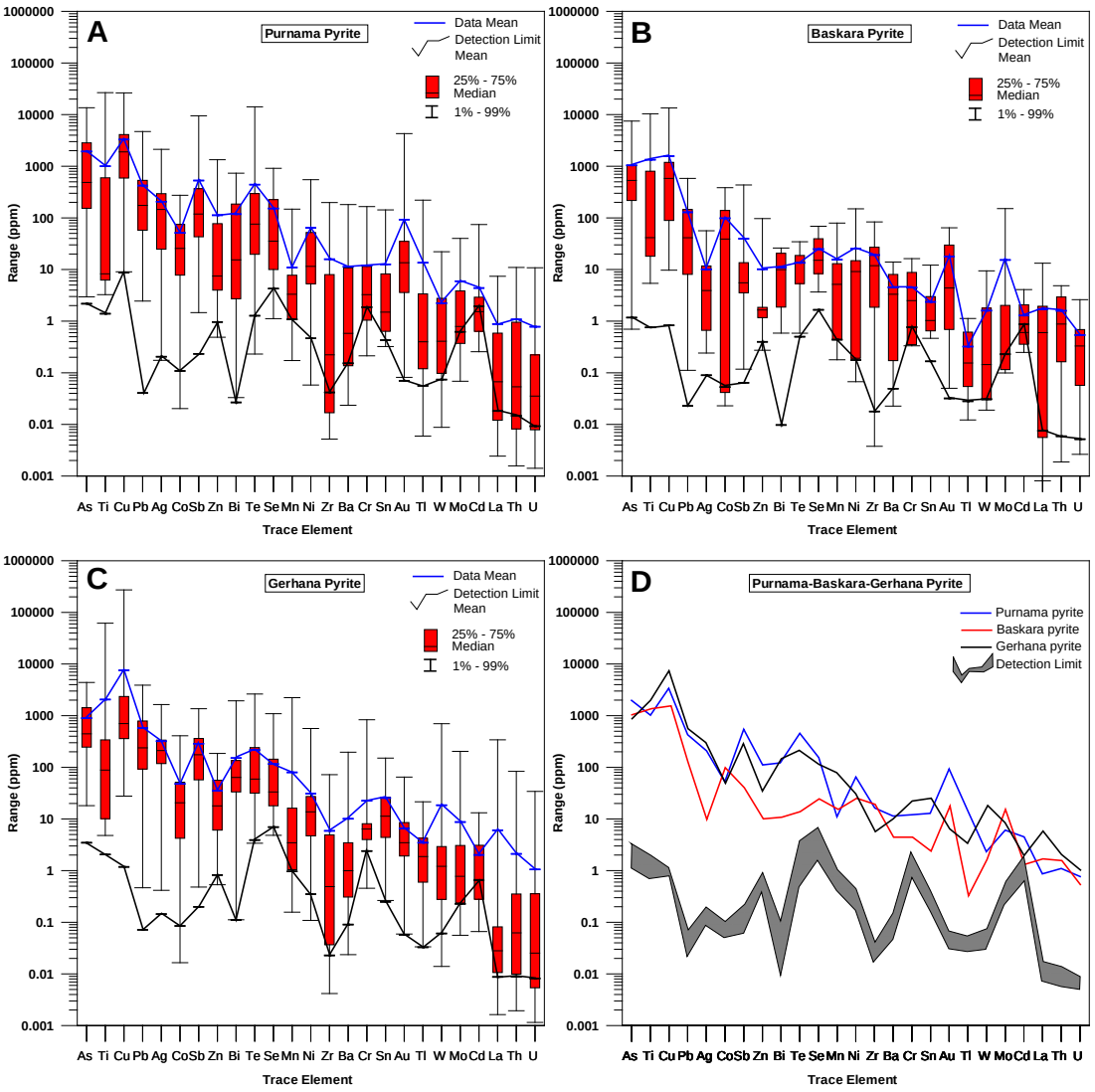

Figure 8.11. Concentration ranges and means for trace element contents in pyrite. A) Purnama deposit. B) Baskara deposit and, C) Gerhana deposit. Comparison of the mean concentration of trace element LA-ICP-MS pyrites from all deposits (D).

8.3.6 Discussion

Pyrites in the advanced argillic or siliceous alteration zones contain higher concentration of trace element compared to pyrite from the other alteration zones. These pyrites were utilized when testing lateral spatial variation.

Three generations of pyrite are recognized. An early stage of well-crystallized pyrite (stage-1) is enclosed by fine (submicron) overgrowths of second stage of poorly crystalline pyrite (stage-2). The stage-1 cores have relatively low trace element contents. Conversely, the stage-2 pyrites are very metalliferous. Stage-3 pyrite occurs as filling vugs or fractures

and encompasses poorly crystalline stage-1 and stage-2 pyrite.

The stage-2 pyrite has the greatest total trace element (Cu, Sb, Zn, Bi, Te, Se and Ni) content compared to stages-1 and stage-3 pyrite. Stage-2 pyrite has higher Au grades (97.2 ppm Au) compared to stage-1(3.3 ppm) and stage-3 (2.3 ppm Au) pyrite. Stage-2 and stage-3 pyrite have similar trace element distributions and variations but the absolute concentrations are different. Stage-1 pyrite has the lowest average concentrations of almost all elements (Figures 8.8c and 8.8d).

Pyrites from the Purnama and Gerhana deposits contain higher concentrations of Cu, Pb, Ag, Sb, Zn, Bi, Te, Se and Sn compared to pyrites from Baskara. Gold is elevated in pyrite for Purnama. Despite the distinctly elevated concentrations of most elements in pyrite from Purnama, higher concentrations of Cu, Zn and Co occur in pyrite from Gerhana. The average concentration of gold in the Purnama (92.3 ppm Au) and Gerhana (17.8 ppm Au) pyrites are greater than Baskara pyrites (6.6 ppm Au). Another distinction between the three deposits is the strong correlation in the Purnama pyrites between Au-Te and Au-Se. This relationship was not seen at Baskara and Gerhana. Pyrites from Baskara have lower Te and Mo and elevated Sb concentrations.

In contrast, pyrites from the advanced argillic alteration zone directly above the Baskara deposit are distinguished by lower concentrations of Ag, Sb, Zn, Bi, Te, Se, Sn and Tl. Only Au and Mo show any sign of enrichment in pyrite at Baskara. Among the deposits, Baskara pyrite has the lowest trace element concentrations, with significantly lower concentrations of Ag, Sb and Bi.

The trace elements (Au, Ag, Sb, Bi, Te, Se and Sn) that define the advanced argillic or siliceous alteration compositional signature are found in highest concentrations in the pyritic overgrowths of stage-2 pyrite, and are most elevated in the pyrite overgrowths from Purnama. This relationship may reflect a difference of pyrite compositions, such as Purnama being Au-rich compared to the other deposits; or it may be representative of the whole hydrothermal system. These data also suggest the possible use of covariations of Au-Sb, Au-Cu, Au-Te, Au-Ag, Au-Se, Sb-Ag, Sb-Te, and Sb-Se to distinguish between the various Martabe high-sulfidation deposits/prospects. These relationships may be an important characteristic of pyrites hosted in areas of high-sulfidation system related to mineralized zones and may prove to be an important tool when searching for buried deposits.

8.4. Enargite

8.4.1 Ore microscopy

A summary of the observations made from the ore microscopy study of enargite is given below. This study shows that there are at least two main groups of enargite:

(1) The first group contains enargite/luzonite that commonly occurs as coarse grains with striations and relatively clean surfaces. This group occurs as veins, veinlets and aggregates or minor patches up to centimeters in size. The aggregates may show subangular-subhedral grain boundaries. Enargite/luzonite may be altered to covellite and digenite and may contain a few inclusion pits (Figure 8.12).

(2) In the second group, enargite/luzonite mostly occurs as medium to fine grains with very irregular shapes. This enargite is rich in inclusions and also has a distinct pitted texture (Figures 8.13 and 8.14). Tiny tetrahedrite-tennantite inclusions are present in this enargite/luzonite (Figure 8.14).

The distinction between enargite and luzonite-famatinite can readily be made under the microscope. Luzonite-famatinite is pinkish and mostly shows polysynthetic twinning, whilst enargite has a more grayish tinge and no polysynthetic twinning.

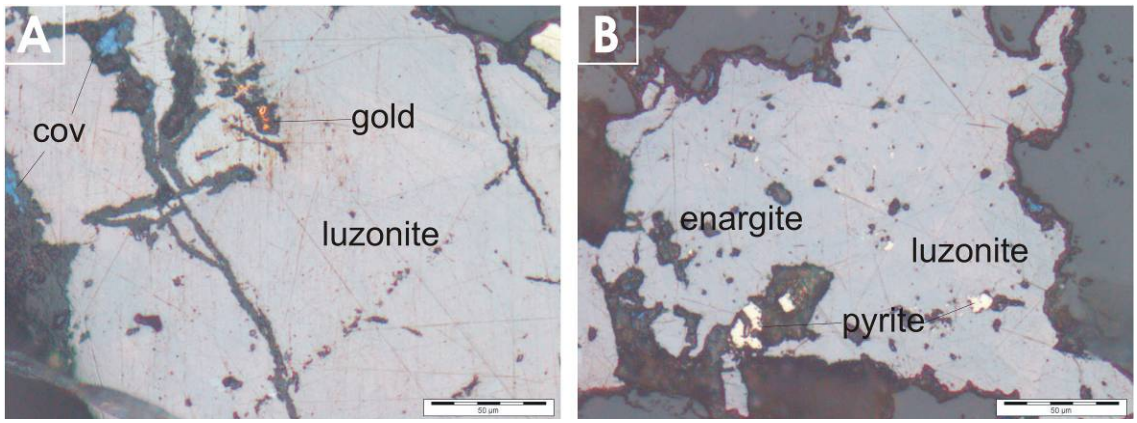

Figure 8.12. A) Reflected light photomicrograph showing a clean surface of enargite. The coarse enargite shows also polysynthetic twinning. B) Reflected light microscopy showing textures of enargite form as overgrowths on pyrite.

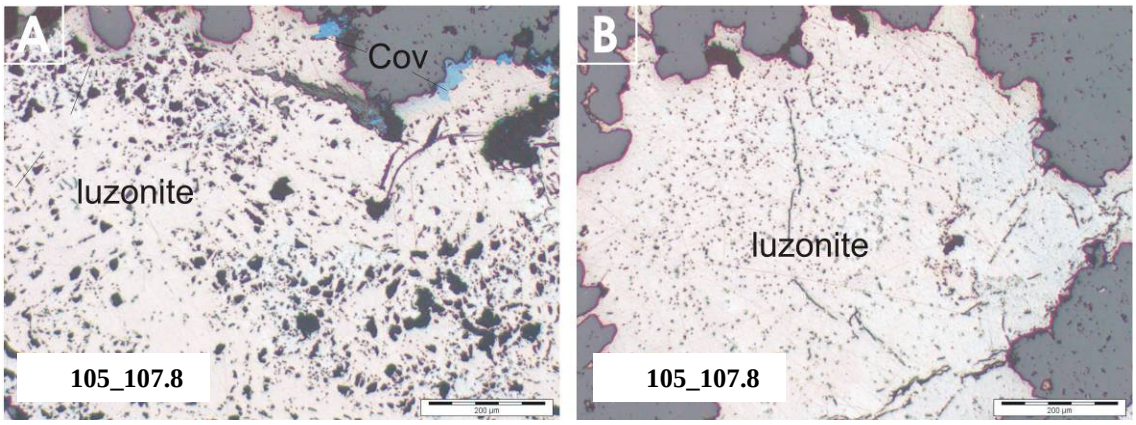

Figure 8.13. Reflected light microscopy images (A) Irregular shaped enargite with heavily pitted-enargite or luzonite. (B) Pinkish enargite/luzonite shows relatively a small but very intensive pit.

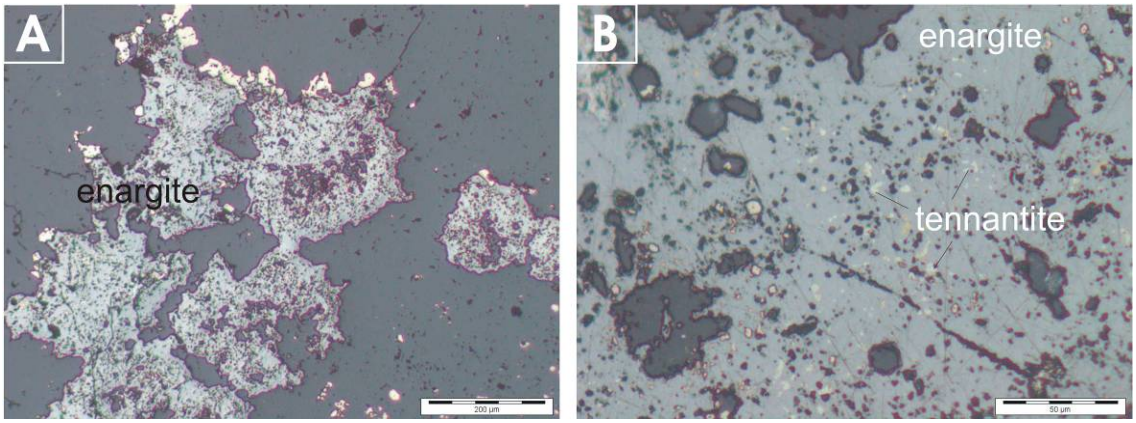

Figure 8.14. Reflected light microscopy showing of (A) Irregular shaped enargite with tetrahedrite-tennantite inclusions. (B) Tetrahedrite-tennantite inclusions in enargite.

8.4.2 EPM results

A summary of average EPM data for enargite is given in Table 8.2. The contents of S, As and Cu in enargite (Cu_3AsS_4) are ideally 32.57%, 19.02% and 48.41%, respectively. EPM analyses indicate near-stoichiometric enargite compositions for the majority of Martabe samples. Antimony contents are variable, with average values up to 7.3 wt % (sample EMP064-85.2). In general, except for the main components (S, As and Cu), only Sb is found in concentrations greater than 1 wt. %, whilst other minor elements, such as Fe, Te, Se, Ag and Au, are in lower concentrations (Te can be up to 0.7 wt %). In order to determine how much Sb can be contained in enargite and to what extent the As-Sb substitution takes places in Cu_3AsS_4 – Cu_3SbS_4 (enargite-luzonite-famatinite) both the As and Sb concentrations from every analysis have been investigated (Figure 8.15; Appendix 5). Figure 9.15 illustrates that the As-Sb substitution within one specimen can be very variable. If enargite and luzonite occur together, the latter is generally richer in Sb but often the compositional ranges overlap (Springer, 1969).

High Sb/As ratios in enargite occur mainly at Purnama and Gerhana, while the ratio is commonly low at East Purnama (Figure 8.15). Back-scattered electron images show that enargite crystals have distinct zoning which relates to variation of As-Sb concentration (Figure 8. 17). Gold occurs in heavily-pitted enargite (Figures 8.13 and 8.14; Table. 8.2) and may be as inclusions. Gold is also presented associating with tennatite-tetrahedrite. Tellurium is also concentrated in the heavily pitted enargite.

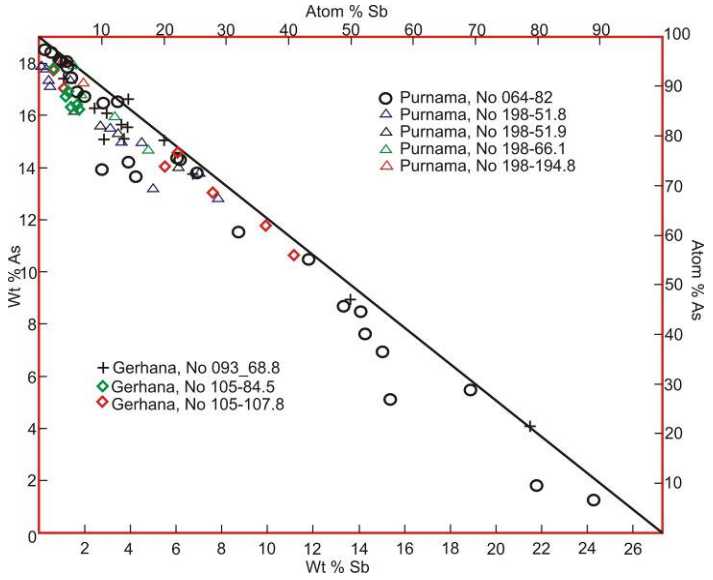

Figure 8.15. Plot of the arsenic against antimony from EMP data of enargite samples analyzed in this study (n=82 points). The line indicate where the measured values should be if the measurements and the correction procedure were closely accurate. Complete individual grain data points are in Appendix 5.

Table 8.2. The summary of EMP data for selected enargite samples. Data for individual sample represents the mean of individual grain data points (n=82). Dash line (-) indicates below detection limit.

No	Elements	Fe	As	S	Au	Cu	Zn	Pb	Bi	Ag	Sb	Te	Se	Total
	Sample_Id	(%)	(%)	(%)	(%)	(%)	(%)	(%)	(%)	(%)	(%)	(%)	(%)	
1.00	EMP064_85.2	0.08	12.94	31.58	0.03	46.60	0.12	-	0.16	0.12	7.29	0.69	0.35	99.94
2.00	EMP198_51.8	0.11	15.93	32.15	0.02	47.28	-	-	0.54	0.02	2.65	0.43	0.26	99.38
3.00	EMP198_51.9	0.03	15.02	31.43	0.11	47.13	-	-	-	-	3.41	1.57	0.02	98.73
4.00	EMP198_66.1	0.61	16.10	31.81	-	46.23	-	-	-	0.03	2.82	0.25	0.03	98.83
5.00	EMP198_194.8	-	17.88	33.13	-	48.08	-	-	-	0.24	1.38	-	-	100.68
6.00	EMP093_68.8	0.04	14.32	31.54	-	46.63	0.51	0.03	-	0.14	4.99	0.45	0.04	98.69
7.00	EMP105_84.5	0.19	16.17	31.37	-	45.95	0.04	-	-	0.34	0.96	0.16	0.04	95.22
8.00	EMP105_107.8	0.07	14.18	32.02	-	47.51	-	-	0.31	-	6.01	0.07	0.37	100.54

8.4.3 LA-ICP-MS results

A summary of enargite LA-ICP-MS data is shown in Figure 8.16 and listed in Appendix 5. There is significant variability in most elements analyzed, and particularly in Te, Bi, Fe, Sn, Se, Au, Pb, Mo, W and Ba. Almost all elements are consistently above LA-ICP-MS detection limits (Figure 8.18; Appendix 5) with the exception of Cd, La, Th and U, whose mean value (42 ppm, 0.1 ppm, 0.2 ppm and 0.1 ppm) are close to the respective detection limits. Elements with the highest mean concentrations (other than Sb) are Te (3.9%), Bi (1.2%), Fe (0.7%), Sn (0.3%), Ag (0.3%) and Se (0.2%).

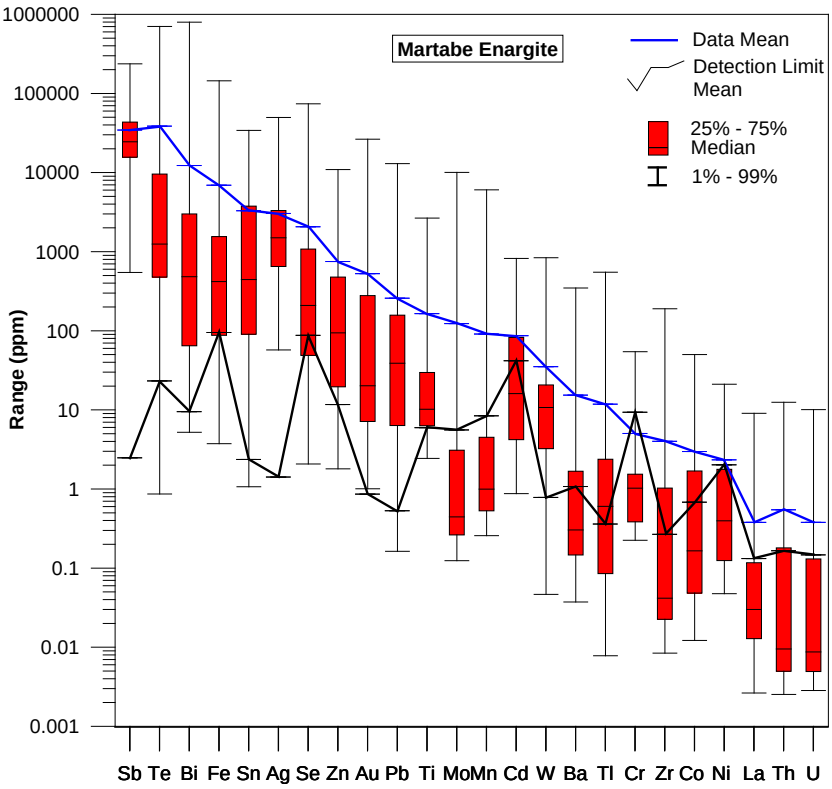

Figure 8.16. Range of enargite LA-ICP-MS trace element data for all analyses. The mean (blue line) of all analyses and detection limits (black line) of each element are shown.

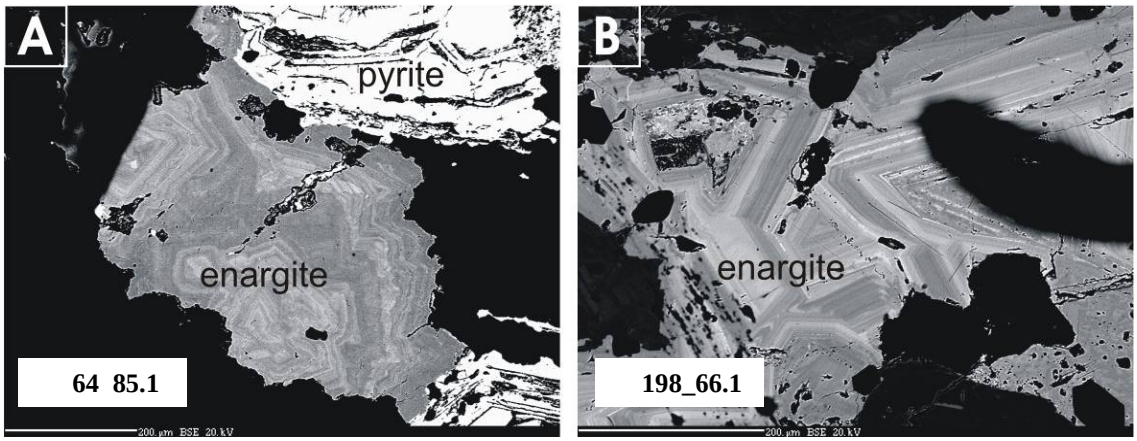

Figure 8.17. Back-scattered electron images showing enargite crystals with dark and light zoning patterns which are related to variation of As-Sb concentration. The light coloured zones indicate higher Sb concentration.

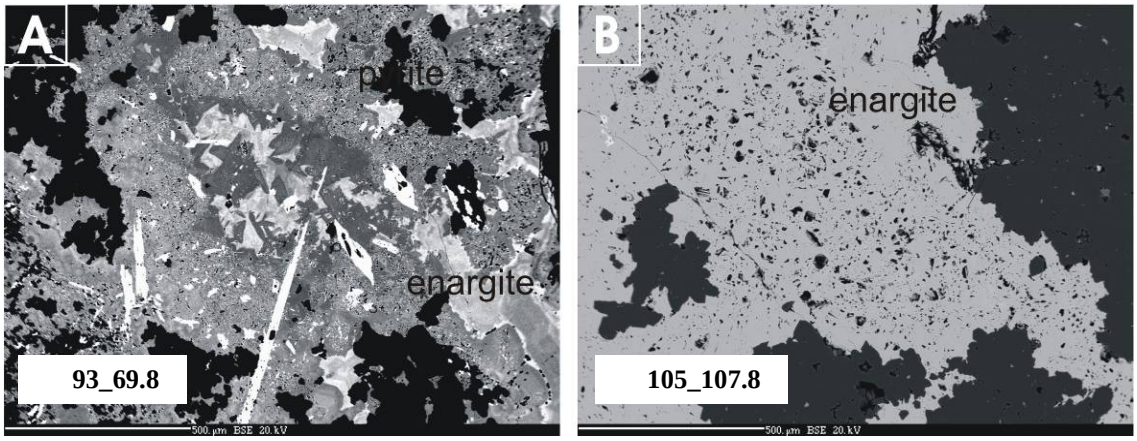

Figure 8.18. (A) Back-scattered electron images showing irregular zoning and inclusions in enargite. (B) Abundant pits in the enargite. SEM analyses indicate this enargite has Au-Sn-Pb and Sb-Bi-Te inclusions.

A direct comparison between the LA-ICP-MS and EPM data cannot easily be made, because the sample size of the two techniques is significantly different. The larger beam size used for LA-ICP-MS analysis provides a better estimate of the 'bulk' composition of individual enargite grains and can be used to sample across small zones of compositional variability. For example, both Au and Bi are close to below detection for EPM analyses (Appendix 8.2), although very high values are reported by LA-ICP-MS techniques. Based on LA-ICP-MS analyses, three groups have been identified:

(1) Group A: LA-ICP-MS analytical patterns are flat and even. These features are mostly seen for elements with concentrations several times above background level. However, most samples show relatively simple LA-ICP-MS compositional chart patterns (Figure 8.19).

(2) Group B: Elements in this group generally show irregular, uneven patterns. Elements in this group are also characterized by wide concentration variations within each grain(Figure 8.20).

(3) Group C: Elements that were found to occur in levels mostly below detection limit.

Table 8.3. Enargite element groups on the basis of LA-ICP-MS analytical measurements and chart patterns.

Group A – Flat (mostly high, evenly distributed)	**Group B – Irregular** (variable levels when present)	**Group C** (below detection)
Fe, Sb, Ag, Te, Au, Bi, W, Pb and Sn	Ag, Te, Sb, Bi and Au, Sn, Pb	Co, Th, La, U

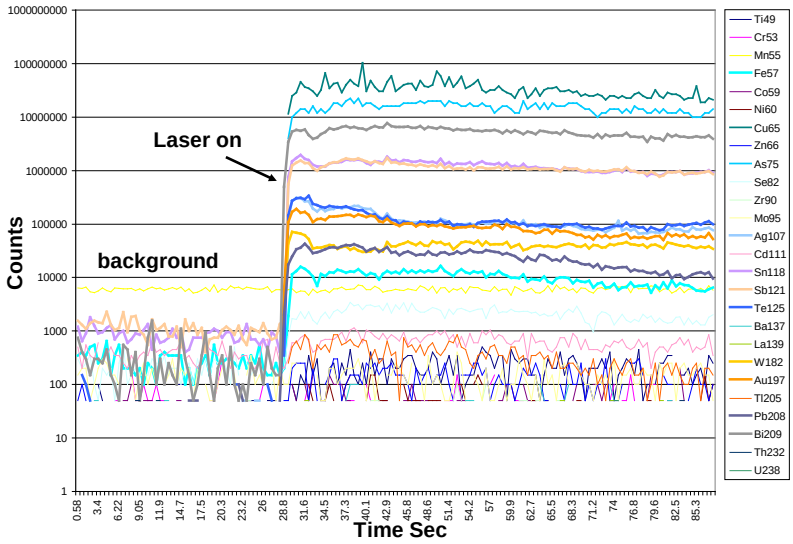

Figure 8.19. Laser ablation traces for selected trace elements in enargite. Flat to smooth varying trace elements patterns indicates elements within enargite crystal structure (elevated in Fe, Sb, Ag, Te, Au, Bi, W, Pb and Sn).

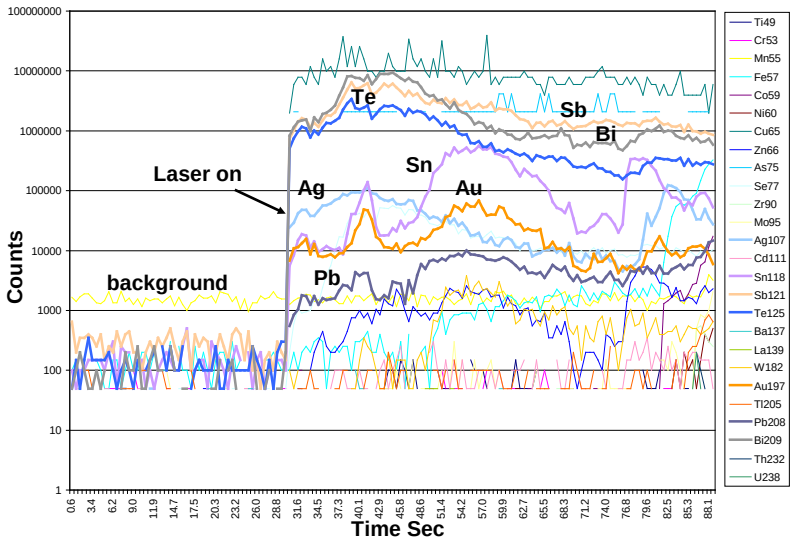

Figure 8.20. Laser ablation traces for selected trace elements in enargite. This time chart shows enargite with elevated and complex variations of Au-Sn-Pb and Ag-Sb-Bi-Te.

The micro-scale compositional variability in enargite is the result of either growth zones and/or inclusions. LA-ICP-MS analyses indicate substantial incorporation of Fe, Te, Bi and Sb in enargite. Other elements such as Sn, Se, Ag and Sn occur in complex and variable combinations. Complex growth zoning was also observed locally in enargite (i.e., Figures 8.16 and 8.17) and is due primarily to different combinations of Fe-Sb-Bi-Te-Se-Sn, but overall there are very few consistent elemental correlations in enargite. Rare Bi-selenides and Sn-bearing phases are also present. There are only a few samples with Zr-Ti-bearing inclusions. The most common inclusion types are Au (± Ag-Sn-Pb) bearing phases, as well as inclusions containing variable combinations of Fe-Sb-Bi-Te-Ag. As indicated in Table 8.4, Sb is weakly correlated with Te, and to a lesser extent Sn. Similarly, weak correlations between Ag-Bi, Te-Se, and Te-Sb are apparent. Ag-Sb and Ag-Te are moderately correlated.

8.5 Discussion

Results from LA-ICP-MS analyses indicate that Fe, Sb, Ag, Te, Au, Bi, W, Pb and Sn are enriched in enargite. LA-ICP-MS analyses also show that these elements occur in three groups based on their nature of concentration or distribution (Table 8.3). The Group A elements, consisting of Fe, Sb, Ag, Te, Au, Bi, W, Pb and Sn, display uniform flat spectra during analysis, and commonly occur at concentrations several times above the LA-ICP-MS detection limits. The uniform spectra for Group A elements suggest that they are structurally bound within the crystal lattice. The Group B elements show very irregular spectra during analysis. They have variable concentration which is due to complicated growth zones, multi-element inclusions or developments along crystal defects. Group C elements occur in levels mostly below detection limit (Table 8.3).

Table 8.4. Correlation matrix (Pearson) showing 'r' values of selected elements based on LA-ICP-MS analyses of all Martabe enargite (Data in Appendix 5).

MARTABE

Sb	1.00																	
Te	0.22	1.00																
Bi	0.07	0.64	1.00															
Fe	0.06	-0.05	0.01	1.00														
Sn	0.10	-0.12	-0.06	0.14	1.00													
Ag	0.49	0.46	0.24	0.04	0.00	1.00												
Se	0.62	0.08	0.20	-0.18	0.07	-0.55	1.00											
Zn	0.28	0.39	0.56	0.03	0.46	0.37	0.53	1.00										
Ni	0.33	0.01	-0.04	0.51	0.16	0.27	-0.02	0.28	1.00									
Ti	0.04	0.00	0.08	0.32	0.46	0.03	0.05	0.30	0.14	1.00								
Mo	0.65	0.06	0.01	0.05	0.00	0.56	0.03	0.33	0.49	-0.03	1.00							
Au	0.21	0.44	0.05	-0.01	-0.02	0.80	0.05	0.08	-0.02	-0.01	0.08	1.00						
Cd	0.09	-0.07	0.04	0.24	0.46	0.06	0.01	0.41	0.39	0.29	0.04	-0.04	1.00					
Tl	0.65	0.18	0.22	0.13	-0.02	0.56	0.23	0.48	0.45	0.03	0.92	0.07	0.07	1.00				
W	0.28	0.09	0.13	0.28	0.16	0.30	0.12	0.35	0.28	0.48	0.49	0.07	-0.03	0.54	1.00			
Pb	0.09	0.59	0.99	0.03	-0.03	0.25	0.93	0.61	0.02	0.09	0.07	0.01	0.06	0.30	0.18	1.00		
Ba	0.04	0.29	0.56	0.01	-0.07	0.16	0.52	0.32	0.20	0.07	0.00	-0.02	0.16	0.12	0.06	0.57	1.00	
Zr	0.00	-0.04	-0.01	0.38	0.21	-0.02	-0.02	0.12	0.12	0.75	-0.01	-0.01	0.08	0.07	0.78	0.01	0.01	1.00
	Sb	Te	Bi	Fe	Sn	Ag	Se	Zn	Ni	Ti	Mo	Au	Cd	Tl	W	Pb	Ba	Zr

8.5.1 Gold distribution in sulfide minerals

Although no visible gold was observed in hand specimen, it has been recognized in optical microscopy. In the sulfide zones, Au content ranges up to 10 ppm. This leads to the hypothesis that sulfide (and sulfosalt) minerals may contain submicroscopic Au.

Analyses of enargite/luzonite from a pinkish coarsely crystalline, late-stage vein which cuts across the breccia from Gerhana assayed up to 10 ppm Au. Gold contents are more consistent in samples with Cu sulfosalts, particularly enargite. At the 100 ppm detection limit, three EMP analyses of enargite from Purnama yielded values of 0.03 to 0.11 wt.% of Au (Table 8.2).

8.5.1.1 Nature of occurrence of Au in sulfide minerals

The nature of Au in the enargite is of particular interest in the Martabe district, as Au is the main contributor to the economic viability of the deposits. In this study, Au is above detection in most enargite samples, with maximum values up to 26,400 ppm (Figure 8.18; Appendix 5). The lack of a significant correlation of Au with other elements (Table 8.4) can be attributed to the variety of forms of Au within the enargite.

In general, three distinct patterns of gold distribution are revealed by LA-ICP-MS analytical traverses across enargite. In most cases, the Au exhibits smooth LA-ICP-MS traces and therefore it is interpreted to occur within the crystal lattice (Danushevsky et al., 2006). In the second form, Au occurs in complicated growth zones and/or multi-

element inclusions within the enargite. In these cases, there is a strong association of Au with zones of variable Fe-Ag-Te-Se-Bi-Sb. In rare cases, Au occurs as distinct inclusions associated with Bi and Sn. At Martabe, Au occurs primarily as electrum or in association with tellurides, selenides, Bi and Sn-bearing phases.

8.5.2 Silver distribution in sulfide minerals

Enargite contains up to 569 ppm Ag with a mean value of 7 ppm Ag. But this is unlikely to represent the total distribution of Ag in Martabe. Purnama (mean= 14 ppm Ag) and Gerhana (12 ppm Ag) have the highest mean values of Ag compared to the other deposits. Silver minerals are rarely identified in hand specimen or polished section.

EMP analyses (Table 8.1) consistently show no detectable Ag in any grains of pyrite, whereas analyses in enargite may contain up to 0.34% Ag at Gerhana and 0.24% Ag at Purnama.

8.5.3 Controls on Sb replacement in enargite

The phase relationships between enargite and the luzonite-famatinite solid-solution series have been studied, and the nature and temperature dependence of Sb substitution in enargite is generally well known (Posfai and Buseck, 1998). Luzonite (Cu_3SbS_4) is the low-temperature form of enargite (Skinner, 1960), although above ~280°C, the formation of either enargite or luzonite-famatinite is generally controlled by the Sb/As ratio in the fluid (Skinner, 1960; Maske and Skinner, 1971). Enargite can contain up to about 6 wt.% Sb which is equal to about 20 mol% Cu_3SbS_4, whilst in luzonite Sb may range up to 20 wt. % Sb (70 mol% Cu_3SbS_4) (Springer, 1969).

At Martabe, Sb contents of enargite are variable, averaging about 3.6 wt.% (Appendix 5). The highest Sb/(Sb+As) ratio occurs in enargite from the Purnama and Gerhana deposits (Figure 8.15), but there is no clear or consistent zonation in Sb to As values away from the Purnama to other prospects. A comparison of Sb/(Sb+As) ratios in samples indicates that there are high Sb/(Sb+As) values in enargite from the Purnama and Gerhana deposits with a broad trend of increasing Sb/Sb+As from the East Purnama to main Purnama deposit (Figure 8.15 and 8.21).

A comparison of enargite Sb/(Sb+As) ratios to the fluid inclusion homogenization temperature has been studied at the Lepanto deposit, Phillipines (Hedenquist et al., 1998). This study suggested that Lepanto has a general trend of decreasing fluid tempera-

ture from the main zone to the outer margin (Hedenquist et al., 1998). However, there is not a similar trend in samples from deposits in the Lepanto district and the Sb/(Sb+As) ratios vary at a range of temperatures. The Hedenquist et al. (1998) study suggested that while there is a general control on decreasingnSb contents in enargite with decreasing temperature in the Lepanto ore body, high Sb values do not solely correlate with high temperature.

Mineralizing fluids at Purnama and Gerhana appear to have had generally higher Sb/(Sb+As) contents, compared to the fluids sourced from the East Purnama and probably Baskara. However, low Sb relative to As contents in Baskara is seen in the LA-ICP-MS data, thus it is assumed that Baskara fluids had a low Sb/(Sb+As) ratio. The variation in Sb/As content of the enargite may be attributed to different fluid source or the deposition mechanism was not similar efficient for Sb in both prospect.

8.5.4 Spatial distribution of trace elements in enargite

Trace element substitution in Cu-sulfosalts has previously been recognized and shown to vary with distance from some epithermal ore bodies, although specific element enrichments or depletions appear to vary between deposits (Takagi and Brimhall, 1998; Camprubi et al., 2001). Similar results are observed in the Martabe district, where several elements are preferentially enriched, or depleted, show vary from one deposits to another deposits (Figures 8.21 to 8.26).

Iron and Ag are relatively constant throughout the district. In enargite, Sb, Au, Te, Se, Bi and Sn show similar distribution patterns where these elements are relatively enriched in Purnama and Gerhana, but depleted in Baskara. Silver is preferentially enriched in the Gerhana deposit, along with Sn, Zn, Pb and Sn, but these elements are lower in concentration in enargite from both Baskara and Purnama. Iron, Ag, Zn and Pb have higher concentrations at Baskara compared to Purnama, while Te, Se and Bi are lower in the Baskara enargite (Figures 8.21d and 8.26).

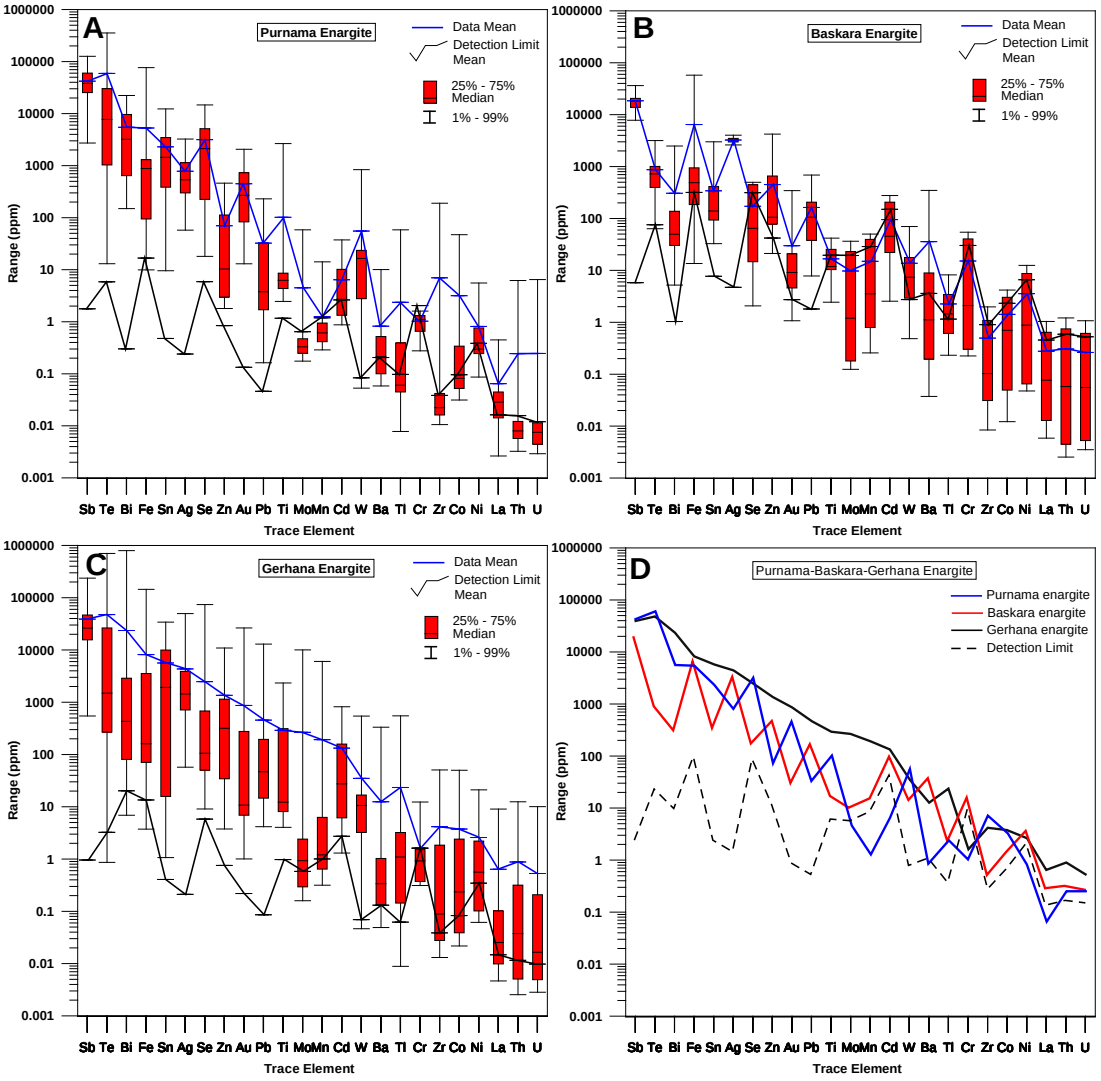

Figure 8.21. Range and average of enargite trace element contents from (A) Purnama, (B) Baskara and (C) Gerhana. (D) Comparison of the average of trace elements LA-ICP-MS enargite from all deposits.

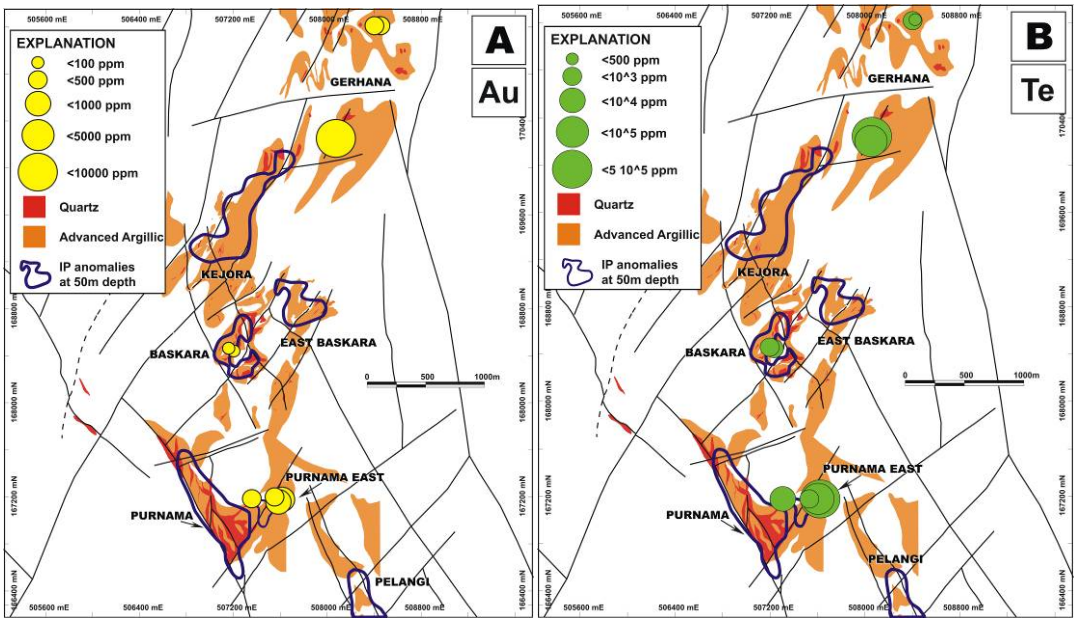

Figure 8.22. Thematic bubble map showing (A) Au and (B) Te in enargite, based on mean LA-ICP-MS results.

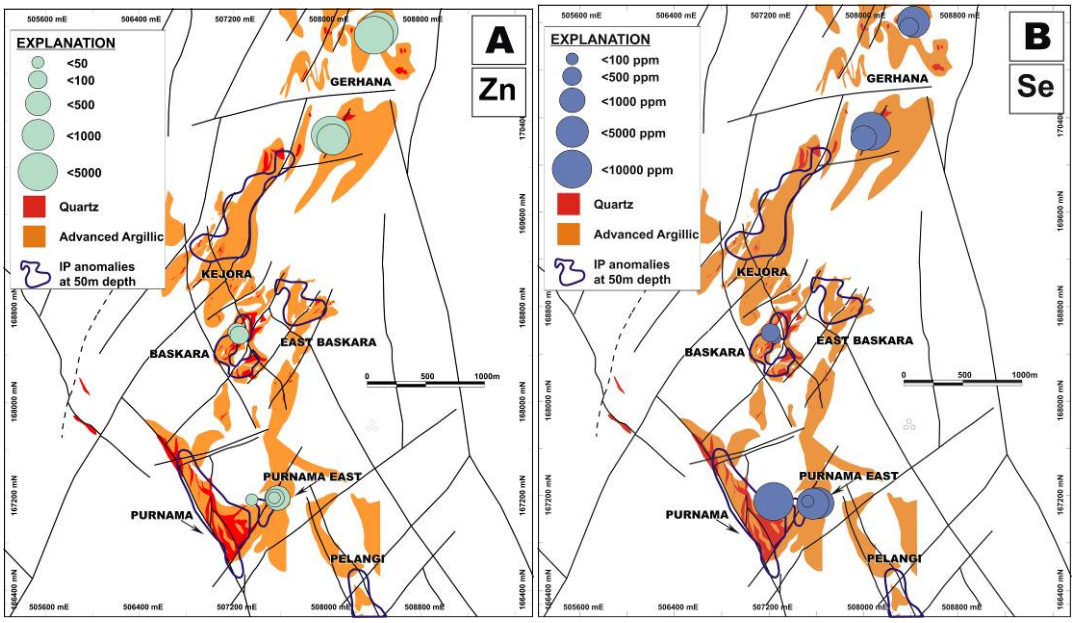

Figure 8.23. Thematic bubble map showing (A) Zn and (B) Se in enargite, based on LA-ICP-MS results.

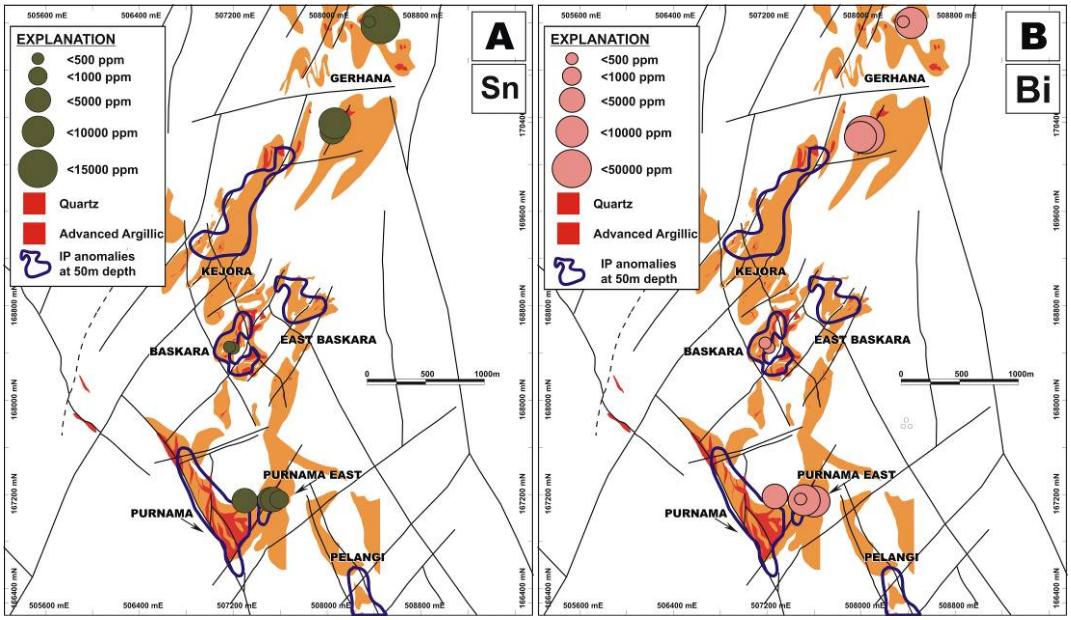

Figure 8.24. Thematic bubble map showing (A) Sn and (B) Bi in enargite, based on LA-ICP-MS results.

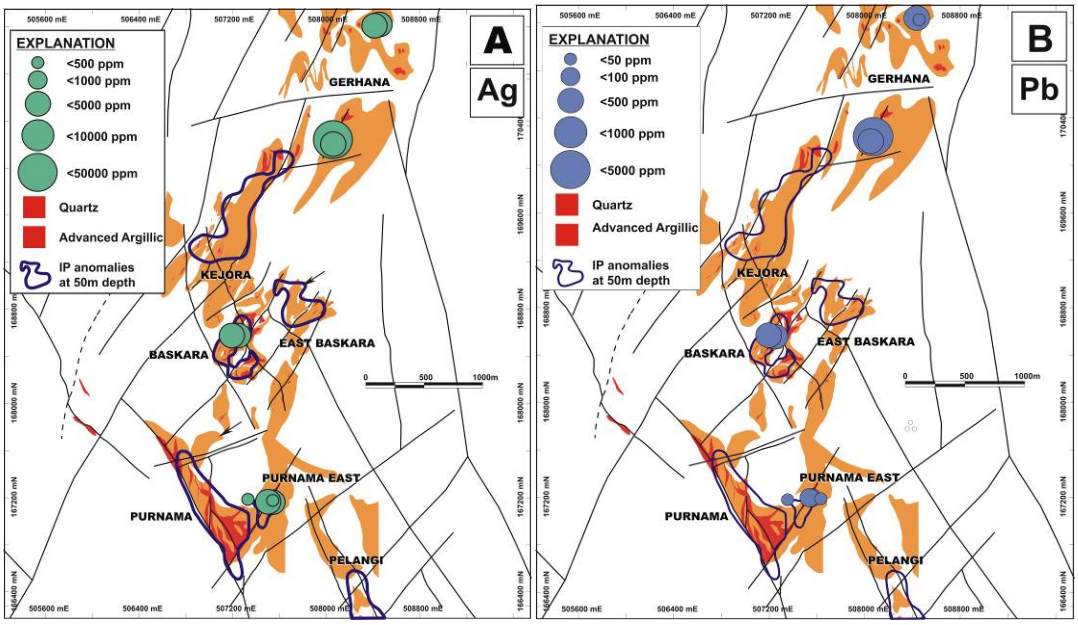

Figure 8.25. Thematic bubble map showing (A) Ag and (B) Pb in enargite, based on LA-ICP-MS results.

8.5.3 Conclusion

This study reports a LA-ICP-MS study of trace element substitution in pyrite and enargite. The LA-ICP-MS methodology described by Danushevsky et al. (2006) for analysis of pyrite and other sulfides has been found in this study to be applicable to enargite. Results indicate significant variability in trace element compositions of pyrite

and enargite from a single deposit and across deposits at the Martabe. The LA-ICP-MS technique has significant advantages over EPM studies; with LA-ICP-MS detection limits one to two orders of magnitude below electron microprobe analyses.

In the Martabe district, results from this study have shown significant incorporation of both Sb and Fe in enargite, at values locally exceeding l wt. %. There is also significant variability in most elements analyzed, and particularly in Fe, Te, Bi, Sn, Se, Au, Pb, Mo, W and Ba. Almost all elements are consistently above ICP-MS detection limits with the exception of Cd, La, Th and U that are close to detection. In general, the most abundant trace elements in enargite are those that also form discrete sulfosalt, selenide, and telluride accessory phases.

Although there is significant variability in some elements between individual grains and/or samples, general trends in the spatial distribution of some elements suggest enrichment in Au, Se and Te in the Purnama and Gerhana system, where the paleo- temperatures were probably the highest. Elements such as Ag, Zn and Pb, to a lesser extent Fe and Pb, are enriched in the enargite in the centre of the Gerhana ore body, whereas Zn (±Se) are enriched in enargite distal to Gerhana and Purnama.

CHAPTER 9

STABLE ISOTOPE GEOCHEMISTRY

9.1 Introduction

Stable isotope analyses have been used to evaluate the characteristics and source of different mineral components and provide a measure of fluid-rock interaction. The studies have been a powerful tool in the study of hydrothermal and volcanic systems (Ohmoto and Rye, 1979; Ohmoto, 1986; Ohmoto and Goldhaber, 1997; Rye e al., 1992; Rye, 1993).

Stable isotope techniques have not been applied to the Martabe deposits prior to this study and the results are used here to provide further constraints on the ore genesis model. Stable isotope data were generated for sulfides ($\delta^{34}S$), quartz ($\delta^{18}O$) and sulfates ($\delta^{34}S$, $\delta^{18}O$, and δD) (Figure 9.1, Appendix 8) from various deposits, including Purnama, Baskara, Gerhana and Pelangi. Enargite and pyrite were the main sulfides analyzed as they are sufficiently coarse-grained to be extracted manually for conventional analysis. Alunite, barite and native sulfur were selected from veins, breccias and vugs across multiple paragenetic stages.

Isotopic calculations are based on fractionation equations by Ohmoto and Lasaga (1982) for SO_4 (solid and aqueous)-H_2S; Ohmoto and Rye (1979) for sulfide-H_2S and sulfide-sulfide; Stoffregen et al. (1994) for alunite SO_4-OH; Zeng et al. (1994), Zheng (1993) for quartz-H_2O; Zheng (1999) for barite-H_2O; Sheppard and Gilg (1996) for dickite (kaolinite)-H_2O and Gilg and Sheppard (1996) for dickite (kaolinite)-hydrogen (Table 9.2).

9.2 Analytical and methods

9.2.1 $\delta^{34}S$ analytical method

Sulfur data were obtained for ore-stage pyrite and enargite, native sulfur, alunite and barite. All analyses were conducted at the Central Science Laboratory (CSL), the University of Tasmania. Sulfur isotope analyses were carried out on sulfide minerals drilled from samples of coarse-grained sulfides and sulfates using conventional methods (after Robinshon and Kuksabe, 1975). All sulfur isotope ratios were measured on a VG Micromass 602D mass spectrometer, under the supervision Christine Cook, following the method of Wasserman et al. (1994). Results are expressed in standard $\delta^{34}S$ per mil (‰)

notation, relative to the Canyon Diablo Troilite (CDT). Analytical uncertainty is $\pm$ 0.2 per mil.

9.2.2 δD and $\delta^{18}O$ analytical methods

Quartz, dickite and alunite were separated from hand samples using a fine diamond drill. Quartz was hand-picked from the crushed samples. The quartz samples were collected from vein and vugs. The dickite and alunite samples were purified by sedimentation and checked to ensure that they were nearly free of quartz and other minerals. Possible contamination of hand-picked samples was reduced by microscopic screening and SWIR analysis. The oxygen and hydrogen isotope data for quartz, alunite and dickite were measured at the GNS-Stable Isotope Laboratory of New Zealand under the supervision Dr. Kevin Faure, according to the methods of Shard (1996). Oxygen was extracted from samples for isotope analyses using a CO_2-laser and BrF_5 (Sharp, 1990). Oxygen results are expressed in standard $\delta^{18}O$ per mil (‰) relative to standard mean ocean water (SMOW). Oxygen isotope values are reported in the $\delta^{18}O$ notation, relative to VSMOW. Samples were normalized to the international quartz standard NBS-28 using a value of +9.6 per mil (‰). Values for four NBS-28 standards analyzed with the samples had values that varied by less than 0.1 per mil. Samples and standards were heated overnight to 150°C prior to loading into the vacuum extraction line. These were then evacuated for approx 6 hours. Blank BrF_5 runs were done until the yield was less than 0.2 micro moles oxygen. Oxygen yields were recorded and CO_2 gas analyzed on a Geo20-20 mass spectrometer (Faure, pers. comm).

Alunite and dickite were analyzed on a HEKAtech high temperature elemental analyzer coupled with a GV Instruments IsoPrime mass spectrometer. Samples were pyrolyzed at 1400°C, in silver capsules. All samples were analyzed in triplicate (Faure, pers. comm.). To ensure that clays were dickite and nearly free of quartz and other minerals, samples with a similar texture and color collected at different depths have been checked by X-ray diffractometry and SWIR analysis. Then the samples were purified by gravity sedimentation.

All results are reported with respect to VSMOW, normalized to international standards IAEA-SO-5 and IAEA-SO-6 with reported $\delta^{18}O$ values of +12.0‰ and –11.0‰. The analytical precision for these measurements are better than 1.0‰.

9.3 Sources and evolution of fluids

In all types of volcanic-hosted epithermal deposits, end-member fluids from two primary sources are typically involved: magmatic and meteoric (Cooke and Simmons, 2000). The isotopic compositions of each may evolve through reaction with wall rock or by mixing with one another (Bethke et al., 2005; Rye et al., 2005).

The low-pH environment during acid-sulfate alteration at the volcanic-hosted epithermal deposits enables of isotope equilibrium among all aqueous species in the hydrothermal fluids and between aqueous species and minerals (Ohmoto and Lasaga, 1982; Rye, 2005). The sulfur-isotope fractionations between coexisting sulfide and sulfate minerals and the oxygen-isotope fractionation between quartz and alunite as well as between the sulfate and OH sites in alunite, provide potential geothermometers (Bethke et al., 2005). The presence of these hydrous minerals both in alteration and in vein-filling stages at Martabe helps the identification of sources and evolution of fluids.

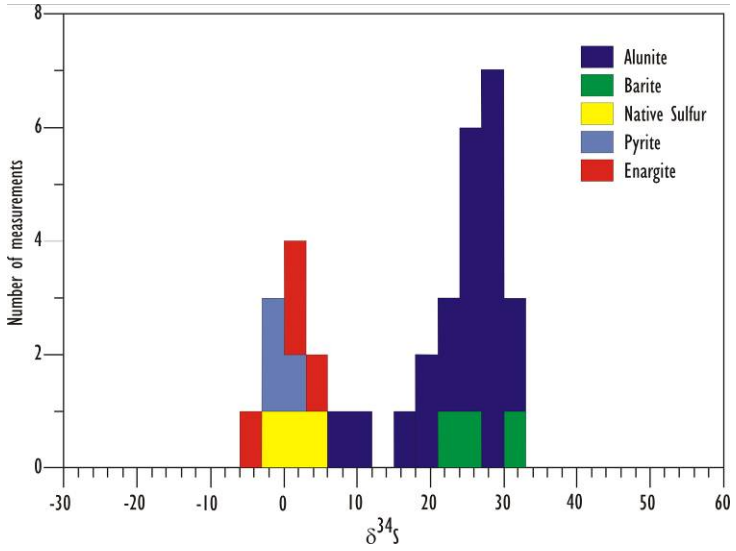

Figure 9.1. Summary of sulfur isotope data for Martabe district. Some enargite and pyrite samples were very fine grained and may have been contaminated by sulfate minerals.

9.3.1 Composition of magmatic and meteoric water

The isotopic composition of aqueous fluid generated during the crystallization of the magma body underlying Martabe is not known. It may be estimated from unaltered samples of the Martabe quartz-rich dacite or hornblende-quartz pyric andesite porphyry; assuming it to be representative of source magma. The boxes for primary magmatic water (PMW; Taylor, 1979), and felsic magmatic water (FMW; Taylor, 1992) in Figure 9.2A are conventional references, as are the meteoric water and kaolinite lines. The composition of

magmatic water from a given area may fall outside these boxes, and water of other origins may have compositions that fall within them. At least during the early stages of leaching and formation of alunite, a component of magmatic water containing acid volatiles is probably present in the Martabe hydrothermal systems. However, from Figure 9.2 the magmatic water component clearly mixed with meteoric waters even in the acid sulfate-alunite stage, whereas meteoric water dominated in the marginal zone of argillic alteration and quartz vein.

The $\delta^{18}O_{H2O}$ composition of the present meteoric water in the Martabe district is not known. However, a present-day local meteoric water at the Sibayak Geothermal Field, 100 km north of the Martabe district at 700–1310 masl (meter above sea level) has values of $\delta^{18}O$= –8.1 to –11.0‰ and δD= –50.1 to –73.3‰ (Abidin et al., 2005). Therefore, values of $\delta^{18}O_{H2O}$= –9.5± 1.5‰ and δD= –61.7± 11.6‰ are adopted for this discussion.

9.4 Magmatic-hydrothermal alteration

The isotopic composition of water in fluids responsible for advanced argillic alteration at Martabe can be calculated from alunite δD and $\delta^{18}O$ values using the fractionation coefficients determined experimentally by Stoffregen et al. (1994). Because the sulfate site is more reliable than the hydroxyl site for the retention of primary oxygen-isotope compositions in alunite, $\delta^{18}SO_4$ was used in these calculations (Bethke et al., 2005; Rye, 2005). Temperatures were taken from alunite–pyrite sulfur-isotope geothermometry, where available. Values for alunite and associated fluids are plotted in Figure 9.2A along with those for dickite alteration.

These $\delta^{34}S$ results are consistent with the sulfides, sulfosalts, and hypogene alunite forming from the same acid fluid at 200°C to 250°C (the temperature range for an equilibrium fractionation of 28-25‰ in $\delta^{34}S$ between sulfide and sulfate in fluid; Ohmoto and Rye, 1979). These result are similar to those for hypogene sulfides and sulfates from high-sulfidation system where textural relationships suggesting equilibrium was established (e.g., Marysvale, Utah, Cunningham et al., 1984; Lepanto, Hedenquist and Gracia, 1990; Summitville, Rye et al., 1992 and Rodalquilar, Arribas, 1992; Bethke et al., 2005). The $\delta^{34}S$ values of 9.0‰ of alunite may be a steam heated alunite which was slightly lighter than $\delta^{34}S$ value of hypogene sulfate and these values are consistent with a similar steam heated origin alunite in Pascua (Deyell et al., 2004). However, the late veinlets of alunite formed from the low-temperature (non-equilibrium) oxidation of sulfide will have a similar isotopic composition to the sulfide minerals (Hedenquist et al., 1994).

The total S isotope ($\delta^{34}S_{\Sigma S}$) composition of the original fluid composition in Martabe was not previously known. In a hydrothermal system with a $\delta^{34}S_{\Sigma S}$of 1‰, alunite typically would have values of 15‰ to 30‰, depending on the $\delta^{34}S$ temperature of deposition and H_2S/SO_4^{2-} ratio of the system (Rye, 2005). However, the isotopic $\delta^{34}S$ concentration of H_2S gas from three production wells of Sibayak Geothermal Field shows average value i.e. –3.3‰, –3.7‰ and –4.3‰ respectively (average –3.8‰); and the average $\delta^{34}S$ value of H_2S from steam vent discharge is –1.7‰o. The value is more depleted than production wells and this value is believed to be close to the $\delta^{34}S$ magmatic sulfur or influenced by magmatic origin or sources (Abidin et al., 2005). Assuming the intrusive value of ~–4‰ for the total $\delta^{34}S$ of Martabe fluids, an isotopic mass balance using an average of –2‰ for the sulfide and 26‰ for the sulfate indicate that the sulfide/sulfate ratio of original fluid was about 4:1 or 5:1. Native sulfur has an isotopic composition of –0.6‰ to 3.1‰ (average 1‰; Appendix 8), therefore the $\delta^{34}S_{\Sigma S}$ composition is assumed to be between the two values (–3.8‰ to 1‰) (Figures 9.2 or 9.3).

9.4.1 $\delta^{18}O_{H2O}$values of quartz vein-forming fluids

The $\delta^{18}O$ composition of the residual quartz was not known previous to this study. It is convenient to label these Purnama and Pelangi vein groups with respect the distance from Baskara deposit (assumed Baskara as a conduit for the district) as proximal and distal, respectively, to distinguish them form each other (Figure 9.2b). Both the distal/peripheral quartz veins from Pelangi (assumed 150°–180°C) and proximal quartz veins of Purnama (assumed 180°–200°C) exhibit similar plot patterns related to depth and $\delta^{18}O$ compositions indicating light isotopic values for their waters, less than 0‰ (–2 to –11‰) (Figure 9.2A; Appendix 8). Most $\delta^{18}O$ compositions have isotopic values for their waters plotting in a range of –6 to –10‰. The Purnama vein sample has a slightly lighter $\delta^{18}O_{H2O}$ value compare to the Pelangi vein. Most $\delta^{18}O_{H2O}$veins are consistent with equilibrium with water equivalent to present day local meteoric water at the Sibayak geothermal field $\delta^{18}O$= –8± 2‰ (Abidin et al., 2005). Exceptions are slightly heavy values for a near-surface sample from Purnama deposit (~440 masl). The concave D-shape form of the quartz field at about 340 masl (Figure 9.2b) possibly suggests the adding of fluids with isotopically heavy or unequal concentrations which flow at 340 masl. Overall, the $\delta^{18}O$ values of quartz veins fall on a broad trend that shows a slightly decrease with depth (Figure 9.2b).

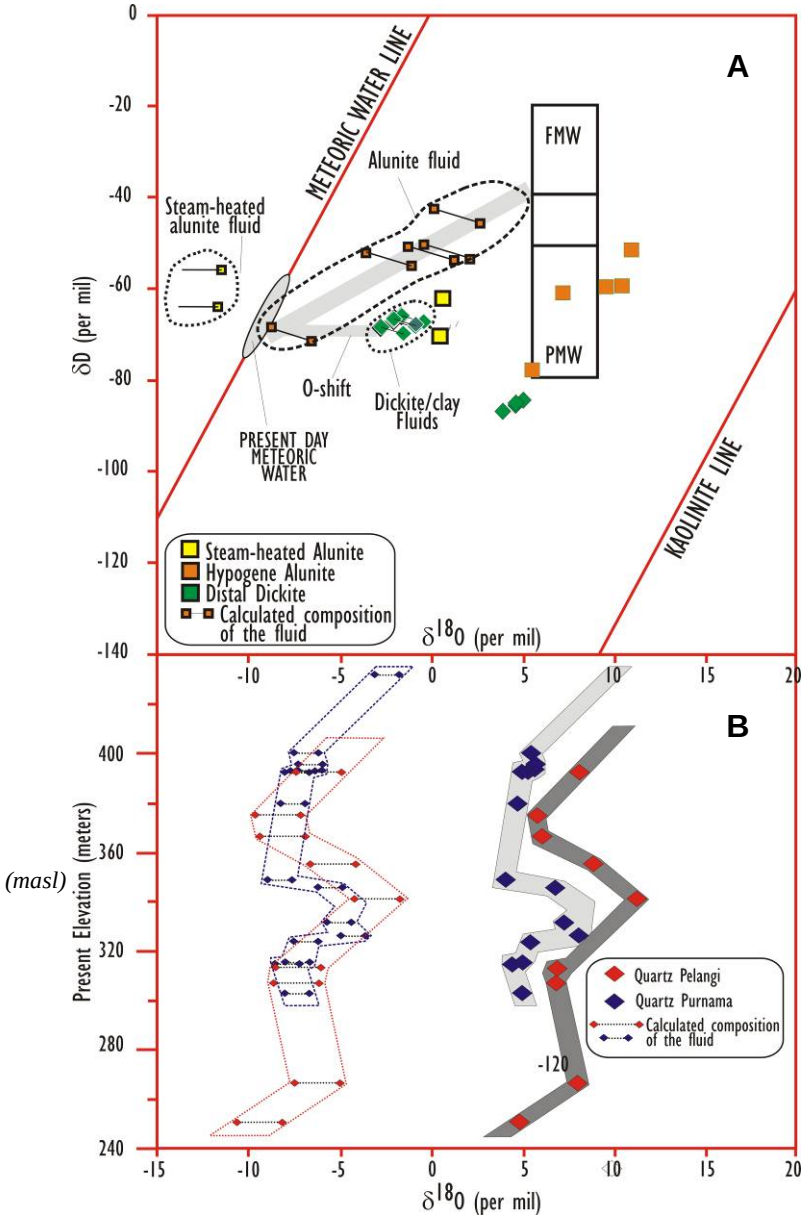

Figure 9.2. Diagram showing the results of isotopic analysis of: (A) alunite and dickite (δD vs. $\delta^{18}O$, plotted on the top) and (B) quartz veins ($\delta^{18}O$ vs. elevation, plotted on bottom). The calculated compositions of the fluids in equilibrium with these minerals are shown. The compositions of local meteoric water (oval), meteoric water and kaolinite lines and Primary Magmatic Water (PMW) and Felsic Magmatic Water (FMW) (Taylor, 1974) boxes are plotted for reference. A fit line (shaded) through the hypogene alunite fluids and the Felsic Magmatic Water (FMW) fluids end member extends to an isotopic composition similar to present local meteoric water and identical in δD values to the dickite/kaolinite fluid. Thus the isotopic composition of alunite records mixing of magmatic and meteoric waters, whereas the marginal clays (dickite/kaolinite), and possibly the quartz vein, indicate that meteoric water dominated on the margins of the quartz bodies, variably shifted in oxygen isotope composition due to exchange with wall rocks. Two alunites from Baskara and Purnama have an isotopic composition which indicates they possibly formed in a steam-heated environment after evaporation of local groundwater (fluid composition calculated for a steam-heated temperature range (150°–180°C)). Temperatures used for fluid calculations are listed in Appendix 8.

Pelangi and Purnama quartz veins were presumably precipitated from similar fluids ($\delta^{18}O$ ~–8‰) (Figure 9.2) and therefore precipitation temperatures of both veins can be inferred from the quartz-H_2O fractionation equation of Zheng (1993).

For comparison, a study in Nansatsu deposit revealed the quartz crystals in vugs of the quartz bodies and the later veinlets have the same composition as the residual silica; and they have heavier isotopic values for their waters than quartz veins (deep or peripheral vein) (Hedenquist, 2005). The $\delta^{18}O$ values determined on fine-grained quartz in the groundmass of vuggy quartz, quartz veins, deep veins are similar at a given locality has the overlap values. The values overlap with those reported by Larson (1987) for similar material from Summitville. However, no quartz sample has been taken and analyzed for isotope study from either vugs or fine-grained quartz in the groundmass vuggy quartz at Martabe.

9.4.2 Alunite and sulfide relations

The δD_{H2O} values of the fluids causing alunite alteration are substantially different from those of meteoric water at the time of mineralization and are consistent with a dominantly magmatic source. A total of seven alunites that were pure enough for $\delta^{34}S$, $\delta^{18}O_{SO4}$, δD isotopic analyses indicate a different trend for their associated waters. Based on the alunite-water fractionation factors ($\delta^{18}O_{SO4\text{-}H2O}$) given by Stoffregen et al. (1994), and temperatures of 200°C and 250°C (based on S-isotope data), the composition of fluids responsible for forming the alunite was calculated. The data for hypogene alunite/magmatic-hydrothermal alunite from the advanced argillic alteration have variable $\delta^{34}S$ (24.9‰ to 32.3‰), $\delta^{18}O_{SO4}$ (5.6‰ to 11.0‰), and δD (–62‰ to –51.2‰) values over limited ranges, with the exception of one sample with a δD value of ~–78‰. Most sulfides and native sulfur exhibit relatively a large range values of $\delta^{34}S$ (–5.2‰ to 11.0‰) and $\delta^{34}S$ (–0.58‰ to 3.2‰), respectively (Figures 9.1 and 9.2A; Appendix 8). Alteration alunite and sulfides has similar isotope value from their each stages of paragenesis. Such isotopic characteristics typify magmatic-hydrothermal alunite and sulfides in high-sulfidation Au-Ag deposits (Rye et al., 1992; compilations by Arribas, 1995; Corbett and Leach, 1998).

Two of the seven alunite samples (APSD73_71 and APSD344_165) are relatively light compared to the other five samples, for both $\delta^{18}O$ and δD, and are almost similar to the composition of steam vents at the cone of Sibayak mountain ($\delta^{18}O$= –2.9‰ and δD= –44.9‰) (Abidin et al., 2005). The other five samples fall on a mixing trend between high temperature fluids and local meteoric water. Another 'distal' alunite fluid

(APSD352_107.5) is plotted within the fluids line which originally from dickite-forming fluid point (Figure 9.2A; Appendix 8). The $\delta^{18}O$ and δD trend of mixing between volcanic condensates and meteoric water is similar to that noted for fumarole vapor and related acid fluids at Sibayak mountain (Abidin et al., 2005) and elsewhere around the circum Pacific (Giggenbach, 1992).

The alunite data in Figure 9.2A suggests a trend towards both lower $\delta^{18}O$ and δD. The patterns may suggest several possible physical or chemical processes, as indicated by the shaded arrows in Figure 9.2A that shifted the $\delta^{18}O_{H2O}$ of the fluids and produced a roughly ~25‰ spread in δD.

Thus, this trend represents a modification of the isotopic composition of evolved magmatic water in fluids by further exchange with wall rocks at high water-rock ratios during acid-sulfate alteration. Such a shift would be expected to result from the intense leaching that led to the formation of the vuggy-silica zones and to the replacements of feldspar by alunite. Then mixing of evolved magmatic fluid with unchanged meteoric water would shift fluid compositions to lower δD_{H2O} and $\delta^{18}O_{H2O}$values, and could be the cause of the trend in values for the alunite samples indicated in Figure 9.2A.

9.4.3 Sulfate–sulfide $\delta^{34}S$ equilibrium and thermometry

Sulfur isotopic fractionations between alunite intergrown with pyrite indicates temperatures (calculate from $\Delta^{34}SO_4$–H_2S between 15-25 ‰) ranging from 233° to 293°C and averaging 258.5°C (n=7 pairs; Appendix 8 and Figure 9.5). Such values are consistent with those determined by sulfur isotopic and/or fluid-inclusion thermometry from other high-sulfidation Au-Ag deposits and with the efficacy of magmatic SO_2 disproportionation to $H_2S+SO_4^{2-}$ below 400°C (Bethke, 1984; Stoffregen, 1987; Rye et al., 1992; Fifarek et al., 2005). Although experimental data indicate sulfur isotopic exchange between aqueous sulfate and sulfide species is kinetically inhibited, rates of exchange reach a maximum at low pH at all temperatures (Ohmoto and Lasaga, 1982). For example, according to Ohmoto and Lasaga (1982), in the alunite-stable range of pH ~2.5, the sulfate–sulfide isotopic equilibrium is approached in hours to days at 150° to 350°C. As discussed by Rye (2005), such sulfur isotopic equilibration is typical of magmatic-hydrothermal deposits and is a function of the relatively slow ascent of a magmatic vapor plume. These experimental results imply that alunite–pyrite isotopic equilibrium was also closely approached or attained during the alteration and mineralization stages at Martabe, and the results corroborate the general reliability of sulfate–sulfide geothermometers in the magmatic-hydrothermal

environment.

Figure 9.3 summarizes the sulfur isotope data on sulfur-bearing minerals and a typical sulfate-sulfide pair from Martabe district. The sulfur isotope values on native sulfur indicate that the $\delta^{34}S$ value of bulk sulfur in the underlying magmas was about ~0‰. As discussed in Section 9.4, the $\delta^{34}S_{\Sigma S}$ composition is assumed to be between range of –3.8‰ and 1‰. $\delta^{34}S$ values for hydrothermal sulfides are similar to those of native sulfur, whereas values for pre-ore alunite and barites are much higher than those for the hydrothermal sulfides.

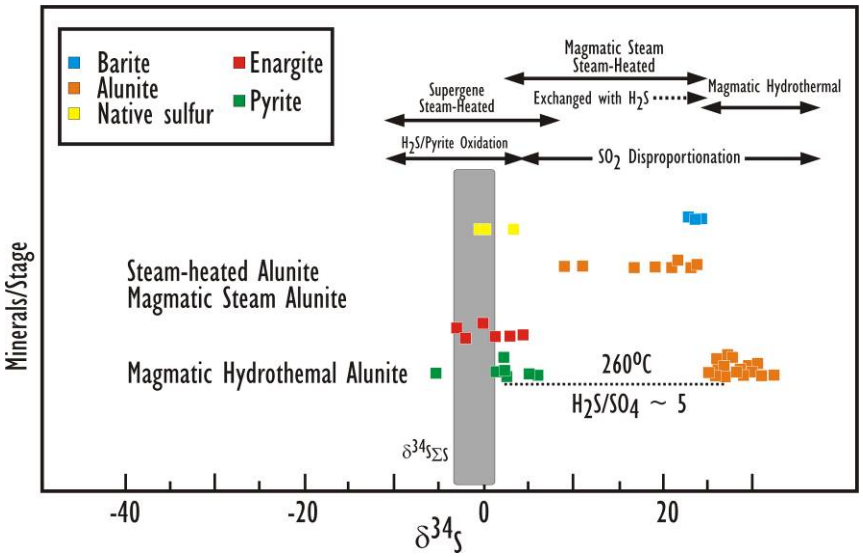

Figure 9.3. $\delta^{34}S$ values of pyrite, alunite and barite from vein and fracture-void filling. Tie lines show a sulfur isotope average temperature and H_2S/SO_4 of fluid for a typical alunite-pyrite pair. Shaded zone shows calculated $\delta^{34}S_{\Sigma S}$ for the system was between –3.8‰ and 1‰ (Appendix 8).

Even though the fluids precipitated abundant sulfates, they were clearly H_2S rich with average H_2S/SO_4 ratios of about 5:1 as shown by the tie line in Figure 9.3 for a typical pyrite-alunite pair (Rye, 1993). These systematics indicate that the hydrothermal fluids were much more reducing than the primary magmatic fluids. The $\delta^{34}S$ values of alunite and coexisting pyrite from Martabe are typical of magmatic hydrothermal acid sulfate alteration zones and similar to other high-sulfidation system (e.g., Rye et al., 1992). The data are consistent with the possibility that the sulfuric acid was derived from the disproportionation of SO_2 during the condensation of magmatic vapor at an average temperature of about 260°C. SO_2 begins to react with condensed water vapor in the plume to form sulfuric acid and H_2S at about 400°C according to the reaction :

$$4SO_2 + 4\ H_2O = 3H_2SO_4 + H_2S.$$

Increasing amounts of H_2SO_4 and H_2S are produced as the temperature decreases. The H_2SO_4 attacks the rocks to form acid sulfate alteration assemblages. H_2S reacts with iron in the system to form pyrite (Holland, 1965; Rye et al., 1992).

The $\delta^{34}S$ and $\delta^{18}O$ isotope data on the SO_4 in alunite and calculated fluid composition are shown in Figure 9.4. The narrow range of calculated $\delta^{18}O_{H2O}$(~–8 ±2‰) values for the fluids is consistent with the hypothesis that the disproportionation of SO_2 took place in nearly exchanged magmatic fluids. As demonstrated by the $\delta^{34}S$ values for alunite fluids (Figure 11.4A). Figure 11.4A summarizes the hydrogen and oxygen data of alunite and various sulfates in the system. The calculated alunite fluids at Martabe have a narrow range of δD of meteoric water during ore deposition, defined from analyses of fluids in late stage minerals as about 28‰. Clearly mixing was a major cause of mineralization in the veins. The important lesson at Martabe is that, sandwiched in between igneous events, a magmatic vapor phase followed by hypersaline and saline liquid-phase fluids rose to very high levels and initially displaced the meteoric water in the host rocks. Although these fluids were of magmatic origin, exchange with deep crystalline rocks apparently controlled their redox state and isotopic composition.

9.4.4. $\delta^{18}O_{H2O}$ and $\delta^{18}D_{H2O}$ values of alunite-forming fluids

Correlation of both $\delta^{18}O$ and $\delta^{18}D$ values of the magmatic-hydrothermal alunite and the calculated $\delta^{18}O_{H2O}$ and δD_{H2O} values of the alunite-forming fluids is shown in Figure 9.2A. The temperatures used to calculate the fluid values were derived from alunite-pyrite sulfur isotopic fractionations (Appendix 8). Fluids associated with the formation of magmatic-hydrothermal alunite range from large values ($\delta^{18}O_{H2O}$=0.1‰ and δD_{H2O}= –45‰) to progressively lower values ($\delta^{18}O_{H2O}$= –3.6‰ and δD_{H2O}= –55‰) along a trend that suggests a mixing of magmatic fluid and unexchanged meteoric water (Figure 9.2A). The magmatic end-member fluids isotopically resembles a fluid inferred to have equilibrated with felsic magma (Figure 9.2A). Although the actual isotopic composition of meteoric water at this time and location is unknown, the estimated $\delta^{18}O$ and δD values are similar to those determined for meteoric groundwater present in the vicinity of the Sibayak Geothermal Field (Abidin et al., 2005). A projection of these data trend to the meteoric water line implies an approximate meteoric groundwater composition at the time of Martabe mineralization ~>2.5 to <3.3 my ago is –8 ±2‰ for $\delta^{18}O_{H2O}$ and –65 ± 8‰ for δD.

If simple mixing between meteoric and magmatic fluids is assumed, then the magmatic-hydrothermal alunite precipitated from magmatic-dominant fluids (Figure 9.4). Deviations from the fluid mixing trend to lower $\delta^{18}O_{H2O}$ values evident in a few

compositions of alunite-forming fluid may be related to the involvement of steam-heated fluids or minor water-rock isotopic exchange.

9.4.5 Alunite and barite $\delta^{34}S$ and $\delta^{18}O_{SO4}$ relations

The distribution of magmatic hydrothermal alunite $\delta^{34}S$-$\delta^{18}O_{SO4}$ values is plotted in Figure 9.4 relative to the predicted compositions of magmatic-hydrothermal sulfate that equilibrated with a fluid of $\delta^{18}O$=~8‰, $\delta^{34}S_{\Sigma S}$=~0 to 1‰, and H_2S/SO_4=5 at temperatures of 150° to 400°C. Oxygen isotopic fractionations for alunite $SO_4^{2-}{}_{H2O}$ (Stoffregen et al., 1994) indicate that alunite $\delta^{18}O_{SO4}$ values should be ~5‰ larger than those for aqueous sulfate at these temperatures. The Martabe alunite has predicted $\delta^{34}S_{SO4}$ value consistent with magmatic, but the $\delta^{18}O_{SO4}$ sulfate values range up to 11‰ less than those of magmatic sulfate (Figure 9.4). These lower alunite $\delta^{18}O_{SO4}$ values are consistent with the involvement of isotopically light meteoric water in the alunite-forming fluids, as noted previously.

Barite veins cut most of the lithologies including hydrothermal breccias and the main-stage mineralization. At shallower levels, base metals are absent and goethite and jarosite occur with the barite. In Summitville, the oxidized-Fe minerals associated with barite in the shallow part of the system resulted from supergene oxidation (Gray and Coolbaugh, 1994). Barite deposition along with the jarosite and goethite, base metals, and gold, were not weathering products, but instead they were formed by the mixing of hypogene fluids and steam-heated waters that had drained back into the ore zone (e.g., Holland and Malinin, 1979; Redd and Spychcer, 1986; Stoffregen, 1987).

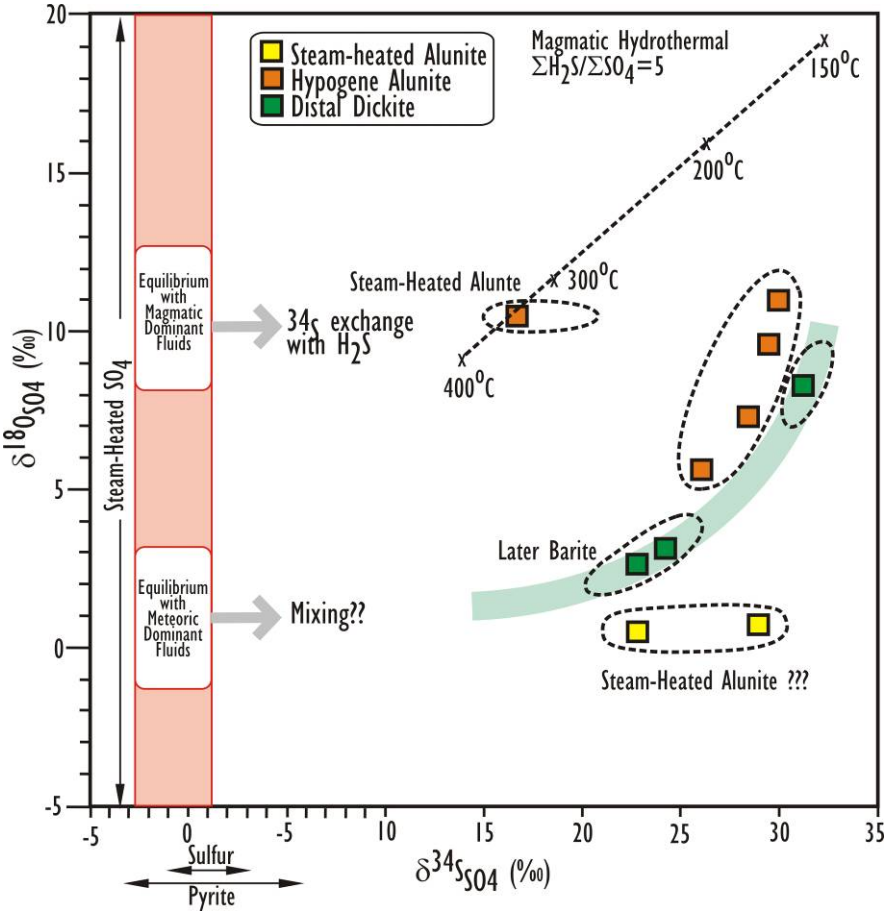

Figure 9.4. Plot of $\delta^{34}S_{SO4}$ vs. $\delta^{18}O_{SO4}$ for alunite and barite samples. The correspondence $\delta^{34}S_{SO4}$ and $\delta^{18}O_{SO4}$ values with those for alunite for all but only one barite sample indicates that the sulfate in that barite was of magmatic origin. Also illustrated is the shift to higher $\delta^{34}S_{SO4}$ values with SO_4^{2-} - H_2S isotopic exchange for steam-heated alunite and the possible composition of steam-heated sulfate incorporated into isotopically light barite (modified from Fifarek et al., 2005). See text for discussion.

Three of the Martabe barites have variable and broadly correlated $\delta^{34}S_{SO4}$ and $\delta^{18}O_{SO4}$values of 22.8‰ to 31.2‰ and 2.6‰ to 8.3‰, respectively (Figure 9.4; Appendix 8). The $\delta^{18}O_{SO4}$ values for most of the barite samples are slightly lower than the values for alteration alunite at corresponding $\delta^{34}S$ values. One sample of barite has a sulfate isotopic value similar to those of the 'low'-temperature magmatic-hydrothermal alunite, although the other two samples have relatively lower $\delta^{34}S_{SO4}$ and $\delta^{18}O_{SO4}$ values.

The two barite samples from Gerhana (APSD105_49.5 and APSD100_24.2) with $\delta^{34}S_{SO4}$ values of 22.8 to 24.3‰ and low $\delta^{18}O_{SO4}$ values of 2.6 to 3.1‰ (Figure 9.4) were collected at an elevation of 282 masl and 331 masl and are associated with jarosite/goethite and significant Au values. If the temperature of this barite deposition was <150°C, the $\delta^{18}O_{SO4}$ of the parent fluid was <–8.0‰ (Appendix 8; Zheng, 1999), indicating a substantial meteoric component. The major component of aqueous sulfate of these samples was most likely derived from the oxidation of H_2S in a steam-heated environment

overlying the main alteration-mineralisation zone. In the more neutral and lower temperature solutions typical of barite deposition during late-stage fluid mixing, sulfur-isotope exchange between aqueous sulfate and sulfide is kinetically inhibited (Ohmoto and Lasaga, 1982); thus isotopic equilibrium among sulfur species would be reflected in the precipitated barite.

The overall trend of the barite "field" suggests either the mixing of, or a temporal, shift between two end member sulfates, one magmatic and the other near-surface oxidation of H_2S in the presence of dominantly meteoric fluids ($\delta^{18}O_{H2O}$= 12.90 to 12.40‰) (Figure 9.4). In large part, the difference between alunite-water and barite-water oxygen-isotope fractionations may also be due to a greater influence of meteoric water on the $\delta^{18}O_{SO4}$ of the barite, and to temperature variations. The aqueous sulfate for most of the barite equilibrated with fluids that had almost the same $\delta^{34}S_{SO4}$ and $\delta^{18}O_{H2O}$ as did the alunite alteration and was clearly derived from magmatic sources (Figure 9.4).

Therefore fluids that deposited most veins and vugs of barite at Martabe were dominated by the aqueous sulfate derived from the oxidation of H_2S in a steam-heated environment overlying the main alteration-mineralisation zone, and that the fluid represent a further neutralization of the system. Variable degrees of mixing of such fluids with overlying steam-heated water during the late-stage collapse of the hydrothermal system are likely to have occurred, such as at Periena, Peru (Fifarek and Rye, 2005) and Summitville (Bethke et al., 2005).

9.4.6 Dickite minerals

Dickite $\delta^{18}O$ values are from 3.9‰ to 5.1‰, whereas the δD values fall in a narrow range of –84‰ to –87‰. The dickite has lower $\delta^{18}O$ and δD values than that of magmatic-hydrothermal alunite (Figure 9.2A; Appendix 8). The $\delta^{18}O$ values of fluids responsible for dickite/kaolinite formation during acid-sulfate alteration, calculated using the kaolinite and waters fractionation factors of Shepperd and Gilg (1996) and assuming a temperature range of 180°–200°C, are similar to those $\delta^{18}O$ value obtained for alunite. The δD_{H2O} values calculated using the equations of Gilg and Sheppard (1996), extend, however, to lower values (Figure 9.2A).

$\delta^{18}O_{H2O}$ and δD_{H2O} values of dickite (clay)-forming fluids

The temperatures of dickite formation at Martabe are poorly constrained. Therefore, the isotopic values of clay-forming fluids were calculated using temperatures based on the following assumptions and comparisons (Fifarek et al., 2005): (1) the temperatures were $\leq$250°C, a typical value for magmatic-hydrothermal alunite formation, because most clay samples are formed later than or as a halo to alunite alteration; (2) temperatures were within the stability ranges of relevant clay minerals in geothermal–epithermal environments (Hedenquist et al., 2000); (3) temperatures were 25°C lower for later fracture-filling clays than for their alteration counterparts; and (4) ~<180°C for fracture and vug-filling (Appendix 8).

The calculated fluids have a δD value of about –66‰ to –68‰ at 180°C, a bit higher than present-day local meteoric water in Sibayak (δD = –65 ±8‰) (Abidin et al., 2005). However the $\delta^{18}O_{H2O}$ is shifted (enriched) by ~5–8‰ from the meteoric water line and very minimal shift in δD_{H2O} if isotopic exchange with andesitic rocks occurs continuously during convection (Figure 9.2A). The results indicate that the dickite-forming fluids had $\delta^{18}O_{H2O}$ values equivalent to those of alunite-forming fluids, rich in meteoric water but had generally lower δD_{H2O} values (Figure 9.2A). A similar isotopic relation between clay (kaolinite) and alunite source fluids is observed at Summitville (Bethke et al., 2005) and Nansatsu (Hedenquist et al., 1994). As shown in Figure 9.2A, the field for dickite-forming fluids at Martabe is adjacent to and subparallel to that for alunite-forming fluids.

However, the position and orientation of the field for the dickite (clay)-forming fluid is highly dependent on the assumed depositional temperatures. For example, the use of different assumed temperatures for clays would generate a sub-horizontally oriented field of clay-forming fluids (Figure 9.2A). For example, assumed temperatures of 100° to 150°C instead of 180° to 200°C (Appendix 8) would position most dickite-forming fluids shifted closely to the fluid-mixing trend for alunite.

It is interpreted that the narrow range of δD and $\delta^{18}O$ values of the dickite (clay)-forming fluid suggest that the dickite formed in dilution zones as evolved magmatic fluids mixed with surrounding exchanged meteoric water, whereas alunite formed from dominantly evolved magmatic water. Another possibility is that both alunite and dickite formed from dominantly evolved magmatic water, but dickite underwent retrograde hydrogen isotopic exchange with highly exchanged meteoric water as proposed above for the deep alunite samples (Figures 9.2 and 9.4). The relatively low δD_{H2O} values of the

dickite-forming fluids clearly indicate mixtures of magmatic and meteoric fluids, where the magmatic component is generally smaller than that of the alunite-forming fluids. This possibility also indicates that the dickite zone was developed by wallrock neutralization with minimal mixing with the surrounding meteoric water.

9.5 Steam-heated alunite

Steam-heated alunite has variable $\delta^{34}S$ values (9‰ to 28.9‰) but has relatively uniform $\delta^{18}O_{SO4}$ (~0.6 ±0.1‰) and δD values (–69.7‰ to –61.7‰) (Appendix 8). These alunite samples are isotopically indistinguishable from magmatic-hydrothermal alunite.

9.5.1 $\delta^{18}O_{H2O}$ and δD_{H2O} values of steam-heated alunite fluids

The assumed δD values and oxygen isotopic temperatures (150° to 180°C) for steam-heated alunite at Martabe indicate fluid compositions (approximately δD_{H2O}~–58±5‰; $\delta^{18}O_{H2O}$~–12 ± 1‰) within a value range of the magmatic-hydrothermal alunite parental fluids (Appendix 8; Fig. 9.2A). The field of steam-heated fluids shown in Figure 9.2A is drawn to encompass an average dickite-forming fluid ($\delta^{18}O_{H2O}$=1.5‰ and δD_{H2O}= –68‰) and an alunite-forming fluid (APSD 352_107.5; $\delta^{18}O_{H2O}$= –7.0‰ and δD_{H2O}= –71‰) related to samples of possible steam-heated origin. The dickite sample is located in proximity to steam-heated alteration. These alunite samples were classified as a magmatic-hydrothermal type, but with the possibility of a $\delta^{34}S$–$\delta^{18}O_{SO4}$ signature of steam-heated alunite.

These data suggest that the two samples, and possibly a few others, may have formed in the steam-heated environment or may have exchanged with steam-heated fluids. The similarity in $\delta^{18}O_{H2O}$ and particularly δD_{H2O} values of steam-heated and magmatic-hydrothermal fluids indicates a strong magmatic influence in the steam-heated environment.

9.5.2 $\delta^{34}S$ and $\delta^{18}O_{SO4}$ relations of steam-heated alunite

Most of the analyzed steam-heated alunite samples from Martabe have $\delta^{34}S$ values similar to those of magmatic-hydrothermal alunite, with an exception exhibiting relatively low $\delta^{34}S$ (9.0‰) values (sample APSD 156_93.7). Oxidation of H_2S gas in the vadose zone produces sulfate with a $\delta^{34}S$ value approximating that of the source H_2S and which has a

potentially wide range of δO_{SO4} values (Rye et al., 1992).

For Martabe, such steam-heated sulfate would have a $\delta^{34}S_{SO4}$ value of ~5.0± 5‰ and 16‰ on the basis of an average $\delta^{34}S_{sulfide}$ values of 1.0 ± 4‰, and would have a $\delta^{18}O_{SO4}$value that reflects formation in the presence of steam, steam condensate, and atmospheric oxygen. The unusual compositions of the steam-heated alunite require that, following percolation to the water table, the sulfate generated in the vadose zone isotopically exchanged with aqueous or streaming H_2S and magmatic–meteoric fluids at temperatures of 150° to 180°C. This exchange step enriched the sulfate in $\delta^{34}S$ by about 10‰ to 32‰ relative to the initial value (~1‰) and yielded a uniform $\delta^{18}O_{SO4}$ value of 13‰ (Figures 9.4 and 9.5).

9.6 Sulfur source and speciation

9.6.1 $\delta^{34}S_{\Sigma S}$ and H_2S/SO_4

The sources of the sulfur in the Martabe deposit can be interpreted from the $\delta^{34}S$ composition of total sulfur ($\delta^{34}S_{\Sigma S}$) in the magmatic-hydrothermal fluids. This parameter and the SO_4/H_2S ratio of the fluids may be derived from a $\delta^{34}S_{alunite}$ vs. $\delta^{34}S_{pyrite}$ plot of coexisting magmatic-hydrothermal alunite and pyrite (Figure 9.5).

The absolute value of the slope of the line is equivalent to R, the SO_4/H_2S molar ratio. An array of R lines is shown in Figure 9.5 for SO_4-H_2S isotopic exchange in a systems in which $\delta^{34}S_{\Sigma S} = 0$. The theoretical and mathematical basis for δ–δ diagrams was developed for oxygen-isotope data by Gregory and Criss (1986) and Criss et al. (1987). Isotherms plot as straight lines of +1 slope in $\delta - \delta$ space (Gregory and Criss, 1986), as illustrated for alunite–pyrite equilibration between 200° and 700°C in Figure 9.5. A theoretical upper temperature limit is reached at $\Delta x\text{-}y=0$, which is the isotherm that passes through the origin. This isotherm represents a locus of points corresponding to different $\delta^{34}S_{\Sigma S}$ compositions and the convergence of their related linear arrays of constant R. For the example of $\delta^{34}S_{\Sigma S}=0$, the related array converges on the origin (Figure 9.5). Consequently, linear data trends with slopes can be used to estimate R (i.e., absolute value of slope m=R), and the intercept of the trend projection with the isotherm passing through the origin is an estimate of $\delta^{34}S_{\Sigma S}$, which may be read directly from the abscissa or ordinate axis (Fifarek et al., 2005).

The Martabe data on a $\delta^{34}S_{sulfate} - \delta^{34}S_{sulfide}$ diagram (Figure 9.5) form a subhorizontal linear cluster that spans isotherms corresponding to the calculated temper-

atures of ~230° to 380°C. The data correlate poorly because of the limited range of $\delta^{34}S_{pyrite}$ relative to $\delta^{34}S_{alunite}$, and the determination of a representative trendline is particularly sensitive to uncertainties related to analytical accuracy and model assumptions (equilibrium isotopic exchange, constant R, constant $\delta^{34}S_{\Sigma S}$ closed-system behavior). A linear regression analysis of the Martabe data results in a best-fit line with a slope of 0.11 and a derived $\delta^{34}S_{\Sigma S}$value of~+1 (Figure 9.5).

The total S isotope ($\delta^{34}S_{\Sigma S}$) composition of the original fluid composition in Martabe is not known. The $\delta^{34}S$ of the bulk sulfur in the magma and in the fluids that exsolved from it can be estimated from $\delta^{34}S$ data on igneous minerals if data on the temperature, sulfur fugacity, and oxidation state of the magma are available (Bethke et al., 2005). However, for a hydrothermal system with a $\delta^{34}S_{\Sigma S}$ of ~1‰, alunite typically would have values of 15‰ to 30‰, depending on the $\delta^{34}S$ temperature of deposition and H_2S/SO_4^{2-} ratio of the system (Rye, 2005).

Currently, such data do not exist for the lithologies in the Martabe district. However, an estimate can be made from the $\delta^{34}S$ data on sulfate from the Sibayak Geothermal Field, 100 km north of the Martabe district. The isotopic $\delta^{34}S$ concentration of H_2S gas from three production wells of Sibayak Geothermal Field, shows average values of –3.3‰, –3.7‰ and –4.3‰, respectively (average–3.8‰); and the average $\delta^{34}S$ value of H_2S from steam vent discharge is –1.7‰. The value is more depleted than production wells and supposing that value is close to the $\delta^{34}S$ magmatic or influenced by magmatic origin or sources (Abidin et al., 2005). Native sulfur in Martabe has an isotopic composition of –0.6‰ to 3.1‰ (average 1‰), therefore if these values are a reasonable estimate, the $\delta^{34}S$ of the bulk sulfur in the magma lies between the two values (–3.8‰ to 1‰) (Figure 9.5).

Estimates of both $\delta^{34}S$ of the magma and SO_4^{2-}/H_2S_{aq} of fluids separated from it can be obtained from a plot of $\delta^{34}S$ of H_2S_{aq} in equilibrium with sulfide minerals vs. $\delta^{34}S$ of SO_4^{2-} in equilibrium with coexisting sulfate minerals, assuming that equilibrium was obtained between the aqueous species in the fluids. Overall, the $\delta^{34}S$ compositions of alunite–pyrite pairs from Martabe suggest equilibrium exchange over a temperature range of 180° to 320°C from sulfide-dominant fluids with $\delta^{34}S_{\Sigma S}$ ~1‰. Assuming the intrusive value of ~1‰ for the total $\delta^{34}S$ of Martabe fluids, an isotopic mass balance using an average of –2‰ for the sulfide and 26‰ for the sulfate indicates that the sulfide/sulfate ratio of the original fluid was about 4:1 or 5:1.

Figure 9.5 is such a plot for alunite–pyrite pairs produced by acid-sulfate alteration at Martabe. Lines of constant ΔSO_4–H_2S_{aq} with a positive 1:1 slope are plotted for temperatures from 200° to 700°C on the basis of the equations of Ohmoto and Lasaga (1982). A line representing ΔSO_4–H_2S=0‰ is also plotted and scaled for $\delta^{34}S$ for the bulk sulfur in the system. Dotted lines representing R values ($R=SO_4^{2-}/H_2S_{aq}$) of 0, 1, and infinity are plotted for bulk sulfur $\delta^{34}S$ values of 0‰ and 5‰. The $\Delta^{34}SO_4$–H_2S lines for their temperatures estimated from the pyrite–alunite fractionation. Although Figure 9.5 cannot be used in a strict analytical sense, the plot allows estimates of the evolution of the bulk sulfur and the SO_4^{2-}/H_2S_{aq} of the system.

The dashed line through the points for two 230° and 380°C pyrite–alunite pairs indicates that the fluid was H_2S_{aq}-dominant at an almost constant SO_4^{2-}/H_2S_{aq} during its ascent from the carapace of the source magma, implying that the system was buffered by the wall rocks during ascent. During the intense leaching leading to the vuggy quartz alteration, the combined processes of SO_2 disproportionation and pyrite deposition changed the bulk ^{34}S of the system and the fluid became strongly SO_4^{2-}/H_2S_{aq} -dominant as indicated by the early vertical dashed line through the pyrite–alunite points (as shown in Bethke, 2005; Fatarek, 2005), the wallrocks having lost their buffering capacity. This evolution of the redox state of the sulfur species from dominantly reduced to dominantly oxidized is obvious from the fact that, in the quartz–alunite alteration zone, the $\delta^{34}S$ of the sulfate is nearly constant while that for the pyrite undergoes a much greater change.

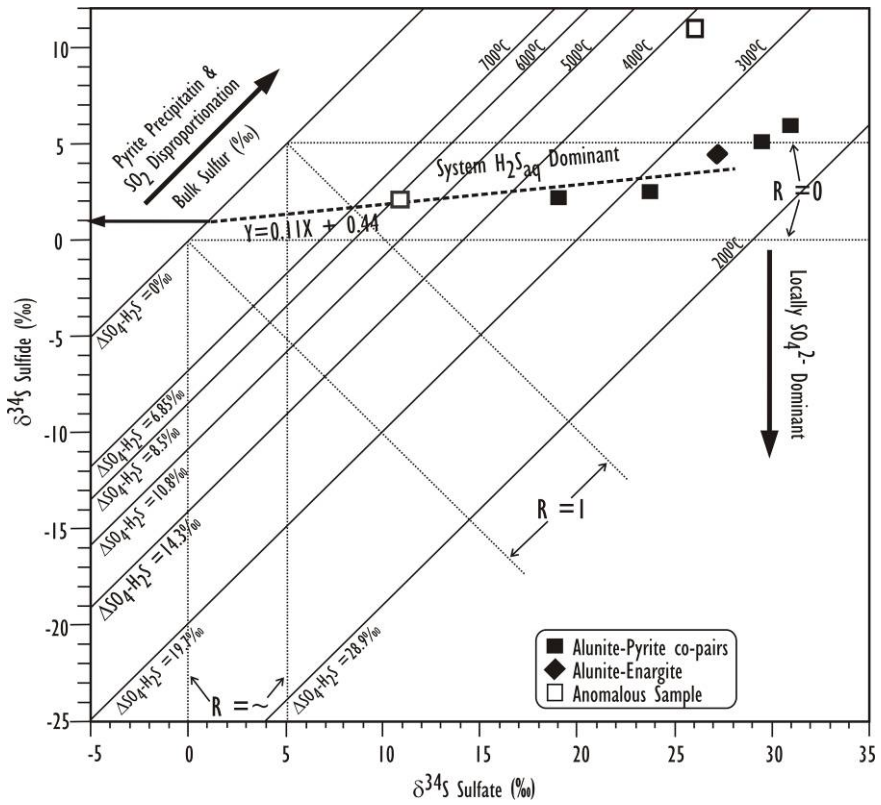

Figure 9.5. Diagram of $\delta - \delta$ for $\delta^{34}S$ in aqueous sulfide and sulfate species in sulfide (pyrite, enargite) and alunite pairs (squares) formed during acid-sulfate alteration. The nearly horizontal slope of the dashed line through pyrite–alunite point, and a cluster of the about 250°C pyrite–alunite points indicates that the system was H_2S_{aq}-dominant in the magma and during ascent into the acid-sulfate alteration zone due to buffering by the wallrocks. The dashed line is the best-fit representation of the Martabe data, excluding one sample (see text), and has a slope equivalent to the absolute value of the SO_4^{2-}/H_2S_{aq} ratio of 0.11. Extrapolation of the dashed line to the 45° line for $\Delta^{34}SO_4–H_2S=0‰$ shows that the initial isotopic composition of the bulk sulfur in the system was near +1‰ (read from the abscissa or ordinate) and remained so until reaching the zone of intense acid-sulfate alteration. Precipitation of pyrite and increasing disproportionation of SO_2 during wall rock alteration changed the bulk isotopic composition of the aqueous sulfur species to increasingly larger values, as indicated by the shaded arrow, causing the fluids to become SO_4^{2-} dominant.

As noted in Section 9.4.5, the $\delta^{34}S$ values for two barites samples was interpreted to have been precipitated from fluids involving steam-heated waters; and another single barite sample of the second group is similar to those for magmatic hydrothermal alunite. The relatively high $\delta^{34}S$ values for the second group of barite samples, and the $\Delta^{34}S$ between barite and associated sulfides, are similar enough to those for the pre-ore alunite and pyrite to indicate that the late-stage ore fluids had a sulfur isotopic geochemistry similar to that of the earlier acid-sulfate fluids. This reflects the conclusion that the oxidation state of the fluids for both stages was buffered by the same deep rocks that controlled the H_2S/ SO_4^{2-} of the alunite alteration fluids at a value >1 prior to disproportionation of SO_2.

9.7 Discussion

9.7.1 Acid sulfate alteration

The isotopic systematics of acid sulfate alteration at Martabe is similar to that documented other high-sulfidation Au-Ag deposits and is consistent with the magmatic-hydrothermal genetic model (e.g., Bethke, 1984; Stoffregen, 1987; White, 1991; Rye et al., 1992; Rye, 1993; Arribas, 1995; Giggenbach, 1997; Corbett and Leach, 1998; Hedenquist et al., 1998, Cooke and Simmons, 2000). A mineralizing intrusion below the Martabe deposit likely crystallized from magma. Magmatic vapor separating from the brine slowly ascended along structures and condensed into meteoric groundwater primarily at the level of the permeable volcaniclastic and breccias units. Buffering of the rising fluids by Fe^{2+} in rocks below the lithologies (andesites and possibly Mesozoic metasedimentary rocks) generated a reduced (H_2S/SO_4 ~5), highly acidic condensate with a $\delta^{34}S_{\Sigma S}$ value of ~1‰. Acid was generated through the separation of HCl and HF gasses and the disproportionation of SO_2 to H_2S and HSO_4^- at temperatures ranging from 380° to 230°C. The alteration zonation resulted from a progressive neutralization of the acid fluids as they migrated away from fluid and vapor conduits now marked by zones of vuggy quartz. Thermodynamic modeling (e.g., Stoffregen, 1987; Reed, 1997) indicates that vuggy quartz forms through the extreme leaching of rocks at a pH ~1 and that alunite–quartz is stable at a pH ~2.5, intermediate argillic assemblages at pH~4, and propylitic assemblages at a pH ~5.5.

9.7.2 Ore fluids

A model for high-sulfidation epithermal deposits has been widely proposed that main-stage ore mineralization results from the introduction of the degassed residual magmatic-hydrothermal brines that provided vapor for the early acid sulfate alteration (e.g., White, 1991; Corbett and Leach, 1998; Cooke and Simmons, 2000). Because of degassing, these fluids are expected to be more saline, metal-rich, and reduced than the previous fluids. Vapor-rich fluid inclusions are apparently associated with some high-salinity fluid inclusions, which suggest that the brines boiled, at least temporarily (Fifarek et al., 2005). The isotopic similarity between alunite and clay (dickite), suggests a compositional similarity between the fluids. Indeed, the occurrence of alunite-sulfide and clay (dickite)-sulfide veinlets in wallrocks of identical alteration assemblages suggests that some fracture filling and alteration formed nearly contemporaneously from the same fluids. Temperature estimates based on isotopic reactions do not reveal a systematic increase with depth. For example, maximum temperatures apparently increase from ~233°C above 591 m to

>290°C at 425–450 m and then decrease to ~241°C at around 464 m (Figure 9.2B; Appendix 8). Such a thermal profile, if accurate, is suggestive of a fluid plume that formed when hot acidic fluids rising along structures in the host rock porphyries encountered the permeable volcaniclastic rocks, slowed in velocity, and dispersed upward and outward. Cooler meteoric dominant groundwater would have been drawn into the plume near the volcaniclastics-lava contact, and lateral fluid flow may have occurred along the strike of the orebody. These inferred hydrodynamics are consistent with the subvertical-shaped vuggy quartz zone from Baskara, in the central part, to the subhorizontal -shaped vuggy quartz zone from Purnama or Gerhana- in the peripheral part of the deposit.

9.7.3 Steam-heated environment

The isotopic compositions calculated for the Martabe steam heated alunite, dickite, and related fluids indicate a dominant magmatic influence in the steam-heated environment. Relationships among SO_4-H_2S fractionation, temperature, pH, and rates of isotopic exchange are described in Rye (2005), which are based on data and interpretations by Ohmoto and Lasaga (1982). The assumed temperatures and magmatic isotopic signature of the Martabe steam-heated fluids suggest that condensed magmatic-hydrothermal fluids displaced meteoric groundwater in the host breccias or volcaniclastic rocks up to the water table.

The combination of factors that could have led to this result includes a high rate of vapor injection into the groundwater, a low rate of groundwater recharge, and an intrinsically low discharge rate due to the absence of major structures that would have channeled flow to hot springs on the flanks of the deposit. Vapor condensation can ultimately transfer sufficient heat to the fluid phase to initiate boiling. This process and (or) non-condensing magmatic steam supplied H_2S and isotopically light sulfate to the vadose zone and groundwater near the water table. Such high-level vapor–fluid interactions apparently created the high-temperature low-pH steam-heated environment that promoted appreciable SO_4^{2-}-H_2S isotopic exchange and the generation of isotopically heavy steam-heated sulfate.

The boiling of magmatic acid fluids can further enhance SO_4^{2-}-H_2S isotopic exchange by decreasing the fluid pH (Reed, 1997). A pH below that of alunite stability (<2) would have the dual effect of increased isotopic exchange rates (Ohmoto and Lasaga, 1982) and, in the absence of a precipitating sulfate minerals, increased sulfate residence times. A very low pH may be attained in siliceous rocks with little buffering capacity, such as those produced by vuggy quartz alteration or intense steam-heated alteration along

faults. Consequently, a lowering of the steam-heated environment into vuggy quartz rock would have been particularly conducive to the attainment of SO_4^{2-}-H_2S equilibrium in the steam-heated fluids at Martabe.

9.7.4 Barite fluids

A the concave-up J-shaped form of the barite field in Figure 9.4 indicates the mixing of two fluids with isotopically distinct sulfate in unequal concentrations. The isotopically heavy end member sulfate has a strong magmatic-hydrothermal signature, whereas the isotopically light end member sulfate most likely formed in a steam-heated meteoric-water-dominant environment. Assuming the isotopically light barite ($\delta^{18}O$ ~0‰) precipitated at ~150°–180°C, a temperature typical of the steam-heated environment, then the fluid for this end member barite had a $\delta^{18}O_{H2O}$ value of approximately –9‰, a composition similar to that of some goethite-forming fluids. However, the low solubility of barite under most hydrothermal conditions indicates that appreciable amounts of Ba and SO_4^{2-} were not transported together in either end member fluid; barite precipitation typically is in response to the mixing of a Ba-rich fluid and a SO_4^{2-}-rich fluid (Holland and Malinin, 1979). At Martabe, Ba may have been supplied to barite depositional sites near the level of the water table either by a sulfate-deficient third fluid, which seems implausible, or by magmatic vapors. An example of evidence for the transport of Ba in magmatic vapors is provided by data from Tambo (Deyell et al., 2005).

The presence at Martabe of steam-heated sulfate with magmatic-hydrothermal isotopic signatures provides another possible explanation for the barite data. At low water/rock ratios, magmatic acid sulfate fluids may evolve through water–rock reactions to a reduced fluid deficient in SO_4^{2-}, with substantial Ba derived from the leaching of earlier precipitated alteration barite and with significant concentrations of Ag and lesser Au (Reed, 1997). Such a fluid may have mixed with steam-heated fluids to generate the late void-filling barite ±acanthite at Martabe. In this case, the barite data may record the transition from an early isotopically heavy steam-heated sulfate that had equilibrated with magmatic-hydrothermal fluids at the water table to a later isotopically light steam-heated sulfate that underwent minimal SO_4^{2-}-H_2S exchange in cooler meteoric-water-dominant fluids. Consequently, the J-shaped field of barite data in Figure 9.4 would not represent a mixing trend involving two distinct sources of sulfate, but a temporal shift in the isotopic composition of sulfate derived from a single (steam-heated) source. Moreover, in the analyzed suite of samples, barite with low isotopic values is generally at lower elevations than barite with high isotopic values (Appendix 8), which suggests that a dropping water

table accompanied the transition to meteoric-dominant fluids and the collapse of the system.

9.8 Summary

The dominant lithological control of alteration–mineralization at the Martabe deposit is linked to the isotopic signatures of alunite and barite through fluid mixing and the kinetics of SO_4^{2-}-H_2S isotopic exchange. Magmatic vapor condensing in meteoric groundwater generated acid sulfate fluids that reacted with the volcanic host rocks to produce a zoned alteration suite typical of high-sulfidation epithermal Au-Ag deposits.

Dispersed fluid flow resulted in relatively large volumes of vuggy quartz-and alunite-quartz–altered rock. Alunite of this stage reflects equilibrium SO_4^{2-}-H_2S isotopic exchange over temperatures of 380° to 230°C in fluids that maintained a constant redox potential and H_2S/SO_4^{2-}ratio due to reaction with wallrock Fe^{2+}. During periods of high vapor influx, the hydrodynamic conditions allowed magmatic-hydrothermal fluids to displace meteoric groundwater up to the water table and to generate temperature (180°–150°C and low-pH (~2) steam-heated fluids with a magmatic signature. Unusually rapid SO_4^{2-}-H_2S isotopic exchange rates for this environment permitted the complete equilibration of steam-heated sulfate with H_2S at and immediately below the water table, as recorded in some steam-heated alunite. Pulses of magmatic steam from the degassing magma penetrated the deposit, but the hydrodynamic contrast at the lava-volcaniclastic rock contact slowed the ascent of the steam, which allowed the incorporation of groundwater and the time for partial SO_4^{2-}-H_2S isotopic exchange prior to precipitation of magmatic-steam alunite.

A descending water table during the late collapse of the hydrothermal system resulted in the progressive incursion of meteoric water into the steam-heated environment, as is recorded in the isotopic composition of barite and then deposited goethite±hematite after sulfides. This oxidizing hydrothermal stage leached sulfides, redistributed metals, and possibly enriched the deposit to ore grades.

CHAPTER 10

EVOLUTION OF THE MARTABE VOLCANIC AND DOME COMPLEX AND MINERALISING HYDROTHERMAL SYSTEM

10.1 Martabe volcanic and dome emplacement

The Martabe district is a discrete Pliocene dome complex surrounded by Early to Late Miocene sedimentary-volcanic sequences, including the diatreme breccias that record a complex sequence of tectonic, phreatic and phreatomagmatic brecciation.

Formation of the Martabe district in the Miocene commenced with the Angkola basaltic andesite-volcaniclastic (Tmav and Tmab) and Toru porphyritic andesitic (Tmtv) volcanic units, following by eruption of a series of phreatic-phreatomagmatic breccias and emplacement of flow domes.

A fiamme-rich tuffaceous rock found in Gerhana (drill holes APSD 103 and 105), indicating previous volcanic activity. These fiamme-rich tuffaceous rocks are poorly sorted, heterolithic, lithic tuff with carbonized wood fragments and are overlain by unstratified, partly welded pyroclastic rocks. This association is typical of a maar volcano setting in which a base surge deposit is formed by a phreatomagmatic eruption directed radially outwards from the vent (Cas and Wright, 1987), and subsequent eruptions deposit airfall tuffs. Juvenile diatreme breccias or volcanic vents are recognized because domes may not be subsequently emplaced preferentially within these original volcanic conduits (Turner, 1997).

Previous 1:10,000 scale mapping at Martabe reveals some characteristics of the various breccias and dome. On aerial photographs, the Baskara and Kejora domes are surrounded by a 2 km diameter circular feature. Laminated, lacustrine sedimentary rocks occur at Purnama, and may have accumulated in a shallow depression formed by the diatreme eruption. The breccia vent provided a highly permeable conduit for fluids, probably resulting in early fumaroles, and acid-sulfate activity around the maar volcano with silicification of marginal tuffs and lacustrine sediments (Turner, 1997).

Unstratified-weakly stratified, poorly sorted breccias with sparse but distinctive silicified clasts are preserved on the margins of the diatreme at Baskara and Purnama East. These may be interpreted as a tuff ring deposited from shallow, phreatomagmatic eruptions which breached the partly silicified lake sediments (Turner, 1997). This sequence

explains the presence of silicified fragments in tuffs, as noted at Purnama East and north Pelangi. The distribution of lacustrine sedimentary rocks throughout the Martabe area indicated the presence of a series of vent-filling lakes. Lakes may also form in the depressions between volcanic centers or pull-apart structure, which is common elsewhere in Sumatra, but at Martabe there is a strong association of these sedimentary rocks with the diatreme centers.

The following section outlines a sequence of events that produced the Martabe dome and breccias, and highlights the key evidence, such as alteration and mineralization for each stage. Figures 10.1 to 10.11 illustrate the series of events that formed the Martabe diatreme/dome complex and its relationship to enclosing units, structural framework, alteration, mineralization and present day erosion level.

A Stage- 1

Formation of the Martabe district commenced with the deposition of Pre-Tertiary Tapanuli Metasedimentary rocks (Put) which were intruded by the 208 Ma Uluhalanagodang granite (Mpi). In the Late Oligocene-Miocene, the Sibarus sedimentary rocks (Tms) and 16 Ma Angkola basaltic volcanic flows-volcaniclastic breccia (Tmav) and Toru porphyritic andesite volcanic rock (Tmtv) were emplaced adjacent to the Uluhalanagodang granite and Tapanuli Metasediments. The lithologies are emplaced by normal and strike slip faults, related to splays of the Sumatra Fault System (SFS), which was active from at least the Late Mesozoic (Barber, 2000) or Triassic (Pulunggono et al., 1992). Meteoric water started to descend down the faults.

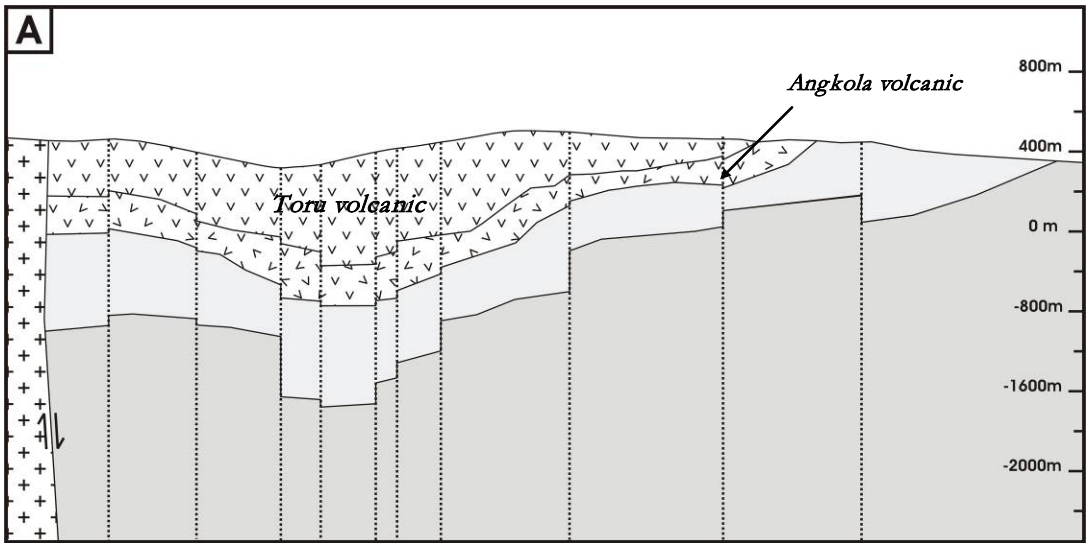

Figure 10.1. Stage-1 showing Pre-Tertiary Tapanuli metasedimentary rocks (Put) (dark grey) intruded by the 208 Ma Uluhalanagodang granite (Mpi). Deposition of Miocene Sibarus sedimentary formation (Tms) (light grey) and volcanic flows adjacent to Pre-Tertiary metasedimentary rocks and granite. These lithologies then are juxtaposed by faults which are related to the Sumatran Fault System (SFS).

B. Stage-2 Intrusion of felsic magma

Intrusion of felsic magma along existing structures that were active during stage-1 (Figure 10. 2). Meteoric water descends down through the faults into units adjacent to the felsic intrusions. Interaction of meteoric water with magma initiated early hydrothermal convection (low-sulfidation fluid). Formation of argillic and prophylitic alteration due to hydrothermal fluid convection is interpreted to have occurred after emplacement of these intrusions. The fluid-magma interaction possibly caused some phreatic eruptions near the surface; and hydraulic brecciation in sedimentary rocks may also have occured adjacent to these intrusions. The hydraulic brecciation is probably caused by heated groundwater seeding deeper into the sedimentary rocks.

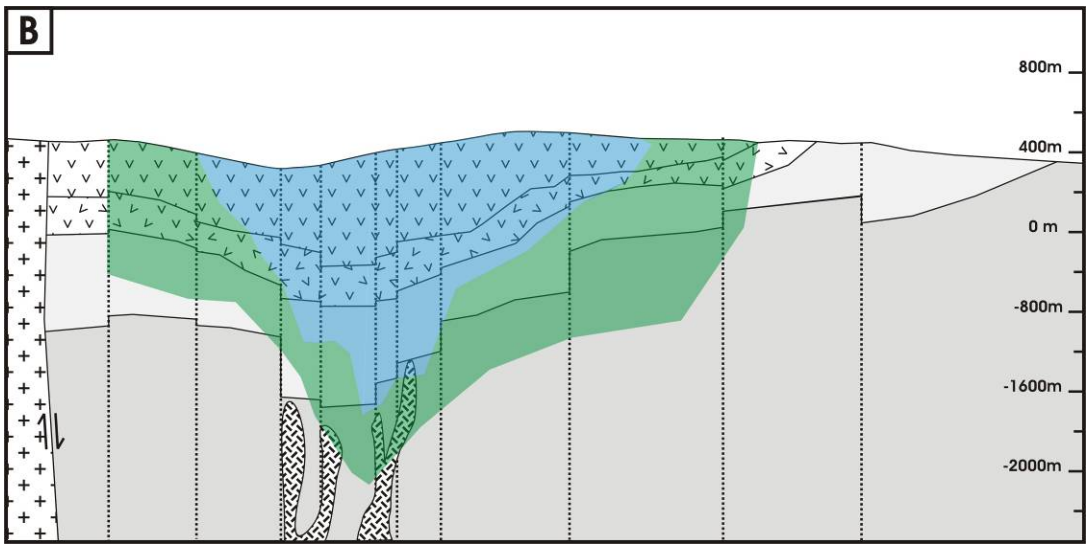

Figure 10.2. Stage-2 showing earlier intrusion of felsic magma along the faults. Intrusion of rhyolitic stocks (dash) through the same faults system generated early argillic alteration (blue). Propylitic alteration (green) formed away from the intrusions.

C. Stage-3 Phreatomagmatic and phreatic eruptions

The felsic intrusions continued to move up along the existing faults and triggered phreatomagmatic and phreatic eruptions into the active hydrothermal system. Phreatomagmatic eruptions are created when magmas ascend to shallow depths and explosively interacted with shallow groundwaters (Lorenz, 1973, 1983). The eruptions (Figure 10.3) produced mainly large unstratified, polymict breccias within the centers of pipes or cones (thick red arrow) and weak- to well-stratified, wet pyroclastic base surge and fall-out eruptions (thin red arrow) at the rims of the vent and on the surface. Volcaniclastic debris from syn-volcanic reworking may have fallen back back into the eruption crater (dashed arrows).

In the subsurface, the products of the phreatomagmatic explosions were mainly polymict, unstratified breccia. These breccia are typically matrix-supported with sub-angular to sub-round fragments and are inferred to have undergone either transport and abrasion, or recycling (e.g., Houghton and Smith, 1993). Sub-facies of polymict-monomictic breccias which have preserved the wispy textures of juvenile magmatic clast textures are also recognized. At surface, the eruptions products were recognized as base surge and fallout deposits placed around a developing maar. Stratified-facies breccias at East Purnama and northeast of Gerhana are interpreted as wet base surge and co-surge fallout deposits on the basis of their bedding forms, which are consistent with deposition from high velocity gas-supported particle transport (Fisher and Waters, 1970; Walker, 1984). Relict felsic fragments and accretionary lapilli were found in both stratified and unstratified breccias.

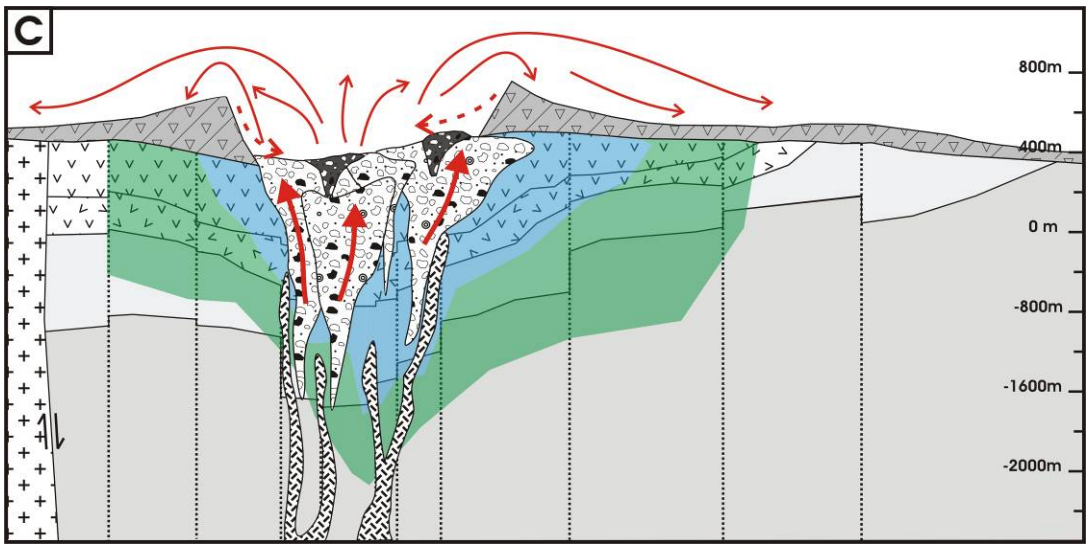

Figure 10.3. Stage-3 showing the intrusion of felsic magma continued up through the faults encountering groundwater and triggered eruptions creating a diatreme. A maar lake was formed and silicification from fumaroles may have occurred. The lake sediments were disrupted by later phreatomagmatic eruptions, which formed unstratified-stratified breccia containing silicified clasts on the margins of the vent.

D. Stage-4 Widening the diatreme

Phreatomagmatic eruptions continue to excavate the conduit and widen the diatreme producing multiple crosscutting breccias (Figure 10.4). Excavation of the diatreme was accompanied by collapse of the upper portions of the maar rim along ring faults, and/or other pre-existing structures. However, no clear evidence for ring faults and collapse structures was found on surface. Widening of the vent caused these breccias to collapse and slump into the diatreme pipe. Blocks of wall rocks, earlier diatreme breccia

phases and bedded pyroclastic deposits slumped into the conduit to be preserved as coherent blocks or disaggregated into later diatreme breccias.

Stratified facies breccias are interpreted to have formed at the surface. There is a transition from bedded to weakly stratified and massive facies with depth. In contrast, on the surface some, remnants of stratified facies breccias may be covered or crosscut by subsequent eruption products. At the northeast of Gerhana and east of Purnama, poorly sorted, heterolithic and lithic tuffs with carbonized wood fragments are overlain by unstratified to weakly stratified, partly welded pyroclastic rocks. The size of clasts diminishes rapidly away from the main centers, which indicates a local source. This association is typical of a maar volcano setting in which a base surge deposit is formed by a phreatomagmatic eruption directed radially outwards from the vent (Cas and Wright, 1987), and subsequent eruptions deposit air fall tuffs. The eruption vent of a maar volcano may also be termed a diatreme breccia. Maar volcanoes typically comprises a series of small <1.5 km diameter, vents forming a volcanic field (Lorenz, 1973). Lacustrine sediments began to deposit in the low part of the water.

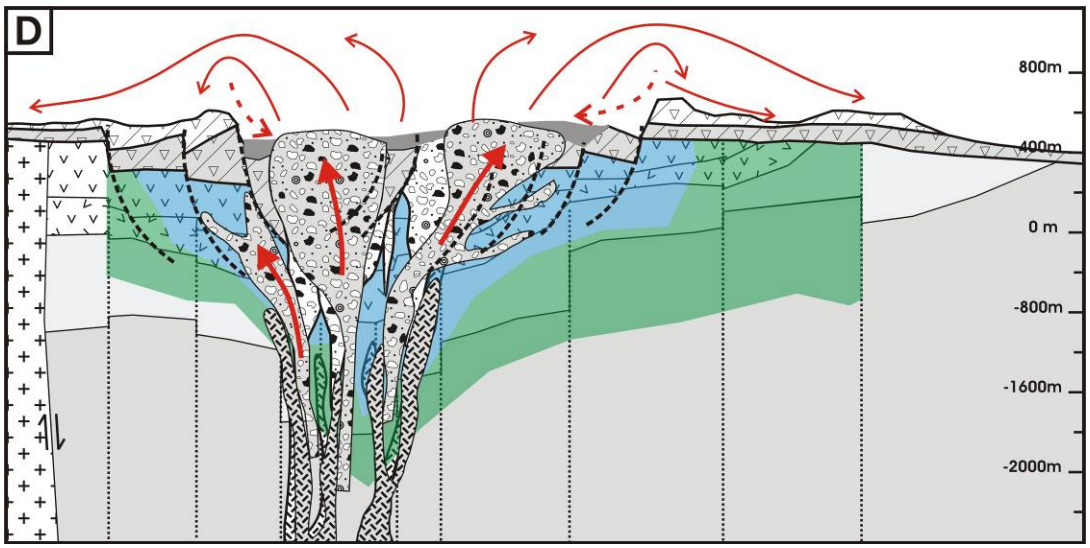

Figure 10.4. Stage-4 showing how the eruption continues to excavate and widen the diatreme conduit producing multiple crosscutting breccias. Collapse of the diatreme walls also caused widening. Lacustrine sediments began to deposit in the low part of the water.

E. Stage-5 High-sulfidation alteration

The diatreme breccia vent provided a highly permeable conduit for fluids (Figure 10.5), probably resulting in early fumarole activity within and around the maar, with silicification of wall and lacustrine sediments. Unstratified, poorly sorted breccias containing distinctive silicified clasts are preserved on the margins of the Baskara domes. These are interpreted as a tuff ring deposited from shallow, phreatomagmatic eruptions

that breached the partly silicified lake sediments (Figure 10.4). This sequence of events explains the presence of silicified fragments in breccias that have subsequently been silicified, as observed at Purnama, Gerhana and Pelangi. High temperature extremely acid (high-sulfidation) fluids that were generated during condensation of magmatic volatiles into a meteoric water reservoir, create the leached rocks. These volatiles derive from degassing magma at depth and include relatively oxidized component of SO_2 gas, as well as HCl, CO_2, H_2S and HF (i.e., Hedenquist et al., 1993, Cooke and Simmons, 2000). The zonation of acid-sulfate assemblages is due to progressive neutralization of the acidic fluid by meteoric fluids (Figure 10.5). Advanced argillic alteration formed, comprising alunitic and kaolinitic sub-types but no mineralization accompanied this alteration. However, the extent and morphology of the vuggy quartz formation depended on how the rising acidifying vapor phases and the influx of meteoric water flow into a porous zone.

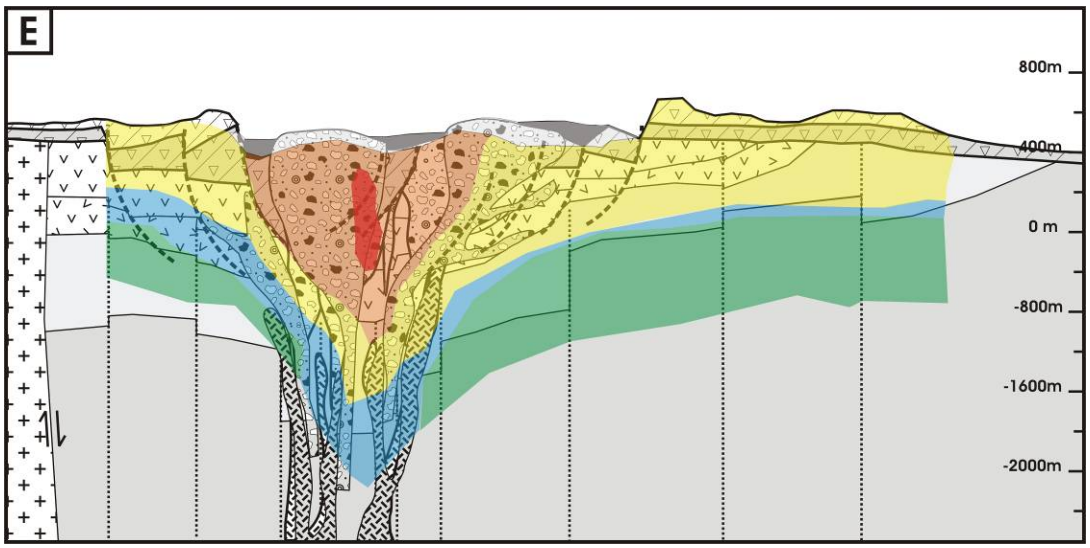

Figure 10.5. Stage-5 showing acid-sulfate alteration generated during condensation of volatile component into a meteoric water reservoir to create the leached rocks; but no mineralization accompanied this alteration. Note: vuggy-quartz (red), alunitic (orange), kaolinitic (yellow), argillic (blue) and propylitic alteration (green) alteration.

F. Stage-6 Low-sulfidation veining

After stage-5 ceases the system returns to hydrothermal convection of meteoric water (low-sulfidation fluid) along structures in an extensional structural regime (Figure 10.6). Boiling of this fluid occurred resulting in deposition of low Au-Ag in quartz-chalcedony veins.

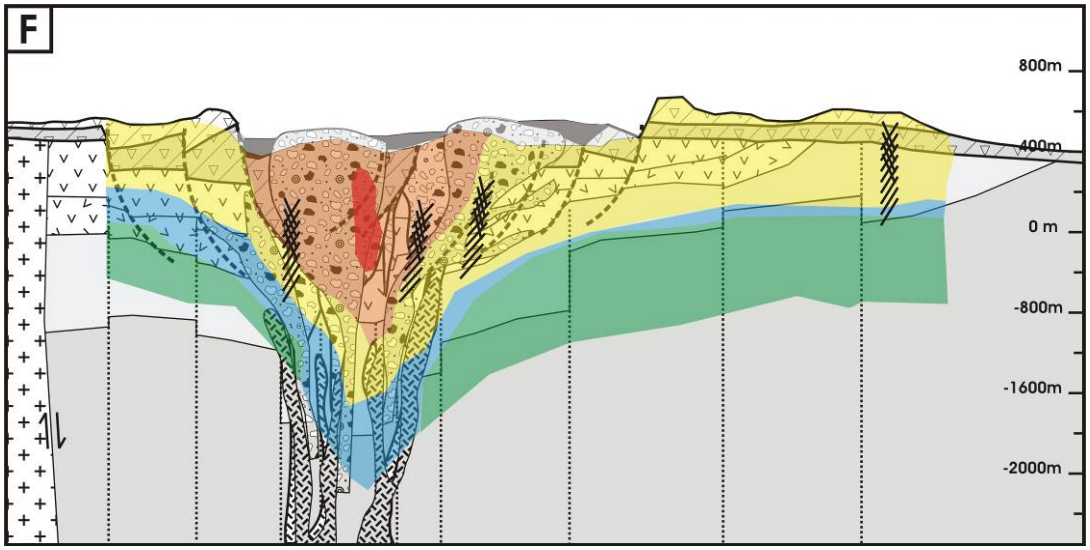

Figure 10.6. Stage-6 showing that after high-sulfidation alteration ceased, the system returns to the convection of near-neutral pH meteoric water (low-sulfidation fluid) resulting in Au-Ag in quartz-chalcedony veining (black hatch pattern) along structures in an extensional structural regime.

G. Stage-7 Dome formation

Intrusion of contemporaneous dacite and hornblende andesite into the diatreme breccia complex to create the dome complex, and which triggered minor phreatomagmatic and widespread phreatic eruptions. The breccia vents provided the channel ways for movement of large volumes of magma to surface or near-surface levels. The source of the magma, and the heat source for all hydrothermal activity was likely an underlying batholith. Late-stage phreatomagmatic breccia may have also occurred but this was not common (Turner, 1997).

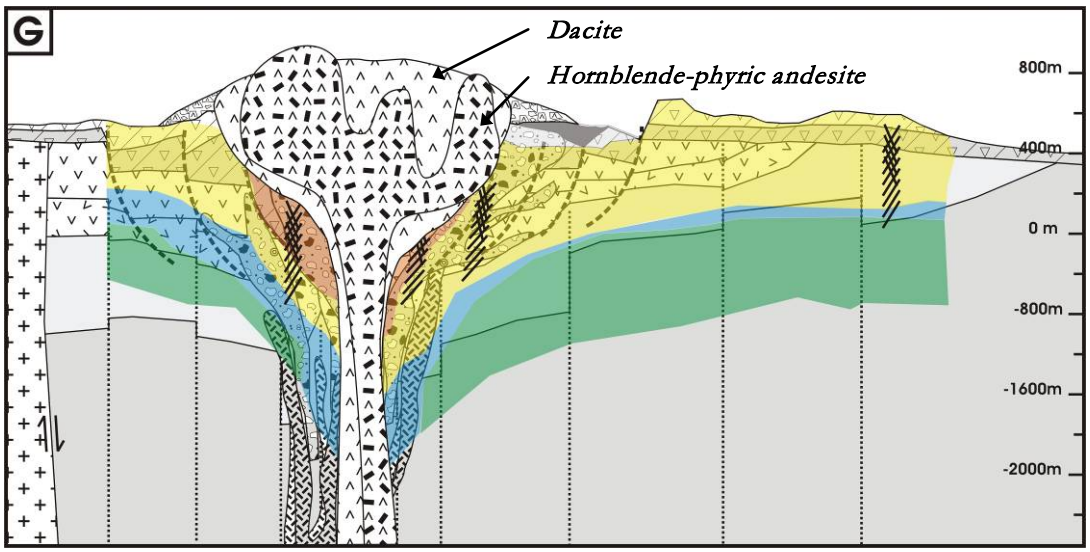

Figure 10.7. Stage-7 showing dacite and hornblende-phyric andesite dome forming through the existing structures and diatreme/breccias complex.

H. Stage-8 Hydrothermal brecciation

The dacite dome was emplaced and interacted with meteoric water causing hydrothermal convection of a low-sulfidation fluid with overpressure leading to hydrothermal brecciation (Figure 10.8). Argillic alteration is widespread. Volcaniclastic or lacustrine sediments were fluidized and pumped through older breccia phases along contemporaneous faults. Collapse of the maar and diatreme along ring faults and/or other structures likely occurred.

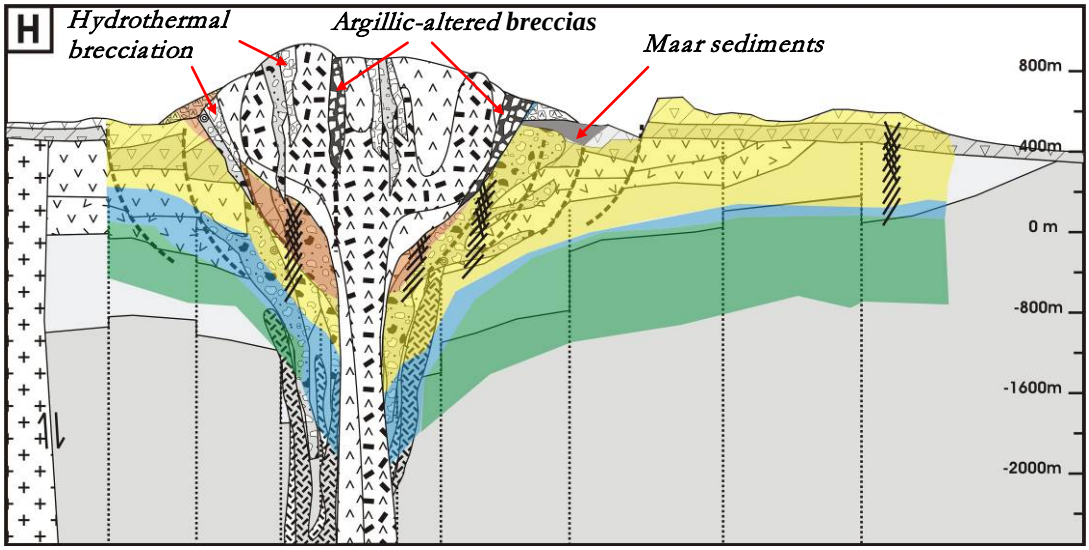

Figure 10.8. Stage-8 showing hydrothermal brecciation and argillic alteration after emplacement of a dome. Return to hydrothermal convection of meteoric water (low-sulfidation fluid), with overpressure leading to hydrothermal brecciation. Maar sediments were fluidized and pumped through older breccia phases along faults.

I. Stage-9 High-sulfidation mineralization

High-sulfidation alteration formed and the introduction of magmatic metal-rich high-sulfidation fluid depositing Cu-Au mineralization occurred. Mineralisation consists of pyrite and enargite/luzonite (red dash line), and lesser covellite (typically at deeper levels) and local, peripheral tennantite-tetrahedrite (Figure 10.9). During this stage a silica cap is formed.

J. Stage-10 Late stage phreatic brecciation

Late stage phreatic brecciation occurs mainly along faults breaking through the silica cap. Hornblende-phyric andesite clasts in late stage phreatic brecciation occur mainly along the contact fault. Clay breccias indicate that minor phreatic eruptions may have occurred during intrusion of hornblende-phyric andesite. The hydrothermal system ceases.

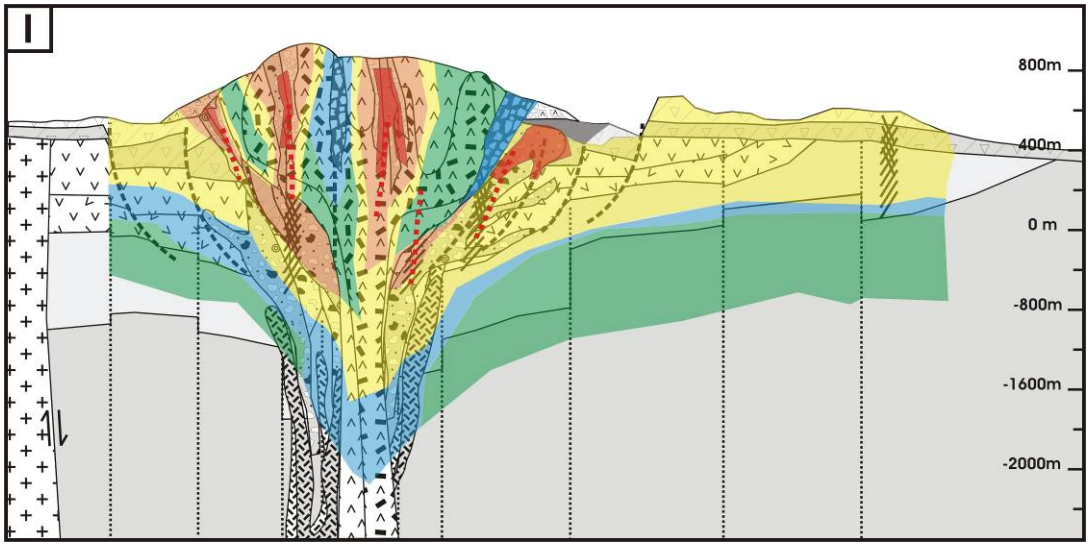

Figure 10.9. Stage-9 showing the introduction of magmatic metal-rich high-sulfidation fluid depositing Au-Ag±Cu mineralization. Mineralisation consists of pyrite and enargite/luzonite (red dash line). Note: vuggy-quartz (red), alunitic (orange), kaolinitic (yellow), argillic (blue) and propylitic alteration (green) alteration.

K. Stage-11 Oxidation and erosion

Uplift, oxidation and erosion produced the present topography, including scree areas and highly anomalous soil geochemistry (Figures 10.10 and 10.11).

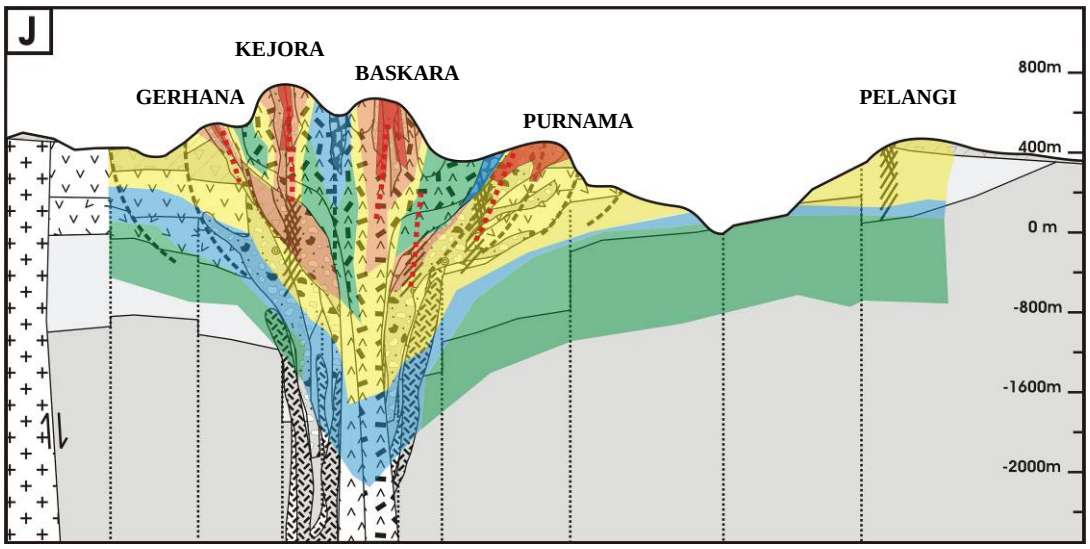

Figure 10.10. Schematic representation of the present day distribution of alteration and mineralisation in the Martabe district. See Figure 10.9 for alteration legend.

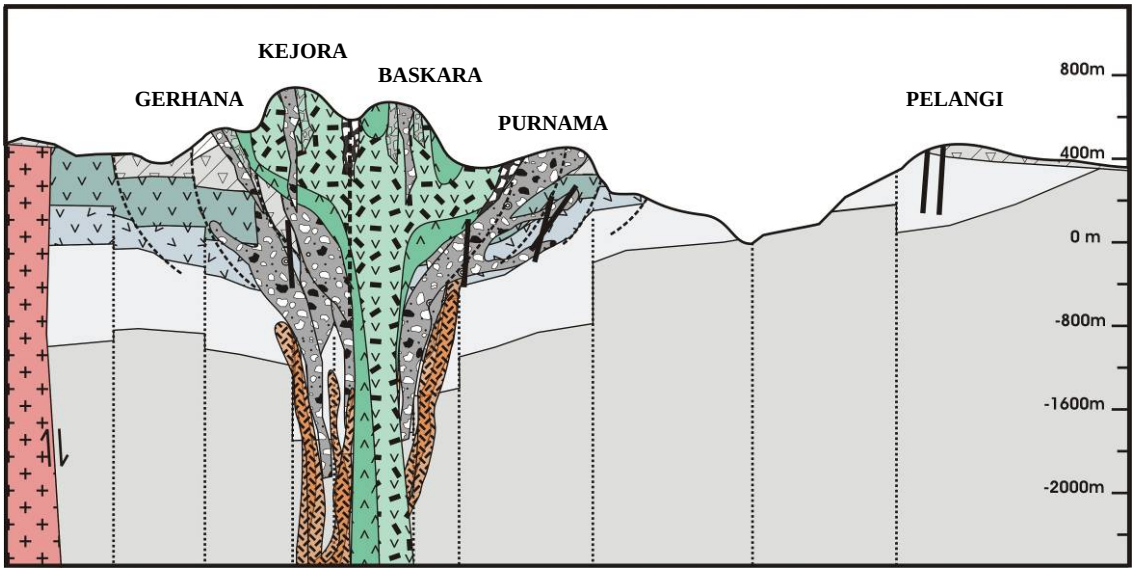

Figure 10.11. Schematic of geology of the Martabe district and relationship to structural framework and present day erosion level.

10.2 Comparison with other flow dome complexes

Domes generally occur as discrete features, in small clusters along linear structures and in volcanic centers, or as multi-stage domes (Cunningham and Ericksen, 1991) and may form in a variety of volcanic settings, e.g., in craters of stratovolcano such as Mount St Helens (Swanson et al., 1987) and Choquelimpie in northern Chile (Gropper et al., 1991); or on caldera margins, at Rodalquilar in southern Spain (Rytuba et al., 1990) and Summitville in Colorado (Grey and Coolbaugh, 1994). Domes may also intrude sedimentary rocks without contemporaneous volcanic activity, as at Chinkuashih, Taiwan (Folinsbee et at., 1972) and Kelian (Davies, 2002).

The Julcani volcanic center in south-central Peru comprises an extensive flow dome field with numerous coalescing individual flow domes which is unusual (Petersen et al., 1977). The Julcani flow dome complex hosts acid-sulphate deposits. The mineralization is strongly controlled by structures and has an Ag-Bi-Pb-Cu-Au-W assemblage. Alteration is also limited to structures; therefore many of the domes are only weakly altered. Age relationships for dome-related alteration and mineralization from selected dome-related deposit are shown in Table 10.1.

Table 10.1. Comparison between alteration and mineralization ages from selected dome-related deposits. All ages in Ma.

DEPOSIT	PRE-MINERAL DOME (Ma)	ALTERATION *I* MINERALIZATION (Ma)	POST-MINERAL VOLCANISM (Ma)	REFERENCE
Summitville, Colorado	22.9-22.8 ± 0.6 rhyodacitic	22.4-22.5 ± 0.5 alunite	20.9 - 19.2 ± 0.8 rhyolitic flow	Mehnert et al. (1973)
Goldfield, Nevada	21.3 ± 0.3 rhyodacitic	20.7 ± 0.4 aluniteillite	20.6 ± 0.4 rhyolite flow	Silberman and Ashley (1970)
Red Mountain Colorado	23.6-21.3 rhyodacitic	23.1 ± 0.10 sericite		Lipman et al. (1976)
Nevados del Famatina Argentina	5.0 ± 0.3 rhyodacitic	3.8 ± 0.2 sericite		Losada-Calderon et al. (1994)
Julcani, Peru	10.13±0.03 dacitic	9.83±0.08 alunite	9.67±0.05 rhyodacitic	Nobleand Silberman (1984)
Cerro Rico de Potosi Bolivia	13.8 ± 0.2 Dacitic	13.76 ±0.10 sericite		Cunningham et al. (1996)
Rodalquilar Spain	11.1 ± 0.4 Dacitic	10.4 ± 0.6 alunite	9.0 ± 0.6 andesitic flow	Arribas et al(1995)
Yanacocha, Peru	Dacite porphyry, ignimbrite	10.9-11.5		Turner (1997)

10.3 Evolution of the alteration system

10.3.1 Formation of early hypogene alteration

Because different types of alteration have different geochemical signatures and variable significance to Au mineralization at Martabe, it is important to understand the likely genesis of the alteration assemblages. The following interpretation is largely based on comparison of data for Martabe obtained by this thesis with other acid-sulfate deposits and by analogy with alteration in active geothermal systems.

Acid-sulfate deposits with disseminated Au mineralization, such as Summitville in Colorado, have a core of vuggy quartz (Grey and Coolbaugh, 1994). These leached rocks are considered to result from extremely acidic fluids that were generated during condensation of volatiles into a meteoric water reservoir (Hedenquist et al., 1994). These volatiles are derived from degassing magma at depth and include a relatively oxidized component of SO_2 gas, as well as HCl, CO_2, H_2S and HF. Similar gases are recognized in the flux of some active volcanoes such as the Poas volcano in Costa Rica and White Island

in New Zealand with attendant intense, shallow acid-sulfate alteration (Brantley et al., 1987; Hedenquist et al., 1993). A principal reaction causing the extreme acidity is the formation of H_2SO_4 by disproportionation of SO_2. For alumina to become soluble at temperatures of ~250°C requires pH levels of <2 (Stoffregen, 1987).

A consequence of the gas transport of a reactive phase is that reaction with wall rock is limited to the zone of condensation, which explains an apparent lack of continuity with depth in most acid-sulfate deposits. The zonation of alteration assemblages around the core of vuggy quartz is due to progressive neutralization of the acidic fluid by meteoric fluids (Figure 10.12). The sharpness of some alteration boundaries reflects more rapid neutralization as a result of meteoric water influx and changes in porosity of the wall rocks. The extent and morphology of the quartz result from a balance between the upflowing acidifying vapor phases and the influx of meteoric water into an increasingly porous zone.

Several aspects of the alteration at Martabe are atypical, notably the extent of massive and compact quartz-alunite alteration. The intensely silicified cap generally conforms to the upper several meters of the flow domes and precursor pyroclastic rocks, such as in the top of Purnama and Baskara. According to Fournier (1985), simple cooling is most effective in depositing quartz from solution or vapor. Therefore, the emplacement of hot magma domes into water-laden tuffs with resulting rapid cooling may have formed massive quartz. However, textural evidence indicates that much of the compact silicification occurred after formation of the vuggy quartz, which formed within existing flow domes. Compact quartz is present in both porous tuffs and rocks of the flow domes; therefore the vuggy quartz probably provided the necessary porosity for continuing quartz deposition in the upper, cooler parts of the system (Figure 10.12). Isotopic dating at Martabe and in many other high-sulfidation deposits associated with domes shows that the time between dome emplacement and alteration may be less than 0.5 Ma and is rarely greater than 1 Ma (Table 10.1).

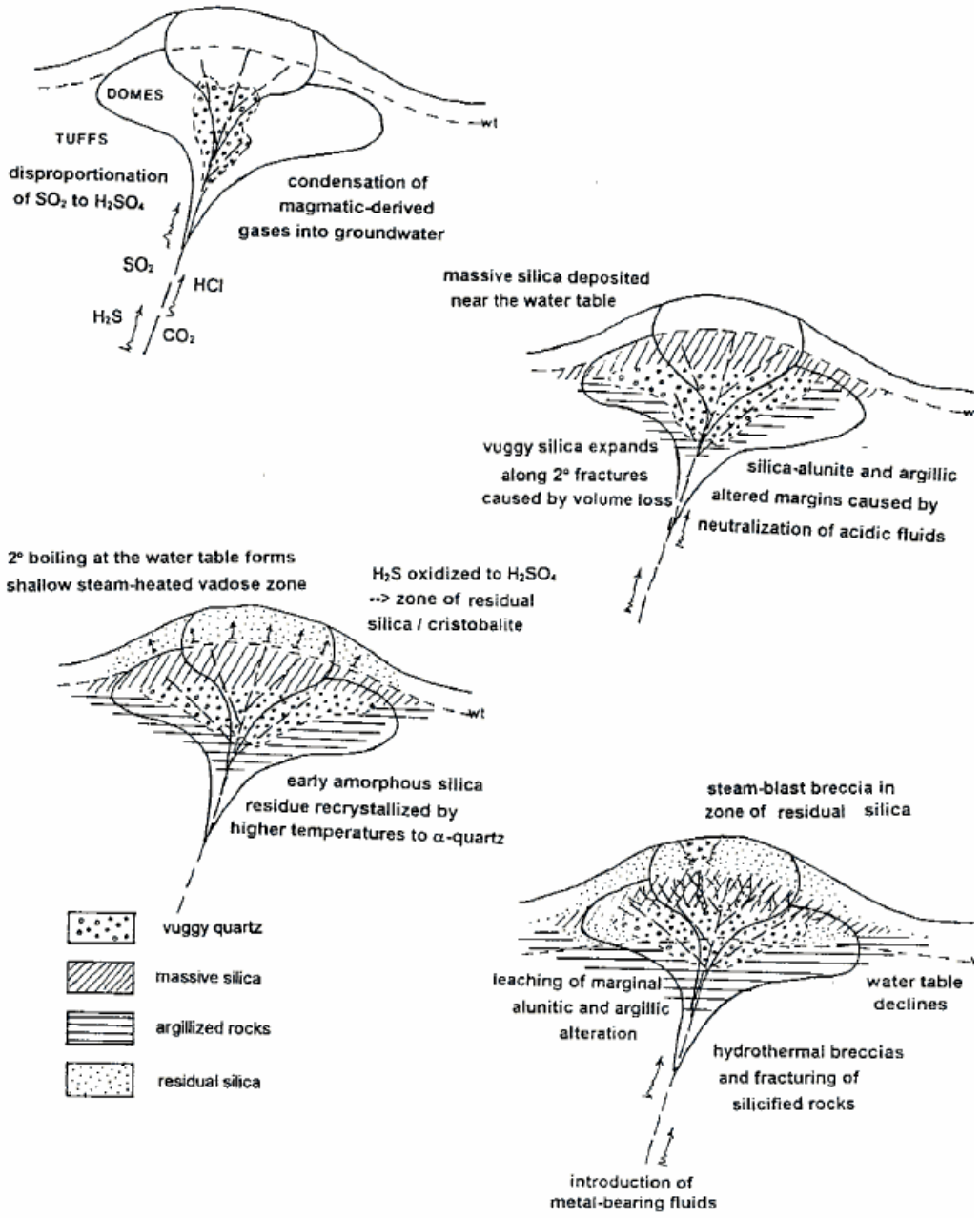

Figure 10.12. Sequence of diagrams illustrating the development of hypogene alteration around flow domes. Note that the initial alteration is restricted to fractures in the flow domes (Turner, 1997).

During formation of the vuggy quartz, isochemical leaching dissolved the host rock with deposistion of a framework of amorphous silica which subsequently recrystallized to fine-grained quartz (Hedenquist, 1994). On the margins of this leached zone, silica in solution may precipitated as silica gel due to the deposition of alunite (Fournier, 1985), that recrystallized to form mottled quartz-alunite alteration.

Pyrophylite and diaspore are generally thought to form at deeper levels in an acid-sulfate system, at temperatures greater than 240°C (Reyes, 1991). However, observations at

Martabe do not corroborate either deeper levels of formation, or higher temperatures. In a fluid supersaturated in silica, pyrophyllite can form at lower temperature (Hempley et al., 1980).

In acid-sulfate systems both alunite and kaolinite may form by several processes, and at different stages. Rye et al. (1989) defined three types of alunites that can be distinguished by S isotopic analyses:

(i) hypogene alunite formed by ascendant SO_2-rich, magmatic fluids,

(ii) alunite formed in the steamed-heated zone above the paleo-water table,

(iii) supergene alunite formed by the oxidation of sulfides,

Although S and O isotopes are useful discriminants, with experience, each of these types of alunite can be recognized in the field by their morphology, mode of occurrence and associate minerals (Sillitoe, 1993), as described in Table 10.2.

Kaolinite intimately admixed with hypogene alunite is probably also hypogene, whereas vug- and fracture-filling kaolinite may have formed during the later stages of hydrothermally activity, or during supergene oxidation. Highly crystalline, well-ordered kaolinite and dickite are indicative of the higher temperatures associated with hypogene alteration. In hand specimen, kaolinite from the oxidized zones is indistinguishable from hypogene kaolinite, but this distinction is possible by consideration of associated minerals, or isotopic studies. In the marginal argillic zone, the ratio of illite to smectite tends to decrease outward from the centre of alteration. This change is attributed to increased illite at higher temperatures (Harvey and Browne, 1991). However, the changes in clay proportions also reflect a trend of neutralization in the acidic fluids that formed the vuggy quartz, with illite being more stable in acidic conditions.

Table 10.2. Types of alunite and criteria for field identification (Rye et al., 1989).

Alunite Type	Field Description	Associated Minerals	Occurrence at Martabe
Hypogene	-crystalline -white to pale pink or yellowish -replacement of feldspars or illite -matrix in hydrothermal breccias	Recrystallized cherty quartz	very common
Steam-heated zone	-very finely crystalline to earthy -massive replacement	Cristobalite powdery quartz	minor
Supergene	veins of cryptocrystalline alunite in the oxidized zone	Fe-oxides sulfates native S	minor but widespread

10.3.2 Formation of zones of residual quartz

Porous, powdery quartz, formed by strong acidic leaching above the water table in active and recent geothermal fields. This type of SiO_2 was described by White et al. (1964) at the silica pit and steaming ground at Steamboat Springs, Nevada. In contrast, vuggy and massive quartz forms only below the water table (Sillitoe, 1993), as products of hypogene alteration. Cristobalite is the product of low-temperature acidic fluids formed by the condensation of H_2S-bearing steam into cool groundwater above the water table. This steam is derived from a deeper zone of boiling, probably associated with the vuggy quartz alteration (Figure 10.12). With time, cristobalite may recrystallize to fine-grained quartz. On the margins of the residual quartz steam-heated zone, fine-grained alunite and kaolinite may form in cooler zones (Sillitoe, 1993).

At Martabe these lower-temperature mineral assemblages are minor, and may have largely been eroded. The planar base of the blanket-like bodies of quartz therefore corresponds closely to the paleo-water table, which has important implications for reconstruction of the paleo-hydrological system, the transport metals, and evidence for structural displacements.

Steeply dipping, overprinting residual quartz is also present on the margins of the hypogene vuggy quartz and advanced argillic alteration. This reflects a lowering of the water table, probably in the waning stages of hydrothermal activity, where descending relatively cool, acidic fluids overprinted the hypogene alteration. This fluid had no effect on the vuggy quartz, but reacted with alunite and clays to form cristobalite, alunite and kaolinite. Much of the marginal clay alteration would be impermeable to this fluid, so leaching was focused along the contacts. This explains the presence of porous quartz instead of a quartz-alunite assemblage in parts of some deposits.

Steam-heated, acidic waters are unable to transport most metals, but Hg, a volatile, can be transported in the vapour phase and precipitated. Under these conditions native S may also form by the oxidation of H_2S. As a result, the high-level quartz blanket is devoid of any anomalous elemental content other than Hg and S. In contrast, the porous quartz formed by lowering of the water table may have preserved the Au content of the hypogene alteration, resulting in low, but anomalous Au values where the quartz-alunite zone was overprinted by the argillic zone. Mercury was also mobilized and redeposited as cinnabar in these zones.

10.3.3 Formation of supergene oxidation

The Martabe dome complex has undergone relatively shallow supergene oxidation, considering the rates of uplift and erosion in Sumatra. Oxidation probably commenced soon after formation of the deposits. However, there is some early oxidized zones still preserved along with shallow-level features of the volcanism and hydrothermal activity.

Some workers have argued that oxidation is part of the hypogene alteration, resulting from relatively oxidized gas content (e.g., Stoffregen, 1987). If this were the case then the contact with oxidation should be upwardly flaring, rather than the almost flat-lying base that is observed. The remnants of sulfide trapped within silicified parts of the oxidized zone are also difficult to reconcile with hypogene oxidization.

10.4 Ore formation and controls

The paragenetic sequence was drawn through observation of cross-cutting relationship, structural orientation, internal textures and mineralogy. The paragenetic and mineralogical data are discussed in the context of the hydrothermal evolution of the Purnama and Baskara deposits.

10.4.1 Ore mineral paragenesis

A paragenesis sequence for the mineralogy generalized from all prospects is shown in Figure 10.13. It is important to note that no single prospect contains all stages of mineralization and that the extent of hydrothermal alteration, ore and gangue mineral and supergene effects varies widely as functions of precursor rock type, process, degree of fracturing, porosity, and permeability. Petrographic studies on 118 polished thin sections supported by logging and other analyses (XRF, XRD, and PIMA) suggest a principal sequence of alteration/mineralization system in Martabe that is the combination of low-sulfidation and high-sulfidation fluids that caused the complex ore mineralogy, textures and paragenesis.

Pyrite is the dominant sulfide formed in all alteration stages. Early (stage-1 py) is fine-grained to moderate grained. This pyrite occurs as disseminated and clusters resulting from sulfidation of Fe-bearing primary minerals, such as pyroxene hornblende, biotite and accessory mineral (magnetite) in the basaltic to andesitic rocks. This pyrite commonly occupies the original shapes of the phenocrysts. Iron is leached from titanomagnetite to

form pyrite, leaving skeletal rutile or anatase. Within parts of the quartz-pyrite alteration, pyrite deposition continued episodically to form overgrowth on pre-existing pyrite. Late (stage-2) pyrite formed in association with gold mineralization. In vuggy quartz alteration, pyrite was apparently stable, although pitting and corrosion textures suggest that some pyrite was leached, probably in the most acidic core of the altered zones.

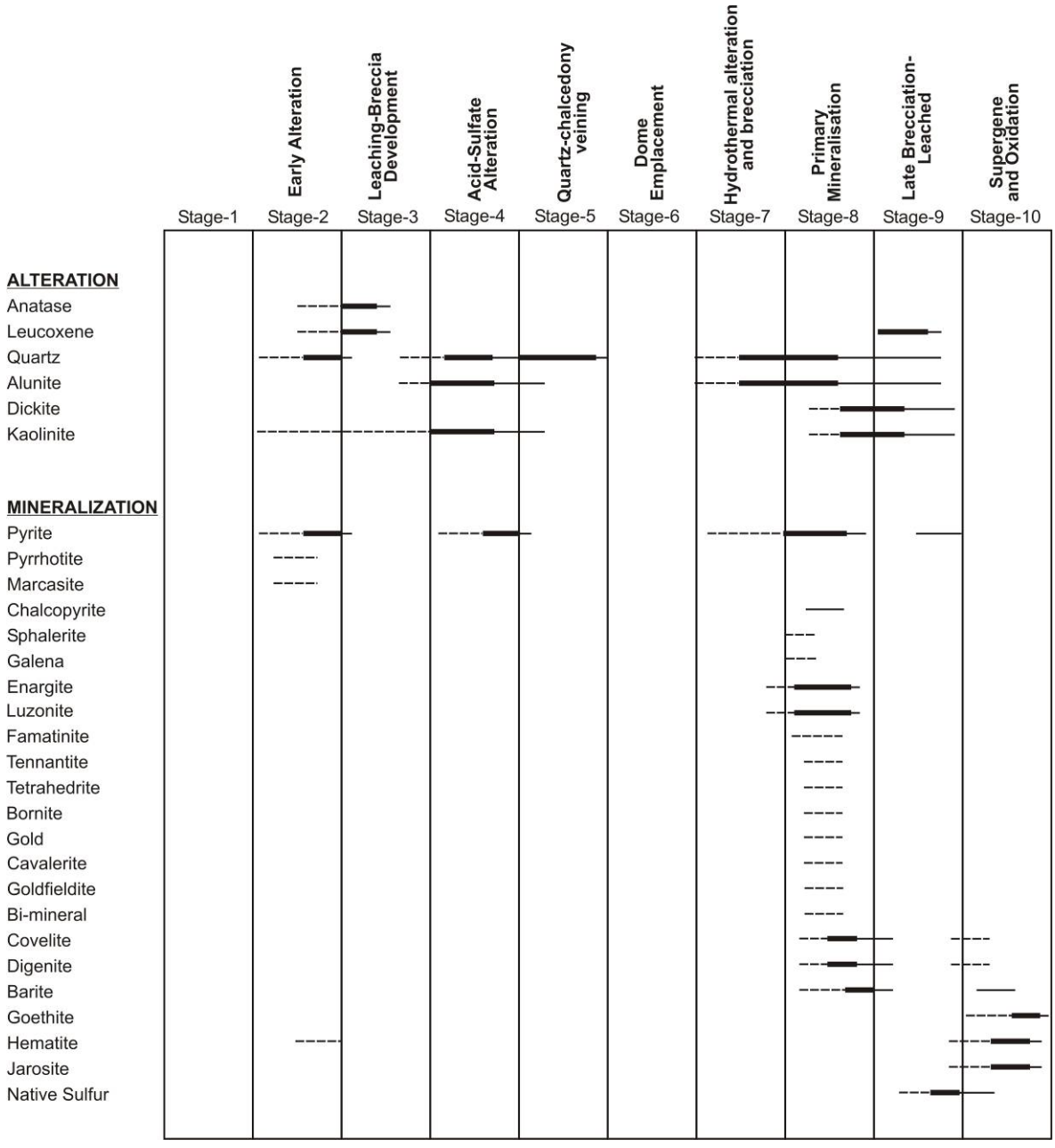

Figure 10.13. A paragenetic sequence for ore and gangue minerals associated with the epithermal mineralization at Martabe.

In the Martabe deposits, and other acid-sulfate systems (i.e., Yanacocha, Lepanto, El-Indio), vuggy quartz alteration is an essential precursor to the main stage of

mineralization. It forms a porous host rock into which subsequent mineralizing fluids are introduced. At Martabe, the Cu-sulfosalt and base metal mineralization precipitated after leaching and brecciation, with enargite, tennantite-tetrahedrite, covellite±base metal sulfides deposited in leached voids, fractures and breccia matrices. Stage-2 and stage-3 generations of pyrite are also probably post-brecciation, and their relationship with the Cu-sulfides is indicated by deposition of either enargite/luzonite-covellite/digenite depending on the availability of Cu, As or Sb in pyrite. Local variations in the paragenetic sequence developed during mineralization, but the sequence pyrite - enargite/luzonite±tennantite-tetrahedrite±sphalerite/galena - covellite/digenite is clearly defined.

Secondary covellite and digenite probably formed during the final stages of primary mineralization. These encrust enargite and leached pyrite and filled leached voids. Barite also filled leached voids, which may suggest that it formed during oxidation. However, barite is also encountered in some depth in the sulfide zone as fracture fill. Therefore, it probably formed in the later stages of hypogene mineralization but only in the upper levels of the deposits, which have been subsequently oxidized.

Late pyrite-dickite/kaolinite was precipitated in fractures. The later fractures extend beyond the siliceous alteration into the argillic alteration zone with an assemblage of pyrite, sphalerite, galena, tennantite, Ag sulfosalts (?) and, in places, minor enargite and covellite. These minerals tend to be Ag-rich, but the enargite may also carry anomalous Au. Brecciated opal and/or late phreatic breccia are also found, it is probably a result of steam-blast eruptions, sourced at the water table. Many fragments of siliceous rocks (including opaline rocks?) have been transported upwards, into the zone of this breccia zone, and deposited on the surface at Purnama. Lowering of the water table during the waning stages of hydrothermal activity, enabled acidic fluids to transport and redeposit much more widespread native sulfur by oxidation of H_2S, extending into the sulfide zone.

During oxidation of sulfides, a range of Fe-oxide and sulfate minerals were formed such as; hematite, goethite, kaolinite, oxides and alunite. This late overprinting of advanced argillic alteration resulted from supergene processes. Within the siliceous alteration, the acidity of the supergene fluids could not affect quartz, but did remobilize some of the elements in the ores; e.g., Cu was probably extensively leached and redeposited at the water table or brecciated oxide zone. Copper anomalies in soil at western Purnama illustrate the remobilization process of Cu. However, no copper oxide minerals are recognized in that area. During oxidation of highly sulfidic zones, as seen in Purnama and Gerhana, Au may be mobilized and concentrated to form higher grade pods or along structures, but

elsewhere there is little evidence for remobilization. In Purnama, high Au grades are encountered between contact clay altered and oxidized quartz altered breccias.

10.4.2 Ore distribution controls

10.4.2.1 Structural controls

Primary structural controls are not obvious in most of the Martabe gold deposits. However, underlying structures have controlled the emplacement of the domes, demonstrated by the N-S to north-northeast – south-southwest alignment, but these structural controls have not produced strike-continuous gold mineralization.

The Purnama and Baskara deposits illustrate some of the structural processes involved in dome and breccia formation and subsequent mineralization. At Purnama, a steep, curvilinear to linear structure apparently exerts a fundamental control on the distribution of higher-grade Au mineralization. In section, this structure is vertical to steeply east-dipping, with a shallow eastward flaring of mineralization. This is interpreted as the collapsed margin or ring of an original dome. Late-stage movement on part of this structure has displaced residual SiO_2 downward to the SW. The resurgent dome may originally have been the site of a diatreme breccia, as suggested by the remnants of lacustrine sediments within the semi-circular topographic low at Purnama East.

An alternative structural interpretation is that a northeast-trending, left-lateral fault formed a zone of dilation and localized the ore bodies at Baskara. Mineralization at Baskara is also controlled by a left-lateral, east-west fault. The north-northeast structural trend and sense of movement concur with that indicated for the Baskara Fault zone at east Baskara. The southern end is traversed by a WNW-trending structural corridor which exerted a fundamental control on subsequent magmatic and hydrothermal activity. The corridor is about ~500 m wide, and separates the Baskara and Purnama deposits. North of this structural corridor, the rocks are intensely altered hydrothermally brecciated and contain abundant Fe oxides, but very little Au mineralization has been found. However, to the south, mineralization at Baskara extends beyond the limits of the structural corridor.

10.4.2.2 Lithology and alteration controls

To date, Purnama is the only known Au deposit at Martabe which exhibits a significant lithological control. Most of the Au mineralization occurs in a tabular body

above the contact of siliceous alteration of polymict breccia and porphyritic andesite with illite-smectite alteration of polymict breccia. At least two breccia units are recognized, diatreme breccias which cross cut all units, and lower volcaniclastic breccia (Tmab) with hyaloclastic and hematized matrix. The highest Au grades of Purnama were directly below the illite-smectite alteration of polymict breccias that had no anomalous surface Au geochemistry.

The contact between rocks of the flow dome and monomict-polymict breccias also controlled the deposit's location and shape. Underlying rocks are clay-pyrite to quartz-alunite altered, with background to low Au grades. Where fluids breached the domes and penetrated more porous tuffs, vuggy quartz developed which became a preferred zone for subsequent Au mineralization.

Breccias act both as favorable, relatively porous horizons for fluid infiltration, and as aquicludes which prevent upward fluid flow. These contrasting controls depend on both original rocks textures, i.e., the degree of welding and presence of vitrophyric margins, and alteration characteristics such as the development of vuggy quartz or clay alteration of glass (Turner, 1997). In many high-sulfidation systems, the vuggy quartz has enhanced porosity and thereby access of mineralizing fluids (Hedenquist et al., 1984; Sttoffregen, 1987). This process has been important at Baskara and possibly Punama, but is not essential for Au mineralization. The brecciated quartz at Purnama and Baskara lacks significant vugginess apart from fractures and breccias. At Kejora, Au mineralization is mainly hosted in quartz-alunite alteration, with very little development of vuggy quartz, but consequently, the average grade is lower.

Thicker breccias units on the periphery of the Baskara, Kejora and eastern Gerhana are potential exploration targets for underlying mineralization, even in the absence of surface geochemical anomalies and alteration and mineralization, and therefore are less likely to host major Au deposits.

10.5 Transport, deposition and sources for metals

Three mechanisms may have introduced ore metals during the later stages of alteration:

(i) metals are transported in the vapor phase from a degassing magma (Vennemann et al., 1993),

(ii) metals are deposited from a saline, metal-rich fluid, which followed the dominantly gaseous phase (White, 1991; Hedenquist et al., 1994),

(iii) early acidic alteration is overprinted by low-sulfidation mineralization (Berger and Henley, 1989).

In the first case deposition is due primarily to mixing and dilution with cooler, meteoric fluids, and in the second case by depressurization and cooling. In both these cases the mineralization is an integral part of the same hydrothermal system, and not a fortuitous coincidence of two different processes, which is required by the third model. The association of some sulfides with kaolinite at Martabe suggests that at least the early mineralizing phase was moderately acidic. Bening and Seward (1994) and Hedenquist et al. (1994) identified $AuHS^{\circ}$ and $AuCl_2^-$ respectively, as potential complexes for transport of Au in relatively acidic fluids.

The source of the metals is more contentious. It is logical that a solidifying magma would expel a metal-bearing fluid, and there is clear evidence of voluminous magmatism, but the metals in the Martabe system could also derive from leaching of older metal-bearing deposits(may be some buried porphyry Cu deposit below Martabe that is causing pre-enrichment), or from deeper basement rocks. For a comparison, there is also a porphyry Cu (Au, Mo) in Aceh, North Sumatra (i.e., Ise-ise prospek) about 100 km from the district, which could be pre-enriched metal sources for leaching and re-concentration to a other high sulfidation deposited called Miwah which is close to the Ise-ise prospek.

10.5.1 Post-ore events

Four main post-ore events have affected the Au mineralization, some of which have been discussed, and might be relevant to further exploration in the district: (i) formation of a blanket of residual quartz, (ii) post-mineral volcanism, (iii) post-mineral faulting, and (iv) supergene oxidation.

The cap of residual quartz formed in the upper part of the hydrothermal system due to secondary boiling at the water table. This is directly analogous to fumarolic areas in active geothermal systems. For exploration, this cap is a blanket with no anomalous content of metals, apart from Hg, and potentially may conceal mineralized rocks below. During the later stages of hydrothermal activity the water table commonly subsides or collapses, perhaps due to lower thermal input accompanying collapse of the hydrothermal system, and/or due to seismic activity. In some systems this collapse, combined with erosion may lead to telescoping of an epithermal system with deeper-level porphyry mineralization (Sillitoe, 1994), but at Martabe this is not recognized. However, as the water table descended, acidic fluids modified the hypogene alteration by leaching marginal alunite

and clays. This alteration is limited to < 100 m of vertical extent. In the waning stages of hydrothermal activity, Martabe was again ruptured and subjected to renewed magmatic activity.

10.6 Styles of mineralization and comparison with other high-sulfidation systems

Mineralization in the Martabe district is typical of acid-sulfate or high-sulfidation system (Hedenquist, 1987). Here, 'acid-sulfate' refers to the type of alteration, stressing the quartz-alunite alteration association, and 'high-sulfidation' to the mineralization, which highlights the sulfidation state of sulfur in the key minerals, i.e., enargite and covellite (Barton and Skinner, 1979). This usage emphasizes that the processes of alteration and mineralization may be separate, although part of the same hydrothermal system; i.e., acid-sulfate alteration is possible without attendant mineralization.

High-sulfidation mineralization typically forms within a continuum of deposit types with subdivisions into Nansatsu type, emphasizing the role of lithology, and El-Indio-type, emphazing structure (White, 1991). In the district like Martabe, and larger districts like Yanacocha and others, these controls can be recognized so it is inadequate to attribute formation of the deposits to a single process. In the following paragraphs a spectrum of major ore controls for the Martabe district are presented with examples from selected deposits.

High-sulfidation Au deposits are rarer than low-sulfidation Au deposits, and display a wide range of variations in volcanic setting, morphology and ore controls. The Yanacocha district is amongst the largest of these deposits, but is quite different from Pueblo Viejo and El lndio, which are atypical of most high-sulfidation systems. To date, Yanacocha lacks the high-grade Au mineralization that characterized direct shipping ore from El lndio (Jannes et al., 1990), and the high-grade breccia pipes in the Chinkuashih deposits (Folinsbee et al., 1972). Characteristics of high-sulfidation systems which distinguish them from other epithermal deposits are well described (Ashley, 1982; Sillitoe, 1983; Bonham, 1986; Heald et al., 1987; Arribas, 1995). Some of these characteristics are summarized and compared (Table 10.3), emphasizing those that appear to be uncommon or unique at Martabe.

Table 10.3: Summary of the characteristics of high-sulfidation systems compared to Martabe.

No	General characteristics	Martabe
1	most commonly Tertiary age, but some Proterozoic	Martabe dome complex from 3.8 to 2.1 Ma.
2	associated with proximal, calc-alkaline, andesitic to rhyolitic rocks	high-K calc-alkaline andesitic to dacitic rocks in the main Martabe
3	variety of volcanic settings including stratovolcanoes, calderas, domes and maar - diatreme complexes calderas, domes and maar - diatreme complexes	coalescing flow domes with diatremes, maar is possible (at northern Gerhana)
4	commonly occur in association with high-level porphyritic intrusions, or flow domes	dacitic domes and later porphyritic andesitic flow intrusions/dikes/stocks
5	commonly a core of vuggy quartz and advanced argillic alteration enveloped by argillic and outer propylitic alteration.	core of vuggy-massive quartz, marginal advanced argillic (alunitic and kaolinitic) and argillic alteration, with peripheral prophylitic alteration.
6	advanced argillic zone characterized by quartz - alunite -± kaolinite ± dickite ± pyrite ± pyrophyllite ± diaspore ± barite ± jarosite and Fe oxides	characteristic assemblage as described
7	evidence of phase(s) of strong leaching	both hypogene leaching which produced vuggy quartz and steam-heated residual quartz.
8	Au mineralization disseminated in vuggy quartz, or in fractures, breccias and major structures; rarely veins	disseminated and fracture breccia - controlled Au mineralization.
9	lithological and/or structural ore controls, ore mostly hosted in vuggy quartz/advanced argillic zones.	core controlled by fundamental structures, lithological contacts, vuggy quartz, margins to diatreme breccias and proximity to late-stage dacitic/andesitic intrusions.
10	Au mineralization invariably after alteration, often late in the paragenesis	up to *2* stages of mineralization after main-stage alteration; possibly contemporaneous with neutral-pH argillic alteration in diatreme and andesitic intrusions.
11	sulfide ore minerals: pyrite, enargite*I* luzonite, covellite, native Au, minor electrum, Ag sulfosalts, tennantite*I* tetrahedrite, goldfieldite, tellurides, chalcocite. galena, sphalerite, chalcopyrite.	characteristic assemblage as described
12	dominant geochemical association of Au, Cu, As, Ag subordinate Zn, Pb, Hg, Sb, Te, Sn, Mo, W	highly anomalous Au, Ag, Sb, As, Pb, Hg; subordinate Bi, Te, Ba

10.7 Implications for exploration

Most deposits in the Martabe district result from a combination of physical controls on the deposition of Au. It is inappropriate to identify and apply a single process as a Martabe-type model for exploration. The monomict, jigsaw- fit breccias, which formed adjacent to explosive diatreme activity in response to quartz-phyric dacitic and hornblende-phyric andesite magmatism, are an attractive exploration target, but this series of events is not applicable to all deposits in the district. Another problem, exemplified at Purnama and Baskara, are the complex, multi-phase sequence of magmatic events, alteration, breccias and mineralization. It is unrealistic to expect that all deposits in the district will reflect this same sequence. Table 10.3 summarizes the most significant ore controls recognized in each of the major deposits or prospects in Martabe district.

Structural controls are not easily interpreted because of the complex history of Martabe (Davies, 2003). Multiple faults and fractures were active, but many were not related to the mineralization. Although fundamental structures controlled emplacement of the domes these may, or may not, have continued to influence alteration and mineralization. The north-northeast trend of a fault which separates Purnama and Pelangi, possibly reflecting a major structure, is not recognized in the distribution of Au at Martabe, whereas northeast and northwest trending structures are important. In the absence of a district-wide structural framework, each deposit must be considered separately. Curvilinear structures are at least as important as linear ones and may denote the margins of diatreme breccias, domes, or zones of large-scale collapse.

A control of lithology on Au distribution has not been widely demonstrated. Although possibly an important concept for exploration, most breccias are on the margins of the Martabe domes, away from the main centers of hydrothermal activity. Contacts between domes of different ages may also have focused Au mineralization, but are difficult to recognize.

Diatreme breccias have various characteristics that can guide exploration. Circular features in aerial photography and satellite imagery are preliminary guides. Breccia textures, components and morphology provide clues to phreatomagmatic events. Intense marginal crackle-type breccias may enhance secondary porosity in otherwise massive quartz, permitting mineralization. Silicified zones on the margins of diatreme breccias tend to be strongly fractured and brecciated in contrast to argillized margins. New targets for mineralisation based on interpreted curviplanar structure and interpreted the margins of diatreme breccias are shown in Figures 10.14 and 10.15.

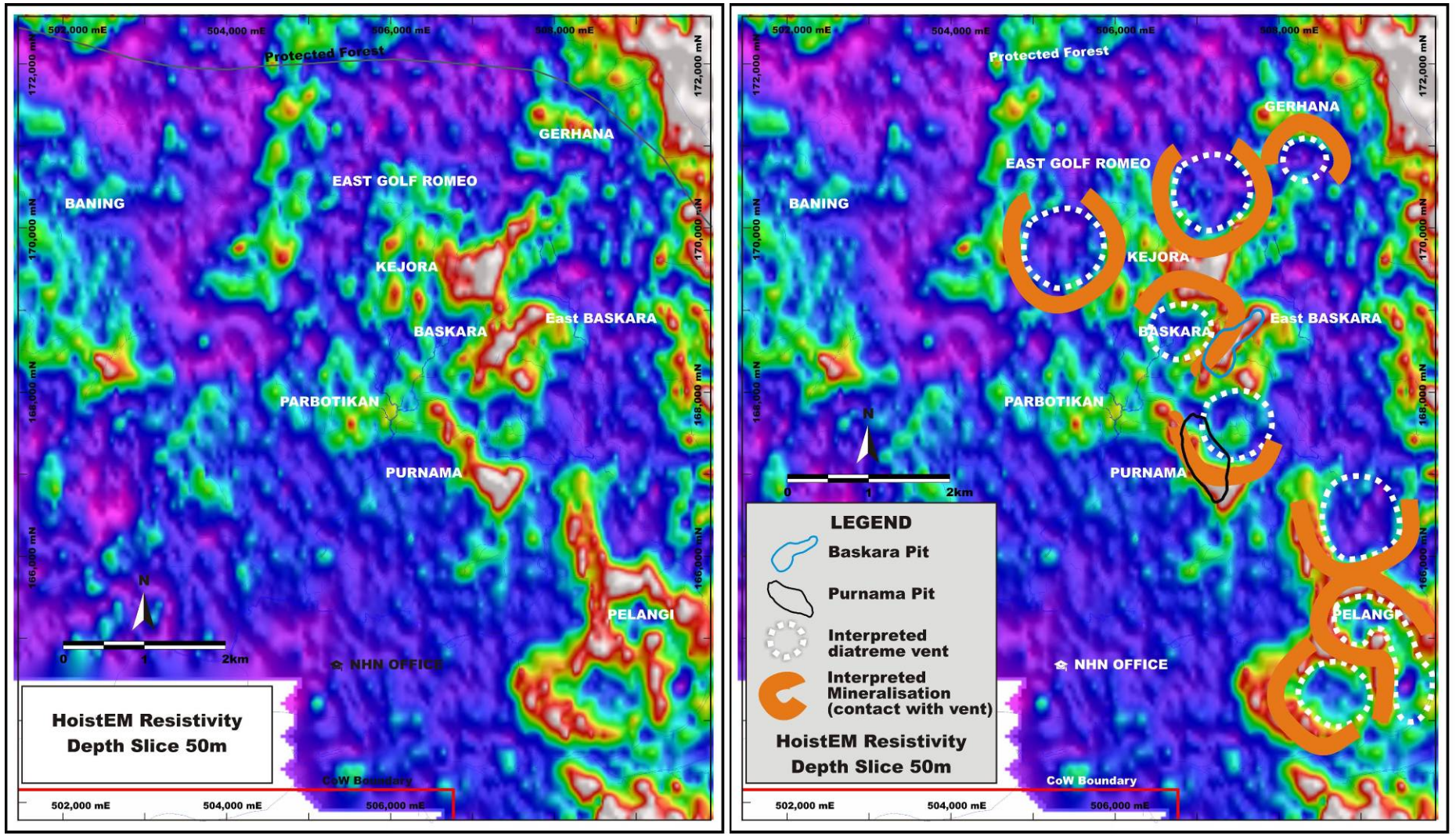

Figure 10.14. (A) HoistEM resistivity depth slice at 50 m. (B) New targets for mineralisation (orange line) based on interpreted curviplanar structures and diatreme vents defined by HoistEM anomalies.

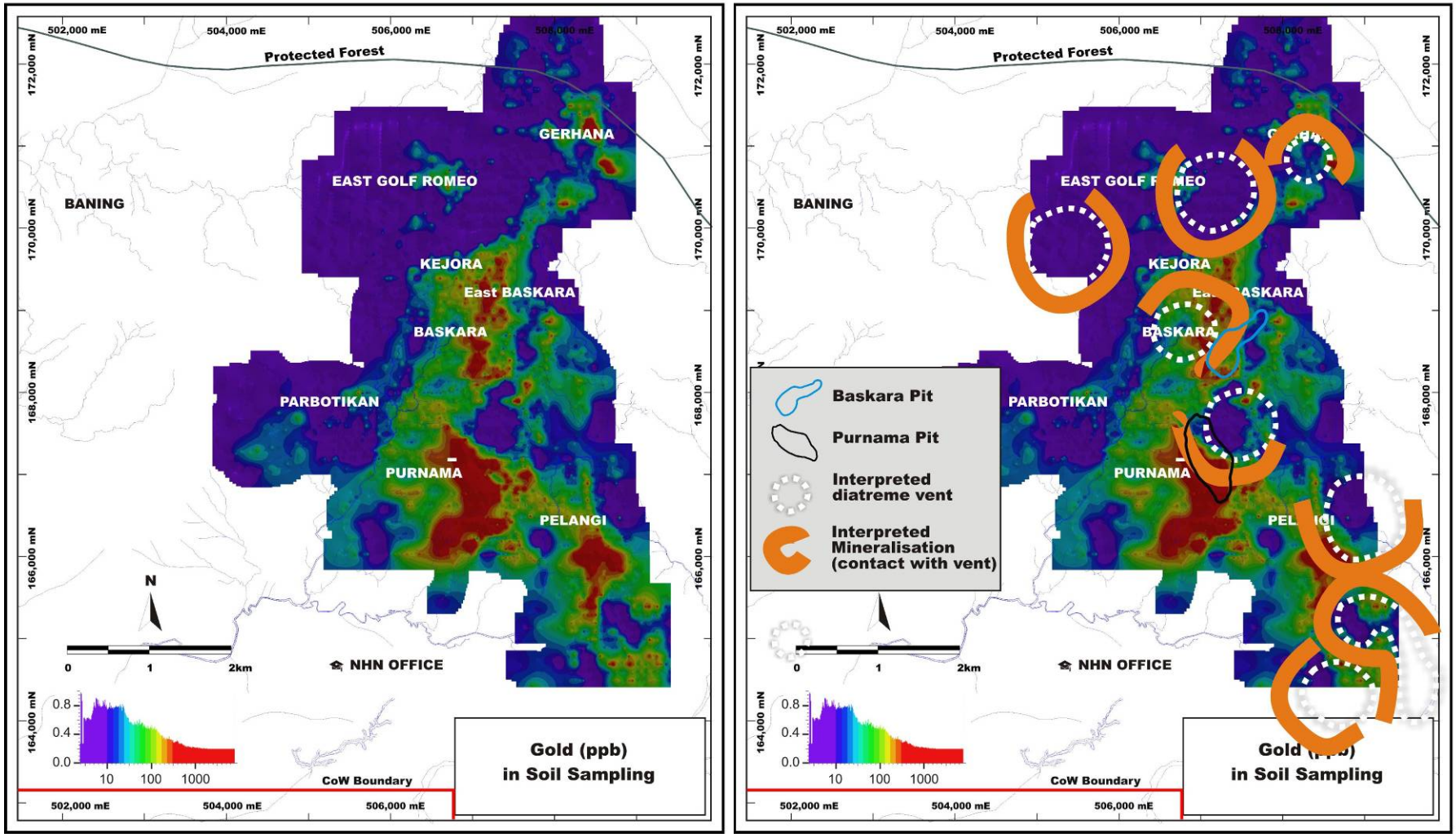

Figure 10.15. (A) Distribution of Au in soils. (B) New targets (orange line) based on interpreted curviplanar structure and diatreme vents overlying Au anomalies n soils.

CHAPTER 11

CONCLUSIONS AND RECOMMENDATIONS

The Martabe Au district, situated on the north-west coast of Sumatra, Indonesia, consists of four high-sulfidation epithermal Au deposits over an 8 km strike length: Purnama, Baskara, Kejora and Gerhana and one low-sulfidation epithermal Au deposit, Pelangi. Resources have been estimated for the three principal known deposits, Purnama, Baskara and Pelangi. Resources are 91.2 Mt @ 1.5 ppm Au and 19 ppm Ag for Purnama, 36.6 Mt @ 1.0 ppm Au and 4 ppm Ag for Baskara, and 10.4 Mt@ 1.1 ppm Au for Pelangi. Reserves are based on an optimized open-pit mine design which extends approximately 900 m north-south along strike; the Purnama reserve is 35.7 Mt @ 1.9 ppm Au and 26 ppm Ag.

Regionally, Sumatra has been influenced by multiple tectonic, magmatic and metallogenic processes which are responsible for formation of the diverse styles of precious and base metals deposits. Many different deposit types and mineralization styles appear to occur in clusters and belts. At least five different mineralization belts/events have been recognized including: (i) base metal mineralization related to Paleozoic sedimentary basins, (ii) tin mineralization related to Early-Mesozoic magmatism, (iii) base metal mineralization related to Mid-Late Mesozoic magmatism (iv) base-precious metal mineralization related to Early Tertiary and Miocene-Pliocene magmatism and (v) precious metal mineralization related to Neogene magmatism.

Martabe is located in the western Sunda Banda magmatic arc within and adjacent to a Late Tertiary porphyritic dacite and andesite dome and diatreme complex that was emplaced into a volcano-sedimentary sequence comprising interlayered sandstone, siltstone, carbonaceous mudstone and andesite lava flows. Martabe is located near a series of fault splays of the Sumatra Fault System and this structural framework has played an important role in the formation of the deposits.

At Martabe there are a wide variety of distinctive breccias within the dome and diatreme complex. The origins and processes of these breccias are varied and include phreatomagmatic, phreatic, tectonic and hydraulic brecciation. There are complex overlaps in these processes and it is likely that the breccias preserved today are the product of hybrid brecciation processes.

Whole-rock geochemical data for coherent volcanic rocks in the Martabe district indicates that there are four characteristically different volcanic suites; a basalt suite, a basaltic-andesite suite, an andesite site and a dacite suite. The Martabe coherent volcanic rocks have geochemical similarities and appear to be co-genetic. Generally, they have

similar immobile element characteristics suggesting that the andesitic to basaltic volcanism generated at a plate margin in a back-arc setting.

Observations, mapping and core logging in this study has led to a better understanding of the diatreme breccias and associated intrusions, which are closely associated spatially with the Purnama, Baskara, Kejora, Pelangi and Gerhana Au-Ag deposits. Numerous and multiple breccias, including phreatomagmatic, phreatic, tectonic and hydraulic breccias were identified. Recognition of stratified and unstratified breccias, base surge deposits and overlying airfall tuffs, indicate that the initial setting was a maar volcanic field, containing multiple diatreme vents.

Intrusion of felsic magma into a fault-bounded blocks of brecciated carbonaceous mudstone (part of Sumatran Fault System) within an active hydrothermal system resulted in phreatomagmatic brecciation at Martabe. The presence of juvenile magmatic clasts with delicate wispy texture and cuspate margins, in situ rhyolite clasts associated with dacitic-andesitic dykes and base surge (stratified breccia) deposits are the key pieces of evidence for a phreatomagmatic origin.

The Purnama diatreme breccia was emplaced in a structural corridor between Pelangi and Baskara. The Purnama deposit is located at the margin of a diatreme. The mineralized zone is limited to the northern and western sides of the diatreme, and the mineralization flares upward and outward away from the margin of the breccia.The ore body at Baskara is within the core of the Martabe dome complex. The Baskara and Pelangi deposits have a strong structural control.

The flow dome complex formed at ca. 3.8± 0.5 Ma (quartz-phyric dacite) and 3.1±0.4 to 2.8± 0.3 Ma (hornblende-phyric andesite), and extensive alteration closely followed emplacement of the domes at 3.30± 0.11 to 2.14± 0.10 Ma (alunite). These periods of hydrothermal activity indicate that the magmatic/hydrothermal system was active from 3.8 to 2.1 Ma and the main-stage alteration occurred within 0.5–0.8 Ma of dome emplacement.

All identified economic and sub-economic gold-silver mineralization and the alteration of the district displays a zonal pattern of alteration typical of high-sulfidation epithermal systems, with the presence of a low-sulfidation epithermal system at the periphery (i.e., Pelangi). In general, the alteration at Martabe consists of siliceous (quartz dominant), advanced argillic (alunitic and kaolinitic), argillic and propylitic zones. The 'alunitic' advanced argillic alteration assemblage consists of quartz+alunite± dickite/kaolinite±pyrite; the 'kaolinitic' advanced argillic assemblage refers to quartz+kaolinite/dickite±alunite ±pyrite; the argillic assemblage contains illite-smectite-montmorillonite-pyrite±quartz; and the propylitic assemblage consists of

chlorite+epidote+calcite ±illite/sericite±pyrite±quartz. Alteration is typically zoned from a core of brecciated, massive and vuggy quartz that grades outwards through advanced argillic alteration (alunitic and kaolinitic) to argillic alteration that is surrounded by a peripheral zone of pervasive propylitic alteration. Economic Au mineralization is hosted within the siliceous and advanced argillic alteration zones. The alteration zones most likely occurred as multiple stages within combining centers and formed contemporaneously with the Martabe flow dome magmatism. Although alteration is widespread, Au mineralization is restricted to discrete centers clustered around the main dome complexes. Textural relationships clearly indicate that the main periods of Au introduction followed hypogene alteration.

Gold-silver mineralization in the district characterizes the high-sulfidation type of epithermal deposit, based on the sulfide and sulfosalt mineral assemblage and widespread advanced argillic alteration. Ore types include sulfide, transitional and oxide. Ore mineralization consists of enargite-luzonite+tetrahedrite-tennantite-pyrite in veins, vugs and as breccia matrix. Jarosite, hematite and goethite are the most common products of oxidation. Gold is present as micron-sized native Au grains associated with quartz, Fe-oxides, enargite-luzonite, tetrahedrite-tennantite and covellite-digenite.

Purnama consists of disseminated Au-Ag mineralization distributed sub-horizontally within and adjacent to the western perimeter of the diatreme with both strong lithological and structural controls. A quartz matrix-supported breccia contains the majority of high-grade ore, although lower grade mineralized zones occur within pervasive advanced argillic-alunitic altered breccias and advanced argillic-kaolinitic altered andesite. At Baskara, mineralization is sub-vertical and spatially associated with phreatic and phreatomagmatic breccia bodies emplaced along NE-striking faults. The best precious metal mineralization at Baskara occurs the contact between breccia bodies and the dacite-andesite dome. Locally, Au- and Agbearing, low-sulfidation quartz veins and vein stockworks of Pelangi and Purnama cross-cut the high-sulfidation mineralization.

Results of a LA-ICP-MS study of trace-element mineral chemistry in pyrite and enargite indicate significant variability in trace-element compositions of pyrite and enargite from a single deposit and across deposits at Martabe, particularly in Fe, Te, Bi, Sn, Se, Au, Pb, Mo, W and Ba. Almost all elements are consistently above ICP-MS detection limits with the exception of Cd, La, Th and U that are close to detection. In general, the most abundant trace elements in enargite are those that also form discrete sulfosalt, selenide, and telluride accessory phases. General trends in the spatial distribution of some elements suggest enrichment in Au, Se and Te in the Purnama and

Gerhana deposit. Elements such as Ag, Zn and Pb, to a lesser extent Fe and Pb, are enriched in the enargite in the centre of the Gerhana ore body, whereas Zn (± Se) are in enriched enargite distal form Purnama and Gerhana.

Metal zoning based on multi element assay data from drill cores at Baskara and Purnama show the strong correlation between Au and Ag. While As, Sb, Te and Pb have higher levels at Purnama and have a stronger correlation with Au than at Baskara. Baskara has higher Cu and Bi levels and greater positive correlation with Au suggesting it may be closer to a magmatic fluid source. Nickel occurs at the base of the oxidation zone or within the sulfide zone. Similarly, higher Cu concentrations are observed to occur at the sulfide zone or at the margin with the oxidation zone. A strong negative correlation of Au is observed with Zn and Mg. Zinc and Mg form a broad halo surrounding the Au mineralization, as well as below the zone of oxidation or within the sulfide zone.

Hydrothermal alteration at Martabe alteration is typical of many mineralized high-sulfidation Au deposits. This alteration is zoned around a core of vuggy quartz (siliceous alteration), formed by acidic fluids, and probably due to condensation of SO_2-rich vapors into groundwater. Much of the vuggy quartz formed initially within the domes, which were controlled by primary structural conduits that did not penetrate the overlying breccias. As the zone of vuggy quartz expanded, increased mixing of acidic fluids and meteoric water, resident in the porous breccia, rapidly cooled the rising fluids causing widespread deposition of quartz high in the system. As a result, the hydrothermal system became sealed, and high temperatures in the central zone caused recrystallization of the amorphous silica to fine-grained quartz, grading successively outwards to chalcedony and opal. Wallrock reactions with the acidic fluids and cooling produced the zoned alteration assemblages. Subsequent phreatic eruption activity also formed diatreme breccias after the main-stage alteration and almost certainly contributed to the fracturing and hydrothermal brecciation. This eruption activity was probably initiated by the intrusion of hornblende-phyric andesite intrusions, stocks or dikes, and was accompanied by a near-neutral pH phase of argillic alteration.

Above the paleo-water table, a steam-heated zone of alteration formed due to deeper boiling fluids. Like steaming ground in active geothermal fields, this zone was strongly leached to form porous cristobalite with marginal alunite and kaolinite. With time the cristobalite recrystallized to fine crystalline, powdery quartz, as seen on the top of Purnama. This zone is devoid of anomalous metals apart from Hg. The planar base of the residual quartz is a good indicator of the paleo-water table level, which provides information on the paleohydrology, subsequent structural dislocations, and levels of erosion.

In the waning stages of hydrothermal activity, the water table descended and residual quartz overprinted the marginal argillic and quartz - alunite assemblages. During supergene oxidation Au dissociated from Cu, As and Ag, which were leached or incorporated in new oxide and sulfate minerals. Gold and Ag contents of most deposits remained little changed between the oxide and sulfide zones, but at Purnama Au is locally coarsened and its values upgraded. During both leaching and oxidation, a volume reduction caused fine fracturing, brecciation and minor fault displacement.

The control of alteration–mineralization at the Martabe deposits is linked to the isotopic signatures of alunite and barite through fluid mixing and the kinetics of SO_4^{2-}-H_2S isotopic exchange. Magmatic vapor condensing in meteoric groundwater generated acid sulfate fluids that reacted with the volcanic host rocks to produce a zoned alteration halo typical of high-sulfidation epithermal Au–Ag deposits. A descending water table during the late collapse of the hydrothermal system resulted in the progressive incursion of meteoric water into the steam-heated environment, as is recorded in the isotopic composition of barite and then deposited goethite±hematite after sulfides. This oxidizing hydrothermal stage leached sulfides, redistributed metals, and possibly enriched the deposit to ore grades.

Development of the main fault (i.e., Purnama and Pelangi faults) in Martabe was very crucial for the emplacement of the intrusions and subsequent mineralization at Martabe. In addition, syn-mineral faulting, brecciation and fracturing provided numerous permeable zones within the altered rocks enhancing movement of metal-bearing fluids and localization of gold. Purnama is a composite deposit that is structurally-lithology controlled, whereas Baskara is a more structurally controlled of high-sulfidation deposit.

In summary, the sequence of events that formed the Martabe diatreme/dome complex and associated alteration and mineralization is interpreted to be:

(i) Down faulting of pre-Miocene sedimentary units.

(ii) Intrusion of felsic magma along existing structures. Interaction of meteoric water with magma initiated early hydrothermal convection (low-sulfidation fluid). Formation of argillic and prophylitic alteration.

(iii) Felsic intrusions continued to move up along the existing faults and triggered phreatomagmatic and phreatic eruptions (diatreme formation).

(iv) Phreatomagmatic eruptions continue to excavate the conduit and widen the diatreme producing multiple crosscutting breccias.

(v) High temperature, extremely acid (high-sulfidation) fluids from condensation of magmatic volatiles caused advanced argillic alteration. No precious-metal mineralization accompanied this alteration.

(vi) Hydrothermal system returns to hydrothermal convection of meteoric water (low-sulfidation fluid). Formation of Au-Ag-bearing, quartz-chalcedony veins.

(vii) Intrusion of dacite and hornblende andesite into the diatreme creating the dome complex. Triggering of phreatomagmatic and phreatic eruptions.

(viii) Domes interacted with meteoric water causing hydrothermal convention of a low-sulfidation fluid with overpressure leading to hydrothermal brecciation.

(ix) Introduction of magmatic, metal-rich, high-sulfidation fluid depositing Cu-Au mineralization (disseminated and fracture-controlled pyrite-enargite-luzonite-tennantite-tetrahedrite).

(x) Late-stage phreatic brecciation.

(xi) Oxidation, erosion and weathering.

The Martabe Au-Ag deposits show a complex interplay of intrusive events, phreatomagmatic, phreatic, and hydrothermal brecciation and differing stages of hydrothermal (low- and high-sulfidation) fluid introduction. The superposition of both high- and low-sulfidation mineralizing events increases the precious metal content of the mineralization, and adds to the overall exploration potential of the district.

Exploration implications

Implications of these studies for exploration in the Martabe district are as follows:

(i) Main prospective areas for additional Au mineralization are near the margin of dome complexes rather than on the periphery of the system.

(ii) Siliceous cap rocks may cover underlying Au mineralization, implying only minor anomalous surface geochemistry.

(iii) The north-south trend of the siliceous alteration zone and resistivity response at Pelangi and South Pelangi, may overlie mineralized zones which have no or low geochemical expression at the surface.

(iv) Argillized dacitic intrusions and diatreme breccias are considered to be good proximal guides to Au mineralization.

(v) Thick breccias overlying flow domes are potential hosts for Au mineralization.

(vi) Major, underlying structural zones that controlled the emplacement of the domes, eruption of phreatomagmatic breccias, and intrusion of dacitic rocks, are likely a fundamental control on the location of Au mineralization.

Regional scale features and relationships that controlled the location of the Martabe district and may be important for exploration include:

(i) North-north west trending structural corridor within which the Martabe dome complex and its intersection with the north-northeast alignment.

(ii) A large Hg anomaly is probably a fundamental guide to locate Au mineralization,

(iii) Martabe was discovered by follow-up of very low Au BLEG anomalies (14 ppb) in stream sediments.

Recommendations for future research

This study was a field-oriented study that provides a framework for understanding the geological evolution of the district and mineralization. Many detailed problems on specific deposits remain unaddressed. This investigation does not include fluid inclusion or detailed deposit-specific studies. Such studies are warranted, to provide a detailed understanding of the geological characteristics and geochemical signatures of each of the major deposits, and

hopefully would complement the work presented. Exploration-oriented research in the Martabe district is strongly recommended. Specific recommendations are:

(i) Each major prospect/deposit in the district warrants detailed mapping, alteration, geochemical and structural studies. Some of this work should accompany exploration, and some would benefit from independent studies.

(ii) High-sulfidation deposits are typically not conducive to detailed fluid inclusion studies because the main-stage alteration and mineralization rarely form quartz with suitable inclusions. However, crystalline quartz in vugs and the late-stage barite crystals should provide suitable material for additional fluid inclusion studies.

REFERENCES

Abidin, A., Alip, D., Nenneng, L., Ristin, P. I., Fauzi, A. 2005. In: Use of isotope techniques to trace the origin of acidic fluids in geothermal systems, International Atomic Energy Agency, IAEA-TECDOC-1448, p.37-60.

Aldiss, D, T, Whandoyo, R., Sjaefudien, A.G. & Kusjono., 1983. The Geology of the Sidikalang and part of Sinabang Quadrangles (0518 and 0618), Sumatra. Scale 1:250000. Geological Survey of Indonesia, Bandung.

Aldiss, D.T., Aspden, J.A., Clarke, M.C.G., Djunuddin, A., Kartawa, W., Miswar, S.J., Thompson, R., and Whandoyo, R. 1983. The Geology of the Lubuksikaping Quadrangle (0716), Sumatra Scale 1:250,000. Geological Survey of Indonesia, Bandung.

Andrews, M.J. 1996. Indonesian projects. Information Brief of Meekatharra Minerals Ltd.

Andrews, M.J, Dods, G.H. and Hewitt, W.V. 1991. Methods and approach to exploration for hard rock and alluvial gold in Indonesia. In: Proceedings World Gold '91. Australian Institute of Mining and Metallurgy, 259-269.

Aspden, J.A., Stephenson, B., Cameron, N.R. 1982a. Tectonic Map of Northern Sumatra (1:1,500,000). Directorate of Overseas Surveys, Keyworth.

Aspden, J.A., Kartawa, W., Aldiss, D.T., Djunuddin, A., Whandoyo, R., Diatma, D., Clarke, M.C.G and Harahap, H., 1982b. The Geology of the Padangsidempuan and Sibolga Quadrangles (0617 and 0717), Sumatra. Scale 1:250 000. Geological Survey of Indonesia, Bandung.

Arribas, A., Jr., 1995. Characteristics of high sulphidation epithermal deposits and their relation to magmatic fluid. In: J.F.H. Thompson (ed). Magmas, Fluids, and Ore Deposits, Mineralogical Association of Canada Short Course. Vol.23, p 419-454.

Ashley, R.P., 1982. Occurrence model for enargite-gold deposits, in Erickson, R.L., ed., Characteristics of Mineral Deposit Occurrences: United States Geological Survey, Open File Report 82-795, p. 144-147.

Barber, A.J., 2000. The origin of the Woyla Terranes in Sumatra and the Late Mesozoic evolution of the Sundaland margin. Journal of Asian Earth Sciences, 18, 713-738.

Barber, A.J., and Crow, M.J. 2003. An evaluation of Plate Tectonic models for the development of Sumatra. Gondwana Research, 20, 1-28.

Barber, A.J., Crow, M.J., and De Smet, M. E. M.., 2005. Chapter 14 Tectonic Evolution, in Sumatra: Geology, Resources and Tectonic Evolution (A. J. Barber, M. J. Crow and J. S. Milsom, eds), Geological Society, London, Memoirs, 2005; 31: 234 - 259.

Barber, A.J., and Crow, M.J, 2005. Chapter 13 Structure and structural history in Sumatra: Geology, Resources and Tectonic Evolution (A. J. Barber, M. J. Crow and J. S. Milsom, eds), Geological Society, London, Memoirs, 2005; 31: 175 - 233.

Barton, P.B., Jr., and Skinner, B.J., 1979. Sulfide mineral stabilities. In: H.L. Barnes (ed), Geochemistry of Hydrothermal Ore Deposits. Wiley Interscience, New york., 278-403.

Behre Dolbear Consultant., 2009. Independent technical Review Martabe Gold-Silver Project-Sumatra, Indonesia, Technical report to Smart Rich Energy Finance Ltd, 64 p.

Bellon, H., Maury, R.C., Sutanti, Soeria-atmadja, R., Gotten, J., and Polve, M. 2004. 65 m.y.-long magmatic activity in Sumatra (Indonesia) from Palaeocene to Recent. Bulletin de la Societe geologique de France, 175, 61-72.

Bening and Seward, L.G., and Seward, T.M., 1994, The solubility of gold as $AuHS^0$ in high temperature hydrosulfide solutions. Beih.z.European Jour. Mineral., 6-1.24.

Ben-Avraham, Z., and Emery, K.O., 1973. Structural framework of Sunda Shell. American Association of Petroleum Geologists Bulletin, 57, 2323-2366.

Bennett, J.D., Bridge, D.Mc., Cameron, N.R., Djunuddin, A., Ghazali, S.A., Jeffery, D.H., Kartawa, W., Keats, W., Rock, N.M.S., Thompson, S.J., and Whandoyo, R. 1981a. The Geology the Banda Aceh Quadrangle, Sunuttra (1:250000). Geological Research and Development Centre, Bandung.

Bennett, J.D., Bridge, D.Mc., Cameron, N.R., Djunuddin, A., Ghazali, S.A., Jeffery, D.H., Kartawa, W., Keats, W., Rock, N.M.S., Thompson, S.J., and Whandoyo, R. 1982b. The Geology of the Tapaktuan Quadrangle (0519), Sumatra. Scale 1:250000. Geological Research and Development Centre, Bandung.

Bennett, J.D., Bridge, D.Mc., Cameron, N.R., Djunuddin, A., Ghazali, S.A., Jeffery, D.H., Kartawa, W., Keats, W., Rock, N.M.S., Thompson, S.J., and Whandoyo, R.. 1981c. The Geology of the Langsa Quadrangle (0420), Sumatra. Scale 1:250 000. Geological Research and Development Centre, Bandung.

Berger, B.R., and Eimon, P.I., 1983, Conceptual models of epithermal metal deposits in Shanks, W.C., ed., Cameron Volume on Unconventional Mineral Deposits: Society of Mining Engineers, New York, p. 191-205.

Berger, B.R., and Henley, R.W., 1989, Advances in the understanding of epithermal gold-silver deposits, with special reference to the western United States, in Keays, R.R., Ramsay, W.R.H., and Groves, D.I. eds., The Geology of Gold Deposits: The Perspective in 1988: Economic Geology, Monograph 6, p. 405-423

Bethke, P.M., Rye, R.O., Stoffregren, R.E., Vikre, P., 2005. Evolution of the magmatic-hydrothermal acid-sulfate system at Summitville, Colorado: integration of geological, stableisotope, and fluid-inclusion evidences. Chem. Geol. 215, 281– 315.

Bethke, P.M., 1984. Controls on base- and precious-metal mineralization in deeper epithermal environments. U.S. Geol. Surv. Open-File Rep. 84–890.

Berger, B.R., and Henley, R.W., 1989, Advances in the understanding of epithermal gold-silver deposits, with special reference to the western United States, in Keays, R.R., Ramsay, W.R.H., and Groves, D.I. eds., The Geology of Gold Deposits: The Perspective in 1988: Economic Geology, Monograph 6, p. 405-423.

Bonham, H.F., Jr., 1986. Models for volcanic-hosted epithermal precious metal deposits: a review. In: proceedings, International Volcanological Congress, Symposium 5, Hamilton, New Zealand, 1986, 13-17.

Brantley, S.L, Borgia, A., Rowe, G., Fernandez, J.F., and Reynolds, J.R., 1987. Poas volcano crater acts as a condenser for acid metal-rich brine. Nature, Vol 330. No 6147, 470-472.

Buchanan, L.J., 1981, Precious metal deposits associated with volcanic environments in the southwest, in Dickson, W.R. and Payne, W.D., eds., Relations of Tectonics to Ore Deposits in the Southern Cordillera: Arizona Geological Society Digest, v. 14, p. 237-262

Busby-Spera, C.J., and White, J.D.L., 1987, Variation in pepertite textures associated with differing host-sedimemt propoerties: Bulletin of Volcanology, v 49, p. 765-775.

Cameron, N. R., Clarke, M.C.G., Aldiss D,T., Aspden, J.A. and Djunuddin. 1980. The geological evolution of northern Sumatra. In: lndonesesian Petroleum Association, Proceedings of the 9th Annual Convention, Jakarta, 1980, 9, 149-187.

Camprubí, A., Canals, À., Cardellach, E., Prol-Ledesma, R.M., and Rivera, R., 2001a, The La Guitarra Ag-Au low sulfidation epithermal system, Temascaltepec district, Mexico: Vein structure, mineralogy, and mineral chemistry: Society of Economic Geologists Special Publication, v. 8, p. 133–158.

Camprubí, A., Cardellach, E., Canals, À., and Lucchini, R., 2001b, The La Guitarra Ag-Au low sulfidation epithermal system, Temascaltepec district, Mexico: Fluid inclusion and stable isotope studies: Society of Economic Geologists Special Publications, v. 8, p. 159–185.

Carlile, J.C., and Mitchell, A.H.G., 1994, Mamgamtic arcs and associated gold and copper mineralisation in Indonesia: Journal of Geochemical Exploration, v. 50, p. 91-142.

Carman, G.D., 1994, Genesis of the Ladolam gold deposit, Lihir Island, Papua New Guinea: Unpub. PhD Thesis thesis, Monash University, 263 p.

Cas, R.A.F., and Wright, J.V., 1987, Volcanic successions: modern and ancient. A geological approach to processes, products and successions, Chapman & Hall, Londo, 528 p.

Chouinard, A., Paquette, J., and William-Jones, A.E., 2005. Cystallographic controls on trace-element incorporation in auriferous pyrite from the pascua epithermal high-sulfidation deposit, Chile-Argentina, The Canadian MineralogistVol. 43, pp. 951-963

Chouinard, A., William-Jones, A.E., Leonardson, R.W., Hodgson, C.J., Silva, P, Tellez, C., Vega, J., and Rojas, F., Geology and Genesis of the Multistage High-Sulfidation Epithermal Pascua Au-Ag-Cu Deposit, Chile and Argentina, Society of Economic Geologists, Economic Geology, v. 100, pp. 463–490

Claveria, R.J.R., 2001. Mineral Paragenesis of the Lepanto Copper and Gold and the Victoria Gold Deposits, Mankayan Mineral District, Philippines, Resources Geology, vol. 51, p. 97-106.

Cobbing, E.J., 2000. The Geology and Mapping of Granite Batholiths. Lecture Notes in Earth Sciences 96. Springer, Berlin.

Cobbing, E.J., and Mallick, D.I.J., 1984. Preliminary Report, Indonesia.Report of the Overseas Directorate, British Geological Survey, No.MP/84/2, p. 1-45.

Cobbing, E.J., Mallick, D.I.J., Pitfield, P.E.J., and Teoh, L.H. 1986. The granites of the Southeast Asian Tin Belt. Journal of the Geological Society of London, 143, p. 537-550.

Cobbing, E.J., Pitfield, P.E.J., Darbyshire, D.P.F & Mallick, D.I.J., 1992. The granites of the Southeast Asian Tin Belt. Overseas Memoirs of the British Geological Survey, 10.

Cobbing, E.J., 2005, Chapter 5 Granites, in Sumatra: Geology, Resources and Tectonic Evolution (A. J. Barber, M. J. Crow and J. S. Milsom, eds), Geological Society, London, Memoirs, 2005; v.31, p 54-62

Cooke, D.R., Simmons, S.F., 2000. Characteristics and genesis of epithermal gold deposits. In: Hagemann, S.G., Brown, P.E. (Eds.), Gold in 2000, Rev. Econ. Geol., vol. 13, p. 221– 244.

Corbett, J.G., and Leach, T.M., 1998, Southwest Pacific Rim gold-copper systems: Structure, alteration, mineralization: Society of Economic Geologist Special Publication, v.6, p. 237.

Criss, R.E., Gregory, R.T., Taylor Jr., H.P., 1987. Kinetic theory of oxygen isotopic exchange between minerals and water. Geochim. bCosmochim. Acta 51, p. 1099–1108.

Crow, M.J and van Leeuwen, T.M., 2005, Metallic mineral resources, in Sumatra: Geology, Resources and Tectonic Evolution (A. J. Barber, M. J. Crow and J. S. Milsom, eds), Geological Society of London Memoirs V. 31, 147-174.

Crow, M.J., and A. J. Barber, A.J., 2005. Map: Simplified geological map of Sumatra; in Sumatra: Geology, Resources and Tectonic Evolution (A. J. Barber, M. J. Crow and J. S. Milsom, eds),. Geological Society, London, Memoirs, 31 NP.

Cunningham, C.G., and Ericksen, G.E., 1991 , Explroation guides for precious-metal deposits in volcanic domes. Seventh Annual V.E. McKelvey Forum on Mineral and Energy Resources, U.S. Geological Survey Circular 1062, 15-16.

Cunningham, C.G., Zartman, R.E., McKee, E.H., Rye, R.O., Naeser, C.W., Sanjines, O.V., Ericksen, G.E., and Tavera, F.V., 1996. The age and thermal history of Cerro Rico de Potosi, Bolivia. Mineral Deposita, 31, 374-385.

Cunningham, C.G., Rye, R.O., Steven, T.A., and Mehnert, H.H., 1984, Origins and exploration signficance of replacement and vein-type alunite deposits in the Marysvale volcanic field, west-central Utah: Economic Geology, v. 79, p. 50–71.

Dalimunthe, P., Hendrawan, D, Arianto, B., and Norris, R.G. 1996. Beukah Pro,wect. Unpublished Report PT Rio Tinto Indonesia.

Dalimunthe, P., Norris, R.G., and Heryawan, B. 1997a. Summary of exploration activities Upper lse-lse Prospect, 1989-1996. Unpublished Report PT Rio Tinto Indonesia.

Dalimunthe, P., Norris, R.G., Hendrawan., D and Heryawan, B.1997b. Summary of exploration activities Upper and Lower Tengekereng Prospects 1989-1996. unpublished Report, PT Rio Tinto Indonesia.

Danyushevsky L, Gilbert S (2005) Laser Ablation ICPMS methodology, CODES University of Tasmania, unpublished report, 9 p

Davies., A.G.S., 2002. Geology and Genesis of the Kelian Gold deposits, East Kalimantan, Indonesia Unpub. PhD Thesis thesis, University of Tasmania University, 405 p.

Davies, B., 2002. Report on the structural review of the Martabe project, Newmont Horas Nauli, internal memorandum, 5 p.

Deyell, C.L., Rye, R.O., Landis, G.P., and Bissig, T., 2004, Alunite in an evolving magmatic-hydrothermal system: The Tambo high-sulfidation deposit, El Indio district, Chile: Chemical Geology.

Deyell, C.L., Rye, R.O., Landis, G.P., Bissig, T., 2005. Alunite and the role of magmatic fluids in the Tambo highsulfidation deposit, El Indio–Pascua belt, Chile. Chem. Geol. 215, 185– 218.

De Smet, M.E.M and Barber, A.J., 2005, Tertiary stratigraphy. In: Sumatra, Geology, Reosurces and Tectonic Evolution (eds) barber, A.J., Crow, M.J., and Milsom, J.. Geological Society, London, Memoirs 2005; v. 31; p. 86-97

Einaudi, M.T., Hedenquist, J.W., and Inan, E.E., 2003, Sulfidation state of fluids in active and extinct hydrothermal sytems: Transitions form porphyry to epithermal environments in Society of Economic Geologists Special Publication 10, p. 285-312.

Eubank, R.T., and Makki, A.C, 1981. Structural geology of the Central Sumatra back-arc basin. In: Indonesian Petroleum Association, Proceedings of the lOth Annual Convention, Jakarta, 1981, 10, 153-196.

Ewart, A., 1982. The mineralogy and petrology of Tertiary–Recent orogenic volcanic rocks: with special reference to the andesitic basaltic compositional range. In: Thorpe, R.S. (Ed.), Andesites: Orogenic Andesites and Related Rocks. John Wiley, New York, pp. 25– 95.

Fifarek, R.H., Rye, R.O., 2005. Stable-isotope geochemistry of the Pierina high-sulfidation Au–Ag deposit, Peru: influence of hydrodynamics on lithological control of hydrodynamics on SO_4^2 - H_2S isotopic exchange in magmatic-steam and steam heated environments. Chem. Geol. 215, 253–279

Fisher, R.V., and Waters, A. C., 1970. Base surge bed forms in maar volcanoes: American Journal of Science, v.268, p.157-180.

Folinsbee, R.E., Kirkland, K., Nekolaichuk, A., and Smejkal, V., 1972, Chikuansih: a gold pyrite-enargite-barite hydrothermal deposit in Taiwan. Geol. Soc. America. Mem., 135, 323-335.

Fournier, R. O., 1985. The behaviour of silica in hydrothermal solutions. In: B.R. Berger and P.M. Bethke (eds), Geology and Geochemistry of Epithermal Systems. Society of Economic Geologists, Reviews in Economic Geology, Vol. 2. 46-62.

Fitch, T.J., 1972. Plate convergence, transcurrent faults and internal deformation adjacent to South-East Asia and the western Pacific. Journal of" Geophysical Research, 77, 4432-4460.

Fontaine, H., and gafoer, S., (eds) 1989. *The Pre-Tertiary Fossils of Sumatra and their Environments.* CCOP Technical Papers, 19, United Nations, Bangkok.

Gasparon, M. and Varne, R. 1995. Sumatran Granitoids and their relationship to Southeast Asian terranes. Tectonophysics, 251, 277-299.

Giggenbach, W.F., 1992, Magma degassing and mineral deposition in hydrothermal systems along convergent plate boundaries: Economic Geology, v. 87, p. 1927–1944.

Giggenbach, W.F., 1997. The origin and evolution of fluids in magmatic-hydrothermal systems. In: Barnes, H.L. (Ed.), Geochemistry of Hydrothermal Ore Deposits, 3rd ed. Wiley, New York, pp. 737–796.

Gilg, H.A., Sheppard, S.M.F., 1996. Hydrogen isotopic fractionation between kaolinite and water revisited. Geochim. Cosmochim. Acta 60, 529– 533.

Gray, J.E., Coolbaugh, M.F., Plumlee, G.S., Atkinson, W.W., 1994. Environmental geology of the Summitville mine, Colorado. Econ. Geol. 89, 2006–2014.

Gregory, R.T., Criss, R.E., 1986. Isotopic exchange in open and closed systems. In: Valley, J.W., Taylor Jr., H.P., O'Neil, J.R. (Eds.), Stable Isotopes in High Temperature Geological Processes, Rev. Min., vol. 16, pp. 91–127.

Grey, J.E., and Coolbaugh, M.F., 1994. Geology and geochemistry of Summitville, Colorado: an epithermal acid sulfate deposit in a volcanic dome. Econ. Geol., 89/8. 1906-1923

Gropper, H., Calvo, M., Crespo, H., Bisso, C.R., Cuadra, W.A., Dunkerley, P.M., and Aguirre, E., 1991. The epithermal gold-silver deposit of Choquelimpie, northern Chile. Economic geology. 86, 1206-1221.

Hall, R.. 1998. The plate tectonics of Cenozoic SE Asia and the distribution of land and sea. In: Hall, R., and Holloway, J.D. (eds) Biogeography and Geological Evolution of SE Asia. Backbuys Publishers, Leiden, 99-131.

Hall, R.. 2002. Cenozoic geological and plate tectonic evolution of SE Asia and the SW Pacific: computer-based reconstructions, model and animations. Journal of Asian Earth Sciences, 20, 353-431.

Hamilton, W. 1977. Subduction in the Indonesian region. In: TALWANI, M. & PITMAN III, W.C. (eds) Island arcs, Deep Sea Trenches and Backarc Basins. American Geophysical Union, Maurice Ewing Series, 1, 15-31.

Hamilton, W. 1979. Tectonics of the Indonesian Region. United States Geological Survey Professional Paper 1078.

Hanson, R. E., and Hargrove, U.S., 1999, Processes of magma/wet sediment interaction in a large-scale Jurassic andesitic peperite complex, northern Sierra Nevada, California: Bulletin of Volcanology v.60, p. 610-626.

Hanson, R.E., and Wilson, T.J., 1993. Large-scale rhyolite peperites (Jurassic, Southern Chile): Journal of Volcanology and Geothermal research, v.54, p.247-264.

Harlan, J.B., Jones, M.J., Sutopo, B and Hoschke, T., 2005. Discovery and Characterization of the Martabe Epithermal Gold Deposits, North Sumatra, Indonesia, Geological Society of Nevada SYMPOSIUM 2005 - Window to the world

Hariwidjaya, and Suharsono, 1990. Report on the follow-up geochemical work in Lubukgadang area, West Sumatra. Exploration Geochemistry Section, Geochemistry and Information Division, Directorate of Mineral Resources.

Hall, R. 1996. Reconstructing SE Asia. In: HALL, R. & BLUNDELL, D. (eds) Tectonic Evolution of Southeast Asia. Geological Society, London, Special Publications, 106, 153-184.

Harvey, C.C., and Browne, P.R.L., 1991, Mixed-layer geothermometry in the Wairakei geothermal field,New Zealand. Clays and Clay Minerals, 39, 614-621.

Hayba, D.O., Bethke, P.M., Heald, P., and Foley, N.K., 1985, Geologic, mineralogic, and geochemical characteristics of volcanic-hosted epithermal precious metal deposits, in Berger, B.R., and Bethke, P.M., eds., Geology and Geochemistry of Epithermal Systems: Society of Economic Geologists Reviews in Economic Geology, v. 2, p. 129-168.

Heald, P., Foley, N.K., and Hayba, D.O., 1987, Comparative anatomy of volcanic hosted epithermal deposits: acid-sulfate and adularia-sericite types: Economic Geology, v. 82, p. 1-26.

Hedenquist, J.W., Arribas Jr., A., Gonzalez-Urien, E., 2000.bExploration for epithermal gold deposits. In: Hagemann, S.G., Brown, P.E. (Eds.), Gold in 2000, Rev. Econ. Geol., vol. 13, pp. 245–277. Hehuwat, F. 1976. Isotopic age determinations in Indonesia: the state of the art. In: 2nd Regional Conference on the Geology of South East Asia, Jakarta, 1975. Proceedings Seminar on Isotopic Dating. Bangkok, May, 1975. United Nations ESCAP CCOP Technical Publication, 3, 135-157.

Hedenquist, J.W., Arribas Jr., A., Gonzalez-Urien, E., 2000. Exploration for epithermal gold deposits. In: Hagemann, S.G., Brown, P.E. (Eds.), Gold in 2000, Rev. Econ. Geol., vol. 13, pp. 245–277.

Hedenquist, J.W., 1987, Mineralization associated with volcanic related hydrothermal systems in the Circum Pacific Basin, in Horn, M.K., ed., Transactions of the 4th circum Pacific energy and mineral resources conference, 17-22 August 1987, Singapore: Tulsa, American Association of Petroleum Geologists, p. 513-523

Hedenquist., J.W., Arribas. A. Jr., and Reynolds, T.J., 1998. Evolution of an intrusion-centered hydrothermal system; Far Southeast-Lepanto porphyry and epithermal Cu-Au deposits, Philippines. Economic Geology; July 1998; v. 93; no. 4; p. 373-404Large et al, 2009)

Hedenquist, J.W., Simmons, S.F., Giggenbach, W.F., and Eldridge, C.F., 1993. White Island, New Zealand volcanic hydrothermal system represents the geochemical environment of high-sulphidation Cu and Au ore deposition. Geology, 21, 731-734.

Hedenquist, J.W.., 1987. Mineralization associated with volcanic-relayted hydrothermal systems in the circum-Pacific basin. Circum-Pacific basin. Circum-Pacific Energy and Mineral Conference, 4th, Singapore, August 17-22, 1986, Transactions, 513-524.

Hedenquist, J.W. Matsuhisa, Y., Izawa, E., White, N. C., Giggencah, W.F., and Aoki, M., 1994. Geology, geochemistry and origin of high-sulphidation Cu-Au minerlisation in the Nansatsu district, Japan.

Hedenquist, J.W., Arribas Jr., A., Reynolds, J.T., 1998. Evolution of an intrusion-centered hydrothermal system: Far Southeast-Lepanto porphyry and epithermal Cu–Au deposits, Philippines. Econ. Geol. 93, 373–404.

Hendrawan, D., Norris, R.G., Pietoyo, A., Setiawan, B and Dalimunthe, P. 1996. Abong prospect. Unpublished Report, PT Rio Tinto Indonesia.

Hendrawan, D., Harsthorn, G and Salastyono, 2001. Year 2001 Annual Report for exploration conducted on the Sumatra zinc project. Unpublished Report, PT Rio Tinto Exploration.

Hendrawan, D., Norris, R.G., Pietoyo, A., Setiawan B & Dalimunthe. P. 1996. Abong prospect. Unpublished Report, PT Rio Tinto Indonesia.

Henley, R.W and Etheridge, M.A. 1995. The structural and hydrodynamic framework for epithermal exploration. In: Mauk, J.L., and George, D.D, S.T. (eds) Pacrim '95, Australian Institute of Mining and Metallurgy, 269-277.

Henley, R.W., and Ellis, A.J., 1983. Geothermal systems, ancient and modern. Earth Science Reviews, v.19, p. 1-50.

Hertrijana, J.J., Jones, M.L., Hehuwat, P and Harlan, J.B., 2005. Martabe High Sulphidation gold deposits, North Sumatra, Indonesia, IAGI Special Issues 2005, Indonesia Mineral and Discoveries, p. 59-73.

Hickman, R.G., Dobson, P.F., van Gerven, M., Sagala, B.D.,and Gunderson, R.P.: ectonic and stratigraphicevolution of the Sarulla graben geothermal area, North Sumatra, Indonesia, Journal of Asian Earth Sciences, 23, (2004), 435-448.

Holland, H.D., Malinin, S.D., 1979. The solubility and occurrence of non-ore minerals. In: Barnes, H.L. (Ed.), Geochemistry of Hydrothermal Ore Deposits, 2nd ed. Wiley, New York, pp. 461– 508.

Houghton, B.F., and Smith, R.T., 1993, Recycling of magmatic clast during explosive eruptions: estimating the true juvenile content of phreatomagmatic volcanic deposits: Bulletin of volcanology, v.55, p.414-420.

Hutchison, C.S and Taylor, D. 1978. Metallogenesis in S.E. Asia. Journal of Geological Society; London, 135, 407-428.

Hutchison, C.S. 1983. Multiple Mesozoic Sn-W-Sb granitoids of Southeast Asia. In: Roddick, J. A (ed.) Circum-Pacific Plutonic Terranes. Geological Society of America Memoir, 159, 35-60.

Hutton, C.O., 1950, Studies of heavy detrital minerals: Geol. Soc. Am. Bull., v. 61, p. 635.
Houghton, B.F., and Smith, R.T., 1993, Recycling of magmatic clasts during explosive erupstions: estimating the true juvenile content of phreatomagmatic volcanic deposits: Bulletin of Volcanology, v.55, p. 414-420.

Jannas, R.R., Bowers, T.S., Petersen, U., and Beane, R.E., 1999, High-sulfidation deposit types in the El Indio district, Chile: Society of Economic Geologists Special Publication, v. 7, p. 27–59.

Imtihanah. 2000. Isotopic dating of igneous sequences of the Sumatra Fault System. M.Phil thesis, London University.

Irvine, T.N and Baragar, W.R.A. 1971 A guide to the classification of the common volcanic rocks. Canadian Journal of Earth Sciences, 8, 523 -547.

Ishihara, S., 1981. The granitoid series and mineralization. Economic Geology, 75th Anniversary Volume, p. 458–484

Jannas, R.R., Bowers, T.S., Petersen, U., Beane, R.E., 1999. High-sulfidation deposit types in the El Indio District, Chile. In:Skinner, B.J. (Ed.), Geology and Ore Deposits of the Central Andes, Soc. Econ. Geol. Spec. Pub., vol. 7, pp. 27– 59.

Karig, D.E., Suparka, S., Moore, G.F. and Hehunassa, P.E. 1979. Structure and Cenozoic evolution of the Sunda Arc in the central Sumatra region, ln: Watkins, J.S., Montadert, L. and Dickerson, P.W (eds) Geological and Geophysical Investigations of the Continental Margins. American Association of Petroleum Geologists Memoirs, 29, 223-237.

Katilli, J.A. 1973. Geochronology of west Indonesia and its implication on plate tectonics. Tectonophysics, 19, 195-212.

Katilli, J.A. 1974a. Sumatra. In: Spencer, A.M. (ed.) Mesozoic-Cenozoic Orogenic Belts. Geological Society, London, Special Publications, 4, 135-158.

Kallagher, H.J. 1989. The structural and stratigraphic evolution of the Sunda Forearc Basin, North Sumatra Indonesia. Ph.D. Thesis, University of London.
Kavalieris, I. 1988. The characteristics of epithermal mineral occurrences in the Bengkulu Province, Sumatera. In: Goode, A.DT., Snyth, E.L., Birch, W.D. and Bosma, L.L., (compilers) Bicentential Gold 88. Geological Society of Australia, Sydney, Abstract 23, 316.

Kusumadinata, KK. 1979. Data Dasar Gunungapi Indonesia. Volcanological Survey of Indonesia.

Kuno, H. 1969. Andesite in time and space. Bulletin of the Oregon Department of Geoloyg and Mineral Industry, 65, 13-20

Le Maitre, R.W., Bateman, P., Dudek, A., Keller, J., Lameyre, J.. Le Bas, M.J., Sabine, P.A., Schmid, R., Sorensen, H., Streckeisen, A., Woolley, A.R. & Zanettin, B., 1989. A Classification of Igneous Rocks and Glossary of terms: Recommendations of the International Union of Geological Sciences Subcommission on the Systematics of Igneous Rocks. Blackwell Scientific Publications, Oxford, U.K.

Larson, P.T., Taylor, H.P., 1987. Solfataric alteration in the San Juan Mountains, Colorado: oxygen isotope variations in a boiling hydrothermal environment. Econ. Geol. 82, 1019– 1036.

Lawless, J.V., 1988, Punctuated equilibrium and paleohydrology: Proceedings of the 10th New Zealand geothermal workshop, Auckland, New Zealand, 1988, p.165-170.

Levet, B.K, Jones, M..L, and Sutopo, B., 2003. The Purnama gold deposit in the Martabe District of North Sumatra, Indonesia SMEDG-AIG Symposium, Friday 10 October, 2003, Asian Update on Mineral Exploration and Development - Put a Tiger in Your Tenement, 8p.

Lindgren, W., 1922, A suggestion for the terminology of certain mineral deposits, Economic Geology, v. 17, p. 292-294.

Lindgren, W., 1933, Mineral deposits: New York, McGraw-Hill, 930 p

Lipman, P.W., Fisher, F.S., Mehnert, H.H., Naeser, C.W., Luedke, R.G., and Steven, T.A., 1976. Multiple ages of mid-Tertiary mineralization and alteration in the western San Juan Mountains, Colorado. Economic Geology, 71, 571-588.

Lorenz, V., 1973, On the formation of maars: Bulletin of Volcanology, v. 37, p. 183-204.

Lorenz, V., 1986, On the growth of maars and diatremes and its relevance to the formation of tuff rings: Bulletin of volcanology, v.48, p.265-274

Losada-Calderon, A.J., McBride. S.L., and Bloom, M.S., 1994. The Geology and 40Ar/39Ar geochronology of magmatic activity and related minerlaization in Nevados del Famatina Mining District, La Rioja province, Argentina. Journal of South American Earth Sciences, 7/1. 9-24.

MacLean, W.H. and Barrett, T.J., 1993. Lithogeochemical methods using immobile elements. Journal of Exploration Geochemistry, v. 48, p.109-133.

Maske, S. and Skinner, B.J. (1971) Studies of the sulfosalts of copper: I. Phases and phase relations in the system Cu-As-S. Economic Geology, 66, 901–918.

McCarthy, A.J. and Elders, C.F., 1997. Cenozoic deformation in Sumatra: oblique subduction and the development of the Sumatran Fault System. In: Fraser, A.J. and Matthews, S.J. (eds) Petroleum Geology of Southeast Asia. Geological Society, London, Special

Publications, 126, 355-363.

McCourt, W.J., Crow, M.J., Cobbing, E.J. and Amin, T.J. 1996. Mesozoic and Cenozoic plutonic evolution of SE Asia: evidence from Sumatra, Indonesia. In: Hall, R., and Blundell, D.J. (eds) Tectonic Evolution of Southeast Asia. Geological Society, London, Special Publications, 106, 321-335.

Mehnert, H.H., Lipman, P.W., and Steven, T.A., 1973. Age of mineralization at Summitville, Colorado, as indicated by K-Ar dating of alunite. Econ. Geol., 68, 399-412.

Metcalfe, I. 1996. Pre-Cretaceous evolution of SE Asian terranes. In: Hall, R., and Blundell, D.J. (eds) Tectonic Evolution of Southeast Asia. Geological Society, Lonodon, Special Publications, 106, 97-122.

Metcalfe, I 2000. The Bentong-Raub Suture Zone. Journal of Asian Earth Science, 18, 691-792.

Metcalfe, I. 2006 Palaeozoic and Mesozoic tectonic evolution and palaeogeography of East Asian crustal fragments: The Korean Peninsula in context. Gondwana Research 9, 24-46.

Meyer, C. and Hemley, J.J., 1967, Wallrock alteration, in Barnes, H.L., ed., Geochemistry of Hydrothermal Ore Deposits: New York, Holt, Reinhart andWinston, p. 166-235.

Ransome, F.L., 1907, The association of alunite with gold in the Goldfield district, Nevada: Economic Geology, v. 2, p. 667-692.

Middlemost, E. A. K. 1975. The basalt clan. Earth Science Reviews, Vol. 11, p. 337-364.

Middleton, T.W. 2003. The Diari-Sedex Zn-Pb project, North Sumatra Indonesia--Discovery to Feasibility. Paper presented at SMEDGAIG Symposium 2003, Asian update on mineral exploration and development, Sydney, 10 October 2003.

Neumann van Padang, M. 1951. Catalogue of the Active Volcanoes of the World, including solfatara fields. Part 1: Indonesia. International Volcanological Association, Napoli.

Noble, D.C., nd Silberman, M.L., 1984. Evolution volcanica y hidrotermal y cronologia de K-Ar del distrito minero de Julcani,Peru. Soc. Geol. Del Peru, Vol. Jubilair, LX Aniversario, Fasciculo 5, 1 – 35.

Ohmoto, H., Goldhaber, M.B., 1997. Sulfur and carbon isotopes. In: Barnes, H.L. (Ed.), Geochemistry of Hydrothermal Ore Deposits, 3rd ed. Wiley, New York, pp. 517–611.

Ohmoto, H., and Lasaga, A.C., 1982, Kinetics of reactions between aqueous sulfates and sulfides in hydrothermal systems: Geochimica et Cosmochimica Acta, v. 46, p. 1727–1746.

Ohmoto, H., Rye, R.O., 1979. Isotopes of sulfur and carbon. In: Barnes, H.L. (Ed.), Geochemistry of Hydrothermal Ore Deposits, 2nd ed. Wiley, New York, pp. 509–567.

Ohmoto, H., 1986. Stable isotope geochemistry of ore deposits. In: Valley, J.W., Taylor Jr., H.P., O'Neil, J.R. (Eds.), Stable Isotopes in High Temperature Geological Processes, Rev. Mineral., vol. 16, pp. 491– 559.

Page, B.G.N, Bennett, J.D., Cameron, N.R., Bridge, D. McC., Jeffery, D.H., Keats, W., and Thaib, J. 1978. Regional geochemistry, geological reconnaissance mapping and mineral exploration in northern Sumatra, Indonesia. In: JONES, M.J. (ed.) Proceedings of the 11th Commonwealth Mineralogical and Metallurgical Congress', Hong Kong, 455-462.

Page, B.G.N, Bennett, J.D., Cameron, N.R., Bridge, D. McC., Jeffery, D.H., Keats, W., and Thaib, J. 1979. A review of the main structural and magmatic features of northern Sumatra. Journal of the Geological Society, London, 136, 569-579.
Pearce J.A., and Cann J.R., 1973, Tectonic setting of basic volcanic rocks determined using trace element analyses. Earth Planet Sci Lett 19: 290-300.

Pearce, J.A. and Norry, M.J., 1979. Petrogenetic Implications of Ti, Zr, Y, and Nb Variations in Volcanic Rocks. Contributions to Mineralogy and Petrology, 69: 33-47.

Peccarillo, A. & Taylor, S.R., 1976. Geochemistry of the Eocene calc-alkaline volcanic rocks from the Kastamonu area northern turkey. Contributions to Mineralogy and Petrology, Vol.58, p.63-81.

Posavec, M., Taylor, D., van Leeuwen, T., and Spector, A. 1973. Tectonic controls on volcanism and complex movements along the Sumatran Fault System. Bulletin of the Geological Society of Malaysia, 6, 43-60.

Posfai, M., and Buseck., P.R. 1998. Relationships between microstructure and composition in enargite and luzonite. American Mineralogist; April 1998; v. 83; no. 3-4; p. 373-382
Petersen, U., Noble, D.C., Arenas, M.J., and Goodell,P.C., 1977. Geology of the Julcani mining district, Peru. Econ. Geol., 72, 931-949.

Pulunggono, A and Cameron, N.R..1984. Sumatran microplates, their characteristics and their role in the evolution of the Central and South Sumatra basins. In: Indonesian Petroleum Association, Proceedings of the 13th Annual Convention, 13, 1221 - 1443.

Reed, M., Spycher, N., 1986. Calculation of pH and mineral equilibria in hydrothermal waters and application to geothermometry and studies of boiling and dilution. Geochim.
Cosmochim. Acta 48, 1479– 1492.

Reed, M.H., 1997. Hydrothermal alteration and its relationshipto ore fluid composition. In: Barnes, H.L. (Ed.), Geochemistry of Hydrothermal Ore Deposits, 3rd ed. Wiley, New York, pp. 303– 365.

Reyes, A.G., 1991. Mineralogy, distribution and origin of acid alteration in Phillippine geothermal systems. Om: Matsuhisa, Y., Aoki, M., and Hedenquist, J.W (Eds), High-temperature Acid Fluids and Associated Alteration and Mineralization, Report no 277, Geological Survey of Japan, pp. 59-66.

Rock, N.M.S, Syah, H.H., Davis, A, A.E., Hutchison, D., Styles, M.T., Lena, Rahayu. 1982. Permian to Recent volcanism in northernnSumatra, Indonesia; a preliminary study of its distribution, chemistry and peculiarities. Bulletin Volcanologique, 45, 128-152.

Roache, M.W., Allen, S.R., and McPhie, J., 2000, Surface and subsurface facies architecture of a small hydroexplosive, rhyolitic centre in the Mesoproterozoic Gawler Range Volcanics, South Australia: Journal of Volcanology and Geothermal Research, v. 101, p. 237-259.

Rock, N.M.S., Aldiss, D.T., Aspedn, J.A., Clarke, M.C.G, Djunuddin, A., Kartawa, W., Miswar, S.J., Thompson, R and Whandoto, R., 1983. The Geology of the Lubuksikaping Quadrangle (0716), Sumatra Scale 1:250 000. Geological Survey of Indonesia, Directorate of Mineral Resources, Geological Research and Development Centre, Bandung.

Rollinsoin, H.R., 1993, Using Geochemical Data: Evaluation, Presentation, Interpretation, Longman, UK. 352 pp.

Rye, R.O., 1993, The evolution of magmatic fluids in the epithermal environment: The stable isotope perspective: ECONOMIC GEOLOGY, v. 88, p. 733–753.; Rye, R.O., 1993, The evolution of magmatic fluids in the epithermal environment: The stable isotope perspective: Economic Geology, v. 88, p.733–753.

Rye, R.O., 2005, A review of the stable isotope geochemistry of sulfate minerals in selected igneous environments and related hydrothermal systems: Chemical Geology. 215, 185– 218.

Rye, R.O., Bethke, P.M., and Wasserman, M.D., 1992, The stable isotope geochemistry of acid-sulfate alteration: Economi Geology, v. 87, p. 225–262.

Rye, R.O., Bethke, P.M., and Wasserman. M.D., 1989. Diverse origins of alunite and acid sulphate alteration: stable isotope systematics. United States Departement of the interior, Geological Survey. Open-File Report 89-5.

Rytuba, J.J., Arribas, A. Jr., Cunningham, C.G., McKee, E.H., Podwysocki, M.H., Smith, J.G., Kelly, W.C., and Arribas, A., 1990. Mineralized and unmineralized calderas in Spain; part II, evolution of the Rodalquilar caldera complex and associated gold-alunite deposits. Mineral Deposita, 25 S29-S39.

Samuel, M.A and Harbury, N.A. 1996. The Mentawai fault zone and deformation of the Sumatra forearc in the Nias area. In: Hall, R and Blundell, D.J. (eds) Tectonic Evolution of Southeast Asia. Geological Society, London, Special Publications, 106,337-352.

Schwartz, M., and Askury, A.K.1990. Granite magmatism and tin-tungsten metallogenesis in the Kuantan-Dungun area, Malaysia. Bulletin of the Geological Society of Malaysia, 26, 147-179.

Self, S., 1983, Large-scale phreatomagmatic silicic volcanism: a case study from new Zealand: Journal of Volcanology and Geothermal Research, v.17, p.433-469.
Sheridan MF and Wohletz KH, 1981, Hydrovolcanic explosions: the systematics of water-tephra equilibration. Science 212: 1387-1389.
Shervais, J.W., 1982, Ti-V plots and the petrogenesis of modern and ophiolitic lavas: Earth and Planetary Science Letters, v. 59, p.101-118.

Sheppard, S.M.F., Gilg, H.A., 1996. Stable isotope geochemistry of clay minerals. Clay Miner. 31, 1–24.

Silberman, M.L., and Ashley, R.P., Age of ore deposition at Goldfield, Nevada, from potassium-argon dating of alunite. Econ. Geol., 65, 352-354.

Sillitoe, R.H., 1973. The tops and bottoms of porphyry copper deposits. Econ. Geol. 68, 799–815.

Sillitoe, R.H., 1977, Metallic mineralization affiliated to subaerial volcanism: a review. in Volcanic Processes in Ore Genesis: Geological Society of London Special Publication 7, p. 99-116.

Sillitoe, R.H., 1983, Enargite-bearing massive sulfide deposits high in porphyry copper systems. Econ. Geol., 78, 348-352.

Sillitoe, R.H. 1991. Gold metallogeny of Chile-an introduction. Economic Geology 86. p.1187-1205.

Sillitoe, R.H., 1993. Epithermal models: genetic types, geometrical controls and shallow features. Assoc. Canada Special Paper 40, 403-417.

Sillitoe, R.H., 1994. Errosion and collapse of volcanoes: causes of telescoping in intrusion centred ore deposits. Geology, 22, 945-948.

Sillitoe, R.H. 1997. Characteristics and controls of the largest porphyry copper-gold and epithermal gold deposits in the circum-Pacific region. Australian Journal of Earth Sciences, 44, 373-388.

Sillitoe, R.H., and Hedenquist, J. W., 2003, Linkages between Volcanotectonic Settings, Ore-Fluid Compositions, and Epithermal Precious Metal Deposits in Volcanic, Geothermal, and Ore-Forming Fluids: Rulers and Witnesses of Processes within the Earth, Special Publication No 10, Society of Economic Geologists, p. 315-345.

Skinner, B.J. (1960) Assemblage enargite-famatinite, a possible geothermometer. Geological Society of America Bulletin, 71, 1975.

Springer, G. (1969) Compositional variations in enargite and luzonite. Mineralium Deposita, 4, 72–74.

Stoffregen, R., 1987. Genesis of acid-sulfate alteration and Au-CU-Ag mineralization at Summitvile, Colorado. Econ. Geol., 82, pp. 1575-1591.

Stephens, B., Sphepherd, T.J., Bowles, J.F.W., and Brook, M. 1987. Gold mineralization and skam Development near Muara Sipongi,West Sumatra, Indonesia. Economic Geology, 82, 1732-1749.

Steven, T.A. and Ratte, J.C., 1960, Geology and ore deposits of the Summitville district, San Juan Mountains, Colorado: United States Geological Survey, Professional Paper 343, 70 p.

Stoffregen, R., 1987, Genesis of acid sulfate alteration and Au-Cu mineralization at Summitville: Economic Geology, v. 82, p. 1575-1591.;

Sutopo, B., Jones, M.L., and Levet, B.K., - 2003, The Martabe gold discovery: A high sulphidation epithermal gold-silver deposit, North Sumatra, Indonesia in Proc. NewGenGold 2003 Conference, Louthen Media, Perth, Australia, pp 147-158. pp 517-525.

Sutopo, B., Gemmell, J.B., and Levet., B.L., 2006. Characteristics of Sub-Microscopic Gold and Trace Element Geochemistry of Enargite in the Martabe High-Sulfidation Epithermal Deposits, North Sumatra, Indonesia

Stoffregen, R.E., Rye, R.O., and Wasserman, M.D., 1994. Experimental studies of alunite: I. 18O-16O and D-H fractionation factors between alunite and water at 250-450°C: Geochimica et Cosmochimica Acta, v. 58, p. 903–916.

Stoffregen, R., 1987, Genesis of acid-sulfate alteration and Au-Cu-Ag mineralization at Summitville, Colorado: Economic Geology, v. 82, p. 1575–1591.

Bellier, O. & Sébrier, M. 1994. Relationship between tectonism and volcanism along the Great Sumatran Fault Zone deduced by SPOT image analyses. *Tectonophysics,* 233, p. 215–231.

Simmons, S.F.; White, N.C.; John, D.A. 2005. Geological characteristics of epithermal precious and base metal deposits. In Economic Geology One Hundredth Anniversary Volume (Hedenquist, J.W.; Thompson, J.F.H.; Goldfarb, R.J.; Richards, J.P.; editors). Society of Economic Geologists. p. 485-522

Stacey, J.S., Kramer, J.D., 1975. Approximation of terrestrial lead isotope evolution by a two-stage model. Earth Planet Sci. Lett. 26, p. 207-221.

Steiger, R.H., and Jager, E., 1977. Subcommission on geochronology: convention on the use of decay constants in geo- and cosmochronology. Earth and Planetary Science Letters, 36, p. 359 - 362.

Swanson, D.A., Dzurisin, D., Holcomb, R.T., Iwatsubo, E.Y., Chadwick, W.W. Jr., Casadevall, T.J., Ewert, J.W., and Heliker, C.C., 1987. Growth of the lava dome at Mount St. Helens, Washington, (USA), 1981-1983. In: Fink, J.H., (ed), The emplacement of silicic domes and lava flows. The Geological Society of America, Special Paper 212, 1-16.

Thorpe, R. S., Francis, P. W, Hammill M. & Baker M.C.W., 1982. The Andes. Andesites. Ed Thorpe, R.S., pp. 187-205.

Takagi, T. K., and Brimhall, G. H, 1998, Effect of trace element content on the optical properties of enargites and their distribution in the Agua Rica copper deposit, Argentina: Geological Society of America, 1998 Annual Meeting, Abstracts with Programs, v. 30, no. 7, p. 75.

Taylor, B.E., 1992. Degassing of H2O from rhyolitic magma during eruption and shallow intrusion, and isotopic composition of magmatic water in hydrothermal systems. Japan Geol. Surv. Rep. 279, 190– 194. Wasserman et al. (1994).

Turner, S.J., 1986. Fluid inclusion, alteration and ore mineral studies of an epithermal mineralised vein system: Mount Kasi, Vanua Levu, Fiji. In: Proceedings, Interntional Volcanological Congress, Symposium 5, Hamilton, New Zealand, February, 1986, 87-94

Turner, S.J., 1997. The Yanacocha Epithermal Gold Deposits, Northern Peru: High-Sulfidation Mineralization in a flow dome setting. Unpub. PhD Thesis thesis, The Colorado School of Mines. 362 p.

Turner, S.J., 2002, Comments and Recommendations on Martabe Project; Unpublished Internal Memorandum, Newmont Mining Corporation.

Turner, S.J.,2004, Martabe Geochronology, Unpublished Internal Email and Memorandum, Newmont Mining Corporation.

Taylor Jr., H.P., 1979. Oxygen and hydrogen isotope relationships in hydrothermal mineral deposits. In: Barnes, H.L. (Ed.), Geochemistry of Hydrothermal Ore Deposits, 2nd ed. Wiley, New York, pp. 236– 318.

Urashima, Y., Sato, M., and Sato, E., (1981) The Iwato gold ore deposits, Kagoshima Prefecture, Japan, Mining Geol., Spec. Issue 10, 1-14.

Valentine, G.A., and Fisher, R.V., 2000, Pyroclastic surges and blasts, Encylopedia of Volcanoes, p. 571-580.

van Leeuwen, T.M., Leach, T.M., Hawke, A.A., and Hawke, M.M., 1990, The Kelian disseminated gold deposit, East Kalimantan, Indonesia: Journal of Geochemical Exploration, v.35, p.1-1.

van Bemmelen, R.W. R.W. 1949. The Geology of Indonesia. Martinus Nijhoff, The Hague, Netherlands.

van Bemmelen, R.W.. 1954. Mountain building. Martinus Nijhoff, The Hague.

van Bemmelen, R.W., R.W. 1970. The Geology of Indonesia (second edition)

van Leeuwen, T.M. & Poole, A.N. 1978. The primary tin and lead/zinc potential of Belitung Island, West Indonesia. Unpublished report PT Rio Tinto Indonesia

van Leeuwen, T.M. 1994. 25 years of mineral exploration and discovery in Indonesia. Journal of Geochemical Exploration, 50, 13-90. Whitford, 1975 Widiyantoro and Van der Hilst, 1996

Vennemann, T.W., Muntean, J.L., Kesler, S.E., O'Neil, J.R., Valley, J.W., and Russell, N., 1993. Stable isotope evidence for magmatic fluids in the Pueblo Viejo epithermal acid-sulfate Au-Ag deposit, Dominican Republic. Econ. Geol., 88, 55-71.

Wajzer, M.R. 1986. The geology and tectonic evolution of the Woyla Group, Natal area, North Sumatra. PhD thesis, University of London. Wilson, 1989).

Walker, G.P.L, 1984, characteristic of dune-bedded pyroclastic surge bedsets: Journal of Volcanology and Geothermal Research, v.20, p.281-296.

White, D.C., Thompson, G.A., and Sandberg, C.H., 1964. Rocks, structure and geologic history of steamboat Springs thermal area, Washoe County, Nevada. United States Geological Survey, Professional Paper 458B, 63 pp.

White, N.C., and Hedenquist, J.W., 1990, Epithermal environments and styles of mineralization: variations and their causes, and guidelines for exploration, in Hedenquist, J., White, N.C., and Siddeley, G. eds., Epithermal Gold Mineralization of the Circum-Pacific, Geology, Geochemistry, Origin and Exploration, II: Journal of Geochemical Exploration, v. 36, p. 445-474.

White, N.C., 1991. High sulfidation epithermal gold deposits: characteristics and a model for their origin. In: Matsuhisa, Y., Aoki, M., Hedenquist, J.W. (Eds.), High Temperature Acid Fluids and Associated Alteration and Mineralization, Geol. Surv. Japan Rep., vol. 277, pp. 9 – 20.

White, N.C., and Hedenquist, J.W., 1995, Epithermal gold deposits: styles, characteristics, and exploration: Society of Economic Geologists Newsletter, October, 1995, n. 23. White et al., 1995;

Wiedenbecket, M., Alle, P., Carfu,.F., Griffin, W.L., Meier, M., Oberli, F., von Quadt, A., Roddick, J.C., and Spiegel, W., 1995. Three natural zircon standards for U-Th-Pb, Lu-Hf, trace elements and REE analyses. Geostandards Newsletter 19, 1-23.

Williams, P.R., Thompson, T.B., Powell, J.L., and Dubar, W.W., 2000, Gold-bearing breccias of the rain Mine, Carlin trend, Nevada: Economic Geology, v. 95, p.391-404.

Williams, H.H. and Eubank, R.T. 1995. Hydrocarbon habitat in the rift graben of the Central Sumatra Basin, Indonesia. In: Lambiase, J.J. (ed.) Hydrocarbon Habitat in Rift Basins. Geological Society, London, Special Publications, 80, p.331–371.

Williamson, A & Fleming, G.J. 1995. Miwah prospect high sulphidation Au-Cu mineralisation, northern Sumatra, Indonesia. In: PACRIM '95.Australian Institute of Mining and Metallurgy, 637-642.

Winchestwer, J.A. and Flyod, P.A., 1977. Geochemical discrimination of different magma series and their differentiation products using immobile elements. Chemical Geology, 20, 325-343.

Wormald, P.J., Orr, T.O.H., and Hodkinson, I. (1991) The Mount Leyshon gold mine (N.E. Queensland), an intrusive breccia and igneous complex.W orld Gold 91, Proceedingsp,. 223-232. AustralasianI nstitute of Mining and Metallurgy, Parkville, Australia.

Young, R.D. and Johari, S. 1978. The Tangse copper-molybdenum prospect, Indonesia. In: Nutalaya, P. (ed.) Proceedings of 3rd Regional Conference on Mineral Resources SE Asia. Asian Institute of Technology, Bangkok, 377-386.

Zheng Y.-F. (1999) Oxygen isotope fractionation in carbonate and sulfate minerals. Geochemical Journal 33, p. 109–126.

Zheng, Y.F. (1993). Calculation of oxygen isotope fractionation in anhydrous silicate minerals. Geochimica et Cosmochimica Acta 57, p. 1079–1091.